# Analysis of Chemical Compositions of 15 Different Cold-Pressed Oils Produced in Turkey: A Case Study of Tocopherol and Fatty Acid Analysis

**Veysel U. Celenk[1]** , **Z. Pinar Gumus [1,2*]** , **Zeliha Ustun Argon[3,4]** , **Mevlut Buyukhelvacigil[4]** , **Ercument Karasulu[1,5]**

[1] Ege University, Drug Research and Pharmacokinetic Development and Applied Center, ARGEFAR, 35100, Bornova, Izmir, Turkey
[2] Ege University, Institute on Drug Abuse, Toxicology and Pharmaceutical Science, BATI INSTITUTE**,** 35100, Bornova, Izmir, Turkey
[3] Necmettin Erbakan University, Eregli Faculty of Engineering and Natural Sciences, 42310 Eregli, Konya
[4] Zade Vital Pharmaceuticals Inc., KOS Güzel Konak Sok. 42300 Karatay, Konya, Turkey
[5] Ege University, Faculty of Pharmacy, Department of Pharmaceutical Technology, 35040, Bornova, Izmir, Turkey

**Abstract:** Many people tend to prefer natural foods and supplements nowadays. Considering this tendency, this study assessed the most significant in quality and purity parameters tocopherol and fatty acid compositions of cold-pressed oils, namely black cumin, sesame, sunflower, poppy, pomegranate, nettle, pumpkin, grape, safflower, flax, canola seed, wheat germ, peanut, hazelnut, and walnut. This study deals with the sample preparation and validation of tocopherols using an HPLC-FLD method for simultaneous determination of α-β-γ-, and δ-tocopherols, and analysis of fatty acid methyl esters (FAME) with using GC-FID. The validated HPLC method was applied for the tocopherols' analysis and measurement uncertainty was calculated for tocopherols and some fatty acids. The obtained data were evaluated by using principal component analysis to show the relationship between quality parameters and seed oils. Wheat germ, hazelnut, safflower, and sunflower oils have the highest tocopherol contents respectively with a predominance of α-tocopherol. Seed oils' fatty acid compositions were classified according to proportions of oleic, linoleic, and other fatty acids. This study shows that the evaluated seeds are valuable sources of natural antioxidants and some specific and polyunsaturated fatty acids. The applied method can also be helpful for the industry to obtain quality analysis approach.

**INTRODUCTION**

Cold-pressed seed oils have health-beneficial factors and significant chemical properties and some consumers tend to prefer natural, nutritional, and safe food supplements for preventing illnesses, maintaining internal and external wellness. There are some different extraction techniques to obtain oil from oily fruits and seeds, these being organic solvent extraction, screw-press or hydraulic press, the cold-press technique does not require an external heat either organic solvent (1-4). The oil was purified by settling, filtering, and centrifuging only (5). Cold-pressing is simple, ecologically friendly, and needs less energy for the process. If the cold-press method is compared with the other extraction methods, especially with supercritical carbon dioxide ($CO_2$) extraction, with regards to the investment's cost of the equipment and the cost of the last product, the cold press method is found less expensive and needs less labor than other extraction techniques (6, 7). Therefore, high-quality oils can be obtained by cold-pressing technique with lower costs and this method can be used for commercial production. Amounts of oil were shown to have final volume differences according to extraction techniques. The oil yield of the cold-pressing technique is lower than hot-pressing, solvent, and supercritical carbon dioxide ($CO_2$) extraction (8). In recent years, interest and demand of consumers to use cold-pressed oil have increased because cold-pressed oils are natural, nutritional, and safe food products (9, 10). Cold-pressed seed oils have great dietary value, specific sensory properties, health-beneficial factors and significant chemical properties because neither heat treatment nor any organic solvent were used to obtain oil from the raw material (3, 10). Thus, natural antioxidants and beneficial phytochemicals such as tocopherols, fatty acids, sterols and antioxidant phenolic compounds are protected at higher levels in cold pressed oils (11-14).

The quality and processing of seed oils are the main determinants of fatty acid composition and tocopherol content that support the reduced risk of coronary heart disease, geriatric diseases, anti-inflammatory and anti-proliferative effects on the types of cancer (15-17).

Tocopherols are important lipo-soluble antioxidants for the protection of human health because they preserve the oil against to lipid oxidation and they are effective against to the activities causing oxidative stress (18-20). When a natural tocopherol is compared to synthetic ones, especially α-tocopherol is superior for radical chain-breaking. It is a lipid-soluble antioxidant and increase the resistance of LDL to oxidation. α-tocopherol, γ-tocopherol has specific biologic activity that potentially protects against to the chronic diseases, such as inflammation (21).

The seed oils have rich mono-unsaturated and poly-unsaturated fatty acids (PUFA) (22). The human body can produce all fatty acids except linoleic acid and α-linolenic acid which are the simplest members of family of PUFA. PUFA regulate biological functions which range from blood pressure and blood clotting to the correct development and functioning of the brain and nervous system and it also has important role in the composition of all cellular membranes (23-25). Oleic acid, a mono-unsaturated fatty acid, has shown activity in cancer prevention, compared to polyunsaturated fatty acids, making it much less susceptible to oxidation and contributing to the antioxidant action, high stability, and long shelf life because oleic acid has a role in preventing oxidative stress (26, 27). It is thought that the reason for the chronic diseases being seen less in societies fed with Mediterranean diets having high oleic acid amount (28).

Because of the above-described and recognized importance of the fatty acid and tocopherol compositions, the main idea of this study is to determine fifteen cold-pressed oils' tocopherol and fatty acid compositions. These were black cumin seed, wheat germ, sesame seed, sunflower seed, poppy seed, pomegranate seed, nettle seed, peanut, pumpkin seed, walnut, hazelnut, grape seed, safflower seed, flax seed, and canola seed oils. For this purpose, the reliable, sensitive, and practical sample preparation methods for tocopherols were developed and validated for designation of the quality of these different cold-pressed oils produced in Turkey. In addition, fatty acid methyl esters (FAME) of cold-pressed seed oils were analyzed. Hence, the results from the present study can be taken and used to classify the quality and purity of cold-pressed oils in the market and also the seed oils which are used as natural supplements. Principal component analysis was applied to find out markers for each seed oil and classified according to composition of the oil.

## MATERIAL AND METHOD

### *Seed Oil Samples*
Seed samples were obtained from different geographical regions of Turkey where seed production of particular types are concentrated. Table 1 lists and shows the regions where the seeds were collected in Turkey. ZADE cold-pressed oils were produced at cold-pressing plants of the Zade Vital Pharmaceuticals, Inc.

During the cold-press process, the temperature was kept below 40 °C. Neither solvent nor heating process was used to protect physicochemical properties of the oil. The cold-press machine was used by 3-4 kg seed/h capacity depending on the seeds' differences. Settling out the sediments has been done by storing the cold-pressed oil in stainless steel intermediate tanks for one day. The next day, filtration of oil was completed by using 1 μm

pores filtration paper. In the last step, the cold pressed oils were filled into 200 mL amber glass bottles and kept at 25 °C and at 60 % relative humidity until the analysis was conducted.

**Table 1:** Production regions of seeds at Turkey.

| Seeds | Regions |
| --- | --- |
| Black Cumin Seed | Central Anatolia - Aegean |
| Wheat Germ | Central Anatolia-All regions |
| Sesame Seed | Mediterranean |
| Sunflower Seed | Central Anatolia-All regions |
| Poppy Seed | Central Anatolia - Aegean |
| Pomegranate Seed | Aegean – South eastern Anatolia |
| Nettle Seed | City of Hatay in Mediterranean region |
| Flax Seed | Aegean - Central Anatolia –Black Sea |
| Peanut | South eastern Anatolia |
| Pumpkin Seed | Central Anatolia - All regions |
| Walnut | Central Anatolia –Black Sea |
| Hazelnut | Black Sea |
| Grape Seed | Aegean |
| Safflower Seed | Central Anatolia |
| Canola | Central Anatolia |

### *Reagents*

All the reagents were purchased from J.T. Baker, LabScan, and Sigma–Aldrich and they were either chromatographic or analytical grade. Millipore ultrapure water (Type I) was used for all analyses. FAME mix (including 37 fatty acids) (Supelco) was used as a standard for determination of retention time of fatty acids. Tocopherol Set (Merck) was used for calibration and validation as a standard which is including four-vial pack containing α, β, γ, and δ-tocopherols.

### *Chromatographic conditions*

Chromatographic analyses were carried out on an Agilent HPLC-FLD system using silica columns (5 µm particle size, L × I.D. 25 cm × 4.6 mm, LiChrosorb SI 60) for separation and quantification. 290 nm and 330 nm were selected as excitation and emission wavelengths, respectively. n-Hexane:2-propanol (99.5:0.5) mixture was used as the mobile phase for tocopherol isomers at a flow rate of 0.8 mL/min. Sample preparation for tocopherol analysis was done according to a modified method of the American Oil Chemists' Society (AOCS) Lipid Library (29). The cold saponification method was used in the standard method for sample preparation. This method of sample preparation is both long and costly. In this study, oils were prepared with a more practical and inexpensive method. In the

assay, 0.5 g of seed oils were dissolved in 10 mL of hexane then vortexed. 20 µL of the homogeneous solution was injected into the HPLC system at 25 °C.

FAME analysis was applied according to COI/T.20/Doc. No 33 for cold-pressed oils (30). Identification of the fatty acids was done according to their retention times. The quantitative analysis was carried out by determination of the area ratio under the relevant peak to the sum of the areas under all the peaks for the fatty acids. FAME analysis was performed with an Agilent 6890 GC-FID system. A Supelco 2560 capillary column (100 m x 0.25 mm ID x 0.2 µm) and 1:100 split ratio was used. Inlet and detector temperatures were 250 °C and 260 °C, respectively. The temperature program was as follows; the oven temperature was held at 140 °C for 1 min and then increased to 240 °C at a rate of 4 °C/min and held for 5 min.

### Preparation of standard and calibration solutions
Stock solutions (1000 µg/mL) of the tocopherols were prepared in n-hexane. The working standard solutions were diluted with n-hexane from the stock solutions. Concentration ranges of calibration solutions were 1.25-200.00 µg/mL for all tocopherols. Triplicate injections (20 µL) were made for each concentration of tocopherols. The peak areas, the excitation at 290 nm and the emission at 330 nm wavelengths were plotted against to the corresponding concentrations to make the calibration graphs, and the linear regression equations were calculated.

The samples were prepared by weighing approximately 0.500 g (± 0,001 g) of seed oil into a 10 mL volumetric flask, adding 8 mL of n-hexane followed by 5 minutes of sonication in ultrasonic bath and then made up to volume to 10 mL with n-hexane and then sonication was repeated for 5 minutes for tocopherol analyses. The procedure of sample preparation was very practical thus time spent on sample preparation was reduced compared with cold-saponification methods at the AOSC Official Methods (31).

### Principal Component Analysis (PCA)
Principal Component Analysis was executed to show the relationship and differences between seed oils. The multivariate analyses were performed using the MINITAB 15 Statistical Software. The data for all tocopherols and fatty acids were performed using by the PCA (the Ward algorithmic method chemometric methods). The results of PCA were visualized by scores and loading plots. The score plots were made by contact between principal groupings and observations. The loading plots were pointed out the importance of each variable for the analyses, loading plots and were used to explain the relationship between variables.

 **RESULTS AND DISCUSSION**

HPLC method coupled with fluorescence detection was developed to make it an available, suitable, and practical procedure for the quality control analysis of tocopherols. The proposed HPLC-FLD method was validated according to the ICH guidelines in terms of some validation parameters (32). The GC-FID standard method was used according to IOC for determination of FAME (30).

### *Optimization of Chromatographic Conditions*

The mobile phases were optimized within different solvents according to resolution of isomers, peak symmetry, tailing factor, and theoretical plate number. The best separation between the four isomers of tocopherols had been with the use of a LICHROSORB SI 60 column. The best chromatogram was obtained with an isocratic elution of the mobile phase system consisting of n-hexane:2-propanol (99.5:0.5) (v:v) mobile phase. The excitation and emission wavelengths were selected according to literatures (29-31). The quantification was achieved using a fluorescence detector based on peak area measurement.

### *Validation of Proposed Methods*

A validation study was carried out for all isomers of tocopherols. The linearity of the HPLC-FLD method was assessed by analyzing a series of eight different concentrations for each tocopherol. Table 2 presents the linearity and sensitivity data and statistical parameters for the method including parameters of linear regression equations, coefficients, concentration ranges, standard deviations (SD) and relative standard deviation (RSD %) of the intercept and the slope. The coefficient values ($R^2 \geq 0.9997$) were shown that regression analysis has had a good linearity and RSD% of the slope, and intercept values which were found less than 0.10 % and 2.00%, respectively.

The limits of detection (LOD) and limits of quantification (LOQ) were calculated based on signal-to-noise ratio values in according to the ICH guidelines. The given data in Table 2 has shown that the method is sensitive enough to detect concentrations for the analyzed compounds.

**Table 2:** Linearity and sensitivity of proposed HPLC-FLD methods.

| | Alpha Tocopherols | Beta Tocopherols | Gamma Tocopherols | Delta Tocopherols |
|---|---|---|---|---|
| Linear range (µg/mL) | 1.25-200 | 1.25-200 | 1.25-200 | 1.25-200 |
| Slope | 19.902 | 23.201 | 24.910 | 40.058 |
| Intercept | 25.142 | 34.558 | 33.033 | 61.229 |
| S.D. of Slope | 0.009 | 0.012 | 0.007 | 0.003 |
| S.D. of Intercept | 0.429 | 0.453 | 0.332 | 0.442 |
| R.S.D of Slope (%) | 0.049 | 0.054 | 0.028 | 0.008 |
| R.S.D of Intercept (%) | 1.709 | 1.309 | 1.006 | 0.721 |
| $R^2$ | 0.9998 | 0.9997 | 0.9997 | 0.9997 |
| LOD (µg/mL) | 0.034 | 0.023 | 0.023 | 0.045 |
| LOQ (µg/mL) | 0.113 | 0.075 | 0.076 | 0.148 |

The injection repeatability and extraction reproducibility for the proposed method were studied at 12.5 µg/mL and 0.100 µg/mL concentration level for each compound using six replicate determinations through the same day. The repeatability was calculated for retention times of analytes, too. The values of injection repeatability of areas and retention times and values of extraction reproducibility of analytes were shown in Table 3.

**Table 3:** Injection repeatability of areas and retention times and values of extraction reproducibility of analytes for proposed HPLC-FLD methods.

| | Alpha-Tocopherols | Beta-Tocopherols | Gamma-Tocopherols | Delta-Tocopherols |
|---|---|---|---|---|
| Injection repeatability mean area (mAU*s) | 298.44 | 340.74 | 370.08 | 617.70 |
| Injection repeatability (R.T for analytes) | 7.949 | 14.663 | 16.184 | 27.512 |
| S.D of area | 1.87 | 2.39 | 2.10 | 2.47 |
| S.D of R.T. | 0.07 | 0.17 | 0.18 | 0.34 |
| RSD of area | 0.63 | 0.70 | 0.57 | 0.40 |
| RSD of RT | 0.91 | 1.17 | 1.14 | 1.23 |
| Reproducibility of analytes | 100.96 | 101.04 | 100.87 | 100.59 |
| SD | 0.62 | 0.70 | 0.17 | 0.35 |
| RSD | 0.61 | 0.69 | 0.17 | 0.35 |

The accuracy parameters of methods were studied at three concentration levels for each compound with three replicate injections. The recovered concentrations were calculated using the calibration equations and recoveries of isomers showed that the method was acceptable for determination of the tocopherols in the seed oils (Table 4).

**Table 4:** Accuracy of proposed HPLC-FLD methods at three different concentrations.

| Recovery mg/kg | Alpha-Tocopherol (mean±SD) | Beta-Tocopherol (mean±SD) | Gamma-Tocopherol (mean±SD) | Delta-Tocopherol (mean±SD) |
|---|---|---|---|---|
| 80 | 99.61±0.12 | 100.36±0.12 | 98.76±0.39 | 100.64±0.40 |
| 100 | 100.76±0.81 | 101.33±0.83 | 100.85±0.19 | 100.44±0.31 |
| 120 | 100.80±0.28 | 100.83±0.37 | 100.10±0.11 | 99.42±0.09 |

The specificity is defined as the ability to contact clearly with the analyte in the presence of components that may be expected to be present, such as degradation products and matrix components (ICH, 2016). Table 5 shows resolution (RS), tailing factor (T), and theoretical plate number (N) values of all tocopherols.

**Table 5:** Resolution, tailing factor, and theoretical plate number of tocopherols.

|  | Alpha-Tocopherol | Beta-Tocopherol | Gamma-Tocopherol | Delta-Tocopherol |
|---|---|---|---|---|
| RT (min) | 7.949 | 14.663 | 16.184 | 27.512 |
| $R_S$ | 11.83 | 14.94 | 2.66 | 14.25 |
| T | 1.149 | 1.154 | 1.155 | 1.154 |
| N | 7809 | 10597 | 10755 | 11596 |

Tocopherol isomers have shown good RS that means the tocopherol peaks were separated from other isomers. Good peaks were obtained from the proposed method for quantification of tocopherols according to T and N values.

### Measurement Uncertainty for two methods

The standard GC method was applied according to IOC for fatty acid methyl esters. In this study, uncertainty of measurement (u) was calculated for both HPLC and the GC method. The same sample was prepared according to sample preparation procedure for each analysis and then injected to the GC and HPLC systems. The samples were analyzed for two replicate determinations of each compound, that is to say, two samples each day for ten consecutive days with measurement every day. The results were given as mean ± u for some selected fatty acid methyl esters and all tocopherol isomers in Table 6.

Uncertainty of measurement was necessary for the reliability of the results and routine analysis laboratories.

### Application of the developed method

The optimized methods were applied to fifteen cold pressed seed oils. The representative chromatograms were obtained from the assayed seed oils were illustrated in Figures 1 and 2. Hazelnut chromatogram were selected as an example.

**Table 6:** Uncertainty of measurements of tocopherols and some selected fatty acids.
(Fatty acids were expressed as %, tocopherols were expressed as μg/mL)

| Analytes | Mean±u | Analytes | Mean±u |
|----------|--------|----------|--------|
| **Arachidic Acid** | 0.43 ± 0.10 | **Palmitic Acid** | 11.80 ± 2.12 |
| **Behenic Acid** | 0.20 ± 0.08 | **Stearic Acid** | 3.66 ± 0.2 |
| **Gondoic Acid** | 0.38 ± 0.12 | **Alpha  TOH** | 119.72 ± 6.44 |
| **Linoleic Acid** | 21.41 ± 0.59 | **Beta TOH** | 106.56 ± 5.20 |
| **Linolenic Acid** | 2.24 ± 0.19 | **Gamma TOH** | 107.52 ± 4.78 |
| **Oleic Acid** | 58.04 ± 1.04 | **Delta  TOH** | 107.47 ± 3.88 |

Since all tocopherols were present, the hazelnut oil chromatogram was chosen as the sample chromatogram.
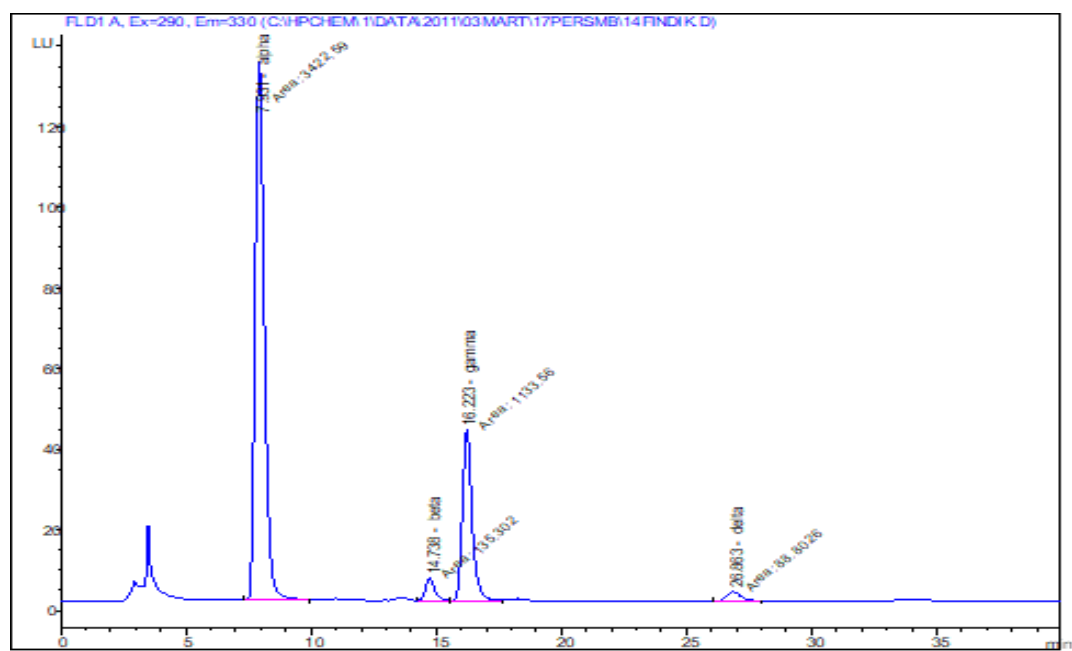


**Figure 1:** HPLC-FLD chromatogram of cold-pressed hazelnut seed oil for tocopherols.
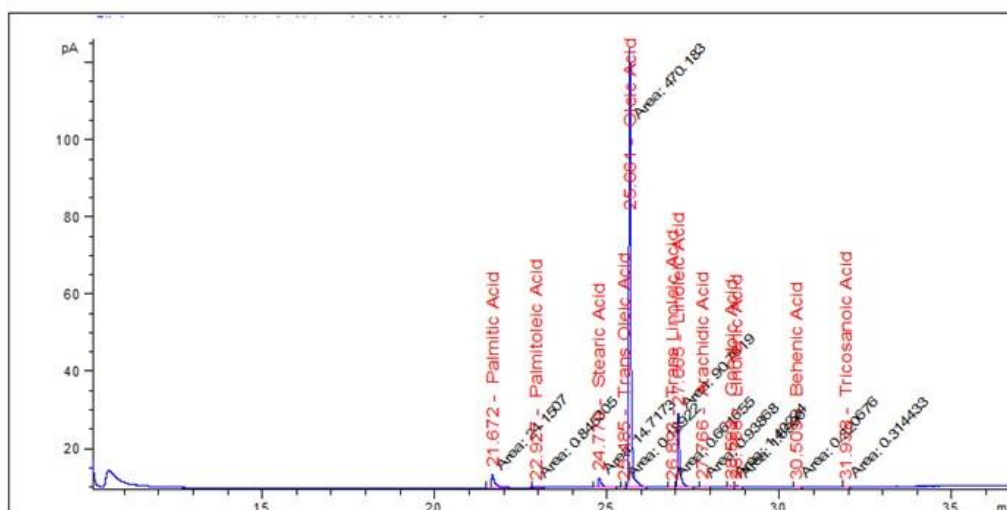
**Figure 2:** GC-FID chromatogram of cold-pressed hazelnut seed oils for fatty acid methyl esters.

It can be concluded that the acceptable analytical performance of the proposed method supports its appropriateness for the routine analysis to determine tocopherols in seed oils for quality controls. Table 7 shows tocopherol content of fifteen cold-pressed seed oils.

**Table 7:** Amount of tocopherols for fifteen cold-pressed seed oils. Tocopherols were expressed as µg/mL.

| Oil/Tocopherols | Alpha-Tocopherol | Beta-Tocopherol | Gamma-Tocopherol | Delta-Tocopherol |
|---|---|---|---|---|
| **Sunflower Seed** | 920.37±1.86 | 37,3±1.25 | 1.23±0.15 | nd |
| **Poppy Seed** | 32.86±2.62 | nd | 276.07±6.30 | 1.87±0.21 |
| **Sesame Seed** | 53.73±1.50 | nd | 482.33±2.65 | 6.86±0.21 |
| **Pomegranate Seed** | 72.37±2.35 | nd | 2625±6.35 | 61.33±1.93 |
| **Nettle Seed** | 19.4±0.62 | nd | 573.03±4.09 | 9.16±0.35 |
| **Flax Seed** | 7.46±0.35 | nd | 434±2.56 | 4.26±0.21 |
| **Peanut** | 114.7±2.45 | 1.36±0.15 | 45.5±0.75 | 9.92±0.09 |
| **Pumpkin Seed** | 25.73±1.21 | nd | 678±3.20 | 10.01±0.08 |
| **Walnut** | 27.23±0.51 | nd | 417.73±3.14 | 37.36±0.66 |
| **Wheat germ** | 2556.07±10.26 | 1061.53±6.80 | 89.46±1.14 | nd |
| **Hazelnut** | 1218.83±7.41 | 42.20±0.35 | 320.43±2.11 | 13.87±0.31 |
| **Grape Seed** | 82.37±1.32 | 0.27±0.01 | 83.84±1.42 | 20.24±0.41 |
| **Black Cumin Seed** | 58.13±1.88 | nd | 185.34±3.05 | nd |
| **Canola** | 235.12±3.17 | nd | 412.86±5.07 | nd |
| **Safflower Seed** | 1063.25±4.96 | 18.41±0.64 | 45.56±1.18 | nd |

n=3 mean±SD SD: standard deviation nd: not detected.

The wheat germ oil was found to be with the highest $\alpha$-tocopherol amount among the other cold-pressed oils. Wheat germ oil itself has the highest tocopherol content of all vegetable

oils up to about 2,500 mg/kg and also the highest content of α-tocopherol (33, 34). These effects are attributed to the high concentration of bioactive compounds present in the germ.

In this study, the highest α-tocopherol level was found in the wheat germ oil as 1218 mg/kg. The hazelnut oil had the next highest level among the other seed oils and it could be considered compatible with other previous studies (35, 36). The safflower and sunflower oils were also found with a high content of α-tocopherol among other fifteen different types of cold-pressed oil. In another study, three types of tocopherols were found in safflower oil in various amounts; α-tocopherol, β-tocopherol, and γ-tocopherol ranging from 46.05 to 70.93 mg/100 g, 0.85 to 2.16 mg/100 g and trace amount to 0.45 mg/100 g of oils, respectively (37). For the sunflower seeds, Świgło *et al.* (2007) found similar results by the highest level of α- tocopherol among other tocopherols (38). The differences between the amounts could be considered to be from the raw materials 'countries of origin, different cultivars, geographical and growing conditions. The pomegranate seed oils have the highest amount gamma tocopherols and delta tocopherols. All seed oils have alpha and gamma tocopherols which have shown that seeds' oils could be used for human health protection (39).

The seed oils were classified into three groups according to their fatty acid compositions with a high oleic acid, linoleic acid and others which differ in terms of other fatty acids. In the study, as shown in the Supplementary Material (SM1a), oleic acid contents of hazelnut oil, canola oil, peanut oil, sesame seed oil, and pumpkin seed oil were found with the highest percentage levels by 77.043±0.466, 61.854±0.094, 45.191±0.192, 38.374±0.075, 36.481±0.200 respectively. These data were found dissimilar with the other studies about general fatty acid composition of mentioned oil (40, 41).

Linoleic acid content of the fifteen different oils (SM1b) has been evaluated and poppy seed oil, nettle seed oil, sunflower seed oil, grape seed oil and safflower oil were found to have the highest percentage rates with 71.920±0.949, 66.624±0.231, 64.952±0.312, 63.455±0.793, 58.217±0.365 respectively. These results were also similar with the other studies (42, 37, 12).

Among the other fatty acid compositions, linolenic acid content were found very high for flax seed oil (54,77%) and walnut oil (11,33%) as expected from other studies (43, 12, 44). Besides, pomegranate seed oil distinctly has punicic acid at the rate of 80,92%. Considering the other studies showing a range 55.8 to 86.6%, our results might be considered within a high level (45-47). The wheat germ was shown to have differences

with a palmitic acid ratio by 16,60% as it could be seen in SM1c, agreeing with the other studies (48,49).

### *Principal Component Analysis (PCA)*

As stated above, 15 different seed oil samples were analyzed to determine their tocopherol contents and fatty acid methyl esters. Thus, classification of the samples according to some selected parameters was performed with PCA. The punicic acid was not evaluated because only pomegranate seed oil has this fatty acid. Figure 3, the score plots of all data of tocopherols and fatty acid methyl esters were indicated in the one main group according to PC1 and PC2.
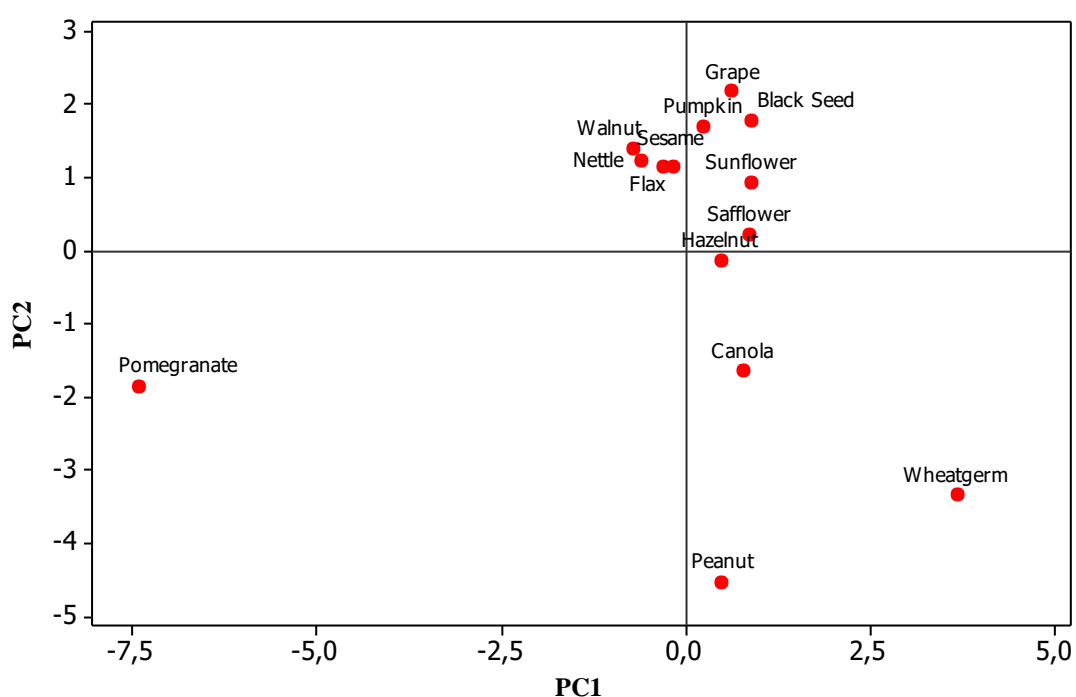


**Figure 3:** Score plot of FAME and tocopherols.

The pomegranate seed, canola, wheat germ, peanut oils were separated from all other seed oils.

When the PCA was accomplished, the results of the modelling power analysis was showed that tocopherols and minor fatty acids were the most effective variables to discriminate the seed oils from the others, as seen in the loading plot in Figure 4.
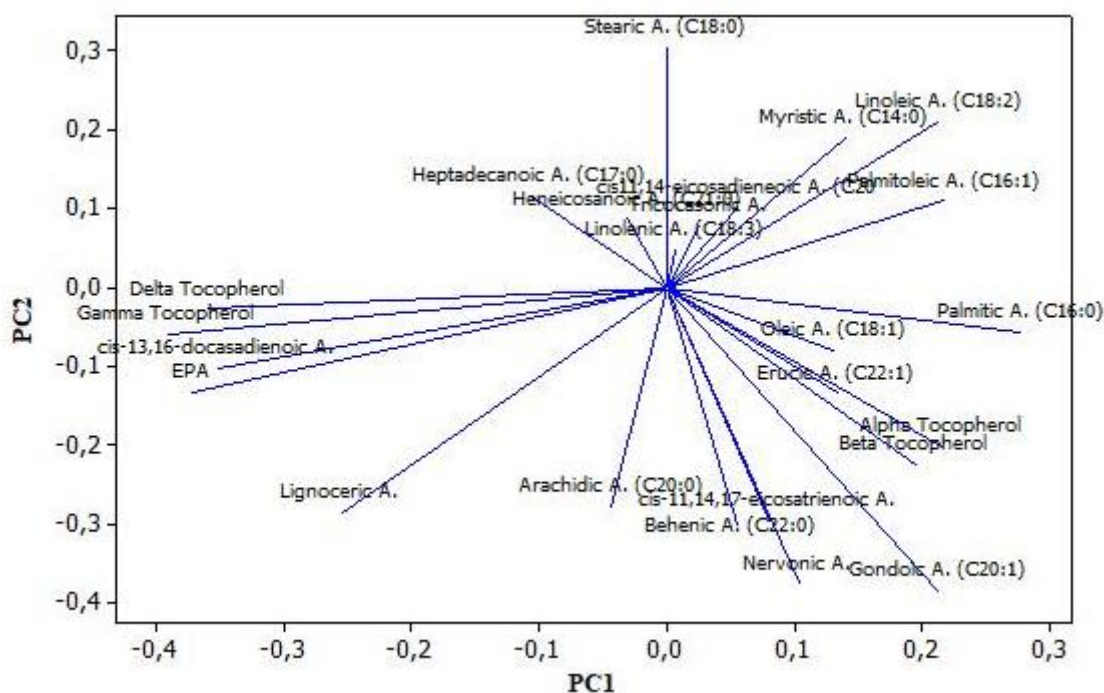
**Figure 4:** Loading plot of FAME and tocopherols.

The delta and gamma tocopherols, *cis*-13,16-docosadienoic acid, and EPA play an important role on the differentiation of pomegranate seed oil. The alpha and beta tocopherols, oleic acid and palmitic acid differentiate wheat germ oil from other seed oils. Minor fatty acids have a role in the differentiation of peanut oils. They are gondoic, nervonic, behenic, arachidic and *cis*-11,14,17-eicosatrienoic acids. The grape seed, walnut, pumpkin seed, sesame seed, nettle seed, flax seed, black cumin seed, safflower seed, sunflower seed, and hazelnut oils were distinguished with the effect of linoleic and linolenic acid.

 **CONCLUSION**

To the best of our knowledge, this is the first report that describes the quantitative determination of fatty acid methyl esters and tocopherols in fifteen cold-pressed oils. The major parameters of cold-pressed seed oils were shown by using principal component analysis.

This study proposes a quick and more practical methodology regarding conventional applications, especially for tocopherol analysis, for raw materials evaluation, and the acceptance step to determine, where time matters, the appropriate raw material for the intended usage. This is also applicable during routine analysis, quality control, and stability

studies of the last products like soft gelatin capsules containing cold-pressed oils. Additionally, the methodology will help with the classification of the quality of cold-pressed oils in the market. The proper utilization of the methodology to analyze and control quality can determine to which the most appropriate applications different oils should be used.

For further research projects and the manufacturing process for industry, these results were shown that fifteen different oils from Turkey's different regions might be preferred as a natural source of antioxidants and essential fatty acids like omega 3, 6, 9, and some specific fatty acids components like punicic acid. All the above-mentioned seeds from the region can be interesting and useful either for applications of food, pharmaceutical, cosmetic, or chemical industries. The cold-pressed oils from the area can be considered as a valuable source for natural antioxidants, poly-unsaturated fatty acids and some specific fatty acids. Also, the applied and validated method can help the industry for a more practical approach for quality analysis.

## ACKNOWLEDGMENTS

## COMPLIANCE WITH ETHICAL STANDARDS

The authors declare that they have no conflict of interest.

## REFERENCES

1. Teh SS, Morlock GE. Effect-directed analysis of cold-pressed hemp, flax and canola seed oils by planar chromatography linked with (bio)assays and mass spectrometry. Food Chemistry. 2015;187:460–468.

2. Topkafa M. Evaluation of chemical properties of cold pressed onion, okra, rosehip, safflower and carrot seed oils: triglyceride, fatty acid and tocol compositions. Analytical Methods 2016;8:4220–4225.

3. Yu LL, Zhou KK, Parry J. Antioxidant properties of cold-pressed black caraway, carrot, cranberry, and hemp seed oils. Food Chemistry. 2005;91:723–729.

4. Teh SS, Birch J. Physicochemical and quality characteristics of cold-pressed hemp, flax and canola seed oils. Journal of Food Composition and Analysis. 2013;30:26–31.

5. Van Hoed V, Barbouche I, De Clercq N, Dewettinck K, Slah M, Leber E, Verhé R. Influence of filtering of cold pressed berry seed oils on their antioxidant profile and quality characteristics. Food Chemistry. 2011;127:1848–1855.

6. Nam UG, Nam D. Some physicochemical properties, fatty acid composition and antimicrobial characteristics of different cold-pressed oils. La rivista italiana delle sostanze grasse, XCII, 2016;187-200.

7. Lampi, A.M., ve Heinonen, M. Berry seed and grapeseed oils,  Gourmet and health-promoting specialty oils,  In R. A. Moreau  A. Kamal-Eldin,   AOCS Press, Urbana, IL, 2009:215–236.

8. Yilmaz E, Aydeniz B, Güneşer O, Arsunar ES. Sensory and physico-chemical properties of cold press-produced Tomato (*Lycopersicon esculentum* L.) Seed Oils. Journal of American Oil Chemist Society. 2015;92:833-842.

9. Thanonkaew A, Wongyai S, McClements DJ, Decker a E. Effect of stabilization of rice bran by domestic heating on mechanical extraction yield, quality, and antioxidant properties of cold-pressed rice bran oil (*Oryza saltiva* L.). LWT - Food Science and Technology. 2012;48:231–236.

10. Gharibzahedi SMT, Mousavi SM, Hamedi M, Rezaei K, Khodaiyan F. Evaluation of physicochemical properties and antioxidant activities of Persian walnut oil obtained by several extraction methods. Industrial Crops and Products. 2013;45:133–140.

11. Lutterodt H, Slavin M, Whent M, Turner E, Yu L. Fatty acid composition, oxidative stability, antioxidant and antiproliferative properties of selected cold-pressed grape seed oils and flours. Food Chemistry. 2011;128:391–399.

12. Bozan B, Temelli F. Chemical composition and oxidative stability of flax, safflower and poppy seed and seed oils. Bioresource and Technology.2008;99:6354–6359.

13. Kozłowska M, Gruczyńska E, Ścibisz I, Rudzińska M. Fatty acids and sterols composition, and antioxidant activity of oils extracted from plant seeds. Food Chemistry. 2016;213:450–456.

14. Gumus ZP, Guler E, Demir B, Barlas FB, Yavuz M, Colpankan D, Senisik a. M, Teksoz S, Unak P, Coskunol H, Timur S. Herbal infusions of black seed and wheat germ oil: Their chemical profiles, in vitro bio-investigations and effective formulations as Phyto-Nanoemulsions. Colloids and Surfaces B: Biointerfaces. 2015;133:73–80

15. Ağ Şeleci̇ D, Gümüş ZP, Yavuz M, Şeleci M, Bongartz R, Stahl F, Coşkunol H, Timur S. Scheper T. A case study on in vitro investigations of the potent biological activities of wheat germ and black cumin seed oil. Turkish Journal of Chemistry. 2015;39:801–812.

16. Argon Ustun Z, Gökyer A. Determination of physicochemical properties of *Nigella sativa* seed oil from Balıkesir region, Turkey. Chemical and Process Engineering Research. 2016; 41:43–46.

17. Abdallah IB, Tlili N, Martinez-Force E, Rubio AGP, Perez-Camino MC, Albouchi A, Boukhchina S. Content of carotenoids, tocopherols, sterols, triterpenic and aliphatic alcohols, and volatile compounds in six walnuts (*Juglans regia* L.) varieties. Food Chemistry. 2015;173:972–978.

18. Butinar B, Bučar-Miklavčič M, Mariani C, Raspor P. New Vitamin E isomers (gamma-tocomonoenol and alpha-tocomonoenol) in seeds, roasted seeds and roasted seed oil from the Slovenian pumpkin variety "Slovenska golica. Food Chemistry. 2011;128:505–512.

19. Parcerisa J, Richardson DG, Rafecas M, Codony R, Boatella J. Fatty acid, tocopherol and sterol content of some hazelnut varieties (*Corylus avellana* L.) harvested in Oregon (USA). Journal of Chromatography A. 1998;805:259–268.

20. Guler E, Barlas FB, Yavuz M, Demir B, Gumus ZP, Baspinar Y, Coskunol H, Timur S, Bio-active nanoemulsions enriched with gold nanoparticle, marigold extracts and lipoic acid: In vitro investigations. Colloids and Surfaces B: Biointerfaces. 2014;121:299–306.

21. Saldeen K, Saldeen T. Importance of tocopherols beyond a-tocopherol: evidence from animal and human studies. Nutrition Research. 2005;25:877–889.

22. Fine F, Brochet C, Gaud M, Carre P, Simon N, Ramli F, Joffre F. Micronutrients in vegetable oils: The impact of crushing and refining processes on vitamins and antioxidants in sunflower, rapeseed and soybean oils. European Journal of Lipid Science and Technology. 2016;118:680-697.

23. Wall R, Ross RP, Fitzgerald GF, Stanton C. Fatty acids from fish: the anti-inflammatory potential of long-chain omega-3 fatty acids. Nutrition Reviews. 2010:68(5):280–289.

24. Patterson E, Wall R, Fitzgerald GF, Ross RP, Stanton C. Health Implications of High Dietary Omega-6 Polyunsaturated Fatty Acids Corporation Journal of Nutrition and Metabolism, 2012;Article ID 539426:16.

25. Das Un. Essential fatty acids: biochemistry, physiology and pathology. Biotechnology Journal, 2006;1(4):420–439.

26. Owen RW, Mier W, Giacosa A. Phenolic compounds and squalene in olive oils: the concentration and antioxidant potential of total phenols, simple phenols, secoiridoids, lignans and squalene. Food Chemical Toxicology. 2000;38:647-659.

27. Visioli F, Galli C, Galli G, Caruso D. Biological activities and metabolic fate of olive oil phenols. European Journal of Lipid Science and Technology. 2002;104:677-684.

28. Waterman E, Lockwood B. Active Components and Clinical Applications of Olive Oil. Alternative Medicine Review. 2007;12(4):331-42.

29. AOCS, Lipid Library, http://lipidlibrary.aocs.org/ , Last Accessed: June, (2017)

30. IOC, http://www.internationaloliveoil.org  COI/T.20/Doc. No 33. Last Accessed: June, (2017)

31. AOCS Official Method Ce 8-89 Determination of tocopherols and tocotrienols in vegetable oils and fats by HPLC.

32. ICH, International Conference on Harmonization Guidelines (ICH Q2B, validation of analytical procedures, methodology).

http://www.ich.org/products/guidelines/quality/quality-single/article/validation-of-analytical-procedures-text-and-methodology.html, Last Accessed: June, (2017)

33. Dunford NT. Health benefits and processing of lipid-based nutritionals. Food Technology. 2001;55(11):38-44.

34. Piras A, Rosa A, Falconieri D, Porcedda S, Dessì MA, Marongiu B. Extraction of oil from wheat germ by supercritical CO2. Molecules. 2009;14:2573-2581.

35. Crews C, Hough P, Godward J, Brereton P, Lees M, Guıet S, Wınkelmann W. Study of the main constituents of some authentic hazelnut oils. Journal of Agricultural and Food Chemistry. 2005;53:4843-4852.

36. Ozdemir M, Ackurt F, Kaplan M, Yildiz M, Loker M, Gurcan T, Biringen G, Okay A, Seyhan FG. Evaluation of new Turkish hybrid hazelnut (*Corylus avellana* L.) varieties: Fatty acid composition, α-tocopherol content, mineral composition and stability. Food Chemistry. 2001;73:411-415.

37. Matthaus B, Özcan MM, Al Juhaimi FY. Fatty acid composition and tocopherol profiles of safflower (*Carthamus tinctorius* L.) seed oils. Natural Product Research. 2015; 29(2):193-6.

38. Gliszczyńska-Świgło A, Sikorska E, Khmelinskii I, Sikorski M. Tocopherol content in edible plant oils. Polish Journal of Food and Nutrition Sciences.  2007;57:4(A):157-161.

39. Ozturk Kirbay F, Geyik C, Guler E, Yesiltepe O, Gumus ZP, Odaci Demirkol D, Coskunol H, Timur S. Testing of bioactive-nanovesicles on hepatotoxicity of atypical antipsychotics via digital holography. Colloids and Surfaces B: Biointerfaces. 2017;152:289–295.

40. Nzikou JM, Matos L, Bouanga-Kalou G, Ndangui CB, Pambou-Tobi NPG, Oomah BD, Mazza G. Health benefits of phytochemicals from selected Canadian crops, TrAC - Trends in Analytical Chemistry. 1999;10:193-198.

41. Mitra P, Ramaswamy HS, Chang KS. Pumpkin (Cucurbita maxima) seed oil extraction using supercritical carbon dioxide and physicochemical properties of the oil. Journal of Food Engineering. 2009;95:208–213.

42. Guil-Guerreroa JL, Rebolloso-Fuentesa MM, Torija Isasab ME. Fatty acids and carotenoids from Stinging Nettle (*Urtica dioica* L.). Journal of Food Composition and Analysis. 2003;16:111–119.

43. Singh KK, Mridula D, Rehal J, Barnwal P. Flaxseed: a potential source of food, feed and fiber. Critical Review Food Science and Nutrition. 2011;51(3):210-22.

44. Comba A, Maestri DM, Berra MA, Garcia CP, Das UN, Eynard AD, Pasqualini ME. Effect of ω-3 and ω-9 fatty acid rich oils on lipoxygenases and cyclooxygenases enzymes and on the growth of a mammary adenocarcinoma model. Lipids in Health and Disease. 2010;9:112.

45. Fadavi A, Barzegar M, Azizi MH. Determination of fatty acids and total lipid content in oil seed of 25 pomegranates varieties grown in Iran. Journal of Food Composition and Analysis. 2006;19:676–680.

46. Kaufman M, Wiesman Z. Pomegranate oil analysis with emphasis on MALDI-TOF/MS triacylglycerol fingerprinting. Journal of Agricultural and Food Chemistry. 2007;55:10405–10413.

47. Alcaraz-Mármol F, Nuncio-Jáuregui N, Calín-Sánchez A, Carbonell-Barrachina AA, Martínez JJ, Hernández F. Determination of fatty acid composition in arils of 20 pomegranates cultivars grown in Spain. Scientia Horticulturae. 2015;197:712–718.

48. Megahed MG. Study on stability of wheat germ oil and lipase activity of wheat germ during periodical storage. Agricultural and Biology Journal of North American. 2011;2(1):163-168.

49. Brandolini A, Hidalgo A. Wheat germ: not only a by-product. International Journal Food Science and Nutrition. 2012;63(1):71-74.

　　　　**RESEARCH ARTICLE**

# Dissipative Particle Dynamics Simulation Parameters and Interactions of A Hydrogel

**Gökhan KAÇAR [1, 2]** iD

[1] Trakya University, Department of Genetics and Bioengineering, 22030 Edirne/Turkey

[2] Laboratory of Physical Chemistry, Department of Chemical Engineering and Chemistry, Eindhoven University of Technology, Eindhoven, The Netherlands

**Abstract:** In this work, we report a parameterization procedure to compute the parameters of a hydrogel consisting of a hydrophilic polymer and a cross-linker. The system is parameterized so that coarse-grained dissipative particle dynamics (DPD) simulations can be performed. Proper computation of the simulation parameters is crucial in order to represent the inherent chemical nature of the hydrogel and to model the correct structure. The polymer is parameterized by considering different volumes for coarse-grained beads. Moreover, the hydrogen bond interactions should be represented and properly defined in the simulations. To that purpose, we use a recently introduced parameterization procedure that incorporates the attraction as a result of the hydrogen bond interactions between relevant beads. This paper serves as an example of how the realistic simulation parameters of a hydrophilic polymer can be straightforwardly computed by leading to a proper determination of the structure and properties. The computational background, the procedures and the results of the computation are reported and discussed in this paper.

**Keywords:** Dissipative Particle Dynamics method, coarse-grained simulations, polymers.

**\*Corresponding author. E-mail:** gokhankacar@trakya.edu.tr.

**INTRODUCTION**

Hydrophilic polymers are widely used in biomedical area as hydrophilicity is desired for various properties, such as lubricity, biocompatibility, wear comfort, and anti-fouling, which would reduce the risk of infection or different clinical problems (1-5). A thorough understanding of the proper structure and dynamics of such materials will pave the way of designing new materials with distinctive features for special purposes. In this work, we study the interactions and structural properties of a hydrogel that is formed by the reaction of a hydrophilic polymer and a cross-linker. Being a hydrogel, the material interacts with water during functioning. The material that we investigate in this work is a cross-linked PEG. PEG was previously studied by performing extensive molecular dynamics simulations for example, to model drug encapsulation (6), to stabilize insulin (7) or to model drug release (8). Moreover, there are also coarse-grained simulation approaches to obtain its structure by Lee and co-workers (9), by Prasitnok and co-workers to study its structure in wet environment (10), and in more complex environments such as attached to lipids (11) or dendrimers (12).

In this work, molecular and mesoscopic scale interactions are studied since intrinsic time and length scales that are valid for the creation of hydrogel structure are at nano- and micro-second levels. The simulation method is referred to as Dissipative Particle Dynamics (DPD). DPD is a coarse-grained simulation method where the different number of atoms, that represent different functional groups, are combined to form the so-called *beads*. By this coarse-graining procedure, the polymer can be equilibrated within a reasonable amount of time. DPD is often applied to study the behavior of complex fluids (13), polymers (14-18), surfactants (19), colloids (20) *etc*. The original DPD parameterization requires beads having similar volumes. This is a serious limitation of the method upon application to real molecular systems. In experimental systems, polymers can have beads with different molar volumes. In this work, we use an alternative parameterization method where a pure-liquid density-dependent parameterization is used (17). This procedure results in beads having different volumes. Especially for cross-linked systems, correct representation of bead volumes is extremely important since the resulting structure cannot be corrected after cross-linking. Besides variable bead volumes of polymeric systems, a particular attention should be paid to modeling the hydrogen bond interactions which are present in hydrophilic systems. For that purpose, we use a recently developed parameterization where the hydrogen bond attraction is explicitly modeled in DPD simulations (21). The parameterization procedure for parameterizing the DPD potential involves addition of a Morse potential term to the DPD potential. A similar procedure is performed to study the $\alpha$−helical and $\beta$-sheet structures of proteins (22). In this work, the parameters defining the Morse potential are set arbitrarily in order to create the target protein structure with no scaling by physical units, therefore without taking proper chemistry of beads into consideration. However in our work, we attempted to compute the

hydrogen bonding parameters by considering the exact chemical nature of molecules by combining the results of atomistic simulations with experimental Flory-Huggins parameters. The work in reference (21) demonstrates that the experimental negative volume excess of hydrogen bonding for low molecular weight alcohol and water mixtures can be predicted from coarse-grained simulations.

In this work, we aim to present a parameterization for DPD simulations, where polymeric materials interacting with water can be modeled. The procedure presented herein, extends the applicability of DPD to a wider range of polymers in contact with wet environments. The contents of the paper can be outlined as follows: Initially, the details of the DPD method are discussed. Second, the parameterization procedure and the results of the calculations are given. Finally, the values are discussed to demonstrate a qualitative structural analysis of the hydrogel. This paper targets to introduce a coarse-grained parameterization procedure that can be applied to any hydrophilic material, and to discuss the interactions of the polymer resulting in the equilibrium structure.

## MATERIALS AND METHODS

### Dissipative Particle Dynamics Simulation Method

The total force that applies to a particular bead is the addition of conservative, random, and dissipative forces. The conservative force characterizes the equilibrium structure, while the random and dissipative forces operate collectively and regulate the temperature. The non-bonded potential of DPD is given as:

$$V_{\mathrm{DPD},ij}(r) = \begin{cases} \dfrac{a_{ij}}{2}\left(1 - \dfrac{r}{r_{\mathrm{DPD}}}\right)^2 & r < r_{\mathrm{DPD}} \\ 0 & r \geq r_{\mathrm{DPD}} \end{cases}$$

(Eq. 1)

where $r_{\mathrm{DPD}}$ is the cut-off value, and $a_{ij}$ is the DPD interaction strength between beads $i$ and $j$ in dimensions $k_{\mathrm{B}}T$.

The previously proposed alternative parameterization of DPD dictates the variable volumes of beads as a function of their pure-liquid densities by the relation: (17)

$$a_{ij} = \hat{a}_{ij} + \frac{p}{0.0454(a_{ii}\rho_{i,\mathrm{pure}} + a_{jj}\rho_{j,\mathrm{pure}})}\chi_{ij}k_{\mathrm{B}}T, \qquad \hat{a}_{ij} = \sqrt{a_{ii}a_{jj}}$$

$$\text{with } a_{ii} = \frac{p - \rho_{i,\mathrm{pure}}k_{\mathrm{B}}T}{\alpha\rho_{i,\mathrm{pure}}^2 r_{\mathrm{DPD}}^3}$$

(Eq. 2)

In Eq. 2, $a_{ii}$ and $a_{jj}$ are like-like interactions of beads $i$ and $j$, $\hat{a}_{ij}$ is the neutral interaction parameter, and $\rho_i$ represents the dimensionless number densities of the pure components. The parameter $\alpha$ is taken here as constant and equals to 0.101 for number densities higher than 3, as demonstrated by Groot and Warren's original work on DPD parameterization (23).

There is a linear relation in between $\Delta a_{ij}$ and the experimental quantities following $\Delta a_{ij} = C \times \chi_{ij} k_B T$. Here, $\chi_{ij}$ is the Flory-Huggins parameter (24) and $\Delta a_{ij}$ quantifies the excess repulsion. $C$ is a constant defining the slope of the linear relationship between Flory-Huggins parameter and the DPD parameter, and is equal to 0.286 for a number density of 3. The pressure $p$ is set to represent an overall compressibility value of the mixture and taken as 40 $k_B T/r_{DPD}^3$. Flory-Huggins $\chi_{ij}$ parameter is related to the solubility parameters via the relation:

$$\chi_{ij} = \frac{V_m}{RT} (\delta_i - \delta_j)^2$$

(Eq. 3)

where $\delta$'s are the solubility parameters and $V_m$ is the molecular volume of a bead. The relationship between the $\chi_{ij}$ parameter and the excess repulsion is reported in Groot and Warren's original DPD work (23).

The implementation of hydrogen bonds to DPD method is performed by adding a Morse potential term to the non-bonded DPD potential.

$$V_{Morse} = D_0 \left[ e^{-2\sigma(r-r_0)} - 2e^{-\sigma(r-r_0)} \right], \quad r < r_{DPD}$$

(Eq. 4)

In this equation, $D_0$ represents the strength of the attraction, $\sigma$ quantifies the curvature, and $r_0$ is the equilibrium distance (21). We select a value of $2/r_{DPD}$ for $\sigma$. In Eq. 4, the contribution of hydrogen bonds are not counted for inter-bead distances larger than 1 $r_{DPD}$.

**Hydrophilic polymer structure and the coarse-graining**

The hydrogel consists of a combination of a trimerized hexamethylene diisocyanate (tHDI) cross-linker and a polyethylene glycol (PEG) spacer with a molecular mass of 2000 g/mol. The mixture is at the stoichiometric ratio of 2:3. As previously mentioned, the coarse-graining is performed by partitioning the chemical structure into chemically meaningful units as depicted in Figure 1. In accordance with the stoichiometry, the total number of beads in each chain are set to 1000 for tHDI and 1500 for PEG chains.

**(a)**



**(b)**
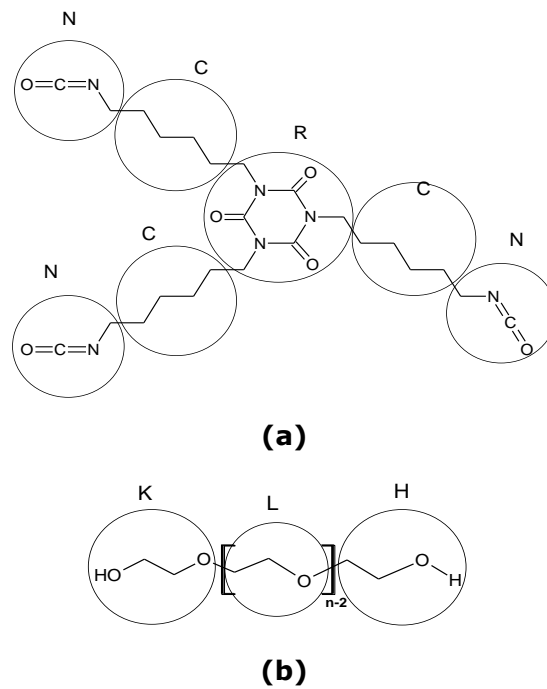
**Figure 1:** Schematic representation of the coarse-grained beads of (a) tHDI and (b) PEG.

**RESULTS AND DISCUSSION**

Initially, the Flory-Huggins interaction parameters which quantify the mixing behavior of the molecules (24) are determined. These parameters are obtained from Eq. 3 by identifying the van Krevelen solubility parameters from group contribution methods (25). Here, Molecular Modeling Pro Software (26) is used. In Table 1, we report the computed $\chi_{ij}$ parameters.

| $\chi_{ij}$ | N (24.58) | C (13.84) | R (29.56) | L, H (25.09) | K (31.86) | N′ (22.01) | W (47.00) |
|---|---|---|---|---|---|---|---|
| **N** | 0.00 | 2.84 | 0.61 | 0.01 | 1.30 | 0.16 | 12.36 |
| **C** | 2.84 | 0.00 | 6.08 | 3.12 | 7.99 | 1.64 | 27.04 |
| **R** | 0.61 | 6.08 | 0.00 | 0.49 | 0.13 | 1.40 | 7.48 |
| **L, H** | 0.01 | 3.12 | 0.49 | 0.00 | 1.12 | 0.23 | 11.79 |
| **K** | 1.30 | 7.99 | 0.13 | 1.12 | 0.00 | 2.39 | 5.63 |
| **N′** | 0.16 | 1.64 | 1.40 | 0.23 | 2.39 | 0.00 | 15.36 |
| **W** | 12.36 | 27.04 | 7.48 | 11.79 | 5.63 | 15.36 | 0.00 |

**Table 1:** Computed Flory-Huggins parameters of the coarse-grained beads. N′ bead represents the reacted N bead upon cross-linking. Values in parentheses indicate the solubility parameters in dimension $(J/cm^3)^{0.5}$. W bead represents single water molecule.

A DPD fluid phase separates out if the value of $\chi$ is above 2 (23). Therefore, the $\chi$ values in Table 1 higher than 2 indicate a phase-separation. The largest difference of $\chi$ value is in between C and K beads, whereas the smallest difference is in between N and L (or H). We named L and H beads differently, although they have the same chemical structures.

The reason is to differentiate the head group and the repeating units of PEG. The repelling interactions of C and K can be explained monitoring the internal chemical structures of C and K beads. The C bead is nothing but a butane molecule which is nonpolar in principle. On the other hand, K bead is a polar molecule that can make hydrogen bonds with particular molecules. According to the values in Table 1, the bead pair that like each other the most is the N and L pair. They are similar in size, both are polar and have high chances to form hydrogen bonds with each other.

If we examine water and polymer bead interactions, it is seen that all beads have a tendency to repel each other. The smallest $\chi$ parameter values are observed in between K and W, and R and W beads among the others. The solubility parameters corresponding to water and polymer beads differ to a large extent. The difference of solubilities and resulting high values of $\chi$ parameters would lead to a large separation of polymer and water beads in the simulations. The exact repulsive nature of the interactions can be analyzed and discussed in the form of self and pairwise interactions of DPD. To that purpose, Eq. 2 and Table 1 are combined to compute the corresponding $a_{ij}$ parameters. The calculated values are given in Table 2.

| $a_{ij}$ | N (0.0113) | C (0.0062) | R (0.0038) | L, H (0.0103) | K (0.0112) | N′ (0.0094) | W (0.0033) |
|---|---|---|---|---|---|---|---|
| **N** | **31.26** | 65.78 | 96.80 | 34.29 | 36.68 | 38.10 | 89.36 |
| **C** | 65.78 | **106.39** | 186.28 | 71.82 | 80.58 | 73.54 | 120.79 |
| **R** | 96.80 | 186.28 | **292.22** | 105.71 | 96.01 | 117.28 | 47.10 |
| **L, H** | 34.29 | 71.82 | 105.71 | **37.55** | 38.73 | 41.93 | 81.08 |
| **K** | 36.68 | 80.58 | 96.01 | 38.73 | **31.37** | 46.46 | 45.89 |
| **N′** | 38.10 | 73.54 | 117.28 | 41.93 | 46.46 | **44.96** | 96.72 |
| **W** | 89.36 | 120.79 | 47.10 | 81.08 | 45.89 | 96.72 | **2.90** |

**Table 2:** DPD interaction parameters $a_{ij}$ of the coarse-grained beads. N′ bead represents the reacted N bead upon cross-linking. The values in parentheses represent the dimensionless number densities of beads $\rho_i$ obtained by $\rho_i = \rho_{i,\text{liquid}} / M_{W,i}$. W bead represents the single water molecule.

We discuss the relative repulsions of beads by considering the difference in the values of pairwise and like-like interactions, which is critical since like-like interactions are different for each bead correlated with the bead volume. For example, the bead having the largest volume is the R bead and the one with the smallest volume is the N bead. Consequently, these beads have the highest and the lowest like-like interaction values, respectively. In line with the Flory-Huggins parameters in Table 1, the most repulsive interaction is in between C and K beads, although the numerical value of corresponding $a_{ij}$ is smaller than most of the values in Table 2, whereas N and L bead pair has the lowest repulsion strength. This means in a simulation, that C and K will be separated, on the other hand, the L bead would like to stay even closer to N bead rather than itself due to a lower $a_{ij}$ value than its like-like interaction value.

The like-like interaction value of water is the lowest among the polymer beads due to its smallest size. However, the pairwise interactions between the water bead and the other type of beads are larger. This indicates a preference of water to stay close to the same type of beads rather than moving near polymer beads. The highest repulsion of water is with the C bead since it is purely composed of carbon atoms. The least repulsion strength is observed in between the R and W beads. This value is even smaller than the like-like interaction of the R bead. The hydrogen bond contribution to solubilities has an influence favoring mixing. Obviously, if these values are used in a simulation, the polymer and water would be phase-separated, with the exception of hydrophilic polymers. The analysis of the DPD parameters solely identifies the importance of contribution of hydrogen bonds to the DPD method.

In this section, we use a parameterization that was recently proposed to add hydrogen bond attraction to the purely repulsive DPD potential (21). The added term will be in the form of a Morse potential. A multi-scale procedure is used to compute the Morse potential parameters which take atomistic molecular dynamics simulations as the basis. In this procedure, the hydrogen bond energy is computed for different hydrogen bonding pairs from the potential energy differences of the mixture and the pure components. The second parameter of the Morse potential, namely the equilibrium hydrogen bond distance, is computed from the radial distribution functions (RDF). The exact form of equations and procedure is given in detail in reference (21).

Upon coarse-graining of the PEG, the repeating unit is solely an ethanol molecule. In this work, we adapted the Morse potential values for the system of interest from the reference study. The repeating unit constitutes a large portion of the mixture due to the rule of stoichiometry. Therefore, the structure of polymer is dominantly characterized by the interactions of this bead. For the rest of the beads, the Morse potential parameters are computed by taking the strength of ethanol-water hydrogen bond interaction as reference and scaling its value with the number of possible hydrogen bonds. For example, the strength of hydrogen bond interaction of R and water beads is computed by multiplying ethanol-water hydrogen bond interaction strength by six, since R bead can make six hydrogen bond interactions with water. In this way, we get a reasonable approximation to the overall hydrogen bond interactions, and at the same time differentiate the hydrogen bond strengths of different materials favoring higher attraction if the number of hydrogen bonds is higher. The equilibrium hydrogen bond distance is taken as the same value for ethanol-water interaction without performing any scaling since the hydrogen bond equilibrium distance does not change significantly according to the type of material as observed in reference (21).

The polymer is in the form of a hydrogel. Therefore, if immersed in, the material can take up a significant amount of water. The hydrogen bond strength and hydrogen bond equilibrium

distance values change as a function of water content in the total mixture. The corresponding values are computed by a linear interpolation using the linear fit parameters reported previously (21). As examples, we demonstrate in Table 3, the Morse potential parameters for two mixtures with different water contents.

As shown in Table 3, the values differ following the variation in water content in the total mixtures. This is a result of the linear increase of the hydrogen bond strength with respect to the decrease in the amount of water in the mixture (21). The strongest hydrogen bond attraction with water is observed for the center bead of tHDI molecule, the R bead, whereas the weakest hydrogen bond attraction with water is formed in presence of the K bead of PEG chain. The hydrogen bond strengths tabulated in Table 3 are a function of the number of possible hydrogen bond connections and the overall molar fraction as dictated by the linear relationship reported in reference (21). The equilibrium hydrogen bond distance values also do change according to the change of the physical length-scale of DPD $r_{DPD}$.

| Bead type | 25% | | | 75% | | |
|:---:|:---:|:---:|:---:|:---:|:---:|:---:|
| | $x_i$ | $D_0$ [$k_B T$] | $r_0$ [$r_{DPD}$] | $x_i$ | $D_0$ [$k_B T$] | $r_0$ [$r_{DPD}$] |
| N | 0.03 | 12.95 | 0.53 | 0.01 | 12.53 | 0.51 |
| R | 0.01 | 37.58 | 0.51 | 0.00 | 37.16 | 0.50 |
| L, H | 0.66 | 13.07 | 0.77 | 0.22 | 8.46 | 0.69 |
| K | 0.02 | 12.63 | 0.51 | 0.01 | 12.42 | 0.50 |
| N′ | 0.03 | 12.95 | 0.53 | 0.01 | 12.53 | 0.51 |

**Table 3:** Morse potential parameters for 25% and 75% water content in the total mixture. $x_i$ represents the molar fraction of individual beads.

## CONCLUSIONS

This paper targets to construct a DPD parameterization scheme where a hydrogel is modeled in order to perform coarse-grained simulations. The beads that constitute the hydrogel are parameterized in such a way that their volumes are set to be different and dictated by their pure-liquid volumes. Moreover, we apply a recently proposed parameterization method where a Morse potential mimics the inter-molecular attraction as a result of the hydrogen bonds. The Morse potential parameters, namely hydrogen bond strengths and equilibrium hydrogen bond distances, are computed by taking the internal chemistry into account. Besides providing the coarse-grained parameterization details, we discuss the inherent interactions that are present and make a qualitative analysis of the structure as well. The validation of the parameterization procedure is saved as a separate future work. The coarse-grained parameterization procedure of the specific polymer reported in this work can be used as a general tool that can be applied to any similar material. Nevertheless, the procedure reported herein would drag attention of the researchers not only from computational but experimental communities.

**ACKNOWLEDGMENTS**

**REFERENCES**

1.      Peppas NA, Hilt JZ, Khademhosseini A, Langer R. Hydrogels in biology and medicine: From molecular principles to bionanotechnology. Adv Mater. 2006;18(11):1345-60.

2.      Lin CC, Metters AT. Hydrogels in controlled release formulations: Network design and mathematical modeling. Adv Drug Deliver Rev. 2006;58(12-13):1379-408.

3.      Drelich J, Chibowski E, Meng DD, Terpilowski K. Hydrophilic and superhydrophilic surfaces and materials. Soft Matter. 2011;7(21):9804-28.

4.      Banerjee I, Pangule RC, Kane RS. Antifouling Coatings: Recent Developments in the Design of Surfaces That Prevent Fouling by Proteins, Bacteria, and Marine Organisms. Adv Mater. 2011;23(6):690-718.

5.      Shirafkan A, Woodward EG, Port MJA, Hull CC. Surface Wettability and Hydrophilicity of Soft Contact-Lens Materials, before and after Wear. Ophthal Physl Opt. 1995;15(5):529-32.

6.      Yu CY, Ma L, Li K, Li SL, Liu YN, Zhou YF, et al. Molecular dynamics simulation studies of hyperbranched polyglycerols and their encapsulation behaviors of small drug molecules. Phys Chem Chem Phys. 2016;18(32):22446-57.

7.      Yang C, Lu DN, Liu Z. How PEGylation Enhances the Stability and Potency of Insulin: A Molecular Dynamics Simulation. Biochemistry-Us. 2011;50(13):2585-93.

8.      Lajunen T, Kontturi LS, Viitala L, Manna M, Cramariuc O, Rog T, et al. Indocyanine Green-Loaded Liposomes for Light-Triggered Drug Release. Mol Pharmaceut. 2016;13(6):2095-107.

9.      Lee H, de Vries AH, Marrink SJ, Pastor RW. A Coarse-Grained Model for Polyethylene Oxide and Polyethylene Glycol: Conformation and Hydrodynamics. J Phys Chem B. 2009;113(40):13186-94.

10.     Prasitnok K, Wilson MR. A coarse-grained model for polyethylene glycol in bulk water and at a water/air interface. Phys Chem Chem Phys. 2013;15(40):17093-104.

11.     Lee H, Pastor RW. Coarse-Grained Model for PEGylated Lipids: Effect of PEGylation on the Size and Shape of Self-Assembled Structures. J Phys Chem B. 2011;115(24):7830-7.

12.     Lee H, Larson RG. Membrane Pore Formation Induced by Acetylated and Polyethylene Glycol-Conjugated Polyamidoamine Dendrimers. J Phys Chem C. 2011;115(13):5316-22.

13.     Hoogerbrugge PJ, Koelman JMVA. Simulating Microscopic Hydrodynamic Phenomena with Dissipative Particle Dynamics. Europhys Lett. 1992;19(3):155-60.

14.     Boek ES, Coveney PV, Lekkerkerker HNW, vanderSchoot P. Simulating the rheology of dense colloidal suspensions using dissipative particle dynamics. Phys Rev E. 1997;55(3):3124-33.

15.     Kacar G, Atilgan C, Ozen AS. Mapping and Reverse-Mapping of the Morphologies for a Molecular Understanding of the Self-Assembly of Fluorinated Block Copolymers. J Phys Chem C. 2010;114(1):370-82.

16.     Kacar G, Peters EAJF, de With G. Structure of a Thermoset Polymer near an Alumina Substrate as Studied by Dissipative Particle Dynamics. J Phys Chem C. 2013;117(37):19038-47.

17.    Kacar G, Peters EAJF, de With G. A generalized method for parameterization of dissipative particle dynamics for variable bead volumes. EPL. 2013;102(4).

18.    Kacar G, Peters EAJF, de With G. Mesoscopic simulations for the molecular and network structure of a thermoset polymer. Soft Matter. 2013;9(24):5785-93.

19.    Can H, Kacar G, Atilgan C. Surfactant formation efficiency of fluorocarbon-hydrocarbon oligomers in supercritical CO2. J Chem Phys. 2009;131(12).

20.    Zeng QH, Yu AB, Lu GQ. Multiscale modeling and simulation of polymer nanocomposites. Prog Polym Sci. 2008;33(2):191-269.

21.    Kacar G, de With G. Hydrogen bonding in DPD: application to low molecular weight alcohol-water mixtures. Phys Chem Chem Phys. 2016;18(14):9554-60.

22.    Vishnyakov A, Talaga DS, Neimark AV. DPD Simulation of Protein Conformations: From alpha-Helices to beta-Structures. J Phys Chem Lett. 2012;3(21):3081-7.

23.    Groot RD, Warren PB. Dissipative particle dynamics: Bridging the gap between atomistic and mesoscopic simulation. J Chem Phys. 1997;107(11):4423-35.

24.    Flory PJ. Principles of Polymer Chemistry. Ithaca, New York: Cornell University Press; 1953.

25.    Krevelen DWv. Properties of Polymers. Amsterdam: Elsevier; 1990.


26.    Molecular Modeling Pro. 6.3.3 ed: Norgwyn Montgomery Software Inc.; 1992.

# Error Analysis of Absolute Rate Coefficient Extrapolated under *Pseudo*-First Order Conditions

**Luca D'Ottone[1] ✉ iD, Enunuwe Chuckunoye Ochonogor[2]\***

[1] UNISA, 0002, Pretoria, South Africa
[2] Cape Peninsula University of Technology, 7705, Cape Town, South Africa

**Abstract:** Computer based simulations for the reaction of nitrogen(II) oxide with the hydroxyl radical have been used to estimate the error associated with the *pseudo*-first order approximation under different simulated conditions. For the absolute rate coefficients, calculated by dividing the *pseudo*-first order constant by the concentration of the reactant in excess, the analysis of the relative error associated with working under *pseudo*-first order conditions shows that for a reactants' ratio higher than 10, the relative error is less than 5%.

**\*Corresponding author:** Enunuwe Chuckunoye Ochonogor;OCHONOGORC@cput.ac.za.

**INTRODUCTION**

The *pseudo*-first order approximation is an important technique used by kineticists to extrapolate absolute rate coefficients ($k_{II}$) of second order reactions with simple mathematical calculations (1,2). The *pseudo*-first order approximation relies on the fact that, in case of a substantial difference between the initial concentrations of the reactants in a second order reaction, the disappearance of one reactant over time would only marginally affect the concentration of the other, and therefore, effectively reduces the order of the reaction from two to one. When the difference in the concentration of the reactants is large enough, *pseudo*-first order conditions are established. On the other hand, when the ratio of the concentration of the reactants approaches each other, the error associated with the absolute rate coefficient extrapolated with first order formalism increases dramatically, and the *pseudo*-first order approximation breaks down. With the advent of more sophisticated mathematical algorithms (3), it has been argued that working under *pseudo*-first order conditions could be considered obsolete. In addition to that, as shown in Table 1, there is substantial confusion with regards to the term of *pseudo*-first order conditions. Table 1 lists the conditions required for *pseudo*-first order according to different authors. The statement *"to a great excess"* has been interpreted by more than ten authors (3), but, as shown in Table 1, there is currently no systematic theoretical treatment addressing this limitation that has been accepted by the scientific community.

**Table 1:** Borders of validity of the *pseudo*-first order conditions reported in selected literature.

|  | **Reference** | **Initial ratio between reagents' concentrations** |
|---|---|---|
| **Specialized Literature** | Sicilio and Peterson, 1961 (4) | 55 to 1 |
|  | O'Ferral and Miller, 1963 (5) | 10 |
|  | Lente, 2015 (6) | 10 |
|  | Espenson, 1995 (7) | 10 |
|  | Corbett, 1972 (8) | 5 |
| **Teaching Literature** | Rawn, 2008 (9) | *"…initial concentration (of A) much greater than the concentration of B."* |
|  | Atkins and De Paula, 2006 (10) | *"…large excess…"* |

Additional confusion is created by the first attempt of Sicilio and Peterson (4) to provide a theoretical analysis of the chemical reactions carried under *pseudo*-first order conditions. While their results were published in the Journal of Chemical Education, which is historically important for the reasons to be further elaborated in this study, validity of their approach may not be relevant to a kineticist. The Sicilio and Peterson's paper (4) reads in part: "*The first part of a reaction is often stressed in the kinetic studies, and unfortunately, it is during this part that the ratio error is greatest. During the latter stages of a reaction, the error decreases rapidly and becomes zero at 100% completion*". Sicilio and Peterson thus implied that looking at the decay in its entirety could possibly lead to better fits under *pseudo*-first order conditions. This is not the case for two main reasons: First, in a *pseudo*-first order reaction, the researchers usually build the kinetic profiles by plotting the concentration of the reactant in deficit over time. When the reaction gets close to completion, the reactant in deficit is almost completely exhausted and its presence is more difficult to detect. Therefore, the relative error becomes more important in comparison with the signal it generates. Second, as shown in Table 2, the propagation of errors in a semi-log plot, such as a first order plot, the relative error for lower values is substantially higher.

**Table 2:** Propagation of error in a semi logarithmic plot: As the value of the variable decreases, the experimental accuracy related to the instrument used for the detection of that variable remains the same. The semi-log scale magnifies the error bars by a factor of about 10 from 0.01 to 0.125.

| Value | Error | Range | Natural Log | Difference |
|-------|-------|-------|-------------|------------|
| 98 | 0.5 | 97.5 | 4.5900 | 0.0102 |
|    |     | 98.5 | 4.5798 |    |
| 8 | 0.5 | 8.5 | 2.1400 | 0.1251 |
|   |     | 7.5 | 2.0149 |    |

If both of these limitations of the 1961 Sicilio and Peterson's (4) analysis are taken into account, the conclusions of their reasoning lose reliability. In 1963, O'Ferral and Miller (5) published a note, also in the same journal, refuting the conclusions of Sicilio and Peterson on the basis that most kineticists work under experimental conditions that are well within the range of functionality allowed for the *pseudo*-first order conditions. Corbett (8), published simulation results for a hypothetical reaction, again in the very same journal, showing that a 2% error could be achieved even if the initial ratio of concentrations of the two reagents was about 2. Other references (6, 7, 9, and 10) discuss the limits of the *pseudo*-first order conditions, but do not provide a theoretical

framework to support their discussions. One of the controversies in the kinetic community is whether the *pseudo*-first order approximation is a reliable tool. Although the *pseudo*-first order approximation is used almost since the inception of chemical kinetics as a specific discipline (7), modern techniques such as non-linear least square fitting without any transformation of axis made possible by modern computer processing, make the this approximation look at least obsolete if not inadequate (6), anonymous reviewer to (1) and anonymous reviewer to the present work. The question is open for discussion in the kinetic community, and while the present work is not designed to take a stand in either direction, it is the intention of the author to produce a solid background for the estimate of the error introduced by working under *pseudo*-first order conditions. More recently, the robustness of the *pseudo*-first order conditions was reviewed by Schnell and Mendoza (11), and by Pedersen and Bersani (12). These more recent studies are focused on applications of the *pseudo*-first order approximation to the analysis of enzymatic reactions. Instead of helping to reach conclusions of broad validity, their application is limited to a very narrow field of the art.

## MATERIALS AND METHODS

Computer simulations of chemical kinetics have been used since the 1970s (13) and currently are a well-established methodology to mimic chemical systems (14). Java-based chemical simulator Billite TENUA (15) was used to simulate the validity of the *pseudo*-first order approximation on the reaction of nitrogen(II) oxide (IUPAC name nitric oxide or systematic IUPAC name oxidonitrogen) with the hydroxyl radical. This recombination reaction is a well-known system (2,16) that follows a simple mechanism (17). The generally accepted mechanism for the reaction of the hydroxyl radical with nitrogen(II) oxide (18) consists of three elementary steps, including the collision of the reactant molecules to form an energized adduct, $[HONO]^*$:

$$NO + OH \rightarrow [HONO]^* \qquad \text{(Eq. 1)}$$

Followed by stabilization of the adduct:

$$[HNOO]^* + M \rightarrow Products \qquad \text{(Eq. 2)}$$

The decomposition of the energized adduct back into the original reactants:

$$[HNOO]^* \rightarrow NO + OH \qquad \text{(Eq. 3)}$$

Adduct $[HONO]^*$ is formed in the first step of the mechanism, and it can either back dissociate or stabilize into products. The internal structure, and the possible isomeric configurations of adduct $[HONO]^*$ have been discussed elsewhere (2,16) and it is most likely to follow the bond sequence HOHO, as other possible structures for this state are energetically unfavourable. M represents the third body; a third molecule that it is not consumed in the reaction, but that plays a significant role by stabilizing the adduct by

removing from it the excess energy, in turn favouring the formation of the reaction products. In the system that was reproduced in this study M is helium gas. The *pseudo-first* order approximation assumes the following order of concentrations: $[M] >> [NO] >> [OH]_0$. The overall reaction can be written as follows:

$$NO + OH + M \rightarrow Products \tag{Eq. 4}$$

To simulate experimental conditions, the initial concentration of NO can be varied in the range of $10^{12}$ - $10^{16}$ , in large excess with respect to the $[OH]_0$, typically kept at $10^{12}$ molecules cm$^{-3}$. Simulated OH temporal profiles are then analysed assuming simple first order exponential behaviour to determine k'.

$$[OH]_t = [OH]_0 x \exp(-k^\wedge t) \tag{Eq. 5}$$

With reference to equation 5, $k^\wedge = k_{II} \times [NO] + k_d$, where $k_{II}$ is the absolute rate coefficient for the reaction, and $k_d$ is the loss of OH due to other factors, such as wall collisions, reactions with its precursor, self-reaction, and others. The reaction rate is derived using the following equation:

$$rate = k^\wedge \times [OH] \tag{Eq. 6}$$

The absolute rate coefficients are calculated by dividing $k^\wedge$ by the concentration of the reactant in excess. Alternatively, absolute rate coefficients can be extrapolated with the least square mean, from linear fits of the plot $k^\wedge$ against [NO] for each different pressure with the assumption that:

$$k_d << k_{II} \times [NO] \tag{Eq. 7}$$

This second technique, also referred as the second order plot or linearization method, minimizes potential experimental errors as it dilutes the effect of the relative concentrations on the determination of the absolute rate coefficient over a relatively wide range of concentrations. On the other hand, it is slightly more elaborated and not all researchers necessarily use it, particularly in solution. Since in the simulation $k_d$ is set to be null, Equation 7 is then reduced to:

$$k_{II} = k^\wedge \times [NO]^{-1} \tag{Eq. 8}$$

The bimolecular rate coefficient for the reaction $k_{calc}$ is obtained from simulated OH decays for different ratios of $r = [NO]_0/[OH]_0$. Ratios are then compared with the accepted values of $k_{II}$ at room temperature under different pressures, including 50, 200, and 600 Torr. The percentage error is then derived as:

$$\varepsilon = 100 \times (k_{true} - k_{calc})/k_{true} \tag{Eq. 9}$$

The different estimates for the percentage errors are tabulated and analyzed. Table 3 shows the absolute rate coefficient calculated with NASA-JPL expression (19) at 298.15 K for three different pressure values. All data treatment was performed with Microcal Origin (20).

**Table 3:** Absolute rate coefficient for the reaction of nitrogen(II) oxide with hydroxyl radical calculated with NASA-JPL expression (19) at 298.15 K under 50, 200, and 500 Torr of helium.

| p (Torr) | $k_{II}$ [cm$^3$ molecule$^{-1}$ s$^{-1}$] |
|:---:|:---:|
| 50 | $1.4 \times 10^{-12}$ |
| 200 | $5.0 \times 10^{-12}$ |
| 500 | $1.0 \times 10^{-11}$ |

**RESULTS AND DISCUSSION**

Hydroxyl radical temporal decays were simulated for at least three orders of magnitude, i.e. from $10^{12}$ [molecules cm$^{-3}$] to $10^9$ [molecules cm$^{-3}$] respectively at 50, 200, and 500 Torr at 298.15 K. Figure 1 represents five typical simulated decays at 298.15 K, under 50 Torr of total pressure, assuming helium to be the bath gas at different relative concentrations of the reactants ranging from 20 to 100 . The decays are linear for at least three orders of magnitude and the temporal resolution between points (ε) was adjusted to allow a sufficient number of points for each curve. The slope calculated by least-square fit of each curve represents the *pseudo*-first order constant k^ [s$^{-1}$].
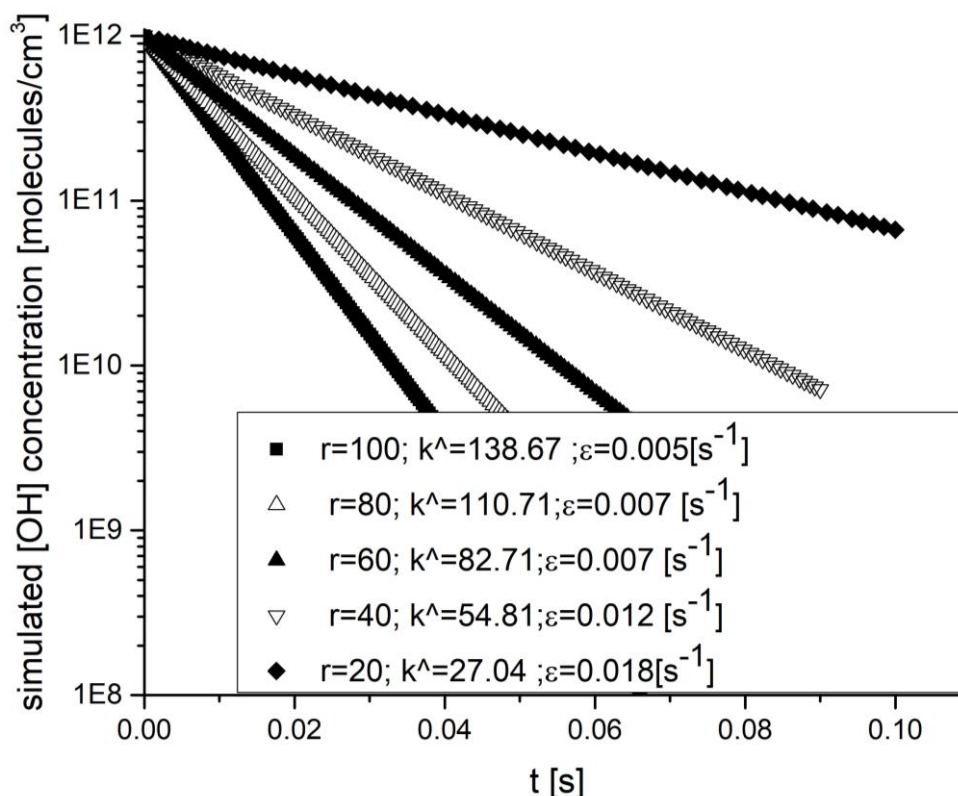


**Figure 1.** Typical simulated temporal profiles for different ratios of initial concentration of reactants between 20 and 100.

Figure 1 shows five typically simulated temporal profiles of the hydroxyl radical in the reaction with nitrogen(II) oxide at 298.15 K, under 50 Torr of total pressure. This is

when assuming helium to be the bath gas, at different relative concentrations of the reactants ranging from r = 20 to r = 100.

The temporal profiles (decays) represented in Figure 1 are substantially linear over a three orders of magnitude drop of concentration of the reactant in defect, suggesting no systemic deviation from a first order kinetic decay. Shown in Figure 2, however, are simulated hydroxyl radical temporal decays under the same conditions of pressure and temperature of the ones represented in Figure 1. The temporal profiles represented in Figure 2 are the outcome of simulations run with relative reactant concentrations ranging from 1 to 5 showing a substantial loss of linearity in a semi logarithmic plot in the first part of the decay. The loss of linearity of the temporal profile is a first indication that the *pseudo*-first order conditions are only partially met in this range of relative concentrations, and that the least square fit of the data point may lead to unreliable conclusions.
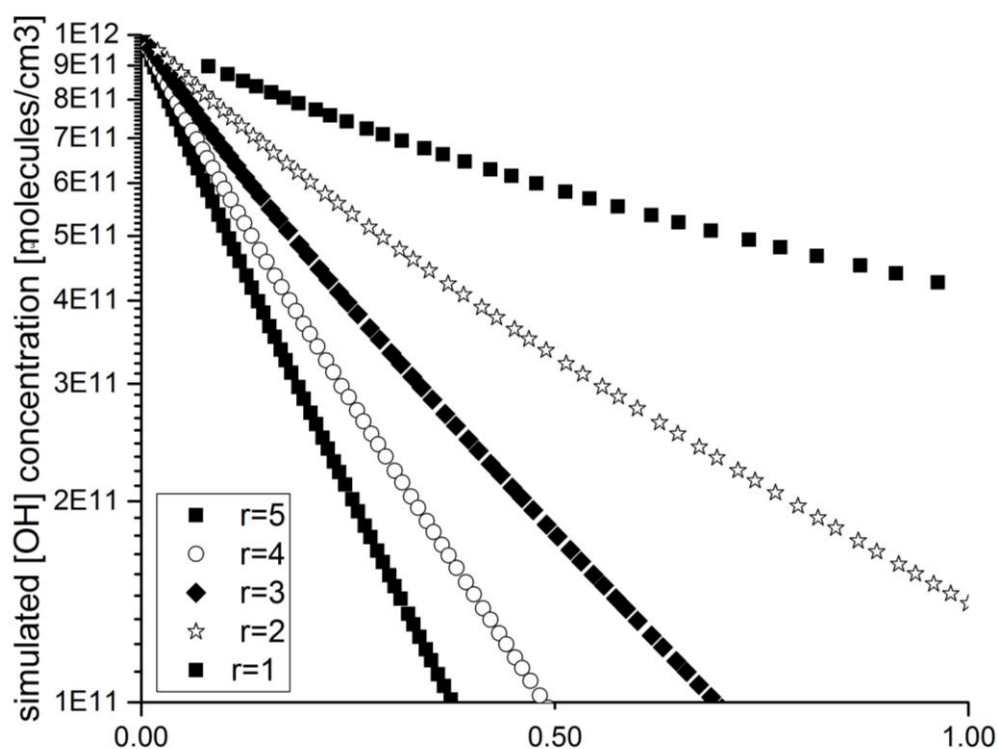


**Figure 2:** Typical simulated temporal profiles for different ratios of initial concentrations of reactants approaching to 1.

Figure 2 represents five typically simulated temporal profiles of the hydroxyl radical in the reaction with nitrogen(II) oxide at 298.15 K, under 50 Torr of total pressure, assuming helium to be the bath gas, at different relative concentrations of the reactants ranging from r = 1 to r = 5. Absolute rate coefficients $k_{II}$ [$cm^3$ molecule$^{-1}$ s$^{-1}$] are then calculated by dividing the *pseudo*-first order constants $k^$ by the concentration of the reactant in excess. Alternatively, they are determined as the slope of the second order

plot, where k^ is plotted against the different concentrations of the reactant in excess, in this case the nitrogen(II) oxide.

Figure 3 shows the simulated *pseudo*-first order constant plotted against the concentration of nitrogen(II) oxide. The plot of in this figure is constructed with simulated data. Therefore, $k_{II}$ extrapolated from it is expected to be the same $k_{II}$ fed into the model, unless the breakdown of the *pseudo*-first order approximation.
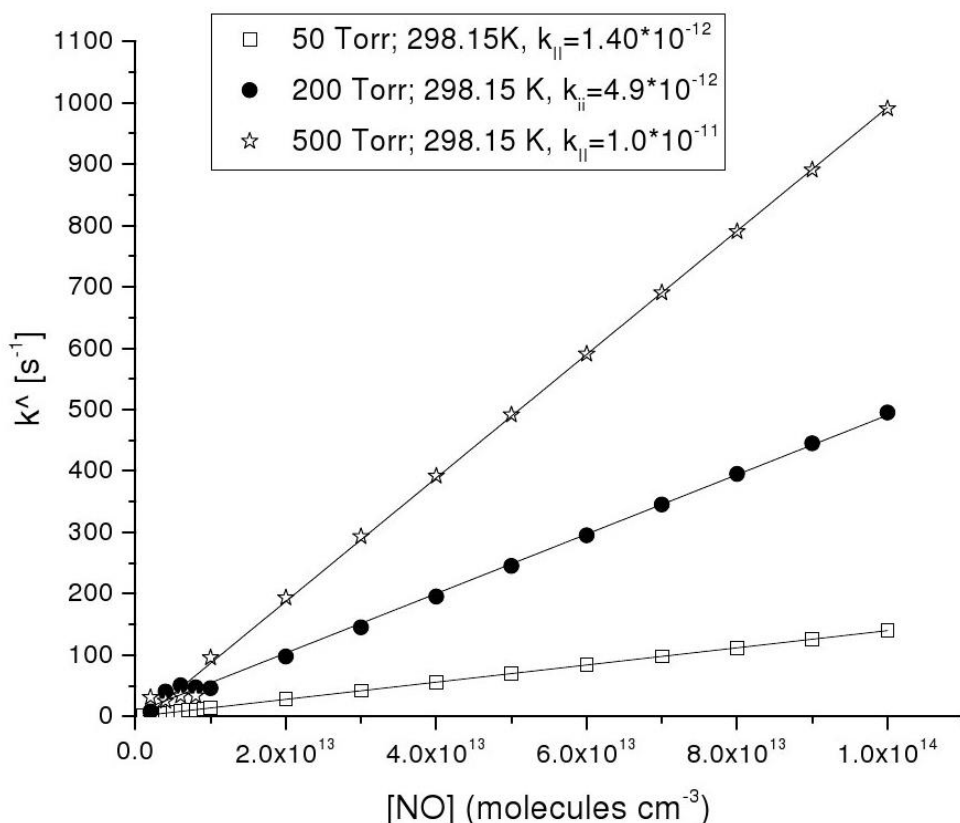


**Figure 3:** Second order plot of the simulated *pseudo*-first order rates versus the concentration of nitrogen(II) oxide at 298.15 K, under 50, 200, and 500 Torr of Helium. The absolute kinetic constant $k_{II}$ [$cm^3$ molecule$^{-1}$ s$^{-1}$] is determined as the least square slope of the linear fit.

Once the absolute rate coefficient is extrapolated for each different simulated condition, its value is compared with the literature value used as input in the simulation mechanism. The relative error is then calculated with Equation 9. Table 4 illustrates the output of the relative error calculation on the absolute rate coefficient derived in the simulation done in the present study. The data tabulated in Table 4 show that for r greater than 10 the relative error introduced by using the *pseudo*-first order approximation is less than 5%. If the absolute rate coefficient instead of being calculated independently as the ratio of the *pseudo*-first order constant k^ by the concentration of nitrogen(II) oxide are calculated with the second order plot, a ratio as low as 5 can be

attained with an error less than 5%. The data of Table 4 are reported in Figure 4 where the relative percentage error is plotted against the relative concentrations of the reactants. If a 5% relative ratio is considered to be acceptable, then the conclusions of O'Ferral and Miller (5) would set the tone for the proper determination of an acceptable level of uncertainty associated with *pseudo*-first order conditions.

**Table 4**: Relative error calculated with Equation 9.

| r | k' [s$^{-1}$] | [OH] [molecules cm$^{-3}$] | [NO] [molecules cm$^{-3}$] | $k_{II(calc)}$ [cm$^3$ molecule$^{-1}$ s$^{-1}$] | $k_{II(true)}$ [cm$^3$ molecule$^{-1}$ s$^{-1}$] | error |
|---|---|---|---|---|---|---|
| 1 | 0.0846 | $10^{12}$ | $10^{12}$ | $8.46 \times 10^{-13}$ | $1.4 \times 10^{-12}$ | 94% |
| 2 | 1.944 | $10^{12}$ | $2 \times 10^{12}$ | $9.72 \times 10^{-13}$ | $1.4 \times 10^{-12}$ | 31% |
| 3 | 3.236 | $10^{12}$ | $3 \times 10^{12}$ | $1.08 \times 10^{-12}$ | $1.4 \times 10^{-12}$ | 23% |
| 4 | 4.616 | $10^{12}$ | $4 \times 10^{12}$ | $1.15 \times 10^{-12}$ | $1.4 \times 10^{-12}$ | 18% |
| 5 | 6.072 | $10^{12}$ | $5 \times 10^{12}$ | $1.21 \times 10^{-12}$ | $1.4 \times 10^{-12}$ | 13% |
| 6 | 7.387 | $10^{12}$ | $6 \times 10^{12}$ | $1.23 \times 10^{-12}$ | $1.4 \times 10^{-12}$ | 12% |
| 7 | 8.726 | $10^{12}$ | $7 \times 10^{12}$ | $1.25 \times 10^{-12}$ | $1.4 \times 10^{-12}$ | 11% |
| 8 | 10.57 | $10^{12}$ | $8 \times 10^{12}$ | $1.32 \times 10^{-12}$ | $1.4 \times 10^{-12}$ | 6% |
| 9 | 11.92 | $10^{12}$ | $9 \times 10^{12}$ | $1.32 \times 10^{-12}$ | $1.4 \times 10^{-12}$ | 5% |
| 10 | 13.35 | $10^{12}$ | $1 \times 10^{13}$ | $1.33 \times 10^{-12}$ | $1.4 \times 10^{-12}$ | 5% |
| 20 | 27.04 | $10^{12}$ | $2 \times 10^{13}$ | $1.35 \times 10^{-12}$ | $1.4 \times 10^{-12}$ | 3% |
| 30 | 40.91 | $10^{12}$ | $3 \times 10^{13}$ | $1.36 \times 10^{-12}$ | $1.4 \times 10^{-12}$ | 3% |
| 40 | 54.81 | $10^{12}$ | $4 \times 10^{13}$ | $1.37 \times 10^{-12}$ | $1.4 \times 10^{-12}$ | 2% |
| 50 | 68.75 | $10^{12}$ | $5 \times 10^{13}$ | $1.38 \times 10^{-12}$ | $1.4 \times 10^{-12}$ | 2% |
| 60 | 82.71 | $10^{12}$ | $6 \times 10^{13}$ | $1.38 \times 10^{-12}$ | $1.4 \times 10^{-12}$ | 2% |
| 70 | 96.73 | $10^{12}$ | $7 \times 10^{13}$ | $1.38 \times 10^{-12}$ | $1.4 \times 10^{-12}$ | 1% |
| 80 | 110.7 | $10^{12}$ | $8 \times 10^{13}$ | $1.38 \times 10^{-12}$ | $1.4 \times 10^{-12}$ | 1% |
| 90 | 124.68 | $10^{12}$ | $9 \times 10^{13}$ | $1.39 \times 10^{-12}$ | $1.4 \times 10^{-12}$ | 1% |
| 100 | 138.67 | $10^{12}$ | $1 \times 10^{14}$ | $1.39 \times 10^{-12}$ | $1.4 \times 10^{-12}$ | 1% |

.

**Figure 4:** Error analysis plot: Relative error on the absolute rate coefficient for the reaction with nitrogen(II) oxide at 298.15 K under 50 Torr of helium.

## CONCLUSIONS

Computer based simulations for the reaction of nitrogen(II) oxide with the hydroxyl radical have been used to estimate the error associated with the *pseudo*-first order approximation under different simulated conditions. The analysis of the relative error associated with the *pseudo*-first order conditions shows that for a reactants' ratio higher than 10, the relative error is less than 5%, thus supporting the view expressed by O'Ferral and Miller (5) and Kiss (3). Further and more comprehensive research may be needed to generalize these results, with specific reference to more complex systems like the reaction of nitrogen(IV) oxide with the hydroxyl radical  (21). Other aspects of this problem suitable for further investigation are related to the transferability of the conclusion of the present study to the practicality of experiments, especially in the range of low signal to background ratio, where it is not always possible to observe a temporal profile for three orders of magnitude.

## ACKNOWLEDGMENTS

## REFERENCES

1. Pettine M, D'ottone L, Campanella L, Millero FJ, Passino R. The reduction of chromium (VI) by iron (II) in aqueous solutions. Geochim Cosmochim Acta. 1998;62(9):1509–1519.

2. Di Loreto G, d'Ottone L. Kinetics of the OH initiated oxidation of nitrogen monoxide. Ann Chim. 2004;94(12):899–910.

3. Kiss V, Ősz K. Double Exponential Evaluation under Non-Pseudo–First-Order Conditions: A Mixed Second-Order Process Followed by a First-Order Reaction. Int J Chem Kinet. 2017 Aug 1;49(8):602–10.

4. Sicilio F, Peterson MD. Ratio errors in pseudo first order reactions. J Chem Educ. 1961 Nov;38(11):576.

5. O'Ferrall RAM, Miller SI. Letters to the editor. J Chem Educ. 1963 May 1;40(5):269.

6. Lente G. Deterministic kinetics in chemistry and systems biology: the dynamics of complex reaction networks [Internet]. Springer; 2015. Available from: https://books.google.com/books?hl=en&lr=&id=ygYyBwAAQBAJ&oi=fnd&pg=PR5&dq=le nte+deterministic+kinetics+in+chemistry+and+system+biology&ots=rSn1Y7o9Vr&sig= WDlkJGkWaJhg8y5OTskW-bYSPL4

7. Espenson JH. Chemical kinetics and reaction mechanisms [Internet]. Vol. 102. Citeseer; 1995. Available from: http://citeseerx.ist.psu.edu/viewdoc/download?doi=10.1.1.831.7089&rep=rep1&type=pd f

8. Corbett JF. Pseudo first-order kinetics. J Chem Educ. 1972 Oct 1;49(10):663.

9. Rawn D. Fundamental Chemical Principles. Towston, MD; 2008.

10. Atkins PW. Paula J de 2006 Physical Chemistry. Oxford: Oxford University;

11. Schnell S, Mendoza C. The condition for pseudo-first-order kinetics in enzymatic reactions is independent of the initial enzyme concentration. Biophys Chem. 2004 Feb 1;107(2):165–74.

12. Pedersen MG, Bersani AM. Introducing total substrates simplifies theoretical analysis at non-negligible enzyme concentrations: pseudo first-order kinetics and the loss of zero-order ultrasensitivity. J Math Biol. 2010 Feb;60(2):267–83.

13. Edelson D. Computer Simulation in Chemical Kinetics. Science. 1981;214(4524):981–6.

14. Belov AA, Kalitkin NN, Kuzmina LV. Modeling of chemical kinetics in gases. Math Models Comput Simul. 2017 Jan 1;9(1):24–39.

15. Barshop BA, Wrenn RF, Frieden C. Analysis of numerical methods for computer simulation of kinetic processes: development of KINSIM--a flexible, portable system. Anal Biochem. 1983 Apr 1;130(1):134–45.

16. Jamal A, others. Allowed energetic pathways for the three-body recombination reaction of nitrogen monoxide with the hydroxyl radical and their potential atmospheric implications. Orbital- Electron J Chem. 2010;2(2):168–179.

17. Lindemann FA, Arrhenius S, Langmuir I, Dhar NR, Perrin J, Lewis WM. Discussion on "the radiation theory of chemical action." Trans Faraday Soc. 1922;17:598–606.

18. IUPAC | International Union of Pure and Applied Chemistry Project Details [Internet]. IUPAC | International Union of Pure and Applied Chemistry. [cited 2017 Oct 10]. Available from: https://iupac.org/projects/project-details/

19. Sander SP, Friedl RR, Golden DM, Kurylo MJ, Moortgat GK, Wine PH, et al. Chemical Kinetics and Photochemical Data for Use in Atmospheric Studies Evaluation Number 15 [Internet]. 2006 Jul. Available from: https://ntrs.nasa.gov/search.jsp?R=20090033862

20. Microcal Origin [Internet]. Northampton, MA: OriginLab; Available from: www.originlab.com

21. D'Ottone L, Campuzano-Jost P, Bauer D, Hynes AJ. A Pulsed Laser Photolysis−Pulsed Laser Induced Fluorescence Study of the Kinetics of the Gas-Phase Reaction of OH with NO2. J Phys Chem A. 2001 Nov 1;105(46):10538–43.

# Boronic acid-functionalized silica microparticles for isolation of flavonoids from *Hypericum perforatum*

**Onur Çetinkaya[1],\*, Hüseyin Çiçek [2], Şeyda Kıvrak [3], Gülsen Tel Çayan[4]**

[1] *Maria Curie-Sklodowska University, Faculty of Chemistry, 20-031, Lublin/Poland*
[2] *Mugla Sitki Kocman University, Faculty of Science, Department of Chemistry, 48000, Muğla, Turkey*
[3] *Mugla Sitki Kocman University, Faculty of Health Sciences, 48000 Muğla, Turkey*
[4]*Muğla Sıtkı Koçman University, Muğla Vocational School, Department of Chemistry and Chemical Processing Technologies, 48000 Muğla, Turkey*

**Abstract:** We have selectively separated *cis-* and/or *vicinal*-diol-containing flavonoids from *Hypericum perforatum* (HP) by adsorption/desorption used aminophenylboronic acid (APBA) functionalized uniform (1.6 μm) silica microparticles (BASPs) synthesized *via* the Stöber method. Silica particles were alkylated via its terminal –OH by 3-aminopropyl trimethoxysilane (APTS), glutaraldehyde (GA) and APBA. The results from model adsorption studies were indicated that these microparticles selectively had adsorbed quercetin and rutin but partially apigenin. The antioxidant and antiradical activities of the desorption solution were slightly higher than the post-adsorption solution. These results indicated that the BASP selectively adsorbed the *cis-* and/or *vicinal* antioxidant and antiradical flavonoids.

## INTRODUCTION

Flavonoids play some important roles in biological and physiological systems of plants (1). They are widely used in health products, cosmetics, and medicines (2-7). Although solvent extraction is the conventional technique (8) to isolate them, this approach leads to environmental pollution due to the large amounts of residual solvents. In addition, these methods are insufficient for the specific isolation of some precious types of flavonoids.

An alternative method for the selective isolation of some types of flavonoids and enrichment of the antioxidant activity of plants involve the uses of adsorbent beads that possess a high surface area and specific functionalities on their surfaces (9-13). In general, the adsorbents used in these studies (*e.g.,* cross-linked polystyrene-based beads) are hydrophobic. The polar/nonpolar ratios can be varied on modification and functionalization of these beads to generate adsorption selectivity to specific types of flavonoids.

Conventionally, uniform micron and submicron silica particles are functionalized with carbon chains, which were selective to some polar/nonpolar groups, have been employed in the columns used in liquid chromatography (14). Hydrophobic interactions and hydrogen bonding can be evaluated as two primary forces to purify or identify the flavonoids. As an alternative packing material or adsorbent, we already reported boronic acid based uniform APBA functionalized poly(chloromethyl styrene-co-divinylbenzene) particles for *cis-* and *vicinal* diol containing flavonoids (15).

Herein we reported silica based microparticles that successfully adsorbed *cis-* and *vicinal* diols (quercetin and rutin as model flavonoids) as compared to the isolated hydroxyl compounds (apigenin). The extraction study was performed on the ethyl acetate extract of *Hypericum perforatum*. As well known, flavonoids possess some antioxidant and antiradical activities. These biological active flavonoids can be selectively separated from the plant extracts. In addition, the prepared uniform microparticles might be useful as the future candidates to be used in liquid chromatography.

## MATERIAL AND METHODS

The tetraethyl orthosilicate (TEOS, 98%, Aldrich, Steinheim, Germany) precursor was used in the synthesis of silica microspheres. *N*-cetyl-*N,N,N*-trimethylammonium bromide (CTAB, 99%, Merck, Darmstadt, Germany) and dodecylamine (DDA, 98%, Aldrich, Steinheim, Germany) were selected as templating agents. Ethanol (99 %, Sigma-Aldrich, Steinheim, Germany) was used for the

preparation of the dispersion medium. Ammonium hydroxide ($NH_4OH$, 25 %, J.T. Baker, USA) was selected as a catalyst. An aminopropil silane (APTS) (97 %, Aldrich, Steinheim, Germany) and anhydrous toluene (Sigma-Aldrich, USA) were used in the first derivatization step of the silica particles. In the second step, glutaraldehyde (GA, 25 %, Merck, Hohenbrunn, Germany) and aminophenylboronic acid (APBA, 95 %, Aldrich, USA) were used in the boronic acid-functionalization of the particles.

Quercetin hydrate (>95 %, Aldrich, Steinheim, Germany), rutin hydrate (95 %, Sigma, China), and apigenin (95 %, Sigma, USA) were employed as model flavonoids and used in adsorption experiments. Methanol (GC grade, Merck, Darmstadt, Germany), ethanol (Sigma-Aldrich, Steinheim, Germany), and distilled water were used to prepare the adsorption and desorption solutions. 4-(2-Hydroxyethyl)piperazine-1-ethanesulfonic acid (HEPES, 99.5 % Sigma, Steinheim, Germany) was employed to adjust the pH of the solutions. The absorption values of the media were measured with a UV-visible spectrophotometer (Shimadzu W-1601).

Agilent Technologies 1260 Infinity HPLC (high-performance liquid chromatography) (ZORBAX, Eclipse SB-C18, 7 µm, 4.6 mm x 250 mm, Agilent, USA) was used in the chromatography experiments. As a mobile phase, a mixture of methanol–acetonitrile (99.9%, Sigma-Aldrich, France)-ultra distilled water (40:15:45, v/v/v, isocratic) containing 1% acetic acid (100%, Riedel-de Haën, Germany) was selected.

For the free radical scavenging, antioxidant activity, and total flavonoid determination experiments, analytical grade 1,1-diphenyl-2-picrylhydrazyl (DPPH) (85 %, Aldrich, 98 Steinheim, Germany), β-Carotene (97 %, Fluka, USA), Tween-40 (Merck, USA), linoleic acid (99 %, Aldrich, Augsburg, Germany), potassium acetate (>99.0, Merck, Barcelona, Spain), and aluminum nitrate (98.5 %, Merck, Germany) were used. Ethanol and ethyl acetate (99.5 %, Sigma–Aldrich, Steinheim, Germany) were employed as the solvent for the extraction of the plant leaves.

**Synthesis of silica microparticles**

The synthesis of BASPs was consisted by four stages, *i.e.* the synthesis of silica microparticles, amine functionalization, activation with glutaraldehyde, and attachment of the APBA ligand. The first stage is the production of silica particles bearing hydroxyl groups on their surface (16), as schematically shown in Fig. 1.
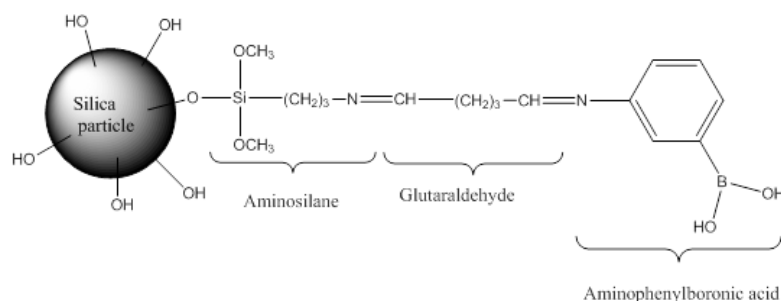
**Figure 1:** Representation of functionalized silica microparticles.

Silica microparticles were produced using by the conventional sol-gel method at room temperature (17-21). Ethanol (130 mL), distilled water (70 mL), DDA (1.34 g), and CTAB (0.14 g) were mixed in a sealed Pyrex glass bottle until a homogenous solution was obtained. A $NH_4OH$ solution (0.8 mL) was added to solution and immediately stirred. This step was followed by the slow addition of TEOS (5 mL) and the medium was shaken for 2 min. Then, the bottle was firmly closed and stored for 24 h at room temperature. The silica microparticles were washed in two steps to remove surfactants from the interior. First, the silica microparticles were placed in 100 mL of isopropanol and shaken at 70 °C for 12 h in a shaker (22). Then, the silica microparticles were centrifuged to precipitate and washed again using the same procedure described above. In the last step, the silica microparticles were washed for 30 min under sonication in an ultrasonic ice bath with a concentrated mixture of HCl/ethanol (15/120, v/v) to remove residual surfactants (23). The latter washing process was repeated three times. Silica microparticles bearing hydroxyl functional groups on their surface, which are suitable for derivatization, were obtained.

**Grafting of amine functional group onto the silica microparticles**
A small amount of the washed silica microparticles (1.26 g) were dried in an oven at 120 °C. Then, the particles were placed in 10 mL of anhydrous toluene under magnetic stirring (24,25). An excess amount of (3-aminopropyl)triethoxysilane (2 mL), which was dispersed in a tube containing 2 mL of anhydrous toluene, was slowly added to this medium in 10 min under a nitrogen atmosphere and stirred for 2 h to complete the grafting. The particles were centrifuged, placed in 10 mL of anhydrous toluene and washed under stirring. The last washing process was repeated two times. Then, the particles were washed under sonication in an ultrasonic water bath with a HCl/ethanol mixture for 10 min and with distilled water followed by drying in a vacuum oven at 60 °C for 24 h (26).

**Activation of the amino-capped silica microparticles with glutaraldehyde**
The amino-capped silica microparticles were dispersed in a phosphate buffer (0.067 M $KH_2PO_4$ 0.067 M $Na_2HPO_4$) at a pH of 8. Then, 4 mL of GA (25 %) was added dropwise to this solution under stirring (27,28), and the reaction was maintained for 5 h. The silica microparticles became

red that was a sign of successful activation. These particles were washed with distilled water three times.

## APBA attachment to the silica microparticles activated with GA

APBA was attached to the terminal aldehyde on the silica microparticles. For this purpose, 300 mg of APBA was dissolved in 40 mL of distilled water. The pH of this solution was adjusted to 8.0 using 0.1 M NaOH. Approximately 1 g of the amino functionalized silica microparticles was added to the medium under stirring at 200 rpm. The pH of this medium was adjusted to 9.0 with 0.1 M NaOH. The suspension was stirred for 12 h and then centrifuged. The particles were washed for 12 h with a 50 mL of a 1 N NaCl solution, which was adjusted to a pH of 10. Finally, the particles (BASPs) were washed with 0.1 M HCl and distilled water (27). The FT-IR spectra of the particles at each derivatization step were recorded on a Nicolet iS10 FT-IR spectrometer using KBr pellets.

## Model flavonoid adsorption experiments with BASPs

The equilibrium adsorption capacity (Q) (mg flavonoid/g particle) of quercetin, rutin, and apigenin with BASPs were determined in methanol/HEPES buffer (85/25, mL/mL) at 8.5 pH using a UV spectrophotometer per the method of Çetinkaya *et al.* (15). All buffers used for adsorption of model flavonoids, were prepared from methanol/HEPES mixture and specific pH values were adjusted with 0.1 N NaOH.

To show the *cis* and/or *vicinal*-diol selectivity of the adsorbent particles in a mixture, rutin, quercetin and apigenin were used. First, 20 μL solutions of each flavonoid of different concentrations in a methanol/HEPES buffer (pH 8.5) were injected to the HPLC; their retention time versus concentration and calibration curves were determined. Then, the flavonoid mixture in the methanol/HEPES buffer at pH 8.5 was prepared by adjusting the concentration of each flavonoid in the mixture to 25 g/mL. Adsorption was repeated with APBA-attached poly(CMS-co-DVB) particles as described before. The adsorption medium was centrifuged and a supernatant was injected to HPLC. The mobile phase was a mixture of methanol–acetonitrile–water (40:15:45, v/v/v) and 1 % acetic acid as an eluent; column flow rate: 1 mL/min.

## Adsorption experiments with BASPs from HP stem extracts

To investigate the efficiency of BASPs against antiradical and antioxidant activity, ethyl acetate extracts of HP stems (Mugla Turkey) were used in adsorption/desorption experiments. The equation (1) was used to calculate the desorption percent of the adsorbed extract from the adsorbent (29).

*% Desorption = [Desorbed amount (mg)/ Adsorbed amount (mg)] x 100*          (1)

**Activity measurements using the adsorption solutions**

The total flavonoid content (mg flavonoid/g dry weight of extract) of the ethylacetate, adsorption and desorption media were determined separately as described by Moreno *et al.* (30).

Free radical scavenging (DPPH) and *β*-carotene-linoleic acid assay were used to determine the activities of the ethyl acetate extract and adsorption solutions (Ads). In the DPPH method, the free radical scavenging activity was calculated using Equation 2 (31),

$$DPPH\ Scavenging\ Effect\ (\%) = (A_0\text{-}A_1/A_1)\ 100 \qquad (Eq.\ 2)$$

where $A_0$ and $A_1$ are the absorbences of the control and sample solutions, respectively. The antioxidant activity was determined using the β-carotene-linoleic acid assay was performed according to the literature method (32).

**RESULTS AND DISCUSSIONS**

**Characterization of silica microparticles**

The diameters of the synthesized silica microparticles were found between 1.5-1.7 μm by Scanning Electron Microscope (SEM) (JEOL JSM-7600F) (Fig. 2). The pore volume, average pore diameter, specific surface area and external surface area of the silica microparticles were measured by Brunauer–Emmett–Teller (BET) analysis being 0.288 cm$^3$/g, 14 Å, 560 m$^2$/g, and 14.61 m$^2$/g, respectively. According to IUPAC, the physical adsorption isotherm of the particles could be represented as a *Type I* isotherm (33).



(a)                          (b)                          (c)
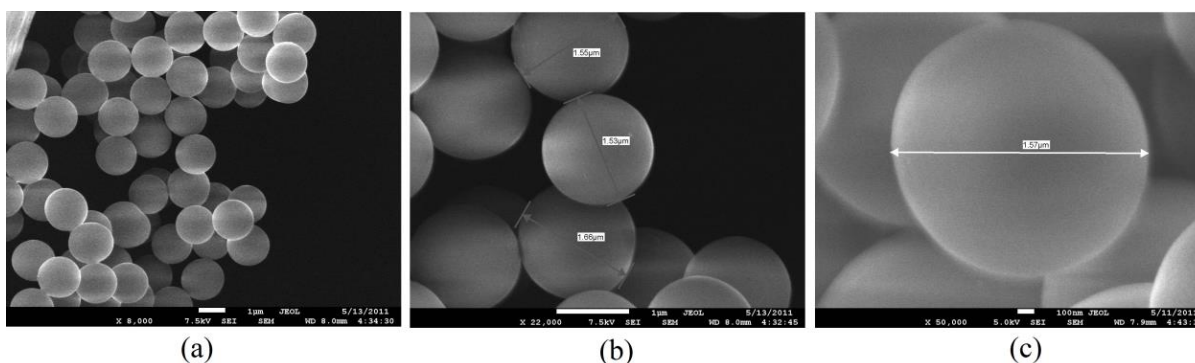
**Figure 2:** SEM photographs of synthesized silica microparticles (magnifications a: 8,000x; b: 22,000x, c: 50,000x).

The prepared BASPs had a smaller pore volume and the pore size compared to poly(7-oxonorbornene-5,6-dicarboxylic acid-block-norbornene) [poly-(ONDCA-b-NBE)]-coated silica particles that had a 50 Å pore size, 7 μm diameter, 0.8 cm$^3$/g pore volume and 420 m$^2$/g surface

area (34). The very small pore volume and porosity properties of BASPs had a disadvantage in adsorption experiments due to their less inner surface area. However, the surface properties, monodispersity and sub-micron particle size of BASPs made it suitable for use in liquid chromatography for the fast determination of flavonoids in plant extracts (34) and could be an alternative to octadecyl-type silica particles (14). Pore size enlargement, which could be achieved by post-synthetic hydrothermal treatment under specific conditions or using by oligomeric and polymeric templates (20), was not applied in this study.

**FT-IR analysis of the APBA-functionalized silica microparticles**

The silica microparticles were derivatized via the hydroxyl groups on their surface. The first step was involved the covalent attachment of the methoxy group of the silane compound (APTS) via condensation with hydroxyl groups on the surface of the silica particles. The FTIR spectra of synthesized silica microparticles itself (a), washed with HCl/Ethanol (b), modified with APTS (c) and modified with APBA (d) are given in Figure 3.

The band located at 3500 $cm^{-1}$ corresponds to the Si-OH vibration as seen in Figure 3(a). The band between 1950 $cm^{-1}$ and 1850 $cm^{-1}$ can be attributed to the Si-O-Si vibration (27, 35). Another band at 1640 $cm^{-1}$ is most likely due to the OH bending vibration. The two bands located at 2850-2950 $cm^{-1}$ correspond to the symmetric and asymmetric stretching vibrations of $CH_2$ and $CH_3$; present in the CTAB and DDA structures. After the microparticles were washed with HCl and ethanol mixture, these bands nearly disappeared (Figure 3(b)).
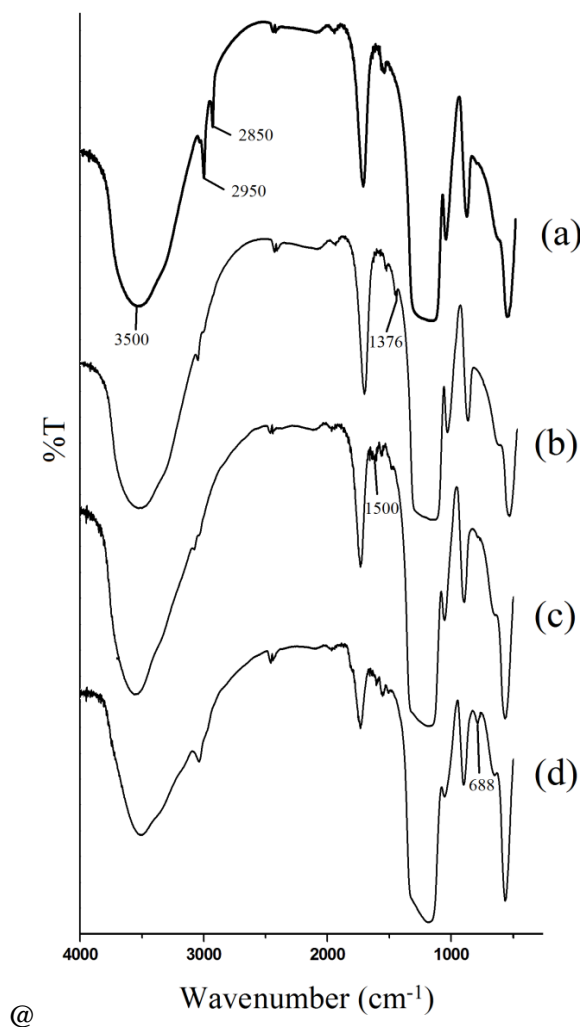
**Figure. 3:** FT-IR spectra of silica microparticles at different functionalization stages; (a) after synthesis, (b) after washed with HCl/ethanol (c) modified with APTS (d) modified with APBA.

In Figure 3 (c), the disappearance of the band located at 1376 $cm^{-1}$ corresponds to the missing Si-OH. The band at 1500 $cm^{-1}$ was due to the secondary amine of APTS (36). The GA attachment is determined by the change in color of the particles due to the shift reaction occurring between the APTS functionalized silica particles and GA. Due to GA and APBA attachment to the surface of the silica particles, the intensity of symmetric and asymmetric stretching vibration bands of the $CH_2$ and $CH_3$ peaks at approximately 2940 $cm^{-1}$ were increased and peak between 3000-3500 $cm^{-1}$ came to fruition (Figure 3 (d)). In addition, the peak that appeared at 688 $cm^{-1}$ (Figure 3d), which was not observed in Figure 3 (c) due to the aromatic structure of APBA.

**Model flavonoid adsorption with BASPs**

The selectivity of BASPs for the *cis* and *vicinal*-diol (rutin) and *vicinal*-only-diol-containing model flavonoids (quercetin) were studied. Apigenin was selected as a model flavonoid that does not contain either *cis*- or *vicinal*-diol. The maximum solubility of quercetin was calculated as 0.02

mg/mL. To compare each flavonoid, this value was employed to investigate the effect of the pH on the adsorption capacity.

At a pH of about 8.5, the geometry of BASPs converts from trigonal to a tetrahedral (37). The tetrahedral formation is the most suitable form to capture *cis-* and/or *vicinal*-diols. Therefore, the adsorption capacity of quercetin was higher at a pH 8.5 compare to the pH values (Fig. 4).
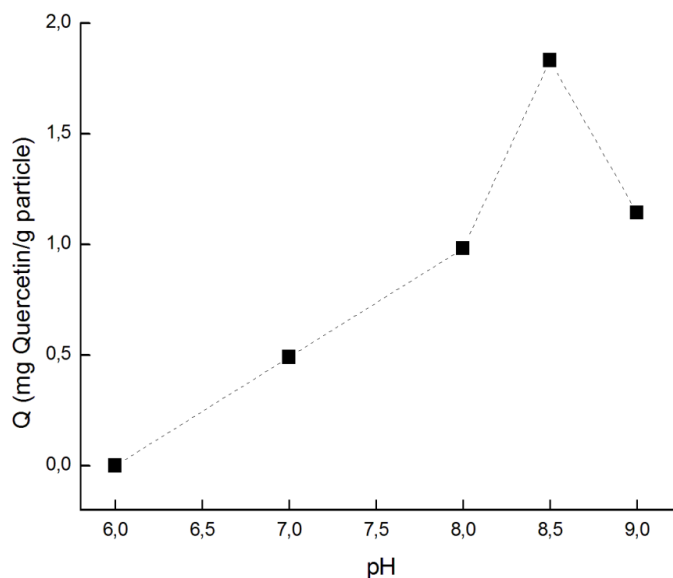


**Figure 4:** Quercetin adsorption capacity of BASPs at different pHs, temperature: 20 °C, initial quercetin concentration: 0.02 mg/mL.

The variation in the maximum adsorption capacity as a function of pH using BASPs for quercetin, rutin, and apigenin were also comparatively studied. The adsorption capacity at a pH 8.5 of apigenin, which does not contain *cis-* either *vicinal*-diol group, was less than that of rutin and quercetin (Figure 5). At this pH, the adsorption capacity of quercetin and rutin was 2 and 3 mg/g particle, respectively.
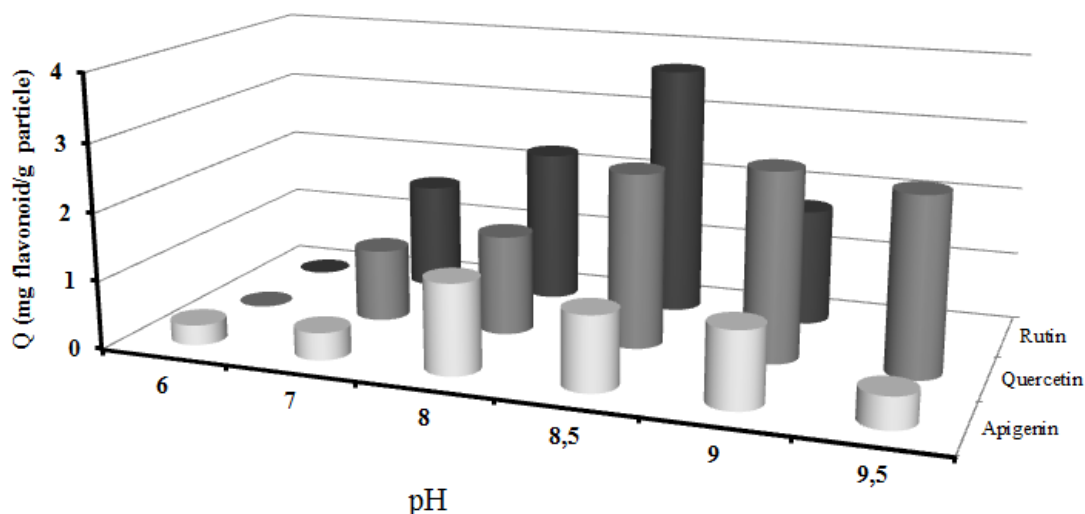
**Figure 5:** Adsorption capacities of BASPs against quercetin, rutin and apigenin at different pHs; temperature: 20 °C, initial flavonoid concentration: 0.02 mg/mL.

The molecular weight of rutin is twice than that of quercetin. In this study, g/mL of the samples were used instead of moles/mL. From that point of view, the rutin concentration (in moles) becomes half of that for quercetin. As Figure 6 shows, almost similar amount of Desp (rutin and quercetin) were obtained by BASPs. As a whole, the amount of rutin adsorbed on the BASPs become twice as that of quercetin. It may be explained by the fact that the binding probability of quercetin carrying one *vicinal*-diol group to bond to the boronic acid of BASPs is same with rutin carrying *cis-* as well as *vicinal*-diols.

The steric effect of rutin might negatively affect its adsorption on the adsorbent. However, the adsorption capacity of apigenin, which did not contain *cis*-diol groups, did not increase with pH and was less than that of *cis-* and *vicinal*-diol-containing rutin and *vicinal*-diol containing quercetin in the alkaline pH region. However, its amount of adsorption capacity was not rendered negligible which could be attributed to the nonspecific adsorption of apigenin on the adsorbent particles. The nitrogen on the spacer arm (Fig. 1) attached to the silica particles can make a hydrogen bond via the -OH located on the apigenin. Therefore, a comparable amount of apigenin can be isolated with BASPs particles, and this amount does not depend on pH.

The maximum adsorption capacity for quercetin was found as approx. 22 mg/g particle (Figure 6 and Table 1). The compatibility of quercetin adsorption with two well-known adsorption models *i.e.* Langmuir and Freundlich (29,37) was also tested. The $q_o$ values obtained from the Langmuir and Freundlich models were found as 15.43 mg/g and 22 mg/g, respectively, very close to each other. The "K" and "$R^2$" values, which are the equilibrium constant and the coefficient of determination, respectively, were calculated as 17.05 and 0.9755, respectively. $R^2$ obtained from Langmuir model

is sufficiently high as compared to the Freundlich model *i.e.* 0.8515. Therefore, the quercetin adsorption process can be adequately represented by the Langmuir model. However, the model parameters calculated for the Freundlich model were not acceptably suitable for representing this process.
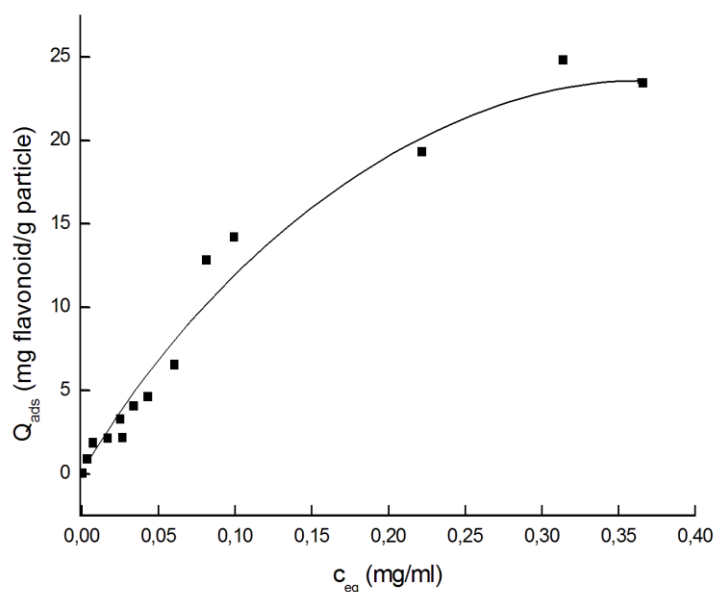


**Figure 6:** The variation of equilibrium quercetin concentration with initial quercetin concentration for BASPs, temperature: 20 °C, initial flavonoid concentration: 0.02 mg/ml, pH: 8.5.

**Table 1** Langmuir and Freundlich model parameters calculated for adsorption of quercetin by using the data obtained from Fig. 6

| Langmuir | | | Freundlich | | |
|---|---|---|---|---|---|
| $q_o$ (mg/g) | $K$ (mg/ml) | $R^2$ | $n$ | $k$ | $R^2$ |
| 15.43 | 17.05 | 0.9755 | 0.6701 | 0.4217 | 0.8515 |

**Adsorption selectivity of BASPs towards a model flavonoid mixture**

The selectivity of the APBA-attached microparticles to the *cis*- and/or *vicinal*-diols (*i.e.,* quercetin and rutin) is shown in Fig. 7. 2 g of quercetin and 1.9 g of rutin were adsorbed per gram of BASPs. Amounts were obtained from the area under the peaks from HPLC chromatogram. As boronic acid is prone to *cis*- and/or *vicinal*-diols, out of the mixture, the adsorption capacity of apigenin was far more less than the sole apigenin solution. BASPs mostly adsorbed the quercetin and rutin. We can say that, the BASPs selectively adsorbed the flavonoids that contained *cis*- and/or *vicinal*-diols.
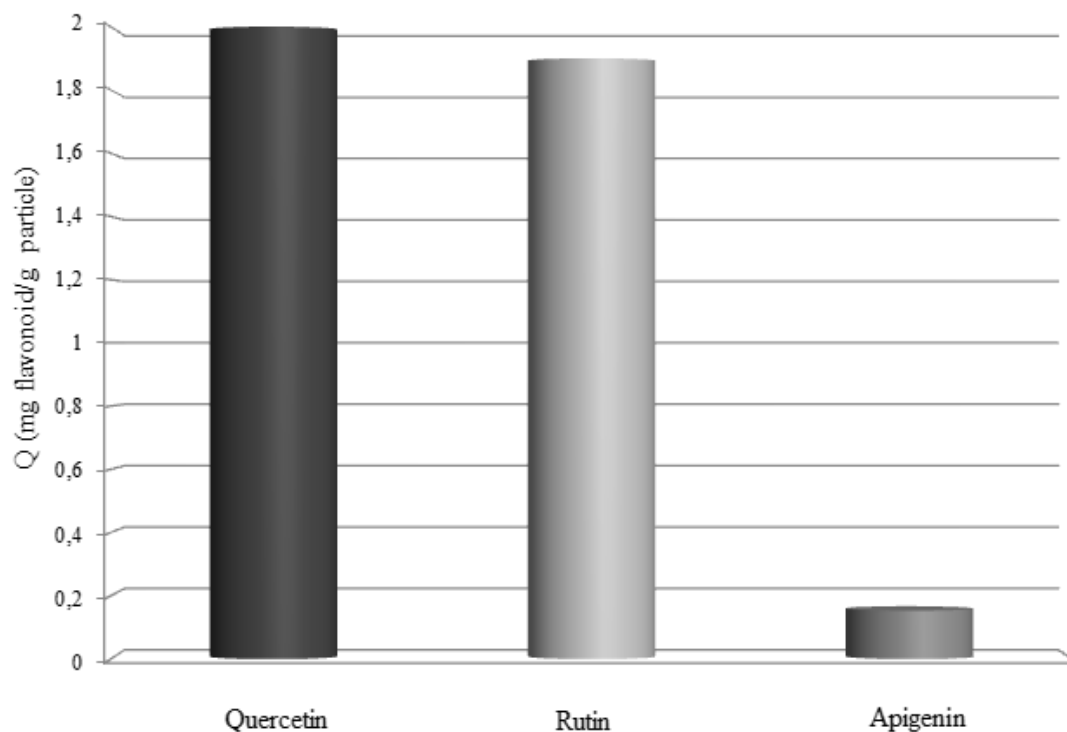
**Figure 7:** Amount of desorbed flavonoids (quercetin, rutin and apigenin) from BASPs after the adsorption, temperature: 20 ºC, initial flavonoid concentration: 0.02 mg/mL, pH: 8.5.

*Adsorption selectivity of BASPs towards ethyl acetate extract of the HP stem*

The adsorption of flavonoids from the ethyl acetate extract of the HP was compared to the HPLC peaks of the original extract as well as the unadsorbed and desorbed solutions. Fig. 8A shows various peaks *i.e.* original ethyl acetate extract (EtOAc), extract after adsorption (Ads), solution after desorption (Desp) and standards (quercetin and rutin). Ethyl acetate extract shows lots of peaks around 27-31 retention time in the chromatogram. The Desp chromatogram also contains peaks at that area. Probably they are peaks related to *vicinal*-diols containing flavonoids, or *cis*-diol sugars. BASPs has selectivity towards the stated diols, but this selectivity is unaffected by the molecular weight of the compounds. the zoomed area of the chromatogram (Fig. 8B) shows the presence of rutin and quercetin in the extract (EtOAc) that was successfully adsorbed by BASPs (Ads) and then desorbed (Desp). However, slight amount of rutin remained in the post-adsorption medium; probably due to the steric effect of rutin.
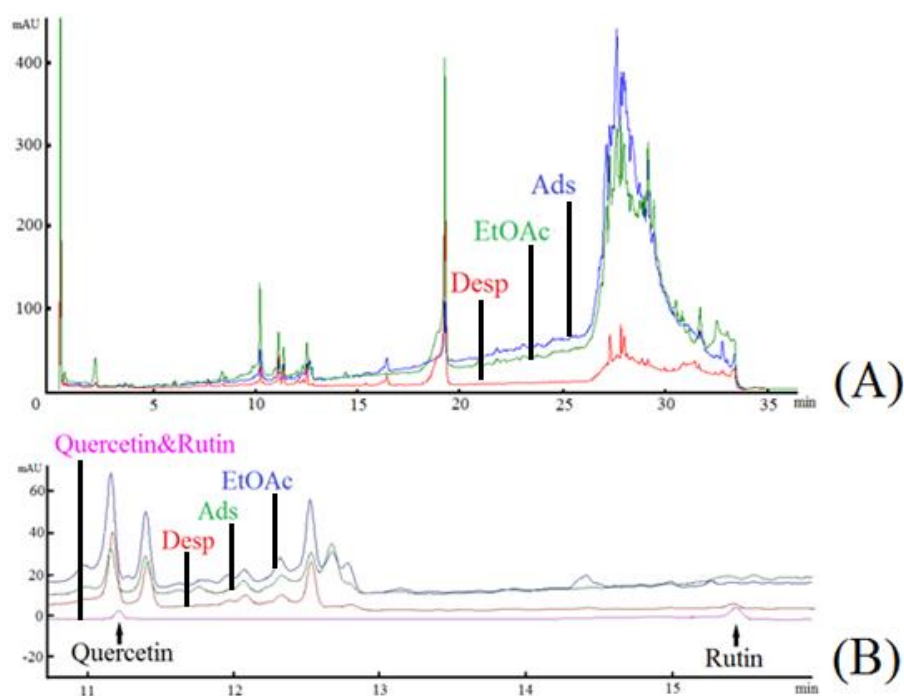
**Figure 8:** The HPLC chromatogram of original ethyl acetate extract of HP stems; (A) Retention time: 0-35 min, (B): Retention time: 10-16 min of (A) with Quercetin and Rutin model flavonoids.

The dry weight of the original ethyl acetate extract (EtOAc) solution, after adsorption (Ads) and of the desorbed solution (Desp) were calculated as 57.4 mg, 39.1 mg, and 18.3 mg, respectively. By using these three values in Eq. (1), the desorption yield was calculated as 100%. This result was obtained with BASPs after the 40th use. It means the prepared microparticles are able to be regenerated with no efficiency loss.

The total flavonoid content (mg flavonoid/g dry weight of extract) of the EtOAc, Ads, and Desp media were approximately determined to be 48.54 mg/g, 20.16 mg/g, and 35.89 mg/g, respectively, as shown in Fig. 9. In this figure, the total flavonoid content of the Desp medium is higher than that of the Ads medium, which indicates the selectivity of BASPs towards the flavonoids.
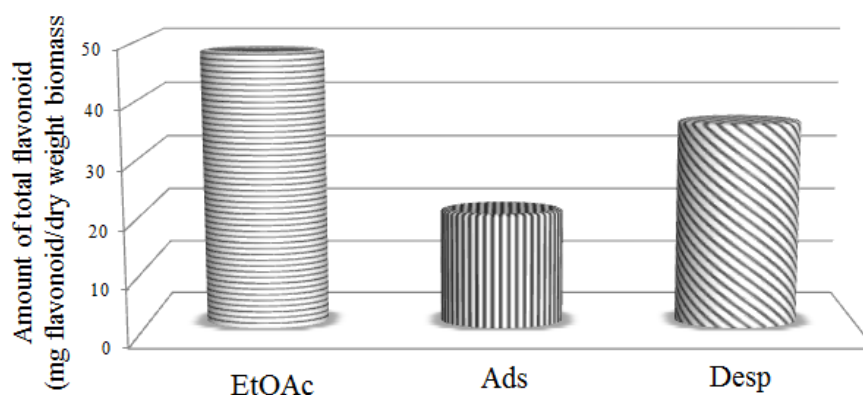
**Figure 9:** Total flavonoid content of the original solution of ethyl acetate extract of HP stems before adsorption (EtOAc), post-adsorption solution (Ads), and desorption solution (Desp).

**Antioxidant and antiradical activities**

The antioxidant activity results with the β-carotene and linoleic system for the ethyl acetate extract of the HP stems are shown in Fig. 10 (A). The antioxidant activities of the three media are in the following order: EtOAc > Desp > Ads. These results are parallel to the flavonoid content of the three media, as shown in Figure 9. According to these results, the adsorbed molecules provides slightly better antioxidant activity than the unadsorbed molecules. The amount of flavonoids in the ethyl acetate extract of the HP stems were reported to be high (38,39). In this study, antioxidant activity observed was higher that was also expected.

The rate of β-carotene bleaching of the ethyl acetate extract of the HP stems and its adsorption/desorption solutions are shown in Fig. 10 (B). An interesting result was observed in Fig. 10 (B) where the desorption solution exhibited a higher antioxidant activity rate than the ethyl acetate and post-adsorption (Desp) solutions.

According to the literature (40,41), flavonoid aglycones (*i.e.,* quercetin, kaempferol and biapigenin) have higher antioxidant activities as compared to other flavonoids. In contrast, the antiradical scavenging properties of glycoside-containing flavonols *i.e.,* rutin, hyperoside, isoquercitrin, and kaempferol were determined as higher than the other components. The base structure of BASP exhibits a hydrophilic character, but their surface is covered with space arms containing polar (amide groups and boronic acid tip) and apolar "$CH_2$" molecules due to APTS/APBA and glutaraldehyde molecules, respectively. A suitable apolar/polar ratio in the adsorbent causes a shift in the adsorption of flavonoids from plant extracts (12). While the increment in this ratio causes an increment in the nonspecific adsorption, its decrease results in a smaller adsorption capacity for flavonoids.

(A)



(B)



(C)
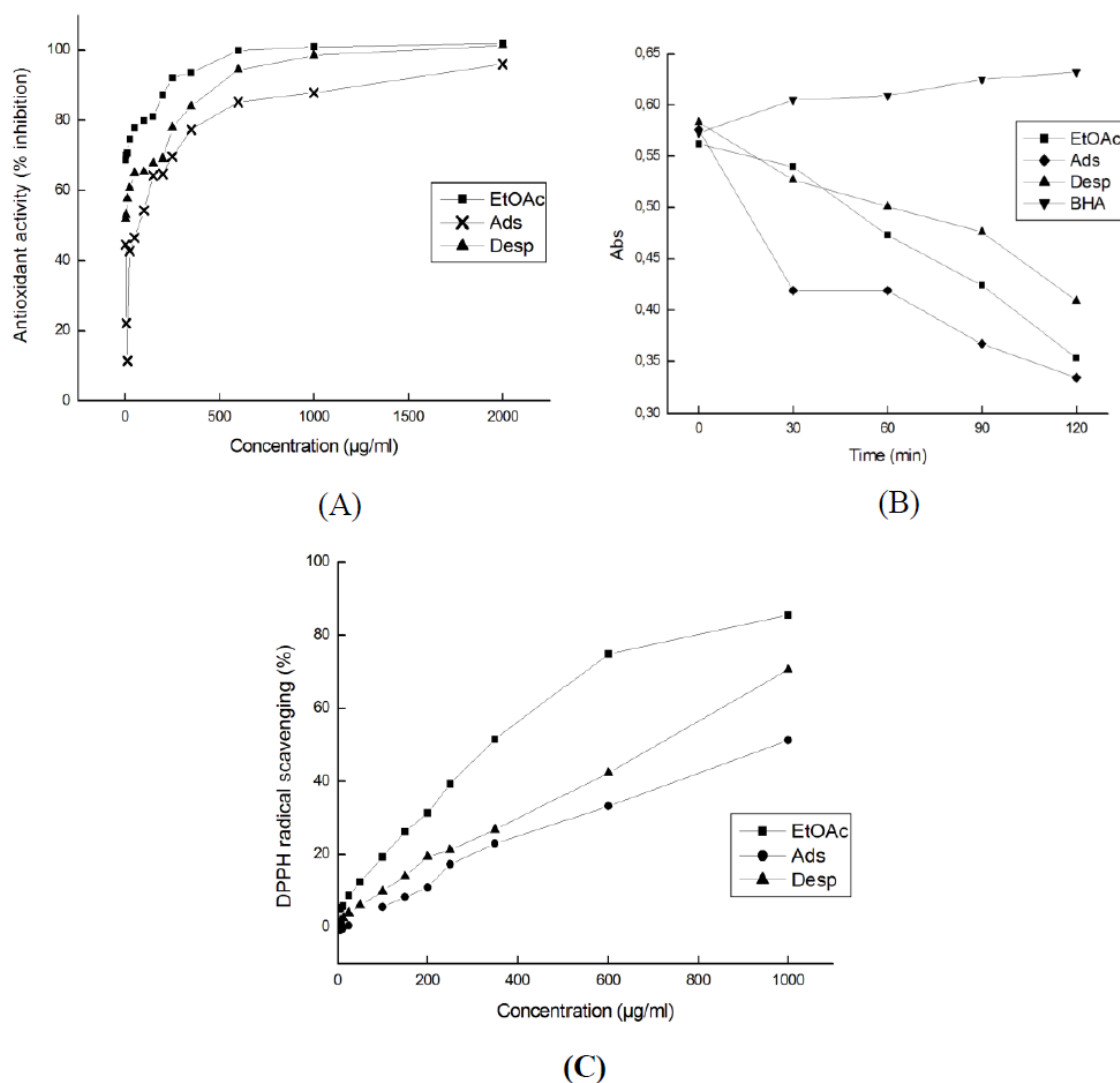
**Figure 10:** Antioxidant activity (A), rate of β-carotene bleaching (BHA: Butylated hydroxyanisole) (B) and DPPH radical scavenging (C) of the original extract solution of the ethyl acetate extract of the HP stems before adsorption (EtOAc), post-adsorption solution (Ads), and desorption solution (Desp).

Considering these observations, the behavior in Fig. 10 (B) can be clarified by adsorption of more apolar flavonoid aglycones bearing antioxidants rather than polar flavonol glycosides. It is likely that a suitable apolar/polar ratio in BASPs might cause quercetin-type flavonoid aglycones moving close to the spacing arm (Fig. 1) to generate a hydrophobic interaction with the hydrophobic sides of the connecting arm and boronic acid affinity interaction with the *cis*-and/or *vicinal*-diols on the boronic acid side groups while simultaneously applying slightly repulsive forces to flavonol glycoside-type molecules. However, there is a possibility for hydrogen bonding interactions between polar flavonol glycosides and the amine groups on spacing arm. Boronic acids prefer to bind *cis*-and/or *vicinal* diols. That is why, it interacted more with the rutin and quercetin as compared to the apigenin. As discussed in our previous study, flavonoid aglycones isolated by BASPs exhibit a high antioxidant capability (15). Therefore, isolated fractions containing more *cis*-

diol-containing flavonoid molecules exhibited high initial antioxidant velocity, as shown in Fig. 10 (B).

For DPPH radical scavenging (Fig. 10C), the trend in the radical scavenging capacity was approximately the same as that for the antioxidant activity shown in Fig. 10 (A). To compare DPPH activities, $EC_{50}$ (effective concentration for 50 % percent activity) values were calculated for EtOAc, Ads, and Desp as 350, 1000 and 730 (µg dwb/mL), respectively.

These results demonstrate that the DPPH activity of the Desp medium was higher than that of the Ads medium, which may be due to the greater adsorption of flavonoids possessing high antioxidant activity and DPPH radical scavenging properties (40).

**CONCLUSIONS**

The APBA-functionalized silica particles (BASPs) synthesized in this study exhibited selectivity towards *cis* ($sp^3$ carbons) as well as *vicinal* ($sp^2$ carbons) diols containing flavonoids. *Cis*-diol-containing flavonoids might be partially isolated with this new adsorbent. However, the presence of other polar/apolar groups present on the silica macroparticles may cause a decrease in the selectivity of the boronic acid groups. Therefore, the DPPH radical scavenging capacity and antioxidant activity of the desorption solution were determined to be lower than that of the original ethyl acetate extract but higher than the post-desorption (Desp) solution. A desorption yield of 100 % for BASPs demonstrates its for studying adsorption phenomena in plant extracts containing *cis*-diol type flavonoids. Uniform adsorbent particles produced in this research have the potential to be used in HPLC chromatography for effective isolating *cis* and/or *vicinal* diols containing compounds.

**ACKNOWLEDGMENTS**

**REFERENCES**

1. Rijke E, Out P, Niessen WMA, Ariese F, Gooijer C, Brinkman UAT. Analytical separation and detection methods for flavonoids. J. Chromatogr. A 2006; 1112:31-63.

2. Middleton E, Kandaswami C, Theoharides TC. The effects of plant flavonoids on mammalian cells:

implications for inflammation, heart disease, and cancer. Pharmacol. Rev. 2000; 52:673–751.

3. Havsteen BH. The biochemistry and medical significance of the flavonoids. Pharmacol. Ther. 2002; 96(2-3):67–202.

4. Georgetti SR, Casagrande R, Di Mambro VM, Azzolini AE, Maria J. Evaluation of the antioxidant activity of different flavonoids by the chemiluminescence method. Am. Assoc. Pharm. Sci. J. 2003; 5(2):1-4.

5. Walle T. Absorption and metabolism of flavonoids. Free Radic. Biol. Med. 2004;7:829-837.

6. Mak P, Leung YK, Tang WY, Harwood C, Ho SM. Apigenin suppresses cancer cell growth through ERB 1. Neoplasia 20068(11):896–904.

7. Bayard V, Chamorro F, Motta J, Hollenberg NK. Does flavanol intake influence mortality from nitric oxide-dependent processes? Ischemic heart disease, stroke, diabetes mellitus, and cancer in Panama. Int. J. Med. Sci. 2007;4(1):53–58.

8. He DH, Otsuka H, Hirata E, Shinzato T, Bando M, Takeda Y. Tricalysiosides A-G: rearranged ent-kauranoid glycosides from the leaves of tricalysia Dubia. J. Nat. Prod. 2002;65:685–688.

9. Aehle E, Grandic SR, Ralainirina R, Rosset SB, Mesnard F, Prouillet C, Maziere JC, Fliniaux MA. Development and evaluation of an enriched natural antioxidant preparation obtained from aqueous spinach (spinacia oleracea) extracts by an adsorption procedure. Food Chem. 2004;86:579-585.

10. Huang J, Liu Y, Wang X. Selective adsorption of tannin from flavonoids by organically modified attapulgite clay. J. Hazard Mater. 2008;160:382–387.

11. Singh SV, Gupta AK, Jain RK. Adsorption of naringin on nonionic (neutral) macroporus adsorbent resin from its aqueous solutions. J. Food Eng. 2008;86:259–271.

12. Geng X, Ren P, Pi G, Shi R, Yuan Z, Wang C. High selective purification of flavonoids from natural plants based on polymeric adsorbent with hydrogen-bonding interaction. J. Chromatogr. A 2009;1216:8331–8338.

13. Li J, Chase HA. Characterization and evaluation of a macroporous adsorbent for possible use in the expanded bed adsorption of flavonoids from ginkgo biloba l. J. Chromatogr. A 2009;1216:8730–8740.

14. Spacil Z, Novakova L, Solich P. Analysis of phenolic compounds by high performance liquid chromatography and ultra performance liquid chromatography. Talanta 2008;76:189–199.

15. Çetinkaya O, Duru ME, Çiçek H. Synthese and characterization of boronic acid functionalized macroporous uniform poly (4-chloromethylstyrene-co-divinylbenzene) particles and its use in the isolation of antioxidant compounds from plant extracts. J. Chromatogr. B 2012;909:51– 60.

16. Kamiya H, Mitsui M, Takano H, Miyazawa S. Influence of particle diameter on surface silanol structure, hydration forces, and aggregation behavior of alkoxide-derived silica particles. J. Am. Ceram. Soc. 2000;83(2):287–293.

17. Grün M, Lauer I, Unger KK. The Synthesis of micrometer- and submicrometer-size spheres of ordered mesoporous oxide MCM-41. Adv. Mater. 1997;9:254–257.

18. Kresge CT, Leonowicz ME, Roth WJ, Vartuli JC, Beck JS. Ordered mesoporous molecular sieves synthesized by a liquid-crystal template mechanism. Nature. 1992;359:710–712.

19. Qi L, Ma J, Cheng H, Zhao Z. Micrometer-sized mesoporous silica spheres grown under static conditions. Chem. Mater. 1998;10:1623–1626.

20. Stöber W, Fink A, Bohn E. Controlled growth of monodisperse silica spheres in the micron size range. J. Colloid. Interface Sci. 1968;26:62–68.

21. Unger KK, Kumar D, Grün M, Büchel G, Lüdtke S, Adam T, Schumacher, K, Renker S. Synthesis of spherical porous silicas in the micron and submicron size range : challenges and opportunities for miniaturized high-resolution chromatographic and electrokinetic separations. J. Chromatogr. A 2000;892:47–55.

22. Büchel G, Grün M, Unger KK, Matsumoto A, Kazuo T. Tailored syntheses of nanostructured silicas: control of particle morphology particle size and pore size. Supramolecular Science 1998;5(7):253-259.

23. Möller K, Kobler J, Bein T. Colloidal suspensions of nanometer-sized mesoporous silica. Adv. Funct. Mater. 2007;17:605-612.

24. Guerrero VV, Shantz DF. Amine-functionalized ordered mesoporous silica transesterification catalysts. Ind. Eng. Chem. Res. 2009;48:10375–10380.

25. Ramkumar A, Lal R. Silica nanoparticle tags for capacitive affinity sensors. Conf. Proc. IEEE Eng. Med. Biol. Soc. 2005;1:266-269.

26. Kecht J, Bein T. Microporous and mesoporous materials oxidative removal of template molecules and organic functionalities in mesoporous silica nanoparticles by H2O2 treatment. Microporous Mesoporous Mater. 2008;116:123–130.

27. Koopal LK, Yang Y, Minnaard AJ, Theunissen PLM, Riemsdijk WHV. Chemical immobilisation of humic acid on silica. Colloid. Surf. A 1998;141:385–395.

28. Park SW, Lee J, Hong SI, Kim SW. Enhancement of stability of GL-7-ACA acylase immobilized on silica gel modified by epoxide silanization. Process. Biochem. 2003;39:359-366.

29. Senel S. Boronic acid carrying (2-hydroxyethylmethacrylate)-based membranes for isolation of RNA. Colloid. Surf. A 2003;219:17-23.

30. Moreno MIN, Isla MI, Sampietro AR, Vattuone MA. Comparison of the free radical-scavenging activity of propolis from several regions of Argentina J. Ethnopharmacol. 2000;71(1–2):109–114.

31. Blois MS. Antioxidant determinations by the use of a stable free radical. Nature 1958;26:1199–1200.

32. İlhami G, Oktay M, Kireçci E, Küfrevioglu Öİ. Screening of antioxidant and antimicrobial activities of anise (pimpinella anisum L.) seed extracts. Food Chem. 2003;83:371-382.

33. Sing KSW, Everett DH, Haul RAW, Moscou L, Pierotti RA, Rouquerol J, Siemieniewska T. Reporting physisorption data for gas/solid systems with special reference to the determination of surface area and porosity. Pure&Appl. 1985;57(4):603-619.

34. Huck CW, Buchmeiser MR, Bonn GK. Fast analysis of flavonoids in plant extracts by liquid chromatography-ultraviolet absorbance detection on poly(carboxylic acid)- coated silica and electrospray ionization tandem mass spectrometric detection. J. Chromatogr. A 2001;943:33–38.

35. Weinstock BA, Yang H, Griffiths PR. Determination of the adsorption rates of aldehydes on bare and aminopropylsilyl-modified silica gels by polynomial fitting of ultra-rapid-scanning FT-IR data. Vib. Spectrosc. 2004;35:145–152.

36. Colthup NB. Spectra-structure correlations in the infra-red region. J. Optical Am. 1950;40:397-400.

37. Çiçek H. Nucleotide isolation by boronic acid functionalized hydrogel beads. J Bioact Compat Polym 2005;20:245-257.

38. Butterweck V, Jurgenliemk G, Nahrstedt A, Winterhoff H. Flavonoids from hypericum perforatum show antidepressant activity in the forced swimming test. Planta Med. 2000;66:3–6.

39. Barnes J, Anderson LA, Phillipson JD. St John's Wort (hypericum perforatum l.): a review of its chemistry, pharmacology and clinical properties. J. Pharm. Pharmacol. 2001;53:583–600.

40. Flausino OA, Zangrossi H, Salgado JV, Viana MB. Effects of acute and chronic treatment with

hypericum perforatum l. (li 160) on different anxiety-related responses in rats. Pharmacol. Biochem. Be. 2002;71:251–257.

41. Silva BA, Ferreres F, Malva JO, Dias ACP. Phytochemical and antioxidant characterization of hypericum perforatum alcoholi c extracts. Food Chem. 2005;90:157–167.

**RESEARCH ARTICLE**

# The Weathering Study of PC/ASA Alloy For Automotive Exterior Applications

**Sinan Öztürk[1a], Semih Ertürk[1], Gürkan Yılmazoğlu[1], Beyhan Haliloğlu[1], Halil İbrahim Okar[1]**

[1]TOFAŞ Türk Otomobil Fabrikası A.Ş., Istanbul Cad. No:574, Bursa 16389, Turkey

**Abstract:** Polycarbonates (PC) are used in automotive industry due to their high physical and mechanical properties like high impact resistance and ductility. Polycarbonates are blended with ABS (Acrylonitrile-Butadiene-Styrene) and ASA (Acrylonitrile-Styrene-Acrylate) terpolymers for interior and exterior applications of automotive components to achieve good physical and mechanical properties. Other reason for choosing such alloys for interior applications is the IZOD impact resistance requirement higher than 40 kJ/m$^2$. Recently, grades of PC/ASA with UV stabilization are developed for non-painted exterior applications. The aim of our study is to investigate whether new developed PC/ASA could be chosen for exterior applications of automotive industry. In this study, the samples are prepared from injection molding and the weathering performance of PC/ASA was tested by a weather-o-meter for 1500 h at a total of 1890 kJ/m$^2$ at 340 nm with a cut-off filter at λ<290 nm. The results are evaluated by FT-IR, DSC, TGA, and SEM. It has been observed that UV degradation of PC/ASA leads to several major changes in its IR spectrum like broad bands occurring in the hydroxyl region around 3300 cm$^{-1}$, and carbonyl stretching region increased intensity around 1728 cm$^{-1}$. The main degradations were based on photo-oxidation and photo-Fries rearrangement of PC. In our study, the photo-oxidation was followed by the color shift to yellowing of the polymer.

**Keywords:** PC/ASA Alloy, weathering, photo-oxidative degradation, automotive exterior applications, thermoplastic.

**\*Corresponding author. E-mail:** suleymansinan.ozturk@tofas.com.tr

## INTRODUCTION

It is possible to modify some properties of deficient polymers in a blend. When the polymers are compatible to be mix in a matrix, the resulting properties are studied for special applications. By controlling the formulation of the material, one can achieve a balanced property with synergistic effect. Polycarbonate (PC) has difficulties in production process due to high melt viscosity. PC has high modulus, high toughness and high impact strength and suitable to be used for blending with other polymers. In the literature, blending with a rubber-toughened thermoplastic Acrylonitrile-Butadiene-Styrene (ABS) has been investigated for observing the mechanical properties (1). Such studies on PC/ABS blends have confirmed that the poor chemical resistance and thermal stability are the main drawbacks of PC/ABS. The butadiene rubber in ABS undergoes chemical aging under UV radiation which decreases the mechanical properties and changes the color (2). ASA terpolymer where butadiene rubber in ABS is replaced with acrylic rubber solves the problem of butadiene degradation. In the case of PC and Styrene-Acrylonitrile (SAN) blends, compatibilizer is required to the blends of PC/ABS and PC/ASA for enhancing the interaction energy. PC and ABS are not totally miscible and requires polar groups and reactive functional polymers for decreasing the interfacial tension between phases (3). Especially for automotive applications where high toughness is required, the interfacial interaction is necessary for welding operations where poor adhesion at welding results into failure (4). Further studies with different compatibilizers were tested for increasing the mechanical properties (5). Such former studies have revealed that thermal and mechanical properties are improved by blending PC and ASA. On the contrary, the drawback of PC/ASA blend is the degradation of PC under UV radiation which is the main objective of this study. The effect of UV degradation on properties and morphology is described.

## MATERIALS AND METHODS

### Materials
The material used was Luran S KR2863 C (Ineos-Styrolution). (Vicat Method A: 150 °C, MFI 260 °C, 5 kg: 18 cm$^3$/10 min, HDT A 1.80 MPa: 109 °C, Izod Notched Method A 23 °C: 600 kJ/m$^2$) The material was injected molded as a complete part with the injection parameters requested by the material supplier. The specimen for UV radiation was prepared by cutting the complete part from the flat surface in dimensions of 65 mm x 140 mm where thickness was 4 mm.

### Accelerated Weathering Test
The aging test was performed according to FIAT 50451 Standards for parts used in vehicle exterior which is used for understanding the behavior of the material under atmospheric agents like light, relative humidity, and temperature. The exposure time was up to 1500 hours. Atlas

Xenon test chamber was used with a black panel temperature of 65 °C ± 3 °C where the air in the chamber was 40 °C ± 3 °C. A Xenon lamp at 340 nm and 0.35 W/m$^2$ light intensity with λ<290 nm cut-off filter (borosilicate/borosilicate) was used. The total irradiation was 1890 kJ/m$^2$. The cycle parameters exposed to the samples were 18 minutes of humidifying and light, and 102 minutes of drying and light (the relative humidity during drying was 60%).

## Characterization

**FT-IR:** The samples are measured by Bruker Tensor II within the range 4000 - 400 cm$^{-1}$. The spectrum was collected by a Diamond crystal attenuated total reflectance (ATR) module, using 24 sample scans and resolution of 4 cm$^{-1}$. The effect of aging on hydroxyl region, carbonyl groups and aromatic groups attached to carbonyl groups were observed.

**Spectrophotometry:** The samples are measured by benchtop spectrophotometer Datacolor 500 (Datacolor). The color measurements were performed by pulsed Xenon flash lamp in the range of 360-700 nm. The sample data was evaluated after obtaining L value (positive ΔL darkness, negative ΔL lightness), a value (positive means red, negative means green) and b value (positive means yellow, negative means blue).

**TG/DTG**: The thermogravimetric analysis was performed using a Mettler Toledo TGA/DSC 1 thermogravimetric analyzer from 30 °C to 600 °C at 20 °C/min under nitrogen atmosphere (60 mL/min). Then the gas is switched to oxygen (60 mL/min) after an isothermal step for 5 minutes and heating up to 800 °C at 20 °C/min. The sample size used was about 5 mg. The degradation onset, degradation maximum, and final degradation temperatures were observed.

**DSC:** The glass transition temperature ($T_g$) of the acrylic rubber, acrylonitrile/styrene and polycarbonate regions were determined by a differential scanning calorimeter (DSC). The test was performed by Netzsch F204. The parameter used was: the temperature range was between -120 °C and 180 °C, two times heating and cooling was applied with a rate of 20 °C/min. The nitrogen flow was 70 mL/min. The second heating curve is used for evaluation. The sample weight was about 5 mg.

**SEM and EDX:** The samples after aging test was examined with SEM Tescan Vega3 XMU (20 kV) and EDS Bruker XFlash 6|30. The coating of the surface was performed by sputtering technique of thin gold-palladium layer before examination.

**RESULTS AND DISCUSSION**

**FT-IR**

After the injection molding of the part, the part is cut from the flat surface. The samples are tested for aging up to 1500 h. The samples are taken out for FT-IR measurement for intermediate time intervals of 250 h, 500 h, 750 h, 1000 h, 1250 h, and 1500 h. In Figure 1, the FT-IR measurements are taken from three different regions and on the same position. The absorbance obtained after averaging three measurements were used for calculating the area under the peak. The area change with increasing amount of irradiation has been plotted in terms of carbonyl groups (1728 cm$^{-1}$) and aromatic groups attached to carbonyl groups (1590 cm$^{-1}$). In Figure 2, the absorbance area of carbonyl groups after 500 h is increasing till 1250 h and in between 1250 h and 1500 h, the absorbance area increase is slowed down. A similar change was also observed for the aromatic groups attached to carbonyl groups. The photo-oxidation of PC has been initiated by UV and oxygen. Up to 500 h, the PC domains did not degrade significantly which could be due to UV stabilizers. In between 500 h and 1250 h, the degradation was more severe. The degradation reactions are initiated and accelerated by the decreasing amount of UV stabilizers. At this stage, yellow photolytic species namely phenylsalicylates, dihydroxybenzophenones, dihydroxybiphenyl and hydroxydiphenyl ether groups were formed (6–8). Due to the humidity in the aging parameters, the photo-yellowing was also accelerated by the chain-scission mechanism which resulted into lower molecular weight polar polymers; consequently the surface was more vulnerable to erosion through hydrolysis (9). After 1250 h, the surface degradation was slowed down by completion of the active sites in PC degradation species and the penetration of the oxygen into the deeper layers was slowed down. After this stage, the photo-oxidation of PC was reduced by the shielding of the polymer with the formation of dihydroxybenzophenone and yellow species (10).
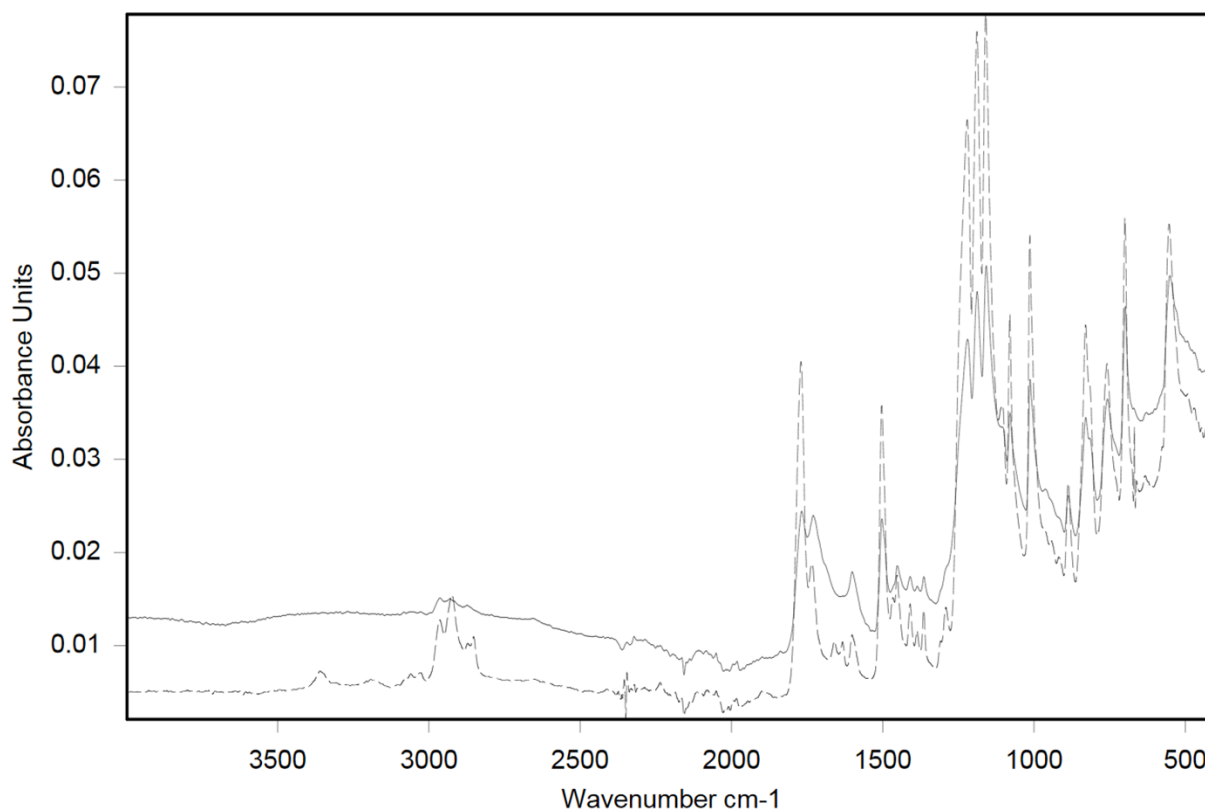
**Figure 1:** FT-IR ATR spectra of PC/ASA before (--) and after aging 1500 h (—).
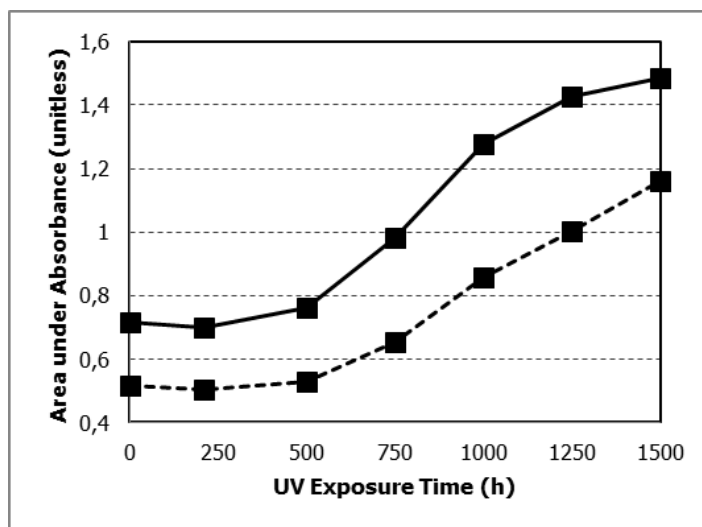


**Figure 2:** Area under absorbance at carbonyl region (—) and aromatic groups attached to carbonyl groups (--) by UV exposure time.

**Spectrophotometry**

The color change of the surface was also measured by the same time intervals. In Table 1, the b value referring to the yellowness of the sample is reported. The surface yellowness was increased after 500 h which refers to the formation of yellow degradation species. The increase was not

slowed down in between 1250 h and 1500 h referring to the fact that the hydrolysis of degradation products by chain-scission was initiated. It is suggested that after long exposure times, the yellowness index increases where degradation continues by photo-oxidation of photo-Fries products (11). The yellowness of the surface decreased after washing the polar degradation byproducts from the surface.

**Table 1:** The color change after UV exposure without washing is reported. *The color change after washing the surface.

|   | 0 h | 250 h | 500 h | 750 h | 1000 h | 1250 h | 1500 h | 1500 h* |
|---|-----|-------|-------|-------|--------|--------|--------|---------|
| **L** | 29.13 | 29.13 | 29.30 | 29.97 | 29.34 | 30.19 | 28.79 | 28.81 |
| **a** | -0.18 | -0.18 | -0.23 | -0.02 | -0.14 | -0.21 | -0.13 | -0.11 |
| **b** | -0.30 | -0.37 | -0.34 | 0.06 | 0.00 | 0.80 | 2.13 | 0.54 |

**TG/DTG**

The TG/DTG curves of PC/ASA before and after aging for 1500 h have been evaluated. In Figure 3, two stages of degradation were observed where the first and second degradation peaks are close to each other. The lower degradation temperature was attributed to the ASA polymers and higher degradation temperature was attributed to the PC polymer in the PC/ASA blend. In Table 2, after the aging the decomposition temperature of both peaks has slightly shifted to the higher temperature. With aging, low molecular mass byproducts have been formed and due to the mobility of the byproducts, the decomposition peak temperature could have shifted to slightly higher temperatures. Since UV degradation has only affected the surface layer and not into the inner layers, the degradation peak temperature did not change drastically.
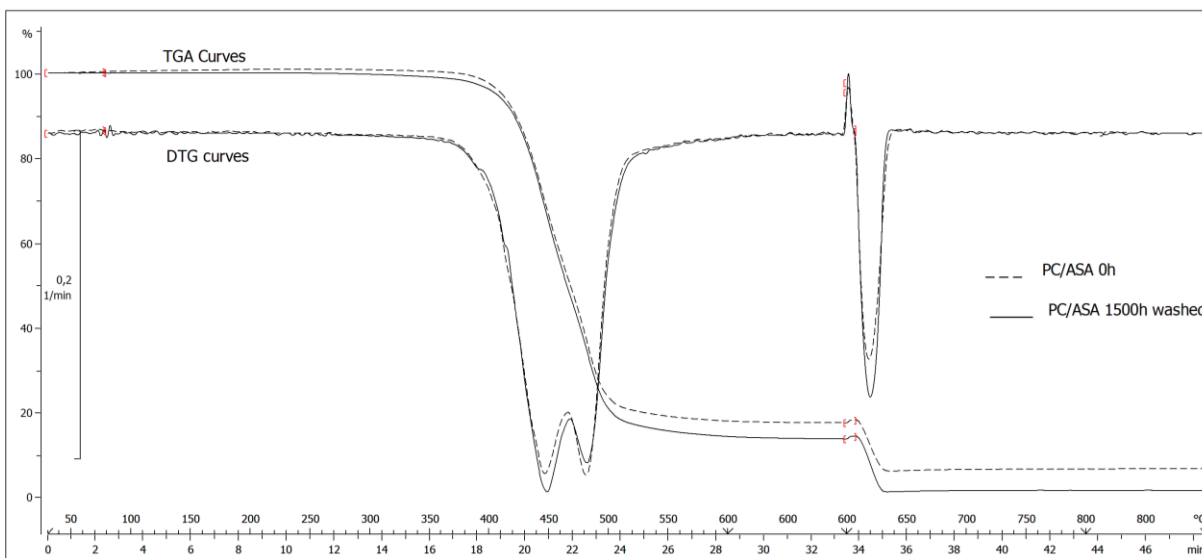


**Figure 3:** TG/DTG curves representing PC/ASA polymer before aging (--) and 1500 h aging after washed (—).

**Table 2:** Representative TG/DTG data of PC/ASA polymer before aging and washed after aging.

| Sample | TGA Degradation Temperature (°C) | | DTG Degradation Peak Temperature (°C) | |
| --- | --- | --- | --- | --- |
| | Onset | End | ASA phase | PC phase |
| Before | 412 | 495 | 442 | 476 |
| After 1500h | 413 | 496 | 444 | 477 |

## DSC

The DSC curve has been evaluated before aging and after aging 1500 h (washed) samples. In Figure 4, three glass transition temperatures were detected. The $T_g$ of polycarbonate was at 141≡C, $T_g$ of acrylonitrile/styrene was at 109 °C and $T_g$ of acrylate was about -44 °C. No major change in the $T_g$ was detected which could be attributed that the amorphous polymers PC and SAN phase have not changed the compatibility. The UV exposure did not penetrate to the deeper layers of the sample.
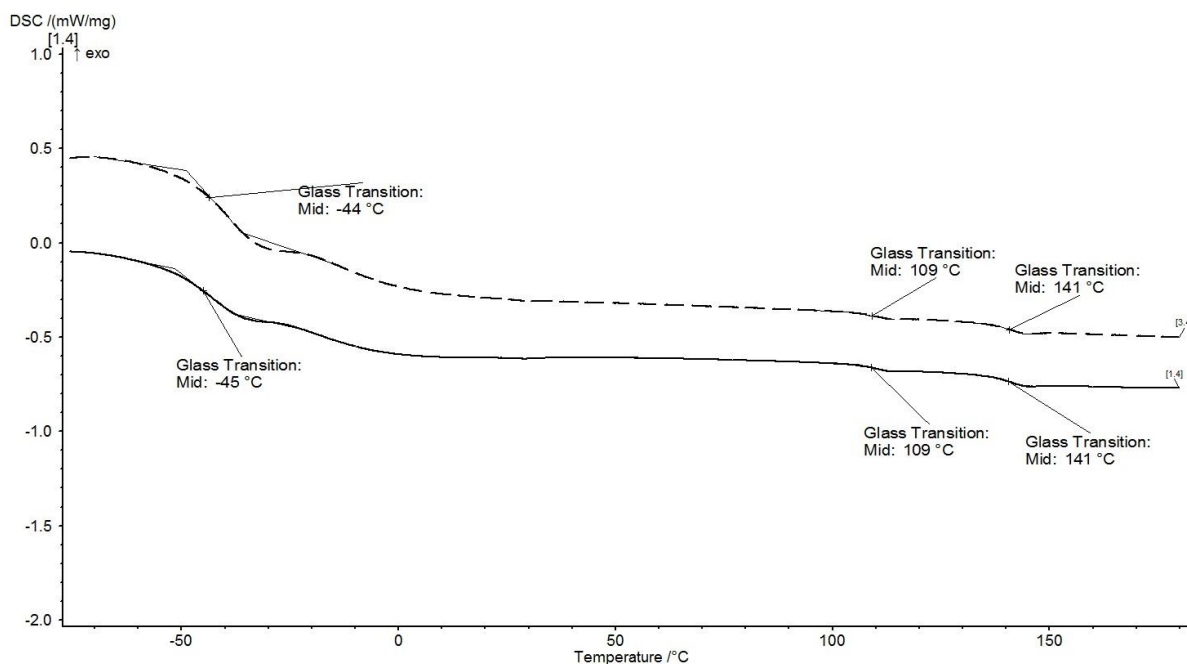


**Figure 4:** DSC curve representing $T_g$ of PC/ASA polymer before (--) and washed after aging (—).

## SEM and EDX

The morphology of the surface after aging was examined by SEM and EDX. The surface of the samples are washed with distilled water and dried with pressurized air. Both the unwashed surface and washed surface have been investigated in order to understand the changes in surface morphology. The unwashed surface after UV radiation for 1500 h was shown in Figure 5. A homogenous distribution of the inorganic fillers which were coming out from the polymer matrix can be observed. Most of the inorganic fillers were more visible meaning that the chemical and

physical detachment was almost completed. In Figure 6, after washing the samples with water and dried with pressurized air, the inorganic fillers were diminished meaning that they have been washed out. When the surface morphology of the washed surface was examined, it has been observed that inorganic fillers are embedded into the matrix. As the humidity forms water soluble polar degradation products after chain-scission, the inorganic filler is detached from the matrix by leaving hollow surface. When EDX analysis was performed on the inorganic filler, carbon, oxygen, titanium, zinc and tin was observed (Figure 7). Metal oxides, mainly titanium dioxide, zinc oxide, and tin oxide, could be used as a UV stabilizer or as a pigment in the matrix. Carbon black is the light screening pigment and blocks UV radiation in most of the polymers. On the other hand, fading pigments are used to compensate the color change throughout the UV exposure. Such pigment masks the color changes and stabilizes the color of the polymer. Until 500 h, the color of the polymer surface was shielded by such stabilizers. The inorganic fillers observed in our analysis is therefore could be regarded as the color fading pigment but also UV stabilizer.
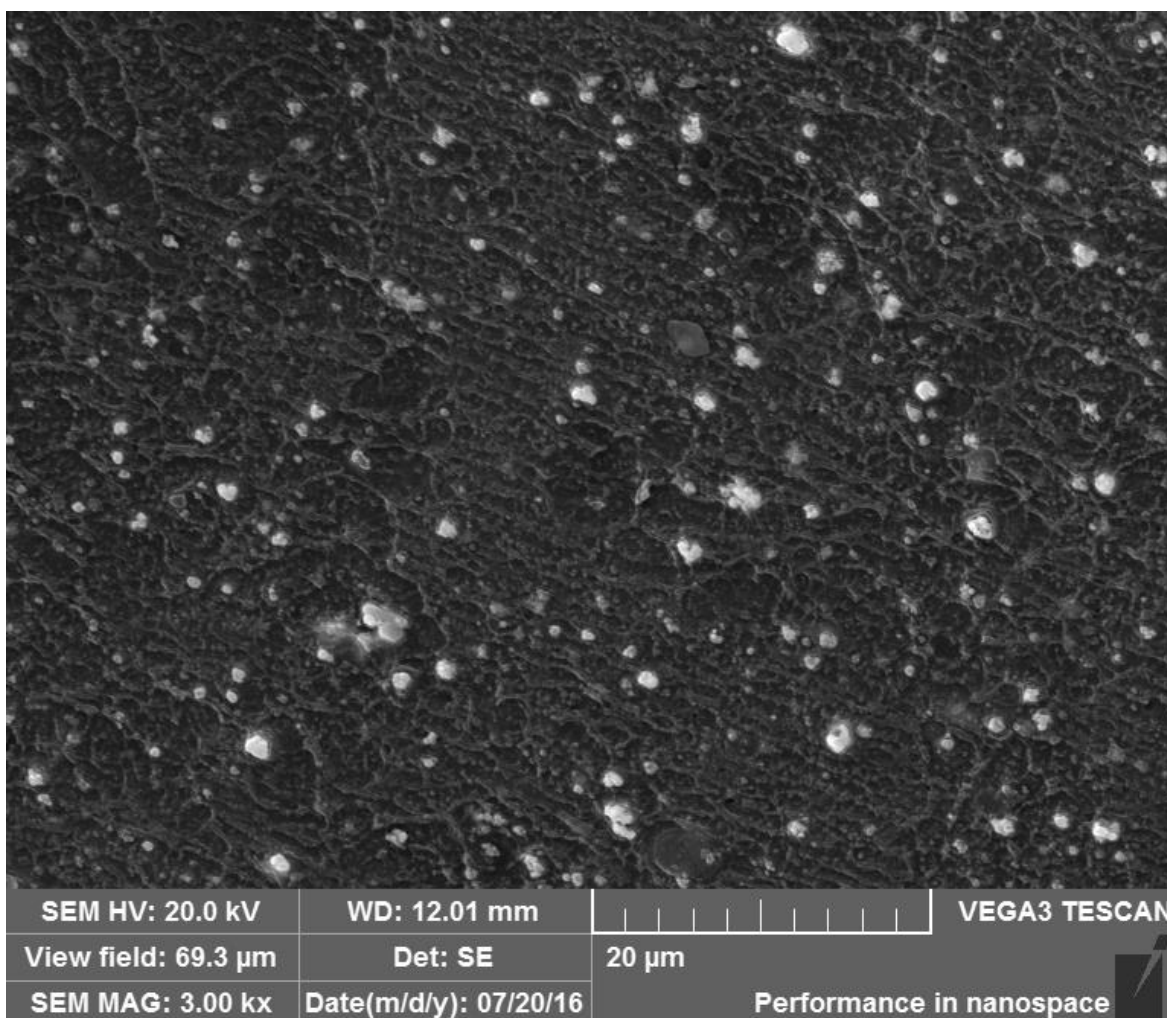


**Figure 5:** SEM of PC/ASA polymer after aging 1500 h before washing.

| SEM HV: 20.0 kV | WD: 11.36 mm | | VEGA3 TESCAN |
| View field: 69.1 µm | Det: SE | 20 µm | |
| SEM MAG: 3.00 kx | Date(m/d/y): 07/20/16 | | Performance in nanospace |
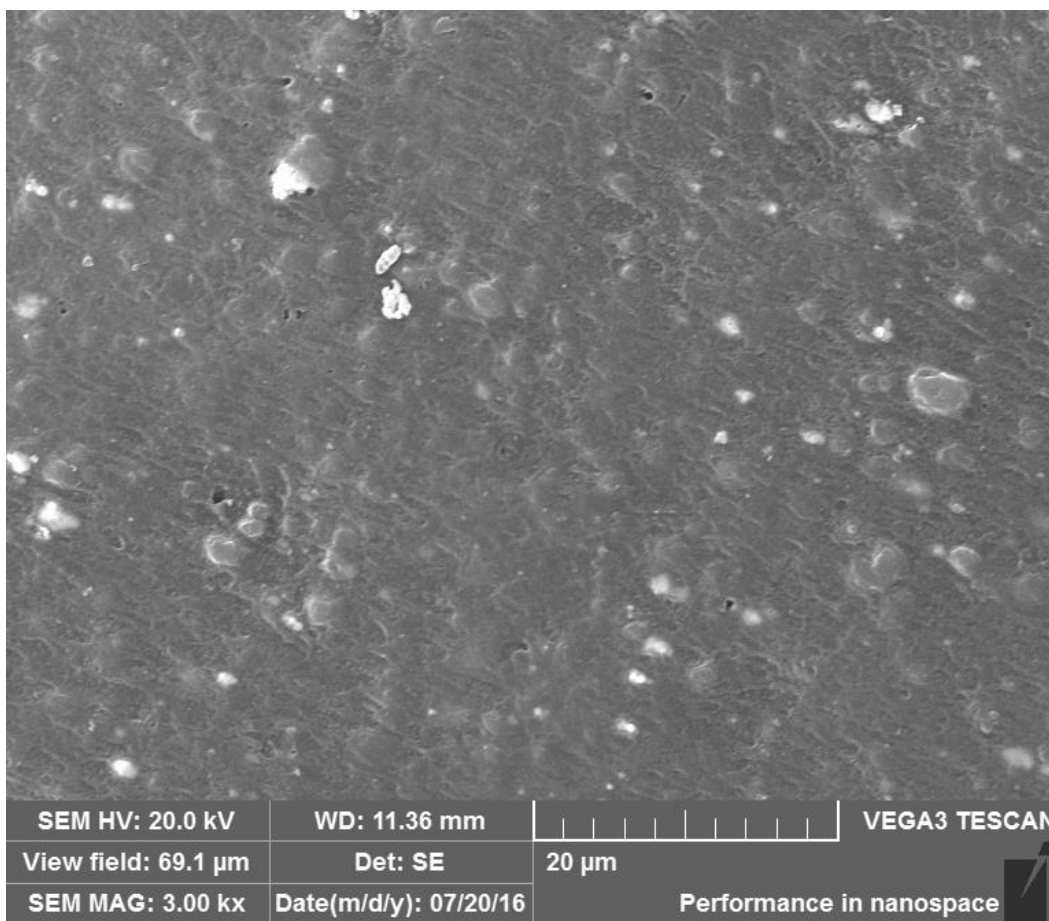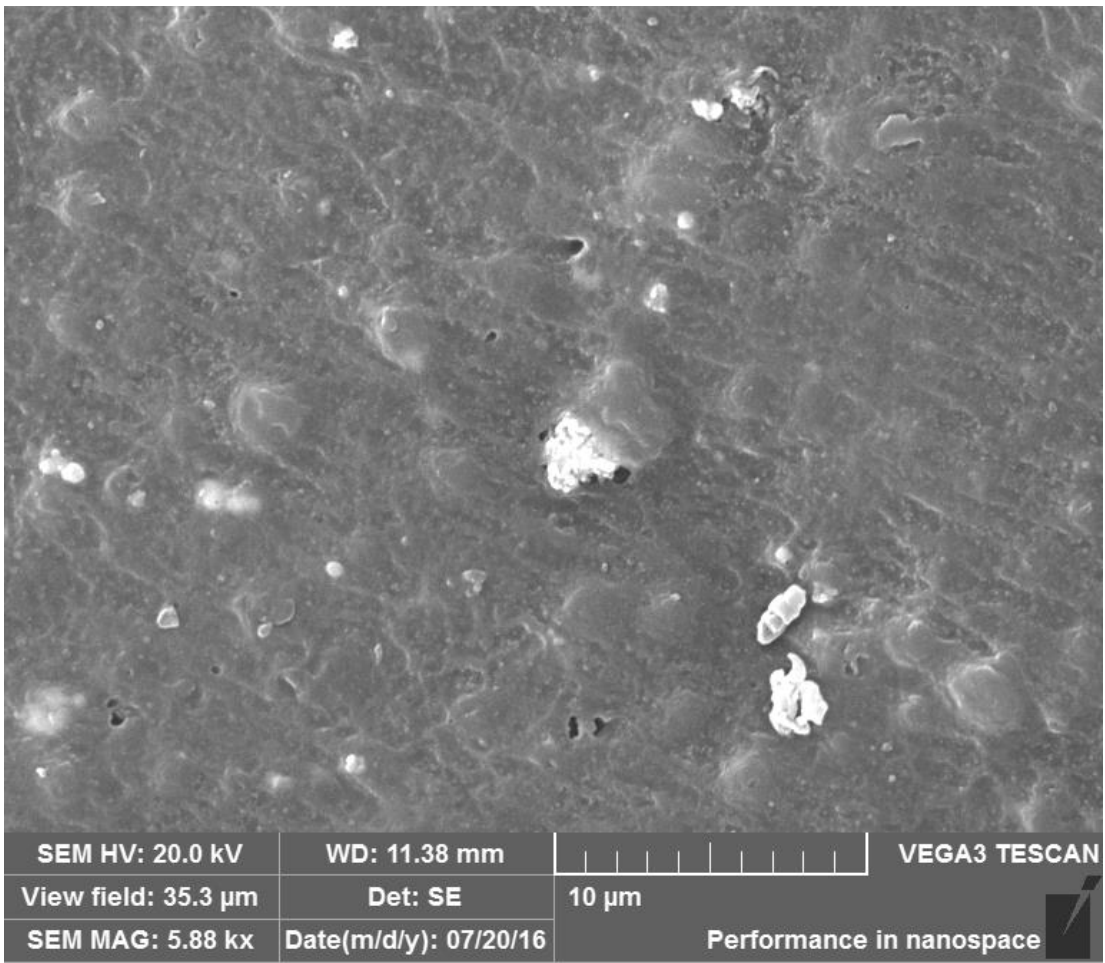
**Figure 6:** SEM of PC/ASA polymer after aging 1500h (washed surface).
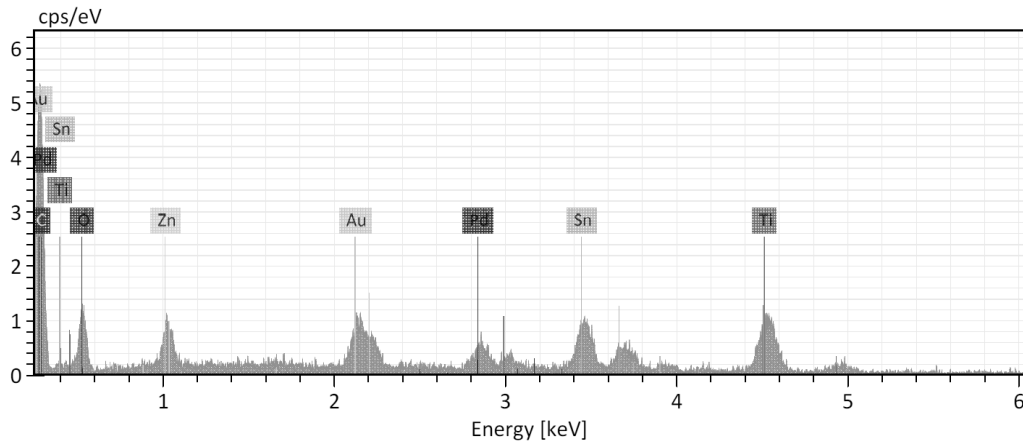


**Figure 7:** EDX on the inorganic spot of PC/ASA polymer after aging 1500 h (washed surface).

**CONCLUSION**

As PC/ASA has good chemical, thermal and mechanical properties, the polymer blend could have been chosen for the exterior applications of automotive industry. Since the polymer matrix of PC/ASA has UV stabilizer, the UV exposure performance for 1500 h at a total of 1890 kJ/m$^2$ was controlled by a weatherometer. The result showed that the degradation of the polycarbonate is accelerated by the UV radiation in the presence of oxygen and humidity. The yellowness of the surface was controlled in time intervals and it has been observed that up to 500 h, the color change is within the control limits. After exposure of sample for 500 h, as the UV radiation degrades the polycarbonate and color fading pigment is detached from the polymer matrix, the UV stabilization effect on the polymer is lost. After 500 h, the predominant UV degradation reactions are photo-Fries rearrangement, photo-oxidation, chain-scission and hydrolysis.

DSC and TGA studies have revealed that no major changes in the thermal properties have occurred. In the FT-IR study, a possible degradation of polycarbonate has been reported in parallel to the previous studies proposed as hydroxyl and carbonyl group formation, chain scission initiated by radicals from the methyl site, recombination reaction, and hydrolysis.

SEM image showed a good dispersion of the inorganic filler. At the end of the aging, most of the inorganic fillers on the surface were able to be washed off by water and pressurized air. The yellowness of the surface has been decreased after washing the water soluble polar degradation byproducts. Nevertheless, still some inorganic filler which were embedded in the structure was visible where others left the surface by leaving hollows on the surface.

In conclusion, PC/ASA developed for application of automotive industry is suitable for interior applications which are not directly exposed to sunlight. On the other hand, it is not applicable to exterior application due to the degradation of PC by UV, oxygen and humidity.

**REFERENCES**

1. Krache R, Debah I. Some Mechanical and Thermal Properties of PC/ABS Blends. Mater Sci Appl. 2011;2(5):404–10.

2. Cheng TW, Keskkula H, Paul DR. Property and morphology relationships for ternary blends of polycarbonate, brittle polymers and an impact modifier. Polymer. 1992 Jan 1;33(8):1606–19.

3. Liu Y, Li H, Ding X, Pan JZW, Cai R. Effect of the compatibilizers on Polycarbonate (PC)/acrylonitrile-butadiene-styrene (ABS) blend. Am J Mater Res. 2014;1(3):48–52.

4. Semba T, Hamada H. Weld Line Strength in PC/ABS Injection Moldings. Int Polym Process. 1999 01;14(4):365–9.

5. Kang MS, Kim CK, Lee JW. PC/ASA blends having enhanced interfacial and mechanical properties. Korea Aust Rheol J. 2006 01;18(1):1–8.

6. Andrady AL, Searle ND, Crewdson LFE. Wavelength sensitivity of unstabilized and UV stabilized polycarbonate to solar simulated radiation. Polym Degrad Stab. 1992;35(3):235–47.

7. Clark DT, Munro HS. Surface and bulk aspects of the natural and artificial photo-ageing of Bisphenol A polycarbonate as revealed by ESCA and difference UV spectroscopy. Polym Degrad Stab. 1984;8(4):195–211.

8. Pryde CA. Weathering of Polycarbonates: A Survey of the Variables Involved. In: American Chemical Society, Polymer Preprints, Division of Polymer Chemistry. ACS, Div of Polymer Chemistry; 1984. p. 52–3.

9. Rivaton A, Sallet D, Lemaire J. The photo-chemistry of bisphenol-A polycarbonate reconsidered: Part 3—Influence of water on polycarbonate photo-chemistry. Polym Degrad Stab. 1986;14(1):23–40.

10. Tjandraatmadja G., Burn L., Jollands M. Evaluation of commercial polycarbonate optical properties after QUV-A radiation—the role of humidity in photodegradation. Polym Degrad Stab. 2002;78(3):435–48.

11. Factor A, Chu ML. The rôle of oxygen in the photo-ageing of bisphenol-A polycarbonate. Polym Degrad Stab. 1980 Sep 1;2(3):203–23.

# Synthesis of New *N*-Phthalimide Substituted Tricyclic Imide Containing Isoxazoline and Bispiro Functional Group as Possible Anti-cancer Agents

## Omer Tahir Gunkara*, Nuket Ocal

Department of Chemistry, Yildiz Technical University, Davutpasa Campus Istanbul 34220, Turkey

**Abstract:** [3+2]-Cycloaddition reactions of *N*-phthalimide substituted tricyclic imide were studied to synthesize their isoxazoline and bispiro derivatives in excellent yields. All new synthesized compounds have been characterized by their FTIR, $^1$H NMR, $^{13}$C NMR, GC/MS and LC/MS (HRMS) analyses.

**Keyword:** [3+2]-Cycloaddition reaction, Azomethine ylide, Bispiromolecules, Isoxazolines, Tetracyclic imides.

**\*Corresponding author.** E-mail: gunkara@yildiz.edu.tr Tel +90-2123834193.

## INTRODUCTION

In recent years, tricyclic imides have been found in many drug molecules. Ocal and co-workers (1-3) have also conducted various investigations on tandospirone which is an antidepressant in Asia and has tricyclic imide structure (4-6). Imides are also very useful intermediates in the synthesis of various natural products (7-12).

In the class of heterocyclic compounds which form the basis of the drug chemistry, isoxazolines have an important place in terms of biological activity due to the oxygen and nitrogen atoms in their structure, are commonly found in natural compounds and pharmaceuticals; they are also versatile synthetic blocks in organic synthesis (13-21).

The most important place in the formation of the isoxazoline, the five-membered ring at the stages of organic synthesis is [3 + 2]-cycloaddition reactions. In this study, 1,3-dipolar adducts were obtained with oximes to obtain the isoxazoline ring (22-24). On the other hand, the reaction of azomethine ylides as 1,3-dipoles (3, 25) with olefinic dipolarophiles forms highly substituted five-membered ring nitrogen heterocycles. This extremely versatile and atom-economical process has been applied toward the syntheses of substituted prolines, which can be used as new catalysts (26, 27) and served as important motifs in many biologically active molecules (28-30).

## EXPERIMENTAL

### Materials and Methods

All reagents and solvents were obtained from commercial suppliers and were used without further purification. The solvents were dried by standard procedures. Reactions were monitored using TLC. Visualizations of the chromatograms were performed with UV light, $KMnO_4$ or Vanillin stain. All melting points are uncorrected and were determined on a Gallenkamp digital thermometer. IR spectra were obtained with a Perkin Elmer Spectrum One FTIR Spectrometer and are reported in terms of the frequency of absorption ($cm^{-1}$). $^1H$ NMR and $^{13}C$ NMR spectra were recorded on a Bruker Avance III-500 MHz NMR spectrometer relative to tetramethylsilane, with coupling constant (J) values in Hertz (Hz). Peak multiplicities are designated by the following abbreviations: s, singlet; d, doublet; dd, double doublet; t, triplet; dt, double triplet; m, multiplet; br, broad. Mass spectra were measured on an Agilent 6890N/5973 GC/IMSD system. High-resolution mass spectra were acquired in the positive ion mode using an Agilent G6530B TOF/Qtof Mass spectrometer.

**Synthesis and Characterization**

*Synthesis of Bicyclic Endic Anhydride* **(1)** (31)

Bicyclic endic anhydride **1** was prepared with freshly distilled cyclopentadiene and maleic anhydride in ethyl acetate at 0 °C with the known procedure (31). White crystals, Yield 82%, m.p. 165-167 °C, $R_f$: 0.42 (20:1, diethyl ether/2-propanol), IR (ATR) 2982, 2956, 1840, 1764, 1666, 1450, 1333, 1228, 1194 cm$^{-1}$, $^1$H NMR (CDCl$_3$, 500 MHz) δ 6.31 (2H, m, H-5, H-6), 3.58 (2H, m, H-2, H-3), 3.51 (2H, m, H-1, H-4), 1.78 (2H, m, H-7a, H-7s) ppm, $^{13}$C NMR (CDCl$_3$, 125 MHz) δ 171.9 (C=Ox2), 136.1 (C-5, C-6), 53.3 (C-2, C-3), 47.7 (C-1, C-4), 40.7 (C-10) ppm, GC-MS (*m/z*) 164 (M$^+$), 121 (C$_8$H$_8$O), 92 (C$_7$H$_8$), 66 (C$_5$H$_6$).


*Synthesis of N-aminobicyclo[2.2.1]hept-5-ene-2-endo,3-endodicarboximide* **(2)** (32)

A solution of hydrazine hydrate (0.6 mL) was added drop wise to bicyclic endic anhydride **1** (1.25 g) in benzene under nitrogen atmosphere. The resulting mixture was stirred at room temperature for 4 hours. White solid was filtered and recrystallized with isopropyl alcohol (32). White crystals, Yield 65%, m.p. 145-147 °C, $R_f$: 0.57 (5:1, ethyl acetate/*n*-hexane), IR (ATR) 3337, 2971, 2953, 2879, 1764, 1691, 1458, 1397, 1207, 1195, 1133 cm$^{-1}$, GC-MS (m/z) 178 (M$^+$), 162 (M$^+$-NH$_2$), 112 (C$_4$H$_2$O$_2$N$_2$), 92 (C$_7$H$_8$), 66 (C$_5$H$_6$).
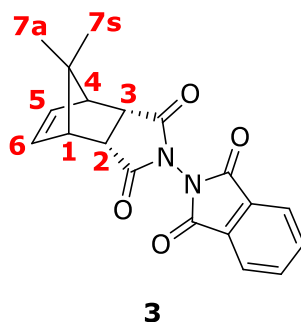


**Figure 1:** Numbering of title compounds.


*Synthesis of N-(1H-isoindole-1,3-dionyl)bicyclo[2.2.1]hept-5-ene-2-endo,3-endodicarboximide* **(3)** (32)

Compound **2** (0.890 g, 5 mmol) was dissolved in 10 mL of acetic acid. Phthalic anhydride (0.740 g, 5 mmol) was added to the solution. The resulting mixture was stirred at reflux overnight. After cooling room temperature, saturated NaHSO$_3$ solution (50 mL) was added, and the mixture was extracted with EtOAc. The aqueous layer was dried over MgSO$_4$, filtered, and concentrated. The product obtained as a brown solid (32). Brown solid, Yield 97%, m.p. 203-205 °C, $R_f$: 0.60 (1:1, ethyl acetate/*n*-hexane), IR (ATR) 2959, 2868, 1737, 1704, 1595, 1468, 1364, 1346, 1232, 1179, 1120 cm$^{-1}$, $^1$H NMR (CDCl$_3$, 500 MHz) δ 7.88-7.93 (2H, m, Ar-*H*), 7.80-7.81 (2H, m, Ar-*H*), 6.33 (2H, brs, H-5, H-6), 3.51 (2H, brs, H-2, H-3), 3.46 (2H, brs, H-1, H-4), 1.82 (1H, d, *J* = 9.14 Hz, H-7s), 1.60 (1H, d, *J* = 9.14 Hz, H-7a) ppm, GC-MS (m/z) 308 (M$^+$), 242 (M$^+$-C$_5$H$_6$), 147 (C$_8$H$_4$O$_2$N), 104 (C$_7$H$_4$O).

*General procedure for the synthesis of compounds* **4-5**

A sealed tube containing ninhydrin (0.178 g, 1 mmol), *N*-methylglycine or *N*-benzylglycine (1 mmol) and compound **3** (0.308 g, 1 mmol) in EtOH/dioxane (1:1, 6 mL) was heated at 65 °C for 6 hours under nitrogen atmosphere. After completion of the reaction with TLC control, the organic phase was concentrated and the residue purified by chromatography on silica gel.

*6-(1,3-Dioxoisoindoline-2-yl)-2-methyl-3,3a,4,4a,8,8a-hexahydro-2H-spiro[4,8-methanopyrole[3,4-f]isoindole-1,2'indene]-1',3',5,7-(6H,7aH)tetraone* **(4)**

Yellow oil, Yield 52%, $R_f$: 0.10 (1:1, ethyl acetate/*n*-hexane), IR (ATR) 2959, 2868, 1737, 1704, 1595, 1468, 1364, 1346, 1232, 1179, 1120 cm$^{-1}$, $^1$H NMR (CDCl$_3$, 500 MHz) δ 7.95-7.97 (2H, m, Ar-*H*), 7.90-7.91 (1H, m, Ar-*H*), 7.78 (2H, dt, *J* = 1.26 and 4.01 Hz, Ar-*H*), 7.74 (2H, dt, *J* = 1.26 and 4.01 Hz, Ar-*H*), 7.69 (1H, brs, Ar-*H*), 3.57 (1H, t, *J* = 9.45 Hz, *N*-C*H$_2$*), 3.20-3.23 (1H, m, H-3), 3.13-3.16 (1H, m, H-2), 2.92 (1H, dd, *J* = 1.57 and 9.45 Hz, H-5), 2.81-2.86 (3H, m, H-1, H-4, *N*-C*H$_2$*), 2.47 (1H, d, *J* = 7.56 Hz, H-6), 2.16 (3H, s, C*H$_3$*), 1.51-1.55 (2H, m, H-7a, H-7s) ppm, $^{13}$C NMR (CDCl$_3$, 125 MHz) δ 202.75 (C=O), 200.8 (C=O), 174.6 (C=O), 172.7 (C=O), 162.9 (C=O), 162.5 (C=O), 152.2 (Ar-*C*), 141.8 (Ar-*C*), 139.7 (Ar-*C*), 136.0 (Ar-*C*H), 135.0 (Ar-*C*H), 130.2 (Ar-*C*), 129.8 (C), 124.8 (Ar-*C*H), 124.6 (Ar-*C*H), 124.4 (Ar-*C*H), 124.2 (Ar-*C*H), 123.6 (Ar-*C*H), 123.1 (Ar-*C*H), 50.5 (*C*H$_3$), 47.4 (*C*H$_2$), 45.3 (*C*H), 45.1 (*C*H), 42.7 (*C*H), 42.4 (*C*H), 42.1 (*C*H), 38.1 (*C*H), 29.7 (C-7) ppm, HRMS (ESI): calcd for [C$_{28}$H$_{21}$N$_3$O$_6$] ([M]$^+$): *m/z* 495.1430, found 496.1812 [M+H]$^+$.

*2-Benzyl-6-(1,3-dioxoisoindoline-2-yl)-3,3a,4,4a,8,8a-hexahydro-2H-spiro[4,8-methanopyrole[3,4-f]isoindole-1,2'indene]-1',3',5,7-(6H,7aH)tetraone* **(5)**

Yellow solid, Yield 32%, m.p. 266-268 °C, $R_f$: 0.48 (1:1, ethyl acetate/*n*-hexane), IR (ATR) 3066, 2954, 2921, 2850, 1737, 1702, 1593, 1468, 1455, 1346, 1288, 1179, 1156 cm$^{-1}$, $^1$H NMR (CDCl$_3$, 500 MHz) δ 7.90-7.92 (2H, m, Ar-*H*), 7.83-7.87 (2H, m, Ar-*H*), 7.76-7.80 (2H, m, Ar-*H*), 7.73-7.75 (2H, m, Ar-*H*), 7.13-7.21 (5H, m, Ar-*H*), 3.50 (1H, d, *J* = 12.92 Hz, C*H$_2$*), 3.45 (1H, d, *J* = 9.45 Hz, C*H$_2$*), 3.39 (1H, d, *J* = 12.92 Hz, C*H$_2$*), 3.14-3.20 (2H, m, H-2, H-3), 2.97 (1H, d, *J* = 10.40 Hz, *N*-C*H$_2$*), 2.82 (1H, t, *J* = 8.19 Hz, H-5), 2.75-2.78 (2H, m, H-1, H-4), 2.70 (1H, d, *J* = 4.41 Hz, H-6), 2.48 (1H, d, *J* = 8.51 Hz, H-7s), 1.53 (1H, d, *J* = 13.55 Hz, H-7a) ppm, $^{13}$C NMR (CDCl$_3$, 125 MHz) δ 202.8 (C=O), 200.4 (C=O), 172.7 (C=O), 172.6 (C=O), 162.9 (C=O), 162.5 (C=O), 142.0 (Ar-*C*), 139.5 (Ar-*C*), 138.6 (Ar-*C*), 135.0 (Ar-*C*H), 132.3 (Ar-*C*H), 130.1 (Ar-*C*), 129.7 (Ar-*C*), 128.8 (Ar-*C*H), 128.6 (Ar-*C*Hx2), 128.4 (Ar-*C*H), 128.0 (C), 128.0 (Ar-*C*H), 127.4 (Ar-*C*H), 127.2 (Ar-*C*Hx2), 127.0 (Ar-*C*H), 124.6 (Ar-*C*H), 123.3 (Ar-*C*H), 59.5 (*N*-C*H$_2$*), 49.7 (*C*H), 46.9 (*C*H), 42.5 (*C*H), 42.3 (*C*H), 39.0 (*C*H), 38.1 (*C*H$_2$), 31.3 (*C*H), 30.8 (C-7) ppm, HRMS (ESI): calcd for [C$_{34}$H$_{25}$N$_3$O$_6$] ([M]$^+$): *m/z* 571.1743, found 572.7224 [M+H]$^+$.

*General procedure for the synthesis of oxime derivatives* **6-9**

Oxime derivatives were prepared with aldehyde, hydroxylamine hydrochloride, and sodium carbonate in ethyl alcohol at room temperature with the known procedure (33-35). A solution of hydroxyl amine hydrochloride (0.417 g, 6 mmol) in 0.5 mL of water and a solution of $Na_2CO_3$ in 1.5 mL of water were added drop wise to the solution of an aldehyde (2 mmol) in 1.5 mL of ethyl alcohol, respectively. Resulting solid was filtered and purified by recrystallization from alcohol.

*4-Chlorobenzaldehyde oxime* **6** (33)

White solid, yield 100%, m.p. 92-94 °C, $R_f$: 0.52 (1:2 ethyl acetate/*n*-hexane), FT-IR (ATR) 3301 (OH), 1589 (C=N), 1496 (C-N), 971 (C-H), 694 (C-Cl) $cm^{-1}$, GC-MS (EI), m/z (%): 155 (M+·, 99), 139 (100), 136 (82), 111 (73), 75 (70).

*2,4-Dimethoxybenzaldehyde oxime* **7** (34)

White solid, Yield 94%, m.p. 103-105 °C, FT-IR (KBr pellet) 2944, 1610, 1504, 1466, 1414, 1270, 1206, 1112, 1026, 922, 832 $cm^{-1}$, $^1$H NMR ($CDCl_3$, 500 MHz) δ 7.73 (1H, s, C*H*=N-OH), 7.0 (1H, d, *J* = 8.5 Hz, Ar-*H*), 6.03 (1H, s Ar-*H*), 6.06 (1H, d, *J* = 8.5 Hz, Ar-*H*), 3.6 (6H, s, 2xOC*H₃*) ppm, calcd for [$C_9H_{11}NO_3$] C 59.66 H 6.11 N 7.70%, found C 60.01 H 6.19%.

*4-Methylbenzaldehyde oxime* **8** (33)

White solid, yield 99%, m.p. 54-55 °C, $R_f$: 0.52 (1:2 ethyl acetate/*n*-hexane), FT-IR (ATR) 3333 (OH), 2994 (CH3), 1572 (C=N), 1497 (C-N), 1028 (C-H) $cm^{-1}$, $^1$H NMR ($CDCl_3$, 500 MHz) δ 8.01 (1H, s, C*H*=N-OH), 7.71 (2H, d, *J* = 7.6 Hz, Ar-*H*), 7.24 (2H, d, *J* = 7.6 Hz, Ar-*H*), 2.21 (3H, s, C*H₃*) ppm, GC-MS (EI), m/z (%): 135 (M+·, 96), 119 (100), 104 (76), 91 (83), 75 (61).

*2-Thiophenealdehyde oxime* **9** (35)

White solid, Yield 98%, m.p. 132-136 °C. FT-IR (ATR) 3320 (OH), 1568 (C=N), 1468 (C-N), 1026 (C-H) $cm^{-1}$.

*General procedure for the synthesis of compounds* **10-13**

The compound **3** (0.154 g, 0.5 mmol) and oxime derivative (*p*-chlorobenzaldehyde oxime, 2,4-dimethoxybenzaldehyde oxime, *p*-methylbenzaldehyde oxime, or thiophene-2-carbaldehyde oxime, respectively) (0.5 mmol) was dissolved in 4 mL of dichloromethane. A solution of NaOCl (0.6 mL) was added drop wise to the reaction mixture at 0 °C. The resulting mixture was stirred at 0 °C overnight. After completion of the reaction, the mixture was extracted with dichloromethane (3x10 mL). The organic phase was dried over $MgSO_4$, filtered, and concentrated.

*3-(4-Chlorophenyl)-6-(1,3-dioxoisoindolin-2-yl)-4,4a,8,8a-tetrahydro-3aH-4,8-methanoisoxazol[3,4-f]isoindole-5,7-dione* **(10)**

White solid, Yield 97%, m.p. 317-319 °C (decomp.), $R_f$: 0.48 (1:1, ethyl acetate/*n*-hexane), IR (ATR) 3004, 2984, 2973, 2953, 1746, 1733, 1468, 1402, 1349, 1207, 1171, 1123 cm$^{-1}$, $^1$H NMR (CDCl$_3$, 500 MHz) δ 7.90-7.92 (1H, m, Ar-*H*), 7.85-7.87 (1H, m, Ar-*H*), 7.78-7.80 (2H, m, Ar-*H*), 7.54 (2H, d, *J* = 8.51 Hz, Ar-*H*), 7.31 (2H, d, *J* = 8.51 Hz, Ar-*H*), 4.90 (1H, d, *J* = 8.19 Hz, H-5), 3.91 (1H, d, *J* = 8.19 Hz, H-6), 3.37-3.38 (2H, m, H-2, H-3), 3.21 (1H, brs, H-4), 3.02 (1H, brs, H-1), 1.86 (1H, d, *J* = 11.35 Hz, H-7s), 1.58 (1H, d, *J* = 11.35 Hz, H-7a) ppm, $^{13}$C NMR (CDCl$_3$, 125 MHz) δ 172.1 (C=O), 171.1 (C=O), 162.9 (C=O), 162.7 (C=O), 155.5 (C), 136.3 (C), 135.4 (C), 130.1 (C), 129.5 (Ar-*C*), 129.4 (Ar-*C*), 129.2 (Ar-*C*), 128.9 (Ar-*C*), 128.2 (C), 126.6 (Ar-*C*), 124.8 (Ar-*C*), 124.5 (Ar-*C*), 123.7 (Ar-*C*), 83.5 (*C*H), 52.7 (*C*H), 51.9 (*C*H), 46.2 (*C*H), 44.9 (*C*H), 42.3 (*C*H), 42.0 (*C*H$_2$) ppm, HRMS (ESI): calcd for [C$_{24}$H$_{16}$ClN$_3$O$_5$] ([M]$^+$): *m/z* 461.0778, found 462.2232 [M+H]$^+$.

*3-(2,4-Dimethoxyphenyl)-6-(1,3-dioxoisoindolin-2-yl)-4,4a,8,8a-tetrahydro-3aH-4,8-methanoisoxazol[3,4-f]isoindole-5,7-dione* **(11)**

Yellow solid, Yield 65%, m.p. 214-216 °C, $R_f$: 0.50 (1:1, ethyl acetate/*n*-hexane), IR (ATR) 3064, 2923, 2850, 2838, 1783, 1738, 1465, 1422, 1344, 1290, 1217, 1177 cm$^{-1}$, $^1$H NMR (CDCl$_3$, 500 MHz) δ 7.87-7.90 (2H, m, Ar-*H*), 7.77-7.79 (2H, m, Ar-*H*), 7.35 (1H, d, *J* = 3.15 Hz, Ar-*H*), 6.86 (1H, dd, *J* = 3.15 and 9.14 Hz, Ar-*H*), 6.80 (1H, d, *J* = 9.14 Hz, Ar-*H*), 4.84 (1H, d, *J* = 8.51 Hz, H-5), 4.31 (1H, d, *J* = 8.51 Hz, H-6), 3.74 (3H, s, OC*H$_3$*), 3.71 (3H, s, OC*H$_3$*), 3.30-3.32 (2H, m, H-2, H-3), 3.15 (1H, brs, H-4), 2.90 (1H, brs, H-1), 1.82 (1H, d, *J* = 11.35 Hz, H-7s), 1.50 (1H, d, *J* = 11.35 Hz, H-7a) ppm, $^{13}$C NMR (CDCl$_3$, 125 MHz) δ 171.8 (C=O), 171.5 (C=O), 163.2 (C=O), 162.9 (C=O), 155.9 (C), 153.4 (Ar-*C*), 151.7 (Ar-*C*), 135.3 (Ar-*C*H), 135.2 (Ar-*C*H), 130.1 (Ar-*C*), 129.7 (Ar-*C*), 124.7 (Ar-*C*H), 124.4 (Ar-*C*H), 117.1 (Ar-*C*), 113.6 (Ar-*C*H), 113.0 (Ar-*C*H), 112.7 (Ar-*C*H), 82.8 (*C*H), 56.1 (O*C*H$_3$), 55.8 (O*C*H$_3$), 51.2 (*C*H), 46.2 (*C*H), 45.7 (*C*H), 44.6 (*C*H), 42.7 (*C*H$_2$), 43.1 (*C*H) ppm, HRMS (ESI): calcd for [C$_{26}$H$_{21}$N$_3$O$_7$] ([M]$^+$): *m/z* 587.1379, found 588.3660 [M+H]$^+$.

*3-(4-Methylphenyl)-6-(1,3-dioxoisoindolin-2-yl)-4,4a,8,8a-tetrahydro-3aH-4,8-methanoisoxazol[3,4-f]isoindole-5,7-dione* **(12)**

White solid, Yield 95%, m.p. 270-272 °C, $R_f$: 0.37 (1:1, ethyl acetate/*n*-hexane), IR (ATR) 3028, 2971, 1746, 1731, 1420, 1349, 1294, 1171, 1111, 724 cm$^{-1}$, $^1$H NMR (CDCl$_3$, 500 MHz) δ 7.89-7.90 (1H, m, Ar-*H*), 7.85-7.86 (1H, m, Ar-*H*), 7.77-7.79 (2H, m, Ar-*H*), 7.49 (2H, d, *J* = 8.19 Hz, Ar-*H*), 7.13 (2H, d, *J* = 8.19 Hz, Ar-*H*), 4.88 (1H, d, *J* = 8.19 Hz, H-5), 3.93 (1H, d, *J* = 8.19 Hz, H-6), 3.35-3.37 (2H, m, H-2, H-3), 3.19 (1H, brs, H-4), 3.04 (1H, brs, H-1), 2.23 (3H, s, C*H$_3$*), 1.87 (1H, d, *J* = 11.35 Hz, H-7s), 1.55 (1H, d, *J* = 11.35 Hz, H-7a) ppm, $^{13}$C NMR (CDCl$_3$, 125 MHz) δ 172.1 (C=O), 171.2 (C=O), 162.9 (C=O), 162.8 (C=O), 156.2 (C), 140.6 (Ar-*C*), 135.3 (Ar-*C*H), 129.9 (Ar-*C*H), 129.7 (Ar-*C*), 129.5 (Ar-*C*), 129.4 (Ar-*C*H), 129.3 (Ar-*C*H), 126.5

(Ar-$C$Hx2), 125.3 (Ar-$C$), 124.6 (Ar-$C$H), 124.4 (Ar-$C$H), 81.9 ($C$H), 52.2 ($C$H$_2$), 45.5 ($C$H), 43.1 ($C$H), 42.5 ($C$H), 36.0 ($C$H), 35.4 ($C$H), 21.3 ($C$H$_3$) ppm,  HRMS (ESI): calcd for [C$_{25}$H$_{19}$N$_3$O$_5$] ([M]$^+$): *m/z* 441.1325, found 442.6204 [M+H]$^+$.

*3-(Thiophen-2-yl)-6-(1,3-dioxoisoindolin-2-yl)-4,4a,8,8a-tetrahydro-3aH-4,8-methanoisoxazol[3,4-f]isoindole-5,7-dione* **(13)**

Beige solid, Yield 85%, m.p. 280-282 °C (decomp.), R$_f$: 0.32 (1:1, ethyl acetate/*n*-hexane), IR (ATR) 3095, 2953, 2921, 2850, 1794, 1737, 1468, 1435, 1345, 1285, 1174, 1118, 700, 670 cm$^{-1}$, $^1$H NMR (CDCl$_3$, 500 MHz) δ 7.90-7.92 (1H, m, Ar-$H$), 7.86-7.87 (1H, m, Ar-$H$), 7.78-7.80 (2H, m, Ar-$H$), 7.32 (1H, dd, *J* = 0.94 and 5.04 Hz, Ar-$H$), 7.17 (1H, dd, *J* = 0.94 and 3.78 Hz, Ar-$H$), 6.99 (1H, dd, *J* = 3.78 and 5.04 Hz, Ar-$H$), 4.91 (1H, d, *J* = 8.19 Hz, H-5), 3.91 (1H, d, *J* = 8.19 Hz, H-6), 3.37-3.39 (2H, m, H-2, H-3), 3.22 (1H, brs, H-4), 3.14 (1H, brs, H-1), 1.92 (1H, d, *J* = 11.35 Hz, H-7s), 1.60 (1H, d, *J* = 11.35 Hz, H-7a) ppm, $^{13}$C NMR (CDCl$_3$, 125 MHz) δ 171.9 (C=O), 171.1 (C=O), 162.9 (C=O), 162.7 (C=O), 152.3 (C), 135.4 (Ar-$C$H), 135.3 (Ar-$C$H), 130.8 (Ar-$C$), 130.1 (Ar-$C$), 129.6 (Ar-$C$), 128.9 (Ar-$C$H), 128.4 (Ar-$C$H), 127.2 (Ar-$C$H), 124.7 (Ar-$C$H), 124.5 (Ar-$C$H), 83.4 (CH), 53.2 ($C$H$_2$), 46.3 (CH), 45.5 (CH), 43.0 (CH), 42.8 (CH), 45.2 (CH) ppm, HRMS (ESI): calcd for [C$_{22}$H$_{15}$N$_3$O$_5$S] ([M]$^+$): *m/z* 433.0732, found 434.0920 [M+H]$^+$.

**RESULT AND DISCUSSION**

In this study, we synthesized bicyclic endic anhydride **1** by Yamamoto's procedure (31). Thereafter, compound **2** was synthesized from the reaction of hydrazonium chloride and bicyclic endic anhydride **1** in benzene at room temperature (32). We continued to prepare *N*-phthalimide substituted tricyclic imide **3** from compound **2** using Kas'yan procedure (32) (**Scheme 1**).
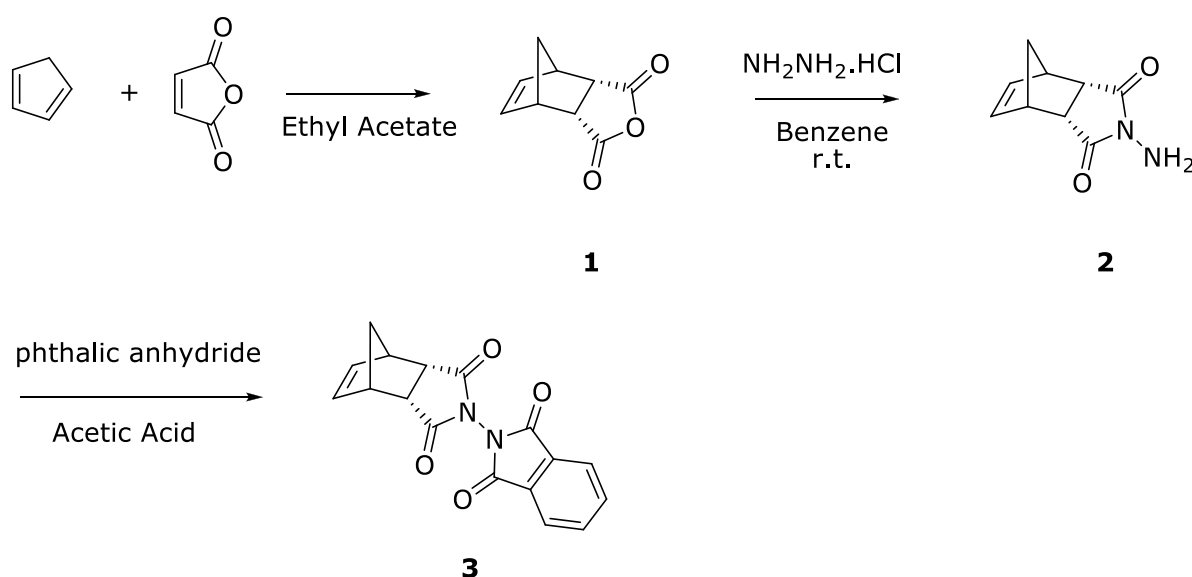


**Scheme 1:** Preparation of Compounds **1-3.**

Our purpose is to prepare new *N*-phthalimide-substituted tricyclic imide with bispiro-functional group because of their importance in biological activity. In order to achieve this purpose, we designed and synthesized the new bispiro tricyclic imide derivatives **4** and **5** from compound **3** in ethanol/1,4-dioxane solvent system at 65 °C in good yields. (**Scheme 2**) In this reaction series, we used ninhydrin and *N*-methylglycine or *N*-benzylglycine to form azomethine ylide in the reaction flask (**Scheme 3**).
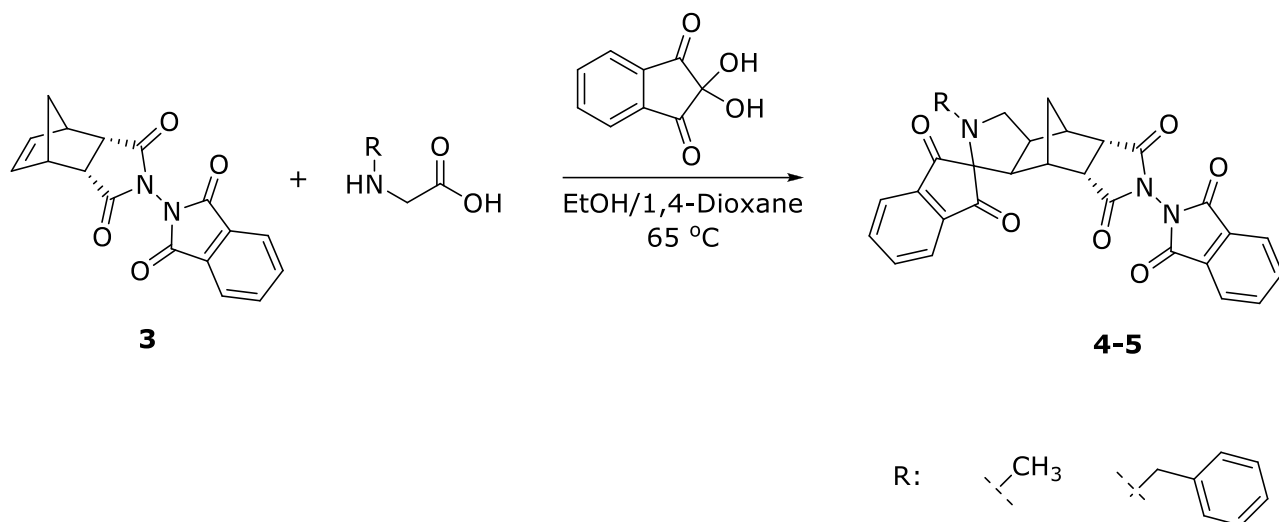


**Scheme 2:** Preparation of Compound **4-5.**
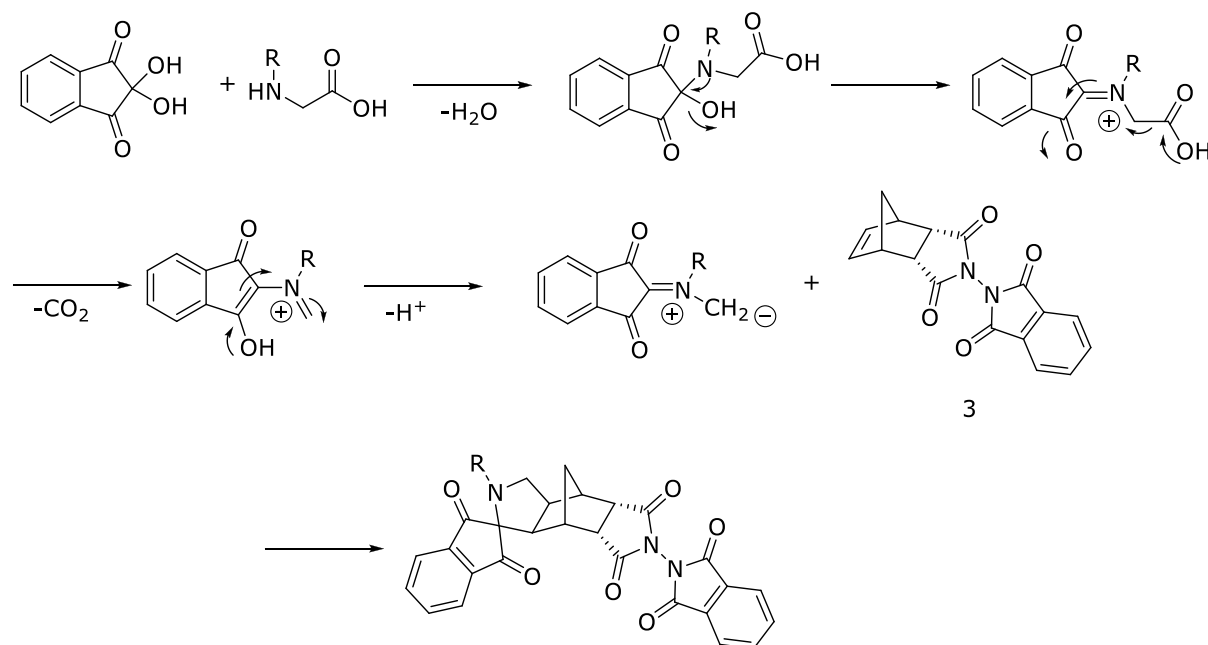


**Scheme 3:** Proposed mechanism of the reaction.

Our other goal is to prepare new *N*-phthalimide-substituted tricyclic imide with isoxazoline group. Because of our synthetic strategy, we firstly synthesized oxime derivatives **6**-**9** with known procedure in excellent yields (33-35) (**Scheme 4**).
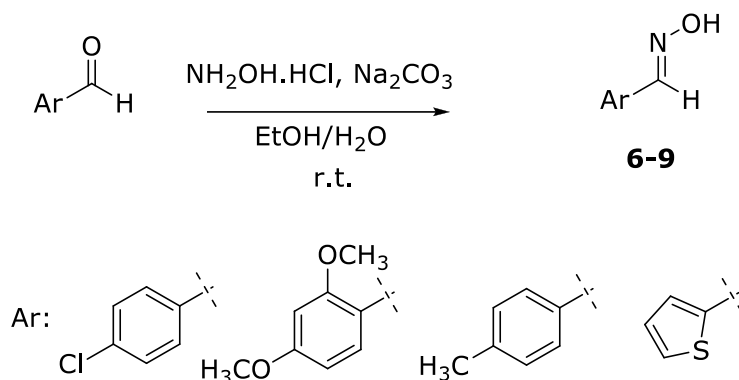
**Scheme 4:** Synthesis of oxime derivatives **6-9**.

In the next step, we synthesized new tricyclic imide derivatives bearing isoxazoline ring **10-13** with 1,3-dipolar cycloaddition reaction using oxime derivatives **6**-**9** as starting materials in dichloromethane solvent system at 0 °C (**Scheme 5**).
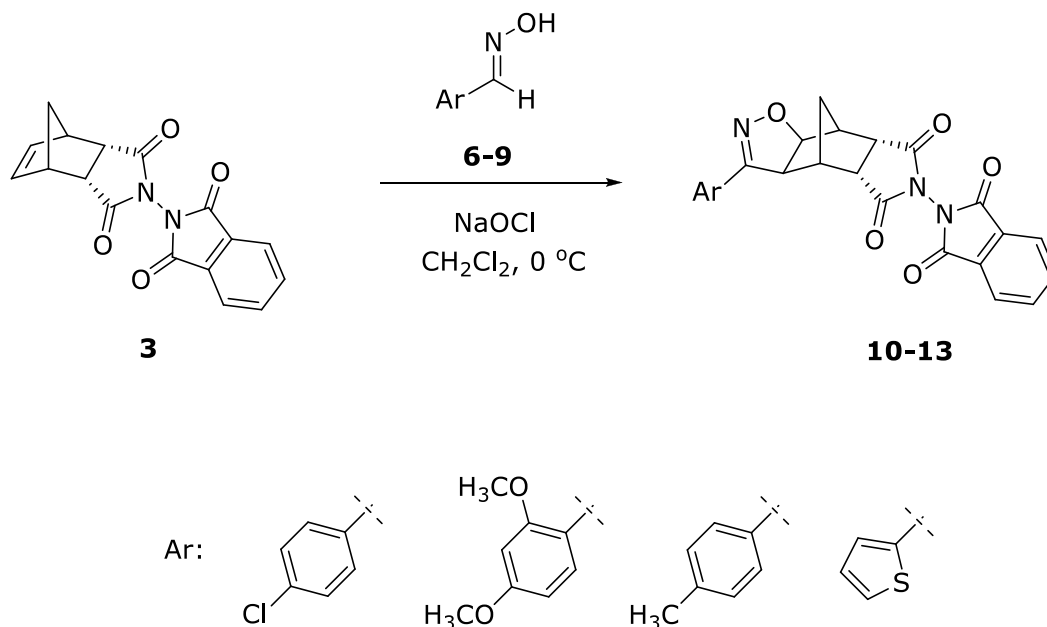


**Scheme 5:** Synthesis of compounds **10-13.**

Overall, we designed and synthesized new bispiro functionalized tricyclic imide molecules and tricyclic imide molecules containing isoxazoline ring as possible anti-cancer agents. We characterized all of the new molecules with $^1$H NMR, $^{13}$C NMR and FTIR spectral data. The reaction of compound **3** with azomethine ylide obtained from ninhydrin and sarcosine gave the desired products; **4** and **5**. $^1$H-NMR spectra of compound **3** showed two alkenic protons (H5 and H6) at 6.33 ppm as a singlet. The absent of alkenic protons in the $^1$H and $^{13}$C NMR spectrum of compound **4** confirmed the structure. $^1$H NMR spectra of compound **4** showed $N$-CH$_2$ protons at 3.57 ppm and four aromatic protons at 7.95–7.97, 7.74 and 7.69 ppm as an additional. $^{13}$C NMR spectra of compound **4** showed four carbonyl carbons with the addition of ninhydrin to the

structure. The $^1$H and $^{13}$C NMR spectrum of compound **5** showed the similar results and confirmed the structure of compound **5**. The $^1$H and $^{13}$C NMR spectrum of compound **10**-**13** proved the 1,3-dipolar cycloaddition reaction occurs. $^1$H-NMR spectra of compound **10** showed protons (H5 and H6) at 4.90 and 3.91 ppm insead of alkenic protons and showed four additional aromatic protons at 7.54 and 7.31 ppm as expected. The $^1$H and $^{13}$C NMR spectrum of compounds **11-13** showed the similar results and confirmed their structures.

 In addition to the $^1$H-NMR, $^{13}$C NMR and FTIR spectral data which were in agreement with the proposed structures, LC-MSMS (Qtof) results of all new compounds showed the expected accurate mass with hydrogen additions.

## CONCLUSION

In conclusion, we synthesized tetracyclic systems that we hope will demonstrate new anti-cancer activity by applying azomethine ylide [3+2]-cycloaddition and 1,3-dipolar cycloaddition reactions to the *N*-phthalimide substituted tricyclic imide molecule. Further work toward exploring anticancer activity of all newly synthesized compounds with MTT essay will be forthcoming.

## REFERENCES

1.      Kulu I, Goksu G, Sucu BO, Kopruceli A, Ocal N, Kaufmann DE. Synthesis of New Aryl-substituted Tandospirone and Epiboxidine Analogues and Isoxazoline Derivatives. Org Prep Proced Int. 2013;45(1):44-56.

2.      Gunkara OT, Sucu BO, Ocal N, Kaufmann DE. Synthesis of new aryl(hetaryl)-substituted tandospirone analogues with potential anxiolytic activity via reductive Heck type hydroarylations. Chem Pap. 2013;67(6):643-9.

3.      Gunkara OT, Sucu BO, Guleli M, Ocal N. Synthesis of New Tandospirone Analogues Carrying 1-(3-(Trifluoromethyl)Phenyl)Piperazine. Synthetic Commun. 2014;44(11):1619-28.

4.      Wieland S, Fischette CT, Lucki I. Effect of Chronic Treatments with Tandospirone and Imipramine on Serotonin-Mediated Behavioral-Responses and Monoamine Receptors. Neuropharmacology. 1993;32(6):561-73.

5.      Trawinski J, Skibinski R. Photolytic and photocatalytic degradation of tandospirone: Determination of kinetics, identification of transformation products and in silico estimation of toxicity. Sci Total Environ. 2017;590:775-98.

6.      Andoh T, Sakamoto A, Kuraishi Y. 5-HT1A receptor agonists, xaliproden and tandospirone, inhibit the increase in the number of cutaneous mast cells involved in the exacerbation of mechanical allodynia in oxaliplatin-treated mice. J Pharmacol Sci. 2016;131(4):284-7.

7.      Mikolajczyk M, Kielbasinski P. Recent Developments in the Carbodiimide Chemistry. Tetrahedron. 1981;37(2):233-84.

8.      Brana MF, Castellano JM, Roldan CM, Santos A, Vazquez D, Jimenez A. Synthesis and mode(s) of action of a new series of imide derivatives of 3-nitro-1,8 naphthalic acid. Cancer Chemother Pharmacol. 1980;4(1):61-6.

9.      Walter WG. Antitumor imide derivatives of 7-oxabicyclo[2.2.1]heptane-2,3-dimethyl-2,3-dicarboxylic acid. J Pharm Sci. 1989;78(1):66-7.

10.     Miyazaki H, Ogiku T, Sai H, Ohmizu H, Murakami J, Ohtani A. Design, synthesis, and evaluation of orally active inhibitors of plasminogen activator inhibitor-1 (PAI-1) production. Bioorg Med Chem Lett. 2008;18(24):6419-22.

11.     Bojarski AJ, Mokrosz MJ, Duszynska B, Koziol A, Bugno R. New imide 5-HT1A receptor ligands - modification of terminal fragment geometry. Molecules. 2004;9(3):170-7.

12.     Ando I, Ohtsuka T, Miki N, Takahashi T, Hayase Y, Hayashi Y. Synthesis and Biological-Activity of Cyclic Imide Derivatives and Related-Compounds. Agr Biol Chem Tokyo. 1989;53(7):2001-3.

13.     Conti P, Dallanoce C, De Amici M, De Micheli C, Klotz KN. Synthesis of new Delta(2)-isoxazoline derivatives and their pharmacological characterization as beta-adrenergic receptor antagonists. Bioorgan Med Chem. 1998;6(4):401-8.

14.     Kaur K, Kumar V, Sharma AK, Gupta GK. Isoxazoline containing natural products as anticancer agents: A review. Eur J Med Chem. 2014;77:121-33.

15.     Ribeiro CJA, Amaral JD, Rodrigues CMP, Moreira R, Santos MMM. Synthesis and evaluation of spiroisoxazoline oxindoles as anticancer agents. Bioorgan Med Chem. 2014;22(1):577-84.

16.     Kozikowski AP. The Isoxazoline Route to the Molecules of Nature. Accounts Chem Res. 1984;17(12):410-6.

17.     Arai MA, Kuraishi M, Arai T, Sasai H. A new asymmetric Wacker-type cyclization and tandem cyclization promoted by Pd(II)-spiro bis(isoxazoline) catalyst. J Am Chem Soc. 2001;123(12):2907-8.

18.     Studer A, Curran DP. A strategic alternative to solid phase synthesis: Preparation of a small isoxazoline library by ''fluorous synthesis''. Tetrahedron. 1997;53(19):6681-96.

19.     Damkaci F, DeShong P. Stereoselective synthesis of alpha- and beta-glycosylamide derivatives from glycopyranosyl azides via isoxazoline intermediates. J Am Chem Soc. 2003;125(15):4408-9.

20.     Fuller AA, Chen B, Minter AR, Mapp AK. Succinct synthesis of beta-amino acids via chiral isoxazolines. J Am Chem Soc. 2005;127(15):5376-83.

21.     Yildirim A, Cetin M. Synthesis and evaluation of new long alkyl side chain acetamide, isoxazolidine and isoxazoline derivatives as corrosion inhibitors. Corros Sci. 2008;50(1):155-65.

22.     Goksu G, Ocal N. 1,3-Dipolar Cycloaddition Reactions of N-Methyl-Substituted Tricyclic Imides. Acta Chim Slov. 2011;58(2):256-61.

23.     Gul M, Ocal N. Heck-type hydroarylations and 1,3-dipolar cycloaddition reactions of new tricyclic hydrazones. Can J Chem. 2010;88(4):323-30.

24.     Kulu I, Gul M, Gunkara OT, Ocal N. Cycloaddition Reactions of Some Tricyclic Imides. Mini-Rev Org Chem. 2013;10(4):409-18.

25.     Gul M, Kulu I, Gunkara OT, Ocal N. Reductive Heck Reactions and [3+2] Cycloadditions of Unsaturated N,N'-Bistricyclic Imides. Acta Chim Slov. 2013;60(1):87-94.

26.     Ahrendt KA, Borths CJ, MacMillan DWC. New strategies for organic catalysis: The first highly enantioselective organocatalytic Diels-Alder reaction. J Am Chem Soc. 2000;122(17):4243-4.

27.     Jen WS, Wiener JJM, MacMillan DWC. New strategies for organic catalysis: The first enantioselective organocatalytic 1,3-dipolar cycloaddition. J Am Chem Soc. 2000;122(40):9874-5.

28.     Obst U, Betschmann P, Lerner C, Seiler P, Diederich F, Gramlich V, et al. Synthesis of novel nonpeptidic thrombin inhibitors. Helv Chim Acta. 2000;83(5):855-909.

29.     Sebahar PR, Williams RM. The asymmetric total synthesis of (+)- and (-)-spirotryprostatin B. J Am Chem Soc. 2000;122(23):5666-7.

30.     Kaffy J, Pontikis R, Carrez D, Croisy A, Monneret C, Florent JC. Isoxazole-type derivatives related to combretastatin A-4, synthesis and biological evaluation. Bioorg Med Chem. 2006;14(12):4067-77.

31.     Yamamoto Y, Yamamoto S, Yatagai H, Ishihara Y, Maruyama K. Lewis Acid Mediated Reactions of Organocopper Reagents - Entrainment in the Conjugate Addition to Alpha,Beta-Unsaturated Ketones, Esters, and Acids Via the Rcu.Bf3 System. J Org Chem. 1982;47(1):119-26.

32.     Kas'yan LI, Tarabara IN, Bondarenko YS, Svyatenko LK, Bondarenko AV. Reactions of 4-amino-4-azatricyclo[5.2.1.0(2,6-endo)]dec-8-ene-3,5-dione with dicarboxylic acid anhydrides. Russ J Org Chem+. 2007;43(7):1014-26.

33.     Galvis CEP, Kouznetsov VV. An unexpected formation of the novel 7-oxa-2-azabicyclo[2.2.1]hept-5-ene skeleton during the reaction of furfurylamine with maleimides and their bioprospection using a zebrafish embryo model. Org Biomol Chem. 2013;11(3):407-11.

34.     Iqbal A, Mohammed AA, Ozair A, Amit N, Subhash CT, Surrinder K. Molecular modelling and snake venom  phospholipase A2 inhibition by phenolic compounds: Structure-activity relationship. Tetrahedron. 2016;114:209-19.

35.     Jung JY, Jung SH, Koh HY, Pae AN, Park WK, Kong JY. Synthesis of piperazinylalkylisoxazoline analogues and their binding affinities for dopamine receptor subtypes. B Korean Chem Soc. 2006;27(11):1861-4.

# Removal of Cesium from Aqueous Solution by Adsorption onto Sivas-Yildizeli (Türkiye) Vermiculite: Equilibrium, Kinetic and Thermodynamic Studies

## Hilmi Arkut AKALIN[1], Ümran HİÇSÖNMEZ[2*], Hatice YILMAZ[3]

[1]Manisa Celal Bayar University, Graduate School of Natural and Applied Sciences, 45030, Muradiye/Manisa, Turkey.

[2]Manisa Celal Bayar University, Faculty of Arts and Science, Department of Chemistry, 45030, Muradiye/Manisa, Turkey.

[3]Dokuz Eylül University, Faculty of Engineering, Department of Mining Engineering, 35390, Tınaztepe/İzmir, Turkey.

**Abstract:** In this study, cesium adsorption performance of raw vermiculite obtained from Sivas-Yıldızeli region of Turkey was investigated using batch adsorption method. In order to obtain the optimum adsorption conditions; different adsorbent dosages, contact times, solution pH's, initial cesium concentrations and temperature ranges were investigated. The concentration of cesium in solution was determined by ICP-OES. Kinetic studies demonstrated that adsorption process was in accordance with pseudo-second order kinetic model and equilibrium isotherm modeling studies showed that the process was compatible with Langmuir, Freundlich and Temkin adsorption isotherm models, indicating that Cs adsorption process had both physical and chemical character. Negative Gibbs energy values obtained from thermodynamic studies revealed that the adsorption process was spontaneous and had a high feasibility. Additionally, the negative enthalpy value indicated that process was exothermic, suggesting that the adsorbed $Cs^+$ ions decreased with increasing reaction temperatures. Positive entropy value showed that disorderliness between solid-liquid phase increased during adsorption. Results clearly indicate that vermiculite mineral has a promising potential in removing $Cs^+$ ions from aqueous media which leads mineral may also be used in decomposing and efficiently removing radioactive cesium from contaminated waters.

**Keywords:** Cesium, vermiculite, adsorption, adsorption kinetic models, adsorption isotherms.

## INTRODUCTION

In 2011, Fukushima Daiichi Nuclear power plant accident occurred and many radionuclides were released into the environment. They caused a great environmental disaster to living metabolisms including humans, animals, and plants nearby because of the contamination provided by these nuclides. Although zeolites were used to prevent the radioactive damage in the power plant facility and surrounding areas, it was not complete enough (1).

Remarkably, ^{137}Cs is one of the most important radionuclides among contaminants released into the environment with nuclear accidents and weapon tests, since it has a very long half-life (30 years) and strong radiation energy (2). Cesium is a crucial radioisotope which can easily move with aqueous media and has almost unlimited solubility in liquid systems, as well as incorporating into soil environment and aquatic organisms, harming them with an untolerated degree of γ and β radiation (3,4). In addition, radiocesium causes significant harm to human health, mostly triggering the incidence of thyroid cancer since it is strongly absorbed by the body via ingestion when exposed to cesium (5).

In order to prevent these negative effects, cesium must be removed from the environment efficiently and adsorption is the most effective method among many techniques used in removing cesium ions in aqueous media such as chemical precipitation, coagulation, membrane process, ion exchange column concerning its low cost, wide range of applicability and the possibility of various types of sorbent selection (6–10). Clay minerals are favorable for adsorption of radioactive components due to their environmental friendly character, abundance and ideal sorption features for specific kinds of metal ions (11).

Vermiculite is a typical 2:1 phyllosilicate clay mineral composed of alumina and magnesia formed between dual tetrahedral silicate sheet and the central chemical structure consists of magnesium octahedral structure (12,13). This mineral has a high surface area, layer charge density, and cation exchange capacity as well as it is reserved worldwide abundance, thus has ideal properties to be used as a powerful removal agent for monovalent cations such as cesium metal (14,15).

For the aim of removing radioactive cesium from radio-contaminated wastes using vermiculite, many studies were conducted since the 1960s, and the mineral was used as an efficient adsorbent for ^{137}Cs in nuclear reactor laboratory column (16–20). Additionally, the Japan Atomic Energy Agency research group (JAEA) investigated the adsorption behavior of radioactive cesium using vermiculite obtained in Fukushima Prefecture, and revealed that vermiculite has a significant potential in adsorbing large amounts of cesium ions due to the local rearrangement of mineral interlayer formation in relation to electrostatic interactions between positively charged cesium ions and oxygen atoms (21). Hence, as the amount of adsorbed cesium ions and the

other mobilized particles, which have similar chemical properties with cesium at one side of interlayer increases, interactions between the other sides of the interlayer is weakened and opposite clay interlayer is separated due to excess concentration of adsorbate ions. With this way, cesium ions at solution media could be gradually adsorbed with newly formed clay layer surface with strong ionic interactions and this sorption approach is called as domino toppling. Domino toppling effect of vermiculite was enlightened by a small angle X-ray scattering method where X-ray irradiates the sample, and the microscopic structure of the sample is determined by analyzing the intensity of the scattered X-ray as a function of the scattering angle.

Since vermiculite has excellent cesium adsorption properties summarized above, we have planned to use vermiculite mineral reserved in Sivas-Karakoç mine of Turkey for efficient removal of cesium ions in aqueous media. For this purpose, we investigated the effect of adsorbent dosage, contact time, pH, initial metal ion concentration, reaction temperature, equilibrium adsorption modeling, kinetic modeling and thermodynamic studies on cesium adsorption, which are important indicators for better understanding the sorption mechanism.

## EXPERIMENTAL METHODS

### Materials

Raw vermiculite was obtained from Organik Madencilik Corporation in Sivas-Yıldızeli region (Sivas-Karakoç mine). Stable $^{133}$Cs as CsCl (Sigma-Aldrich), $HNO_3$ (Merck), HCl (Merck), NaOH (Merck), KCl (Sigma-Aldrich), oxalic acid (Sigma-Aldrich), ammonium acetate (Merck) and other chemicals used in the study were in analytical grade. Stable cesium chloride salt was used in the present study due to its radiochemical similarity with radioactive $^{137}$Cs.

### Apparatus

Hanna HI-221 pH meter, a GFL 1083 batch adsorption shaker, an AX224 Sartorius 220 g analytical scales, a Retsch RM-2OO automatic agate mortar, a Perkin Elmer Spectrum BX FT-IR spectrometer, a Rigaku Miniflex II XRD device, a Panalytical Axios XRF device, a Perkin Elmer Optima 8000 ICP-OES device were used in experiments.

### Preparation of raw vermiculite sample

Vermiculite sample was ground to particle size to 355-400 μm with Retsch RM 200 mortar. In order to remove the water-soluble impurities from the sample, 10 g of raw vermiculite was dispersed in 250 mL distilled water and shaken in a batch shaker for 12 hours. After washing with distilled water, the sample was carefully removed from the glass tube and dried in an oven at 80$^o$C for 4 hours.

## Characterization methods

Physicochemical analysis

Cation exchange capacity (CEC), bulk density and isoelectronic point of vermiculite were obtained with potentiometric technique, pycnometer, and pH difference methods, respectively.

## XRD and XRF analysis

Quantitative chemical analysis of the sample was conducted with an XRF device (Panalytical Axios) in General Directorate of Mineral Research and Exploration Foundation, Analysis and Technology Laboratory, Ankara-Turkey. Mineralogical analysis of the sample was realized with XRD device, equipped with Cu X-ray tube, C monochromator and ICDD database (Rigaku Miniflex II) in Dokuz Eylül University Department of Mining Engineering. XRF analysis provided the quantitative amounts of chemical compounds exist in the mineral formation. XRD analysis enlightened and verified the crystal structure of vermiculite mineral.

## Batch adsorption studies

Stock $Cs^+$ solution (1000 mg/L) was prepared by dissolving 0.1265 g of CsCl in 100 mL of distilled water. After preparation of the stock solution, approximately 3 mL of 0.5 N $HNO_3$ was added to media and the solution was shaken thoroughly. Solution pH values were arranged using 0.01/0.1 N of $HNO_3$ and NaOH. In order to find optimum Cs adsorption conditions; different amounts of adsorbent (0.05, 0.1 and 0.2 g), contact time (1, 2, 3, 4, 5, 6 and 8 hours), solution pH's (3, 4, 6, 7, 8, 9 and 10), initial Cs concentrations (100, 175, 200, 250, 300 mg/L) and reaction temperatures (25, 40, 50, 70°C) were studied and evaluated.

The specific amount of vermiculite mineral was weighed, and adsorption experiments were realized with appropriate CsCl solutions into 50 mL plastic test tubes. pH of the suspension was arranged to the desired level, noted as arrangement pH. The solution volume was rearranged to 25 mL by adding distilled water into the test tubes. The suspension was shaken for a suitable time in a batch shaker and then filtered using blue Whatman filter paper.

Liquid section was poured into the volumetric flask and prepared for ICP-OES analysis (Perkin Elmer Optima 8000). In order to calculate the amount of adsorbed $Cs^+$ ions on vermiculite layer, equation given below was used;

$$Q_e(mg/g) = \frac{(C_0 - C_e)V}{W}$$ **(Eq. 1)**

$Q_e$ = Amount of adsorbed $Cs^+$ ions on vermiculite layer (mg/g)

$C_0$ = Initial $Cs^+$ ion concentration (mg/L)

$C_e$ = Equilibrium $Cs^+$ ion concentration (mg/L)

V = Volume of solution (L)

W = Amount of adsorbent (g)

## Desorption studies

Since cesium is a radioactive isotope, it is crucial to regain $Cs^+$ ions back to solution media according to radioactive waste management laws in order to prevent negative effects caused by radio-contamination. Therefore, It is important to detect the desorption conditions where $Cs^+$ ions are recovered. For this purpose, different eluent solutions were used to regain cesium and observe the desorption conditions under different temperatures. In this respect, $Cs^+$ loaded vermiculite samples were mixed with 10 mL of 0.5 and 1 M of oxalic acid solutions in batch adsorption device under 25, 45 and 65°C for 2 h and recovered suspensions were filtered. Subsequently, aqueous phases were separated and the amount of desorbed $Cs^+$ ions were detected with ICP-OES analysis.

Similarly, $Cs^+$ loaded samples were contacted with 10 mL of ammonium acetate and HCl (0.5 and 1 M) solutions in batch adsorption device under 25 °C for 2 h, filtered and the filtrate was analyzed with ICP-OES. For regeneration of Cs in distilled water media, loaded mineral samples were mixed with 10 mL of distilled water in batch adsorption device under 25 °C for 2 h, then the Cs concentration in the bulk solution phase was determined by ICP-OES. Percentage of desorbed $Cs^+$ ions was calculated using equation given below;

$$\%\text{Desorption efficiency} = \frac{\text{Amount of } Cs^+ \text{ desorbed}}{\text{Amount of } Cs^+ \text{ adsorbed}} \times 100 \qquad \textbf{(Eq. 2)}$$

## Potassium interference effect studies

IA group elements have similar features concerning their molecular orbital structures and electronic configuration. Natural soil samples include many cations such as $Na^+$, $K^+$, $Mg^{2+}$, and $Ca^{2+}$. Especially $K^+$ has an interesting effect of interfering the sorption of $Cs^+$ ions with different kinds of adsorbents regarding its ionic radius and chemical character (22).

Thus, to examine the effects of $K^+$ presence in Cs adsorption, 0.2 g of raw vermiculite sample was weighed and 5 mL of 1265 mg/L CsCl solution included 1000 mg/L $Cs^+$ ions poured into test tubes. At pH 8, the concentration of $K^+$ in solution varied from 100 and 400 mg/L, respectively. The volume of the solution was completed to 25 mL using distilled water and desorption experiments were realized at 25°C for 4 h. Resulting suspension was filtered, and the liquid was recovered for further determination of Cs concentration with ICP-OES.

**RESULTS AND DISCUSSION**

**Physicochemical properties**

Cation exchange capacity (CEC) of raw vermiculite was determined with a potentiometric technique using 0.5 N HCl (23) and calculated as 205 meq/100 g and this is a good value compared with other studies in the literature (24,25).

The bulk density of raw vermiculite samples containing 4% impurity was obtained as  0.909 g/cm$^3$ using pycnometer which is in good terms with the values reported by Organik Madencilik Mining Corporation where the samples were obtained (26).

The isoelectronic point of any adsorbent is crucial since it is an indicator of the point where maximum ionic adsorption takes place at specified pH point, and no uptake of adsorbate ions occur after that pH point, concerning ionic interactions. Hence, the isoelectronic point of raw vermiculite was obtained with given procedure (27): ΔpH value was calculated with the equation ΔpH = $pH_{final}$ - $pH_{initial}$ and the ΔpH (y-axis) vs. pH initial (x-axis) were plotted (not shown). The intercept point of the graph with x-axis was accepted as an isoelectronic point of vermiculite and was determined as pH 7.

**Chemical and Mineralogical  properties**

Chemical components exist in mineral formation was enlightened using XRF technique and given in Table 1. For comparison, chemical analysis of another vermiculite sample obtained from the same region (Sivas-Yıldızeli, Karakoç mine) conducted by Üçgül and Addison (28,29) was investigated and the results demonstrated that $SiO_2$, $TiO_2$ and $Na_2O$ contents of both minerals are similar.

**Table 1:** Chemical composition of raw vermiculite.

| Element Oxides | Percentage (%w/w) |
|---|---|
| $SiO_2$ | 36.3 |
| MgO | 14.6 |
| $Al_2O_3$ | 14.8 |
| $K_2O$ | 4.8 |
| $Fe_2O_3$ | 12.4 |
| $TiO_2$ | 2.7 |
| CaO | 4.2 |
| $Na_2O$ | 0.3 |
| (LOI) Loss of Ignition | 9.10 |

Mineralogical compositions of the raw sample determined by XRD were given in Figures 1 and 2. As shown in Figure 1, it was mainly composed of vermiculite, hydrobiotite, and cordierite while containing minor amounts of calcite, and trace amounts of sanidine.
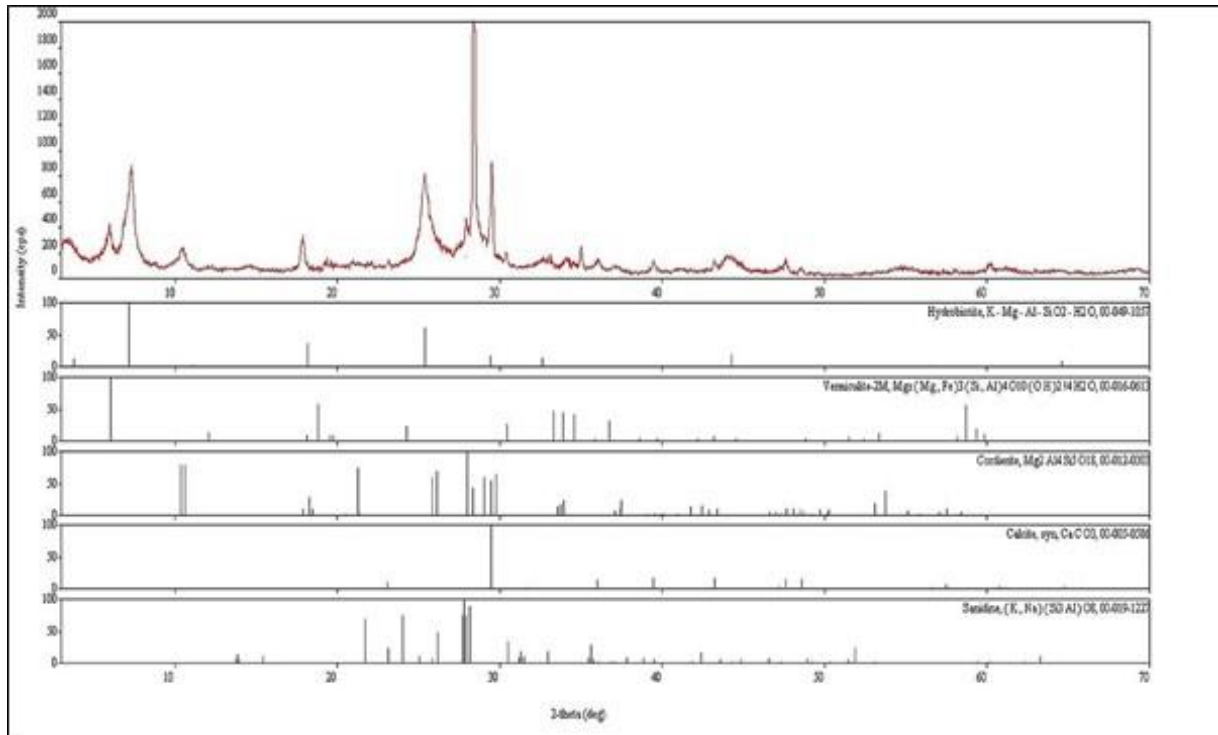


**Figure 1:** XRD diagram of Sivas-Yıldızeli vermiculite and other minerals in the formation.

The basal plane (100) of vermiculite and hydrobiotite mineral crystal structures are swollen when they collect water and organic molecules (such as ethylene glycol). When they are heated, however, the water and hydroxides are removed from their formation. Thus, changes occur in distances between the interlayers and the crystal structure. In order to reveal these changes, oriented samples were prepared by sedimentation. Samples were glycosylated and heated. The glycosylation procedure was materialized at 60 °C for 18 h under exposure to glycol vapor. Additionally, the heating procedure was carried out in oriented mineral samples under 550 °C for 1 h.

After these procedures, XRD diagrams were obtained, and the results were evaluated. According to the results, as seen in Figure 2, the peak corresponding to vermiculite in 15.33 Å was expanded to 18.28 Å. Peaks of other minerals were not affected by glycosylation. Thus, there were not any changes for their peaks. However, it was detected that peaks corresponding to vermiculite and hydrobiotite for the sample materialized under 550 °C for 1 h have been fully removed.

On the other hand, under these conditions two major enormous peaks were seen in 10.16 and 3.34 Å. The reason is, with the heating process; as $H_2O$ and OH groups in the formation of

vermiculite and hydrobiotite were removed; the crystal structure of minerals was decomposed and transformed into an illite formation. Consequently, two characteristic peaks of illite (10.16 and 3.34 Å) were formed (Figure 2).
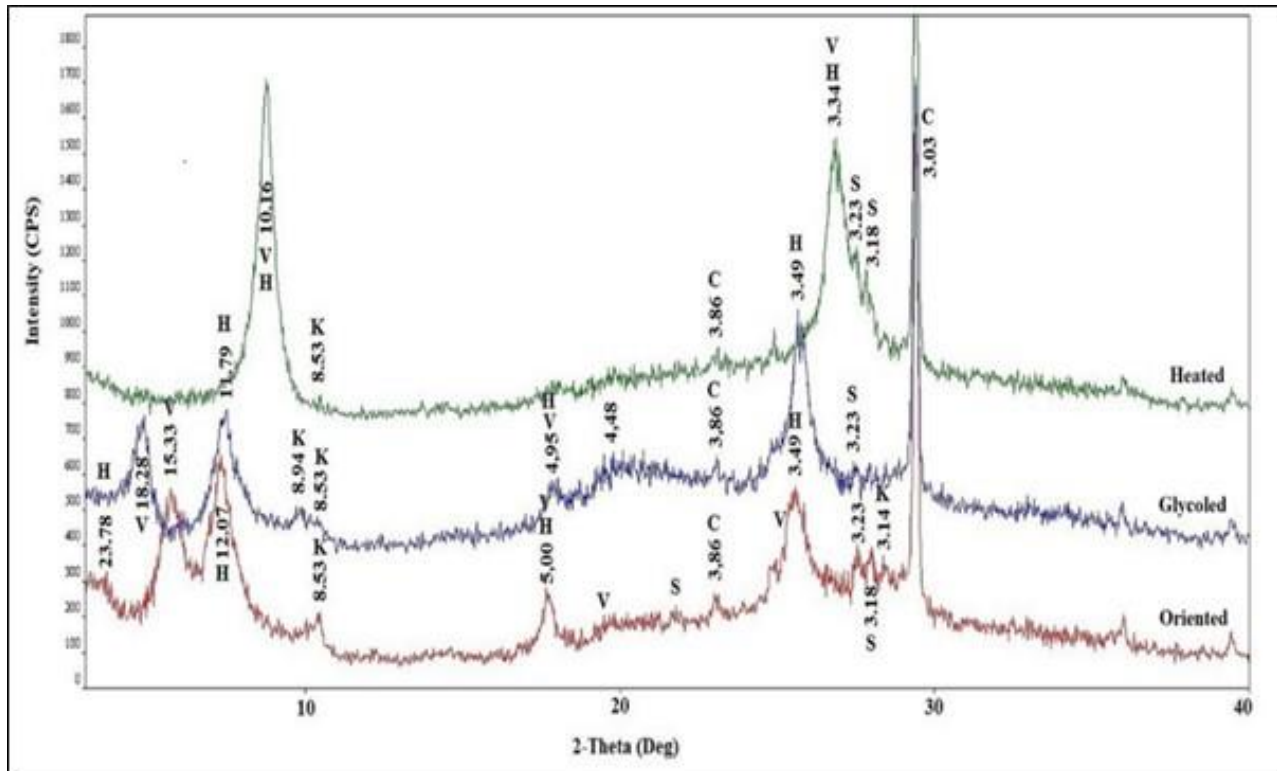


**Figure 2:** XRD peaks of Sivas-Yıldızeli vermiculite.

Cordierite, calcite, and sanidine minerals were affected neither by glycosylation procedure nor by the heating procedure under 550 °C. That is why these minerals are stable under these conditions. Thus, there were not any changes reported in their peaks. Therefore, peaks were unchanged after glycosylation and heating. As known, calcite is calcined at 1000 °C and decomposed as the reaction given below, but it is stable at 550 °C.

$$CaCO_3 \longrightarrow CaO + CO_2$$

In a study conducted by Ehsani (30), the crystal structure of a vermiculite sample obtained from South Africa was enlightened with XRD technique. Ehsani *et al.* investigated XRD peaks of the mineral by exposing it to heat and compared it with an untreated sample. They found that heated vermiculite showed characteristic peaks in 3.34 and 9.98 Å, thus compared with the current study; these peaks are identical with Sivas-Yıldızeli vermiculite, which illustrated 3.34 and 10.16 Å peaks.

As for unheated African vermiculite, peaks shown in 3.47, 4.91 and 11.82 Å are identical with Sivas-Yıldızeli vermiculite, which gave peaks in 3.49, 4.95 and 11.79, respectively. In another

study carried out by Yalçın *et al.* (31), they collected Sivas vermiculite for XRD analysis identification. Peaks found in 3.34 and 9.93 Å are nearly similar with that of peaks obtained in the current study (3.34 and 10.16 Å).

**FT-IR analysis**

Figure 3 illustrated FT-IR spectrum of Sivas-Yıldızeli vermiculite. As seen in the figure, the peak obtained in 3423 $cm^{-1}$ with medium intensity, corresponded to stretching vibrations of OH and silanol groups, peak obtained in 1631 $cm^{-1}$ with low intensity corresponded to bending vibrations of OH groups, major peak obtained in 1012 $cm^{-1}$ with high intensity corresponded to stretching vibrations of Si-O and Al-O and finally, peak obtained in 466 $cm^{-1}$ with high intensity corresponded to vibrations of Si-O-M (M: Si, Al, Mg, Fe) (30).
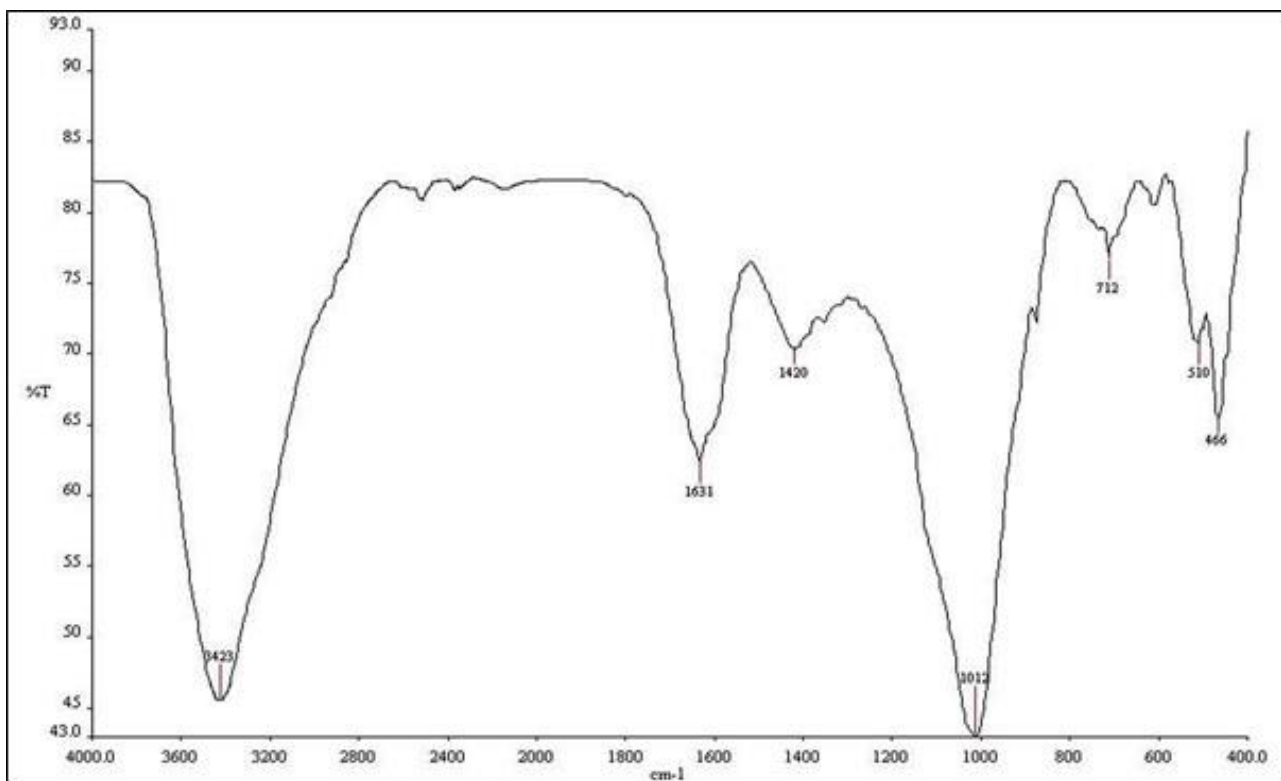


**Figure 3:** FT-IR spectrum of Sivas-Yıldızeli vermiculite.

**Adsorption study**

*Effect of adsorbent dosage*

0.05, 0.1 and 0.2 g of (2 g/L, 4 g/L, and 8 g/ L) raw vermiculite were used to find the optimum adsorbent dosage for cesium adsorption in 25 mL. Results demonstrated that adsorbed $Cs^+$ ions gradually increased with the increasing adsorbent dosage. Thus, the optimum adsorbent dosage for Cs adsorption process was obtained as 0.2 g of vermiculite. Hadadi *et al.* (4) proposed that Cs adsorption on natural vermiculite increased with increasing mineral dosage due to providing more active sites for adsorbing more $Cs^+$ ions in media, as seen in the current study. Kim *et al.* (2) reported that %Cs adsorption values increased with increasing sorbent concentrations.

However, adsorption capacities were decreased due to the increase of unsaturated sorption sites, which was in accordance with our results.

Figure 4 illustrates %Cs adsorption/Qe (mg/g) vs adsorbent dosage (g) plot, respectively. As seen in the figure, increasing the adsorbent dosage from 0.05 to 0.2 g caused a great difference in Cs uptake and the highest Cs sorption yield was obtained as 82.03% using 0.2 g of mineral.
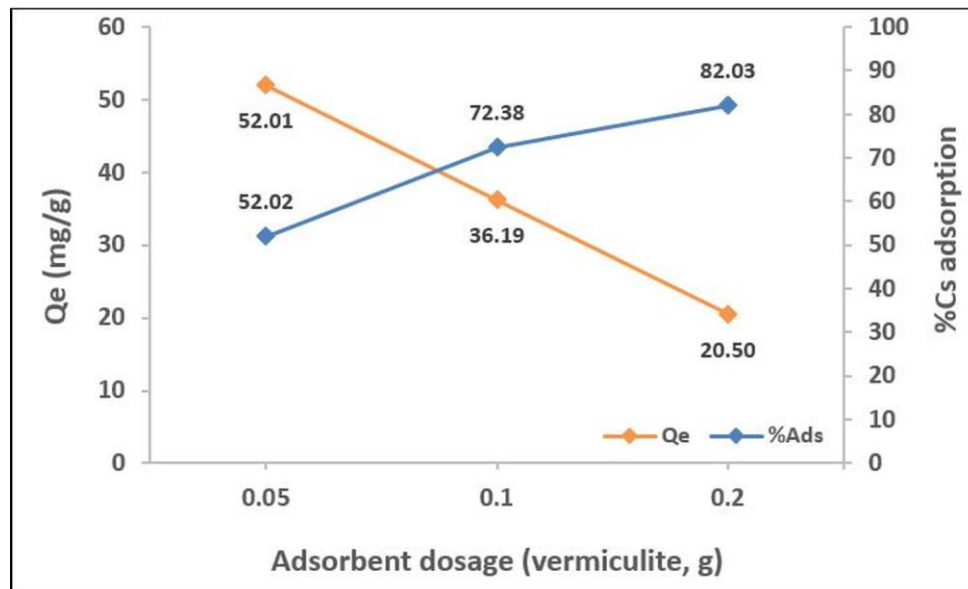


**Figure 4:** Effect of adsorbent dosage (Initial Cs concentration: 200 mg/L; Volume; 25 mL, Solution pH: 6; Contact time: 4 h; Reaction temp: 25°C).

**Effect of contact time and reaction kinetics**

In order to create kinetic modeling regarding the adsorption process, the effect of different contact times on Cs adsorption was investigated. A series of batch contact time experiments were performed to define and evaluate the optimum Cs ion sorption by the vermiculite, and the filtrate solution was checked by ICP-OES after each fraction. Experiments were conducted duplicate, and average %Cs adsorption/Qe values including standard deviations were included.

Results indicate, clearly, that Cs adsorption using vermiculite is not strongly depended on contact time since the equilibrium concentration of adsorbed Cs ions (Qe, mg/g) and adsorbed Cs ion percentage (Cs%) are very close in different time intervals (82% adsorbed Cs for 3 h, 82% for 4 h, 84% for 5 h) (Fig 5). Consequently, the optimum contact time was detected as 5 h.

In literature, similar behaviors have been previously reported about Cs$^+$ adsorption on different types of adsorbents (2,3). Khandaker *et al.* (32) studied the Cs sorption behavior of HNO$_3$ modified bamboo charcoal and the results demonstrated that Cs$^+$ ion uptake has not changed significantly with contact time, as was seen in the current study. Similarly, Yang *et al.* (33) found that Cs adsorption capacity of CuHF modified leather scrap stayed steady between 240 and 480 min (4–8 h), which showed a similar Cs sorption behavior with our study.
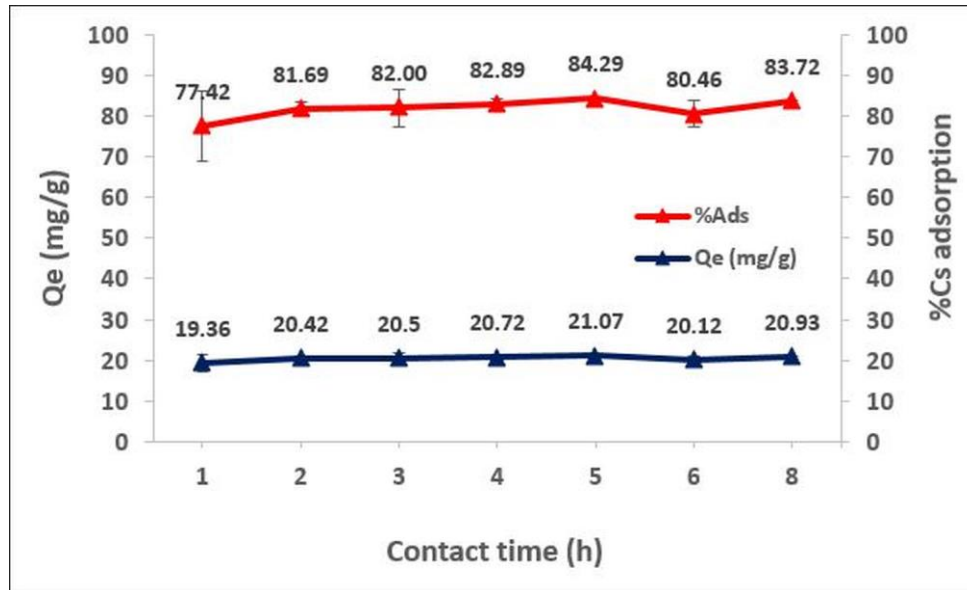
**Figure 5:** Effect of contact time (Adsorbent dosage: 0.2 g; Initial Cs concentration: 200 mg/L; Volume; 25 mL, Solution pH: 6; Reaction temp: 25°C).

## Pseudo-First Order kinetic model (Lagergren model)

This model was found by Lagergren in 1898 and has been applied to many studies since (34). Mathematical expression of Lagergren model is given by Equation 3, where $Q_e$: Amount of Cs ions adsorbed at equilibrium (mg/g), $Q_t$: Amount of Cs ions adsorbed at equilibrium at a specific time interval (mg/g), $k_1$: Lagergren rate constant (1/h), t: Contact time (h). Results of kinetic modeling study are illustrated below, which is built by kinetic parameters, respectively.

$$\log(q_e - q_t) = \log(q_e) - \frac{k_1}{2.303} t \qquad \textbf{(Eq. 3)}$$

Pseudo-first order kinetic rate constant ($k_1$) was determined as 0.1089 $h^{-1}$ and $R^2$ value of pseudo-first order kinetic model was found as 0.386, indicating that Cs-vermiculite adsorption process is not suitable with Lagergren kinetic model (graphic not shown). Theoretical (1.89 mg/g) and experimental Qe (21.75 mg/g) values proved this issue, as they are not even close.

## Pseudo-Second Order kinetic model (Ho model)

Ho and McKay found pseudo-second Order kinetic model in 1999, and this model has a wide variety of applications to various adsorption systems (35). Mathematical expression of Ho model is given in Equation 4, where $Q_e$: Amount of Cs ions adsorbed at equilibrium (mg/g), $Q_t$: Amount of Cs ions adsorbed at equilibrium at a specific time interval (mg/g), $k_2$: Ho rate constant (g/mg.h), t: Contact time (h). Fig 6 represents pseudo-second order kinetic model given for Cs-vermiculite adsorption process, parameters of Ho model applied to the current study is given above.

$$\frac{t}{q_t} = \frac{1}{K_2 q_e^2} + \frac{t}{q_e} \qquad \textbf{(Eq. 4)}$$
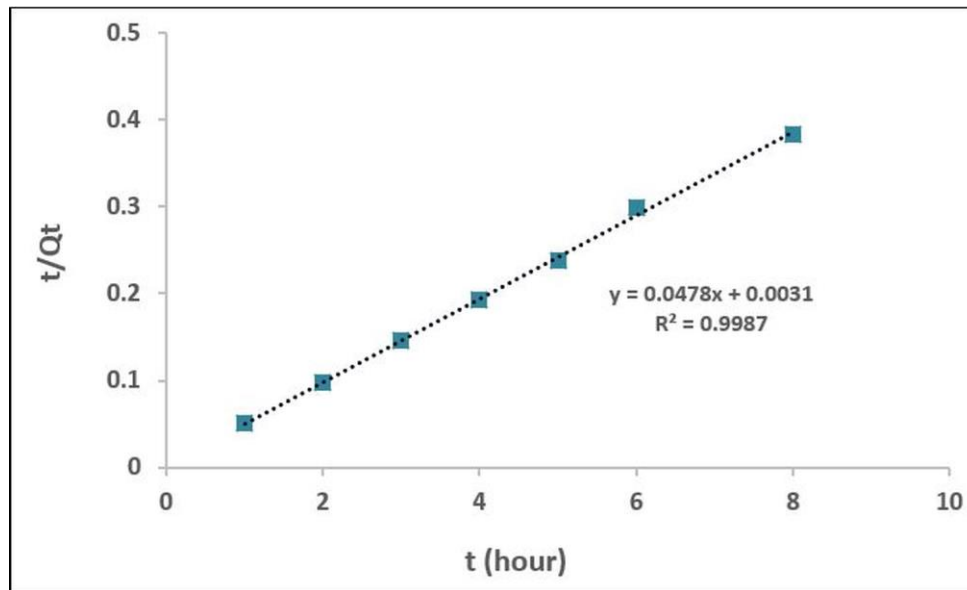


**Figure 6:** Pseudo-Second order Ho kinetic model plot of the Cs-vermiculite adsorption process.

Pseudo-second order kinetic model rate constant ($k_2$) was obtained as 0.7371 g/mg.h. More importantly, high regression value found as 0.9987 and close experimental (21.75 mg/g) and theoretical (20.92 mg/g) Qe values suggested that Cs-vermiculite adsorption operation was in accordance with pseudo-second order kinetic model.

**Elovich kinetic model**

This chemisorption model was established by Zeldowitsch in 1934 (36) and applied to describe the rate of adsorption of carbon monoxide on manganese dioxide that decreased exponentially with an increase in the amount of gas adsorbed (37). Mathematical linear expression of Elovich equation is given in Equation 5 (38), where $Q_t$: Amount of Cs ions adsorbed at equilibrium at a specific time interval (mg/g), α and β: Elovich rate constants, t: Contact time (h). Linear regression value of Elovich Kinetic model was obtained as 0.5695 suggesting that Cs-vermiculite adsorption was not compatible with this model (graphic not shown).

$$q_t = a + b\ln t \qquad \textbf{(Eq. 5)}$$

**Weber-Morris kinetic model (Intraparticle model)**

Adsorption of cesium ions on vermiculite pores is depended upon three stage consecutive stage process; boundary layer diffusion (film diffusion), intraparticle diffusion and adsorption on the porous surface. Briefly, adsorbate molecules ($Cs^+$ ions) soluted in liquid media are mass transferred across the external film layer, which covered the outer section of adsorbent (vermiculite).

After Cs⁺ ions are transferred across this film, they are moved into the inner sections of vermiculite pores, and this is known as intraparticle diffusion. When adsorbate molecules reach the active adsorption sites of the mineral, they are physically adsorbed onto porous layers.

In order to enlighten the type of diffusion kinetics mechanism concerning Cs adsorption onto vermiculite, Weber-Morris kinetic model (intraparticle model) was applied to present data by plotting $q_t$ values against $t^{1/2}$ data.

Weber-Morris kinetic model expression is given in Eq. 6, where $q_t$: Amount of Cs⁺ ions adsorbed in a given moment at equilibrium, $K_{ipd}$: Intraparticle diffusion rate constant, $t^{1/2}$: Root of adsorption contact time, C: Intercept defining the thickness of boundary layer in intraparticle diffusion mechanism. High C values correspond to thicker boundary layer (film layer) covering the external site of an adsorbent molecule (39).

$$q_t = K_{ipd}t^{1/2} + C \qquad \textbf{(Eq. 6)}$$

Intraparticle diffusion model parameters and the characteristics of diffusion kinetics regarding the adsorption of Cs on vermiculite pores are summarized below. For 1, 2, 3, 4, 5, 6, and 8 hours of adsorption, $t_{1/2}$ values were obtained as 1, 1.4142, 1.7320, 2, 2.2361, 2.4495, and 2.8284, respectively.

In the case of intraparticle diffusion is completely affecting the adsorption process, the plot $q_t$ versus $t_{1/2}$ passes through the origin (40), which is not a valid situation in the current experiment as seen in Figure 7.
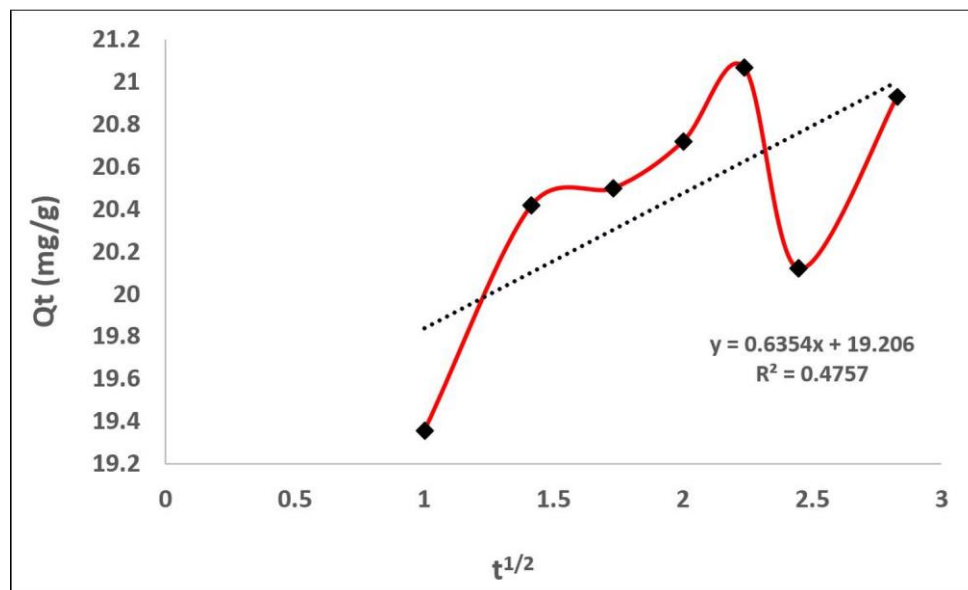


**Figure 7:** Weber-Morris kinetic model plot of Cs-vermiculite adsorption process.

That means that Cs adsorption on vermiculite layer consists of two-stage processes, the first part is rapid boundary layer diffusion and the second part is slower intraparticle diffusion. Consequently, Cs adsorption process onto vermiculite was not compatible with Weber-Morris kinetic model, since $R^2$ value of 0.4757 was quite low and unsatisfactory for the intraparticle process.

**Effect of solution pH**

In order to investigate the effect of pH on Cs adsorption, different solution pH's were studied and evaluated. Solution pH was rearranged to 3, 4, 6, 7, 8, 9 and 10 using appropriate acid/base solutions and pH meter, respectively. As shown in Figure 8, the percentage of adsorbed $Cs^+$ ions and amount of adsorbed $Cs^+$ ions at equilibrium were increased with increasing pH values until pH 9.2.

The reason is due to the negative electrostatic interactions covered the layer of vermiculite causing a more powerful affinity between positive charged Cs ions and mineral layer, thus increasing the amount of $Cs^+$ ions onto mineral (4). Additionally, high alkaline pH values caused the formation of cesium hydroxide complexes as negatively charged $Cs(OH_2)^-$ via hydrolysis, resulting in electrostatic repulsions with mineral layer surface and triggered the decrease in the amount of adsorbed $Cs^+$ (41,42).

Ding *et al.* (43) reported that $Cs^+$ uptake on the clay sample significantly decreased under pH 5 due to the competition between $H_3O^+$ and $Cs^+$ ions in acidic media. However, in more alkaline values, $Cs^+$ uptake was increased concerning the lower competition between $H_3O^+$ and $Cs^+$, more importantly, deprotonation of silanol and aluminol groups, providing a stronger affinity between active sites and cesium (3).
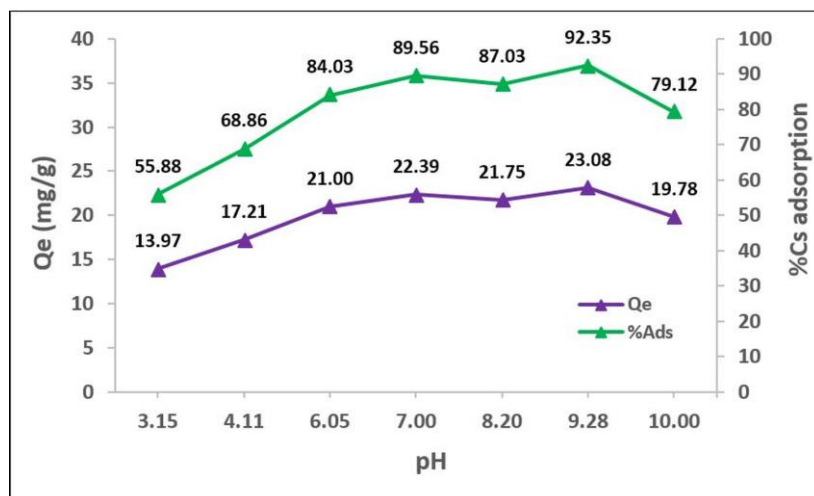


**Figure 8:** Effect of solution pH (Adsorbent dosage: 0.2 g; Initial Cs concentration: 200 mg/L; Volume; 25 mL, Contact time: 5 h; Reaction temp: 25°C).

**Effect of initial Cs concentration and equilibrium isotherm modeling**

Different concentrations of adsorbate and the effects of adsorption were investigated. Fig 9 demonstrates the effect of initial adsorbate concentration on $Cs^+$ adsorption process. Increasing adsorbate concentrations caused an increase in the amount of $Cs^+$ ions adsorbed onto the surface of the mineral, per 1 mg of Cs ion adsorbed in per 1 g of mineral, meaning mg/g. Even the adsorption percentage was found as 99% in 100 mg/L Cs concentration; it was decided to study with 200 mg/L Cs concentration for adsorption experiments.

Seaton *et al.* (44) observed that adsorption capacity of Cs (mg/g) using silica gel embedded phosphotungstic acid gradually increased with increasing Cs initial concentrations. Ding *et al.* (43) found that $Cs^+$ adsorption amount has increased proportionally with augmenting initial Cs concentrations. These results support gradual sorption increase behavior of $Cs^+$ with enhancing initial concentrations in our study.
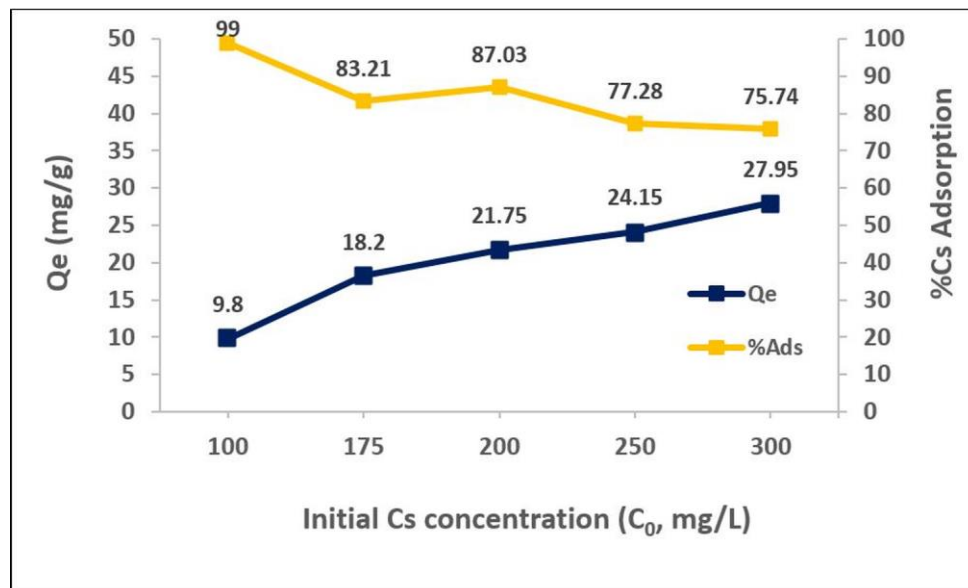


**Figure 9:** Effect of initial Cs concentration (Adsorbent dosage: 0.2 g; Solution pH: 8; Contact time: 5 h; Reaction temp: 25°C).

There are various kinds of adsorption isotherms used in the literature and the most important ones are reported as Langmuir (45), Freundlich (46), D-R (47) and Temkin (48) isotherms. Adsorption isotherms provide the knowledge and relation between the concentration of adsorbate ions in bulk solution and adsorbed amount of them at equilibrium, thus enlightening the efficiency and characteristics of the adsorption process. Present data were exposed to Langmuir, Freundlich, D-R, and Temkin isotherm models for further investigation of adsorption characteristics.

**Langmuir isotherm model**

Irving Langmuir established the Langmuir adsorption isotherm model in 1918 and described the gas-solid phase adsorption on activated carbon using this model (45). The general assumption of Langmuir adsorption isotherm model is that the adsorption takes place in a monolayer section of adsorbent and adsorption energies of adsorbate molecules are identically uniform. Thus, there are not any interactions between adsorbed metal ions on the porous surface of sorbent. Additionally, the processes that are compatible with Langmuir isotherm model are usually characterized by chemical adsorption, meaning after being reached to adsorption saturation point, which is called as maximum monolayer capacity, no following sorptions occur. This model was applied to many studies concerning the adsorption of various metal ions on different kinds of clay minerals for years (49–53).

Langmuir model is expressed in Equation 7, where Ce: Concentration of adsorbate ions in bulk solution at equilibrium (mg/L), Qe: Amount of adsorbed ions on adsorbent surface at equilibrium (mg/g), $Q_{max}$: monolayer saturation capacity (maximum monolayer capacity, mg/g), b: Langmuir constant related to adsorption energy (L/mg). Plotting Ce/Qe against Ce gives the slope of $1/Q_{max}$ and the intercept of $1/bQ_{max}$. Parameters of Langmuir isotherm and adsorption isotherm plot are demonstrated in Fig 10.

$$\frac{C_e}{q_e} = \frac{1}{bQ_{max}} + \frac{C_e}{Q_{max}} \qquad \textbf{(Eq. 7)}$$
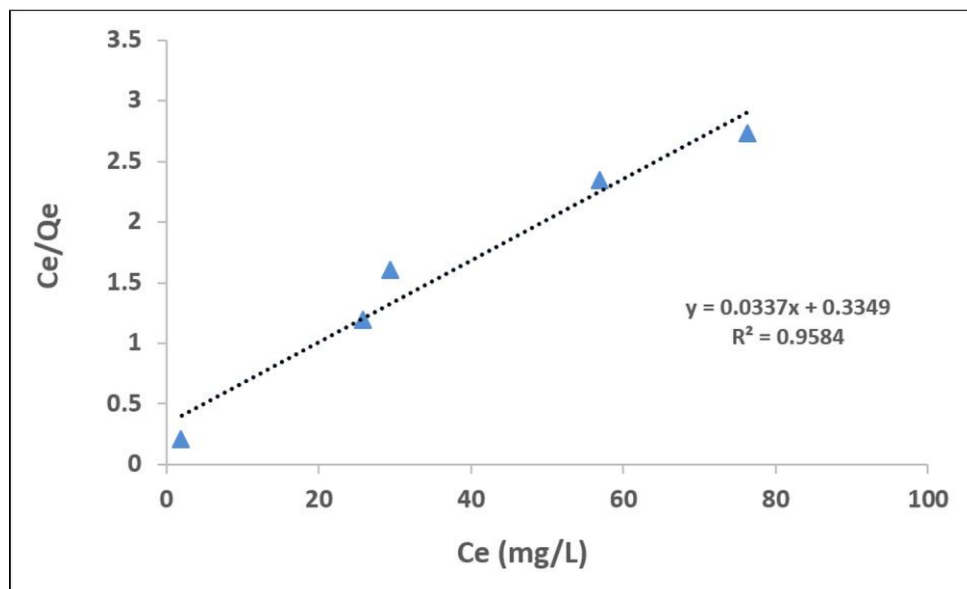


**Figure 10:** Langmuir adsorption isotherm plot for Cs adsorption onto vermiculite.
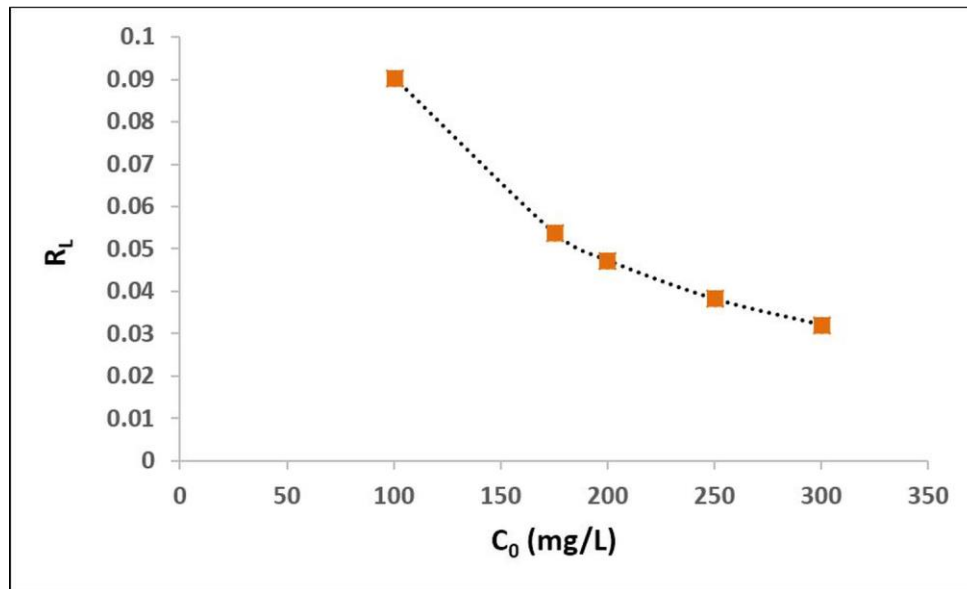
**Figure 11:** Variation of separation factor as a function of initial Cs concentration.

Applicability of Langmuir adsorption isotherm is verified by a dimensionless physicochemical constant given as separation factor, $R_L$. It defines either adsorption nature is favorable or not, thus it is an indicator of sorption feasibility. If $R_L$ value >1: it indicates that the adsorption process is unfavorable, if $R_L$ value is $0 < R_L < 1$: it is favorable, if $R_L = 0$: process is irreversible and finally if $R_L = 1$, it is linear (54). Separation factor ($R_L$) is mathematically illustrated in Equation 8, where $R_L$: separation factor, $K_L$: Langmuir constant (L/mg), $C_0$: Initial adsorbate concentration (mg/L). The connection between separation factor $R_L$ and initial Cs concentration (between 100 and 300 mg/L Cs) is given in Fig 11.

$$R_L = \frac{1}{1 + K_L C_0}$$ **(Eq. 8)**

Cesium adsorption process onto vermiculite surface was compatible with Langmuir isotherm model since linear regression value of Langmuir plot was obtained as 0.9584. Separation factor ($R_L$) values were found as 0.0904, 0.0538, 0.0473, 0.0382, and 0.0321, respectively (for 100-300 mg/L initial Cs). In addition, Langmuir constant related to the adsorption energy b was calculated as 0.1006 L/mg. Maximum adsorption capacity $Q_{max}$ was determined as 29.67 mg/g.

These results indicate that $Cs^+$ ions were adsorbed on a monolayer section of porous vermiculite structure with uniform energies. $R_L$ value being obtained lower than 1 proposed that adsorption of Cs onto the mineral was a favorable process and as seen in Fig 11, increasing initial metal concentrations caused $R_L$ values to gained closer to zero value, meaning higher adsorbate concentrations were more appropriate for favorable Cs adsorption.

**Freundlich isotherm model**

This isotherm model was originally found by Freundlich in 1906 (46) and is based on a contrary idea with Langmuir's isotherm characteristics that the adsorption takes place on a heterogeneous porous surface of adsorbent and adsorption energies (enthalpy) of adsorbate molecules are not identical, referring that sorption enthalpy is dependent on the amount of adsorbate. Also, this model approves that the adsorption enthalpy decreases logarithmically with the increase of adsorbate fractions. Consequently, if an adsorption model is fitted with Freundlich model, it strongly suggests that a physical adsorption process is in effect with lower sorption energy than that of chemisorption (55,56).

Linear form of Freundlich adsorption isotherm model is mathematically expressed in Equation 9 where $q_e$: Amount of adsorbed ions at equilibrium (mg/g), $K_f$: Freundlich constant corresponding to approximate indicator of adsorption capacity (mg/g), 1/n: Adsorption intensity indicating that whether adsorption process is favorable or not, $C_e$: Concentration of metal ions in bulk solution at equilibrium (mg/L). Plotting $\log q_e$ against $\log C_e$ gives the slope of 1/n and the intercept of $\log K_f$, as it is demonstrated in Fig 12.

$$\log q_e = \log K_f + \frac{1}{n}\log C_e \qquad \textbf{(Eq. 9)}$$

1/n value is an important indicator for evaluating whether sorption is favorable or not since, if 1/n = 1, it corresponds that adsorption is linear, 1/n < 1 suggest that adsorption is a physical sorption and fits Freundlich model and finally if 1/n > 1, it means that adsorption is a chemical process. 1/n value also corresponds to the degree of adsorption heterogeneity, meaning the smaller 1/n values express higher heterogeneity (54).
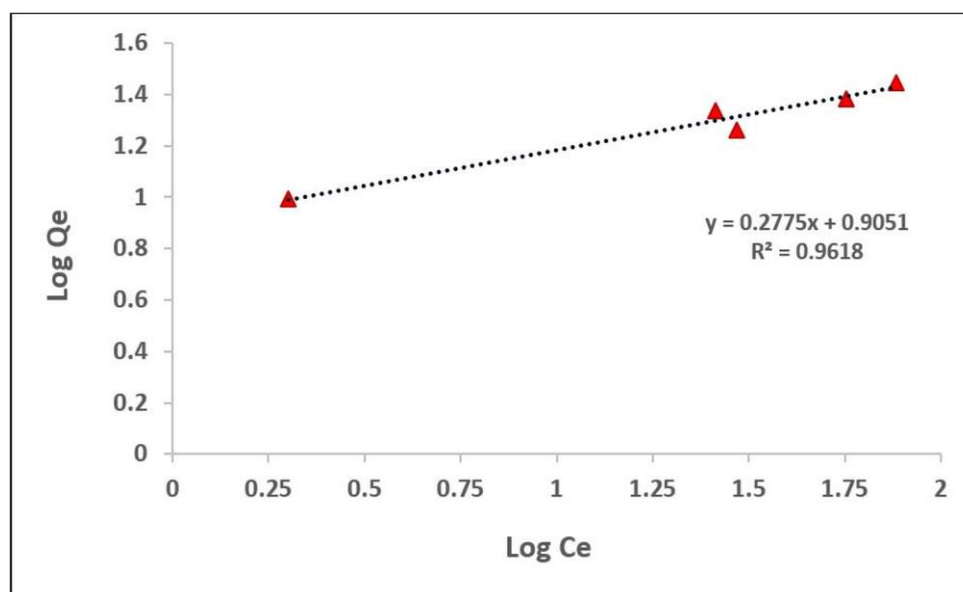


**Figure 12:** Freundlich adsorption isotherm plot for Cs adsorption onto vermiculite.

As displayed in Fig 11, high linear regression value of 0.9618 and excellent 1/n value being calculated lower than unity (n=3.6036, 1/n=0.2775) clearly explains that Cs adsorption onto the porous surface of vermiculite mineral is in accordance with Freundlich adsorption isotherm model and it is an indicator of the presence of a physical sorption. Thereby, these data provide that a physisorption process administrates sorption uptake of positively charged Cs ions onto the vermiculite mineral with a maximum adsorption capacity of 8.037 L/g.

**Temkin isotherm model**

Mikhail Temkin developed this model with a study based on the adsorption of hydrogen gas onto platinum electrodes in acidic solutions in 1940, thus is a modified Langmuir isotherm model (48). On the contrary with Freundlich isotherm model assumption, the model is based on the idea that the adsorption enthalpy decreases not exponentially, but linearly with the increase of adsorbate fractions and the binding energies of adsorbate molecules on the adsorbent surface is uniformly distributed because of the indirect adsorbate/adsorbent interactions (57). Linear form of Temkin isotherm model is displayed in Equation 10, where $q_e$: Amount of adsorbed ions at equilibrium (mg/g), $C_e$: Concentration of metal ions in the bulk solution at equilibrium (mg/L), B: Heat of adsorption constant (j/mol), B = RT/b where b: Temkin isotherm constant referring the heat of adsorption, A: Equilibrium binding constant (L/g), R: Ideal gas constant (8.314 j/mol.K), T: Absolute temperature (°K).

$$q_e = B \ln C_e + B \ln A \qquad \textbf{(Eq. 10)}$$

Figure 13 demonstrates the parameters of Temkin isotherm and plot of $q_e$ versus ln $C_e$ where the slope of the graphic is B and the intercept is B lnA. Temkin isotherm constant b derived from B constant refers to the heat of adsorption and is used to determine the adsorption characteristics, meaning whether the adsorption is a physical or chemical process (58). Empirical results demonstrated that adsorption of Cesium ions onto vermiculite surface showed a physical sorption character since Temkin isotherm constant b was found to be 541.46 j/mol, lower than 8 kJ/mol and this is supported by the results of Freundlich isotherm modeling. In addition, good linear regression value of 0.9139 indicates that adsorption process is fitted with Temkin isotherm model.
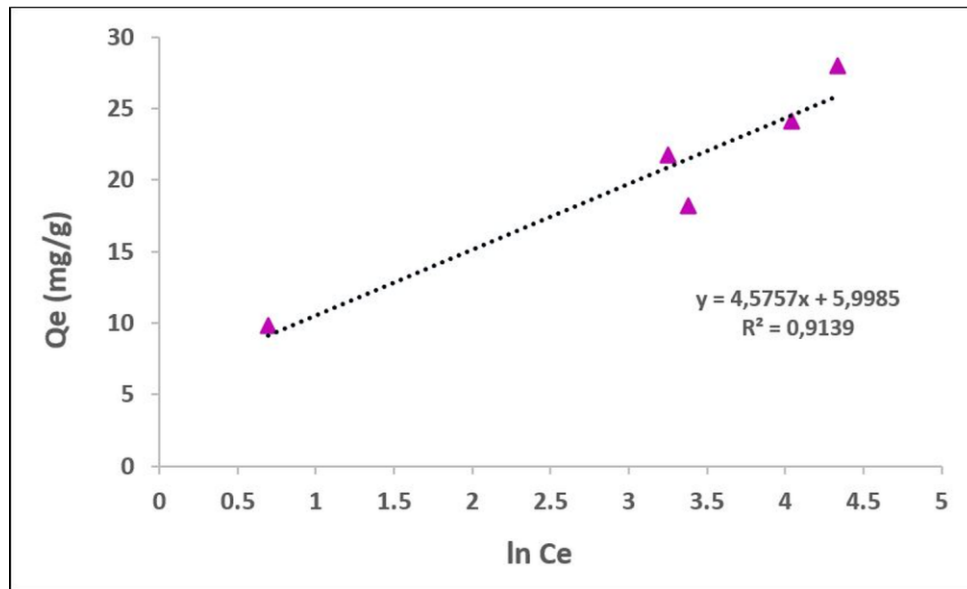
**Figure 13:** Temkin adsorption isotherm plot for Cs adsorption onto vermiculite.

**Dubinin-Radushkevich (D-R) isotherm model**

Dubinin-Radushkevich adsorption isotherm model (47) was developed in 1947 to describe the sorption of vapors onto microporous solids in order to express the adsorption mechanism with a Gaussian energy distribution on a heterogeneous surface. This model assumes that adsorption process follows a pore-filling mechanism and has been used to distinguish the physical and chemical adsorption using isotherm parameters concerning the sorption energy (59). Additionally, this model accepts that the adsorption curve is related to the porosity of adsorbent and often fit well with the high amount of solute activities with mid-range of concentrations. Linear expression of D-R isotherm model is demonstrated in Equation 11, where $q_e$: Amount of adsorbate ions adsorbed at equilibrium (mg/g), $K_{DR}$: D-R isotherm constant ($mol^2/kj^2$) associated with mean free adsorption energy of adsorbate molecules per mole as they are transferred from solution media onto the adsorbent surface (60). $Q_{max}$: Theoretical isotherm saturation capacity (mg/g), $\epsilon$: Polanyi potential (j/mol). Expression of Polanyi potential is also given in Equation 12. The D-R plot of $\ln q_e$ versus $\epsilon^2$ gives the slope of isotherm constant $K_{DR}$ and the intercept of maximum adsorption capacity, $\ln q_{max}$ as it is displayed in Fig 14.

$$\ln q_e = K_{DR} e^2 + \ln q_{max} \qquad \textbf{(Eq. 11)}$$

$$e = RT \ln(1 + \frac{1}{C_e}) \qquad \textbf{(Eq. 12)}$$
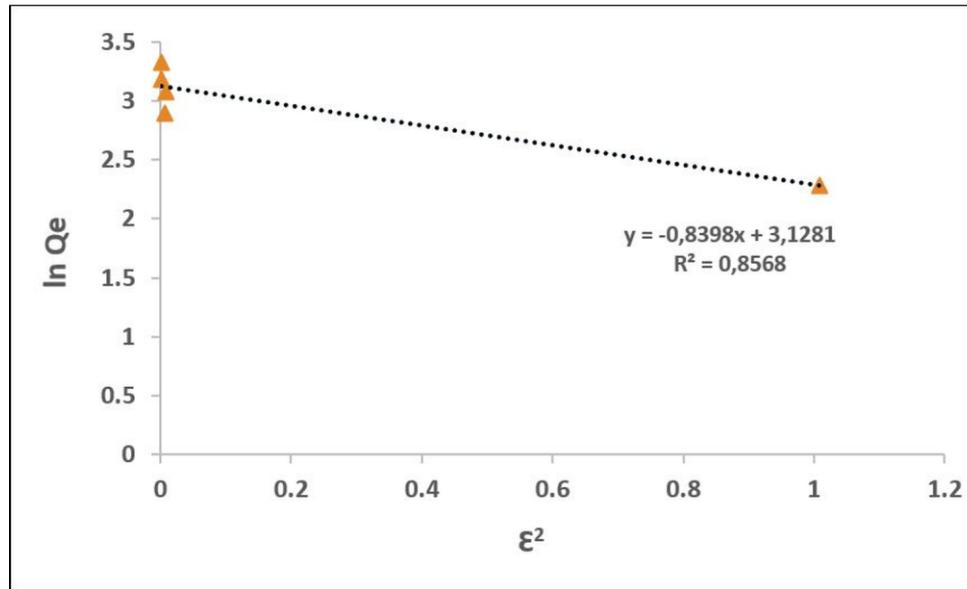
**Figure 14:** Dubinin-Radushkevich adsorption isotherm plot for $Cs^+$ adsorption onto vermiculite.

D-R adsorption isotherm constant; $K_{DR}$ was found as 0.8398 $mol^2/kj^2$ and $Q_{max}$ value corresponding to the maximum adsorption capacity of adsorbent, derived from Equations 11 and 12, was obtained as 22.38 mg/g.

One of the unique characteristics of D-R isotherm model is that it provides the type of sorption process using adsorption energy parameter given as E. According to present model, with the calculation of E; if E < 8 kJ/mol, that refers the adsorption is a physical process (physisorption) with Van der Waals interactions. if 8 < E < 16 kJ/mol, it indicates that adsorption of metal ions on adsorbent is a chemical process with higher sorption enthalpy, more likely with the domination of covalent bond interactions (61). The formula of adsorption energy E is shown in Equation 13.

$$E = \left[ \frac{1}{\sqrt{2K_{DR}}} \right] \qquad \textbf{(Eq. 13)}$$

As demonstrated in Fig 13, D-R isotherm plot is constructed with a temperature-dependent modeling, since $\varepsilon$ and $\varepsilon^2$ values calculated for different temperatures affect the sorption curve, and the data fitted with model lied on the same curve. Adsorption energy is found as 0.772 kJ/mol, which is lower than the value of 8 kJ/mol, indicates that the adsorption of $Cs^+$ ions onto vermiculite surface is a physisorption process. In addition, linear regression value of 0.8568 is an unsatisfactory $R^2$ value, referring that sorption of Cs onto the porous structure of vermiculite mineral is not compatible with D-R isotherm model.

**Effect of temperature and adsorption thermodynamics**

Thermodynamic parameters are essential for the interpretation of the nature and characteristics of adsorption process concerning their physicochemical attributes. Gibbs free energy, adsorption enthalpy, and entropy hold fundamental knowledge about the character of sorption. Gibbs free energy change ($\Delta G^0$), provides the information of whether the sorption process is spontaneous or not, meaning if it is necessary to give an external energy to the system in order to start the adsorption. Adsorption free enthalpy ($\Delta H^0$) change gives the knowledge of the thermal character of the sorption, providing whether the sorption of metal ions on adsorbent is endothermic or exothermic and finally, adsorption free entropy change ($\Delta S^0$) is an indicator of magnitude concerning the disorder among the adsorbate molecules and adsorbent.

If $\Delta G^0 < 0$ (negative): it indicates that the sorption occurs spontaneously without the need for an external energy. If $\Delta G^0 > 0$ (positive), it means the sorption does not take place spontaneously and the reaction mechanism needs a supportive force, mostly the heat energy. Usually, it is favorable for $\Delta G^0$ to be spontaneous (negative value) for ideal sorption mechanism. Physicochemical expression of Gibbs free energy change ($\Delta G^0$) and the equilibrium constant $K_c$ are illustrated between Equation 14 and 17, respectively. R: ideal gas constant (8.314 j/mol.K) and T: absolute temperature (K).

Equilibrium constant ($K_c$) refers the ability of an adsorbent molecule to hold adsorbate ions onto its porous structure and amplitude of adsorbate mobility in the sorption media, regarding the ratio of adsorbed metal ions at equilibrium and concentration of metal ions in bulk solution (62). The general expression of $\Delta G^0$ is given in Eq. 14 and rearranging $\Delta G^0$ as $-RTlnK_c$ from Eq. 15 gives the Eq. 17. The plot of $lnK_c$ versus $1/T$ gives the slope of $\Delta H^0/RT$ and the intercept of $\Delta S^0/R$.

$$\Delta G^0 = \Delta H^0 - T\Delta S^0 \qquad \textbf{(Eq. 14)}$$

$$\Delta G^0 = -RTlnK_c \qquad \textbf{(Eq. 15)}$$

$$K_c = \frac{q_e}{C_e} \qquad \textbf{(Eq. 16)}$$

$$lnK_c = \frac{\Delta S^0}{R} - \frac{\Delta H^0}{RT} \qquad \textbf{(Eq. 17)}$$

Hence, in order to evaluate physicochemical characteristics and thermochemical features of Cs adsorption onto vermiculite, thermodynamic studies were conducted. In this context, $K_c$ ($q_e/C_e$) values for different temperatures (25, 40, 50 and 70 °C) were calculated and different $\Delta G^0$ values for these temperatures were obtained. To calculate $\Delta H^0$ and $\Delta S^0$ values, a graphic of $lnK_c$ versus $1/T$ was plotted (Van't Hoff plot) and was displayed in Fig 16. Thermodynamic parameters of adsorption process are given below. Effect of temperature on Cs adsorption is shown in Figure 15, which shows that $Cs^+$ sorption capacity was decreased with increasing temperatures. Zheng *et al.* (63) observed the same situation, since the temperature increased, Cs uptake on

unmodified montmorillonite diminished. Also, Kim *et al.* (2) reported that Cs sorption gradually decreased with higher temperatures using raw sericite mineral.
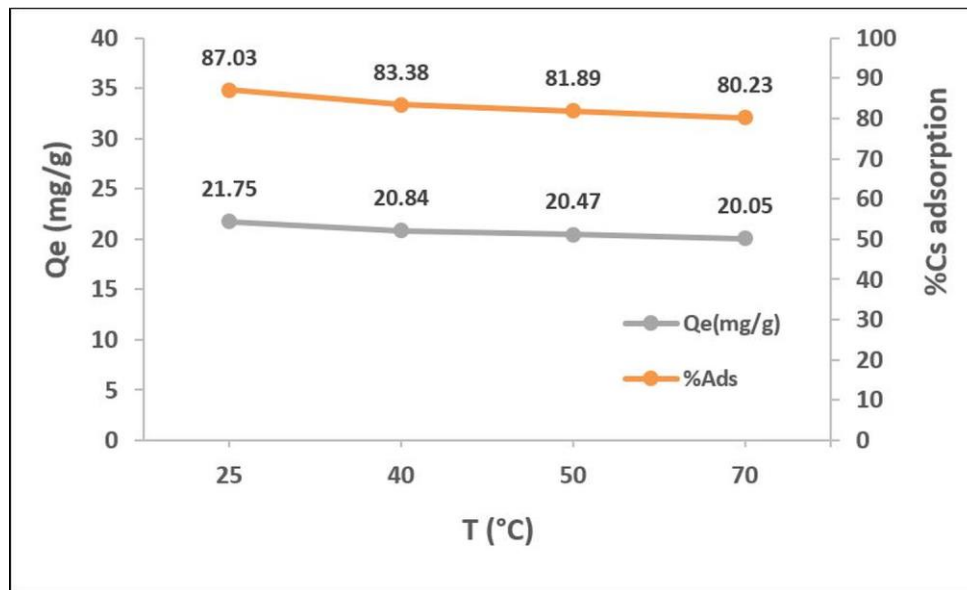


**Figure 15:** Effect of temperature (Adsorbent dosage: 0.2 g; Initial Cs concentration: 200 mg/L; Volume: 25 mL; Solution pH: 8; Contact time: 5 h).
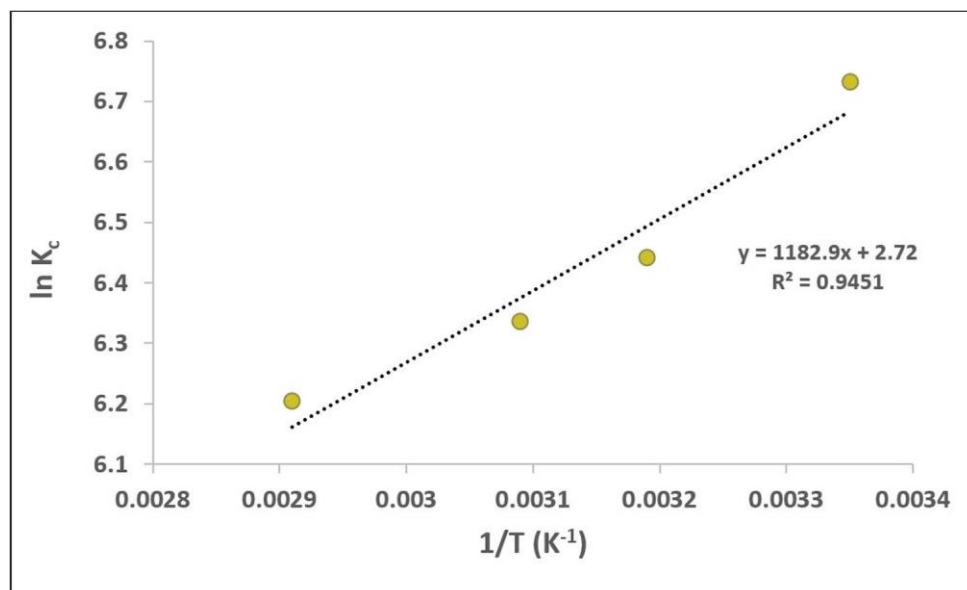


**Figure 16:** Van't Hoff plot of Cs adsorption.

Results demonstrated that cesium adsorption process onto vermiculite mineral occurred spontaneously, since $\Delta G^0$ values were obtained below zero (-15.65, -16.67, -16.76, -17.02 and -17.69 kJ/mol for 25, 40, 50 and 70 °C, respectively) and higher $\Delta G^0$ values with increasing temperatures revealed that spontaneity increased with increasing temperatures.

The negative $\Delta H^0$ value indicated that sorption of $Cs^+$ ions on the mineral surface had exothermic character, meaning as the temperature increased, the amount of adsorbed $Cs^+$ ions were gradually decreased as seen in Figures 24 and 25. Positive $\Delta S^0$ value of 22.61 j/mol.K proved

that the disorderliness among the solid and liquid phases in bulk solution increased during adsorption equilibrium.

The degree of $\Delta H^0$ value provides the knowledge of sorption characteristics, if $\Delta H^0$ value is between 8-25 kJ/mol, the adsorption process is a physisorption and if it is between 83-830 kJ/mol, it is a chemisorption (56). Thus, $\Delta H^0$ value of -9.83 kJ/mol being lower than 25 kJ/mol revealed that Cs adsorption was a physical process with weak interactions between adsorbent and adsorbate molecules. $K_c$ values were decreased with increasing temperatures and that means the mobility of $Cs^+$ ions were increased with gradual increase in adsorption temperature, referring that interactions between adsorbent and adsorbate molecules were weakened and amount of adsorbed $Cs^+$ ions were decreased (62).

Results of our study are compared and interpreted with similar studies in literature and given in Table 2.

**Table 2.** Comparison of current experimental $Cs^+$ adsorption capacities on different adsorbents.

| Adsorbent | $Q_{max}$ (mg/g) | Reference |
|---|---|---|
| Sivas vermiculite (Turkey) | 29.67 | This study |
| Gangneung Sericite (Korea) | 6.68 | (2) |
| Vermiculite (Commercial) | 56.92 | (3) |
| Vermiculite (Natural) | 0.65 | (4) |
| Nitric acid-modified bamboo charcoal | 45.87 | (32) |
| Potassium cobalt hexacyanoferrate modified leather scrap | 36.75 | (33) |
| Nickel modified Akadama clay (Japan) | 16.10 | (43) |
| Silica gel embedded phosphotungstic acid | 20.80 | (44) |
| Ammonium-pillared montmorillonite/$Fe_3O_4$ | 27.53 | (63) |
| Clay from Inshas disposal site, Cairo (Egypt) | 46.30 | (64) |
| Nanocrystalline mordenite | 37.30 | (65) |
| Chitosan impregnated with ionic liquid | 2.85 | (66) |
| Marble | 2.37 | (67) |
| Modified hydroxyl apatite | 69.49 | (68) |

These results suggest that vermiculite is a strong and efficient sorbent for $Cs^+$ removal compared with other clay minerals and various kinds of modified adsorbents. As seen in Table 4, $Q_{max}$ values of some modified adsorbents (nanocrystalline mordenite, nitric acid modified bamboo charcoal, KCoHF modified leather scrap, modified hydroxyl apatite) were higher than that of the present study. However, studied vermiculite is a natural material and this adsorbent can be easily applied with cheap, economic and simple batch sorption procedures in solutions such as water with neutral/low alkaline pH values for Cs removal.

**Cesium desorption studies**

Recovering adsorbates with nuclear character are crucial in preventing radioactive contamination trapped in soil minerals, which are exposed to the natural environment, and living metabolisms. Hence, $Cs^+$ ions were desorbed from adsorbent using different kinds of eluent solutions with various concentrations. Results of desorption study were demonstrated in Figure 17 and Table 3, respectively.
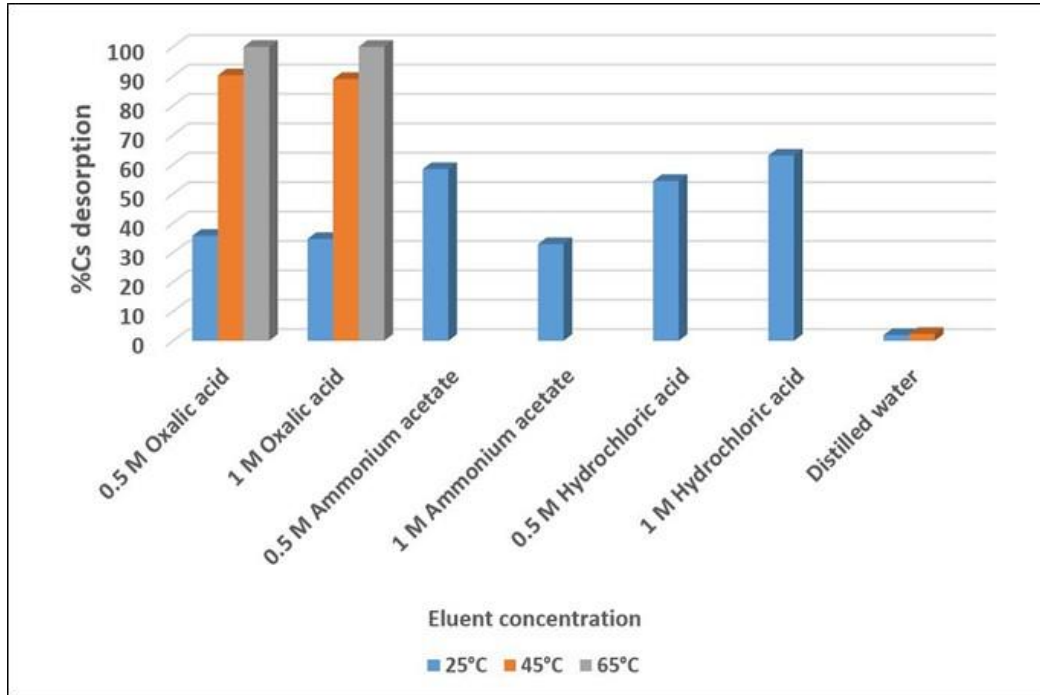


**Figure 17:** $Cs^+$ desorption efficiency against eluent concentration.

Results proved that the most efficient recovery of $Cs^+$ ions from vermiculite surface to solution media occurred using oxalic acid eluent with 89%, 90% and 100% desorption efficiency under 45 and 65 °C (Table 3). The concentration of oxalic acid did not cause a significant difference in desorption efficiency since $Cs^+$ recovery ratios are nearly the same (Figure 17). 0.5 M ammonium acetate solution caused a stronger regain of $Cs^+$ than that of 1 M eluent. As for a strong acid HCl, higher concentration provided a slight increase in Cs recovery ratio, as seen in Table 3.

**Table 3:** Results of Cs desorption studies.

| Eluent (volume= 10 mL) | Concentration of eluent (M) | pH | Batch shaker temperature (°C) | Desorption Cs (%) |
|---|---|---|---|---|
| Oxalic acid | 0.5 | 1.56 | 25 | 35.73 |
| Oxalic acid | 1 | 1.48 | 25 | 34.65 |
| Oxalic acid | 0.5 | 1.46 | 45 | 90.30 |
| Oxalic acid | 1 | 1.48 | 45 | 89.06 |
| Oxalic acid | 0.5 | 1.53 | 65 | 100 |
| Oxalic acid | 1 | 0.63 | 65 | 100 |
| NH$_4$AOc | 0.5 | 5.72 | 25 | 58.44 |
| NH$_4$AOc | 1 | 6.01 | 25 | 32.89 |
| HCl | 0.5 | 0.36 | 25 | 54.38 |
| HCl | 1 | 0.23 | 25 | 63 |
| Distilled water | - | 7.13 | 25 | 1.96 |
| Distilled water | - | 6.93 | 45 | 2.36 |

Desorption and regeneration of Cs in water are necessary because the most of radioactive $Cs^+$ exist in aqueous media after nuclear accidents and fallouts. Small amounts of $Cs^+$ ions were desorbed from adsorbent to water and this indicated that vermiculite trapped Cs into its porous structure strongly, even at higher temperatures than ambient room temperature (45 °C). These results clearly suggest that whether radioactive $Cs^+$ is adsorbed by vermiculite in water media, it does not tend to be transferred to the liquid phase, preventing the radioactive damage to aqueous media and living organisms.

**Potassium interference effect studies**

Results of ion interference study were illustrated in Table 4. When the cesium ion concentration (200 mg/L) is two times higher then the potassium concentration (100 mg/L), Cs adsorption yield was found as 64% and the amount of Cs adsorbed at equilibrium was calculated as 16.22 mg/g. It is still a good uptake in the presence of $K^+$ ions.

**Table 4:** Results of potassium interference effect study
(vermiculite= 0.2 g, V= 25 mL, pH=8, Contact time= 4 h., Cs conc.= 200 mg/L, temp.=25 °C)

| K conc. (mg/L) in solution | Cs, $C_e$ (mg/L) | Cs, $q_e$ (mg/g) | K, $C_e$ (mg/L) | K, $q_e$ (mg/g) | Adsorption Cs (%) | Adsorption K (%) |
|---|---|---|---|---|---|---|
| 100 | 70.28 | 16.22 | 106.30 | none | 64.86 | none |
| 400 | 119 | 10.12 | 289 | 13.88 | 40.50 | 27.75 |

$K^+$ concentration in seawater was given around 9700 µmol/L (approx. 400 mg/L) for normal salinity. As for low solute fresh waters and rivers, it was in the range of 1-50 µmol/L (approx. 0.04-1.95 mg/L) (69). As seen in Table 4, at 400 ppm of K concentration, Cs adsorption yield was found as 40.50%. For seawater with normal salinity, Cs adsorption yield is acceptable considering the strong constraining effect of $K^+$ ions due to similar ionic radius with $Cs^+$ [$RK^+$=1.33 A° (33), $RCs^+$=1.70 A° (70)].

**CONCLUSIONS**

In the current study, Cs removal performance of raw vermiculite obtained from Sivas-Yıldızeli region of Turkey was investigated and 87% of $Cs^+$ ions were adsorbed under optimal conditions. Adsorption process followed pseudo-second order kinetics model with an excellent $R^2$ value of 0.9987. Equilibrium studies revealed that Cs adsorption onto vermiculite layer was compatible with Langmuir, Freundlich, and Temkin isotherm models suggesting that Cs uptake on the mineral surface had both physical and chemical sorption character. The maximum adsorption capacity of natural vermiculite (5 h) calculated from the Langmuir model was 29.67 mg/g at 298 K. The adsorbtion energy value was calculated as 0.772 kJ/mol using D-R isotherm model, being lower than 8 kJ/mol, clearly indicated that the physisorption process was in effect during Cs uptake.

Negative Gibbs energy values obtained with thermodynamic studies showed that adsorption process was spontaneous and had high feasibility, indicating that sorption of $Cs^+$ ions onto vermiculite surface has not needed an extra external energy to realize. Negative and low enthalpy value indicated that sorption was physicochemically exothermic and interactions between adsorbent and adsorbate ions were weak since the percentage of Cs ions adsorbed at equilibrium decreased with increasing temperatures. Consequently, the positive mid-range value of entropy proposed that disorderliness between the solid and liquid phases in the bulk media increased during adsorption.

Desorption studies showed that oxalic acid was the most efficient elution agent since 100% of Cs was completely recovered from solution media. Potassium interference studies revealed that when the concentration of cesium cation was two times higher than potassium (200 mg/L Cs + 100 mg/L K) during the adsorption, approximately 65% of $Cs^+$ ions were adsorbed and the value is acceptable. When the concentration of $K^+$ ions was two times higher than $Cs^+$ ions in solution media (200 mg/L Cs + 400 mg/L K) which included nearly the same potassium content with natural seawater, 40% of Cs was adsorbed. This is a quite satisfactory yield considering the powerful interfering effect of potassium ions. As a consequence, cesium adsorption is decreased with increasing $K^+$ concentrations in solution media.

In conclusion, results gathered in present study is a clear demonstration that vermiculite obtained from Sivas-Yıldızeli-Türkiye has an exceptional potential for removing Cs from aqueous media. It indicates that vermiculite mined with national mining procedures could also be used in any nuclear accident for the purpose of decomposing and removing radioactive ^{137}Cs leaked into water media. This, of course, is expected to contribute to national scientific prestige and national economy, whether efficient removal of ^{137}Cs can also be materialized in light of present results since stable [133]Cs has same radiochemical features with radioactive [137]Cs. Finally, it is expected that the adsorption capacity and $Cs^+$ ion selectivity of raw vermiculite obtained from Sivas-Karakoç mine can be enhanced with chemical modification using various molecules and better results can be taken with modification in future studies.

## ACKNOWLEDGMENTS

## REFERENCES

1. Suzuki N, Ochi K, Chikuma T. Cesium Adsorption Behavior of Vermiculite and It's Application to the Column Method. J Ion Exch. 2014;25(4):122–5.

2. Kim J-O, Lee S-M, Jeon C. Adsorption characteristics of sericite for cesium ions from an aqueous solution. Chem Eng Res Des. 2014 Feb;92(2):368–74.

3. Long H, Wu P, Yang L, Huang Z, Zhu N, Hu Z. Efficient removal of cesium from aqueous solution with vermiculite of enhanced adsorption property through surface modification by ethylamine. J Colloid Interface Sci. 2014 Aug;428:295–301.

4. Hadadi N, Kananpanah S, Abolghasemi H. Equilibrium and Thermodynamic Studies of Cesium Adsorption on Natural Vermiculite and Optimization of Operation Conditions. Iran J Chem Chem Eng IJCCE. 2009 Dec 1;28(4):29–36.

5. Sangvanich T, Sukwarotwat V, Wiacek RJ, Grudzien RM, Fryxell GE, Addleman RS, et al. Selective capture of cesium and thallium from natural waters and simulated wastes with copper ferrocyanide functionalized mesoporous silica. J Hazard Mater. 2010 Oct;182(1–3):225–31.

6. Igwe JC, Abia AA. A bioseparation process for removing heavy metals from waste water using biosorbents. Afr J Biotechnol [Internet]. 2006 Jan 1 [cited 2017 Jun 18];5(11). Available from: https://www.ajol.info/index.php/ajb/article/view/43005

7. Abdel-Ghani NT, Hefny M, El-Chaghaby GAF. Removal of lead from aqueous solution using low cost abundantly available adsorbents. Int J Environ Sci Technol. 2007 Dec;4(1):67–73.

8. Gupta VK, Carrott PJM, Ribeiro Carrott MML, Suhas. Low-Cost Adsorbents: Growing Approach to Wastewater Treatment—a Review. Crit Rev Environ Sci Technol. 2009 Oct 9;39(10):783–842.

9. Kim E-J, Lee C-S, Chang Y-Y, Chang Y-S. Hierarchically Structured Manganese Oxide-Coated Magnetic Nanocomposites for the Efficient Removal of Heavy Metal Ions from Aqueous Systems. ACS Appl Mater Interfaces. 2013 Oct 9;5(19):9628–34.

10. Khan NA, Hasan Z, Jhung SH. Adsorptive removal of hazardous materials using metal-organic frameworks (MOFs): A review. J Hazard Mater. 2013 Jan;244–245:444–56.

11. Uddin MK. A review on the adsorption of heavy metals by clay minerals, with special focus on the past decade. Chem Eng J. 2017 Jan;308:438–62.

12. A. Saleh T, Sarı A, Tuzen M. Chitosan-modified vermiculite for As(III) adsorption from aqueous solution: Equilibrium, thermodynamic and kinetic studies. J Mol Liq. 2016 Jul;219:937–45.

13. Stawinski W, Wegrzyn A, Danko T, Freitas O, Figueiredo S, Chmielarz L. Acid-base treated vermiculite as high performance adsorbent: Insights into the mechanism of cationic dyes adsorption, regeneration, recyclability and stability studies. Chemosphere. 2017 Apr;173:107–15.

14. Gharin Nashtifan S, Azadmehr A, Maghsoudi A. Comparative and competitive adsorptive removal of Ni2+ and Cu2+ from aqueous solution using iron oxide-vermiculite composite. Appl Clay Sci. 2017 May;140:38–49.

15. Malandrino M, Abollino O, Giacomino A, Aceto M, Mentasti E. Adsorption of heavy metals on vermiculite: Influence of pH and organic ligands. J Colloid Interface Sci. 2006 Jul;299(2):537–46.

16. Sawhney BL. Sorption and Fixation of Microquantities of Cesium by Clay Minerals: Effect of Saturating Cations. Soil Sci Soc Am J. 1964;28(2):183.

17. Sawhney BL. Sorption of Cesium from Dilute Solutions. Soil Sci Soc Am J. 1965;29(1):25.

18. Sawhney BL. Unusual Sorption of Caesium by Vermiculite. Nature. 1966 Aug;211(5051):893–4.

19. Sawhney BL. Selective Sorption and Fixation of Cations by Clay Minerals: A Review. Clays Clay Miner. 1972;20(2):93–100.

20. Sikalidis CA, Misaelides P, Alexiades CA. Caesium selectivity and fixation by vermiculite in the presence of various competing cations. Environ Pollut. 1988;52(1):67–79.

21. Japanese Atomic Energy Agency. Radioactive cesium is adsorbed onto vermiculite and biotite, mechanism of cesium adsorption has been clarified [Internet]. Japanese Atomic Energy Agency Sector of Fukushima Research and Development. 2015 [cited 2015 Jan 26]. Available from: https://fukushima.jaea.go.jp/english/topics/pdf/topics-fukushima058e.pdf

22. Staunton S, Dumat C, Zsolnay A. Possible role of organic matter in radiocaesium adsorption in soils. J Environ Radioact. 2002 Jan;58(2–3):163–73.

23. Faithfull NT, editor. Methods in agricultural chemical analysis: a practical handbook [Internet]. Wallingford: CABI; 2002 [cited 2017 Jun 18]. Available from: http://www.cabi.org/cabebooks/ebook/20023165853

24. Santos SSG, Pereira MBB, Almeida RKS, Souza AG, Fonseca MG, Jaber M. Silylation of leached-vermiculites following reaction with imidazole and copper sorption behavior. J Hazard Mater. 2016 Apr;306:406–18.

25. Dias NC, Steiner PA, Braga MCB. Characterization and Modification of a Clay Mineral Used in Adsorption Tests. J Miner Mater Charact Eng. 2015;03(04):277–88.

26. Karakoç Cevherinin Fiziksel ve Kimyasal Özellikleri : Organik Madencilik [Internet]. [cited 2017 Jun 18]. Available from: http://www.organikmadencilik.com/?p=112

27. Dong Z, Qiu Y, Dai Y, Cao X, Wang L, Wang P, et al. Removal of U(VI) from aqueous media by hydrothermal cross-linking chitosan with phosphate group. J Radioanal Nucl Chem. 2016 Sep;309(3):1217–26.

28. Üçgül E. Sivas-Yıldızeli-Karakoç Flogopit Cevherinin Isısal ve Kimyasal Genleşme Özellikleri [Yüksek Mühendislik Tezi]. Hacettepe Üniversitesi; 1997.

29. Addison J. Sivas-Yıldızeli-Karakoç Detaylı Jeolojik Prospeksiyon Çalışması. 2007.

30. Ehsani İ. Bir Vermikülitin Fiziksel, Kimyasal ve Isıl Özellikleri Üzerine Sülfürik Asit Liçinin Etkileri [Yüksek Lisans Tezi]. [Ankara]: Hacettepe Üniversitesi, Fen Bilimleri Enstitüsü, Maden Mühendisliği Anabilim Dalı; 2015.

31. Yalçın H, Bozkaya Ö, Yeşildağ H. Sivas-Yıldızeli Yöresi Ultramafik Platonik Kayaçlarla İlişkili Flogopit Oluşumlarının Kökeni. Yerbilim Üniversitesi Yerbilim Uygul Ve Araşt Merk Derg [Internet]. 2016 Jun 3 [cited 2017 Jun 18];37(1). Available from: http://dergipark.gov.tr/doi/10.17824/yrb.79284

32. Khandaker S, Kuba T, Kamida S, Uchikawa Y. Adsorption of cesium from aqueous solution by raw and concentrated nitric acid–modified bamboo charcoal. J Environ Chem Eng. 2017 Apr;5(2):1456–64.

33. Yang J, Luo X, Yan T, Lin X. Recovery of cesium from saline lake brine with potassium cobalt hexacyanoferrate-modified chrome-tanned leather scrap adsorbent. Colloids Surf Physicochem Eng Asp. 2018 Jan;537:268–80.

34. Lagergren S. About the Theory of So-Called Adsorption of Soluble Substances. K Sven Vetenskapsakademiens Handl. 1898;24(4):1–39.

35. Ho Y., McKay G. Pseudo-second order model for sorption processes. Process Biochem. 1999 Jul;34(5):451–65.

36. Zeldowitsch J. Über den mechanismus der katalytischen oxydation von CO an MnO2. Acta Physicochem URSS. 1934;1:364–449.

37. Ho Y. Review of second-order models for adsorption systems. J Hazard Mater. 2006 Aug 25;136(3):681–9.

38. Low MJD. Kinetics of Chemisorption of Gases on Solids. Chem Rev. 1960 Jun 1;60(3):267–312.

39. Abdel-Ghani NT, Rawash ESA, El-Chaghaby GA. Equilibrium and kinetic study for the adsorption of p-nitrophenol from wastewater using olive cake based activated carbon. Glob J Environ Sci Manag. 2016 Jan 1;2(1):11–8.

40. Nethaji S, Sivasamy A, Mandal AB. Adsorption isotherms, kinetics and mechanism for the adsorption of cationic and anionic dyes onto carbonaceous particles prepared from Juglans regia shell biomass. Int J Environ Sci Technol. 2013 Mar;10(2):231–42.

41. Chen R, Tanaka H, Kawamoto T, Asai M, Fukushima C, Na H, et al. Selective removal of cesium ions from wastewater using copper hexacyanoferrate nanofilms in an electrochemical system. Electrochimica Acta. 2013 Jan;87:119–25.

42. Sakamoto S, Kawase Y. Adsorption capacities of poly-g-glutamic acid and its sodium salt for cesium removal from radioactive wastewaters. J Environ Radioact. 2016 Dec;165:151–8.

43. Ding D, Lei Z, Yang Y, Zhang Z. Efficiency of transition metal modified akadama clay on cesium removal from aqueous solutions. Chem Eng J. 2014 Jan;236:17–28.

44. Seaton K, Little I, Tate C, Mohseni R, Roginskaya M, Povazhniy V, et al. Adsorption of cesium on silica gel containing embedded phosphotungstic acid. Microporous Mesoporous Mater. 2017 May;244:55–66.

45. Langmuir I. The Adsorption of gases on plane surfaces of glass, mica and platinium. J Am Chem Soc. 1918 Sep;40(9):1361–403.

46. Freundlich H. Über die Absorption in Lösungen. Z Für Phys Chem. 1906;57:385–470.

47. Dubinin MM. The Potential Theory of Adsorption of Gases and Vapors for Adsorbents with Energetically Nonuniform Surfaces. Chem Rev. 1960 Apr 1;60(2):235–41.

48. Temkin M, Pyzhev V. Recent modifications to Langmuir isotherms. Acta Physicochim URSS. 1940;12:217–22.

49. Zacaroni LM, Magriotis ZM, Cardoso M das G, Santiago WD, Mendon?a JG, Vieira SS, et al. Natural clay and commercial activated charcoal: Properties and application for the removal of copper from cacha?a. Food Control. 2015 Jan;47:536–44.

50. Bentahar Y, Hurel C, Draoui K, Khairoun S, Marmier N. Adsorptive properties of Moroccan clays for the removal of arsenic(V) from aqueous solution. Appl Clay Sci. 2016 Jan;119:385–92.

51. Khan TA, Singh VV. Removal of cadmium(II), lead(II), and chromium(VI) ions from aqueous solution using clay. Toxicol Environ Chem. 2010 Sep;92(8):1435–46.

52. Priyantha N, Bandaranayaka A. Interaction of Cr(VI) species with thermally treated brick clay. Environ Sci Pollut Res. 2011 Jan;18(1):75–81.

53. Alemayehu D, Singh S, Tessema D. Assessment of the adsorption capacities of fired clay soils from Jimma (Ethiopia) for the removal of Cr (VI) from aqueous solution. Univ J Env Res Technol. 2012;2:411–20.

54. McKay G, Blair HS, Gardner JR. Adsorption of dyes on chitin. I. Equilibrium studies. J Appl Polym Sci. 1982 Aug;27(8):3043–57.

55. Meroufel B, Benali O, Benyahya M, Benmoussa Y, Zenasni M. Adsorptive removal of anionic dye from aqueous solutions by Algerian kaolin: Characteristics, isotherm, kinetic and thermodynamic studies. J Mater Env Sci. 2013;4(3).

56. Vijayakumar G, Tamilarasan R, Dharmendirakumar M. Adsorption, Kinetic, Equilibrium and Thermodynamic studies on the removal of basic dye Rhodamine-B from aqueous solution by the use of natural adsorbent perlite. J Mater Env Sci. 3(1):157–70.

57. Wibowo E, Rokhmat M, Sutisna, Khairurrijal, Abdullah M. Reduction of seawater salinity by natural zeolite (Clinoptilolite): Adsorption isotherms, thermodynamics and kinetics. Desalination. 2017 May;409:146–56.

58. Kyziol-Komosinska J, Rosik-Dulewska C, Franus M, Antoszczyszyn-Szpicka P, Czupiol J, Krzyzewska I. Sorption Capacities of Natural and Synthetic Zeolites for Cu(II) Ions. Pol J Environ Stud. 2015;24:1111–23.

59. Can N, Ömür BC, Altındal A. Modeling of heavy metal ion adsorption isotherms onto metallophthalocyanine film. Sens Actuators B Chem. 2016 Dec;237:953–61.

60. Hasany SM, Chaudhary MH. Sorption potential of Haro river sand for the removal of antimony from acidic aqueous solution. Appl Radiat Isot. 1996 Apr;47(4):467–71.

61. Ibrahim MB, Sani S. Comparative Isotherms Studies on Adsorptive Removal of Congo Red from Wastewater by Watermelon Rinds and Neem-Tree Leaves. Open J Phys Chem. 2014;04(04):139–46.

62. Lian L, Guo L, Guo C. Adsorption of Congo red from aqueous solutions onto Ca-bentonite. J Hazard Mater. 2009 Jan;161(1):126–31.

63. Zheng X, Dou J, Yuan J, Qin W, Hong X, Ding A. Removal of Cs + from water and soil by ammonium-pillared montmorillonite/Fe3O4 composite. J Environ Sci. 2017 Jun;56:12–24.

64. Abdel-Karim A-AM, Zaki AA, Elwan W, El-Naggar MR, Gouda MM. Experimental and modeling investigations of cesium and strontium adsorption onto clay of radioactive waste disposal. Appl Clay Sci. 2016 Nov;132–133:391–401.

65. Lee K-Y, Park M, Kim J, Oh M, Lee E-H, Kim K-W, et al. Equilibrium, kinetic and thermodynamic study of cesium adsorption onto nanocrystalline mordenite from high-salt solution. Chemosphere. 2016 May;150:765–71.

66. Lupa L, Voda R, Popa A. Adsorption behavior of cesium and strontium onto chitosan impregnated with ionic liquid. Sep Sci Technol. 2017 Apr 10;1–9.

67. Hamed MM, Aly MI, Nayl AA. Kinetics and thermodynamics studies of cobalt, strontium and caesium sorption on marble from aqueous solution. Chem Ecol. 2016 Jan 2;32(1):68–87.

68. Metwally SS, Ahmed IM, Rizk HE. Modification of hydroxyapatite for removal of cesium and strontium ions from aqueous solution. J Alloys Compd. 2017 Jun;709:438–44.

69. Talling JF. Potassium — A Non-Limiting Nutrient in Fresh Waters? Freshw Rev. 2010 Dec;3(2):97–104.

70. Onodera M, Kirishima A, Nagao S, Takamiya K, Ohtsuki T, Akiyama D, et al. Desorption of radioactive cesium by seawater from the suspended particles in river water. Chemosphere. 2017 Oct;185:806–15.

# Synthesis and Characterization of Polysulfone-based Graft Copolymers Possessing Quaternary Ammonium Salts via Photoiniferter Polymerization

**Serhat Oran[1], Mehmet Atilla Tasdelen[1]***

[1] Department of Polymer Engineering, Faculty of Engineering, Yalova University, 77100, Yalova, Turkey

**Abstract:** Well-defined polysulfone-based graft copolymers containing quaternary ammonium salts were successfully prepared by photoiniferter method under mild conditions (at room temperature and nitrogen atmosphere). The corresponding macroiniferter agent was sequentially synthesized by chloromethylation and nucleophilic substitution reactions between obtained chloromethylated polysulfone and sodium diethyldithiocarbamate. Upon UV irradiation, this macroiniferter enabled the accomplished grafting of 2-(dimethylamino) ethyl methacrylate onto the polysulfone backbone in a controlled manner. After the successful synthesis of graft copolymers, the tertiary amine groups in the side-chains are readily quaternized using methyl iodide to get desired quaternary ammonium salts containing graft copolymers.

**Keywords:** Graft copolymer; iniferter; polysulfone; photopolymerization; quarternary ammonium salts.

## INTRODUCTION

Polysulfones (PSU) are the family of thermoplastics that have excellent thermal and chemical stability, high radiation degradation resistance, transparency, high rigidity, mechanical strength, and good electrical and film properties (1, 2). To benefit from above-mentioned advantages, they have been used in many applications such as medical devices (hemodialysis), food processing, feeding systems, automotive, electronics, water distillation, gas separation, and fuel cells (3-5). However, these PSU have some drawbacks including stress cracking with certain solvents, poor tracking resistance, and weathering properties. To overcome these limitations and also extend their potential applications, the functionalization of PSU is a subject of considerable interest in recent studies (6, 7). There are two main functionalization methods; (i) functional monomer and (ii) post-functionalization approaches (8). The post-functionalization is most widely applied method in which the desired functionality is attached onto the polymer end- or side-chains of polymers (9, 10). The chemical structure of PSU backbone contains two different repeating units, electron-deficient phenyl sulfone and electron-rich bisphenol A groups that are suitable both electrophilic and nucleophilic substitution reactions for the incorporation of various functional groups. For example, sulfonation, chloromethylation, lithiation, and other methods are successfully applied for the side-chain functionalization of PSU in the literature (9). The grafting method including polymer chains with different chemical natures are attached onto another polymer backbone is a versatile process for the functionalization of polysulfones (11-16). The resulting functional polysulfone graft copolymers exhibit superior properties such as high porosity, wettability, and protein resistance compared to the non-functionalized polysulfones.

The iniferter (initiator-transfer-terminator agent) polymerization is the first controlled radical polymerization method discovered by Otsu and co-workers (17-19). In this method, the radical polymerization proceeds in a controlled manner where "active" and "dormant" propagating chain ends are reversibly equilibrated throughout the polymerization period (20-22). Various macromolecular architectures including telechelic (23, 24) and hyper-branched polymers (25, 26) and also block (27-31) and graft (32) copolymers can be simply synthesized under mild conditions via thermal or photochemical activations.(33, 34)

In this study, firstly, commercially available polysulfone was chloromethylated by a well-known

procedure using paraformaldehyde, trimethylsilyl chloride, and tin (IV) chloride. Then, the obtained polymers were converted to the macroiniferter by changing chloromethyl moieties with diethyl dithiocarbamate groups via nucleophilic substitution reaction. By applying UV irradiation, this macroiniferter (side-chain functional diethyl dithiocarbamate polysulfone) were enabled to conduct the radical polymerization of 2-(dimethylamino) ethyl methacrylate in a controlled manner. As a result of the iniferter polymerization, a well-defined graft copolymer (polysulfone-*g*-poly(2-(dimethylamino)ethyl methacrylate)) was successfully synthesized under mild conditions, *i.e.,* UV irradiation and room temperature. Finally, quaternization experiment using methyl iodide was applied to obtain desired polysulfone graft copolymer containing quaternary ammonium salts. The structures and properties of intermediate and final products were characterized by various techniques including spectroscopic (FT-IR and $^{1}$H-NMR), chromatographic (GPC), and thermal (DSC) analysis.

## MATERIALS AND METHODS

### Materials

Polysulfone (Udel® P-1700, Solvay), paraformaldehyde (95%, Merck), tin(IV) chloride (98%, Alfa Aesar), trimethylsilyl chloride (≥ 99.0%, Aldrich), sodium azide (99%, Merck), sodium diethyldithiocarbamate (BDH Chem.) 2-(dimethylamino)ethyl methacrylate (99%, Merck) and methyl iodide (Aldrich) were used as received. Commercial grade solvents *N,N*-dimethylformamide (≥ 99.8%, Merck), chloroform (≥ 99.8%, Merck), pyridine (≥ 99.0%, Aldrich), dimethyl sulfoxide (VWR) tetrahydrofuran (≥ 99.7%, VWR) and methanol (100%, VWR) were purchased and used as received.

### Chloromethylation of polysulfones

Polysulfone (20 g, 0.5 mmol) was dissolved with chloroform (600 mL) in a 1000 mL glass flask by using ultrasonic bath and then paraformaldehyde (57 mL, 450 mmol) and trimethylsilyl chloride (57 mL, 450 mmol) were added carefully into the mixture (13). After the mixture was stirred for a while, tin(IV) chloride (0.52 mL, 4.5 mmol) was added into this solution and the mixture was stirred at room temperature for 72 hours. All these steps and the reaction were carried out under inert atmosphere.  End of the given time, the product was precipitated into excess methanol. Then, the precipitate was filtered and dried in a vacuum oven at room temperature.

In order to confirm the successful of the chloromethylation process by FT-IR spectroscopy, the chloromethyl groups were converted to azide groups having characteristic band at 2150 cm$^{-1}$. For this purpose, the chloromethylated polysulfone (PSU-CH$_2$-Cl) (1 g, 0.026 mmol) was dissolved in 20 mL of dimethylformamide (DMF) and sodium azide (NaN$_3$) (100 mg, 1.54 mmol) was added into the solution. The mixture flask was wrapped up with alumina film to protect from solar light and then the mixture was stirred at 50 $^0$C for 24 h. Finally, the product was precipitated into excess methanol, filtered, and dried in a vacuum oven at room temperature.

### Synthesis of polysulfone-based macroiniferter (PSU-DDC)

Iniferter functionalized polysulfone (PSU-DDC) was synthesized from the reaction of PSU with sodium diethyldithiocarbomate (35). The PSU-CH$_2$-Cl (500 mg, 0.013 mmol), sodium diethyldithiocarbamate (60 mg, 0.35 mmol) and pyridine (5 mL) were placed to a 100 mL flask. After mixing and dissolution processes had been finished, the mixture flask was stirred in silicon oil bath at room temperature for 24 h. The solution was precipitated into methanol, filtered, and dried in a vacuum oven.

### Synthesis of polysulfone-g-poly(2-(dimethylamino)ethyl methacrylate) (PSU-g-PDMAEMA) via photoiniferter polymerization

PSU-DDC (50 mg, 0.0013 mmol) and DMF (1 mL, 0.013 mmol) were placed into a tube. After PSU-DDC completely dissolved, 2-(dimethylamino)ethyl methacrylate (DMAEMA) (1 mL, 5.94 mmol) was added into the solution tube and nitrogen was bubbled through 2-3 minutes. Then, the tube was irradiated by a UV photoreactor within 300-400 nm wavelength (Philips TL-D 18W) at room temperature for different reaction times. The solution mixture was precipitated into excess amount of hexane and then filtered. The product was dried under vacuum.

### Quarternarization of PSU-g-PDMAEMA

PSU-g-PDMAEMA (165 mg, 0.003 mmol) and THF (5 mL, 0.07 mmol) were added into a flask. After the polymer was completely dissolved, methyl iodide (CH3I) (50 µL, 0.0008 mmol) was carefully added into the solution flask and the mixture was stirred in silicon oil bath at room temperature for 24 h. The mixture was precipitated in hexane and filtered. After filtration, polymers were dried for 24 hours in a vacuum oven.

**Analysis**

A Perkin-Elmer FT-IR Spectrum One B spectrometer was used for FT-IR analysis. The Agilent NMR System VNMRS 500 spectrometer was used at room temperature in $CDCl_3$ with $Si(CH_3)_4$ as an internal standard for $^1$H-NMR analysis. Molecular weights were determined by a Viscotek GPCmax Autosampler system consisting of a pump module (GPCmax, Viscotek, Houston, TX), a combined light-scattering (Model 270 dual detector, Viscotek), and a refractive index (RI) detector (VE 3580, Viscotek). The light-scattering detector ($\lambda_0$=670 nm) included two scattering angles: 7 and 90°. The RI detector was calibrated with polystyrene standards having narrow molecular weight distribution, and hence the quoted molecular weights of the polymers were expressed in terms of polystyrene equivalents. Two columns (7.8 x 300 mm, LT5000L, Mixed, Medium Org and LT3000L, Mixed, Ultra-Low Org) with a guard column (4.6 x 10 mm, Viscotek, TGuard) were used for the chloroform eluent at 35 $^0$C (flow rate, 1 mL/min). Data were analyzed using Viscotek OmniSEC Omni-01 software. Differential scanning calorimetry (DSC) was performed on a Perkin-Elmer Diamond DSC with a heating rate of 10 $^0$C/min under nitrogen flow (10 mL/min).

**RESULTS AND DISCUSSIONS**

There are three main methods for the synthesis of graft copolymers; (i) grafting-onto, (ii) grafting-from and (iii) grafting-through (macromonomers) (36-39). Among them, grafting-from approach is a very useful method since a wide range of monomers can be used together with different reaction conditions (40). In this method, an initiator is attached onto the polymer backbone and subsequent polymerization of second monomer enables to form corresponding graft copolymers. In our case, firstly, iniferter (diethyl dithiocarbamate) group was attached onto PSU backbone by sequantial chloromethylation and nucleophilic substitution reactions. The chloromethylated polysulfone was synthesized according to the well-known procedure (13). Then, its structure was confirmed by FT-IR and $^1$H-NMR techniques in accordance with respect to the literature data (11, 15). Due to overlapping of chloromethyl bands with the characteristic polysulfone bands, determination of chloromethylation was difficult with FT-IR spectroscopy. Therefore, the chlorine atoms were replaced with azide groups that were easily detectable in FT-IR spectroscopy. The characteristic azide band at 2250 cm$^{-1}$ was obviously detected in FT-IR spectrum (Figure 1). Thus, the successful chloromethylation of PSU was proven by FT-IR spectroscopy.
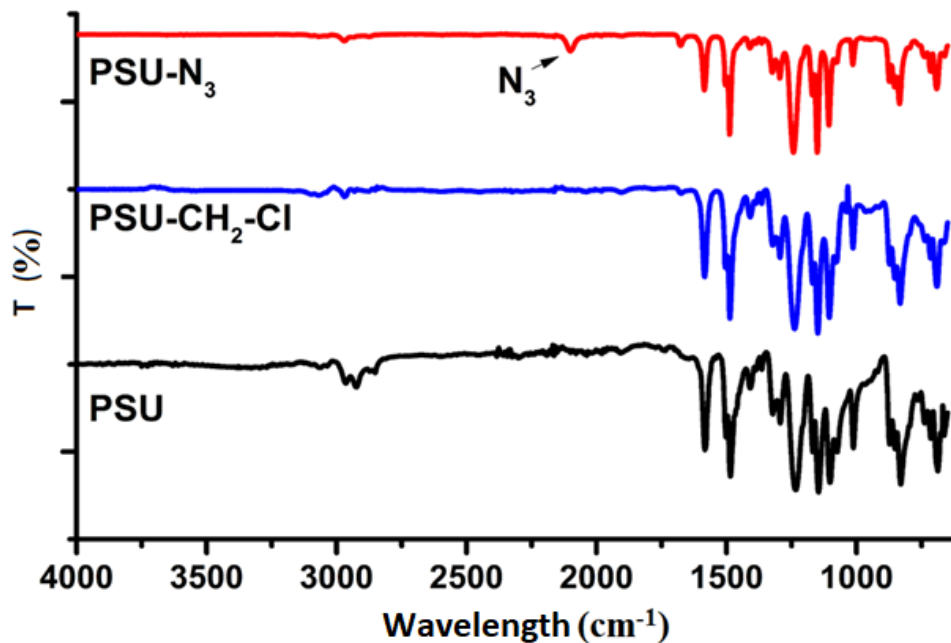
**Figure 1**. FT-IR spectra of neat, chloromethylated- and azide-functionalized polysulfones.

The successful transformation as well as the degree of substitution of chloromethyl group in PSU were determined by ^{1}H-NMR measurement. As can be seen in Figure 2, six methyl protons (a) and two methylene protons (b) of PSU-CH$_2$Cl appeared at 1.7 and 4.6 ppm, whereas four aromatic protons (c) were detected at 7.9 ppm. The degree of substitution of chloromethyl group into PSU backbone was calculated by using integral ratio of b and c protons and it was found as 7%.
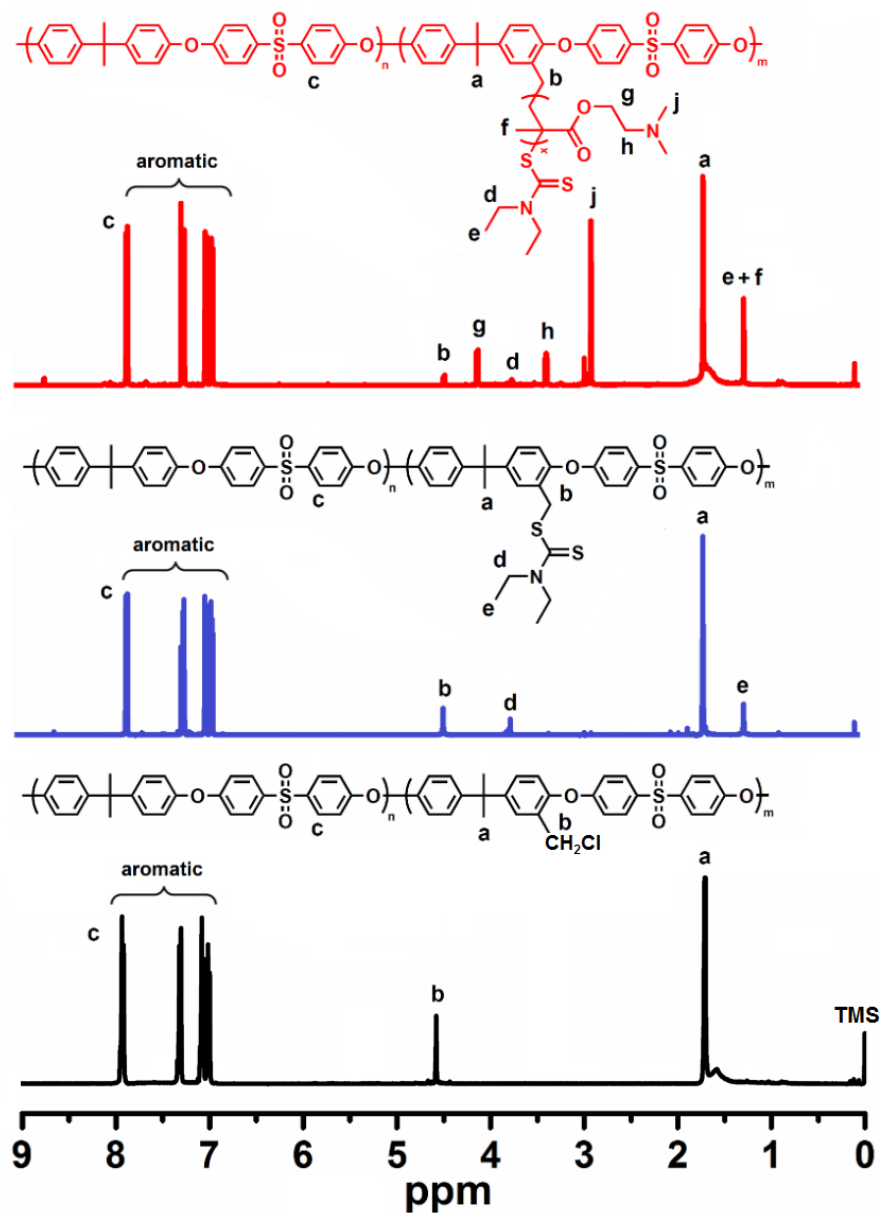
**Figure 2.** $^1$H-NMR spectra of PSU-CH$_2$Cl, PSU-DDC and PSU-*g*-P DMAEMA.

In the second step, the macroiniferter (polysulfone containing diethyl dithiocarbamate) was prepared by nucleophilic substitution reaction of PSU-CH$_2$Cl and sodium diethyl dithiocarbamate according to Scheme 1. The chemical structure of PSU-DDC was monitored by $^1$H-NMR spectroscopy. As can be seen in Figure 2, six methyl (e) and four methylene (d) protons of DDC moieties were

observed at 1.3 and 3.8 ppm. In addition, the characteristic peaks of methyl (a), methylene (b) and aromatic protons (c) were observed at the same regions. These results clearly confirmed the successful transformation from PSU-CH₂Cl to PSU-DDC.
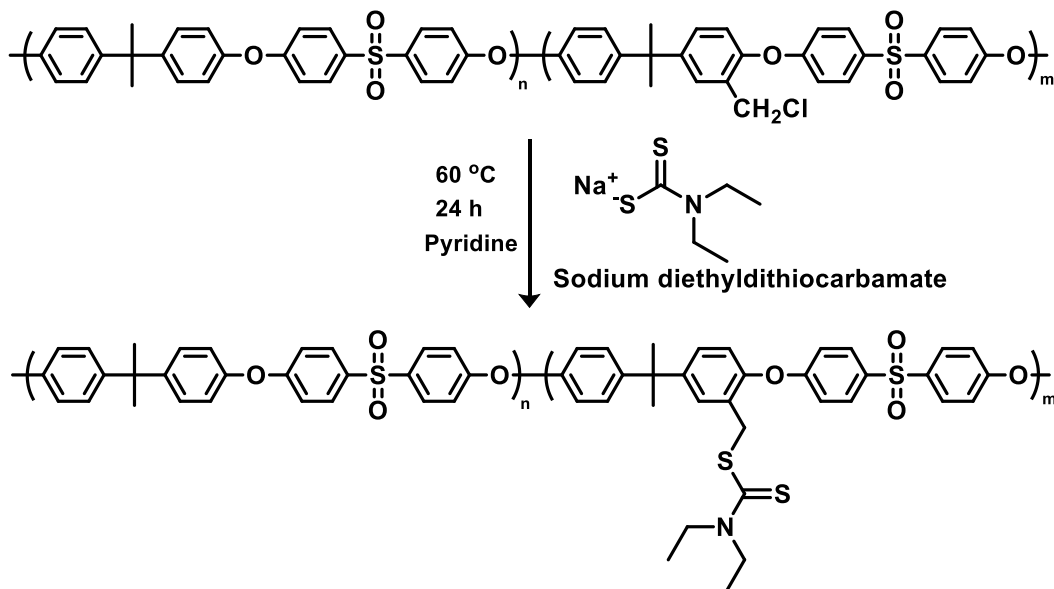


**Scheme 1**. The synthesis of macroiniferter agent (PSU-DDC).

Upon UV exposure, the PSU-DDC macroiniferter generated two types of radicals, an active radical on the PSU backbone and an inactive radical (DDC•). While the active macroradicals could initiate the polymerization of 2-(dimethylamino)ethyl methacrylate (PDMAEMA), the inactive radicals allowed to control the chain growth by eliminating unreversible termination reactions to obtain well-defined PSU-*g*-PDMAEMA graft copolymers (Scheme 2).
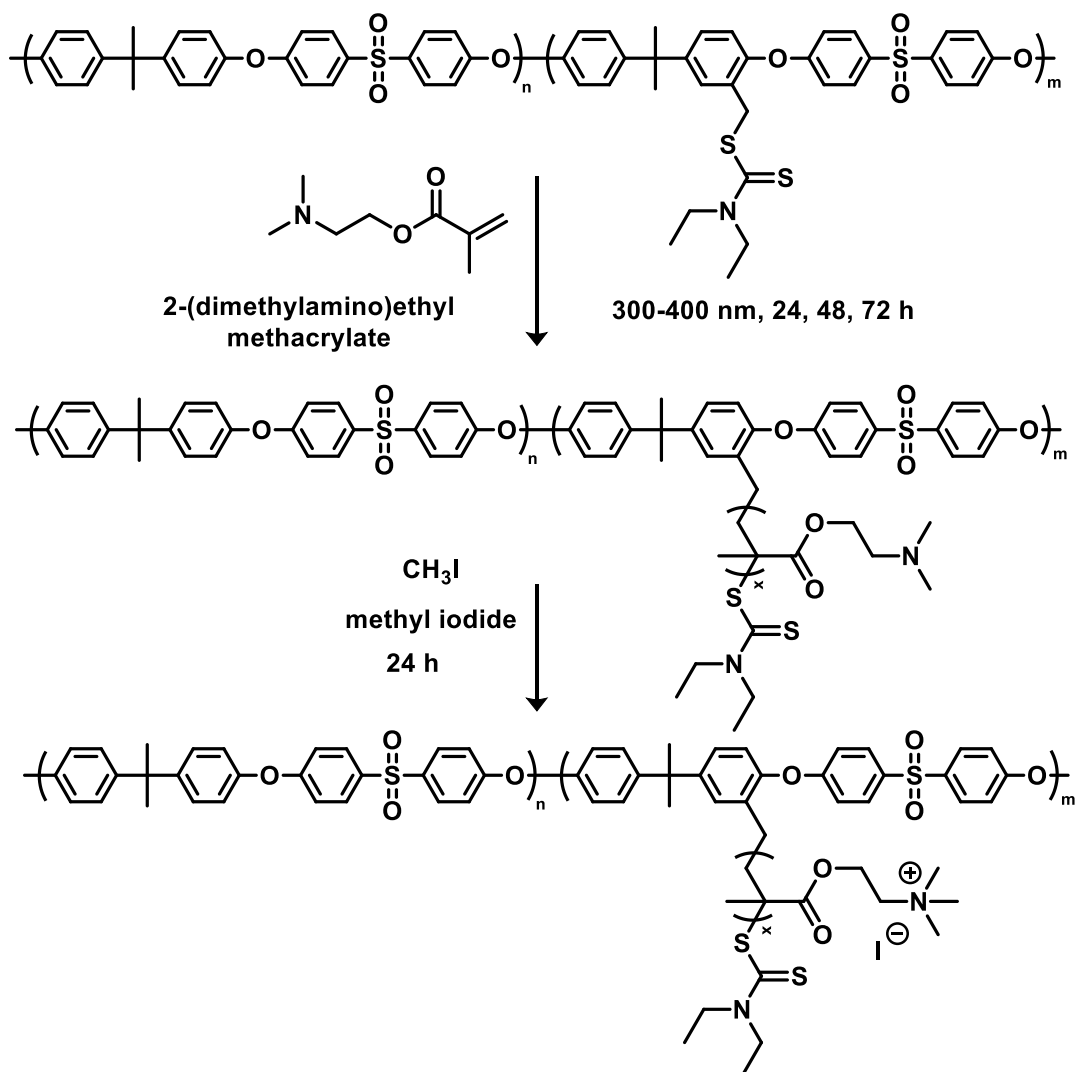
**Scheme 2.** The synthesis of PSU-*g*-PDMAEMA and PSU-*g*-QPDMAEMA.

By changing polymerization time, a series of graft copolymers was obtained and their structures were confirmed by FT-IR and $^1$H-NMR analyses. As shown in Figure 3, the characteristic ester peaks of C=O and C-O-C of PDMAEMA were sharply observed at 1712 and 1100 cm$^{-1}$, whereas the –N(CH)$_3$, –CH and C-C-N bands were seen at 2825, 2775 and 1160 cm$^{-1}$. In addition, the aromatic C=C streching bands of PSU units were displayed at 1590 and 1485 cm$^{-1}$. The graft copolymer structures were also investigated by $^1$H-NMR spectroscopy. Both the aliphatic (a) and aromatic (c) peaks belonging to protons of PSU backbone were clearly appeared at the same region. The new peaks assigned to aliphatic (j,h,g and f) -CH$_2$ and -CH$_3$ protons of PDMAEMA blocks appeared at

2.9, 3.4, 4.1 and 1.5 ppm, respectively. Additionally, the methyl protons of DDC groups were still visible after graft copolymerization as shown in Figure 2.
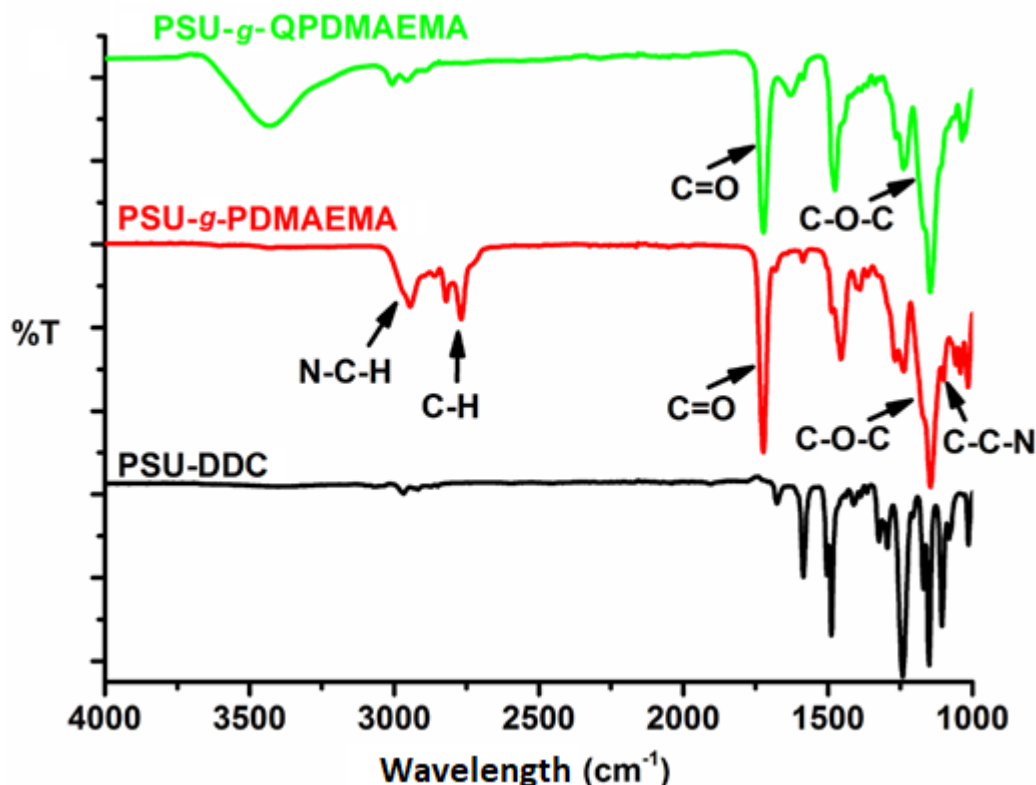


**Figure 3.** FT-IR spectra of PSU-DDC, PSU-*g*-PDMAEMA and PSU-*g*-QPDMAEMA.

The compositions of obtained graft copolymers were determined from the integration ratio of the protons (**c** and **j**) belonging to PSU and PDMAEMA blocks by using ^{1}H-NMR spectroscopy. As a results, the conversions as well as the molecular weights of graft copolymers were gradually increased by increasing the polymerization time. In contrast, the composition of PSU segments in the graft copolymers were paralelly decreased from 68 to 35% (Table 1).

Molecular weight distributions of inital PSU and obtained graft copolymers were investigated by gel permeation chromatography. The peaks belonging to graft copolymers were shifted to lower retention times meaning higher molecular weights than neat PSU backbone. After 72 h grafting process, the molecular weight was shifted from 38.000 g/mol to 121.000 g/mol (Table 1). Furthermore, all graft samples displayed single GPC peak accompanied by relatively narrow molecular weight distributions below 2.10. This result implied that it was not admixed with an

independently formed homopolymer. The single GPC peaks indicated that was no homopolymer contamination of graft copolymerization (Figure 4).
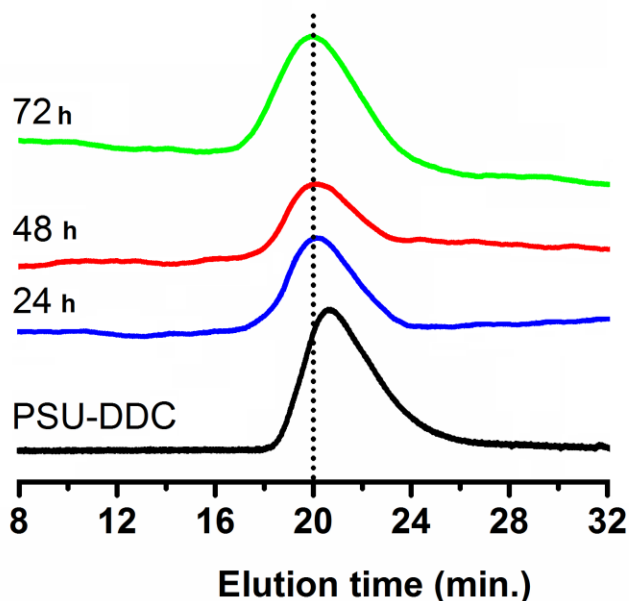


**Figure 4.** GPC curves of PSU-DDC and PSU-*g*-PDMAEMA polymers.

The thermal properties of resulting graft copolymers (PSU-g-PDMAEMA) were investigated by DSC analysis under nitrogen atmosphere and compared with initial PSU-DDC sample. According to DSC analysis, The PSU-DDC displayed a glass transition temperature ($T_g$) around 185 °C. The obtained graft copolymers were displayed only single $T_g$ values at between 105 and 123 °C. In the literature, the $T_g$s of neat PSU and PDMAEMA were determined around 190 and 5 °C, respectively.(40, 41) The $T_g$s of graft copolymers decreased from 123 to 105 °C by increasing composition of PDMAEMA segments (Table 1).

**Table 1.** The characterization results of  PSU-DDc and PSU-g-PDMAEMA polymers.

| Polymer | [Inf]/ [M] | Time (h) | $M_{n,GPC}$ (g/mol)[a] | $M_w/M_n$[a] | Yield (% )[b] | Comp. (%)[c] | $T_g$ (°C)[d] |
|---|---|---|---|---|---|---|---|
| PSU-DDC | - | - | 38.000 | 1.74 | 95 | 100 | 185 |
| PSU-*g*-PDMAEMA-24 | 1/760 | 24 | 53.000 | 1.58 | 47 | 68 | 123 |
| PSU-*g*-PDMAEMA-48 | 1/760 | 48 | 96.000 | 1.75 | 67 | 43 | 112 |
| PSU-*g*-PDMAEMA-72 | 1/760 | 72 | 121.000 | 2.10 | 98 | 35 | 105 |

a)Determined by GPC, b)Calculated gravimetrically, c)Determined by ^{1}H-NMR spectroscopy from the intagration ratio of the protons (**c** and **j**), d)Measured by DSC under nitrogen atmosphere.

After the successful grafting process, the tertiary amine groups in the graft copolymers were quaternized using methyl iodide to get corresponding quaternary ammonium salts containing graft copolymers (PSU-*g*-QPDMAEMA) (Scheme 2). Because of the solubility problems of quaternized graft copolymers, the ^{1}H-NMR spectroscopy and GPC analysis were not performed. The quaternization process was only characterized by using FT-IR spectroscopy. The PSU-*g*-PDMAEMA displayed the characteristic $-N(CH)_3$, $-CH$ and C-C-N bands at 2825, 2775 and 1160 cm$^{-1}$, respectively. After quaternization process, the bands at 2825 and 2775 cm$^{-1}$ of the PDMAEMA segments clearly disappeared. This result confirmed the successful formation of quaternary ammonium salts containing graft copolymers.

## CONCLUSIONS

In conclusion, the PSU-based macroiniferter was successfully synthesized and applied for the polymerization of DMAEMA under mild conditions. This process allowed the successful synthesis of well-defined graft copolymers with high yields. The obtained graft copolymers displayed a single GPC peak with relatively narrow molecular weight distributions. The compositions of PDMEMA segments in the graft copolymers were gradually increased with increasing monomer conversion. All graft copolymers exhibited single $T_g$ value at between 105 and 123 °C. After the successful synthesis of PSU-g-PDMAEMA, the tertiary amine groups in the side chains were readily converted to quaternary ammonium salts to obtain desired quaternary ammonium salts containing graft copolymers.

## ACKNOWLEDGEMENTS

## REFERENCES

1. Ioan S, editor. Functionalized polysulfones: synthesis, characterization, and applications: CRC Press; 2015

October 23.

2. El-Hibri MJ, Weinberg SA. Polysulfones.  Encyclopedia of Polymer Science and Technology: John Wiley & Sons, Inc.; 2002 October 22.

3. Iojoiu C, Marechal M, Chabert F, Sanchez JY. Mastering sulfonation of aromatic polysulfones: Crucial for membranes for fuel cell application. Fuel Cells. 2005;5(3):344-54.

4. Abdelrasoul A, Doan H, Lohi A, Cheng CH. Morphology Control of Polysulfone Membranes in Filtration Processes: a Critical Review. Chembioeng Reviews. 2015;2(1):22-43.

5. Zhu LJ, Song HM, Wang JR, Xue LX. Polysulfone hemodiafiltration membranes with enhanced anti-fouling and hemocompatibility modified by poly(vinyl pyrrolidone) via in situ cross-linked polymerization. Materials Science & Engineering C-Materials for Biological Applications. 2017;74:159-66.

6. Dizman C, Ates S, Uyar T, Tasdelen MA, Torun L, Yagci Y. Polysulfone/clay nanocomposites by in situ photoinduced crosslinking polymerization. Macromolecular Materials and Engineering. 2011;296(12):1101-6.

7. Dizman C, Uyar T, Tasdelen MA, Yagci Y. Synthesis and characterization of polysulfone/POSS hybrid networks by photoinduced crosslinking polymerization. Macromolecular Materials and Engineering. 2013;298(10):1117-23.

8. Yagci Y, Tasdelen MA. Mechanistic transformations involving living and controlled/living polymerization methods. Progress in Polymer Science. 2006;31(12):1133-70.

9. Dizman C, Tasdelen MA, Yagci Y. Recent advances in the preparation of functionalized polysulfones. Polymer International. 2013;62(7):991-1007.

10. Van der Bruggen B. Chemical Modification of Polyethersulfone Nanofiltration Membranes: A Review. Journal of Applied Polymer Science. 2009;114(1):630-42.

11. Yilmaz G, Toiserkani H, Demirkol DO, Sakarya S, Timur S, Torun L, et al. Polysulfone based amphiphilic graft copolymers by click chemistry as bioinert membranes. Materials Science and Engineering: C. 2011;31(5):1091-7.

12. Dizman C, Ates S, Torun L, Yagci Y. Synthesis, characterization and photoinduced curing of polysulfones with (meth) acrylate functionalities. Beilstein journal of organic chemistry. 2010;6.

13. Toiserkani H, Yilmaz G, Yagci Y, Torun L. Functionalization of polysulfones by click chemistry. Macromolecular Chemistry and Physics. 2010;211(22):2389-95.

14. Ates S, Dizman C, Aydogan B, Kiskan B, Torun L, Yagci Y. Synthesis, characterization and thermally activated curing of polysulfones with benzoxazine end groups. Polymer. 2011;52(7):1504-9.

15. Yilmaz G, Toiserkani H, Demirkol DO, Sakarya S, Timur S, Yagci Y, et al. Modification of polysulfones by click chemistry: amphiphilic graft copolymers and their protein adsorption and cell adhesion properties. Journal of Polymer Science Part A: Polymer Chemistry. 2011;49(1):110-7.

16. Dizman C, Altinkok C, Tasdelen MA. Synthesis of self-curable polysulfone containing pendant benzoxazine units via CuAAC click chemistry. Designed Monomers and Polymers. 2017;20(1):293-9.

17. Otsu T, Tazaki T. Living radical polymerization in homogeneous system with phenylazotriphenylmethane as a thermal iniferter. Polymer Bulletin. 1986;16(4):277-84.

18. Otsu T, Yoshida M, Tazaki T. A model for living radical polymerization. Makromolekulare Chemie-Rapid Communications. 1982;3(2):133-40.

19. Tasdelen MA, Yagci Y. Chapter 3 Controlled/Living Radical Polymerization in the Presence of Iniferters. Fundamentals of Controlled/Living Radical Polymerization: The Royal Society of Chemistry; 2013. p. 78-111.

20. Lalevee J, Blanchard N, El-Roz M, Allonas X, Fouassier JP. New photoiniferters: Respective role of the initiating and persistent radicals. Macromolecules. 2008;41(7):2347-52.

21. Tasdelen MA, Durmaz YY, Karagoz B, Bicak N, Yagci Y. A new photoiniferter/RAFT agent for ambient temperature rapid and well-controlled radical polymerization. Journal of Polymer Science Part A: Polymer Chemistry. 2008;46(10):3387-95.

22. Tasdelen MA, Çiftci M, Uygun M, Yagci Y. Possibilities for photoinduced controlled radical polymerizations. Progress in controlled radical polymerization: mechanisms and techniques: ACS Publications; 2012. p. 59-72.

23. Vankerckhoven C, Vandenbroeck H, Smets G, Huybrechts J. Dithiocarbamate telechelic polymers - synthesis and block copolymerization. Makromolekulare Chemie-Macromolecular Chemistry and Physics. 1991;192(1):101-14.

24. Tasdelen MA, Kahveci MU, Yagci Y. Telechelic polymers by living and controlled/living polymerization methods. Progress in Polymer Science. 2011;36(4):455-567.

25. Ishizu K, Ohta Y, Kawauchi S. Kinetics of hyperbranched polystyrenes by free radical polymerization of photofunctional inimer. Macromolecules. 2002;35(9):3781-4.

26. Joung YK, Choi JH, Bae JW, Park KD. Hyper-branched poly (poly (ethylene glycol) methacrylate)-grafted surfaces by photo-polymerization with iniferter for bioactive interfaces. Acta biomaterialia. 2008;4(4):960-6.

27. Watanabe J, Kano K, Akashi M. Bioconjugate polymer by photo-iniferter approach: Hydrophilic random or block copolymer-coated surface. Materials Science & Engineering C-Materials for Biological Applications. 2009;29(7):2287-93.

28. Durmaz YY, Karagoz B, Bicak N, Yagci Y. Synthesis of block copolymers by combination of ATRP and photoiniferter processes. Polymer International. 2008;57(10):1182-7.

29. Cakmak I. Synthesis of multiblock copolymers via macroiniferter. European Polymer Journal. 1998;34(10):1561-3.

30. Acar MH, Yagci Y. Studies on the block copolymerization of methacrylonitrile and hexafluorobutylmethacrlate using phenylazotriphenylmethane as thermal iniferter. Journal of Macromolecular Science-Chemistry. 1991;A28:177-83.

31. Temel BA, Amici J, Sangermano M, Yagci Y. Synthesis of H-shaped complex macromolecular structures by combination of atom transfer radical polymerization, photoinduced radical coupling, ring-opening polymerization, and iniferter processes. Journal of Polymer Science Part A: Polymer Chemistry. 2013;51(21):4601-7.

32. Kwak J, Lacroix-Desmazes P, Robin JJ, Boutevin B, Torres N. Synthesis of mono functional carboxylic acid poly(methyl methacrylate) in aqueous medium using sur-iniferter. Application to the synthesis of graft copolymers polyethylene-g-poly(methyl methacrylate) and the compatibilization of LDPE/PVDF blends. Polymer. 2003;44(18):5119-30.

33. Pan X, Tasdelen MA, Laun J, Junkers T, Yagci Y, Matyjaszewski K. Photomediated controlled radical

polymerization. Progress in Polymer Science. 2016;62:73-125.

34. Tasdelen MA, Yagci Y. Photochemical methods for the preparation of complex linear and cross-linked macromolecular structures. Australian Journal of Chemistry. 2011;64(8):982-91.

35. Al-Kaabi K, van Reenen AJ. Controlled radical polymerization of poly (methyl methacrylate-g-epichlorohydrin) using N, N-dithiocarbamate-mediated iniferters. Journal of applied polymer science. 2008;108(4):2528-34.

36. Gacal B, Durmaz H, Tasdelen M, Hizal G, Tunca U, Yagci Y, et al. Anthracene-maleimide-based Diels-Alder" click chemistry" as a novel route to graft copolymers. Macromolecules. 2006;39(16):5330-6.

37. Demirci G, Tasdelen MA. Synthesis and characterization of graft copolymers by photoinduced CuAAC click chemistry. European Polymer Journal. 2015;66:282-9.

38. Tasdelen MA, Yagci Y, Demirel AL, Biedron T, Kubisa P. Synthesis and Characterization of Block-Graft Copolymers [poly (epichlorohydrin-b-styrene)-g-poly (methyl methacrylate)] by Combination of Activated Monomer Polymerization, NMP and ATRP. Polymer bulletin. 2007;58(4):653-63.

39. Tasdelen MA, Moszner N, Yagci Y. The use of poly (ethylene oxide) as hydrogen donor in type II photoinitiated free radical polymerization. Polymer bulletin. 2009;63(2):173-83.

40. Ates S, Tatar-Guner P, Yagci Y, Levent Demirel A. Synthesis and characterization of polysulfone-g-poly (2-alkyl-2-oxazoline) s. Designed Monomers and Polymers. 2013;16(2):137-44.

41. Goracci G, Arbe A, Alegría A, García Sakai V, Rudić S, Schneider GJ, et al. Influence of Solvent on Poly(2-(Dimethylamino)Ethyl Methacrylate) Dynamics in Polymer-Concentrated Mixtures: A Combined Neutron Scattering, Dielectric Spectroscopy, and Calorimetric Study. Macromolecules. 2015;48(18):6724-35.

# The catalytic activity of Palladium(II) complexes containing PN ligands in the Heck and Suzuki C-C coupling reactions

**Mustafa Kemal Yılmaz[a,*], Mustafa Keleş[b]**

[a]Mersin University, Faculty of Arts and Sciences, Department of Chemistry, 33343 Mersin, Turkey
[b]Osmaniye Korkut Ata University, Faculty of Arts and Sciences, Department of Chemistry, 80000 Osmaniye, Turkey

**Abstract:** A range of iminophosphine (PN) ligands (($C_6H_5$)$_2$P-$C_6H_4$-CH=NR (R=-$C_6H_3$(2-$CH_3$)(4-OH) (**1a**), -$CH_2CH_2C_6H_4$(4-OH) (**1b**) and -$C_5H_3$N(2-$CH_3$) (**1c**))  have been synthesized starting from 4-amino-3-methylphenol, 4-(2-aminoethyl)phenol and 2-amino-3-methylpyridine with 2-(diphenylphosphino)benzaldehyde. The PN ligands were reacted with Pd(cod)Cl$_2$ to give corresponding new Pd(PN)Cl$_2$ metal complexes, (**2a**, **2b** and **2c**). The Heck and Suzuki C-C coupling reactions were examined with catalysts **2a**-**2c** and showed high conversions under the determined conditions with para substituted aryl halides.

**\*Corresponding author**. **E-mail**: mkyilmaz@mersin.edu.tr. Tel.: +90 324 361 00 01; fax: 90 324 361 00 73.

## INTRODUCTION

The palladium-catalyzed cross-coupling reactions of aryl halides with arylboronic acids (Suzuki reaction) and with olefins (Heck reaction) provides a powerful methodology for constructing $C(sp^2)$-$C(sp^2)$ bonds (1). The reason for the intense research is the fact that C-C coupling reactions have been relatively used in several fields such as pharmacological agents, herbicides, and the synthesis of natural products, *etc*. Consequently, researchers have been working to find better catalysts and achieve better yields in these areas which are important for both industrial and scientific purposes (2,3).

Cyclopalladated catalysts display superior catalytic activities in cross-coupling reactions. Phospha-palladacycles were found to be highly efficient catalysts for Heck and Suzuki coupling reactions (4). Although phosphine ligands and their palladium complexes are widely used to catalyze the cross-coupling reactions for a variety of substrates, there have not been enough publications about the application of the iminophosphines and their palladium complexes in C-C coupling reactions. Besides that, the use of iminophosphine ligands, containing both soft phosphorus and hard nitrogen atoms, are generally increases the catalytic activity compared to the homo donor PP and NN ligands. The reason for this is that phosphorus atom can stabilize Pd center in a low oxidation state due to the π-acceptor character, while σ-donor ability of the nitrogen atom makes the Pd center more sensitive to the oxidative addition during the catalytic cycle.  So PN ligands and their palladium(II) complexes have been identified as efficient catalysts for Heck (5,6) and Suzuki (7,8) reactions.

In this study, we have prepared new palladium(II) complexes (**2a-c**) to be used in the Heck and Suzuki cross-coupling reactions. The results demonstrate that PN type phosphine palladium(II) complexes are easily synthesized, and are also highly efficient complexes for the C-C cross-coupling reactions.

## MATERIALS AND METHODS

All reactions were carried out under nitrogen or argon atmosphere using conventional Schlenk glassware. All solvents were dried using established procedures and then immediately distilled under nitrogen atmosphere prior to use. 4-amino-3-methylphenol, 4-(2-aminoethyl)phenol, and 2-amino-3-methylpyridine obtained from Sigma-Aldrich Chemie GmbH (Steinheim, Germany) were used without further purification. The [Pd(cod)Cl$_2$] (9) and 2-(diphenylphosphino)benzaldehyde (10) were prepared as described in the literature.

Microanalysis was performed using a LECO CHNS 932 instrument. The $^1$H NMR (400.1 MHz) and $^{31}$P{$^1$H} NMR (162.0 MHz) spectra were recorded at 25 °C with DMSO-$d_6$ and CDCl$_3$ on a Bruker NMR spectrometer; $^{13}$C NMR were recorded on a Varian Mercury 100.6 MHz NMR spectrometer. $^{31}$P{$^1$H} NMR spectra were recorded with complete proton decoupling and reported in ppm using 85% H$_3$PO$_4$ as external standard. The coupling products were analyzed by a Perkin Elmer Clarus 500 series gas chromatograph equipped with a flame ionization detector and Elite-1 capillary column with 30 m×0.25 mm×0.25 µm film thickness. Thin-layer chromatography (TLC) was used for monitoring the reactions.

### Preparation of Pd(II) complexes

The **1a-c** were prepared as described in the literature (11).

### Preparation of [PdCl$_2$(Ph$_2$P-C$_6$H$_4$-CH=N-C$_6$H$_3$(2-CH$_3$)(4-OH))] (2a)
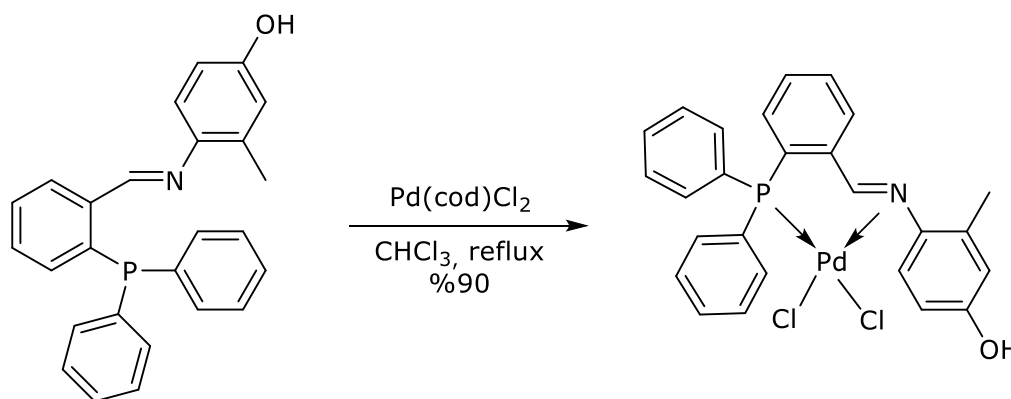


**Scheme 1:** Synthesis of complex **2a.**

To a solution of Pd(cod)Cl$_2$ (145 mg, 0.51 mmol) in CHCl$_3$ (10 mL) was added **1a** (200 mg, 0.51 mmol). The mixture was stirred for 6 h. Then the addition of diethyl ether caused to form a yellow solid which was filtered off and dried to give the title compound **2a**. Yield 263 mg (90%), mp.: 255-256 °C. $^1$H NMR (400.1 MHz, DMSO-$d_6$): δ (ppm) 9.47 (s, 1H), 8.59 (s, 1H), 8.20-8.12 (dd, $J$= 6.9, 4.2 Hz, 1H), 7.95 (t, $J=8.3$ Hz, 1H), 7.81 (t, $J=7.6$ Hz 1H), 7.73-7.69 (m, 2H), 7.65-7.59 (m, 4H), 7.54-7.48 (m, 4H), 7.02 (dd, $J=10.3$, 7.8 Hz, 1H), 6.78-6.74 (m, 1H), 6.58-6.52 (m, 2H), 2.09 (s, 3H). $^{13}$C NMR (100.6 MHz, DMSO-$d_6$): δ (ppm) 168.12 (d, $J_{PC}$=8.9 Hz, 1C, $\underline{C}$H=N), 156.06 (s, 1C), 143.93 (s, 1C), 137.77 (d, $J_{PC}$=8.6 Hz, 1C), 136.55 (d, $J_{PC}$=15.7 Hz, 2C), 134.87 (d, $J_{PC}$=7.4 Hz, 1C), 133.95 (s, 1C), 133.53 (d, $J_{PC}$=11.0 Hz, 4C), 132.28 (d, $J_{PC}$=2.7 Hz, 1C), 131.27 (s, 1C), 129.16 (d, $J_{PC}$=11.8 Hz, 4C), 126.44 (s, 1C), 125.84 (s, 1C), 124.53 (s, 2C), 119.88 (s, 1C), 116.62 (s, 1C), 112.19 (s, 1C), 18.66 (s, 1C). $^{31}$P NMR (162.0 MHz, DMSO-$d_6$): δ (ppm) 28.78 (s). Anal. calcd. for C$_{26}$H$_{22}$Cl$_2$NOPPd: C, 54.52; H, 3.87; N, 2.45 %. Found: C, 53.73; H, 4.37; N, 2.09 %. **2b** and **2c** were prepared as described in procedure **2a.**

## 2.2.4. Preparation of [PdCl$_2$(Ph$_2$P-C$_6$H$_4$-CH=N-(CH$_2$)$_2$-C$_6$H$_4$-(4-OH))] (2b)
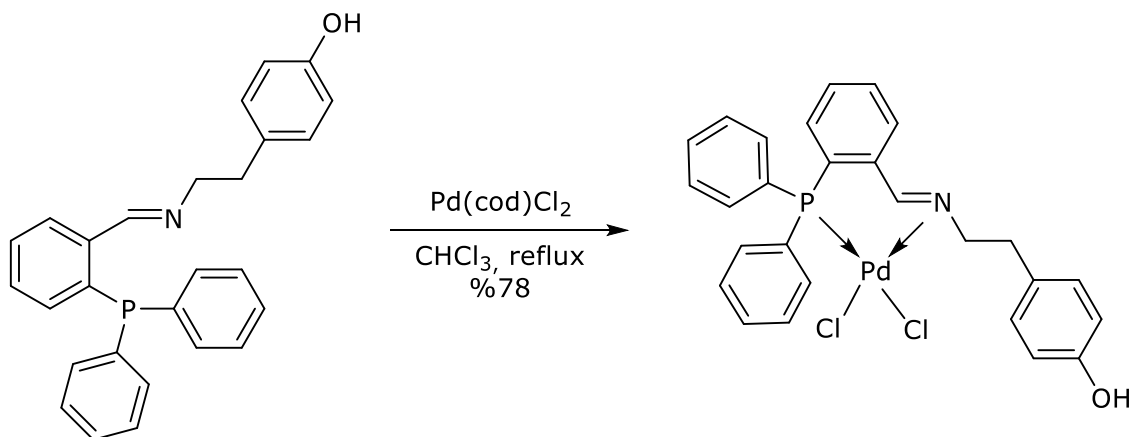


**Scheme 2:** Synthesis of complex **2b.**

Yield 233 mg (78%), mp.: 203-204 °C. $^1$H NMR (400.1 MHz, DMSO-$d_6$): δ (ppm) 9.23 (s, OH, 1H), 8.53 (s, CH=N, 1H), 7.96-7.90 (m, 2H), 7.78 (t, $J$=7.5 Hz 1H), 7.71 (td, $J$=6.4, 1.0 Hz, 2H), 7.61 (td, $J$=7.6, 2.7 Hz, 4H), 7.47 (dd, $J$=12.9, 7.3 Hz, 4H), 7.01 (dd, $J$=10.0, 8.0 Hz, 1H), 6.80 (d, $J$=8.4 Hz, 2H), 6.59 (d, $J$=8.4 Hz, 2H), 4.46 (t, $J$=15.5 Hz, NCH$_2$, 2H), 2.69 (t, $J$=15.6 Hz, CH$_2$Ph, 2H). $^{13}$C NMR (100.6 MHz, DMSO-$d_6$): δ (ppm) 165.70 (d, $J_{PC}$=8.9 Hz, 1C, C̲H=N), 155.86 (s, 1C), 136.72 (d, $J_{PC}$=16.1 Hz, 1C), 136.50 (d, $J_{PC}$=8.6 Hz, 4C), 134.30 (d, $J_{PC}$=7.9 Hz, 1C), 133.72 (d, $J_{PC}$=11.1 Hz, 2C), 133.34 (d, $J_{PC}$=2.2 Hz, 1C), 132.33 (d, $J_{PC}$=2.7 Hz, 1C), 129.46 (s, 1C), 129.08 (d, $J_{PC}$=11.9 Hz, 4C), 127.55 (s, 1C), 125.99 (s, 1C), 125.39 (s,1C), 119.72 (d, $J_{PC}$=9.6 Hz, 4C), 115.19 (s, 1C), 66.82 (s, 1C), 35.93 (s, 1C). $^{31}$P NMR (162.0 MHz, DMSO-$d_6$): δ (ppm) 30.93 (s). Anal. calcd. for C$_{27}$H$_{24}$Cl$_2$NOPPd: C, 55.27; H, 4.12; N, 2.39 %. Found: C, 54.67; H, 4.67; N, 2.17 %.

## 2.2.4. Preparation of [PdCl$_2$(Ph$_2$P-C$_6$H$_4$-CH=N-C$_6$H$_3$N-(2-CH$_3$))] (2c)
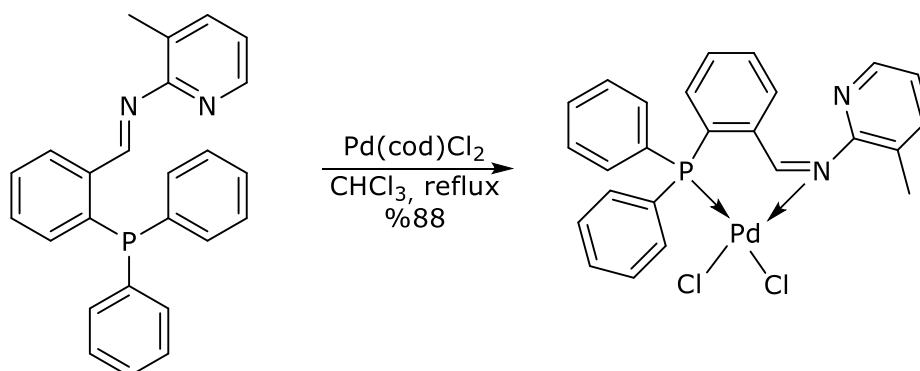


**Scheme 3:** Synthesis of complex **2c.**

Yield 250 mg (88%), mp.: 165 °C. $^1$H NMR (400.1 MHz, DMSO-$d_6$): δ(ppm) 8.82 (s, 1H, HC=N), 8.31-8.24 (m, $2$H), 7.98 (t, $J$=7.6 Hz, 1H), 7.87 (t, $J$=7.6 Hz, 1H), 7.72-7.66 (m, 3H), 7.66-

7.59 (m, 6H), 7.56 (d, $J$=7.2 Hz, 2H), 7.29 (dd, $J$=7.6, 4.8 Hz, 1H), 7.17 (dd, $J$=10.1, 7.9 Hz, 1H), 2.25 (s, 3H, CH$_3$). $^{13}$C NMR (100.6 MHz, DMSO-$d_6$): δ (ppm) 168.93 (d, $J_{PC}$=8.5 Hz, <u>C</u>H=N), 161.53 (s, 1C), 145.06 (s, 1C), 139.31 (s, 1C), 138.83 (d, $J_{PC}$=8.4 Hz, 2C), 135.81 (d, $J_{PC}$=15.7 Hz, 1C), 135.52 (d, $J_{PC}$=7.5 Hz, 2C), 134.43 (s, 1C), 133.67 (d, $J_{PC}$=11.0 Hz, 2C), 132.20 (d, $J_{PC}$=2.6 Hz, 1C), 129.06 (d, $J_{PC}$=11.9 Hz, 4C), 128.40 (s, 1C), 126.79 (s, 1C), 126.26 (d, $J_{PC}$=14.1 Hz, 4C), 123.22 (s, 1C), 18.10 (s, 1C, <u>C</u>H$_3$). $^{31}$P NMR (162.0 MHz, DMSO-$d_6$): δ (ppm) 28.03 (s). FT-IR, (KBr, cm$^{-1}$) υ: 3063 (CH$_{Ar}$), 2982 (CH$_3$), 1614 (C=N), 1432 (P-Ph). Anal. calcd. for C$_{25}$H$_{21}$Cl$_2$N$_2$PPd: C, 53.84; H, 3.80; N, 5.02 %. Found: C, 54.69; H, 3.34; N, 4.00 %.

### General procedure for the Heck coupling reaction

A Schlenk tube was charged with the base (1.20 mmol) and the organic solvent (2.0 mL) under nitrogen atmosphere followed by aryl halide (1.00 mmol), olefin (1.20 mmol), and Pd(II) catalyst (1.00 % mol). The flask was sealed under N$_2$ atmosphere and placed in an oil bath and then the reaction mixture was stirred at appropriate temperatures for required times. After completion of the reaction, the mixture was cooled and extracted with ethyl acetate (3x20 mL). The extracts were washed with brine and dried over MgSO$_4$ and then the solvent was evaporated.

### General procedure for the Suzuki coupling reaction

A Schlenk tube was charged with the base (2.00 mmol) and the organic solvent/H$_2$O (3.0/3.0 mL) under nitrogen atmosphere followed by aryl halide (1.00 mmol), phenylboronic acid (1.50 mmol) and Pd(II) catalyst (1.00 % mol). The flask was sealed under N$_2$ atmosphere and placed in an oil bath and then the reaction mixture was stirred at appropriate temperatures for required times. The reaction mixture was cooled and poured into water (5 mL) and extracted with CHCl$_3$ (3x20 mL). The extracts were washed with brine and dried over MgSO$_4$ and the solvent was then evaporated.

### RESULTS AND DISCUSSION

The ligands, **1a**-**c,** were previously synthesized by treating 2-(diphenylphosphino)benzaldehyde (*o*-Ph$_2$PPhCHO) with appropriate primary amines 4-amino-3-methylphenol, 4-(2-aminoethyl)phenol and 2-amino-3-methylpyridine, respectively. The Pd(II) complexes **(2a-2c)** of the iminophosphine ligands were prepared under argon atmosphere using Schlenk techniques as shown in Schemes 1-3.

### Characterization of the iminophosphine ligands and their Pd(II) complexes

The synthesized compounds were characterized using FT-IR and $^1$H, $^{13}$C, and $^{31}$P-NMR. Quantizations were carried out with elemental analysis.

The $v_{N-H}$ and $v_{C=O}$ bands in the free amine and aldehyde compounds have totally disappeared in Schiff base ligands after the condensation. The displacement of C=N stretching frequencies from 1610-1636 cm$^{-1}$ (**1a**: 1620, **1b**: 1636, **1c**:1610 (11)) in the free Schiff base ligands to lower values of 1603-1613 cm$^{-1}$ (**2a**: 1603, **2b**: 1613, **2c**: 1604 cm$^{-1}$) in the complexes indicating the coordination of imine nitrogen to the palladium center (12–16).

## $^1$H NMR evaluation of the compounds

The $^1$H NMR spectrum of complexes **2a-c** displayed singlets at δ 8.59, 8.53, and 8.82 ppm, respectively, which confirmed the coordination of the imine (-CH=N) nitrogen to the palladium center (free ligands; **1a**; 8.89 ppm, **1b**; 8.88 ppm, and **1c**; 9.57 ppm) (11,17–20). On the other hand, $^1$H-NMR spectra of the compounds demonstrate that the -OH peaks for **2a** and **2b** were observed at 9.47 and 9.43 ppm, respectively. As in the complexes -OH peaks slightly shifted to downfield comparing to the iminophosphine ligands. The aliphatic -CH$_3$ peaks in the structure of **2a** (2.09 ppm) and **2c** (2.25 ppm) appeared as a singlet, and the -CH$_2$-CH$_2$ peaks were found as triplet in the structure of **2b** occurring at 2.69 (N-CH$_2$) and 4.46 ppm (CH$_2$Ph) (21,22).

## $^{13}$C NMR evaluation of the compounds

According to the $^{13}$C-NMR spectra of the ligands, the peaks of the imine (-$\underline{C}$H=N) carbon appeared in the region between 161.1 and 155.3 ppm indicating that the iminophosphine ligands were formed from the reaction of 2-(diphenylphosphino)benzaldehyde and amines (23). Furthermore, the -C-OH peaks for **1a**, **1b**, **2a** and **2b** appeared at 156.50, 156.06, 156.52 and 155.86 ppm, respectively. The -CH$_3$ peaks in the structure of **1a** and **2a** appear at 17.54 and 18.66 ppm as for the -CH$_2$-CH$_2$- peaks in the structure of **2b** occur at 66.82 (N-CH$_2$) and 35.93 (CH$_2$Ph) ppm. The $^{13}$C NMR peaks of the phenyl carbons appeared at 143.93-112.19 **(2a)**, 136.72-115.19 **(2b)** and 145.06-123,22 ppm **(2c)** (24).

## $^{31}$P NMR Evaluation of the Compounds

$^{31}$P-NMR peaks appeared at -13.54 (**1a**), -13.97 (**1b**), -13.76 (**1c**), 28.78 (**2a**), 30.93 (**2b**) and 28.03 (**2c**), respectively. The $^{31}$P NMR signals of the complexes which appeared downfield shift shows that the ligands are coordinated to the palladium center via phosphorus atom (25). Based on NMR and FT-IR analysis of the ligands and palladium complexes, the ligands are coordinated to the palladium atom through the imine nitrogen and the phosphorus atom (26,27).

Elemental analysis for C, H and N of ligands **1a**-**1c** and Pd(II) complexes **2a**-**2c** have indicated that the metal-ligand ratio of complexes was 1:1.

**Heck Reaction**

First of all, the optimal conditions for the catalytic application of Pd(II) complexes in Heck reaction were identified. Different bases (NEt$_3$, Na$_2$CO$_3$, NaOAc and K$_2$CO$_3$), different temperatures (80, 100, 120 and 140 °C) and different solvents (toluene, 1,4-dioxane, DMF, and NMP) were tested to determine the optimum conditions. The progress of the reaction was monitored by GC analysis. Among the preliminary studies, K$_2$CO$_3$ was found to be best base and the N-methylpyrolidone (NMP) was found to be most suitable solvent at 140 °C. After optimization of the reaction conditions, the reactions of electronically activated and deactivated aryl bromides and aryl chlorides with substituted styrenes were also examined and moderate to good yields were obtained using catalysts **2a-c**. The results are given in Table 1. All of the reactions are performed with 1.0 mol% of catalysts in NMP as solvent at 140 ˚C with K$_2$CO$_3$ acting as base.

**Table 1:** Reaction of aryl bromides with halogenated styrenes.
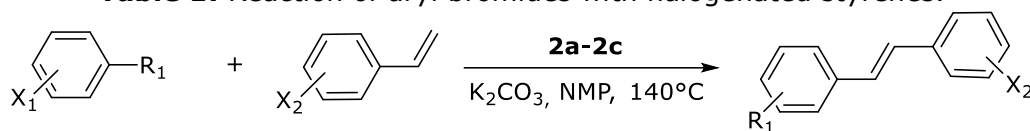


| Entry | $X_1$ | $R_1$ | $X_2$ | Conv. (%)[a] | | |
|---|---|---|---|---|---|---|
| | | | | 2a | 2b | 2c |
| 1 | o-Br | CO(CH₃) | o-Cl | 93 | 42 | 98 |
| 2 | m-Br | CO(CH₃) | " | 96 | 97 | 89 |
| 3 | p-Br | CO(CH₃) | " | 98 | 92 | 94 |
| 4 | p-Br | COH | " | 88 | 45 | 71 |
| 5 | Br | H | " | 50 | 85 | 17 |
| 6 | o-Br | CO(CH₃) | m-Cl | 62 | 72 | 14 |
| 7 | m-Br | CO(CH₃) | " | 96 | 99 | 76 |
| 8 | p-Br | CO(CH₃) | " | 98 | 91 | 88 |
| 9 | p-Br | COH | " | 93 | 98 | 98 |
| 10 | Br | H | " | 58 | 63 | 48 |
| 11 | o-Br | CO(CH₃) | p-Cl | 76 | 79 | 87 |
| 12 | m-Br | CO(CH₃) | " | 96 | 98 | 99 |
| 13 | p-Br | CO(CH₃) | " | 94 | 98 | 99 |
| 14 | p-Br | COH | " | 85 | 85 | 94 |
| 15 | Br | H | " | 87 | 49 | 75 |
| 16 | o-Br | CO(CH₃) | o-Br | 72 | 17 | 91 |
| 17 | m-Br | CO(CH₃) | " | 64 | 46 | 88 |
| 18 | p-Br | CO(CH₃) | " | 93 | 36 | 95 |
| 19 | p-Br | COH | " | 85 | 10 | 91 |
| 20 | Br | H | " | 10 | 6 | 7 |
| 21 | o-Br | CO(CH₃) | m-Br | 76 | 50 | 59 |
| 22 | m-Br | CO(CH₃) | " | 90 | 97 | 99 |
| 23 | p-Br | CO(CH₃) | " | 97 | 98 | 47 |
| 24 | p-Br | COH | " | 60 | 97 | 96 |
| 25 | Br | H | " | 12 | 5 | 4 |
| 26 | o-Br | CO(CH₃) | p-Br | 72 | 64 | 18 |
| 27 | m-Br | CO(CH₃) | " | 83 | 97 | 98 |
| 28 | p-Br | CO(CH₃) | " | 88 | 78 | 99 |
| 29 | p-Br | COH | " | 86 | 90 | 93 |
| 30 | Br | H | " | 5 | 1 | 21 |

[a]Reaction conditions: aryl bromide (1.00 mmol), styrene (1.20 mmol), K₂CO₃ (1.20 mmol) and 0.01 mmol catalyst in NMP (2.0 mL), 140 °C, 6h.
[b]Conversions were determined by GC based on aryl halide.

The results from the Table 1 indicate that the highest conversion (99%) (Table 1, entries 12, 13, 22, and 28) was achieved with the catalyst **2c** for the reaction between *m*- and *p*-bromo acetophenone, and *m*- and *p*-bromo styrene and *m*-chloro styrene. The reason why the yield in ortho position is lower than that in *m*- or *p*- position is that the substrate is unable to approach to the active center of Pd(0). The lowest conversion (5%) (Table 1, entry 30) was observed in the reaction of bromobenzene with *p*-bromostyrene. When $C(O)CH_3$ or $C(O)H$ substituted aryl bromides were used, the yields were generally high. $C(O)CH_3$ or $C(O)H$ groups activate the phenyl ring and it results in a higher yield. In general, the conversions were high in the test reactions conducted with aryl halides including electron-withdrawing groups as the substitutes. The conversion rates came out lower in the coupling reactions of bromobenzene. In addition, some low conversions are determined due to the occurrence of palladium black and its influence on the reaction rate (Table 1, entry 25, 30, 50, and 60) (28,29).

**Table 2:** Palladium-catalyzed coupling reactions of 2-bromo-6-methoxy naphthalene with styrenes[a].
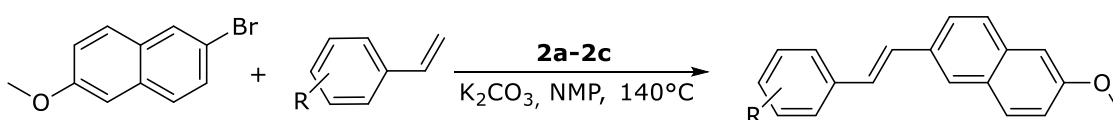


| Entry | R | Conv. | | |
|:---:|:---:|:---:|:---:|:---:|
| | | 2a | 2b | 2c |
| **1** | *o*-Cl | 38 | 60 | 55 |
| **2** | *m*-Cl | 70 | 56 | 63 |
| **3** | *p*-Cl | 92 | 79 | 79 |
| **4** | *o*-Br | 27 | 16 | 19 |
| **5** | *m*-Br | 32 | 23 | 15 |
| **6** | *p*-Br | 17 | 28 | 16 |
| **7** | *o*-CH$_3$ | 57 | 61 | 45 |
| **8** | *m*-CH$_3$ | 72 | 84 | 84 |
| **9** | *p*-CH$_3$ | 95 | 77 | n.r. |
| **10** | *o*-OCH$_3$ | 99 | 37 | 93 |

[a]Reaction conditions: 2-bromo-6-methoxy naphthalene (1.00 mmol), olefin (1.20 mmol), $K_2CO_3$ (1.2 mmol) and 0.01 mmol catalyst in NMP (2 mL), 140 °C, 6h.
[b]Conversions were determined by GC based on aryl halide.

Finally, Heck reaction was carried out with 2-bromo-6-methoxynaphthalene which is an important chemical in medicinal chemistry and used in the synthesis of naproxen (30). In the reaction between the substituted styrenes and 2-bromo-6-methoxynaphthalene using the

catalyst **2a** *o*-methoxy styrene gave the highest conversion (99%) (Table 2, entry 10) while *p*-bromo styrene gave the lowest conversion (17%) (Table 2, entry 6). The reaction yield was found high when active groups such as -methyl and -methoxy bound to the phenyl ring. It was determined to be low when halogens were used. This is because -methoxy or -methyl groups increase the interest of the substrates to Pd(0), and it causes an easier binding. When halogens on the phenyl ring are compared, the conversion found from the -chloro attached to phenyl ring was partially higher than that of the -bromo attached to phenyl ring (Table 2). The electron-withdrawing effect of -chloro group is higher than that of -bromo group, and it reduces the electron density of 2-bromo-6-methoxy naphthalene. This increases the interest of 2-bromo-6-methoxy naphthalene to Pd(0).

**Suzuki Reaction**

The same way as in the Heck C-C coupling reaction, firstly, the optimal conditions for defining the catalytic efficiency of Pd(II) complexes were determined for the Suzuki reaction. In order to determine the optimal conditions, organic and inorganic bases (NEt$_3$, Na$_2$CO$_3$, NaOAc, and K$_2$CO$_3$), different temperatures (80, 100, 120, and 140 °C) and solvents (toluene, 1,4-dioxane, DMF and NMP) were tested in the reaction of bromo benzene and phenyl boronic acid. At the end of the reaction, samples were analyzed with GC. The results confirm that the conversion was low at 80 °C in NMP when compared to other solvents such as toluene, 1,4-dioxane, and DMF.

After determining optimal conditions, the results showed that the conversion rose up to as high as 99 percent at the temperature of 80 °C, in the presence of Na$_2$CO$_3$ in the DMF solvent. The catalytic experiments were conducted with different aryl halide and boronic acid derivatives at 80 and 25 °C (31). Comparing among -bromo acetophenones, p-bromo acetophenone is slightly higher than ortho- and *m*-bromo acetophenone (Table 3, entries 3, 8 and 13). The bromo-positioned at meta- and para- causes a steric hindrance, and it results in partially low conversion. Therefore, the substrate cannot be coordinated to the Pd center well.

**Table 3:** The results of the reactions between aryl bromide and 2-naphthalene boronic acid.
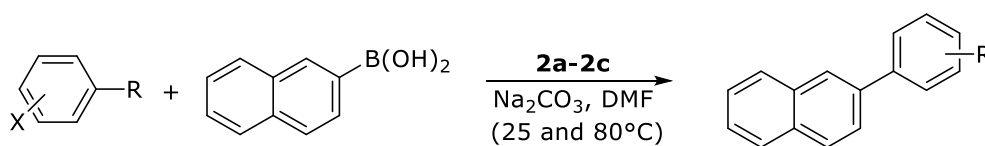


| Entry | Catalyst | X | R | Conv. (%)[a] | |
|:---:|:---:|:---:|:---:|:---:|:---:|
| | | | | 25°C | 80°C |
| 1 | 2a | o-Br | CO(CH$_3$) | 60 | 65 |
| 2 | " | m-Br | CO(CH$_3$) | 53 | 55 |
| 3 | " | p-Br | CO(CH$_3$) | 69 | 68 |
| 4 | " | p-Br | C(O)H | 77 | 79 |
| 5 | " | Br | H | 65 | 68 |
| 6 | 2b | o-Br | CO(CH$_3$) | 2 | 9 |
| 7 | " | m-Br | CO(CH$_3$) | 10 | 63 |
| 8 | " | p-Br | CO(CH$_3$) | 98 | 98 |
| 9 | " | p-Br | C(O)H | 85 | 91 |
| 10 | " | Br | H | 46 | 49 |
| 11 | 2c | o-Br | CO(CH$_3$) | 67 | 82 |
| 12 | " | m-Br | CO(CH$_3$) | 39 | 54 |
| 13 | " | p-Br | CO(CH$_3$) | 77 | 89 |
| 14 | " | p-Br | C(O)H | 80 | 93 |
| 15 | " | Br | H | 61 | 66 |

[a]Reaction conditions: aryl bromide (1.00 mmol), 2-naphthaleneboronic acid (1.20 mmol), K$_2$CO$_3$ (1.20 mmol) and 0.01 mmol catalyst in DMF/H$_2$O 2/2 mL), 6h.
[b]Conversions were determined by GC based on aryl halide.

According to the GC analyses, the Suzuki reaction of 4-biphenylboronic acid and aryl bromide using the catalyst **2b**, the highest conversions of 99 percent (Table 4, entries 8 and 9), were achieved in the reactions with p-bromoacetophenone and p-bromobenzaldehyde. The reason why the conversions from the aldehyde and ketone group in para position are higher than those for ortho and meta aldehyde and ketone group is that the steric hindrance is low in para position, and it easily coordinates to Pd(II) center (Table 3, entry 6).

For the reaction between biphenyl and aryl bromide, the highest conversion was obtained 74% at 25 °C and 92% at 80 °C. The lowest conversion at 25 and 80 °C was calculated to be 12% and 15%, respectively (Table 4, entry 1). As shown in Table 4 entry 9, catalyst **2b** gave excellent results for the synthesis of carbaldehyde derivative compounds in the room temperature.

**Table 4.** The Suzuki reaction between aryl bromides and 4-biphenylboronic acid.

Ph—B(OH)$_2$ + R—Br $\xrightarrow[\substack{Na_2CO_3,\ DMF \\ (25\ ^\circ C\ and\ 80\ ^\circ C)}]{\textbf{2a-2c}}$ Ph——R
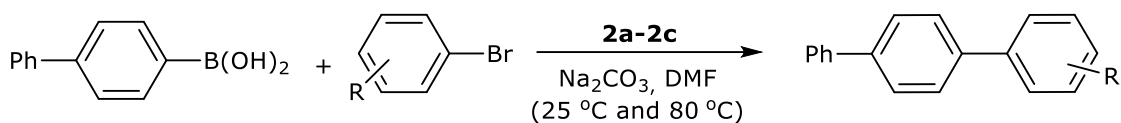
| Entry | Catalyst | R | Conv. (%)[a] | |
|:-----:|:--------:|:----:|:-----:|:-----:|
| | | | 25 °C | 80 °C |
| 1 | **2a** | $o$-CO(CH$_3$) | 12 | 15 |
| 2 | " | $m$-CO(CH$_3$) | 25 | 74 |
| 3 | " | $p$-CO(CH$_3$) | 47 | 67 |
| 4 | " | $p$-C(O)H | 74 | 92 |
| 5 | " | H | 60 | 87 |
| 6 | **2b** | $o$-CO(CH$_3$) | 4 | 20 |
| 7 | " | $m$-CO(CH$_3$) | 15 | 76 |
| 8 | " | $p$-CO(CH$_3$) | 91 | 99 |
| 9 | " | $p$-C(O)H | **99** | **99** |
| 10 | " | H | 67 | 87 |
| 11 | **2c** | $o$-CO(CH$_3$) | - | 12 |
| 12 | " | $m$-CO(CH$_3$) | 57 | 66 |
| 13 | " | $p$-CO(CH$_3$) | 65 | 79 |
| 14 | " | $p$-C(O)H | 98 | 98 |
| 15 | " | H | 51 | 65 |

[a]Reaction conditions: aryl halide (1.00 mmol), 4-biphenylboronic acid (1.20 mmol) K$_2$CO$_3$ (1.20 mmol) and 0.01 mmol cat., DMF/H$_2$O 2/2 mL), 6h.
[b]Conversions were determined by GC based on aryl halide.

When the catalytic efficiencies were analyzed with GC, the best conversion percentage in the reactions between 2-bromo-6-methoxy naphthalene, 2-naphthalene boronic acid and 4-biphenyl boronic acid was determined to be 91 percent when the catalyst **2b** was used and 69 percent with the catalyst **2a** (Table 5, entries 2-3). As seen in Table 5, the conversions were found to be low or average. Due to the steric effect of the substrates, the substrates are inability to approach to palladium active center, and it results in low conversions.

**Table 5:** The results of the reaction between 2-bromo-6-methoxy naphthalene and arylboronic acids.

| Entry | Catalyst | ArB(OH)$_2$ | Product and conv. (%)[a] |
|---|---|---|---|
| 1 | **2a** | | %30[b] %39[c] |
| 2 | " | | %18[b] %69[c] |
| 3 | **2b** | | %32[b] %91[c] |
| 4 | " | | %42[b] %76[c] |
| 5 | **2c** | | %42[b] %76[c] |
| 6 | " | | %36[b] %71[c] |
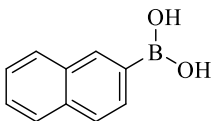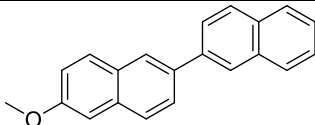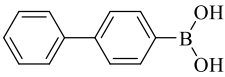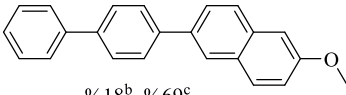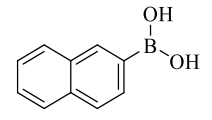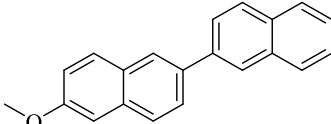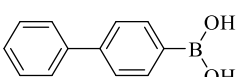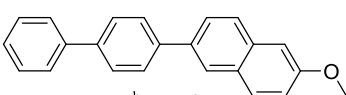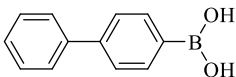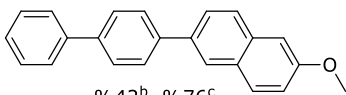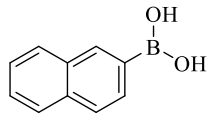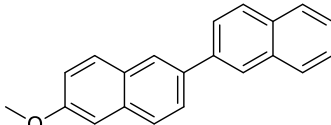
Reaction conditions: 2-bromo-6-methoxy naphthalene (1 mmol), arylboronic acid (1.20 mmol), K$_2$CO$_3$ (1.20 mmol) and 0.01 mmol of catalyst, DMF/water, 2/2 mL, 6h.
[a]Conversions were determined by GC based on 2-bromo-6-methoxynaphthalene.
[b]25 °C.
[c]80 °C.

## CONCLUSIONS

A new series of iminophosphine-Pd(II) complexes with PN ligands have been synthesized and characterized using spectroscopic techniques. The $^{31}$P{$^1$H} NMR and FTIR results of the complexes indicate that the coordination of the iminophoshine ligand with Pd(II) occurs via phosphorus and nitrogen atoms. The complexes have been tested as catalysts for Heck and Suzuki reactions. The C-C coupling reactions put into practice with catalysts **2a**-**2c** show high conversions under the determined conditions with para- substituted aryl halides. Besides, the high conversion of some substrates at 25 °C shows that the catalysts are active.

## ACKNOWLEDGEMENT

## REFERENCES

1.  Aydemir M, Baysal A, Gümgüm B. Synthesis and characterization of tris{2-(N,N-bis(diphenylphosphino) aminoethyl} amine derivatives: Application of a palladium(II) complex as a pre-catalyst in the Heck and Suzuki cross-coupling reactions. J Organomet Chem. 2008 Dec;693(26):3810–4.

2.  Scrivanti A, Beghetto V, Matteoli U, Antonaroli S, Marini A, Crociani B. Catalytic activity of η2-(olefin)palladium(0) complexes with iminophosphine ligands in the Suzuki–Miyaura reaction. Role of the olefin in the catalyst stabilization. Tetrahedron. 2005 Oct;61(41):9752–8.

3.  Nadri S, Joshaghani M, Rafiee E. Biphenyl-based phosphine: A well-defined, air-stable, and efficient ligand for the Mizoroki–Heck reaction. Appl Catal Gen. 2009 Jun;362(1–2):163–8.

4.  Herrmann WA, Böhm VP., Reisinger C-P. Application of palladacycles in Heck type reactions. J Organomet Chem. 1999 Mar;576(1–2):23–41.

5.  Iyer S, Kulkarni GM, Ramesh C. Mizoroki–Heck reaction, catalysis by nitrogen ligand Pd complexes and activation of aryl bromides. Tetrahedron. 2004 Feb;60(9):2163–72.

6.  Reddy KR, Surekha K, Lee G-H, Peng S-M, Liu S-T. Palladium(II) Complexes with Phosphorus−Nitrogen Mixed Donors. Efficient Catalysts for the Heck Reaction. Organometallics. 2000 Jun;19(13):2637–9.

7.  Doherty S, Knight JG, Scanlan TH, Elsegood MR, Clegg W. Iminophosphines: synthesis, formation of 2, 3-dihydro-1H-benzo [1, 3] azaphosphol-3-ium salts and N-(pyridin-2-yl)-2-diphenylphosphinoylaniline, coordination chemistry and applications in platinum group catalyzed Suzuki coupling reactions and hydrosilylations. J Organomet Chem. 2002;650(1):231–248.

8.  Cheng J, Wang F, Xu J-H, Pan Y, Zhang Z. Palladium-catalyzed Suzuki–Miyaura reaction using aminophosphine as ligand. Tetrahedron Lett. 2003;44(37):7095–7098.

9.  Drew D, Doyle JR, Shaver AG. Cyclic Diolefin Complexes of Platinum and Palladium. In: Cotton FA, editor. Inorganic Syntheses [Internet]. Hoboken, NJ, USA: John Wiley & Sons, Inc.; 2007 [cited 2017 Nov 24]. p. 47–55. Available from: http://doi.wiley.com/10.1002/9780470132449.ch11

10. Laue S, Greiner L, Wöltinger J, Liese A. Continuous application of chemzymes in a membrane reactor: Asymmetric transfer hydrogenation of acetophenone. Adv Synth Catal. 2001;343(6–7):711–720.

11. Keleş M, Şahinoğlu C, Emir DM, Mart M. New iminophosphine–Ru (II) complexes and their application in hydrogenation and transfer hydrogenation. Appl Organomet Chem. 2014;28(10):768–772.

12. Nobre SM, Monteiro AL. Pd complexes of iminophosphine ligands: A homogeneous molecular catalyst for Suzuki–Miyaura cross-coupling reactions under mild conditions. J Mol Catal Chem. 2009;313(1):65–73.

13. Jeffery JC, Rauchfuss TB, Tucker PA. Metal complexes of diiminodiphosphines. Structural and reactivity patterns. Inorg Chem. 1980 Nov;19(11):3306–15.

14. Rülke RE, Kaasjager VE, Wehman P, Elsevier CJ, van Leeuwen PWNM, Vrieze K, et al. Stable Palladium(0), Palladium(II), and Platinum(II) Complexes Containing a New, Multifunctional and Hemilabile Phosphino−Imino−Pyridyl Ligand: Synthesis, Characterization, and Reactivity. Organometallics. 1996 Jan;15(13):3022–31.

15. Crochet P, Gimeno J, Borge J, García-Granda S. Novel ruthenium(ii) complexes containing imino- or aminophosphine ligands for catalytic transfer hydrogenation. New J Chem. 2003 Jan 20;27(2):414–20.

16. Kwong H-L, Lee W-S, Lai T-S, Wong W-T. Ruthenium catalyzed asymmetric transfer hydrogenation based on chiral P,N,O Schiff base ligands and crystal structure of a ruthenium(II) complex bearing chiral P,N,O Schiff base ligands. Inorg Chem Commun. 1999 Feb;2(2):66–9.

17. Reddy KR, Surekha K, Lee G-H, Peng S-M, Chen J-T, Liu S-T. Study of Insertion of Olefins and/or Carbon Monoxide into Phosphine- Imine Palladium Methyl Complexes. Organometallics. 2001;20(7):1292–1299.

18. Wang C, Friedrich S, Younkin TR, Li RT, Grubbs RH, Bansleben DA, et al. Neutral Nickel(II)-Based Catalysts for Ethylene Polymerization. Organometallics. 1998 Jul;17(15):3149–51.

19. Lavery A, Nelson SM. Dinuclear intermediates in the oxidation of pendant olefinic groups of palladium (II)-co-ordinated Schiff-base ligands. J Chem Soc Dalton Trans. 1984;(4):615–620.

20. Alder MJ, Cross WI, Flower KR, Pritchard RG. Azo-phosphine containing complexes of Group 6 metal carbonyls: crystal and molecular structure of [Mo(CO)5{1-(4-ethylphenylazo)-6-diphenylphosphino-naphthalen-2-ol}]. J Organomet Chem. 1998 Oct;568(1–2):279–85.

21. Korostylev A, Bondarev O, Lyubimov S, Kovalevsky AY, Petrovskii P, Davankov V, et al. New palladium (II) complexes of (N, N-dimethylamino) alkoxy-1, 3, 2-oxazaphospholidine ligands. Inorganica Chim Acta. 2000;303(1):1–6.

22. Mahamo T, Mogorosi MM, Moss JR, Mapolie SF, Chris Slootweg J, Lammertsma K, et al. Neutral palladium(II) complexes with P,N Schiff-base ligands: Synthesis, characterization and application as Suzuki–Miyaura coupling catalysts. J Organomet Chem. 2012 Apr;703:34–42.

23. Radulović V, Bacchi A, Pelizzi G, Sladić D, Brčeski I, Andjelković K. Synthesis, Structure, and Antimicrobial Activity of Complexes of Pt(II), Pd(II), and Ni(II) with the Condensation Product of 2-(Diphenylphosphino)benzaldehyde and Semioxamazide. Monatshefte Für Chem - Chem Mon. 2006 Jun;137(6):681–91.

24. Mogorosi MM, Mahamo T, Moss JR, Mapolie SF, Slootweg JC, Lammertsma K, et al. Neutral palladium (II) complexes with P, N Schiff-base ligands: Synthesis, characterization and catalytic oligomerisation of ethylene. J Organomet Chem. 2011;696(23):3585–3592.

25. Keleş M, Yılmaz MK. Palladium(II) complexes with aminomethylphosphine ligands as catalysts for the heck reaction. Heteroat Chem. 2012;23(5):466–71.

26. Keles M, Aydin Z, Serindag O. Synthesis of palladium complexes with bis(diphenylphosphinomethyl)amino ligands: A catalyst for the Heck reaction of aryl halide with methyl acrylate. J Organomet Chem. 2007 Apr;692(10):1951–5.

27. Garrou PE. .DELTA.R-ring contributions to phosphorus-31 NMR parameters of transition-metal-phosphorus chelate complexes. Chem Rev. 1981 Jun;81(3):229–66.

28. Smith RC, Bodner CR, Earl MJ, Sears NC, Hill NE, Bishop LM, et al. Suzuki and Heck coupling reactions mediated by palladium complexes bearing trans-spanning diphosphines. J Organomet Chem. 2005 Jan;690(2):477–81.

29. Pramick MR, Rosemeier SM, Beranek MT, Nickse SB, Stone JJ, Stockland, RA, et al. Coupling of Aryl Halides with Aryl Boronic Acids with $P(C_6H_5)(2\text{-}C_6H_4Cl)_2$ as the Supporting Ligand. Organometallics. 2003 Feb;22(3):523–8.

30. Harrington PJ, Lodewijk E. Twenty Years of Naproxen Technology. Org Process Res Dev. 1997 Jan;1(1):72–6.

31. Sabounchei SJ, Panahimehr M, Ahmadi M, Nasri Z, Khavasi HR. Four-coordinate Pd(II) complexes containing non-symmetric phosphorus ylides: Synthesis, characterization, and catalytic behavior towards Suzuki reaction. J Organomet Chem. 2013 Jan;723:207–13.

**RESEARCH ARTICLE**

# Synthesis and Structural Analysis of Some New Sulfanyl Amino 1,4-Naphthoquinone Derivatives

**Hatice YILDIRIM [1], \***
[1] Istanbul University, 34320, Istanbul, Turkey

**Abstract:** In this study, some new sulfanyl-substituted amino 1,4-naphthoquinone derivatives which possess two electron-donating groups in the amino fragment were synthesized and their structures were analyzed by spectroscopic techniques. First, 2-chloro-3-[(2,4-dimethoxyphenyl)amino]naphthalene-1,4-dione (**3a**) and 2-chloro-3-[(3,5-dimethoxyphenyl)amino]naphthalene-1,4-dione (**3b**) were obtained from the reactions of dichloro-1,4-naphthoquinone (**1**) with 2,4-dimethoxyaniline and 3,5-dimethoxyaniline. In the following step, the compounds **3a**,**b** were reacted with aliphatic nucleophiles; ethyl-, 1-propyl-, and 1-pentyl mercaptan. S-nucleophiles attacked the carbon atom of 1,4-naphthoquinone core and displaced the chlorine atom to create target molecules; 2-arylamino-*3*-(ethylthio)naphthalene-1,4-dione **(5a,b)**, 2-arylamino-3-(propylthio)naphthalene-1,4-dione **(5c,d)**, 2-arylamino-3-(pentylthio)naphthalene-1,4-dione **(5e,f)** derivatives. The structures of the synthesized compounds were elucidated by utilizing 1D and 2D NMR techniques with additional spectroscopic data (mass and FTIR).

**INTRODUCTION**

Quinoic structures are quite valuable compounds because of having a wide range of applications. Such compunds allow electronic transition between molecules due to their reduction states. They have three oxidation states; one state is quinone, another state is semiquinone, which is one-electron reduced form of quinone, and the last one is also catechol or hydroquinone which is two-electron reduced form of quinone. These different oxidation states of quinone structures make them very crucial for chemical science (1). For instance, the reduction properties of quinones stand out in the field of energy storage. Quinones give reversible redox reactions at high potential. Although they are not practical because of their insolubility in electrolyte solutions, quinones are able to use as electron-active species in flow battery (2-5).

Quinones have not only some practices in the field of energy storage but also have biological effects such as antitumor, antifungal, antibacterial, and phytotoxic activities. Salinisporamycin and hygrocin A, containing 1,4-napthoquinone core, have antimicrobial and anticancer effects (6, 7). In particularly, since the test results of these naphthoquinone derivatives presenting low cytotoxic effects, the interest of synthesis of new naphthoquinone compounds has increased.

The amino 1,4-naphthoquinone structure plays a key role for synthesis of many bioactive molecules. It is possible to see amino and thioether derivatives of 1,4-naphthoquinone in the impressive bioactivity studies. They have a variety of pharmacological properties such as antibacterial, antifungal, antiviral, anti-inflammatory, and anti-cancer (1, 8-12). Some sulfanylamino-1,4-naphthoquinone derivatives have been evaluated against a full panel of 60 primary human tumor cell lines derived from nine human cancer types. Among the tested compounds, it has been observed that the structure **I** affects the growth of two colon cancer cells, HCT116 and HCT15, and of two leukemia cells, MOLT-4 and SR. The structure **II** has also low cytotoxicity against the NCI-H23 cancer line (9) (Figure1)
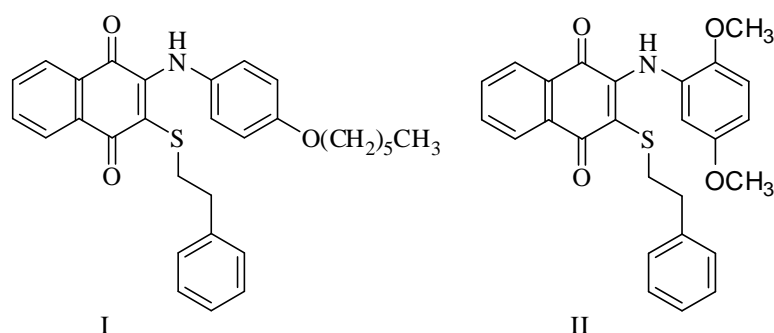


**Figure 1**. Example structures of sulfanylamino-1,4-naphthoquinones (**I**) and (**II**).

In previous studies, the effect of the electron-withdrawing groups on the biological activity of molecule has been investigated and the results of these studies have showed that amino- and/or

sulfanyl- derivatives of 1,4-naphthoquinone act as good antibacterial and antifungal agents against different pathogens. The sort of electron-withdrawing group(s) and also their position(s) in the amine ring have an influence upon the activity (8, 10, 13, 14). In this study, some novel sulfanylamino-1,4-naphthoquinone derivatives have been obtained from the nucleophilic substitution reactions of 1,4-napthoquinones possessing an aryl amine substituent which has two electron donating groups, in the 2,4- and 3,5-positions of phenyl ring, with alkyl mercaptans. The products have been purified by column chromatography and characterized by FTIR, 1D/2D NMR and mass spectroscopy.

## MATERIALS AND METHODS

All reagents were commercially obtained from commercial suppliers and used without further purification unless otherwise noted. The purity of reaction products was routinely monitored by thin-layer chromatography on analytical thin layer chromatography (TLC), which was purchased from Merck KGaA (silica gel 60 $F_{254}$) based on Merck DC-plates (aluminum-based). Visualization of the chromatogram was performed by UV light (254 nm). Column chromatographic separations were carried out using silica gel 60 (Merck, 63–200 $\mu$m particle size, 60–230 mesh). All NMR spectra were acquired using a Varian UNITY INOVA 500 MHz spectrometer equipped with AutoX PFG probe operating at a proton observation frequency of 499.7 MHz and a carbon observation frequency 125.7 MHz at 25 °C in $CDCl_3$ as the solvent. $^1$H NMR spectra and $^{13}$C NMR spectra in $CDCl_3$ referred to the solvent signal center at $\delta$ 7.25 and $\delta$ 77.0 ppm, respectively. Standard abbreviations indicating multiplicity were used as follows: s (singlet), bs (broad singlet), d (doublet), dd (doublet of doublets), t (triplet), td (triplet of doublets), q (quartet) and m (multiplet). The one-bond J(CH) coupling constant was 146 Hz and the long range J(CH) coupling constant was 8 Hz for 2D spectra. FTIR spectra were recorded using Jasco FT/IR-4700 spectrometer with high resolution 0.4 $cm^{-1}$ using ATR accessory. Mass spectra were obtained on a Thermo Finnigan LCQ Advantage MAX MS/MS spectrometer equipped with an ESI (Electrospray ionization) sources. Melting points (mp) were determined with a Buchi B-540 melting point apparatus and were uncorrected.

### *General Procedure:*
In this study, two types of synthetic procedures were used to obtain substituted 1,4-naphthoquinone derivatives.

*General Procedure for Preparation of the 2-arylamino 1,4-naphthoquinone Derivatives (**3a-b**)*
2-Chloro-3-[(2,4-dimethoxyphenyl)amino]naphthalene-1,4-dione (**3a**) and 2-chloro-3-[(3,5-dimethoxyphenyl)amino]naphthalene-1,4-dione (**3b**) were obtained from the reactions of 2,3-dichloro-1,4-naphthoquinone (**1**) with 2,4-dimethoxyaniline (**2a**) and 3,5-dimethoxyphenyl amine (**2b**) according to previous literature reported (1, 13, 15).

*General Procedure for Preparation of the 2-arylamino-3-sulfanyl-1,4-naphthoquinone Derivatives (**5a-f**)*

2-Arylamino-3-chloro-1,4-naphthoquinone derivatives (**3a,b**) (1 mmol) and the aliphatic thiols (**4a-c**) (1.5 mmol) in the presence of Et₃N were stirred in CHCl₃ (5 mmol) at room temperature for 6-8 hours. The resulting solution was extracted with 100 mL chloroform then washed with water (3x100 mL) and dried over calcium chloride. The solvent was removed *in vacuo*. The purification of product was subjected to column chromatography on silica gel using a proper solvent mixture such as chloroform-petroleum ether (2:1 or 3:1, v/v).

*2-(2,4-Dimethoxyphenylamino)-3-(ethylthio)naphthalene-1,4-dione* **5a** was synthesized from 2-chloro-3-[(2,4-dimethoxyphenyl)amino]naphthalene-1,4-dione (**3a**) and ethanethiol (**4a**) as a dark purple viscous product by using the general procedure. Yield: 0.088 g, 81%. FTIR (ATR) ν(cm⁻¹): 3312 (-NH), 3060 (CH$_{arom.}$), 2924, 2833 (CH$_{aliph.}$), 1662 (C=O), 1590 (C=C). ¹H NMR (500 MHz, *CDCl₃*) δ (ppm): 8.16 dd, *J:7.65, 0.93Hz*, 1H (-CH$_{arom.}$); 8.04 dd, *J: 7.65, 0.92Hz*, 1H (-CH$_{arom.}$); 7.77 bs, 1H (-NH); 7.72  td, *J:7.60, 1.40Hz*, 1H (-CH$_{arom.}$); 7.63 td, *J:7.50, 1.34Hz*, 1H (-CH$_{arom.}$); 6.93 d, *J:8.41 Hz*, 1H(-CH$_{arom.}$); 6.50 t, *J:2.70 Hz*, 1H(-CH$_{arom.}$); 6.48 dd, *J:8.43, 2.63 Hz*, 1H(-CH$_{arom.}$); 3.84 s, 3H (-OCH₃); 3.82 s, 3H, (-OCH₃); 2.58 q, *J:7.40 Hz*, 2H ( -SCH₂); 1.07 t, J:7.40 Hz, 3H (CH₃). ¹³C NMR (125 MHz, *CDCl₃*) δ(ppm): 180.7, 180.5 (C=O), 158.3, 153.3, 146.9, 134.4, 133.7, 132.4, 130.9, 126.7, 126.4, 124.7, 120.9, 113.9, 103.1, 98.8 (-CH$_{arom.}$ and C$_q$), 55.7, 55.5 (OCH₃), 28.0 (-SCH₂), 14.6 (CH₃). MS (GC-MS): *m/z* (%) 370.1 (100, [M]⁺). Anal. Calcd. for C₂₀H₁₉NO₄S (369.43).

*2-(3,5-Dimethoxyphenylamino)-3-(ethylthio)naphthalene-1,4-dione* **5b** was synthesized from 2-chloro-3-[(3,5-dimethoxyphenyl)amino]naphthalene-1,4-dione (**3b**) and ethanethiol (**4a**) as a dark red solid product by using the general procedure. Yield: 0.06 g, 56%; mp 136-138 °C. FTIR (ATR) ν(cm⁻¹): 3295 (-NH), 3064 (CH$_{arom.}$), 2834 (CH$_{aliph.}$), 1648 (C=O), 1584 (C=C). ¹H NMR (500 MHz, *CDCl₃*) δ (ppm): 8.15 dd, *J = 7.81, 0.98 Hz*, 1H (-CH$_{arom.}$); 8.08 dd, *J = 7.81, 0.98 Hz*, 1H (-CH$_{arom.}$); 7.76 bs, 1H (-NH); 7.73 td, *J = 7.32, 1.46 Hz*, 1H (-CH$_{arom.}$); 7.66 td, *J = 7.32, 0.98 Hz*, 1H (-CH$_{arom.}$); 6.26 t, J = 1.96 Hz, 1H (-CH$_{arom.}$); 6.17 d, J = 2.44 Hz, 2H (-CH$_{arom.}$); 3.79 s, 6H (-OCH₃); 2.69 q, *J = 7.32 Hz*, 2H (-SCH₂); 1.08 t, *J = 7.32 Hz*, 3H(-CH₃). ¹³C NMR (125 MHz, *CDCl₃*) δ(ppm): 181.1, 180.3 (C=O), 160.7, 144.8, 140.4, 134.5, 133.5, 132.8, 130.6, 126.8, 126.6, 119.2, 100.6, 96.8(-CH$_{arom.}$ and C$_q$), 55.4 (OCH₃), 28.0 (-SCH₂), 14.6 (CH₃). MS (ESI+) m/z (%): 370.1 (100, [M]⁺). Anal. Calcd. for C₂₂H₁₉NO₄S (369.43).

*2-(2,4-Dimethoxyphenylamino)-3-(propylthio)naphthalene-1,4-dione* **5c** was synthesized from 2-chloro-3-[(2,4-dimethoxyphenyl)amino]naphthalene-1,4-dione (**3a**) and propane-1-thiol (**4b**) as a dark purple viscous product by using the general procedure. Yield: 0.097 g, 87%. FTIR (ATR) ν(cm⁻¹): 3311 (-NH), 2929, 2831 (CH$_{aliph.}$), 1663 (C=O), 1590 (C=C). ¹H NMR (500 MHz,

*CDCl₃*) δ (ppm): 8.17 dd, *J:7.68, 0.92 Hz*, 1H (-CH$_{arom.}$); 8.05 dd, *J: 7.62, 0.96Hz*, 1H(-CH$_{arom.}$); 7.77 bs, 1H (-NH); 7.73 td, *J:7.60, 1.38Hz*, 1H (-CH$_{arom.}$); 7.64 td, *J:7.53, 1.33Hz*, 1H (-CH$_{arom.}$); 6.94 d, *J:8.43 Hz*, 1H (-CH$_{arom.}$); 6.51 t, *J:2.91 Hz*, 1H (-CH$_{arom.}$); 6.48 dd, *J:8.46, 2.64 Hz*, 1H(-CH$_{arom.}$); 3.85 s,3H (-OCH₃); 3.83 s,3H(-OCH₃); 2.54 t, *J:7.34 Hz*, 2H (S-CH₂-), 1.49-1.38 m, 2H (-CH₂); 0.86 t, *J:7.34 Hz*, 3H (-CH₃). ¹³C NMR (125 MHz, *CDCl₃*) δ(ppm): 180.7, 180.6(C=O), 158.3, 153.3, 146.8, 134.3, 133.7, 132.4, 130.9, 126.7, 126.4, 124.7, 120.9, 114.3, 103.1, 98.9 (-CH$_{arom.}$ and C$_q$), 55.6, 55.6 (OCH₃), 35.8 (-SCH₂), 22.9 (-CH₂), 13.3 (CH₃). MS (ESI+) *m/z* (%): 384.1 (100, [M]⁺). Anal. Calcd. for C₂₁H₂₁NO₄S (383.46).

*2-(3,5-Dimethoxyphenylamino)-3-(propylthio)naphthalene-1,4-dione* **5d** was synthesized from 2-chloro-3-[(3,5-dimethoxyphenyl)amino]naphthalene-1,4-dione (**3b**) and propan-1-thiol (**4b**) as a dark red-colored solid product by using the general procedure. Yield: 0.088 g, 79%; mp 73-75 ⁰C. FTIR (ATR) ν(cm⁻¹): 3293 (-NH), 2961, 2920 (CH$_{aliph.}$), 1666, 1633 (C=O), 1591, 1552 (C=C). ¹H NMR (500 MHz, *CDCl₃*) δ (ppm): 8.15 dd, *J:7.62, 1.0Hz*, 1H (-CH$_{arom.}$); 8.08 dd, *J: 7.59, 1.0Hz*, 1H (-CH$_{arom.}$); 7.77 bs, 1H (-NH); 7.73 td, *J:7.55, 1.40Hz*, 1H (-CH$_{arom.}$); 7.66 td, *J:7.52, 1.34Hz*, 1H (-CH$_{arom.}$); 6.27 t, *J:2.17 Hz*, 1H (-CH$_{arom.}$); 6.18 d, *J:2.09 Hz*, 2H (-CH$_{arom.}$); 3.79 s, 6H (-OCH₃); 2.65 t, *J:7.40 Hz*, 2H (-SCH₂); 1.44 q, *J:7.34 Hz*, 2H(-CH₂); 0.86 t, *J:7.35 Hz*, 3H (-CH₃). ¹³C NMR (125 MHz, *CDCl₃*) δ(ppm): 181.1, 180.3 (C=O), 160.7, 144.9, 140.5, 134.5, 133.5, 132.8, 130.6, 126.8, 126.6, 119.4, 100.7, 96.8 (-CH$_{arom.}$ and C$_q$), 55.4 (OCH₃), 35.7 (-SCH₂), 23.0 (-CH₂), 13.3 (CH₃). MS (ESI+) *m/z* (%): 384.1 (100, [M]⁺). Anal. Calcd. for C₂₁H₂₁NO₄S (383.46).

*2-(2,4-Dimethoxyphenylamino)-3-(pentylthio)naphthalene-1,4-dione* **5e** was synthesized from 2-chloro-3-[(2,4-dimethoxyphenyl)amino]naphthalene-1,4-dione (**3a**) and pentan-1-thiol (**4c**) as a dark purple-colored viscous product by using the general procedure. Yield: 0.08 g, 67%. FTIR (ATR) ν(cm⁻¹): 3323 (-NH), 2924, 2844 (CH$_{aliph.}$), 1664 (C=O), 1590, 1547 (C=C). ¹H NMR (500 MHz, *CDCl₃*) δ (ppm): 8.15 dd, *J:7.81, 1.47Hz*, 1H (-CH$_{arom.}$); 8.04 dd, *J:7.81, 1.47Hz*, 1H (-CH$_{arom.}$); 7.76 bs, 1H (-NH); 7.71 td, *J:7.32, 1.46Hz*, 1H (-CH$_{arom.}$); 7.63 td, *J:7.32, 1.46Hz*, 1H (-CH$_{arom.}$); 6.92 d, *J:8.3 Hz*, 1H (-CH$_{arom.}$); 6.48 dd, *J:7.56, 2.68Hz*, 1H (-CH$_{arom.}$); 6.48 dd, *J:16.10, 2.68Hz*, 1H (-CH$_{arom.}$); 3.83 s, 3H (-OCH₃); 3.82 s,3H (-OCH₃); 2.52 t, *J:7.32 Hz*, 2H (-SCH₂); 1.41 -1.34 m, 2H (-CH₂-); 1.23 -1.18 m, 4H(-CH₂-); 0.83 -0.80 m, 3H(-CH₃). ¹³C NMR (125 MHz, *CDCl₃*) δ(ppm): 180.7, 180.6 (C=O), 158.2, 153.2, 146.5, 134.3, 133.7, 132.3, 130.8, 126.7, 126.4, 124.6, 120.7, 114.4, 103.0, 98.8 (-CH$_{arom.}$ and C$_q$), 55.6, 55.5 (OCH₃), 33.7 (-SCH₂), 30.9, 29.1, 22.2 (-CH₂), 13.9 (CH₃). MS (ESI+) *m/z* (%): 412.2 (100, [M]⁺). Anal. Calcd. for C₂₃H₂₅NO₄S (411.51).

*2-(3,5-Dimethoxyphenylamino)-3-(pentylthio)naphthalene-1,4-dione* **5f** was synthesized from 2-chloro-3-[(3,5-dimethoxyphenyl)amino]naphthalene-1,4-dione (**3b**) and pentan-1-thiol (**4c**) as a dark red solid product by using the general procedure. Yield: 0.07 g, 58 %; mp 125-127

°C. FTIR (ATR) ν(cm⁻¹): 3297 (-NH), 2916, 2852 (CH$_{aliph.}$), 1666, 1630 (C=O), 1590 (C=C). ¹H NMR (500 MHz, *CDCl₃*) δ (ppm): 8.18-8.16 m, 1H (-CH$_{arom.}$); 7.76 td, *J:7.51, 1.40Hz*, 2H (-CH$_{arom.}$, -NH); 7.69 td, *J:7.51, 1.40Hz*, 1H (-CH$_{arom.}$); 8.12-8.10 m, 1H (-CH$_{arom.}$); 6.30 t, *J:2.19 Hz*, 1H (-CH$_{arom.}$); 6.20 d, *J:2.20 Hz*, 2H (-CH$_{arom.}$); 3.81 s,6H (-OCH₃); 2.67 t, *J:7.37 Hz*, 2H (-SCH₂); 1.45-1.38 m, 2H (-CH₂-); 1.25-1.21 m, 4H(-CH₂-); 0.85-0.82 m, 3H (-CH₃). ¹³C NMR (125 MHz, *CDCl₃*) δ(ppm): 181.1, 180.4 (C=O), 160.7, 144.7, 140.4, 134.5, 133.6, 132.8, 130.6, 126.9, 126.7, 119.7, 100.7, 96.9 (-CH$_{arom.}$ and C$_q$), 55.5, 55.4 (OCH₃), 33.7 (-SCH₂), 30.8, 29.2, 22.1 (-CH₂), 13.9 (CH₃). MS (ESI+) *m/z* (%): 412.2 (100, [M]⁺). Anal. Calcd. for C$_{23}$H$_{25}$NO$_4$S (411.51).

## RESULTS AND DISCUSSION

The general pathway of the synthesis of 2-arylamino-3-sulfanyl-1,4-naphthoquinones (**5a–f**) was summarized in Scheme 1. The first step was to obtain the starting compounds, 2-chloro-3-[(2,4-dimethoxyphenyl)amino]naphthalene-1,4-dione     (**3a**)     and     2-chloro-3-[(3,5-dimethoxyphenyl)amino]naphthalene-1,4-dione (**3b**), by the nucleophilic substitution of 2,3-dichloro-1,4-naphthoquinone (**1**) reported in the literature (1, 13, 15). In the next step, new sulfanyl-substituted 1,4-naphthoquinones **(5a-f)** containing arylamino substituent with two methoxy groups were obtained and characterized by some spectroscopic methods.
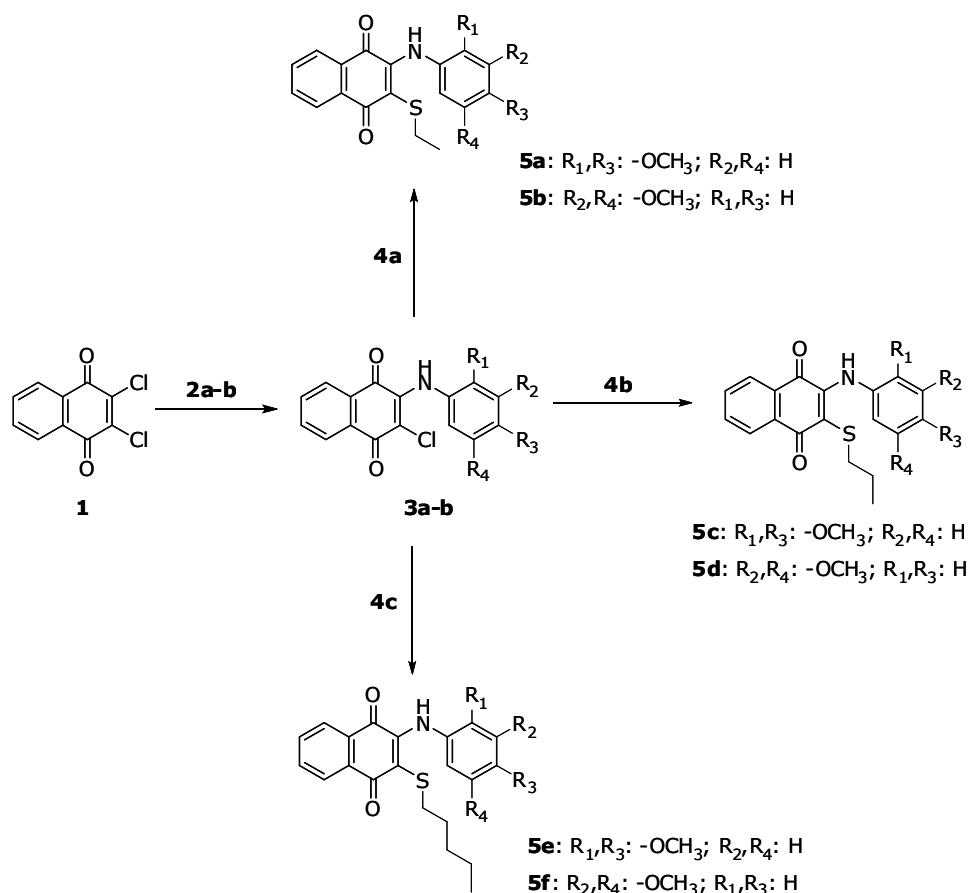


**Scheme 1.** The synthesized 2-arylamino-3-sulfanyl-1,4-naphthoquinone derivatives.

The reactions of compounds **3a,b** with 1-ethyl-, 1-propyl- and 1-pentyl mercaptan took place via nucleophilic substitution. It is known that the addition of a base into the reaction medium reduced the reaction time and also increased the yields of products.

Carbonyl groups are observed at about 180-181 ppm as two peaks which prove being two different substituents in the $^{13}$C NMR spectra. The methoxy groups are in the 2,4- or 3,5- positions of the amine ring. Although some compounds (**5a**, **5c**, **5e**) which have two methoxy groups in the 2,4- position are at about 55.6 and 55.5 ppm as two bifurcate peaks, other compounds (**5b**, **5d**, **5f**) having two methoxy groups in the 3,5- position of amine ring are at 55.4 ppm as only one bifurcate peak. It can be inferred that their distances to amine group (-NH) have an effect on the NMR shifts. In the $^{1}$H NMR spectra of compounds **5a**, **5c**, **5e**, methoxy groups are at between 3.84-3.81 ppm as two singlet peaks even though they are seen at about 3.79 ppm as only one singlet peak in the $^{1}$H NMR spectra of compounds (**5b**, **5d**, **5f**).
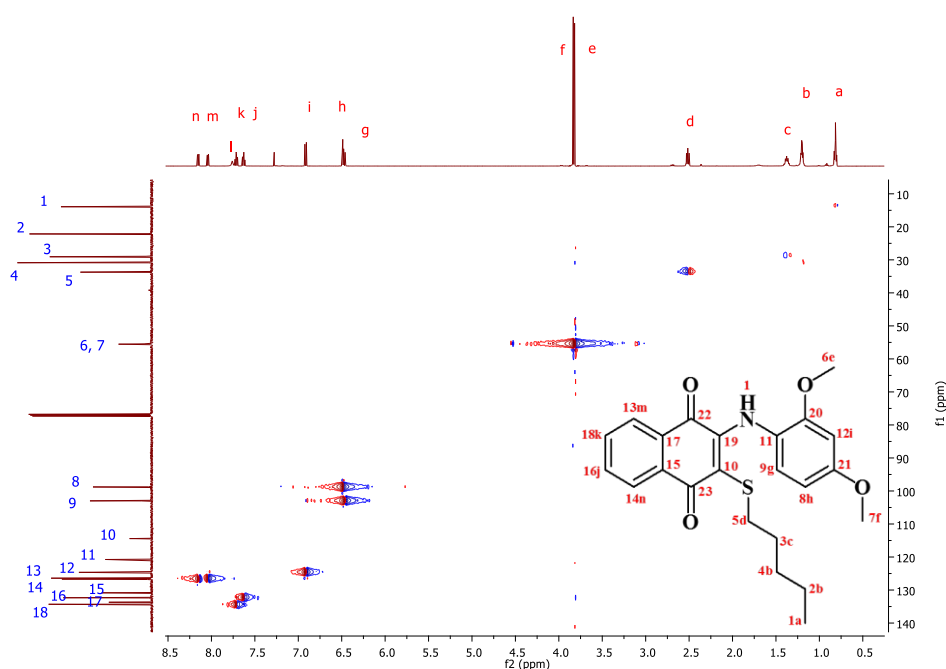


**Figure 1.** Expanded one-bond $^{1}$H-$^{13}$C couplings($\delta$C/$\delta$H 10–140/0.5–8.5 ppm):HSQC of **5e**
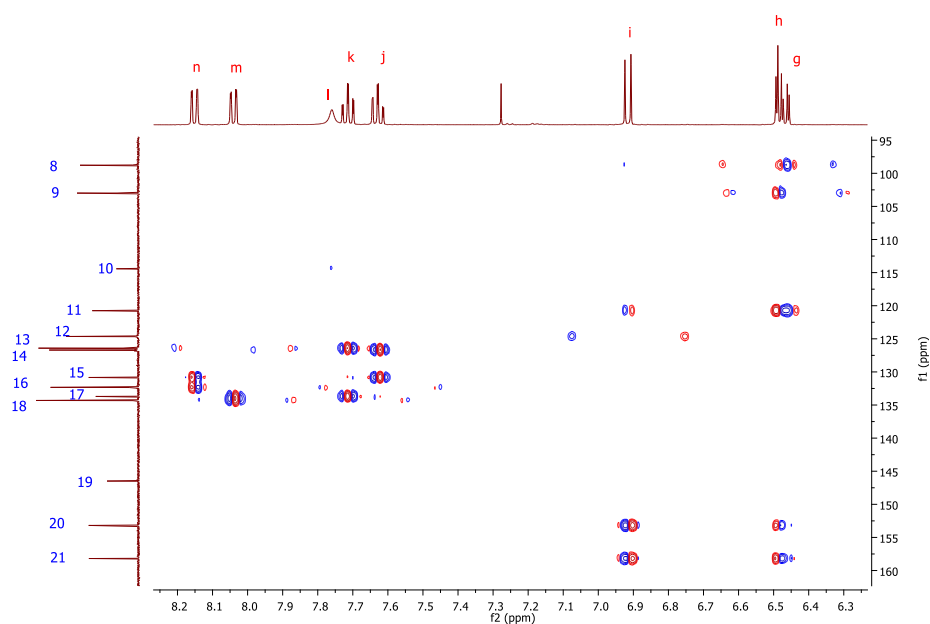
**Figure 2.** Expanded long-range $^1$H-$^{13}$C couplings($\delta$C/$\delta$H 95–165/6.3–8.2 ppm): HMBC spectrum of **5e**

To better understand the structure of compounds, we should look at the 2D $^1$H-$^{13}$C correlation NMR spectra. The HSQC (heteronuclear single quantum correlation) of **5e** spectra presented in the Figure 1 shows the region $\delta_C$/$\delta_H$ 10–140 / 0.5–8.5 ppm. The aliphatic protons labeled *a*, *b*, *c* and *d* are linked to aliphatic carbons labeled *1*, *2*, *4*, *3,* and *5,* respectively. The methyl carbon attached to the oxygen atom signals at $\delta_C$ 55.5 ppm (*6*) and $\delta_C$ 55.6 ppm (*7*) which have two bifurcate peaks correlate to *e* ($\delta_H$ 3.82 ppm) and *f* ($\delta_H$ 3.83 ppm) proton signals. In addition, it is clearly picked out that the aromatic carbons *8* ($\delta_C$ 98.8 ppm), *9* ($\delta_C$ 103.0 ppm), *12* ($\delta_C$ 124.6 ppm), *13* ($\delta_C$ 126.4 ppm), *14* ($\delta_C$ 126.7 ppm), *16* ($\delta_C$ 132.3 ppm), *18* ($\delta_C$ 134.3 ppm) are bound to proton *h* ($\delta_H$ 6.48 ppm), *g* ($\delta_H$ 6.47 ppm), *i* ($\delta_H$ 6.92 ppm), *m* ($\delta_H$ 8.04 ppm), *n* ($\delta_H$ 8.15 ppm), *j* ($\delta_H$ 7.63 ppm) and *k* ($\delta_H$ 7.71 ppm) respectively. In Figure 2, expanded long-range heteronuclear coupling spectrum of **5e** is seen. In the HMBC (Heteronuclear Multiple Bond Correlation) spectra, proton signal *g* ($\delta_H$ 6.47 ppm) correlates to carbon signals *8* ($\delta_C$ 98.8 ppm), *9* ($\delta_C$ 103.0 ppm), and *21* ($\delta_C$ 158.2 ppm) while proton signal *h* ($\delta_H$ 6.48 ppm) correlates to carbon signals *9* ($\delta_C$ 103.0 ppm), *11* ($\delta_C$ 120.7 ppm), *20* ($\delta_C$ 153.2 ppm) and *21* ($\delta_C$ 158.2 ppm). The methyl protons attached to the oxygen atom *e* ($\delta_H$ 3.82 ppm) and *f* ($\delta_H$ 3.83 ppm) also correlate to carbon signals *20* ($\delta_C$ 153.2 ppm) and *21* ($\delta_C$ 158.2 ppm) which means protons *g* and *h* are adjacent to each other in the phenyl ring. Proton *i* ($\delta_H$ 6.92 ppm) correlates to the carbon *8* ($\delta_C$ 98.8 ppm),  *11* ($\delta_C$ 120.7 ppm), *20* ($\delta_C$ 153.2 ppm) and *21* ($\delta_C$ 158.2 ppm) because of belonging to the same ring.
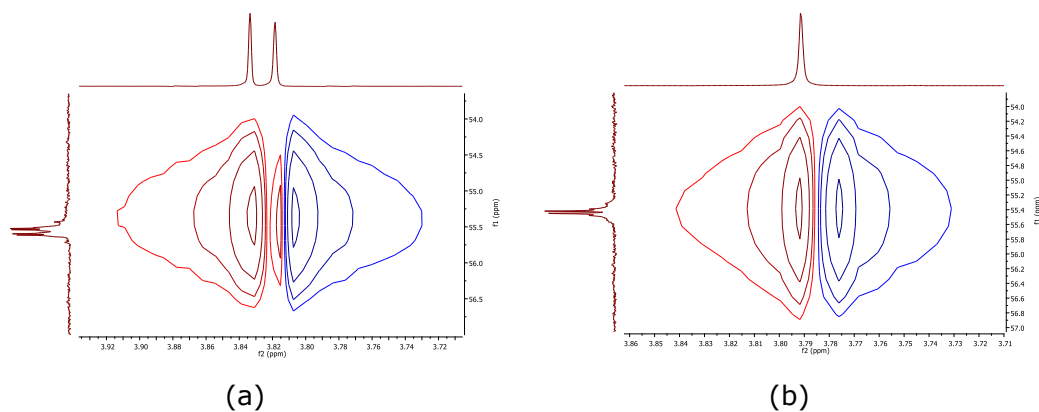
**Figure 3.** (a) Expanded HSQC spectra of **5e** (δC/δH 54–57/3.72–3.92 ppm),
(b) Expanded HSQC spectra of **5b** (δC/δH 54–57/3.71–3.86 ppm)

In Figure 3, the differences between the methoxy signals of compound **5e** and **5b** can be observed. Methoxy groups of compound **5e** and **5b** are in the 2,4-position and 3,5-position of the phenyl ring in order; therefore, there are two cross peaks in the Figure 3 (a) and there is only one cross peak in the Figure 3 (b).

The mass spectra of the new synthesized compounds shows the molecular ion peak as expected.

**CONCLUSION**

In this study, the first step was to synthesize the known amino-substituted 1,4-naphthoquinones (**3a,b**) from the reactions of 2,3-dichloro 1,4-naphthoquinone (**1**) with 2,4-dimethoxyphenyl amine and 3,5-dimethoxyphenyl amine as described in the literature (1, 13, 15). After that, these compounds were used as starting materials to obtain novel sulfanyl-substituted amino 1,4-napthquinone derivatives (**5a-f**). The newly synthesized compounds were acquired in good yields. The structures of these new naphthoquinone derivatives (**5a-f)** were elucidated by one- and two-dimensional NMR techniques in which the differences of positions of methoxy groups on the phenyl ring were detected. In addition, mass spectroscopy and FTIR data helped to specify the structures of new compounds.

The amino and thioether derivatives of naphthoquinones have a wide range of biological activities. Therefore, it is predicted that these novel derivatives of 1,4-naphthoquinone (**5a-f**) will most probably play a significant role in many biological applications.

**REFERENCES**

1. Sieveking I, Thomas P, Estevez JC, Quinones N, Cuellar MA, Villena J, et al. 2-Phenylaminonaphthoquinones and related compounds: Synthesis, trypanocidal and cytotoxic activities. Bioorg Med Chem. 2014;22(17):4609-20.

2. Senoh H, Yao M, Sakaebe H, Yasuda K, Siroma Z. A two-compartment cell for using soluble benzoquinone derivatives as active materials in lithium secondary batteries. Electrochim Acta. 2011;56(27):10145-50.

3. Ding Y, Yu GH. A Bio-inspired, heavy-metal-free, dual-electrolyte liquid battery towards sustainable energy storage. Angew Chem Int Edit. 2016;55(15):4772-6.

4. Huskinson B, Marshak MP, Suh C, Er S, Gerhardt MR, Galvin CJ, et al. A metal-free organic-inorganic aqueous flow battery. Nature. 2014;505(7482):195-211.

5. Ding Y, Li YF, Yu GH. Exploring bio-inspired quinone-based organic redox flow batteries: A combined experimental and computational study. Chem. 2016;1(5):790-801.

6. Matsuda S, Adachi K, Matsuo Y, Nukina M, Shizuri Y. Salinisporamycin, a novel metabolite from Salinispora arenicora. J Antibiot. 2009;62(9):519-26.

7. Cai P, Kong FM, Ruppen ME, Glasier G, Carter GT. Hygrocins A and B, naphthoquinone macrolides from Streptomyces hygroscopicus. J Nat Prod. 2005;68(12):1736-42.

8. Yildirim H, Bayrak N, Tuyun AF, Kara EM, Celik BO, Gupta GK. 2,3-Disubstituted-1,4-naphthoquinones containing an arylamine with trifluoromethyl group: synthesis, biological evaluation, and computational study. RSC Adv. 2017;7(41):25753-64.

9. Bayrak N, Yildirim H, Tuyun AF, Kara EM, Celik BO, Gupta GK, et al. Synthesis, computational study, and evaluation of in vitro antimicrobial, antibiofilm, and anticancer activities of new sulfanyl aminonaphthoquinone derivatives. Lett Drug Des Discov. 2017;14(6):647-61.

10. Bayrak N, Yildirim H, Tuyun AF, Kara EM, Celik BO, Gupta GK. Synthesis, biological, and computational study of Naphthoquinone derivatives containing heteroatoms. J Chem Soc Pakistan. 2016;38(6):1211-21.

11. Tandon VK, Maurya HK, Mishra NN, Shukla PK. Design, synthesis and biological evaluation of novel nitrogen and sulfur containing hetero-1,4-naphthoquinones as potent antifungal and antibacterial agents. Eur J Med Chem. 2009;44(8):3130-7.

12. Rau G, Cretu FM, Andrei AM, Pisoschi CG, Mogosanu GD, Boroghina A, et al. Synthesis and evaluation of antimicrobial activity of new 2-mercapto-3-substituted-1,4-naphthoquinones (I). Farmacia. 2015;63(5):665-9.

13. Tuyun AF, Bayrak N, Yildirim H, Onul N, Kara EM, Celik BO. Synthesis and in vitro biological evaluation of aminonaphthoquinones and benzo[b]phenazine-6,11-dione derivatives as potential antibacterial and antifungal compounds. J Chem. 2015: Artn 645902.

14. Bayrak N. Novel straight-chained sulfanyl members of arylamino-1,4-naphthoquinones: Synthesis and characterization. JOTCSA. 2017; 4(2):121.

15. Luo YL, Chou TC, Cheng CC. Design of antineoplastic agents on the basis of the ''2-phenyl-naphthalene-type'' structural pattern .3. Synthesis and biological activity evaluation of 5H-benzo[b]naphtho[2,3-d]pyrrole-6,11-dione derivatives. J Heterocyclic Chem. 1996;33(1):113-7.

# Synthesis, Characterisation and DFT Calculations of Azo-Imine Dyes

**Sevil Özkınalı[1]\*, Muhammet Serdar Çavuş[2], Büşra Sakin[1]**

[1]Hitit University, Faculty of Science and Literature, Department of Chemistry, 19040, Çorum, Turkey
[2]Kastamonu University, Faculty of Engineering and Architecture, Biomedical Engineering Department, 37100, Kastamonu, Turkey

**Abstract:** In this study, azo dyes containing an imine group were synthesised by coupling *p*-hydroxybenzylidene aniline with the diazonium salts of *p*-toluidine, 4-aminophenol, aniline, *p*-chloroaniline, *p*-fluoroaniline and *p*-nitroaniline. The compounds were characterised by melting point, elemental, UV-Vis and IR analyses as well as ^{1}H-NMR and ^{13}C-NMR spectroscopies. Moreover, the experimental data were supplemented with density functional theory (DFT) calculations. The experimental data on FT-IR and UV–Vis spectra of the compounds were compared with theoretical results. The DFT calculations were performed to obtain the ground state geometries of the compounds using the B3LYP hybrid functional level with 6-311++g(2d,2p) basis set. Frontier molecular orbital energies, band gap energies and some chemical reactivity parameters, such as chemical hardness and electronegativity, were calculated and compared with experimental values. A significant correlation was observed between the dipole moment and polarities of the solvents and the absorption wavelength of the compounds.

*Corresponding Author: E-mail Address: sevilozkinali@hitit.edu.tr; T: 03642277000-1636 F: 03642277005

## INTRODUCTION

Azo dyes have been widely used in various areas, such as textile dyes (1-2), printing systems (2), photoelectronics (3), coloring fibres (4) and optical storage technology. They are also commonly utilised in many biological reactions (5, 6) and in analytical chemistry (7-8). Schiff bases are also an important class of organic compounds that exhibit a broad range of biological activities, including antibacterial (9), antifungal (9), antiproliferative (8), anti-inflammatory (4), antimalarial (8), antipyretic (8) and antiviral (5) properties (6,10). Azo dyes and related Schiff bases containing both imine (-HC=N-) and azo (-N=N-) groups have received much attention in both fundamental and applied research areas. Azo-azomethine dyes containing hydroxyl groups are of particular interest because of the proton tautomerism that exists between the enol-imine and keto-enamine forms (11-14).

Because of the proton-transfer ability of azo-azomethine dyes, they play an important role in many scientific fields; in addition, their tautomers exhibit different optical behaviours and possess different electronic absorption spectra and dyeing properties (1,4,5). The extent to which a tautomer is favoured under certain conditions can play a significant role in terms of its structural and optical behaviours in different medium (6,15). Inter- and intramolecular proton transfer from the phenolic oxygen to the imine nitrogen alters photophysical properties, such as electronic structure and ground- and excited-state dipole moments (5-6). In addition to these solvent effects, substitutions are also important in understanding many chemical and physical behaviours, such as hydrogen bonding and tautomerism of Schiff bases in solutions (5,6). In this study, we examine the relationship between the structural and spectroscopic behaviours of azo dyes containing Schiff bases using density functional theory (DFT) analyses and estimation of singlet ground- and excited-state dipole moments (6).

The literature contains many reports on the successful application of DFT to azo dyes (16-23). In this study, a series of azo dyes containing an imine group were synthesised and characterised using both spectroscopy and Kohn-Sham DFT (24) method. The molecular structures and FT-IR and UV–Vis spectra of the azo-imine dyes synthesised in this study were obtained using the B3LYP method with 6-311++g(2d,2p) basis set. Solvent effects on the absorbance characteristics of the dyes were theoretically studied in solvents of different polarities, such as dichloromethane (DCM), dimethylformamide (DMF) and ethanol (EtOH).

## EXPERIMENTAL PROCESS

All reagents and solvents for synthesis and analysis were purchased from Merck (Germany) and Sigma-Aldrich (US) and were used without further purification. *p*-Hydroxybenzylidene aniline were synthesised and purified according to methods used in previous studies (11,25-27). In this study compounds **2**, **3** and **6** are new compounds and these are given here first time in the literature, also theoretical calculations of all the compounds except **4** are studied for the first time.  Azo-imine compounds were obtained by coupling *p*-hydroxybenzylidene aniline with the diazonium salts of *p*-toluidine, *p*-hydroxyaniline, *p*-chloroaniline, *p*-fluoroaniline and aniline in a 1:1 molar ratio at 0–5°C. The crude products were purified by recrystallisation from EtOH–water. Elemental (C, H and N) analyses were performed using a LECO CHNS-932 elemental analyser (LECO Corporation, US). UV–Vis spectra were obtained using a Genesys 10S UV–Vıs spectrophotometer (Thermo Scientific, UK) with a concentration of $5 \times 10^{-5}$ mol/L of dye in various solvents, such as EtOH, DCM, and DMF. Infrared spectra were obtained using a Class 1 Laser product FTIR (Thermo Scientific, US) in the 400–4000 $cm^{-1}$ range. $^1$H-NMR and $^{13}$C-NMR spectra were obtained using an AC 400 (400 MHz) NMR spectrometer (Bruker, Germany) with deuterated dimethylsulphoxide ($d_6$-DMSO) as a solvent and tetramethylsilane as an internal standard.

### General procedure for synthesising azo-imine dyes

*p*-Hydroxybenzylidene aniline was synthesised by a condensation reaction between *p*-hydroxybenzaldehyde and aniline at a 1:1 molar ratio, as described previously (6,11,25-27), and the reaction mixture was refluxed for 3 h. Azo derivatives were synthesised from the *p*-hydroxybenzylidene aniline by reaction with diazonium salts at 0–5°C. The general synthetic method is depicted in Figure 1.
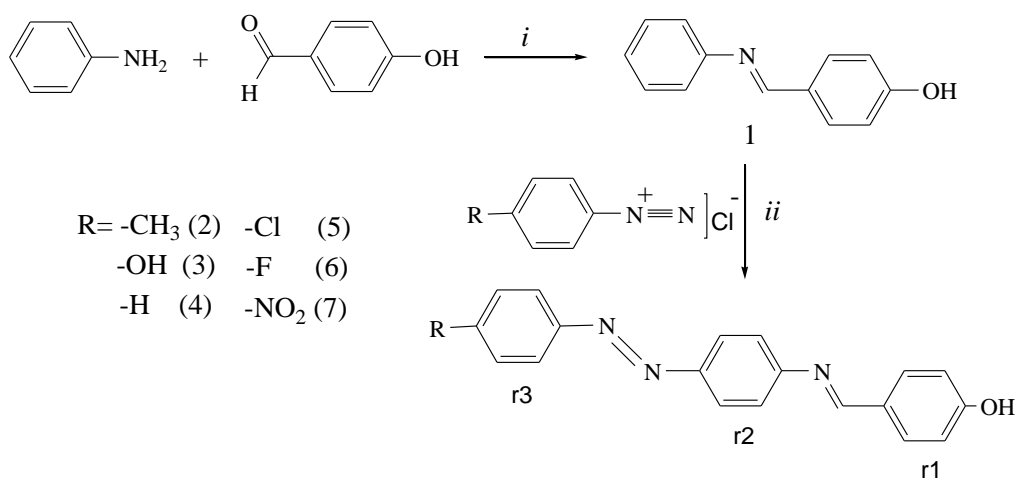


**Figure 1.** Synthesis of azo-imine compounds (*i*) pH=4-5, methanol, reflux, 3 h, (*ii*) NaNO₂, HCl, 0-5°C, r1: Ring ; r2: Ring 2; r3: Ring 3.

**Synthesis of (E)-4-[(phenylimino)methyl]phenol, 1**

Aniline (0.93 g; 0.01 mol) was added dropwise to a solution of p-hydroxybenzaldehyde (1.22 g; 0.01 mol) in 35-mL of EtOH. Four to five drops of acetic acid were added to the solution to reach a pH of 4–5. The reaction mixture was refluxed for 3 h and left to crystallise at room temperature for a day. The yellow product was collected by filtration, washed with cold water, dried and recrystallised from toluene. Yield: 78%, melting point (m.p.): 185°C–186°C. IR: $\nu$=3200-2673 (br, O-H), 3042 (C-H arom.), 1602 (-CH=N-), 1573 (-C=C-), 1283 cm$^{-1}$ (-C-O). $^1$H-NMR (d$_6$-DMSO, ppm): $\delta$= 10.12 (s, H1), 8.45 (s, H4), 7.76 (d, J=8.8 Hz, H3), 7.38 (t, J=5.2 Hz, H7), 7.21 (d, J=4.0 Hz, H6), 7.18 (d, J=4.0 Hz, H5), 6.89 (d, J=8.8Hz, H2) $^{13}$C-NMR (101 MHz, d$_6$-DMSO) $\delta$ 161.09 (C1), 160.48 (C5), 152.47 (C6), 131.14 (C3), 129.59 (C8), 127.98 (C9), 125.78 (C4), 121.33 (C7), 116.31 (C2). Anal. calcd. (%) for C$_{13}$H$_{11}$NO: C 79.16, H 5.62, N 7.10; found: C 78.85, H 5.47, N 7.07

**Synthesis of 4-[[[4-[(4-methylphenyl)azo]phenyl]imino]methyl]-phenol, 2**

Azo-coupled Schiff bases were synthesised using standard coupling methods (6,8,11). p-Toluidine (1 g; 9.33 mmol) was dissolved in 40-mL water containing concentrated HCl solution (2.4 mL; 27.9 mmol) and then diazotised at 0–5°C with a solution of NaNO$_2$ (0.64 g; 9.33 mmol in 4-mL water). The diazonium solution was stirred at 0–5°C for 30 min. Following diazotisation, diazonium salt solutions were added dropwise to a solution of (E)-4-[(phenylimino)methyl]phenol (1,84 g; 9,33 mmol) and 5-g sodium acetate in 25-mL DMF at 0–5°C. The resulting solution was stirred for 3 h at 0–5°C and then acidified with 1 M HCl to precipitate the product. The reddish-brown product was filtered and then washed with cold water before recrystallisation in EtOH/water. Yield: 68%, m.p.: 110–111°C. IR: $\nu$=3551-3071 (br, O-H), 3039 (C-H arom.), 2913,2872 (-C-H, Aliph.), 1602 (-CH=N-), 1652, 1573 (-C=C-), 1514, 1442 (-N=N-), 1283 cm$^{-1}$ (-C-O). $^1$H-NMR (d$_6$-DMSO, ppm) $\delta$= 12.01 (s, H1), 7.97 (s, H4), 7.81 (m, H3), 7.68 (m, H8), 7.43 (m, H6), 7.37 (m, H5), 7.08 (m, H9), 6.67 (m, H2), 1.91 (s, H10) $^{13}$C-NMR (101 MHz, d$_6$-DMSO) $\delta$ 169.08 (C1), 162.56 (C5), 156.45 (C6), 152.52 (C9), 147.89 (C13), 142.68 (C8), 141.57 (C10), 130.35 (C3), 129.83 (C12), 122.80 (C11), 125.41 (C4), 123.95 (C7), 119.58 (C2), 21.45 (C14). Anal. calcd. (%) for C$_{20}$H$_{17}$N$_3$O: C 76.17, H 5.43, N 13.12; found: C 75.74, H 5.28, N 12.65

**Synthesis of 4-[[[4-[(4-hydroxyphenyl)azo]phenyl]imino]methyl]-phenol, 3**

This compound was prepared in a manner similar to that described in section 1.1.2. Yield: 81%, m.p. 186–188°C. IR: $\nu$= 3473-3087 (br, O-H), 3042 (C-H arom.), 1602 (-CH=N-), 1612, 1573 (-C=C-), 1514, 1442 (-N=N-), 1283, 1240, 1163 cm$^{-1}$ (-C-O). $^1$H-NMR (d$_6$-DMSO, ppm) $\delta$= 10.13 (s, H1), 8.45 (s, H4), 7.79 (m, H3), 7.76 (m, H8), 7.20 (m, H6), 7.39 (m, H5), 6.90 (m, H9), 6.87 (m, H2), 10.13 (s, H10, OH) $^{13}$C-NMR (101 MHz, d$_6$- DMSO) $\delta$ 164.12 (C1, C13), 160.41(C5), 152.29 (C9), 156.30 (C6), 145.59 (C10), 143.89 (C8), 131.05 (C3), 129.44 (C12),  124.81 (C4), 124.78

(C11), 121.34 (C7), 116.37 (C2). Anal. calcd. (%) for $C_{20}H_{17}N_3O$: C 71.91, H 4.76, N 13.24; found: C 71.25, H 4.58, N 13.04

### Synthesis of 4-[[[4-phenylazo]phenyl]imino]methyl]-Phenol, 4

This compound was prepared in a manner similar to that described above. Yield: 75%, m.p.: 78–80 °C. IR: $\nu$=3483-3085 (br, O-H), 3041(C-H arom.), 1602 (-CH=N-), 1595 (-C=C-), 1504, 1478 (-N=N-), 1239, 1137 cm$^{-1}$ (-C-O). $^1$H-NMR (d$_6$-DMSO, ppm) $\delta$= 6.10 (s, H1), 7.76 (s, H4), 7.69 (m, H3), 7.49 (m, H8), 7.49 (m, H6), 7.41 (m, H5), 7.38 (m, H9), 6.69 (m, H2), 7.44 (m, H10) $^{13}$C-NMR (101 MHz, d$_6$-DMSO) δ 153.34 (C1,C6), 152.92 (C5, C9), 145.59 (C10), 143.26 (C8), 130.36 (C13), 129.85(C3), 129.65(C12), 125.65 (C4), 122.52 (C11) 122.16 (C7), 113.84(C2)  Anal. calcd. (%) for $C_{19}H_{15}N_3O$: C 75.73, H 5.02, N 13.94; found: C 74.48, H 4.92, N 13.17

### Synthesis of 4-[[[4-[(4-chlorophenyl)azo]phenyl]imino]methyl]-phenol, 5

This compound was prepared a in a manner similar to that described above. Yield: 73%, m.p.: 72–74°C. IR: $\nu$=3301-2648 (br, O-H), 3044(C-H arom.), 1602 (-CH=N-), 1670, 1574 (-C=C-), 1515, 1443 (-N=N-), 1285, 1164 cm$^{-1}$ (-C-O), 840 (-C-Cl). $^1$H-NMR (d$_6$-DMSO, ppm) $\delta$= 12.58 (s, H1), 8.73 (s, H4), 7.75 (m, H3), 7.66 (m, H8), 7.28 (m, H6), 7.44 (m, H5), 7.04 (m, H9), 6.69 (m, H2). $^{13}$C-NMR (101 MHz, d$_6$-DMSO) δ 153.73 (C1), 153.34 (C5), 152.92 (C6), 152.57 (C9), 151.12 (C13), 143.22 (C10), 131.52 (C8), 129.73 (C12), 128.96 (C3), 125.92, 125.57 (C4), 122.82 (C11), 122.17 (C7), 113.77 (C2). Anal. calcd. (%) for $C_{19}H_{14}ClN_3O$: C 67.96, H 4.20, N 12.51; found: C 67.24, H 4.14, N 11.73

### Synthesis of 4-[[[4-[(4-fluorophenyl)azo]phenyl]imino]methyl]-phenol, 6

This compound was prepared in a manner similar to that described above. Yield: 76%, m.p.: 71–72 °C. IR: $\nu$= 3386-2745 (br, O-H), 3042 (C-H arom.), 1602 (-CH=N-), 1572 (-C=C-), 1514, 1443 (-N=N-), 1283, 1163 cm$^{-1}$ (-C-O), 1193 (-C-F). $^1$H-NMR (d$_6$-DMSO, ppm) $\delta$= 12.45 (s, H1), 8.45 (s, H4), 7.79 (m, H3), 7.54 (m, H8), 7.24 (m, H6), 7.41 (m, H5), 7.03 (m, H9), 6.87 (m, H2) $^{13}$C-NMR (101 MHz, $_{d6}$-DMSO) δ 163.75 (C1), 160.43 (C13), 161.04 (C5), 152.46 (C9), 150.14 (C6), 146.84 (C10), 142.30 (C8), 131.14 (C3), 129.16 (C12), 125.71 (C4), 122.83 (C7), 121.33 (C11), 116.56 (C2), 114.56 (C12). Anal. calcd. (%) for $C_{19}H_{14}FN_3O$: C 71.46, H 4.42, N 13.16; found: C 71.34, H 4.38, N 12.87

### Synthesis of 4-[[[4-[(4-nitrophenyl)azo]phenyl]imino]methyl]-phenol, 7

This compound was prepared in a manner similar to that described above. Yield: 77%, m.p.: 128–130°C. IR: $\nu$=3544-3068 (br, O-H), 3047 (C-H arom.), 1602 (-CH=N-), 1572 (-C=C-), 1514, 1442 (-N=N-), 1484, 1388 (-NO$_2$), 1283, 1163 cm$^{-1}$ (-C-O). $^1$H-NMR (d$_6$-DMSO, ppm) $\delta$= 13.03 (s, H1), 8.29 (s, H4), 7.60 (m, H3), 7.58 (m, H8), 7.47 (m, H6), 7.50 (m, H5), 7.53 (m, H9), 7.34 (m, H2)

$^{13}$C-NMR (101 MHz, d$_6$-DMSO) 163.77 (C1), 158.41 (C5), 153.35 (C9), 152.04 (C6), 149.63 (C13), 142.00 (C10), 14167 (C8), 130.16 (C3), 126.39 (C11), 126.19 (C4), 123.95 (C12), 121.73 (C7), 114.25 (C2). Anal. calcd. (%) for C$_{19}$H$_{14}$N$_4$O$_3$: C 65.89, H 4.07, N 16.18; found: C 65.38, H 3.96, N 15.64

**Computational details**

Quantum chemical calculations of azo dyes containing an imine group were performed by the Gaussian 09 software package (28) using Becke's three-parameter exchange functional (B3) (29) combined with the nonlocal correlation functional of Lee, Yang and Parr (LYP) (30) with 6-311++G(2d,2p) basis set. Ground state geometries of the azo-imine dyes in gas and solvent phases were optimised with the same method and basis set without any constraint on the geometry. Vibrational analysis was used to verify whether the optimised structures corresponded to local minima on the potential energy surface. The self-consistent reaction field method and the conductor-polarizable continuum model (31) were used for UV calculations. The vertical excitation energies and oscillator strengths at the optimised ground state equilibrium geometries were calculated for DCM, DMF and EtOH phases using time-dependent DFT computations and the same hybrid functional and basis set, and the UV–Vis absorption properties of the synthesised azo-imine compounds were investigated for these solvents.

The highest occupied molecular orbital (HOMO), lowest unoccupied molecular orbital (LUMO) and electrostatic potential (ESP) surfaces of the optimised forms of the molecules were obtained. Electronegativity ($\chi$) and chemical hardness ($\eta$) were also calculated. The theoretical results proved invaluable in interpreting the experimental IR and UV–Vis spectra of the compounds.

**RESULT AND DISCUSSION**

The UV–Vis spectra of the azo-imine compounds were obtained at a concentration of $1 \times 10^{-5}$ mol/L in EtOH, DCM, DMF and pH of 2 and 12 (in DMF). The UV–Vis spectral results of the compounds are depicted in Table 1. The major absorption peaks with highest extinction coefficients are attributed to π→π* and n→π* transitions at 318–389 nm and 372–521 nm, respectively. A weak n→π* transition was observed as a shoulder peak in the spectra because it overlapped with the strong π→π* transition. Figure 2 shows the UV–Vis spectrum of compound **3**. Increasing the pH and polarity produced a bathochromic shift. In acidic medium, the absorption bands for all compounds were observed in the visible spectral region of 328–501 nm (**Table 1**).

**Table 1.** Experimental and theoretical UV-Vis data of the compounds 2-7.

| Comp. | λmax. EtOH (nm) | Log ε | λmax. CH₂CI₂ | Log ε | λmax. DMF | Log ε | λmax. DMF (pH=2) | Log ε | λmax. DMF (pH= 12) | Log ε | Theoretical | | |
|---|---|---|---|---|---|---|---|---|---|---|---|---|---|
| | | | | | | | | | | | EtOH | CH₂Cl₂ | DMF |
| 2 | 379 | 3,28 | 365 | 3,48 | 350ˢ 391 | 3,26 3,31 | 501 | 3.09 | 352 | 3,24 | 425.4 | 425.8 | 427.4 |
| 3 | 367 | 3,31 | 352 | 3,72 | 373 | 3,88 | 347 378ˢ | 3.84 3.04 | 361 398ˢ | 3,99 3,74 | 430.2 | 430.9 | 432.4 |
| 4 | 318 396 | 3,53 3,87 | 329 372 | 3.62 3.82 | 405 | 3,44 | 390 | 3,26 | 364 412 520ˢ | 4,85 3,75 3.12 | 423.2 | 423.5 | 425.3 |
| 5 | 389 | 3.36 | 370 | 3.88 | 374 | 3.43 | 498 | 3.09 | 410 511 | 3.49 3.40 | 431.9 | 432.4 | 434.0 |
| 6 | 353 380ˢ | 3,71 3.88 | 359 | 3,98 | 323 368 | 3.78 3.85 | 328 350 | 3.88 3.86 | 364 401ˢ 511 | 4,04 3.85 3.41 | 424.2 | 424.8 | 426.3 |
| 7 | 387 | 3.81 | 330 381 | 3.59 3.98 | 392 510ˢ | 3,74 3.04 | 384 490ˢ | 3,47 3.03 | 521 | 3,86 | 397.1 501.4 | 394.4 498.5 | 398.0 504.3 |

λmax. nm, Log ε: L.mol⁻¹.cm⁻¹
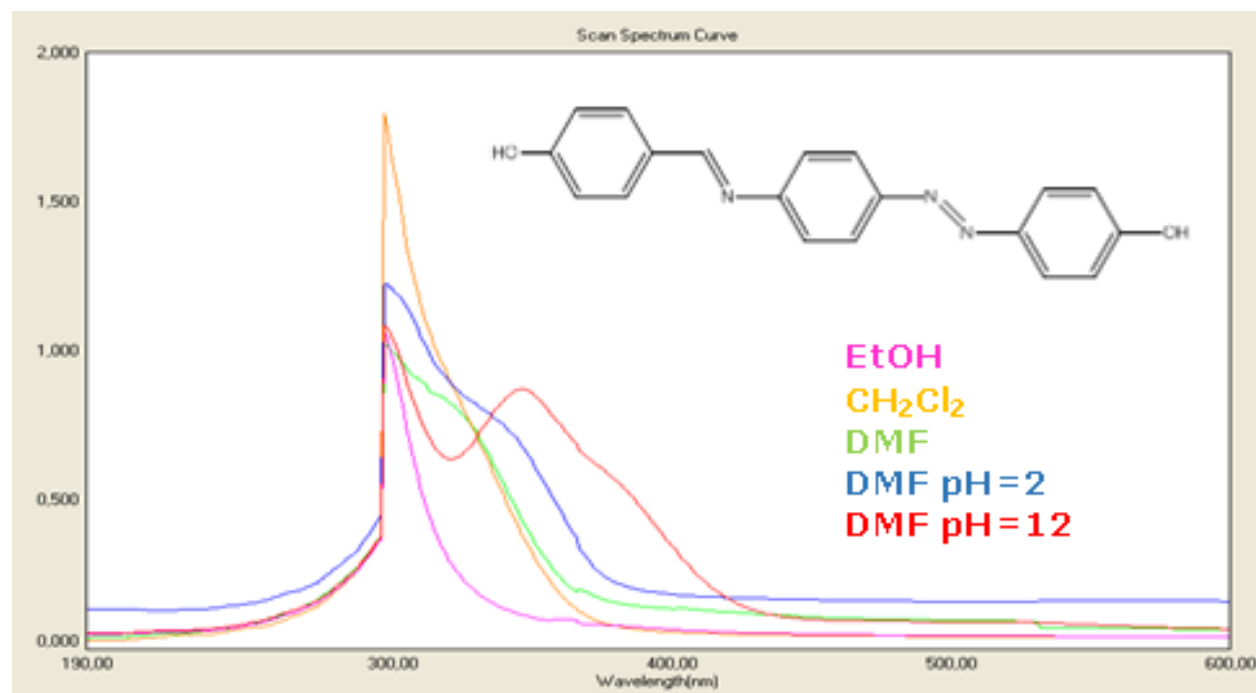


**Figure 2.** The UV-Vis spectra of 4-[[[4-[(4-hydroxyphenyl)azo]phenyl]imino]methyl]-phenol in CHCl3, EtOH, DMF, pH=2 (DMF) and pH=12 (DMF).

Consistent with experimental measurements for the compounds, theoretical calculations of their UV–Vis spectra showed that the absorption wavelengths obtained using DMF as a solvent were generally longer than those obtained using other solvents. The absorption wavelengths of compounds **2**–**7** in DCM and EtOH were found to be at around 425 nm, 430 nm, 423 nm, 432 nm and 424 nm, respectively (Table 1), whereas they were 2 nm higher for the same compounds in DMF. Compound **7**, which bore the $NO_2$ substituent, exhibited two large absorption peaks at 398 and 504 nm. Besides, for the compounds **2**-**6**, the effects of $CH_3$, OH, Cl and F substituents on the absorption wavelengths were determined to be $\lambda_{-Cl} > \lambda_{-OH} > \lambda_{-CH_3} > \lambda_{-F} > \lambda_{-H}$. An increase in the polarity of the solvent elicited a bathochromic shift in the absorption wavelengths of the compounds, that is, the most polar solvent DMF produced a larger effect than the other solvents. A significant correlation was also observed between the dipole moments of the solvents and the bathochromic shifts they produced ($m_{DMF} \approx 3.86$ D, $m_{EtOH} \approx 1.69$ D, $m_{DCM} \approx 1.47$ D, where D is Debye).

The IR absorption of the hydroxyl groups of the compounds occurred as a broad peak band in the range of 3551–2672 cm$^{-1}$ because of intramolecular hydrogen bonding, and the stretching of -HC=N- was observed at 1602 cm$^{-1}$ (5, 6). In addition, weak peak bands appeared in the ranges 3047–3039 cm$^{-1}$ and 2925–2872 cm$^{-1}$, which can be attributed to aromatic C-H and aliphatic =C-H stretching, respectively (Figure 3 and Table 2). The asymmetric and symmetric stretching bands of the azo group (-N=N-) were observed at both 1500 and 1450 cm$^{-1}$. The exact position of these bands varied according to the molecular structure of the compounds, and the strong bands that appeared in the range of 1650–1572 cm$^{-1}$ of the IR spectra can be attributed to aromatic stretching.
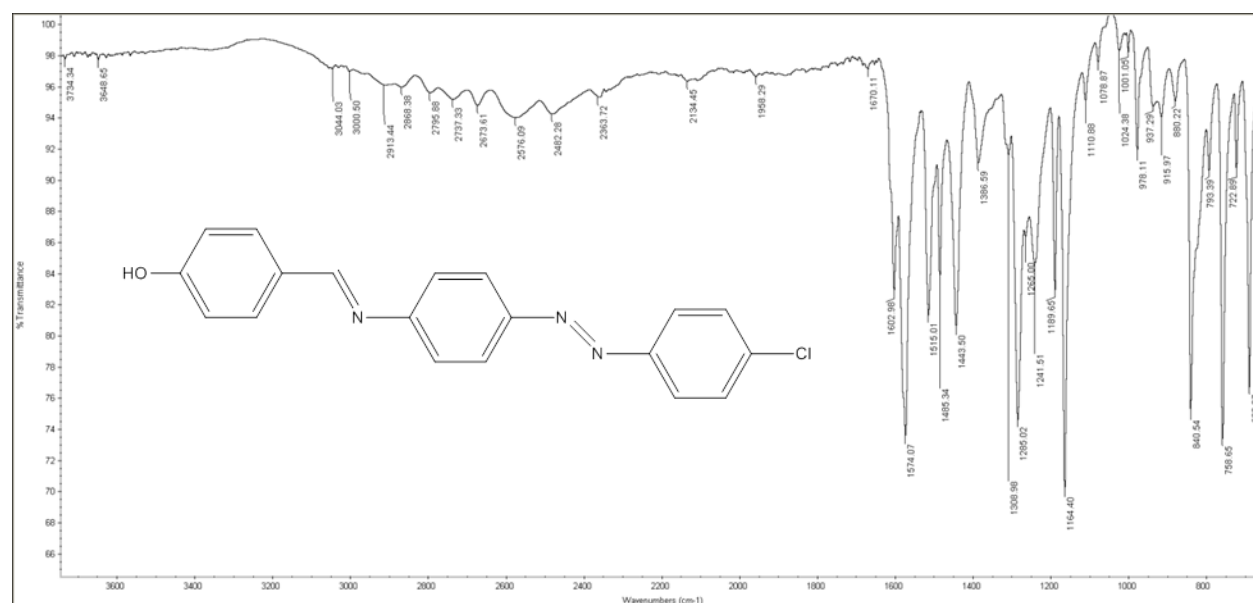


**Figure 3.** The IR spectrum for 4-[[[4-[(4-chlorophenyl)azo]phenyl]imino]methyl]-Phenol

**Table 2.** IR spectral results of compounds **1**-**7.**

| Compound | $\nu_{O-H}$ | $\nu_{C-H}$ Arom. | $\nu_{=C-H}$ Aliph. | $\nu_{C=N}$ | $\nu_{C=C}$ | $\nu_{N=N}$ | $\nu_{Ar-O}$ | Other functional groups |
|---|---|---|---|---|---|---|---|---|
| **1** | 3200-2672 | 3042 | 2914 2863 | 1602 | 1573 | - | 1283 | - |
| **2** | 3551-3071 | 3039 | 2913 2854 | 1602 | 1652 1573 | 1514 1442 | 1283 | 2913 and 2872 ($CH_3$) |
| **3** | 3473-3087 | 3042 | 2923 2872 | 1602 | 1612 1573 | 1514 1442 | 1283 1240 1163 | - |
| **4** | 3483-3085 | 3041 | 2918 2863 | 1602 | 1595 | 1504 1478 | 1239 1137 | - |
| **5** | 3301-2648 | 3044 | 2913 2868 | 1602 | 1670 1574 | 1515 1443 | 1285 1164 | 840 (C-Cl) |
| **6** | 3386-2745 | 3042 | 2924 2874 | 1602 | 1573 | 1514 1443 | 1283 1163 | 1193 (C-F) |
| **7** | 3544-3068 | 3047 | 2925 2864 | 1602 | 1572 | 1514 1442 | 1283 1163 | 1484 and 1388 ($NO_2$) |

As can be seen in Table 3, the theoretical and experimental IR results were in close agreement. However, because the theoretical calculations were performed for single molecules (*i.e.* intermolecular interactions were not taken into account), calculated aromatic and aliphatic =C-H bond vibrations were found to be higher than experimentally determined values. -$CH_3$, -OH, -Cl and -F substituents did not significantly alter the vibration of O-H, whereas $NO_2$ substitution had a more pronounced effect (Table 3). Substituents appeared to have the most effect on N=N vibrations. For example, in unsubstituted compound **4** the -N=N- vibration frequency had its highest value (1534 $cm^{-1}$), and the difference in the electronegativity of the substituents had little effect on other oscillation frequencies except for the -N=N- bond and aromatic C-H vibrations of ring 3. Both the experimental and theoretical results showed that C=N vibrations were particularly unaffected by substituent variation (experimental, 1602 $cm^{-1}$; theoretical, 1679 $cm^{-1}$). All selected oscillation frequencies are shown in Table 3.

**Table 3.** Theoretical IR spectral results of the compounds.

| Compound | $\nu_{O-H}$ | $\nu_{C-H}$ Arom. | $\nu_{=C-H}$ Aliph. | $\nu_{C=N}$ | $\nu_{C=C}$ | $\nu_{N=N}$ | $\nu_{Ar-O}$ | Other functional groups |
|---|---|---|---|---|---|---|---|---|
| **2** | 3832 | 3179 (r2) 3160 (r3) 3158 (r1) | 3011 | 1680 | 1646 1618 1548 | 1490 1438 | 1286 | 3109 3076 3032 (CH$_3$) |
| **3** | 3833 (r3) 3831 (r1) | 3178 (r2) 3159 (r1) 3153 (r3) | 3009 | 1678 | 1642 1612 1527 | 1496 1466 | 1289 (r1) 1281 (r2) | 3833 (O-H) |
| **4** | 3831 | 3199 (r3) 3179 (r2) 3176 (r1) | 3010 | 1679 | 1647 1612 1548 | 1534 1445 | 1290 | - |
| **5** | 3831 | 3218 (r3-weak) 3180 (r2) 3160 (r1) | 3010 | 1679 | 1647 1612 1548 | 1530 1492 | 1290 | 1095 (C-Cl) |
| **6** | 3831 | 3210 (r3-weak) 3179 (r2) 3160 (r1) | 3010 | 1679 | 1647 1612 1527 | 1496 1439 | 1290 | 1238 (C-F) |
| **7** | 3830 | weak (r3) 3205 (r2) 3160 (r1) | 3012 | 1679 | 1647 1611 1528 | 1528 1488 | 1292 | 1359 (NO$_2$) |

r1: ring 1, r2: ring 2, r3: ring 3

The $^1$H-NMR spectra of the compounds were produced using DMSO-d$_6$, and the signals at 7.81 ppm and 6.67 ppm were assigned to the aromatic protons. The signal stemmed from imine group appeared as a singlet in the range of 8.45 and 7.76 ppm. Aromatic protons were observed as doublets and, in a few cases, as overlapping doublets/multiplets. The singlet peak of the OH group appeared at 13.03 and 10.12 ppm except for that of the OH group the compound **4**, which appeared at 6.10 ppm. An additional signal at 1.91 ppm, which was found in compound **2**, was attributed to the CH$_3$ group. Hydroxyl and imine protons were observed as singlet peaks at 13.03 and 8.29 ppm for the H1 and H4 protons in the spectrum of compound **7** (Figure 4). The peak at 7.34–7.60 ppm was attributed to signals from aromatic protons (Table 4). Protons (H2-H7) on the benzene ring adjacent to the nitro group shifted downfield, as expected, due to the unsubstituted benzene protons (H2-H7) in the compound **7**.
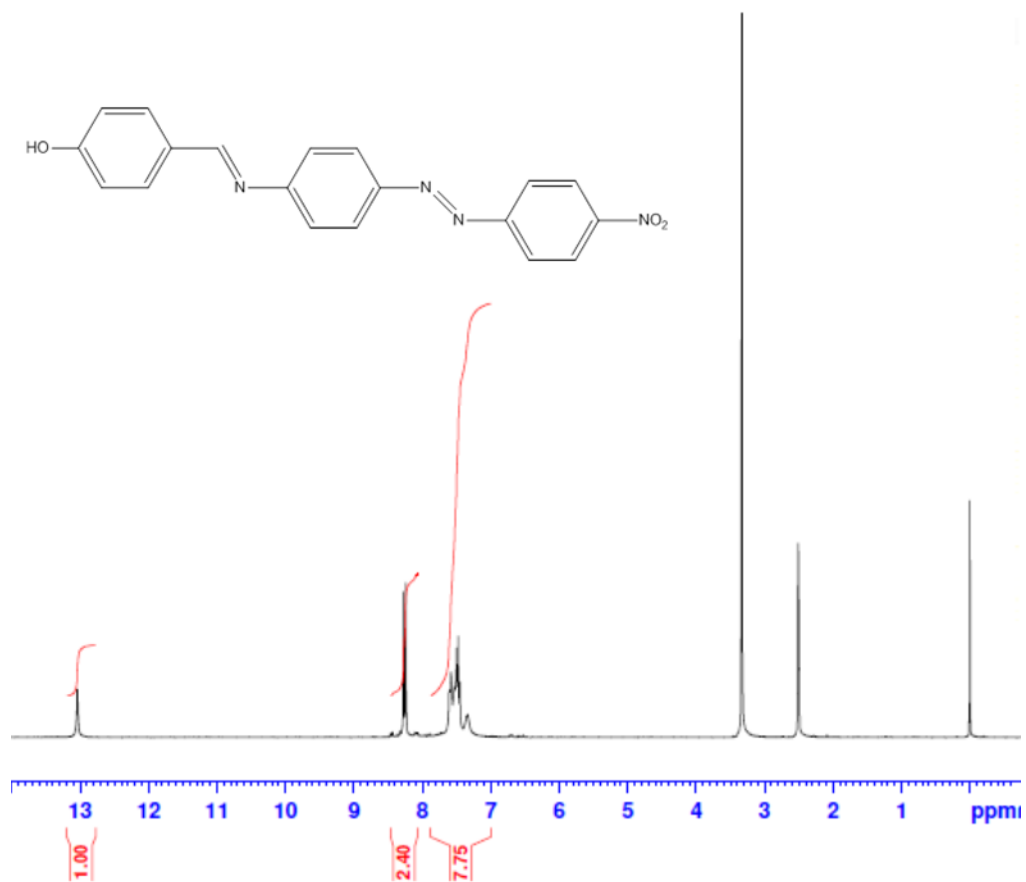
**Figure 4.** The ^{1}H-NMR Spectrum of 4-[[[4-[(4-nitrophenyl)azo]phenyl]imino]methyl]-Phenol

**Table 4.** ^{1}H-NMR spectral results of compounds **1**-**7**.
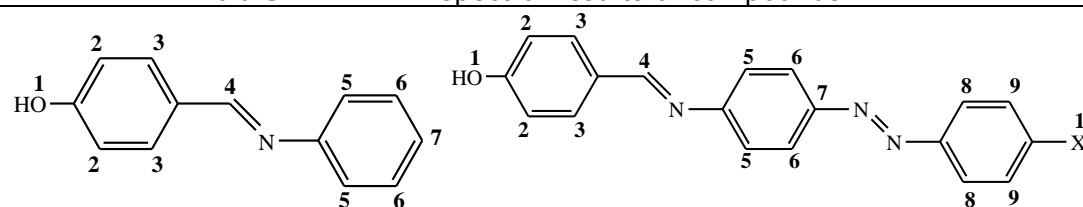


**Compound 1**

**X**= $CH_3$ (**2**), -OH (**3**), -H (**4**), -Cl (**5**), -F (**6**), $NO_2$ (**7**)

|   | H1 | H2 | H3 | H4 | H5 | H6 | H7 | H8 | H9 | H10 |
|---|------|------|------|------|------|------|------|------|------|------|
| **1** | 10.12 (s) | 6.89 (d) | 7.76 (d) | 8.45 (s) | 7.18 (d) | 7.21(d) | 7.38 (t) | - | - | - |
| **2** | 12.01 (s) | 6.67 (m) | 7.81 (m) | 7.97 (s) | 7.37(m) | 7.43(m) | - | 7.68(m) | 7.08(m) | 1.91(s) |
| **3** | 10.13 (s) | 6.87 (m) | 7.79 (m) | 8.45 (s) | 7.39(m) | 7.20(m) | - | 7.76(m) | 6.90 (m) | 10.13(s) |
| **4** | 6.10 (s) | 6.69 (m) | 7.69 (m) | 7.76 (s) | 7.41(m) | 7.49(m) | - | 7.49(m) | 7.38(m) | 7.44(m) |
| **5** | 12.58 (s) | 6.69 (m) | 7.75 (m) | 8.73 (s) | 7.44(m) | 7.28(m) | - | 7.66(m) | 7.04(m) | - |
| **6** | 12.45(s) | 6.87 (m) | 7.79(m) | 8.45 (s) | 7.41(m) | 7.24(m) | - | 7.54(m) | 7.03(m) | - |
| **7** | 13.03(s) | 7.34 (m) | 7.60(m) | 8.29 (s) | 7.50(m) | 7.47(m) | - | 7.58(m) | 7.53(m) | - |

Theoretical calculations showed that the highest molecular energy among compounds **2**–**7** was shown by the unsubstituted compound **4** (−972.776 au) and that there was no relationship between the electronegativity of substituent groups and the molecular energies of the compounds. Compound **5**, bearing the -Cl substituent, had the lowest molecular energy (−1432.400 au). The NO$_2$ substituted compound **7** possessed the lowest HOMO-LUMO energy gap (ΔE) and the highest electronegativity (4.798 eV) and dipole moment (9.914 D). Therefore, compound **7** exhibited the lowest chemical hardness (1.517 eV) and the highest reactivity. Conversely, unsubstituted compound **4** exhibited the highest chemical hardness. Comparison between compounds **4** and **2** showed that the methyl substituent decreased the dipole moment of the compound **4** from 3.6 to 1.5 D.

**Table 5.** Electronic and chemical parameters calculated by B3lyp/6-311++g(2d,2p)

| Compound | $E$ (au) | $E_{homo}$ (eV) | $E_{lumo}$ (eV) | $\Delta E$ | $\eta$ (eV) | $\chi$ (eV) | $m$ (D) |
|:---:|:---:|:---:|:---:|:---:|:---:|:---:|:---:|
| **2** | -1012.105 | -5.862 | -2.455 | 3.406 | 1.703 | 4.158 | 1.501 |
| **3** | -1048.026 | -5.765 | -2.417 | 3.348 | 1.674 | 4.091 | 2.469 |
| **4** | -972.776 | -5.954 | -2.529 | 3.425 | 1.713 | 4.242 | 3.600 |
| **5** | -1432.400 | -6.022 | -2.673 | 3.350 | 1.675 | 4.348 | 5.276 |
| **6** | -1072.046 | -5.992 | -2.593 | 3.399 | 1.700 | 4.293 | 4.903 |
| **7** | -1177.345 | -6.315 | -3.282 | 3.033 | 1.517 | 4.798 | 9.914 |

**E**: Energy, $\Delta E$: $E_{LUMO} - E_{HOMO}$, $\boldsymbol{\eta}$: Chemical Hardness, $\chi$: Electronegativity, **m**: Dipole moment **D:** Debye

As can be seen from Table 5, there is no obvious relationship between the electronegativity of the substituents and that of the compounds **2**–**6**. However, compound **7**, which bore the highest electronegative substituent (NO$_2$), also showed the highest electronegative. However, these data still suggest that a substituent's electronegativity is not necessarily the only criterion that determines the molecular electronegativity of the compound. The calculated electronic and chemical values of the compounds are shown in the Table 5. Furthermore, the calculated HOMO-LUMO and ESP maps of the molecules are given in Figure 5.

| Comp. | HOMO | LUMO | ESP |
|-------|------|------|-----|
| 2 | | | |
| 3 | | | |
| 4 | | | |
| 5 | | | |
| 6 | | | |
| 7 | | | |
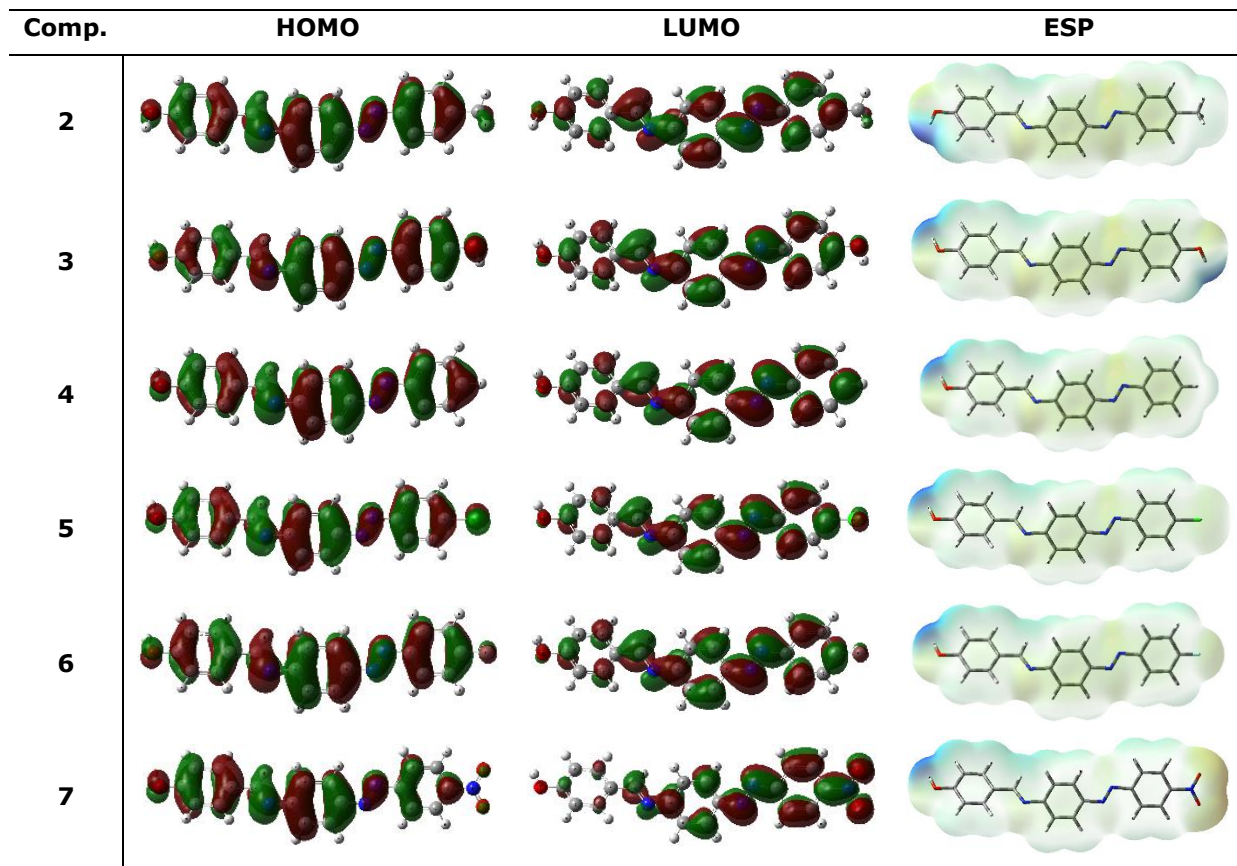


**Figure 5.** HOMO-LUMO and ESP maps of the compounds.

In ^{13}C-NMR spectra, which are shown in Table 6 and Figure 6, the aromatic and imine carbon atoms appear in the same region of 163.77–121.33 ppm, which is in agreement with values reported in the literature (5,8,13). The C1 atom conjugated to the OH group produced a signal downfield from the other carbon atoms, whereas the C5 and C6 atoms were shifted downfield, as expected, due to the nitrogen atom. In the substituted benzene ring, the C13 carbon atom resonated downfield due to a decrease in electron density resulting from the presence of -OH, -Cl, -F or -NO$_2$. Conversely, the presence of the electron-donating -CH$_3$ group resulted in upfield shifts in carbon atoms resonances due to an increase in electron density.
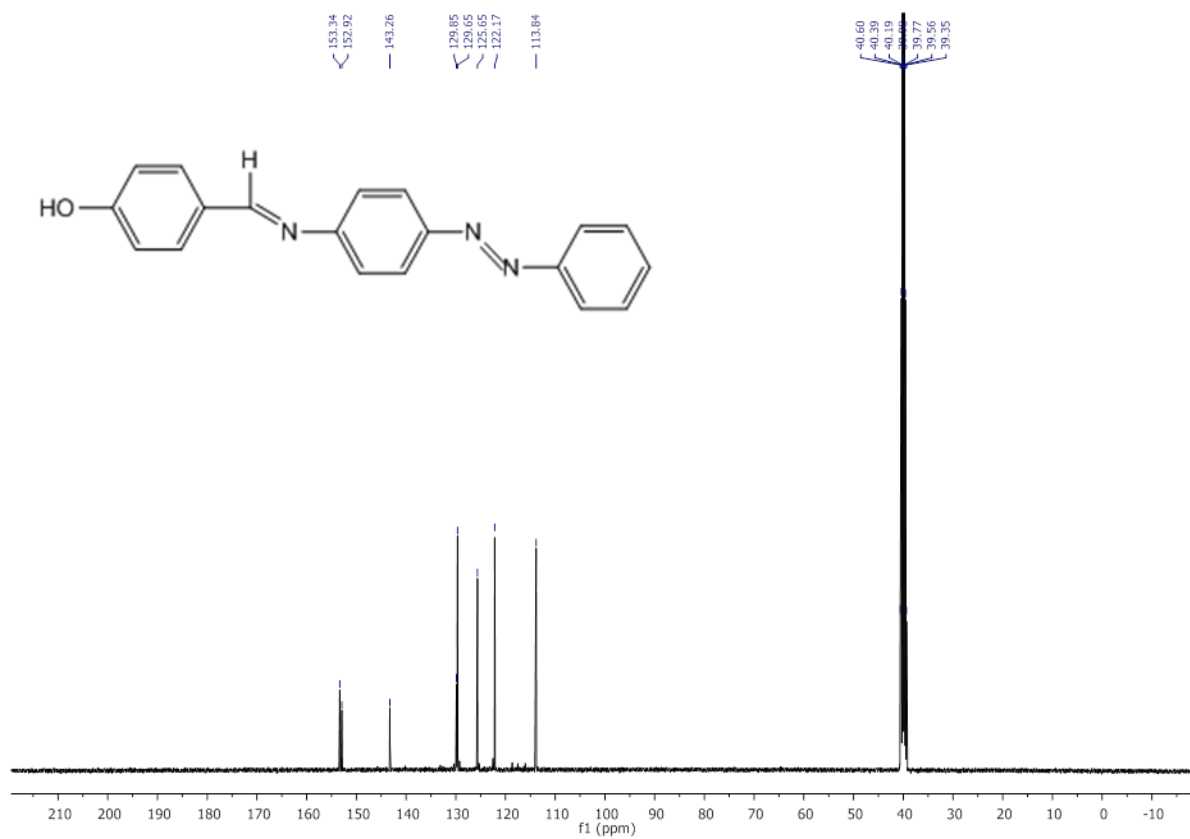
**Figure 6.** The ¹H-NMR Spectrum of 4-[[[4-[(phenyl)azo]phenyl]imino]methyl]-phenol

**Table 6.** $^{13}$C-NMR spectral results of compounds **1**-**7**.
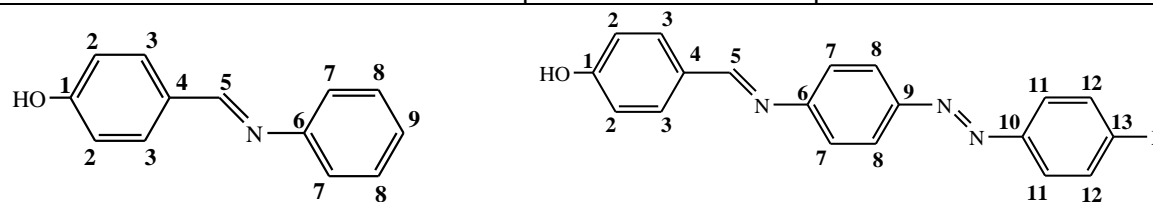


**Compound 1**　　　　　**X**= CH$_3$ (**2**), -OH (**3**), -H (**4**), -Cl (**5**), -F (**6**), NO$_2$ (**7**)

|  | C1 | C2 | C3 | C4 | C5 | C6 | C7 | C8 | C9 | C10 | C11 | C12 | C13 |
|---|---|---|---|---|---|---|---|---|---|---|---|---|---|
| **1** | 161.09 | 116.31 | 131.14 | 125.78 | 160.48 | 152.47 | 121.33 | 129.59 | 127.98 | - | - | - | - |
| **2** | 169.08 | 119.58 | 130.35 | 125.41 | 162.56 | 156.45 | 123.95 | 142.68 | 152.52 | 141.57 | 122.80 | 129.83 | 147.89 |
| **3** | 164.12 | 116.37 | 131.05 | 124.81 | 160.41 | 156.30 | 121.34 | 143.89 | 152.29 | 145.59 | 124.78 | 129.44 | 164.12 |
| **4** | 153.34 | 113.84 | 129.85 | 125.65 | 152.92 | 153.34 | 122.16 | 143.26 | 152.29 | 145.59 | 122.52 | 129.65 | 130.36 |
| **5** | 153.73 | 113.77 | 128.96 | 125.57 | 153.34 | 152.92 | 122.17 | 131.52 | 152.57 | 143.22 | 122.82 | 129.73 | 151.12 |
| **6** | 163.75 | 116.56 | 131.14 | 125.71 | 161.04 | 150.14 | 122.83 | 142.30 | 152.46 | 146.84 | 121.33 | 114.56 | 160.43 |
| **7** | 163.77 | 114.25 | 130.16 | 126.19 | 158.41 | 152.04 | 121.73 | 141.67 | 153.35 | 142.00 | 126.39 | 123.95 | 149.63 |

**CONCLUSION**

The azo-imine compounds synthesised in this study were obtained in a high yield and were characterised by UV–Vis, IR, NMR and elemental analyses. Spectroscopic and elemental analyses revealed the expected results. The UV–Vis electronic absorption and IR spectra of the compounds were determined both experimentally and also computationally using DFT. The UV–Vis spectra of the compounds exhibited two absorption bands in the ranges of 318–389 and 372–521 nm, which were assigned to $\pi{\rightarrow}\pi^*$ and n$\rightarrow\pi^*$ transitions, respectively. ^{1}H- and ^{13}C NMR spectroscopy confirmed the presence of the functional groups, particularly the -N=N- and -HC=N- imine groups, of the compounds.

**REFERENCES**

1. Umape P.G, Patil V.S,  Padalkar V.S, Phatangare K.R, Gupta V.D, Thate A.B, Sekar N, Synthesis and characterization of novel yellow azo dyes from 2-morpholin-4-yl-1,3-thiazol-(5H)-one and study of their azo-hydrazone tautomerism. Dyes and Pigments. 2013;99: 291-298.

2. Gür M., Kocaokutgen H., M. Taş, Synthesis, spectral and thermal characterissation of some azo-ester derivatives containing a 4-acryloyloxy group, Dyes and Pigments, 2007, 72, 101-108.

3. Al-Hamdani A.A.S, Balkhi A.M, Falah A, Shaker S.A, Synthesis and investigation of thermal properties of vanadyl complexes with azo-containing Schiff-base dyes, Journal of Saudi Chemical Society, 2016; 20: 487-501

4. Bitmez Ş, Sayin K, Avar B, Köse M, Karayıldız A, Kurtoğlu M, Preparation, spectral, X-ray powder diffraction and computational studies and genotoxic properties of new azo–azomethine metal chelates, Journal of Molecular Structure. 2014:1076; 213–226

5. Eren T, Köse M, Kurtoğlu N, Ceyhan G, McKee V, Kurtoğlu M,  An azo-azomethine ligand and its copper(II) complex: Synthesis, X-ray crystal structure, spectral, thermal, electrochemical and photoluminescence properties. Inorganica Chimica Acta 2015; 430: 268–279

6. Köse M, Kurtoğlu N, Gümüşsu Ö, Tutak M, McKee V, Karakaş D, Kurtoğlu M, Synthesis, characterization and antimicrobial studies of 2-{(E)-[(2-hydroxy-5-methylphenyl)imino]methyl}-4-[(E)-phenyldiazenyl] phenol as a novel azo-azomethine dye. Journal of Molecular Structure. 2013; 1053: 89–99

7. Kantar C, Mavi, V, Baltas N¸ İslamoğlu F, Şaşmaz S, Novel zinc(II)phthalocyanines bearing azo-containing schiff base: Determination of pKa values, absorption, emission, enzyme inhibition and photochemical properties. Journal of Molecular Structure. 2016; 1122: 88-99

8. Purtas F, Sayin K, Ceyhan G,  Kose M, Kurtoglu M, New fluorescent azo-Schiff base Cu(II) and Zn(II) metal chelates; spectral, structural, electrochemical, photoluminescence and computational studies. Journal of Molecular Structure. 2017; 1137: 461-475.

9. Alaghaz A.M.A, Zayed M. E, Alharbi S. A, Synthesis, spectral characterization, molecular modeling and antimicrobial studies of tridentate azo-dye Schiff base metal complexes. Journal of Molecular Structure. 2015; 1084: 36–45

10. Zakerhamidi M.S, Nejati K, Sorkhabi S.G, Saati M, Substituent and solvent effects on the spectroscopic properties and dipole moments of hydroxyl benzaldehyde azo dye and related Schiff bases. Journal of Molecular Liquids. 2013; 180: 225–234

11. Anitha C, Sheela C.D, Tharmaraj P, Sumathi S, Spectroscopic studies and biological evaluation of some transition metal complexes of azo Schiff-base ligand derived from (1-phenyl-2,3-dimethyl-4-aminopyrazol-5-

one) and 5-((4-chlorophenyl)diazenyl)-2-hydroxybenzaldehyde. Spectrochimica Acta Part A: Molecular and Biomolecular Spectroscopy. 2012; 96: 493–500

12. Nazır H, Yıldız M, Yılmaz H,  Tahir M.N, Ülkü D, Intramolecular hydrogen bonding and tautomerism in Schiff bases. Structure of *N*-(2-pyridil)-2-oxo-1-naphthlidenemethylamine. Journal of Molecular Structure. 2000; 524: 241-250

13. Pal M.K, Kushwah N, Wadawale AP, Manna D, Sudarsan V, Ghanty T.K, Jain V.K, Synthesis, characterization, photoluminescence and computational studies of mono- and diorgano-gallium complexes containing azo linked salicylaldimine Schiff bases. Journal of Organometallic Chemistry. 2015; 776: 98-106

14. Nagy P.I, Fabian W.M.F, Theoretical Study of the Enol Imine-Enaminone Tautomeric Equilibrium in Organic Solvents. J. Phys. Chem. B. 2006; 110: 25026-25032

15. Alaghaz A.M.A, Zayed M. E, Alharbi S. A, Synthesis, spectral characterization, molecular modeling and antimicrobial studies of tridentate azo-dye Schiff base metal complexes. Journal of Molecular Structure. 2015; 1084:  36–45

16. Qian H.F, Tao T, Feng Y.N, Wang Y.G, Huang W, Crystal structures, solvatochromisms and DFT computations of three disperse azo dyes having the same azobenzene skeleton. Journal of Molecular Structure. 2016; 1123: 305-310

17. Atay Ç.K, Gökalp M, Kart S.Ö, Tilki T, Mono azo dyes derived from 5-nitroanthranilic acid: Synthesis, absorption properties and DFT calculations. Journal of Molecular Structure. 2017; 1141: 237-244.

18. Sreenath M.C, Mathew S, Joe H.I, Rastogi V.K, Z-scan measurements of the third-order optical nonlinearities and vibrational spectral studies by DFT computations on azo dye 1-(2-Methylphenylazo)-2-napthol. Optics and Laser Technology. 2017; 97: 390–399.

19 Deshmukh M.S, Sekar N, A combined experimental and TD-DFT investigation of three disperse azo dyes having the nitroterephthalate skeleton. Dyes and Pigments. 2014; 103: 25-33

20. Turkten N, Cinar Z, Photocatalytic decolorization of azo dyes on TiO2: Prediction ofmechanism via conceptual DFT. Catalysis Today. 2017; 287: 169–175

21. Miraftab R, Ramezanzadeh B,  Bahlakeh G, Mahdavian M, An advanced approach for fabricating a reduced graphene oxide-AZO dye/polyurethane composite with enhanced ultraviolet (UV) shielding. Chemical Engineering Journal. 2017; 321: 159–174

22. Erfantalab M, Khanmohammadi H, New 1,2,4-triazole-based azo–azomethine dye. Part III: Synthesis, characterization, thermal property, spectrophotometric and computational studies properties: Experimental and first-principles QM modeling. Spectrochimica Acta Part A: Molecular and Biomolecular Spectroscopy. 2014; 125: 345–352

23. Gür M, Muğlu H, Çavus M.S, Güder A, Sayıner H.S, Kandemirli F, Synthesis, characterization, quantum chemical calculations and evaluation of antioxidant properties of 1,3,4-thiadiazole derivatives including 2- and 3-methoxy cinnamic acids. Journal of Molecular Structure. 2017; 1134: 40-50

24. Kohn W, Sham L.J, Self-consistent equations including exchange and correlation effects. Phys. Rev. 1965; 140:  A1133.

25. Shahab S, Sheikhi M, Filippovich L, Kumar R, Dikusar E, Yahyaei H, et al. Synthesis, geometry optimization, spectroscopic investigations (UV/Vis, excited states, FT-IR) and application of new azomethine dyes. Journal of Molecular Structure. 2017 Nov;1148:134–49.

26. Endre J, Tibor Z., Antimicrobial, ascaricidal, and molluscicidal activities of salicylanilide analogs. Virusforschung und Parasitologie. 1967; 202 (4): 547-62

27. Gogotov, A. F., 4-Hydroxybenzylidenaniline and 4-hydroxyazobenzene derivatives as alternatives to nitrobenzene in the selective decomposition of lignin to vanillin. Russian Journal of Applied Chemistry 2000; 73(2): 324-29

28. Gaussian 09, Revision B.01, Frisch M. J, Trucks G. W, Schlegel H. B, Scuseria G. E, Robb M. A, Cheeseman J. R, Scalmani G., Barone V, Mennucci B, Petersson G. A, Nakatsuji H, Caricato M, Li X, Hratchian H. P, Izmaylov A. F, Bloino J, Zheng G, Sonnenberg J. L, Hada M, Ehara M, Toyota K, Fukuda R, Hasegawa J, Ishida M, Nakajima T, Honda Y, Kitao O, Nakai H, Vreven T, Montgomery J. A, Peralta J. E, Ogliaro F, Bearpark M, Heyd J. J, Brothers E, Kudin K. N, Staroverov V. N, Keith T, Kobayashi R, Normand J, Raghavachari K, Rendell A, Burant J. C, Iyengar S. S, Tomasi J, Cossi M, Rega N, Millam J. M, Klene M, Knox J. E, Cross J. B, Bakken V, Adamo C, Jaramillo J, Gomperts R, Stratmann R. E, Yazyev O, Austin A. J, Cammi R, Pomelli C, Ochterski J. W, Martin R. L, Morokuma K, Zakrzewski V. G, Voth G. A, Salvador P, Dannenberg J. J, Dapprich S, Daniels A. D, Farkas O, Foresman J. B, Ortiz J. V, Cioslowski J, Fox D. J, Gaussian, Inc., Wallingford CT, 2010.

29.Becke AD, A new mixing of HartreeeFock and local density-functional theories. J Chem Phys. 1993; 98:1372-7.

30. Lee C, Yang W, Parr RG. Development of the Colle-Salvetti correlation-energy formula into a functional of the electron density. Phys Rev B 1988; 37: 785-9.

31. Cossi M, Barone V, Cammi R, Tomasi J., Ab initio study of solvated molecules: a new implementation of the polarizable continuum model, Chem. Phys. Lett. 1996;255: 327-335.

# Preparation and Cytotoxicity of Coriandrum sativum L. Oil-Loaded Chitosan Nanoparticles

## Yasemin Budama-Kilinc[1]*, Rabia Cakir-Koc[1], Zeynep Kaya[1]

1Yildiz Technical University, Chemical and Metallurgical Engineering Faculty, Bioengineering Department, 34220, Istanbul, Turkey.

**Abstract:** Coriandrum sativum L. (coriander) oil has antibacterial, antifungal, and antimicrobial activity. This study prepared and characterized chitosan nanoparticles loaded with the oil from Coriandrum sativum L., using an ionic gelation method with tripolyphosphate as the cross-linker. The coriander oil-loaded chitosan nanoparticles were characterized by Zeta Sizer measurements, Fourier transform infrared spectrometry, scanning electron microscopy (SEM), electron dispersive X-ray spectroscopy (EDS), and in vitro release properties. It was shown that chitosan nanoparticles loaded with coriander oil have an average size of 113.5 nm, zeta potential of 16 mV and a polydispersity index of 0.378. The encapsulation efficiency was calculated as 72%. The spherical morphology of the nanoparticles was verified by SEM analysis, and EDS revealed the elemental composition. Furthermore, cytotoxicity analysis using L929 fibroblast cells and the XTT method demonstrated that coriander oil-loaded chitosan nanoparticles, coriander oil, and empty chitosan nanoparticles had no significant cell toxicity.

**Keywords:** Cell culture, chitosan, coriander (Coriandrum sativum L.), cytotoxicity, nanoparticle.

**\*Corresponding author. E-mail:** yaseminbudama@gmail.com; Tel: +90 212 383 46 47; Fax: +90 212 383 46 26.

## INTRODUCTION

*Coriandrum sativum* L. (coriander) is a member of the Apiaceae family and used as a medicinal plant (1). It is an annual, herbaceous plant grown for therapeutic purposes in North and Middle Africa and Asia (2). Coriander oil is one of the prominent essential oils found in the global market (3).

Various pharmacognostic, phytochemical, and pharmacological studies of coriander oil and its bioactive phenolic components have been published (1). Such literature investigations highlight the effectiveness of coriander oil as an antibacterial agent against gram-positive (*Staphylococcus aureus, Bacillus* spp.) and gram-negative bacteria (*Escherichia coli, Salmonella typhi, Klebsiella pneumoniae, Proteus mirabilis, Pseudomonas aeruginosa*) (4). In addition, its antimicrobial activity against pathogenic *Candida albicans* fungus has been illustrated, and it has been shown that coriander oil has significant antibacterial and antifungal activity against all microbes, except antibiotic-resistant *P. aeruginosa* (5).

The main component of coriander oil, linalool, has demonstrated to have anti-cancer activity (6). It is thought to increase the therapeutic index of anthracyclines in the therapy of breast cancer and especially in drug-resistant tumors (7). Other authors have reported that coriander nectar and volatile oils can display anti-inflammatory, as well as anti-oxidant properties (8). *In vivo* and *in vitro* assays indicate that the bioactive components of coriander have hypoglycemic, hypolipidemic, anxiolytic, analgesic, anti-inflammatory, anti-convulsant, anti-helmintic, and hepatoprotective activities (4). However, the use of herbal components is limited due to their low stability. Recently, development of nano-sized formulations, which encapsulate herbal constituents in polymer networks, has gained importance because it is known that the encapsulation techniques preserve the characteristics of medicinal herbal oils, as well as increase their activity due to their nano-size (9).

A wide range of polymers and various polymer combinations are suitable for the encapsulation of nanostructures. Chitosan is commonly used as a wall material polymer because it does not show toxicity. Further advantages of chitosan are its biocompatibility, due to its physical and chemical properties (10), biodegradability, and stability in micro- and nano-sized particles, and under high-temperature conditions (11). For these reasons, chitosan nanoparticles have great importance in controlled drug delivery systems (12, 13).

The antimicrobial activity of coriander oil microcapsules has been studied in a previous work (14). Another study determined the swelling and release attributes of coriander oil encapsulated in microparticles using various materials, such as chitosan, alginate, chitosan/alginate, and chitosan/insulin (15).

However, encapsulation of coriander oil into nano-scale particles has not yet been documented. Therefore, this study aimed to prepare coriander oil-loaded chitosan nanoparticles and characterize their properties by using a Zeta Sizer, scanning electron microscope, Fourier transform infrared (FTIR) spectrometer, and an electron dispersive X-ray spectroscope. The *in vitro* cytotoxicity of the samples was also determined.

## MATERIALS AND METHODS

### Chemicals

Chitosan (75–85% deacetylated, low molecular weight, CAS no. 9012-76-4), sodium tripolyphosphate (TPP, CAS no. 7758-29-4), and Tween 80 (CAS no. 9005-65-6) were purchased from Sigma–Aldrich (St. Louis, MO, USA). Acetic acid (CAS no. 64-19-7), coriander *(Coriandrum sativum* L.*)* oil (99% pure), and 2,3-bis-(2-methoxy-4-nitro-5-sulfophenyl)-2H-tetrazolium-5-carboxanilide (XTT) were obtained from Merck (Darmstadt, Germany). All the chemicals and solvents were of analytical grade and were used without further purification. Ultra-pure water was obtained using a Millipore Milli-Q Gradient System.

### METHODS

### Preparation of coriander oil-loaded chitosan nanoparticles

Coriander oil-loaded chitosan nanoparticles were prepared using a modified version of the ionic gelation method (16). Chitosan (2.5% w:v) was added to 1% (v:v) acetic acid solution and mixed on a magnetic stirrer until a homogeneous solution was obtained. The pH of the solution was adjusted to 4.6–4.8. Next, coriander oil and Tween 80 mixture (1:1 v:v) were combined with a solution of chitosan. In order to obtain a homogeneous solution, the mixture was stirred at room temperature for 2 h. Next, TPP was dissolved in distilled water (0.05%, w:v) and then added drop-wise. The solution was agitated on a magnetic stirrer for 45 min, and finally, ultrasonication was applied.

In order to prepare chitosan nanoparticles, the first two steps were performed as per the coriander oil-loaded nanoparticles. The remaining steps were performed with TPP, in equal amounts as described above, without coriander oil.

### Characterization studies

*Average size, polydispersity, and size distribution with dynamic light scattering (DLS):* Photon correlation spectroscopy was accomplished using a Zeta Sizer Nano ZS (Malvern Instruments, UK) instrument, equipped with a 4.0 mV He-Ne laser (633 nm), operating at 25 °C. This technique enabled assessment of the average size, polydispersity index (PDI), and size distribution of the coriander oil-loaded chitosan and chitosan nanoparticles. Before every

electrophoretic light scattering measurement, each sample was filtered through a 0.2 μm regenerated cellulose membrane (Sartorius, Germany) to remove any impurities from the solutions.

*FTIR spectrometry:* The IR Prestige 21 FTIR spectrometer (Shimadzu, Japan) was used for chemical analyses of the functional groups present in the samples. Measurements were carried out for coriander oil, chitosan nanoparticles, and coriander oil-loaded chitosan nanoparticles, in universal attenuated total reflectance (ATR) mode. The FTIR spectra were collected from eight scans per sample, over the range 4000 to 750 cm$^{-1}$, at 4 cm$^{-1}$ resolution.

*Scanning electron microscopy (SEM) and electron dispersive X-ray spectroscopy (EDS):* The morphology of the coriander oil-loaded chitosan nanoparticles was analyzed using a scanning electron microscope (Zeiss Supra 50 V). Nanoparticle samples were fixed to metal stubs and sputtered with a gold–palladium mixture at a thickness of 100 Å. The imaging was conducted using an accelerating voltage of 20 kV.

*Determination of encapsulation efficiency and loading efficiency:* The standard calibration curve of coriander oil was established by using a UV-Vis spectrophotometer (Shimadzu UV-1280) at 273 nm, to calculate the encapsulation efficiency. Freeze-dried coriander oil-loaded chitosan nanoparticles were mixed with 5 mL of 2 M hydrochloric acid solution and boiled at 95 °C for 30 min. After cooling, 2 mL of ethanol was added, and the solution then centrifuged at 9,000 rpm/25 °C for 5 min (17). The supernatant was analyzed by UV-Vis spectrophotometry at a wavelength of 273 nm. The encapsulation efficiency of coriander oil-loaded chitosan nanoparticles was determined by calculating the concentration of the free coriander oil in the supernatant, from the coriander oil calibration curve.

$$\text{Encapsulation Efficiency (\%)} = \frac{\text{Total drug amount} - \text{Free drug amount}}{\text{Total drug amount}} \times 100 \qquad \text{(Eq. 1)}$$

*In vitro release experiment of coriander oil:* To determine the *in vitro* coriander oil release profiles, the freeze-dried coriander oil-loaded chitosan nanoparticles (20 mg) were placed in a tube containing a 3:2 ratio of PBS (pH 7.4) and ethanol, and incubated at 37 °C with gentle shaking. At specific time intervals, the samples were centrifuged at 9000 rpm/5 °C for 5 min (18). The supernatant volume was taken for analysis, and the equivalent volume of fresh medium was added, followed by measurement at 273 nm, using a UV-Vis spectrophotometer.

The release of coriander oil was determined as detailed in the following equation;

$$\text{Release (\%)} = \frac{\text{Released coriander oil}}{\text{Total coriander oil}} \times 100 \qquad \text{(Eq. 2)}$$

*Cytotoxicity experiments*: An L929 cell line was used for the cytotoxicity studies. The mouse fibroblast cell line NCTC clone 929 (strain L) was derived in 1948 from a C3H/An male mouse. Fibroblast cultures are often used to evaluate materials intended for medical use. The cytotoxicity is taken as an indicator of bioincompatibility. Cells were cultured in a DMEM-F12 medium, supplemented with 10% fetal bovine serum and penicillin-streptomycin. The basal medium is widely used for supporting the growth of many different mammalian cells. The plates were incubated at 37 °C for 3 days in a 5% $CO_2$ incubator until confluency was attained. A trypsinization process was applied to the cells, and the detached cells were obtained by centrifugation.

The L929 cells were seeded (10,000 cells/well) in 96-well flat-bottom microplates with 100 µL of medium. The plates were incubated at 37 °C for 24 h, for attachment to the well bottoms. Various concentrations (3.12, 6.25, 12, and 18 µg/mL) of the chitosan nanoparticles, coriander, and coriander-oil-loaded chitosan nanoparticles were added, respectively, and incubated for another 24 h. The media containing chitosan or nanoparticles were then aspirated, and 100 µL of XTT solution in fresh medium was added to the wells at 0.5 mg/mL (with 7.5 µg/mL phenazine methosulfate). The plates were incubated at 37 °C for 3 h. Afterward, the optical density was measured at 450 nm with a multi-plate reader (Thermo Labsystems Multiscan Ascent 354 Microplate Photometer). Then, the percentage viability was calculated by the following equation:

$$\text{Viability (\%)} = \frac{\text{Absorbance of experimental group}}{\text{Absorbance of control group}} \times 100 \qquad \text{(Eq. 3)}$$

**RESULTS AND DISCUSSION**

In this study, an ionic gelation technique was used to prepare the nanoparticles. Briefly, this method is based on an ionic gelation interaction, formed by the repulsive force between positively-charged chitosan and negatively-charged TPP. This procedure was undertaken to synthesize empty and coriander oil-loaded chitosan nanoparticles. These two types of nanoparticles were examined and compared for their physicochemical properties, such as particle size, zeta potential, and PDI, as well as their biological properties in cell culture.

The average size of the empty and coriander oil-loaded nanoparticles was determined using the DLS technique, with triplicate measurements (Table 1). As seen from Figures 1 and 2, the empty chitosan nanoparticles have a size of 156.2 nm, a zeta potential of 22.4 mV, and a PDI of 0.150, whereas coriander oil-loaded chitosan nanoparticles are 113.5 nm, with a zeta potential of 16 mV and a PDI of 0.378.

**Table 1.** Zeta Sizer results of nanoparticles

| Sample | Size (nm) | PDI | Zeta potential (mV) |
|---|---|---|---|
| Chitosan nanoparticles | 156.2±1.8 | 0.150 | 22.4±1.95 |
| Coriander oil-loaded chitosan nanoparticles | 113.5±3.5 | 0.378 | 16.0±1.1 |
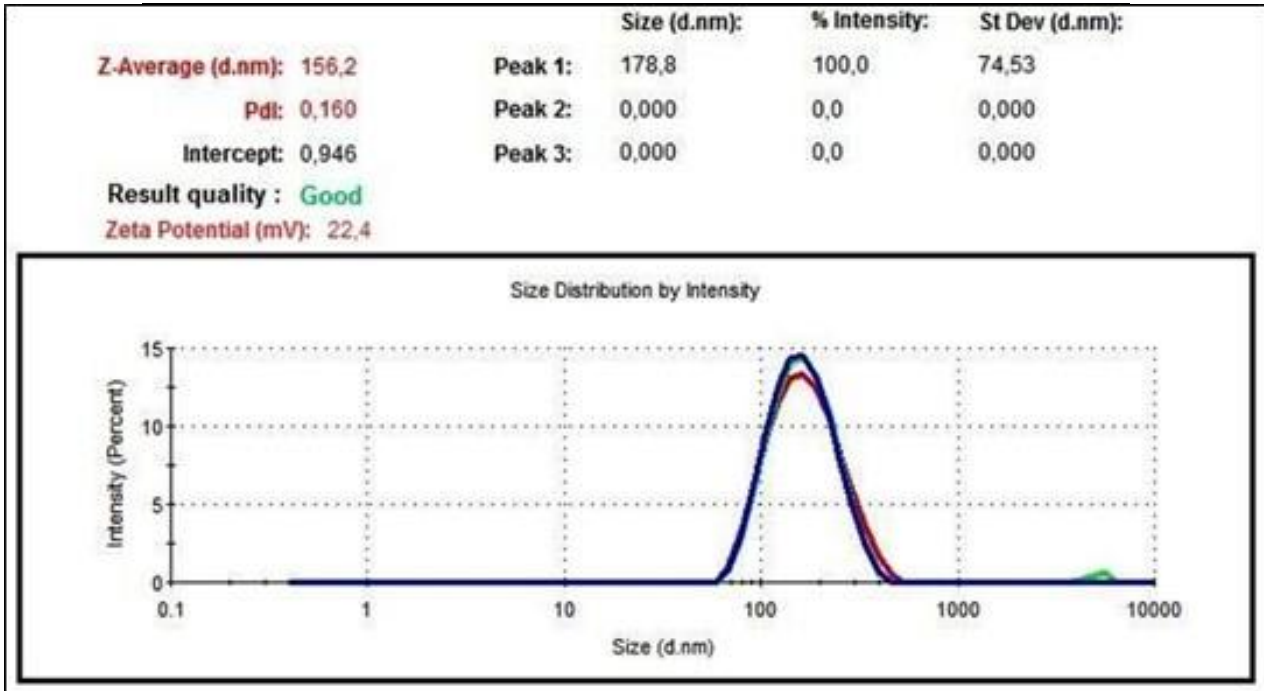


**Figure 1.** The Zeta Sizer result of chitosan nanoparticles.
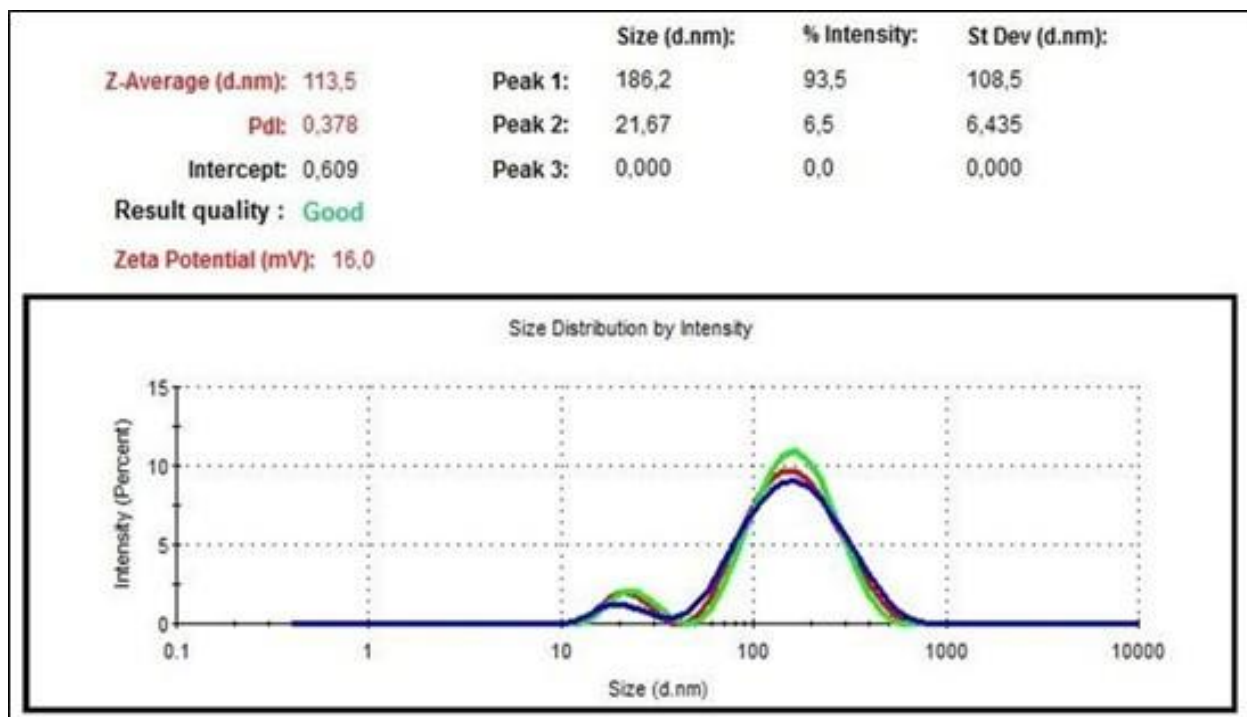


**Figure 2.** The Zeta Sizer result of coriander oil-loaded chitosan nanoparticles.

During the encapsulation process, coriander oil and chitosan polymers are likely to interact with each other. Based on the weak interactions, such as hydrogen bonding, during this process, the conformation of the chitosan nanoparticles loaded with coriander oil may change. The DLS method showed that the size of the chitosan nanoparticles decreased when loaded with coriander. Thus, more compact structures have been formed with the loading of coriander oil into the chitosan nanoparticles.

The coriander oil-loaded chitosan nanoparticles were visualized, using a scanning electron microscope. As can be observed in Figure 3, coriander oil-loaded chitosan nanoparticles have a spherical morphology with some bridging flocculation between the particles.
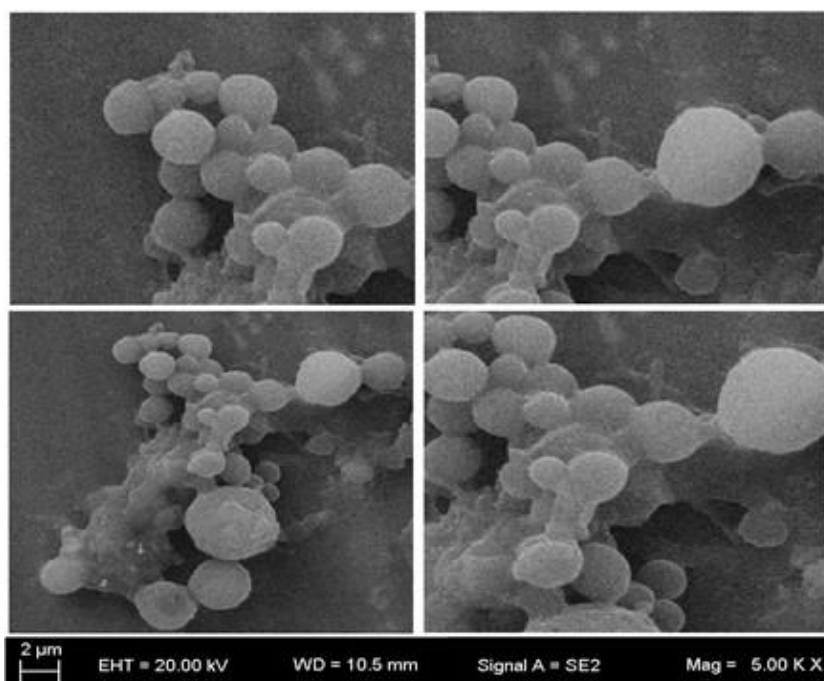


**Figure 3.** Scanning Electron Microscope images of coriander oil-loaded chitosan nanoparticles.

EDS is a chemical analysis method that can be used to determine the elemental composition at a certain point in the imaged area (19). Figure 4 provides the EDS results of the chitosan and coriander oil-loaded chitosan nanoparticles. The EDS spectra (Figure 4A) evidenced that the analysis site of the empty chitosan nanoparticles contained carbon (C), nitrogen (N), and oxygen (O). All these elements are known to exist in the chitosan polymer structure. Similarly, for the two different points of the coriander oil-loaded chitosan nanoparticles analyzed by EDS, Figure 4B reveals that C, N, and O are present. However, when compared to the empty chitosan nanoparticles, the intensities of these peaks were decreased, possibly due to the presence of coriander oil.
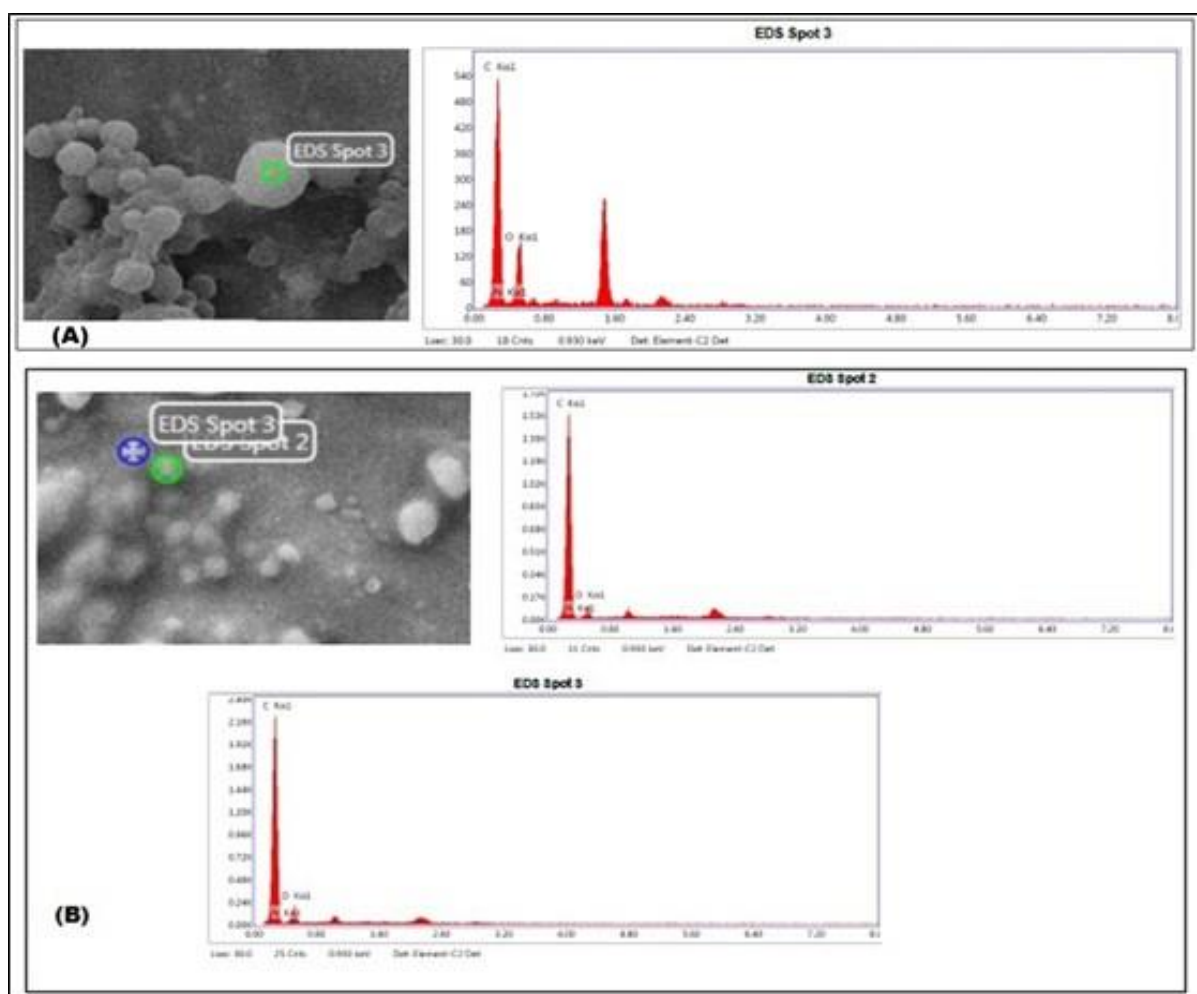
**Figure 4.** Scanning electron microscopy-electron dispersive X-ray spectroscopy results of chitosan **(A)** and coriander oil-loaded chitosan nanoparticles **(B)**.

The nature of the chemical bonds present in the coriander oil, chitosan, and coriander oil-loaded chitosan nanoparticles were identified using FTIR. As illustrated in Figure 5, typically, the vibrations at 3005 cm$^{-1}$ (-OH), 2924 cm$^{-1}$ (C-H), and 2852 cm$^{-1}$ (C-H) observed in the coriander oil analysis are considered to originate from the hydrocarbon groups found in its chemical structure. There is a specific and intense peak at 1745 cm$^{-1}$, arising from the ester groups (C=O) (Figure 5(c)) and the signal at 1165 cm$^{-1}$ is assigned to C-O bonds. When the FTIR spectrum for chitosan nanoparticles was analyzed (Figure 5(a)), -NH vibrations at 1649 cm$^{-1}$ and C-O signals at 1165 cm$^{-1}$ were seen. In Figure 5(b), the FTIR results of the coriander oil-loaded chitosan nanoparticles indicate strong -OH vibrations at 3388 and 2922 cm$^{-1}$. Compared to chitosan alone, coriander oil-loaded chitosan nanoparticles have a significantly sharper intensity at this position. At 1631 cm$^{-1}$, an -NH peak characteristic of the amino group of chitosan is observed. A primary alcohol (C-O) peak specific to coriander oil at 1089 cm$^{-1}$ and a C-H peak at 871 cm$^{-1}$ are also noticed.
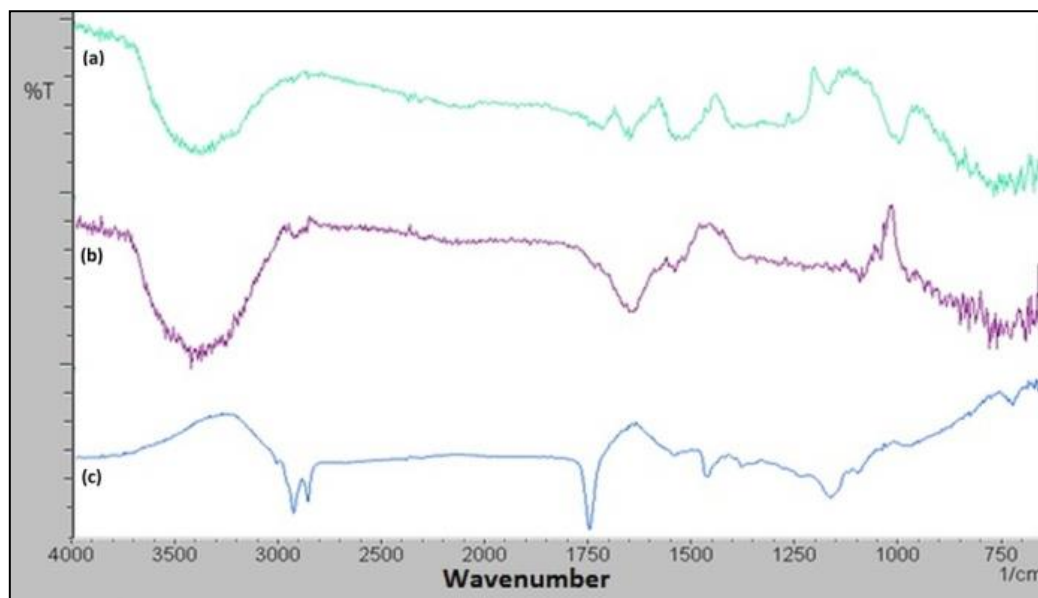
**Figure 5.** Fourier transform infrared spectra of chitosan nanoparticles **(a)**, coriander oil-loaded chitosan nanoparticles **(b)**, and coriander oil **(c)**.

The standard graphic of coriander oil (Figure 6) was constructed, to calculate the encapsulation efficiency of the nanoparticles. The encapsulation of coriander oil into chitosan nanoparticles was confirmed by UV analysis at 273 nm. The encapsulation efficiency of coriander oil was calculated as 72% (Eq. 1).
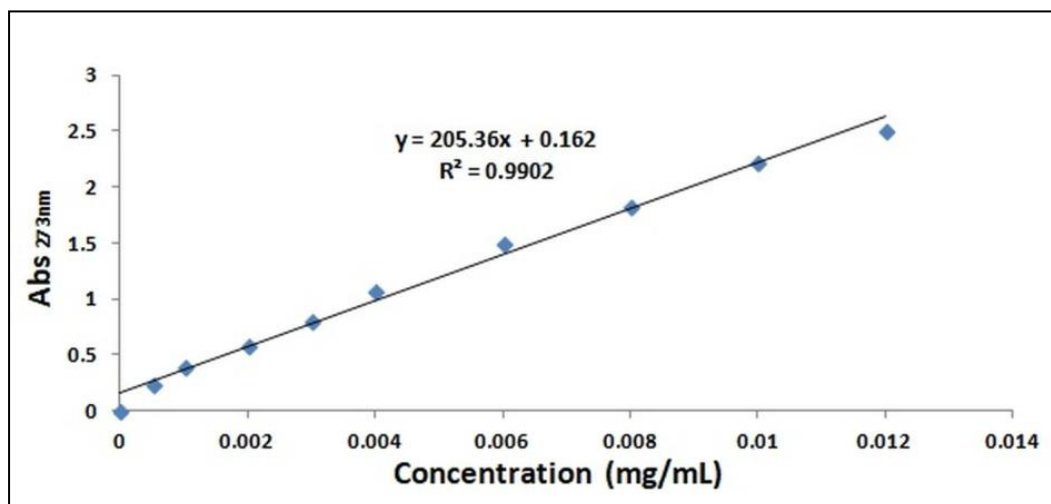


**Figure 6.** The standard calibration curve of coriander oil at 273 nm.

In order to perform the *in vitro* release experiment, the free coriander oil concentration was calculated. The *in vitro* release profile of coriander oil from chitosan nanoparticles is depicted in Figure 7. The amount of coriander oil released at different times was measured by UV-Vis spectroscopy at 273 nm. The experiment was performed for 5 h, and 97% coriander oil was released at the end of the second hour.
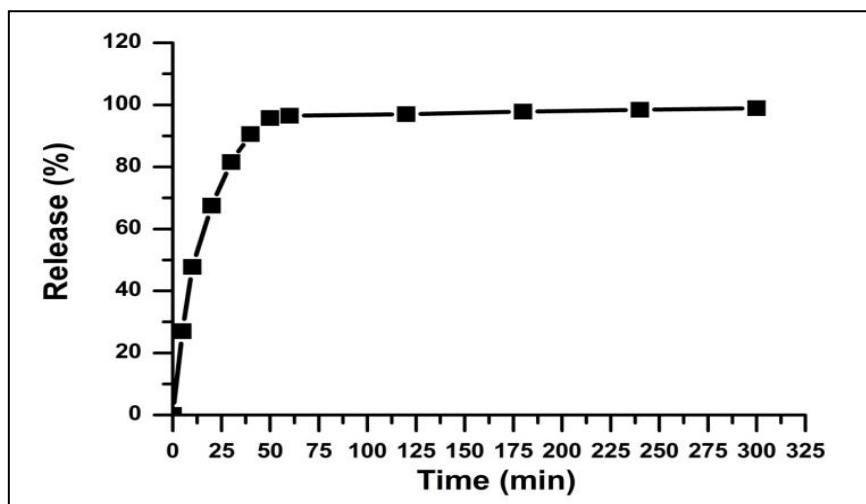
**Figure 7.** *In vitro* release profile of coriander oil-loaded chitosan nanoparticles.

After the characterization experiments of the nanoparticles, the coriander oil, coriander oil-loaded chitosan nanoparticles, and chitosan nanoparticles were used, respectively, at four different concentrations (3.12, 6.25, 12, and 18 µg/mL) in cell culture experiments (Figure 8). Coriander oil, indicated in Figure 8 by the green bars, did not provoke a significant toxic effect on the cells. Cell viability only decreased slightly at 18 µg/mL of coriander oil compared to the control (0 mg µg/mL).
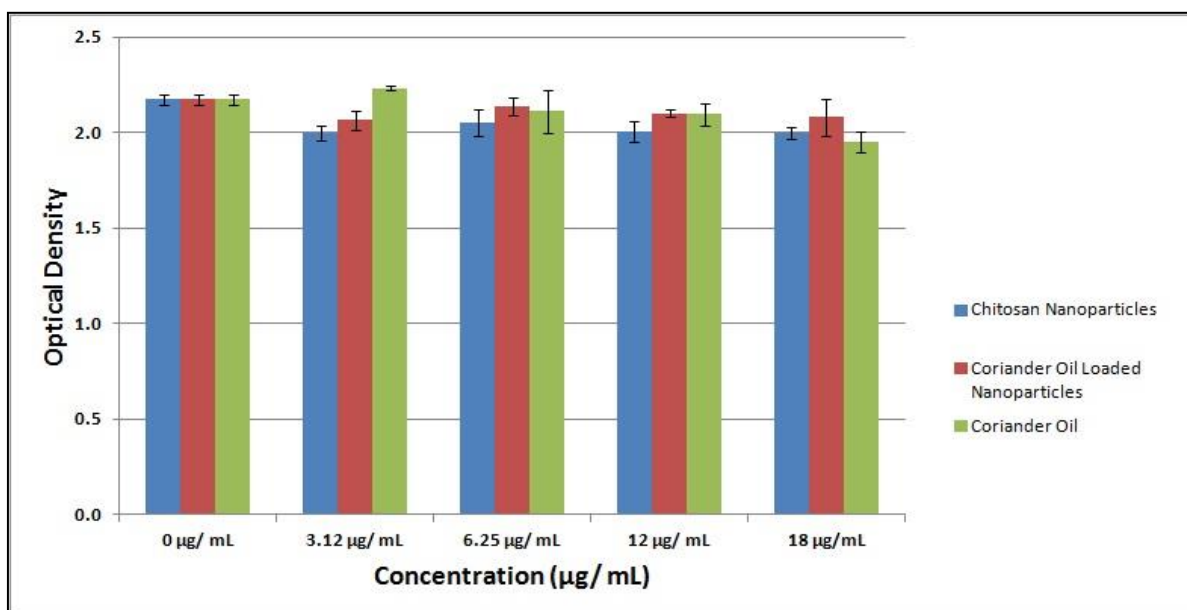


**Figure 8.** Differentiation of L929 cell viability with concentration.

Similarly, the coriander oil-loaded chitosan nanoparticles (Figure 8, red bars) presented no significant decrease in L929 cell viability, at the concentrations investigated. It is known that chitosan is a biocompatible polymer and does not provoke a toxic effect on cells (20). Our cell culture results (Figure 8, blue bars) also support this literature data. The cell viability was very similar to the control group.

Table 2 shows the percentage effect on L929 cell viability after 24 h treatment with coriander oil, chitosan, and coriander oil-loaded chitosan nanoparticles, compared to the control (0 µg/ mL). It is noted that the cell viability is over 90%, even at the longest exposure time investigated.

**Table 2.** Viability (%) of L929 cells exposed to coriander oil, chitosan nanoparticles, and coriander oil-loaded chitosan nanoparticles at different concentrations.

| Sample concentration | Coriander oil-loaded chitosan nanoparticles | Chitosan nanoparticles | Coriander oil |
|---|---|---|---|
| 3.12 µg/mL | 96.47±2.41 | 93.87±1.89 | 126.14±18.60 |
| 6.25 µg/mL | 100.47±1.92 | 96.33±3.19 | 99.13±5.27 |
| 12 µg/mL | 98.65±0.88 | 93.41±2.72 | 98.50±2.77 |
| 18 µg/mL | 97.66±4.00 | 93.81±1.52 | 91.60±2.66 |

**CONCLUSION**

In this study, coriander oil-loaded chitosan nanoparticles, which may be used for various purposes as active agents, were synthesized and characterized. Structural analysis was done by spectroscopy and imaging techniques, and nanoparticle formation was confirmed, with an encapsulation efficiency of 72%. The *in vitro* release studies indicated that the coriander oil present in the chitosan nanoparticles was released at the end of the second hour. These results confirm that coriander oil-loaded chitosan nanoparticles were obtained successfully. Furthermore, cytotoxic effect of obtained coriander oil-loaded chitosan nanoparticles were investigated in comparison with coriander oil and empty chitosan nanoparticles on L929 cells in cell culture assays. According to ISO 10993-5 standards, percentages of cell viability above 80% are considered as non-cytotoxic; within 80%–60% weakly toxic; 60%–40% moderately toxic and below 40% strong cytotoxicity respectively (21, 22). Coriander oil-loaded chitosan nanoparticles were non-toxic, based on an *in vitro* assay with L929 cells.

**CONFLICTS OF INTEREST**

The authors declare that they have no conflicts of interest.

**REFERENCES**

1. Laribi B, Kouki K, M'Hamdi M, Bettaieb T. Coriander (Coriandrum sativum L.) and its bioactive constituents. Fitoterapia. 2015;103:9-26.

2. Diederichsen A. Coriander: Coriandrum Sativum L: Bioversity International; 1996.

3. Lawrence BM. Progress in essential oils. Perfumer & flavorist. 1992;17(5):131-46.

4. Padmaa M. Coriandrum sativum linn: a review. Pharmacol online Newsl. 2009;3:561-73.

5. Matasyoh J, Maiyo Z, Ngure R, Chepkorir R. Chemical composition and antimicrobial activity of the essential oil of Coriandrum sativum. Food Chemistry. 2009;113(2):526-9.

6. Chang M-Y, Shen Y-L. Linalool exhibits cytotoxic effects by activating antitumor immunity. Molecules. 2014;19(5):6694-706.

7. Asgarpanah J, Kazemivash N. Phytochemistry, pharmacology and medicinal properties of Coriandrum sativum L. African Journal of Pharmacy and Pharmacology. 2012;6(31):2340-5.

8. Stashenko EE, Puertas MA, Martínez JR. SPME determination of volatile aldehydes for evaluation of in-vitro antioxidant activity. Analytical and bioanalytical chemistry. 2002;373(1):70-4.

9. Donsì F, Annunziata M, Sessa M, Ferrari G. Nanoencapsulation of essential oils to enhance their antimicrobial activity in foods. LWT-Food Science and Technology. 2011;44(9):1908-14.

10. Shukla SK, Mishra AK, Arotiba OA, Mamba BB. Chitosan-based nanomaterials: A state-of-the-art review. International journal of biological macromolecules. 2013;59:46-58.

11. Rinaudo M. Chitin and chitosan: properties and applications. Progress in polymer science. 2006;31(7):603-32.

12. Agnihotri SA, Mallikarjuna NN, Aminabhavi TM. Recent advances on chitosan-based micro-and nanoparticles in drug delivery. Journal of controlled release. 2004;100(1):5-28.

13. Uhrich KE, Cannizzaro SM, Langer RS, Shakesheff KM. Polymeric systems for controlled drug release. Chemical reviews. 1999;99(11):3181-98.

14. Duman F, Kaya M. Crayfish chitosan for microencapsulation of coriander (Coriandrum sativum L.) essential oil. International Journal of Biological Macromolecules. 2016;92:125-33.

15. Dima C, Pătraşcu L, Cantaragiu A, Alexe P, Dima Ş. The kinetics of the swelling process and the release mechanisms of Coriandrum sativum L. essential oil from chitosan/alginate/inulin microcapsules. Food chemistry. 2016;195:39-48.

16. Calvo P, Remunan-Lopez C, Vila-Jato JL, Alonso M. Novel hydrophilic chitosan-polyethylene oxide nanoparticles as protein carriers. Journal of Applied Polymer Science. 1997;63(1):125-32.

17. Keawchaoon L, Yoksan, R. Preparation, characterization and in vitro release study of carvacrol-loaded chitosan nanoparticles,. Colloids and Surfaces B: Biointerfaces. 2011;84(1):163-71.

18. Hosseini S, Zandi, M., Rezaeia, M., Farahmandghavi, F. Two-step method for encapsulation of oregano essential oil in chitosan nanoparticles: Preparation, characterization and in vitro release study. Carbohydrate Polymers. 2013; 95(1):50-6.

19. Reed SJB, Reed SJB. Electron microprobe analysis: Cambridge University Press Cambridge; 1975.

20. Kumar MNR. A review of chitin and chitosan applications. Reactive and functional polymers. 2000;46(1):1-27.

21. López-García J, Lehocký M, Humpolíček P, Sáha P. HaCaT keratinocytes response on antimicrobial atelocollagen substrates: extent of cytotoxicity, cell viability and proliferation. Journal of functional biomaterials. 2014;5(2):43-57.

22. ISO. 10993-5:2009 Biological Evaluation of Medical Devices. Part 5: Tests for In Vitro Cytotoxicity. International Organization for Standardization. Geneva, Switzerland. 2009.

# Preparation of α-Al₂O₃ Supports for Thin Membrane Fabrication

**Berna Topuz***, Ali Semih Yurttaş, Ali Altunsoy**

Ankara University, Chemical Engineering Department, 06100, Ankara, Turkey

**Abstract:** In this study, macroporous α-alumina supports were prepared by using vacuum assisted filtration of α-Al₂O₃ suspensions with different particle size. The average particle sizes of the powders are 400 and 200 nm. The prepared supports had smooth and uniform surface microstructure and well suited for the fabrication of thin continuous membrane. The microstructure consists of a random close-packing of 200 nm particles led to improved surface uniformity and roughness. ZnO spheres were prepared by homogeneous precipitation and added to the colloidal suspension to modify the support structure and increase the support flux. Structural parameters such as pore diameter and tortuosity of the prepared macroporous supports were estimated by using He, $N_2$, $CO_2$ permeance measurements. Slight pressure dependence in the permeance values indicated the contribution of viscous flow to the Knudsen flow. The supports prepared by alumina powder with a larger particle size exhibited a He permeance of three times higher than that of prepared with a smaller particle size. The addition of ZnO resulted in the increase in He permeance value significantly for the support prepared by 400 nm particles in size. He permeance was in a range of 8.5-8.7x10⁻⁶ mol/(m²sPa) which is very close to the desired value of 1x10⁻⁵ mol/(m²sPa).

**Keywords:** Membrane, support, alumina, high flux, colloidal processing, ZnO.

**\*Corresponding author. E-mail:** topuzb@ankara.edu.tr.

**INTRODUCTION**

Due to the high energy demand in our developing world, designing more energy-efficient processes is one of the significant challenges over the past few decades. Separation-based technologies play a significant role in chemical industries and account for 15% of world's energy consumption (1). Membrane-based separations are attractive in various separation processes due to their low energy consumption and operating cost over other thermally driven separation techniques like distillation. The intense interest towards thermally and mechanically stable ultrathin supported membranes (like zeolite, sol-gel derived ceramic, and MOF) with molecular sieving capability is continuously increasing due to their potential to attain high throughput. The mostly used supported membrane structure is composed of layers with a gradual decrease in pore size and thickness on a macroporous support to minimize the gas resistance through the membrane (2).

The macroporous supports are designed to mechanically hold the thin separative membrane layer and must be chemically inert, thermally stable, and highly permeable. The fabrication of ultrathin supported membranes necessitate the desired surface characteristics of support in terms of roughness and homogeneity. Ultrathin membranes (<500 nm in thickness) on macroporous supports have been prepared for high flux gas separation, vapor permeation, and pervaporation applications (3-6).

Ceramic supports have advantages in terms of their thermal stability and gas flux compared to their polymeric counterparts (7-9). One important disadvantage of macro/mesoporous ceramic supports is their high cost that impedes large scale deployment of thermally stable ceramic/zeolite/MOF membranes. Silica, zirconia, titania, and alumina or their composites are generally used as the membrane support materials (9-13). The supports must be highly porous so the molecules that were released through the membrane layer can also easily pass through the supports without any resistant. They must also be mechanically strong and have a smooth surface for the formation of defect-free continuous thin membrane layer.

Dry pressing, tape casting, and extrusion are the generally used methods for the preparation of ceramic membrane supports, however colloidal processing (slip casting/vacuum-assisted filtration) of statically or sterically stable suspensions allow the fabrication of macroporous supports with appropriate surface properties (14, 15). A smoother surface with less amount of roughness can be obtained by vacuum filtration method in which colloidal processing is used (15). High throughput thin membranes necessitate high flux membrane support with homogeneous surface properties, uniform

192

pore size and macro-defect free surface. The support structure has a great importance for determining the membrane microstructure, membrane performance in terms of selectivity and flux.

In this study, disk-shaped alumina supports with 21 mm in diameter and ~2 mm in thickness were prepared through colloidal processing of α-$Al_2O_3$ powders with different particle size (Baikowski CR-6 and Sumitomo Chemical AKP-50). ZnO spheres were added to the structure in order to increase the permeability of the supports. Single gas (He, $N_2$, $CO_2$) permeation behavior of the supports was determined at different temperature and pressure. Structural parameters of prepared supports were also estimated by single gas permeance measurements.

## MATERIALS AND METHODS

### Preparation of ZnO

ZnO nanospheres were prepared by homogeneous precipitation at 160 °C for 2 hours (16). Zinc acetate dihydrate (Sigma-Aldrich) was dissolved in diethylene glycol (DEG, Merck) with molar ratio of 1:105.4 DEG. After cooling the synthesis solution to the room temperature, ZnO spheres were collected by centrifugation (10000 rpm for 15 min). The ZnO spheres were washed 3 times with ethanol and dispersed in ethanol to be further used in $\alpha$-$Al_2O_3$ support preparation.

### Support Preparation

CR-6 (Baikowski) and AKP-50 (Sumitomo Chemical Company) α-$Al_2O_3$ powders were used to prepare macroporous supports with a thickness and diameter of 2 mm and 21 mm, respectively. The properties of these powders are shown in Table 1.

Electrostatically stable suspensions were first prepared by dispersing the powders in deionized water at pH~2. Electrostatic stability can be provided in aqueous suspension at pH in the 2–3 range for positively charged alumina particles (14). Nitric acid solution (1.44 M) was used for the adjustment of pH. Stable suspensions with 20 vol% $Al_2O_3$ in water were horn-sonicated (Sonics Vibra-Cell VCX130, 130 watts, 0.250″ probe) with an operating power at 80% maximum amplitude, 2 seconds of pause for each 5 seconds sonication sequences for 3 minutes. The suspensions were filtered with 1 µm stainless steel mesh and 3 µL/g-powder n-octanol was added prior to bath sonication at degassing mode for 90 minutes to eliminate the air bubbles in the suspension. ZnO added alumina supports were prepared by adding ZnO spheres into alumina suspension before casting. The amount of ZnO was kept at 3 wt% with respect to the weight of alumina. The presence of ZnO was

expected to modify the pore structure and increase the support flux. The supports were encoded according to their powder particle size and whether they had ZnO (Table 1).

**Table 1**: Support codes and properties of α-Al$_2$O$_3$ powders.

| Support Code | Powder Type | Mean Particle Size (nm) | BET Surface Area (m$^2$/g) | ZnO Addition |
|---|---|---|---|---|
| S400 | Baikowski /CR-6 | 400 | 6 | - |
| S200 | Sumitomo Chemical/AKP-50 | 200 | 10.3 | - |
| S400-Z | Baikowski /CR-6 | | | 3 wt% |
| S200-Z | Sumitomo Chemical/AKP-50 | | | 3 wt% |

Polypropylene cylinder molds (22 mm inner dimension, 70 mm height) were used for casting the supports. The molds were placed vertically on a 0.22 μm nylon membrane (Advantec MFS, Inc.) under partial vacuum (-0.6 bar). Alumina and ZnO-added alumina green compacts were removed from the molds after 2 hours of vacuum filtration and dried overnight at room temperature. The surfaces of the supports were cleaned with pressurized nitrogen (1 bar) before heat treatment. Dried compacts of S400, S400-Z and S200, S200-Z were heat treated at 1000 °C and 900 °C for 3 hours with a heating and cooling rate of 5 °C/min, respectively. The preparation of ZnO-added alumina supports is given schematically in Figure 1.
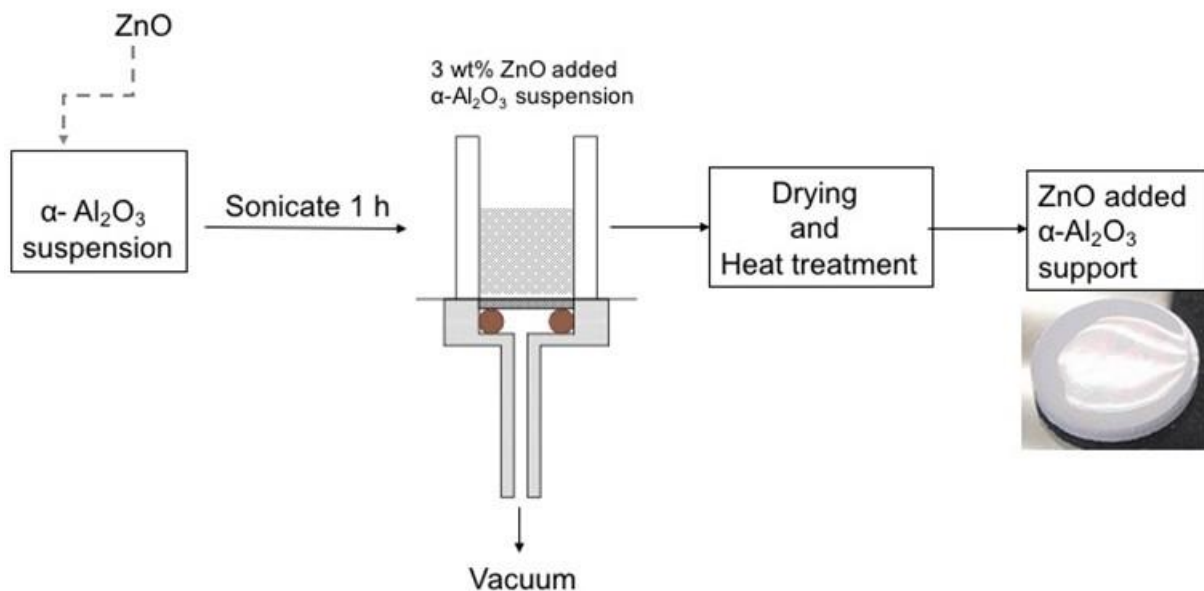


**Figure 1**: A schematic representation for the preparation of ZnO-added alumina supports.

**Characterization**

The morphology and size of the ZnO crystals were determined by field emission Scanning Electron Microscopy (SEM, QUANTA 400F). The samples were sputter coated with a thin

layer of Au-Pd before analysis. After degassing at 250 °C for 4 hours, BET surface area of the ZnO spheres were obtained from $N_2$ adsorption-desorption isotherms (AUTOSORB-6B).

The microstructure of the top and cross-section of the prepared supports were investigated by Scanning Electron Microscopy (SEM - Zeiss EVO 40 and QUANTA 200 FEG). The elemental composition was determined by Energy Dispersive X-ray Spectroscopy. Pore size and pore volume of the supports were determined with Mercury Intrusion Porosimeter (Quantachrome Corporation, Poremaster 60).

**Gas Permeation**

Single gas permeation of He, $N_2$ and $CO_2$ through the prepared supports were determined by using a constant pressure-variable volume membrane test system. The pressure of the feed side was adjusted in order to obtain transmembrane pressures in the 1-3 bar range and kept constant during the permeation experiments. Permeate flow rates were measured for the determination of single gas permeance (mol/$m^2$-s-Pa) values at different temperatures (25 °C-150 °C) for a constant transmembrane pressure of 1 bar.
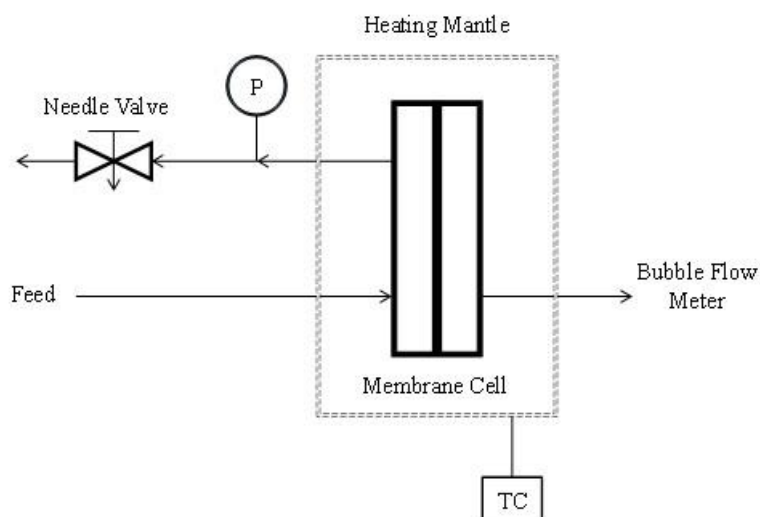


**Figure 2**: Single gas membrane test system.

**RESULTS AND DISCUSSION**

ZnO spheres with a bimodal particle size distribution were synthesized by precipitation. Figure 3.a shows a SEM image of ZnO spheres. The average sphere sizes were estimated from the SEM image as 680±64 nm and 290±90 nm for large and small spheres, respectively. SEM image with high magnification (Figure 3.a, inset) clearly shows that these spheres have rough surfaces. The nitrogen sorption–desorption isotherms of the spheres at 77 K showed a Type IV isotherm with a H2 hysteresis loop (Figure 3.b) indicating the mesoporous nature of ZnO spheres. BET surface area and pore volume of the sample

were 52 $m^2/g$ and 0.075 $cm^3/g$, respectively.
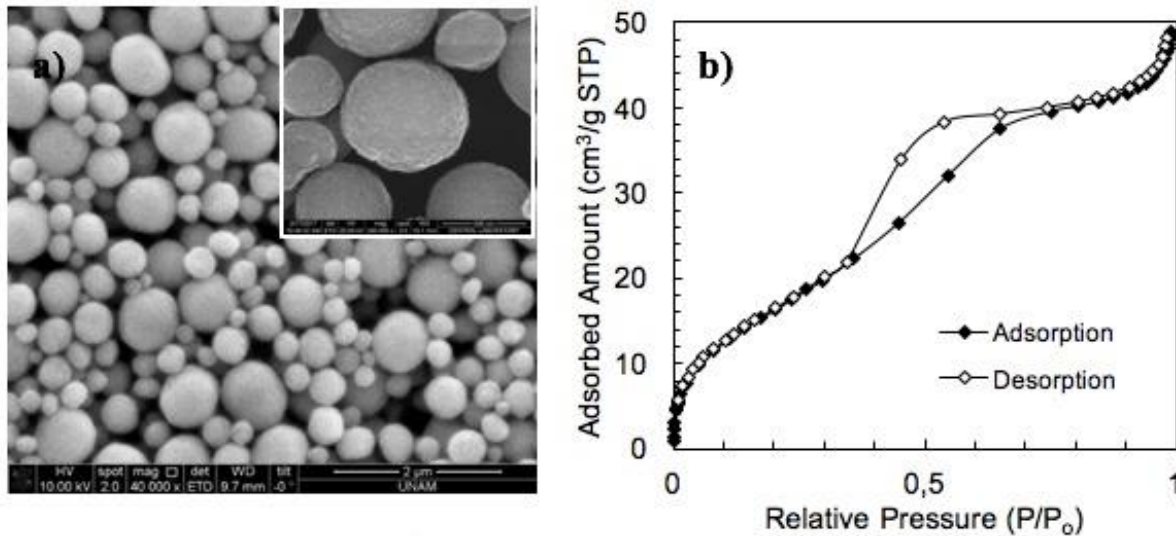


**Figure 3**: (a) SEM micrographs (inset: 200 kX) and (b) $N_2$ adsorption-desorption isotherms of ZnO spheres.

The microstructure of the support before heat treatment can be controlled by the colloidal stability of the suspension. Different colloidal approaches can be used to stabilize the particles in suspensions; *electrostatic stabilization, steric stabilization* and *electrosteric stabilization* (17). To fabricate the support with homogeneous improved properties, colloidal processing of electrostatically stabilized alumina suspension was used. Smooth and homogeneous support surface with roughness less than the membrane thickness is desirable for defect free, continuous thin film formation. Figure 4 shows SEM images of supports prepared by vacuum filtration. We did not observe any surface defects like a print of gas bubbles in the suspension, contamination with a foreign particles or abnormal grain growth. Low surface roughness with well packed particles have been obtained for both supports. Open pore structures were obtained for both types of supports without any partial closure of the surface pores. Figure 4.b shows SEM image of top surface of S200 support which is prepared by suspension with a smaller average particle size. The surface of this support is much smoother and densely packed than that prepared by a larger average particle size (Figure 4.b). Smooth and uniform surface properties may be attributed to the colloidal stability of particles in the suspension. However, the extent of such a large particle stability could be enhanced by using different colloidal approach. A graded morphology through the fracture cross-section of the supports can be seen in Figure 4.c and Figure 4.d. This structure is highly desirable to fabricate high flux crack-free thin membranes with high selectivity. Particle size distribution in the suspensions has a strong impact on the formation of this structure since the smaller particles can packed on top during the filtration

forming uniform surfaces with low surface roughness.
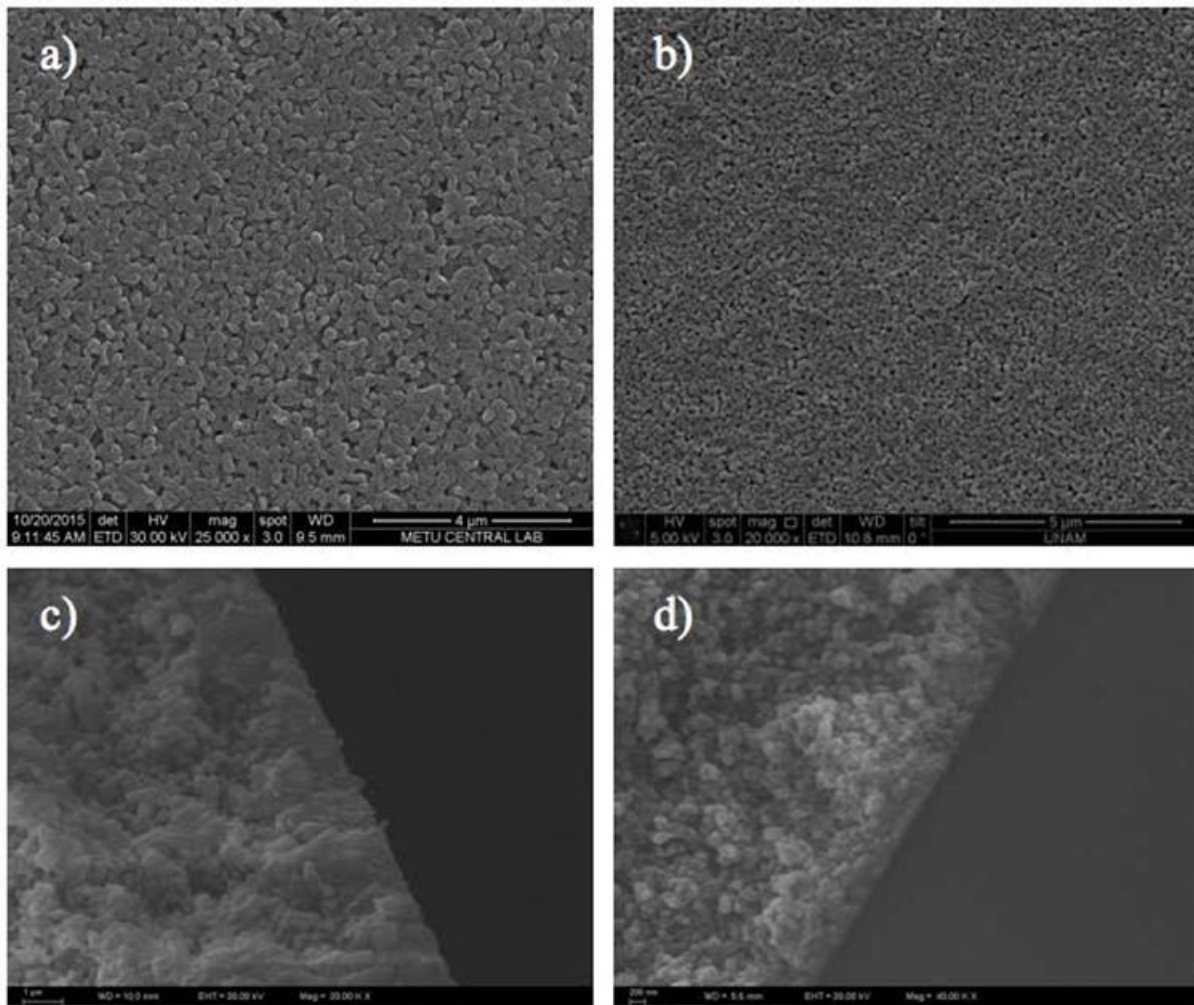


**Figure 4:** SEM images of the α-Al$_2$O$_3$ supports (a) top surface image of S400, (b) top surface image of S200, (c) the fracture of cross-section of S400, (d) the fracture of cross-section of S200.

Figure 5 shows SEM images of the fracture surfaces of ZnO added alumina supports with corresponding EDS spectra. ZnO added microstructure seems to have much larger surface pores. Although ZnO spheres were not observed in the structure, EDS spectra show the elemental constituents of Zn, Al, and O for both type of the supports. Addition of ZnO to the suspension results in the formation of more open structure by retaining the surface roughness sufficient for thin film coating. The presence of ZnO during the consolidation (vacuum filtration) may affect the packing behavior of alumina particles. However, additional porosity might be related to the dissolution of ZnO spheres in the alumina suspension at pH 2. Since ZnO is an amphoteric oxide, it can easily be dissolved in both acids and bases. It has been reported that ZnO particles could be dissolved completely at pH 1 was observed (18). Therefore, ZnO may behave as a pore-forming agent in the support structure by creating new pores after dissolution.
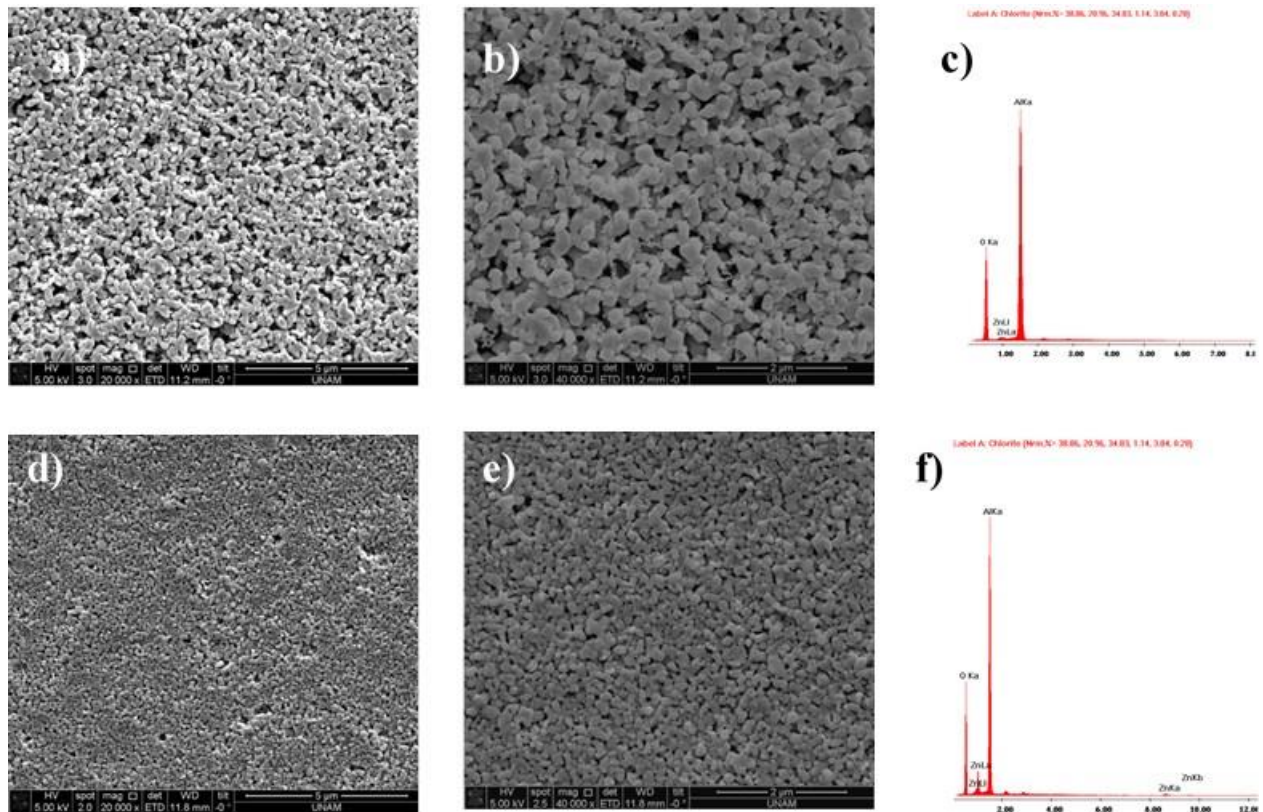
**Figure 5:** SEM images of ZnO added α-Al$_2$O$_3$ supports (a) top surface image of S400-Z (20kX), (b) top surface image of S400-Z (40kX), (c) corresponding EDS spectrum of S400-Z, (d) top surface image of S200-Z (20kX), (e) top surface image of S200-Z (40kX), (f) corresponding EDS spectrum of S200-Z.

The membrane supports prepared by vacuum-assisted colloidal filtration had smooth and homogeneous surface microstructure and well suited for the fabrication of the thin film. The microstructure consists of a random close packing of a smaller particle size led to slightly improved surface uniformity (Figure 4b). However, because of well packed support microstructure, these supports have relatively low permeance based on the targets for inorganic membranes (2). S400 and S200 supports at room temperature, had He permeance values of $5 \times 10^{-6}$ mol/(m$^2$sPa) and $1.3 \times 10^{-6}$ mol/(m$^2$sPa), respectively (Figure 6). These values are 8 and 2 times lower than the desired target value of $1 \times 10^{-5}$ mol/(m$^2$sPa). In Figure 6, the He permeance of prepared supports (S400, S200, S400-Z and S200-Z) is given as a function of transmembrane pressure. From this figure, it is clear that the gas resistance of S400 support is 3 times lower compared to that for S200 support. The difference in permeance values can be explained by the difference in the pore sizes and porosity of two supports. The S400 and S200 supports had total Hg-intrusion porosities of 0.30 with 160 nm pores and 0.25 with 100 nm pores, respectively.

He permeance value has increased significantly upon addition of ZnO. S400-Z support has a He permeance in a range of $8.5-8.7 \times 10^{-6}$ mol/(m$^2$sPa) which is very close to the desired

value of $1 \times 10^{-5}$ mol/(m²sPa). However, the permeance enhancement was not significant for S200-Z support. He permeance increased from $1.3 \times 10^{-6}$ mol/(m²sPa) to $1.7 \times 10^{-6}$ mol/(m²sPa) at 1 bar. The increase in ZnO content in S200 may lead to a stronger effect on the permeance. He permeances through the supports showed slight pressure dependence that indicated the contribution of viscous flow to the Knudsen flow.
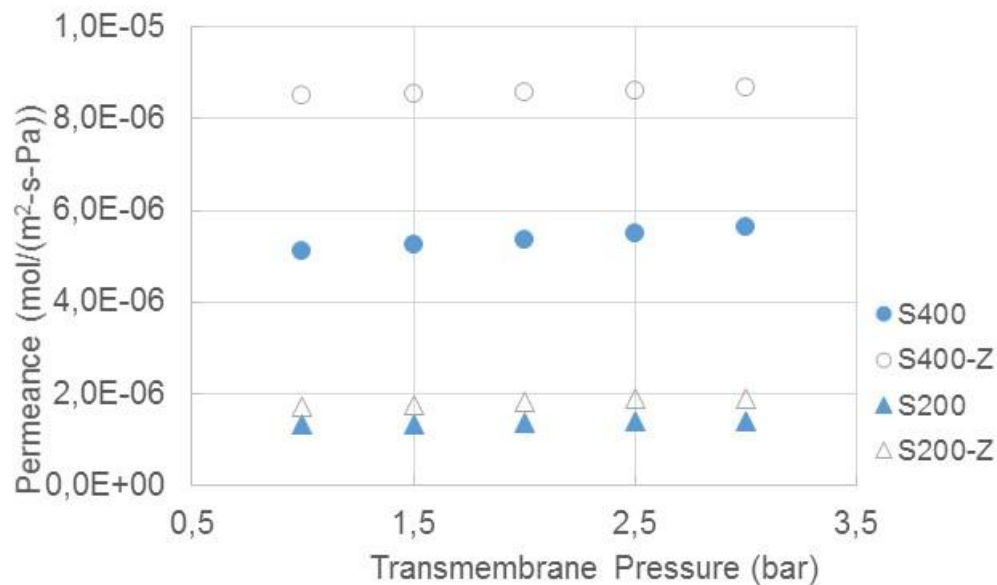


**Figure 6:** Effect of transmembrane pressure on He permeances at 25 °C.

The addition of ZnO improved the permeances of $N_2$ and $CO_2$ as well. Figure 7 shows the single gas permeances of He, $N_2$ and $CO_2$ for the prepared supports. The highest permeance values were obtained for S400-Z supports. Knudsen selectivities of He/$CO_2$ and He/$N_2$ are 3.3 and 2.65, respectively. All prepared supports had almost the same He/$CO_2$ and He/$N_2$ ideal selectivities with a small positive or negative deviation from Knudsen selectivities (Table 2). As a result, ZnO enabled us to increase the support flux by modifying pore structure of S400-Z but less notable influence on S200-Z support flux has been observed.
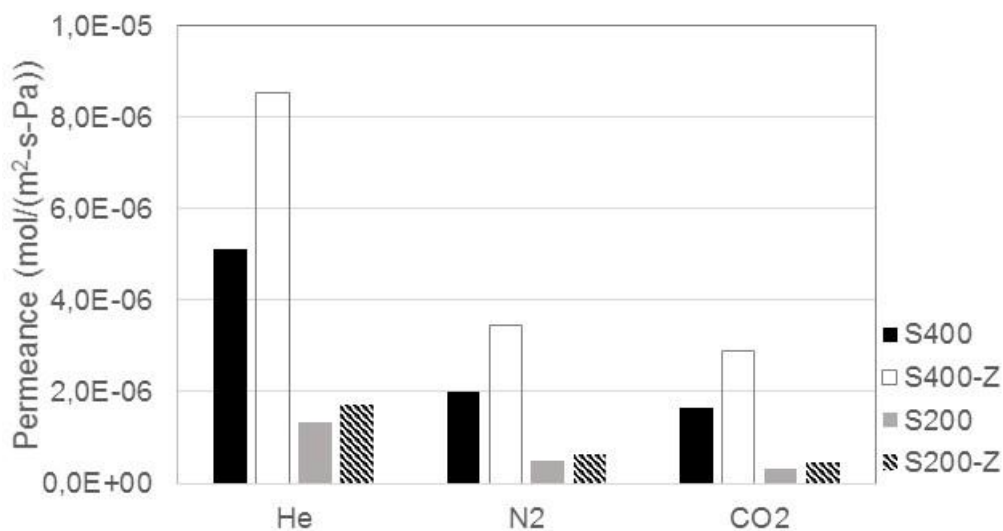
**Figure 7:** He, $N_2$ and $CO_2$ permeances of supports at 25 °C and 1 bar.

**Table 2**: He/$N_2$ and He/$CO_2$ ideal and Knudsen selectivities

| Support Code | He/$N_2$ | He/$CO_2$ | (He/$N_2$)$_{KD}$ | (He/$CO_2$)$_{KD}$ |
|---|---|---|---|---|
| S400 | 2.60 | 3.10 | 2.65 | 3.30 |
| S400-Z | 2.50 | 2.95 | | |
| S200 | 2.80 | 3.95 | | |
| S200-Z | 2.80 | 3.70 | | |

He permeances through the supports as a function of temperature are given in Figure 8. He permeance decreased with decreasing temperature. Knudsen flow effect can be observed in these figures since He permeance for all prepared supports had inverse temperature dependence.
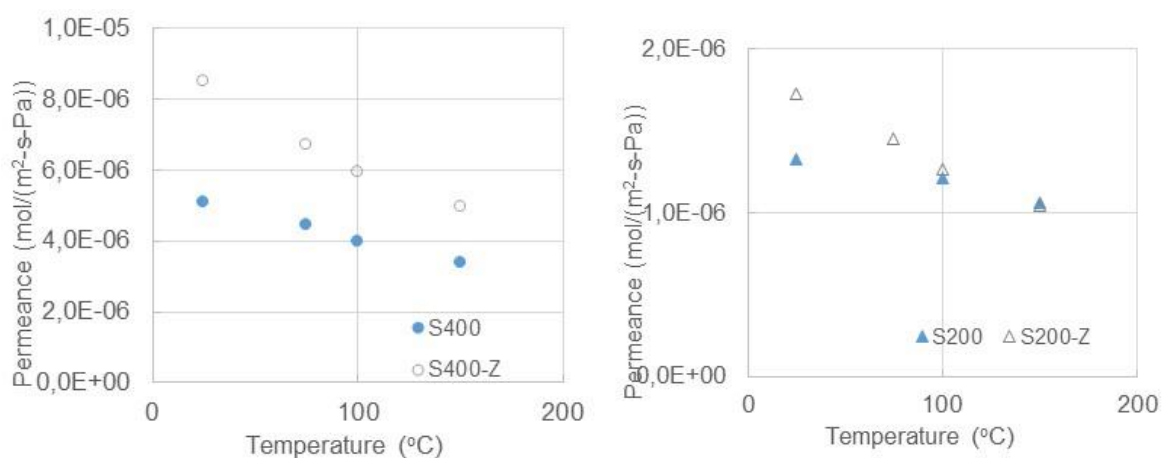


**Figure 8:** (a) He permeances through S400 and S400-Z (left) and S200 and S200-Z supports (right) as a function of temperature.

The Knudsen transport is valid for the pores mostly in mesoporous range between 10 nm and 100 nm, while the viscous flow is dominant in large pores. When the mean free path is comparable to pore size (at intermediate pore size) both viscous and Knudsen flow are significant (19). Since the pore size of the supports exceed 100 nm and observed slight pressure dependency in He permeance He (Figure 6), both Knudsen and viscous flow can be considered to describe the transport mechanism in the supports;

$$F = -\frac{1}{RTl}\left(D_{Kn} + \frac{B_0}{\eta}P_m\right) \qquad \text{(Eq. 1)}$$

where, F is the permeance, R is the gas constant, T is the absolute temperature, $l$ is the support thickness, $P_m$ is the average pressure across the support, $\eta$ is the viscosity. $D_{Kn}$[1] (Knudsen diffusivity) and $B_o$[2] include structural parameters like $\varepsilon$ (porosity), $d_p$ (pore diameter) and $\tau$ (tortuosity). From Eqn. 1, plotting $F$ versus $P_m$ should result in a straight line where intercept and the slope is represented by the contribution of Knudsen flow and viscous flow, respectively. If the Eqn. 1 is rearranged and plotting $Rl(MT)^{0.5}F$ versus $(M/T)^{0.5}$ $P_m/\eta$ gives a straight line in which the structural factors of $K_o$ and $B_o$ can be obtained from intercept and slope, respectively ($M$ is the molecular weight of the gas molecule). Figure 9 shows the change in $RL(MT)^{0.5}F$ with $(M/T)^{0.5}$ $P_m/\eta$ obtained from $N_2$ permeance at temperature of 25°C through the supports and the corresponding linear fitting ($R^2>0.98$). The linear increase in the $N_2$ permeances with mean pressure was observed. In Table 3, calculated structural parameters ($K_o$ and $B_o$) are given for the prepared supports. Differences in the structural parameters indicated that different pore structure formed for all prepared support. The flow induced pore diameter of S200 support was calculated as 115 nm by assuming cylindrical pores which is in agreement with the value of the pore size determined by Hg intrusion measurement (110 nm). Calculated tortuosity (2.3) is also reasonable by using the porosity of 0.25 obtained from Hg-intrusion. Although 2 times higher pore diameter was calculated for S400 support, almost the same tortuosity (2.5) value was calculated by using the Hg-intrusion porosity of 0.3. A higher flow induced pore diameter might be the result of broad pore size distribution o S400 support. Almost same structural parameters obtained for S200 and S200-Z may indicate the small change in porous network upon adding ZnO as confirmed also by small change in gas permeances for both support. The increase in permeance values for S400-Z may be the result of the

---

1 $D_{Kn} = \frac{4}{3}K_0 u$ where $K_o$ ($\frac{1}{4}\frac{\varepsilon}{\tau}d_p$) is the structural factor and $u$ is the mean molecular velocity.

2 $B_0 = \frac{\varepsilon}{\tau}\frac{d_p^2}{32}$

increase in viscous flow contribution to the gas transport resulting low flow induced pore diameter.
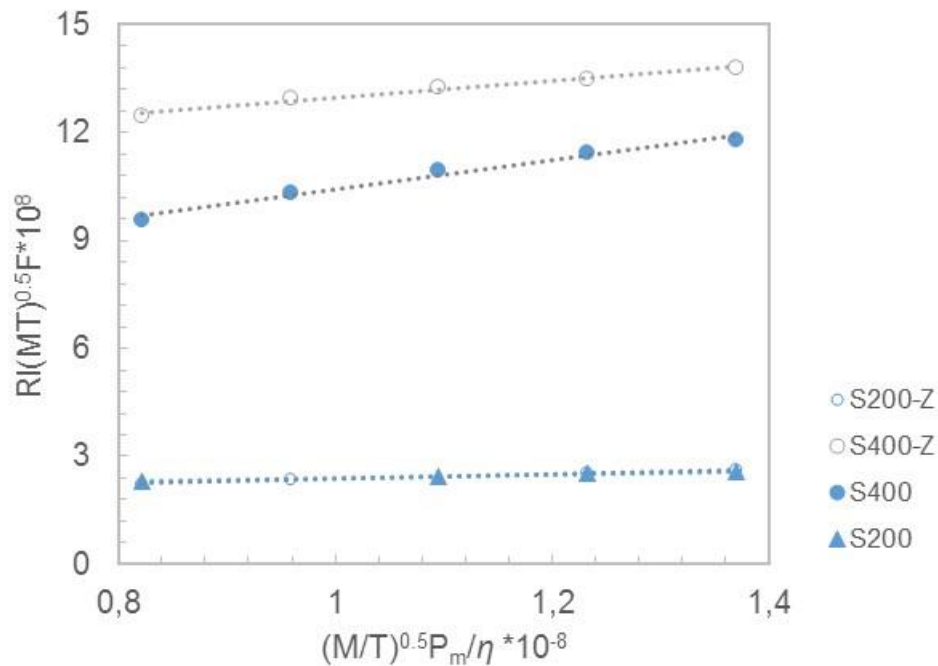


**Figure 9:** The change in $RL(MT)^{0.5}F$ with $(M/T)^{0.5} P_m/\eta$ obtained from $N_2$ permeance at 25 °C.

**Table 3:** Structural parameters obtained from permeance measurements.

| Support Codes | $B_o$ [$10^{17}$] m$^2$ | $K_o$ [$10^9$] m | $D_p$ (nm) | $\frac{\varepsilon}{\tau}$ [-] |
|---|---|---|---|---|
| S400 | 40 | 10.3 | 315 | 0.13 |
| S200 | 4.5 | 3.2 | 115 | 0.11 |
| S400-Z | 33 | 22.6 | 130 | 0.42 |
| S200-Z | 6.7 | 2.8 | 195 | 0.06 |

**CONCLUSIONS**

High-flux macroporous supports with macro-defect free surfaces were successfully prepared by using vacuum-assisted colloidal filtration of alumina suspensions with different particle sizes. The microstructure consists of a random close packing of 200 nm particles led to improved surface uniformity and roughness. However, these supports (S200 and S200Z) exhibited higher gas resistant compared to those prepared with larger particle size. ZnO addition enhanced the He permeance significantly for S400-Z support, but did not affect considerably for S200-Z support. Further research on the influence of added ZnO amount on gas permeances may be clarified the understanding of gas permeation behavior and microstructural changes upon ZnO addition.

**ACKNOWLEDGMENTS**

**REFERENCES**

1. Sholl DS, Lively RP. Seven chemical separations to change the world. Nature. 2016; 532:435-7.

2. Mottern ML, Shqau K, Shi JY, Yu D, Verweij H. Thin supported inorganic membranes for energy-related gas and water purification. International Journal of Hydrogen Energy. 2007; 32(16):3713-23.

3. Agrawal KV, Topuz B, Pham TCT, Nguyen TH, Sauer N, Rangnekar N, et al. Oriented MFI Membranes by Gel-Less Secondary Growth of Sub-100 nm MFI-Nanosheet Seed Layers. Advanced Materials. 2015;27(21):3243-9.

4. Zhou H, Korelskiy D, Sjöberg E, Hedlund J. Ultrathin hydrophobic MFI membranes. Microporous and Mesoporous Materials. 2014;192:76-81.

5. de Vos RM, Verweij H. High-Selectivity, High-Flux Silica Membranes for Gas Separation. Science. 1998;279(5357):1710-1.

6. van Veen HM, Rietkerk MDA, Shanahan DP, van Tuel MMA, Kreiter R, Castricum HL, et al. Pushing membrane stability boundaries with HybSi® pervaporation membranes. Journal of Membrane Science. 2011;380(1):124-31.

7. Bissett H, Zah J, Krieg HM. Manufacture and optimization of tubular ceramic membrane supports. Powder Technology. 2008;181(1):57-66.

8. Mottern M, Chiu W, Warchol Z, Shqau K, Verweij H. High-performance membrane supports: A colloidal approach to the consolidation of coarse particles. International Journal of Hydrogen Energy. 2008;33(14):3903-14.

9. Chang CH, Gopalan R, Lin YS. A comparative study on thermal and hydrothermal stability of alumina, titania and zirconia membranes. Journal of Membrane Science. 1994;91(1–2):27-45.

10. Larbot A, Alami-Younssi S, Persin M, Sarrazin J, Cot L. Preparation of a γ-alumina nanofiltration membrane. Journal of Membrane Science. 1994;97:167-73.

11. Bruni YL, Garrido LB, Aglietti EF. Effect of high alumina cement on permeability and structure properties of ZrO2 composites. Ceramics International. 2012; 38(3):1755-63.

12. Shojai F, Mäntylä T. Monoclinic Zirconia Microfiltration Membranes: Preparation and Characterization. Journal of Porous Materials. 8(2):129-42.

13. Van Gestel T, Vandecasteele C, Buekenhoudt A, Dotremont C, Luyten J, Leysen R, et al. Alumina and titania multilayer membranes for nanofiltration: preparation, characterization and chemical stability. Journal of Membrane Science. 2002; 207(1):73-89.

14. Cesarano J, Aksay IA. Processing of Highly Concentrated Aqueous α-Alumina Suspensions Stabilized with Polyelectrolytes. Journal of the American Ceramic Society. 1988;71(12):1062-7.

15. Agrawal KV, Topuz B, Jiang Z, Nguenkam K, Elyassi B, Francis LF, et al. Solution-processable exfoliated zeolite nanosheets purified by density gradient centrifugation. AIChE Journal. 2013; 59(9):3458-67.

16. Lin L, Zhang T, Liu H, Qiu J, Zhang X. In situ fabrication of a perfect Pd/ZnO@ZIF-8 core-shell microsphere as an efficient catalyst by a ZnO support-induced ZIF-8 growth strategy. Nanoscale. 2015;7(17):7615-23.

17. Lewis JA. Colloidal processing of ceramics. Journal of the American Ceramic Society. 2000;83(10):2341-59.

18. Mudunkotuwa IA, Rupasinghe T, Wu C-M, Grassian VH. Dissolution of ZnO Nanoparticles at Circumneutral pH: A Study of Size Effects in the Presence and Absence of Citric Acid. Langmuir. 2012;28(1):396-403.

19. Gao X, Bonilla MR, Costa JCDd, Bhatia SK. The transport of gases in macroporous α-alumina supports. Journal of Membrane Science. 2012; 409-410:24-33.

# Radical Scavenging Activity and Chemical Composition of Methanolic Extract from *Arum dioscoridis* SM. var. *dioscoridis* and Determination of Its Mineral and Trace Elements

## Erdal YABALAK

Mersin University, Faculty of Arts and Science, Department of Chemistry, Mersin TR-33343, Turkey

**Abstract:** *Arum dioscoridis* SM. var. *dioscoridis* (*A. dioscoridis*) which is a member of Arum L. genus and belonging to Araceae family was extensively analyzed in detail. DPPH free radical scavenging capacity *of A. dioscoridis* was obtained as 0.01091 mg gallic acid (GA) and 0.0929 mg Trolox (Tr) equivalent per mg of extract, respectively, based on DPPH free radical scavenging activity analysis. Chemical composition of *A. dioscoridis* was evaluated and 16 compounds were detected in the methanolic extract using GC-MS. Obtained compounds were assessed for their health benefits according to literature works. 20 elements were obtained in the mineral and trace element analysis by ICP-MS using microwave digestion procedure.

## INTRODUCTION

Araceae is a large plant family represented by 3800 species in 118 genera spreading in a wide range of ecological habitats from sea level to 3000 m of height (1). *Arum* L., which is known as a genus of flowering plants of Araceae family, is represented by 26 species that are distributed in Northern Africa, Mediterranean region, Western Asia, and Europe (2). The species of *Arum* L. have been widely used in folk medicine to prevent several chronic diseases such as stomach acidity, atherosclerosis, cancer, and diabetes. In addition, these plants have been used in traditional treatment methods and were consumed as daily nutrients (3-4). As a member of *Arum* L., *A. dioscoridis* is traditionally used in the Mediterranean gastronomy (5). While Asian, European and especially Turkish people are familiar to Arum taxa, very few studies have been detected concerning *A. dioscoridis*.

Free radical species that are formed as a result of metabolic activities threaten human health. Antioxidants can effectively prevent the tissue or cell damages caused by free radicals through scavenging chain between radicals. Thus, antioxidants protect living cells against many chronic diseases, such as cancer, diabetes, and cardiovascular disease (6-8).

Natural food, including traditional herbs, provide antioxidative components such as polyphenols. Various plants contain phenolic compounds, which are known as powerful antioxidant agents that are used to prevent oxidative reactions (9). In addition, phytochemical compounds, involving polyphenols and other antioxidants, have anti-mutagenic and anti-carcinogenic activities, anti-inflammatory, and neuroprotective effects (10). Therefore, we need to know and consume the food or plants containing antioxidative compounds.

2,2-Diphenyl-1-picrylhydrazyl (DPPH$^\bullet$) free radical scavenging activity method comes to prominence due to its applicability and fastness, comparing various methods used for evaluating antioxidant activity (11) . DPPH$^\bullet$ is used to measure the radical scavenging properties of an electron or hydrogen atom donating components, thanks to its colorful nature (12-14). In the present study, *A. dioscoridis* was investigated for determining its total radical scavenging activities in the methanolic extract.

The identification of mineral and trace element composition and chemical composition of *A. dioscoridis* is another point of the investigation that is firstly done within this work. In addition, mineral and trace element composition of herbs is of great importance and draws researchers' attention due to their medical and nutritional benefits (15). Minerals play a key role in the formation of bio-active components which have great importance for metabolic processes such as human development and health (16). Furthermore, mineral and trace elements can positively or adversely affect health due to the insufficient or excessive intake of them (17). Thus, 20

elements and their levels found in *A. dioscoridis* (B, Na, Mg, Al, P, K, Ca, Cr, Mn, Fe, Co, Ni, Cu, Zn, As, Se, Cd, Sn, Ba, Pb) as well as 16 chemical components were demonstrated by this study.

## MATERIALS AND METHODS

### Materials and instruments

$HNO_3$, HCl, and $H_2O_2$ were obtained from Merck (Darmstadt, Germany), Tr, GA, $C_7$-$C_{40}$ saturated alkane standard mixture and DPPH were obtained from Sigma-Aldrich (St. Louis, MO), Argon and Helium gases were obtained from Linde Gas (Turkey). Syringe filter (0.45 $\mu$L) was supplied by Agilent (Wilmington, DE, USA). Aqueous solutions were prepared using ultra-pure water (Millipore Milli-Q Advantage A10).

Soxhlet apparatus, rotary evaporator (Hei-VAP, Heidolph Instruments, Germany), UV-1601 spectrophotometer (UV-1601, Shimadzu, Japan), GC-MS (GC: 7890A, MS: 5975C, Agilent, USA), ICP-MS equipped with octopole reaction system (Agilent 7500ce, USA), and microwave system (CEM MARS 250/40, CEM Corporation, USA) were used throughout this work.

### Collection and characterization of plant material

Specimens of *A. dioscoridis* were collected from Mersin, Yenişehir, Akkent, open-field, 10-20 m, EY201704 in 15.04.2017 by the author and identified by Assoc. Prof. Dr. Rıza Binzet. The specimens are deposited with a deposit number of 7810 in the research herbarium of the biology department of Mersin University, Turkey.

### Preparation and extraction of the plant sample

*A. dioscoridis* samples were air-dried at room temperature in the dark for 45 days and were milled. 10 grams of crushed and homogenized sample was used in each triplicated Soxhlet extraction experiment. Samples were refluxed with methanol for 4 hours. Each extract was concentrated to 50 mL at 40 °C using a rotary evaporator.

### Radical scavenging activity assay by DPPH radical

Free radical scavenging activity of methanolic extract of *A. dioscoridis* was evaluated according to DPPH method. This method, which we mentioned in our previous work (14) and briefly summarized below, has been previously reported by Dziri *et al.* (18). Firstly, 2 mL of $10^{-3}$ M DPPH solution was added to 1 mL of each concentrated methanolic extract containing 0.5 to 12 mg of dried *A. dioscoridis* per mL of solution. Subsequently, the resulting mixture was kept in the dark for 15 minutes at room temperature to complete the reaction between the components exhibiting antioxidant properties and the DPPH radical. After keeping time, UV absorbance of each sample mixture was recorded at 515 nm. Finally, scavenging activity of samples was calculated in percentages by comparing recorded absorbance of samples and of stock DPPH

solution according to the equation given in our previous work (14). In addition, the $IC_{50}$ value of the methanolic extract of *A. dioscoridis* was determined by using Figure 1 which shows the curves of DPPH free radical scavenging activity against concentration of extracts. Furthermore, the $IC_{50}$ value of the methanolic extract of *A. dioscoridis* was calculated as mg of gallic acid equivalent (GAE) and mg of Trolox equivalent (TrE per mL of the extract, respectively, against DPPH• stock solution according to the previously identified $IC_{50}$ values of GA and Tr, respectively (14).

**Chemical composition assay**

The chemical composition of *A. dioscoridis* was determined by analyzing methanolic extract of *A. dioscoridis* using GC-MS in the scanning range of $M^+=50-550$ m/z. 1 $\mu$L of the concentrated extract was filtered through 0.45 $\mu$L syringe filter and injected to GC-MS injection port (250 °C) in splitless mode. The extract was eluted using HP5-MS capillary column (30m x 0.25 mm x 0.25 μm) at helium gas flow rate of 1.75 mL $min^{-1}$ under fixed 21.21 psi of pressure. The analysis was held for a total of 70 minutes by applying following temperature program for elution of the sample. The temperature of the oven was gradually enhanced after keeping at 50 °C for 2 minutes. Later on, it was enhanced to 100 °C at 5 °C $min^{-1}$ and held for 5 minutes. Then, it was increased to 150 °C at 5 °C $min^{-1}$ and held for 8 minutes. Finally, increased to 250 °C at 5 °C $min^{-1}$ and kept for 15 minutes. The Kováts index of each compound was determined using C7-C40 Saturated Alkane Mixture, a certified reference material, which contains each C7-C40 component in a concentration of 1000 μg in mL of hexane.

**Mineral and trace element composition assay**

Dried samples of *A. dioscoridis* were acid-digested using microwave system. 12 mL of $HNO_3$-HCl digestion mixture and 12 mL of $H_2O_2$ were mixed with 0.5 g of sample in microwave vessels. Then, the vessels were held in the microwave oven for 20 minutes at 200 °C for the digestion process. Finally, the obtained acidic solution was diluted to 50 mL with ultrapure water. The analysis was repeated three times and the average values of obtained results were given along with their standard deviation values in Table 3.

The metal content was determined by ICP-MS applying the following conditions. RF power was set to 1500 W. Flow rates of plasma gas, carrier gas, and auxiliary gas was fixed to 15 L $min^{-1}$, 1 L $min^{-1}$, and 1 L $min^{-1}$, respectively. Nebulizer pump was set to 0.1 rps, and temperature of spray chamber was set to 2 °C. Samples were introduced at a fixed flow rate of 1 L $min^{-1}$. The determinations were carried out by an external calibration method using internal standard mixture formed of Li, Sc, Ge, Y, In, Tb and Bi and prepared in 2 % $HNO_3$ matrix. Ten-point calibration curves using NIST single element reference standards ($R^2 \geq 0.999$) were employed.

**RESULTS AND DISCUSSION**

**Evaluation of extraction method**
Since the selection of the method in the extraction process is a crucial, effective, reliable, and reproducible method is required for extraction of *A. dioscoridis*. Herein, Soxhlet extraction method has a wide application area in scientific works and in industrial applications in the analysis of antioxidant potential and total phenolic content of various matrices (18-20). In addition, methanol can provide high extraction of antioxidative and polyphenolic compounds as indicated in previous works (20-22). The relative ease of evaporation when comparing to water provides an advantage and thus provides ease of operation. Based on the features mentioned above, Soxhlet extraction method was applied in the extraction process and methanol was used as a solvent.

**Evaluation of radical scavenging activity assay**
Application and popularity of DPPH method has been increasing day by day, as it offers many advantages such as being a cheap, easy, rapid, and effective method. In addition, it does not require a sample preparation step (13, 23-25). Thus, DPPH method was performed to evaluate the radical scavenging activity of *A. dioscoridis*. Figure 1 demonstrates the DPPH free radical scavenging activity percentages (inhibition rates) against the concentration of methanolic extracts. In addition, Figure 1 also demonstrates the $IC_{50}$ value of *A. dioscoridis* as 2.422 mg $mL^{-1}$.
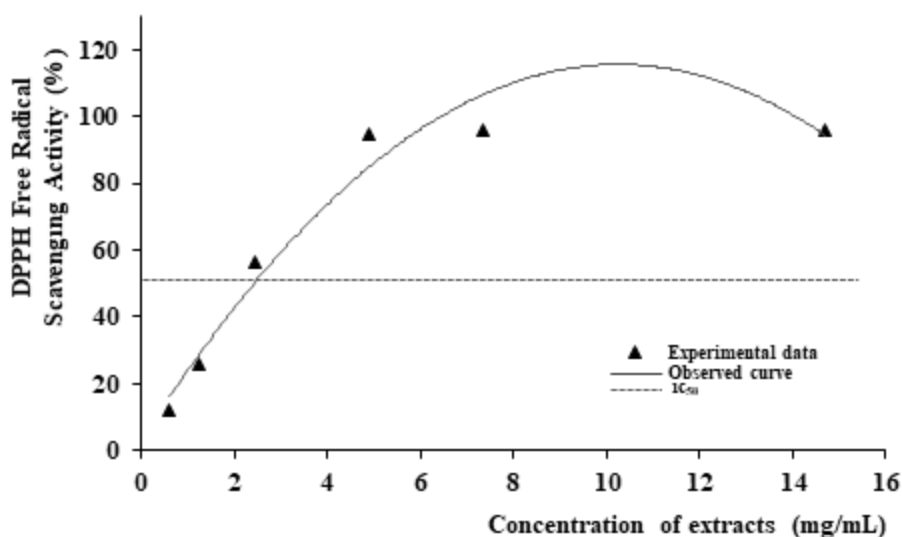


**Figure 1:** DPPH radical scavenging activity of methanolic extract from *A. dioscoridis*.

Furthermore, the radical scavenging capacity of *A. dioscoridis* was evaluated according to GA and Tr standards, which are known as natural and highly antioxidative compounds (26, 27). Thus, the $IC_{50}$ value of *A. dioscoridis* was calculated according to $IC_{50}$ values of GA and Tr, which were given in our previous work (14).

**Table 1:** $IC_{50}$ value of *A. dioscoridis* and radical scavenging activity values of standards and *A. dioscoridis*

| $IC_{50}$ value of *A. dioscoridis* (mg mL$^{-1}$) | $IC_{50}$ values of standards (mg mL$^{-1}$) | | $IC_{50}$ equivalent values of *A. dioscoridis* (mg mL$^{-1}$) | |
|---|---|---|---|---|
| | GA | Tr | GAE | TrE |
| $2.242 \pm 8.185 \times 10^{-3}$ | $0.02642 \pm 7.55 \times 10^{-5}$ | $0.225 \pm 5.292 \times 10^{-3}$ | $0.01091 \pm 7 \times 10^{-5}$ | $0.0929 \pm 8.72 \times 10^{-4}$ |

Table 1 demonstrates the results of radical scavenging activity assay. Results of triplicated experiments were given along with their standard deviations. Radical scavenging activity of *A. dioscoridis* was calculated as $0.01091 \pm 7 \times 10^{-5}$ mg GAE and $0.0929 \pm 8.72 \times 10^{-4}$ mg TrE per mL of extract with the help of the $IC_{50}$ values of GA and Tr of $0.02642 \pm 7.55 \times 10^{-5}$ mg mL$^{-1}$ and $0.225 \pm 5.292 \times 10^{-3}$ mg mL$^{-1}$, respectively.

Kalogeropoulos *et al.* obtained DPPH radical scavenging activity values of ethanolic extracts of 6 propolis samples which are collected from various sites from 0.33 to 1.33 mmol Tr/g ethanolic extract of propolis (28). It was obtained in the present study that *A. dioscoridis* has higher radical scavenging activity than the findings of Kalogeropoulos *et al.*

Oliveira *et al.* analyzed DPPH radical scavenging activity of ethanolic extracts of two different types of commercial tea, and two plants (Brazilian cherry and *Moringa oleifera*) using electrochemical and spectrophotometric methods (29). The lower $IC_{50}$ value, which is known as the concentration of a compound or sample etc. to scavenge DPPH radicals by 50 %, the higher radical scavenging activity. So, it is obvious that *A. dioscoridis* has a reasonably high antioxidative capacity considering these consequences.

**Evaluation of Chemical composition**

16 compounds which are detected in the methanolic extract of *A. dioscoridis* were given in Table 2 along with their retention times ($t_r$), names, chemical formulas, molecular weights (g mol$^{-1}$), peak areas (%), peak qualities (%), Kováts indices (KI), literature retention indices (RIL), and reference numbers.

Accuracy and reliability of gas chromatography method can be increased and standardized by using retention indices. Kováts indices, which can be obtained from the equation developed by Kováts in 1958, are widely used (30-31).  A mixture of saturated alkanes (C7-C40) is analyzed in the GC and Kováts indices are calculated by comparing retention times of each compound with the components of the mixture according to the mentioned equation. In this way, though GC conditions, such as pressure and volume of carrier gas, column length, *etc.* affect retention times, they do not affect the KI. In addition, literature retention indices were given for all compounds in Table 2. It is clearly shown that Kováts indices for detected compounds are sufficiently compatible with the literature retention indices.

The identification of obtained compounds was carried out by a computerized procedure. This method is simply based on matching the mass spectrum of the detected compounds with Wiley 7 Nist05.L and NIST05a.L, which are the mass spectral libraries of the GC-MS system.

When Table 2 is examined, it is seen that all compounds are above 74% of the quality ratios. Furthermore, despite the compounds given in Table 2 show antioxidative properties one by one or collectively, their characteristics may vary widely. The detected compounds were comprehensively evaluated from many perspectives below according to previous works.

Jordán *et al.* obtained the concentration of 2-cyclopentene-1-one (C. No. 1) as 0.50 ppm in passion fruit essence (32). Also, KI of 796.12 for 2-cyclopentene-1-one is compatible with their results (802). 2-cyclopentene-1-one was proved to be effective in the treatment of inflammatory diseases by Ianaro *et al.* (33). Valeric aldehyde (pentanal) (C. No. 2) was reported by Warner *et al.* as a volatile flavor of vegetable oil and could be used as indicators of oil quality (35). 2,3-Dihydro-3,5-dihydroxy-6-methyl-4H-pyran-4-one (C. No. 3) was reported by Xu *et al.* to be found in the extracts of fungus *Paecilomyce* sp. isolated from *Panax ginseng*. They pointed out that the obtained extract has a potential of antifungal and antitumor activities (36).

**Table 2:** Components detected by GC-MS obtained from methanolic extract of *A. dioscoridis*

| C. No. | $t_r$ | Compound Name | Chemical Formula | Molecular Weight (g/mol) | Peak Area (%) | Quality (%) | KI | RIL | Ref. No |
|---|---|---|---|---|---|---|---|---|---|
| 1 | 8.23 | 2-Cyclopentene-1-one | $C_5H_6O$ | 82.10 | 4.4 | 74 | **796.12** | 802 | 32 |
| 2 | 12.66 | Valeric aldehyde | $C_5H_{10}O_2$ | 86.13 | 1.34 | 82 | **735.41** | 698 | 34 |
| 3 | 14.95 | 2,3-Dihydro-3,5-dihydroxy-6-methyl-4H-pyran-4-one | $C_6H_8O_4$ | 144.13 | 3.67 | 94 | **1160.48** | 1162 | 36 |
| 4 | 22.02 | p-Vinylguaiacol | $C_9H_{10}O_2$ | 150.07 | 0.24 | 95 | **1318.65** | 1315 | 37 |
| 5 | 30.14 | Formanilide | $C_7H_7NO$ | 121.14 | 0.13 | 63 | **1620.96** | nd | na |
| 6 | 44.40 | Neophytadiene | $C_{20}H_{38}$ | 278.52 | 0.16 | 91 | **1836.42** | 1830 | 38 |
| 7 | 47.15 | Palmitic acid | $C_{16}H_{32}O_2$ | 256.42 | 0.06 | 86 | **1957.32** | 1957 | 39 |
| 8 | 48.19 | Elaol | $C_{16}H_{22}O_4$ | 278.34 | 0.29 | 95 | **1972.36** | 1960 | 41 |
| 9 | 49.64 | Stearyl alcohol | $C_{18}H_{38}O$ | 270.50 | 0.15 | 58 | **2071.57** | 2084 | 42 |
| 10 | 52.89 | Linoleic acid ethyl ester | $C_{20}H_{36}O_2$ | 308.50 | 0.58 | 99 | **2141.51** | 2144 | 43 |
| 11 | 53.03 | Linolenic acid | $C_{18}H_{30}O_2$ | 278.43 | 1.08 | 99 | **2156.52** | 2154 | 45 |
| 12 | 56.91 | Oleamide | $C_{18}H_{35}NO$ | 281.48 | 3.80 | 87 | **2189.45** | nd | na |
| 13 | 60.83 | 1-Eicosanol | $C_{20}H_{42}O$ | 298.56 | 2.43 | 97 | **2286.74** | 2290 | 47 |
| 14 | 64.80 | 1-Docosanol | $C_{20}H_{46}O$ | 326.61 | 1.87 | 91 | **2501.41** | 2493 | 47 |
| 15 | 68.26 | γ-Tocopherol | $C_{28}H_{48}O_2$ | 416.68 | 0.46 | 90 | **3108.23** | 3074 | 48 |
| 16 | 70.30 | α-Tocopherol | $C_{29}H_{50}O_2$ | 430.71 | 5.57 | 99 | **3152.43** | 3149 | 48 |

tr: Retention times, C. No: Component number, KI: Kováts index, RIL: Retention Index obtained from literature, nd: not detected, na: not available.

Asuming *et al.* detected *p*-vinylguaiacol (2-methoxy-4-vinylphenol) (C. No. 4) in their investigation of essential oil composition of four *Lomatium* Raf. species. They defined the percent of *p*-vinylguaiacol and other components in percent of oil from fruits, stems and leaves, and roots of each herb (37). Palic *et al.* obtained neophytadiene (C. No. 6) as one of the major components of the essential oil of the oriental tobacco, Prilep (38). Also, they pointed out that the extract which contains the mentioned component has antimicrobial activity against the microorganisms (38). In addition, KI value of neophytadiene is in good agreement with their findings. Palmitic acid (hexadecanoic acid) (C. No. 7) was reported as a component of the essential oil of *Phlomis ferruginea* Ten. by Formisano *et al.* Their results for KI value of palmitic is in very good agreement with our results (39). In addition, Lalitharani *et al.* pointed out in their work that palmitic acid has an antioxidative activity potential, in which they identified the components of the ethanolic extract of *Pothos scandens* L. leaf using GC-MS (40). Stearyl alcohol (octadecane-1-ol) (C. No. 9) was found in the extract of Mentha spp. Honey and the Bee-Stomach, which was reported by Jerković *et al.* (42). Linoleic acid ethyl ester (Ethyl linoleate) (C. No. 10) was found as a member of the main fraction of volatile constituents of *Ailanthus excelsa* Roxb. by Tzakou *et al.* (43). In addition, Park *et al.* showed the anti-inflammatory activity of linoleic acid ethyl ester detected in the extract of *Allium sativum* (44). Linoleic acid (C. No. 11) was reported to be found in various percentages composition in essential oil from flowers, leaves, and stems of *Wisteria brachybotrys* by Miyazawa *et al.* (45). Additionally, Hu *et al.* pointed out that Linoleic acid (α-Linolenic acid) (C. No. 11) might reduce the risk of arrhythmia (46). Vedernikov and Roshchin identified 1-eicosanol (eicosyl alcohol) (C. No. 13) and 1-docosanol (behenic alcohol) (C. No. 14) along with two unsaturated fatty acids, linoleic acid, and linolenic acid, in the *Betula pendula* Roth. extract (47). Finally, two bio-active compounds, namely γ-tocopherol (Vitamin E) (C. No. 15) and α-tocopherol (Vitamin E) (C. No. 16), types of vitamin E, were detected in the extract of the methanolic extract of *A. dioscoridis* (49-50). These compounds are also known as the endogenous antioxidant and α-tocopherol is known for its peroxyl radical scavenging activity (51).

**Evaluation of mineral and trace element composition**

Mineral and trace elements have crucial roles in various metabolic processes (52,53). Although deficiency or excess levels of trace elements cause certain diseases (53), some are nutritious for humans (54). Thus, the determination of mineral and trace element is of great importance.

**Table 3:** Concentration levels (ppm) of metals in dried *A. dioscoridis*.

| B | Na | Mg | Al | P | K | Ca | Cr | Mn | Fe |
|---|---|---|---|---|---|---|---|---|---|
| nd | 636.0±5.7 | 1301.4±7.3 | 331.1±2.9 | 218.9±3.4 | 4142.0±9.3 | 14406.6±18.8 | 0.3 ±0.01 | 16.9 ±0.7 | 370.6±3.6 |

| Co | Ni | Cu | Zn | As | Se | Cd | Sn | Ba | Pb |
|---|---|---|---|---|---|---|---|---|---|
| 0.7 ±0.01 | 9.1 ±0.9 | 38.9 ±1.2 | 83.2 ±2.4 | nd | nd | 0.004 ±0.00 | 0.68 ±0.01 | 14.2 ±0.9 | 0.61 ±0.01 |

nd: not dedected

Table 3 demonstrates the concentration values of metals in ppm in the dried mass of *A. dioscoridis*. The highest values were obtained for Ca as 14406.6 ppm and the lowest value was obtained as 0.004 ppm for Cd. However, B, As, and Se were found to remain under detection limits. Comparatively high concentration of Na, Mg, P, K, Ca, Mn, Fe, Cu and Zn, which are known for their nutritional benefits are favorable (54). Nevertheless, trace elements such as Co, Ni, Cd, Sn, Ba, and Pb, which adversely affect human health due to their toxic potential, were obtained in considerably low levels (54, 55).

The soil of planting and the fertilizers used by the plant, as well as the plant structure, are influential in the diversity of the plant's elemental composition (56). However, the presence of Cd and Pb may also be due to exposure of the plant to exhaust fumes or other contaminants, as the plant is collected from the open area within the city.

## CONCLUSION

Being widely used as a food herb and owing medicinal and economic potential, A. dioscoridis has been widely investigated. The overall radical scavenging capacity of *A. dioscoridis* was determined by employing DPPH free radical scavenging activity analysis. $IC_{50}$ values of methanolic extract from *A. dioscoridis* which were determined as GA and Tr equivalents, suggest that *A. dioscoridis* is a functional herb considering its quite high DPPH radical scavenging capacity. Further, the mentioned $IC_{50}$ values put forward the potential of *A. dioscoridis* to be used as a natural antioxidant for the industrial applications. Considering the pharmaceutical and medicinal importance of 16 compounds, which were detected in the methanolic extract of *A. dioscoridis*, they were evaluated separately by comparing literature work. All compounds were shown to be very rich in terms of their diversity and usefulness. In addition, trace and mineral element composition were determined to assess the nutritional value and possible therapeutic or illness effect. Herein, 20 elements were determined by ICP-MS analysis and their concentration values were evaluated. Further studies should be carried out to determine the detailed biochemical and medicinal effect of this herb.

## ACKNOWLEDGEMENTS

## REFERENCES

1. Henriquez CL, Arias T, Pires JC, Croat TB, Schaal BA. Phylogenomics of the plant family Araceae. Mol. Phylogenet. Evol. 2014; 75: 91-102.

2. Farid MM, Hussein SR, Ibrahim LF, Desouky MAE, Elsayed AM, et al. Cytotoxic activity and phytochemical analysis of Arum palaestinum Boiss. Asian Pac. J. Trop. Biomed. 2015; 5(11): 944-7.

3. Sağlik S, Alpinar K, İmre S. Fatty acid composition of the seed oil of Arum italicum miller. J. Food Lipids. 2002; 9:95-103.

4. Karahan F, Kulak M, Urlu E, Gözüacik HG, Böyümez T, Şekeroğlu N, et al. Total phenolic content, ferric reducing and DPPH scavenging activity of Arum dioscoridis. Nat. Prod. Res. 2015; 29: 1678-83
    I

5. Abu-Reidah, IM, Ali-Shtayeh MS, Jamous RM, Arraez-Roman D, Segura-Carretero A. Comprehensive metabolite profiling of Arum palaestinum (Araceae) leaves by using liquid chromatography–tandem mass spectrometry. Food Res. Int. 2015; 70: 74-86.

6. Halliwell B, Guterridge J, Croos C. Free radicals, antioxidants and human disease: Where are we now? J. Lab. Clin. Med. 1992; 119 598-620.

7. Zhang X, Shi Q, Ji D, Niu L, Zhang Y. Determination of the phenolic content, profile, and antioxidant activity of seeds from nine tree peony (*Paeonia* section *Moutan* DC.) species native to China. Food Res. Int. 2017; 97:141-48.

8. Zou Z, Xi W, Hu Y, Nie C, Zhou Z. Antioxidant activity of Citrus fruits. Food Chem. 2016; 196: 885-96.

9. Limmongkon A, Janhom P, Amthong A, Kawpanuk M, Nopprang P, Poohadsuan J, et al. Antioxidant activity, total phenolic, and resveratrol content in five cultivars of peanut sprouts. Asian Pac. J. Trop. Biomed. 2017; 7(4): 332-8.

10. Skendi A, Irakli M, Chatzopoulou P. Analysis of phenolic compounds in Greek plants of Lamiaceae familyby HPLC. J. Appl. Res. Med. Aromat. Plants. 2017; 6: 62-9.

11. Wollinger A, Perrin E, Chahboun J, Jeannot V, Touraud D, Kunz W. Antioxidant activity of hydro distillation water residues from Rosmarinus officinalis L. leaves determined by DPPH assays. Comptes. Rendus. Chim. 2016; 19(6): 754-65

12. Figueiredo C, Barroso J, Pedro L, Scheefeer J. Factors affecting secondary metabolite production in plants: volatile components and essential oils. Flavour Fragr. J. 2007; 22: 206-13.

13. Demirtas I, Erenler R, Elmastas M, Goktasoglu A. Studies on the antioxidant potential of flavones of Allium vineale isolated from its water-soluble fraction. Food Chem. 2013; 136(1): 34-40.

14. Yabalak E, Gizir A. Evaluation of total polyphenol content, antioxidant activity and chemical composition of methanolic extract from *Allium Kharputense* Freyn et. Sint. and determination of mineral and trace elements. J. Turk. Chem. Soc. Sect. A: Chem. 2017; 4: 691-708.

15. Tokalıoğlu Ş. Determination of trace elements in commonly consumed medicinal herbs by ICP-MS and multivariate analysis. Food Chem. 2012; 134(4): 2504-8.

16. Pytlakowska K, Kita A, Janoska P, Połowniak M, Kozik V. Multi-element analysis of mineral and trace elements in medicinal herbs and their infusions. Food Chem. 2012; 135(2): 494-501.

17. Karak T, Bhagat RM. Trace elements in tea leaves, made tea and tea infusion: A review. Food Res. Int. 2010; 43(9): 2234-52.

18. Dziri S, Hassen I, Fatnassi S, Mrabet Y, Casabianca H, Hanchi B, et al. Phenolic constituents, antioxidant and antimicrobial activities of rosy garlic (Allium roseum var. odoratissimum). J. Funct. Foods. 2012; 4(2): 423-32.

19. Edrisi M, Timothy S, Langrish AG. Spray drying bioactive orange-peel extracts produced by Soxhlet extraction: Use of WPI, antioxidant activity and moisture sorption isotherms. LWT-Food Sci. Technol. 2016; 72: 1-8.

20. Ammar I, Ennouri M, Attia H. Phenolic content and antioxidant activity of cactus (Opuntia ficus-indica L.) flowers are modified according to the extraction method. Ind. Crops Prod. 2015; 64: 97-104.

21. Lim YY, Quah EPL. Antioxidant properties of different cultivars of Portulaca oleracea. Food Chem. 2007; 103(3): 734-40.

22. Jo YH, Seo GU, Yuk HG, Lee SC. Antioxidant and tyrosinase inhibitory activities of methanol extracts from Magnolia denudata and Magnolia denudata var. purpurascens flowers. Food Res. Int. 2012; 47: 197-200.

23. Özcelik B, Lee J, Min D. Effects of Light, Oxygen, and pH on the Absorbance of 2, 2-Diphenyl-1-picrylhydrazyl. J. Food Sci. 2003; 68(2): 487-90.

24. Wang Y, Gao Y, Ding H, Liu S, Han X, Gui J, et al. Subcritical ethanol extraction of flavonoids from Moringa oleifera leaf and evaluation of antioxidant activity. Food Chem. 2017; 218: 152-8.

25. Shalaby EA, Shanab SMM. Antioxidant compounds, assays of determination and mode of action. Afr. J. Pharm. Pharmacol. 2013; 7(10): 528-39.

26. Utrera M, Estévez M. Impact of trolox, quercetin, genistein and gallic acid on the oxidative damage to myofibrillar proteins: The carbonylation pathway. Food Chem.2013; 141(4): 4000-9.

27. Schlesier K, Harwat M, Böhm V, Bitsch R. Assessment of antioxidant activity by using different in vitro methods. Free Radic. Res. 2002; 36(2): 177-87.

28. Kalogeropoulos N, Konteles SJ, Troullidou E, Mourtzinos I, Karathanos VT. Chemical composition, antioxidant activity and antimicrobial properties of propolis extracts from Greece and Cyprus. Food Chem. 2009; 116: 452-61.

29. Oliveira GKF, Tormin TF, Sousa RMF, de Oliveira A, de Morais SAL, Richter EM, Munoz RAA. Batch-injection analysis with amperometric detection of the DPPH radical for evaluation of antioxidant capacity. Food Chem. 2016; 192: 691–7.

30. Kovats E, Gas-chromatographische Charakterisierung organischer Verbindungen. Teil 1: Retentionsindices aliphatischer Halogenide, Alkohole, Aldehyde und Ketone. Helv Chim Acta. 1958; 41(7): 1915-32.

31. d'Acampora Zellner B., Bicchi C, Dugo P, Rubiolo P, Giovanni Dugo, Luigi Mondello. Linear retention indices in gas chromatographic analysis: a review. Flavour Fragr. J. 2008; 23: 297-314.

32. Jordán MJ, Goodner KL, Shaw PE. Characterization of the aromatic profile in aqueous essence and fruit juice of yellow passion fruit (Passiflora edulis Sims F. Flavicarpa degner) by GC-MS and GC/O. J. Agric. Food Chem. 2002; 50(6): 1523-8.

33. Ianaro A, Ialenti A. Maffia P, Di Meglio P, Di Rosa M, Santoro MG, Anti-inflammatory activity of 15-Deoxy-$\Delta^{12,14}$-PGJ$_2$ and 2-Cyclopenten-1-one: role of the heat shock response, Mol. Pharmacol. 2003; 64: 85-93.

34. Pino JA, Mesa J, Muñoz Y, Martí MP, Marbot R. Volatile Components from Mango (Mangifera indica L.) Cultivars. J. Agric. Food. Chem. 2005; 53(6): 2213-23.

35. Warner K, Evans CD, List GR, Dupuy HP, Wadsworth JI, Goheen GE. Flavor score correlation with pentanal and hexanal contents of vegetable oil. J. Am. Oil Chem. Soc. 1978; 55(2): 252-6.

36. Xu LL, Han T, Wu JZ, Zhang QY, Zhang H, Huang BK, et al. Comparative research of chemical constituents, antifungal and antitumor properties of ether extracts of Panax ginseng and its endophytic fungus. Phytomedicine 2009; 16: 609-16.

37. Asuming WA, Beauchamp PS, Descalzo JT, Dev BC, Dev V, et al. Essential oil composition of four Lomatium Raf. species and their chemotaxonomy. Biochem. Syst. Ecol. 2005; 33(1): 17-26.

38. Palic R, Stojanovic G, Alagic S, Nikolic M, Lepojevic Z. Chemical composition and antimicrobial activity of the essential oil and $CO_2$ extracts of the oriental tobacco, Prilep. Flavour Fragr. J. 2002; 17: 323-6.

39. Formisano C, Senatore F, Bruno M, Bellone G. Chemical composition and antimicrobial activity of the essential oil of Phlomis ferruginea Ten. (Lamiaceae) growing wild in Southern Italy. Flavour Fragr J. 2006; 21(5): 848-51.

40. Lalitharani S, Mohan VR, Regini GS, Kalidass C. GC-MS analysis of ethanolic extract of Pothos scandens leaf. J. Herb. Medi. Toxicol. 2009; 3(2): 159-60.

41. Kotowska U, Zalikowski M, Isidorov VA. HS-SPME/GC-MS analysis of volatile and semi-volatile organic compounds emitted from municipal sewage sludge. Environ. Monit. Asses. 2012; 184(5): 2893-7

42. Jerković I, Hegić G, Marijanović Z, Bubalo D. Organic extractives from Mentha spp. honey and the bee-stomach: methyl syringate, vomifoliol, terpenediol I, hotrienol, and other compounds. Molecules. 2010; 15(4): 2911-24.

43. Tzakou O, Said A, Farag A, Rashed K. Volatile constituents of Ailanthus excelsa Roxb. Flavour Fragr J. 2006; 21(6): 899-901.

44. Park SY, Seetharaman R, Ko MJ, Kim DY, Kim TH, Yoon MK, et al. Ethyl linoleate from garlic attenuates lipopolysaccharide-induced pro-inflammatory cytokine production by inducing heme oxygenase-1 in RAW264.7 cells. Int. Immunopharmacol. 2014; 19(2): 253-61.

45. Miyazawa M, Marumoto S, Kobayashi T, Yoshida S, Utsumi Y. Determination of characteristic components in essential oils from Wisteria braphybotrys using gas chromatography-olfactometry incremental dilution technique. Rec. Nat. Prod. 2011; 5(3): 221-7.

46. Hu FB, Stampfer MJ, Manson JE, Rimm EB, Wolk A, Colditz GA, et al. Dietary intake of α-linolenic acid and risk of fatal ischemic heart disease among women[1-3]. Am. J. Clin. Nutr. 1999; 69: 890-7.

47. Vedernikov DN, Roschin VI. Extractive compounds of Birch Buds (Betula pendula Roth.): I. Composition of fatty acids, hydrocarbons, and esters. Rus. J. Bioorg. Chem. 2010; 36(7): 894-8.

48. Andriamaharavo NR. Retention Data. NIST Mass Spectrometry Data Center. 2014.

49. Jiang Q, Christen S, Shigenaga MK, Ames BN. γ -Tocopherol, the major form of vitamin E in the US diet, deserves more attention. Am J Clin Nutr. 2001; 74(6): 714-22.

50. Wagner K-H, Kamal-Eldin A, Elmadfa I. Gamma-tocopherol–an underestimated vitamin? Ann. Nutr. metab. 2004; 48(3): 169-188.

51. Rice-Evans CA, Miller NJ, Paganga G. Structure-antioxidant activity relationships of flavonoids and phenolic acids. Free Radic. Biol. Med. 1996; 20(7): 933-56.

52. Prohaska JR. Functions of trace elements in brain metabolism Physiol. Rev. 1987; 67: 858-901.

53. Carvalho ML, Magalhães T, Becker M, von Bohlen A. Trace elements in human cancerous and healthy tissues: A comparative study by EDXRF, TXRF, synchrotron radiation and PIXE. Spectrochim. Acta Part B: At. Spectrosc. 2007; 62(9); 1004-11.

54. Fraga CG. Relevance, essentiality and toxicity of trace elements in human health, Mol. Aspects Med. 2005; 26: 235-44.

55. Karak T, Bhagat RM. Trace elements in tea leaves, made tea and tea infusion: A review. Food Res Int. 2010; 43(9): 2234-52.

56. Cupit M, Larsson O, de Meeûs C, Eduljee GH, Hutton, M, Assessment and management of risks arising from exposure to cadmium in fertilizers-II. Sci Total Environ. 2002; 291: 189-206.

# Examination of the Effects of Activated Carbon Produced from Coal Using Single-Step H₃PO₄/N₂+H₂O Vapor Activation on the Adsorption of Bovine Serum Albumin at Different Temperatures and pH Values

**Atakan Toprak\*[1] and Kadriye Bozgeyik[2]**

*1Department of Chemistry and Chemical Process Technology, Bülent Ecevit University, 67800 Zonguldak, Turkey*[1]

*2Department of Chemistry, Bülent Ecevit University, 67100 Zonguldak, Turkey*[2]

**Abstract:** This study examined protein adsorption equilibrium and kinetics on activated carbon (AC) that we obtained from coal by single-step $H_3PO_4$ activation under $N_2+H_2O$ vapor at 800 °C. Surface properties, pore size distribution, and volumes of AC were determined using volumetric method with $N_2$ adsorption at 77 K. Also, the textural properties were characterized by SEM-EDAX and XRD. The zeta potential values were measured to elucidate the electrostatic interactions between the protein and AC. The obtained AC discrete system was also used as an adsorbent for adsorbing bovine serum albumin (BSA) from aqueous solution. The effects of pH (4.0, 5.0, and 7.4) and temperatures (20, 30 and 40 °C) on the adsorption of BSA on AC were examined. The surface area, micropore, mesopore and total pore volumes of AC were found to be 1175 $m^2/g$, 0.477 $cm^3/g$, 0.061 $cm^3/g$ and 0.538 $cm^3/g$, respectively. The optimum temperature for AC in BSA adsorption was found to be 40 °C and the pH was found to be 4.0. The highest BSA adsorption was found to be 159 mg/g and pH to be 4.0. The experimental equilibrium data were compared with the Langmuir and Freundlich models and found to be compatible with both models. The adsorption process is best described by the pseudo-first-order kinetic model. As a result, it was found out that AC obtained by single step $H_3PO_4/N_2+H_2O$ vapor activation is an effective adsorbent for the adsorption of BSA from aqueous solution.

**\*Corresponding author. E-mail:** atakantoprak2@hotmail.com**. Tel:** + 90 3725563573-156. **Fax**: + 90 3725563574.

## INTRODUCTION

Protein adsorption on surfaces is a very common phenomenon because it is the first step in many biological processes such as trans-membrane signalling or blood coagulation steps (1, 2). Protein adsorption in artificial tissue scaffolds is a key factor for a favorable vascularity (re-formation of vessels) because protein adsorption can cause thrombosis in biomedical implants interacting with blood flow (3). Moreover, protein adsorption can induce adhesion of the possible inflammation of particles, bacteria, cells and their contamination processes (4). Non-specific protein adsorption on sensor surfaces, protein chips or experiment platforms in the fields of analytical science is a serious problem that disrupts the analytical performance of devices. Indeed, there are intensive studies on biocompatible and protein-resistant materials that can be applied to biomedical implants or analytical platforms, and the vast majority of scientific publications in recent years have contributed extensively to this field (5-8). Progress in this area has taken place during the emergence of grafted polymers (such as PEG, PAA) and self-assembled monolayers (SAM) in particular. However, the rules behind protein rejection are still not fully understood, and it is still necessary to better understand the stability of selected surfaces (9-11)

Protein-surface interactions are influenced by both protein properties and surface properties. Surface energy, surface tension, polarity, surface charge, surface wetting potential and morphology are important parameters affecting protein-surface interactions (12). Scientific studies have generally chosen the type of surface adsorbent that can replace implant materials, cell walls, biosensors or membrane filters. Some typical limitations are introduced according to the experimental techniques applied to the model surfaces (such as atomic flat surfaces whose optical transparency, electrical conductivity or flexibility can be affected). Furthermore, protein is also frequently adsorbed on unmodified surfaces such as quartz, mica, glass, metal or graphite, and modified surfaces obtained with chemical modification of these surfaces (3).

Activated carbon is an adsorbent that is highly versatile in its use, with a high surface area, pore structure and a high degree of surface reactivity. Because of its unique porosity and surface morphology, it is specifically in many areas in industry such as gas adsorption, purification and separation of gaseous mixtures, removal of harmful contaminants, processing of urban and industrial wastewater, fuel cells, adsorption of large molecules and as a catalyst in drug synthesis (13-15). The activated carbons are of interest because they are easy to produce, durable and quite cheap compared to other types of adsorbents (16). The adsorption capacity of the activated carbons is due to the presence of pores suitable

to the molecular size of the adsorbent and the interest of functional groups on the surface to the adsorbent.

Two methods (physical and chemical activation) are mainly used for activated carbon production. Physical activation involves carbonization and activation with steam and $CO_2$ at high temperature. Chemical activation involves the activation of samples impregnated with various activating agents (NaOH, KOH, $H_3PO_4$, $ZnCl_2$, *etc.*) in an inert atmosphere (17, 18).

In this study, we tried to examine protein adsorption on activated carbon obtained by sonication and single-step $H_3PO_4/N_2+H_2O$ vapor activation on an coal sample taken from Zonguldak region (Zonguldak is a province located along the Black Sea coast in the northwest of Turkey, and is also known as a major center of coal production). We chose BSA as a model protein, which is a blood plasma protein. Firstly, the characterization of the activated carbon (surface area, pore distribution, micropore volume) was examined by $N_2$ adsorption at 77 K with volumetric methods, and its morphological characteristics were determined with SEM-EDAX and XRD. BSA adsorption equilibrium and kinetics on activated carbon were then examined for different temperatures and pHs. Zeta potential values were also measured to understand protein-surface interaction.

## MATERIALS AND EXPERIMENTAL

### Materials
BSA and other chemicals were purchased from Sigma Aldrich.

### Activated carbon production
Highly volatile A type bituminous coal (ASTM standards) was taken from Zonguldak region as the starting material and it was made into a size of 100-300 μm (19). Since inorganic materials such as Fe, Al, and Si in the coal sample produce water-insoluble residues such as $FePO_4$, $Al(PO_3)_3$ and $SiO_2P_2O_7$ in activation with $H_3PO_4$, they cause low pore formation and adsorption capacity in activated carbon (20, 21). For this reason, the ash removal process was carried out to eliminate the interaction of $H_3PO_4$ with the inorganic substance in the coal. In the ash removal process the coal was first mixed with 20% HCl for 3 hours at 60°C. The treated sample was washed repeatedly using hot distilled water until the pH reached about 7.0. Then the same process was repeated with 25% HF. As a result of the ash removal, the ash content was reduced to 0.4%, having initially been 4.5% (22).

For AC production, the ash-reduced coal with $H_3PO_4$ was mixed at the rate of 3:1 with magnetic stirrer (1000 rpm) at 70 °C. After the mixture was sonicated for 30 minutes at 60 °C, it was transferred to the quartz tube and kept in the drying-oven at 100 °C overnight. In this method, the water vapor connection was made after the mixture was brought to 800°C under $N_2$ (200 mL/min) in a tube furnace. The mixture was activated with $N_2+H_2O$ vapor for 30 min and allowed to cool under $N_2$. AC obtained after activation was washed with hot distilled water until the pH was 7.0 and then dried in an oven at 110 °C.

**AC analysis methods**: The physical characteristics of AC obtained by one-step $H_3PO_4/N_2+H_2O$ vapor activation were calculated using a Quantachrome AS 1C device with $N_2$ adsorption-desorption at 77 K in the range of 0.01-0.995 of $P/P_0$. AC was degassed under vacuum at 150°C for 5 hours before $N_2$ adsorption at 77 K. BET (Brunauer, Emmett and Teller) and Langmuir surface areas, micro ($V_{micro}$), meso ($V_{meso}$) and total pore volumes ($V_T$) were calculated using $N_2$ isotherm at 77 K. The pore size distributions were determined by DFT (Density Functional Theory) method. The micropore volume ($V_{micro}$) was calculated using the Dubinin Radushkevich (DR) model in the range of 0.01-0.05 of $P/P_0$. The total pore volume ($V_T$) was calculated from the volume value of $N_2$ isotherm at $P/P_0.=0.995$. $V_{meso}$ is obtained by subtracting $V_{micro}$ volume from $V_T$. The surface morphology and element percentage of AC were determined by using an FEI QUANTA FEG 450 (SEM-EDAX) device. The diffraction analysis of AC was measured by PAN-analytical's Empyrean device at the range of $2\theta=10-90°$.

**Adsorption experiments**

For the adsorption equilibrium experiment, 100 mL of BSA solutions with an initial concentration of 500 mg/L were prepared in 250 mL capped conical flasks. The pH of the BSA solutions was adjusted with pH=2.8 ($NaH_2PO_4/H_3PO_4$) and pH=10 ($NH_4Cl/NH_3$) buffers. The prepared solutions were placed in a water bath at a constant temperature and constant stirring speed (120 rpm). AC was added to these solutions at a rate of 2-12 g/L and absorbance values of the samples taken at the end of the equilibration period of 420 min were measured at a wavelength 730 nm in the UV-visible spectrophotometer. The remaining protein concentration in the solution was determined by the Lowry method. In the Lowry method, protein is first treated with alkaline copper sulfate in the presence of tartrate. This "incubation" is then followed by the addition of the Folin-phenol reagent. It is believed that the enhancement of the color reaction in the Lowry procedure occurs when the tetradentate copper complexes transfer electrons to the phospho-molybdic/phosphotungstic acid complex ($Mo+6/W+6$, Folin phenol reagent) (23).

To identify protein adsorption kinetics on activated carbon at pH=4, 5 and 7.4, 100 mL of BSA solution with a 500 mg/L initial concentration was taken and 6 g/L adsorbent was added onto it. Protein samples were taken from the mixture before and during the experiment at specific time intervals. Sampling continued until the solution concentration reached constant values. The protein concentration in the solutions obtained was determined by the Lowry method using the UV-visible spectrophotometer. These processes were repeated for temperatures of 20, 30 and 40°C.

**Zeta potential experiments**

The solution at the same initial concentration (500 mg/L) as in the adsorption experiments was used for the zeta potential measurements of BSA. AC suspension was prepared by 0.05 g of AC in 25 mL NaCl (0.9%) solution. Another set of BSA/AC suspension was prepared with 0.05 g of AC in 25 mL BSA (500 mg/L) solution. The pH of the suspensions was adjusted with $NaH_2PO_4.2H_2O/H_3PO_4$ (pH=2.8) and $NH_4Cl/NH_3$ (pH=10) buffers. The zeta potentials of BSA, AC and AC/BSA were determined with the use of a Brookhaven ZetaPlus instrument at constant temperature.

**RESULTS AND DISCUSSION**

**AC characterization**

Figure 1 shows the DFT pore size distribution and $N_2$ adsorption-desorption isotherm of AC at 77 K obtained as a result of single-step $N_2+H_2O$ vapor activation of the mixture at 800 °C after impregnation and sonication of the coal sample of $H_3PO_4$ at the rate of 3:1. The curve of the $N_2$ adsorption isotherm of AC corresponds with Type I isotherm according to IUPAC classification (24). According to this, AC shows that it commonly has a microporous structure. It is also seen that desorption of the adsorption of $N_2$ at 77 K and $P/P_0$ do not correspond in the range of 0.4-0.99 and that hysteresis occurs, which is a result of the capillarity condensation while the gas fills in and bleeds in the mesopore. The hysteresis in AC corresponds with Type H4 according to IUPAC classification. Type H4 is known to be in activated carbon with a slit pore structure. According to the IUPAC classification, porous adsorbents are classified as micropores if they are below 20 Å and as mesopores in the range of 20-500 Å. In the DFT pore size distribution in Figure 1, it is seen that micropores and, at low rate, mesoporous structures are commonly observed. Table 1 shows the surface characteristics of AC calculated from the $N_2$ adsorption-desorption isotherm at 77 K. The BET and Langmuir surface areas of AC were found to be 1175 and 1270 $m^2/g$ respectively. In addition, micropore (calculated with DR model), mesopore and the total pore volume were found to be 0.477, 0.061 and 0.538 cc/g respectively.
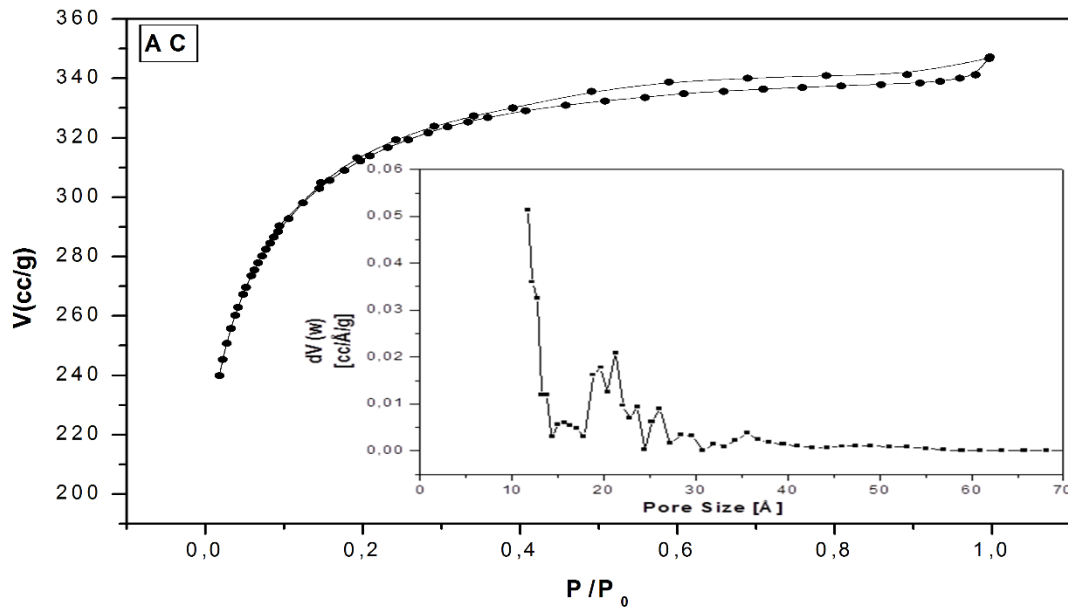
**Figure 1:** $N_2$ adsorption–desorption isotherms at 77 K and pore size distribution for AC prepared by single step $H_3PO_4/N_2+H_2O$ vapor activation at 800 °C.

**Table 1.** Surface and pore structure parameters of AC prepared by single step $H_3PO_4/N_2+H_2O$ vapor activation at 800 °C.

| Sample | Surface Area (m²/g) | | Pore Volumes (cc/g) | | | Pore Sizes (Å) | |
|---|---|---|---|---|---|---|---|
| | *BET* | *Lang.* | $V_{micro}$ | $V_{meso}$ | $V_T$ | *DFT* | *Average* |
| **AC** | 1175 | 1270 | 0.477 | 0.061 | 0.538 | 11.7 | 18.3 |

The surface morphology of AC was observed with SEM-EDAX in Figure 2. When the SEM image is examined, it is seen that there are irregular macroscopic pores and cavities on the surface of AC. It can be said that these pore formations are the result of the vaporization of volatiles such as $CO_2$, CO and $H_2$ from the carbon surface during $H_3PO_4$ and that $N_2+H_2O$ vapor activation, temperature and sonication are also important parameters (25).
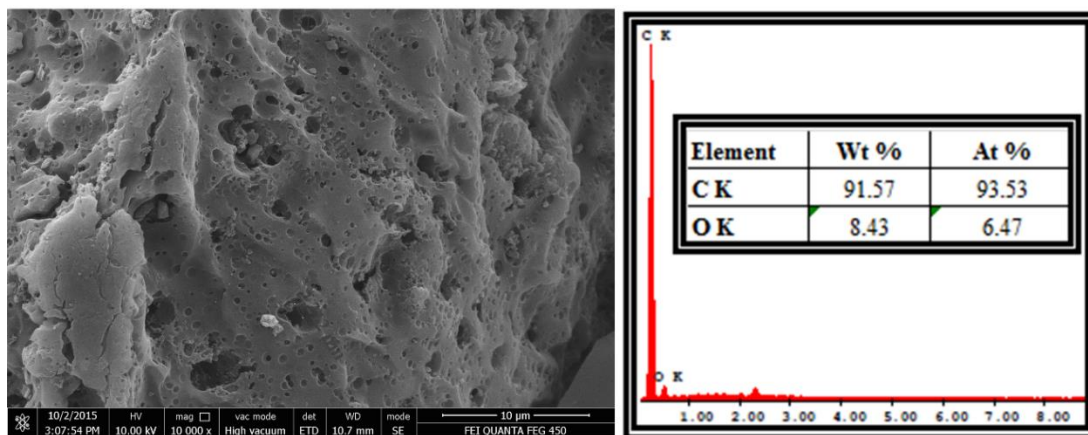


**Figure 2.** SEM image and EDAX analysis of AC.

The XRD pattern of AC is given in Figure 3. It is seen that there are three characteristic peaks in AC at approximately 25°, 43° and 79°. The peaks at 2θ=25° (002 plane) show the stacking structure of the aromatic layers and crystallinity height and 100/101 planes at 2θ=45° show the average crystallinity width. In AC, we can say that crystalline regions develop as sharp peaks at 25° in fragments. The 100/101 plane at 43° and the 110 plane at 79° in AC have weak intensity. This means that the AC shows the presence of small domains of ordered graphene sheets. Peaks at 25° and 43° have narrower and higher intensities, so we can say that it has graphene-like regular crystalline structures similar to the AC produced in the literature (26-29).
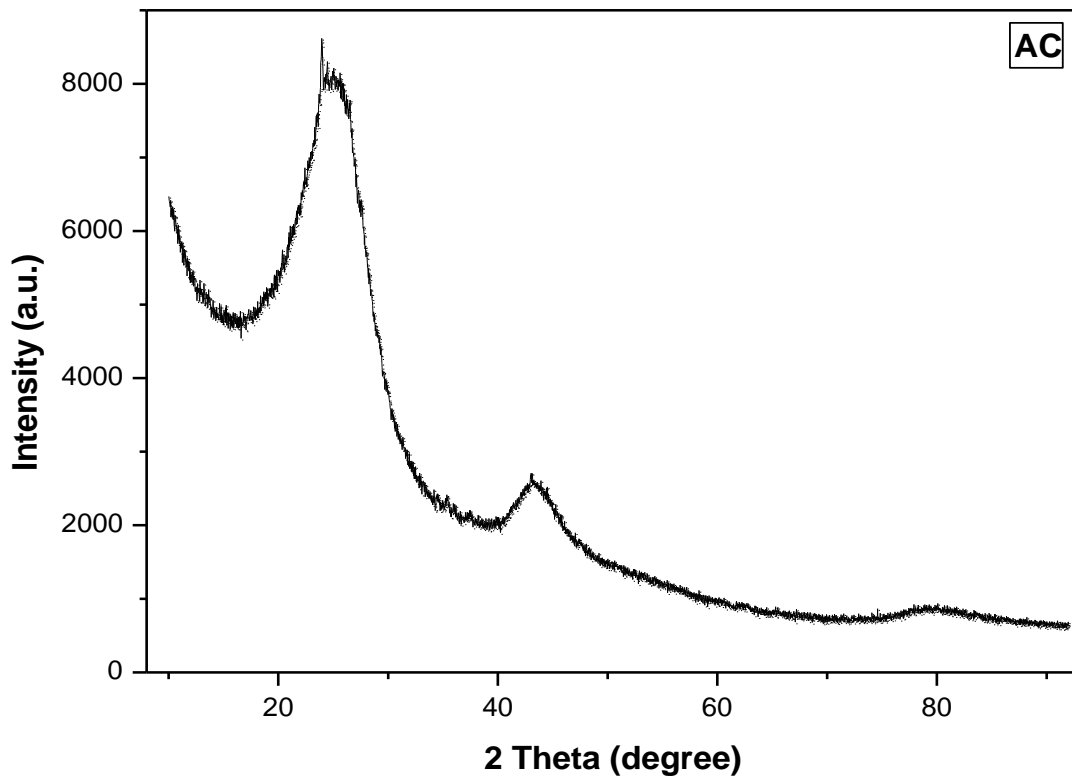


**Figure 3:** X-Ray diffraction patterns of AC.

**Effect of temperature and pH on BSA adsorption**

One of the important factors affecting protein adsorption is temperature. Proteins are subjected to a conformational change between primary structures and quaternary structures due to temperature differences. It is even the case that proteins are denaturalized due to temperature (30).

The effect of temperature on BSA adsorption on AC was determined by observing the changes in the protein concentration in the liquid phase at 20, 30 and 40 °C over time. Figures 4-6 show the effects of temperature at various pHs. In the figures for all pH environments, it is seen that the amount of BSA adsorbed onto AC generally increases as the temperature increases. The increase in adsorption capacity with increasing

temperature can be explained as a result of increases in protein activity leading diffusion to increases on the effective adsorbent surfaces (31). The optimum temperature environment for AC was found to be 40 $^{o}$C at all pH values.
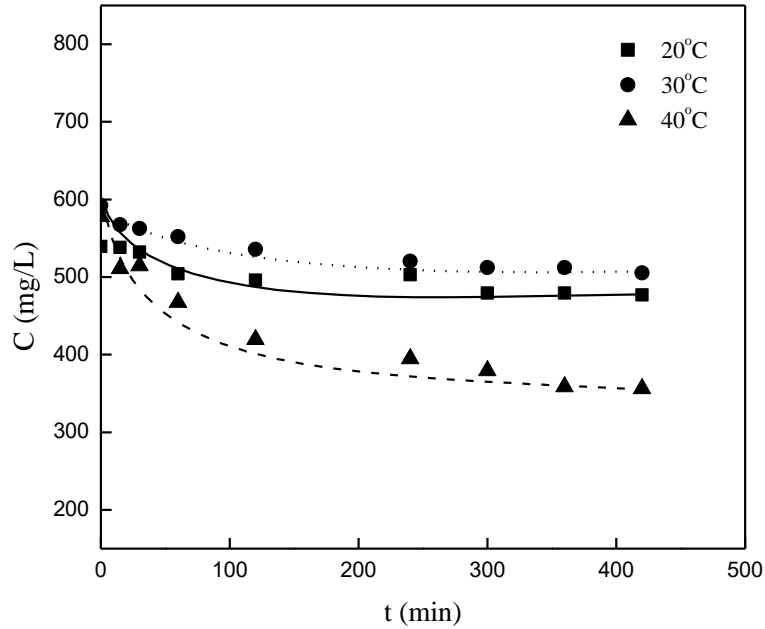


**Figure 4.** Effect of temperature on AC/BSA adsorption at pH=4.0.
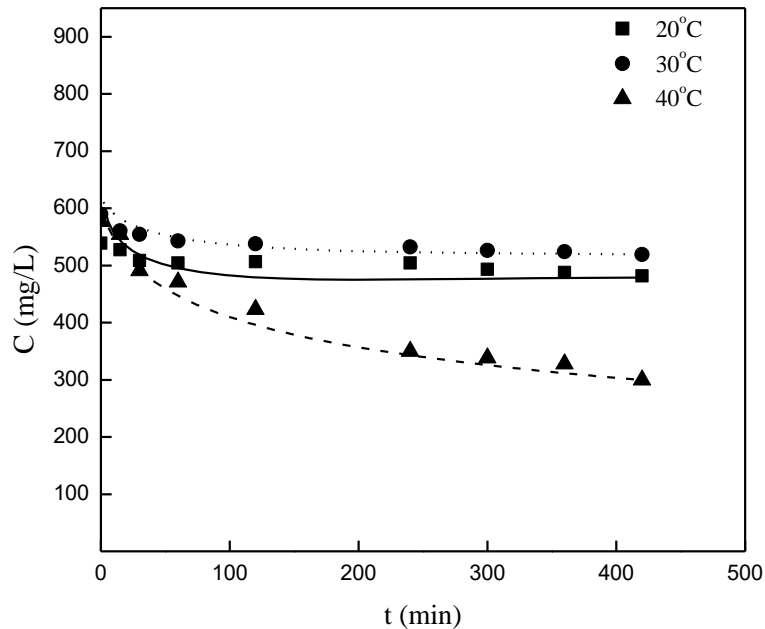


**Figure 5.** Effect of temperature on AC/BSA adsorption at pH=5.0.
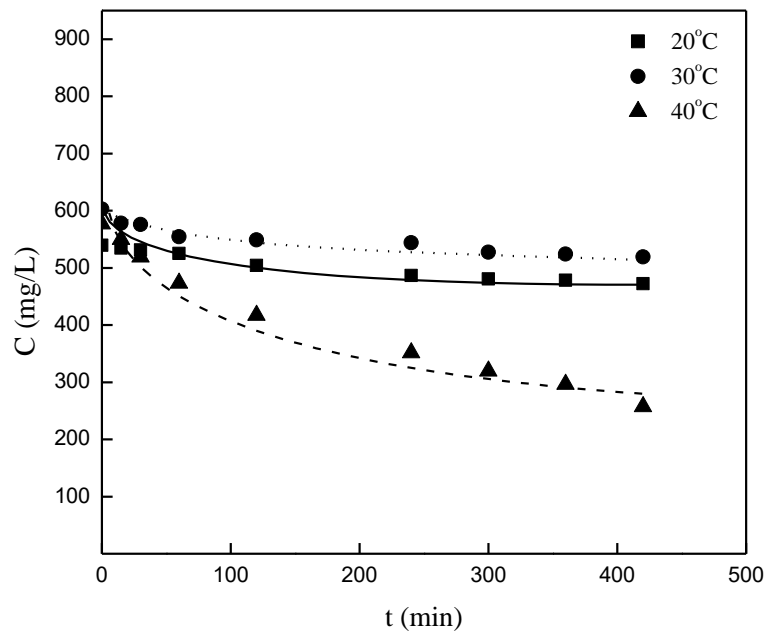
**Figure 6.** Effect of temperature on AC/BSA adsorption at pH=7.4.

**Zeta potential**

Zeta potential measurement is an easy and intelligible method to determine the presence of electrostatic interactions on the surface (32). To elucidate the electrostatic interactions between the surface and protein, the zeta potential values of the adsorbent, protein, and protein-adsorbent were measured.

The graph of zeta potential values measured for BSA, AC and AC/BSA is given in Figure 7. It is seen that zeta potential values of AC suspensions prepared with 0.15 M NaCl solution are negative ((-10)–(-30) mV) in all measured pH environments. The isoelectric point (p$I$) of BSA is found to be about 4.7. BSA has positive zeta potential values at lower pH than p$I$, and negative values at a higher pH. The interaction between positively charged BSA and negatively charged AC particles at pH 4 is a consequence of electrostatic attraction forces. For this reason, the highest protein adsorption capacity for AC was found at pH 4. Zeta potential changes also coincide with the adsorption equilibrium results obtained for AC/BSA. Zeta potential values measured for the AC/BSA also have a negative magnitude but less negative magnitude than AC. This magnitude difference occurred more at pH 5 and 7.4. This is due to the reduction of the negatively charge density on the active carbon surface after the AC surface has been coated with BSA. Although AC and BSA have negative charges at pH 5 and 7.4, it was found that protein was adsorbed on activated carbon surfaces. Even protein and substrate surface have the same charge, in vitro studies have shown that adsorption can occur for albumin. Adsorption was interpreted as an entropic

increase due to the shocks in the 'soft' α-helical structure of serum albumin despite electrostatic repulsion (33).
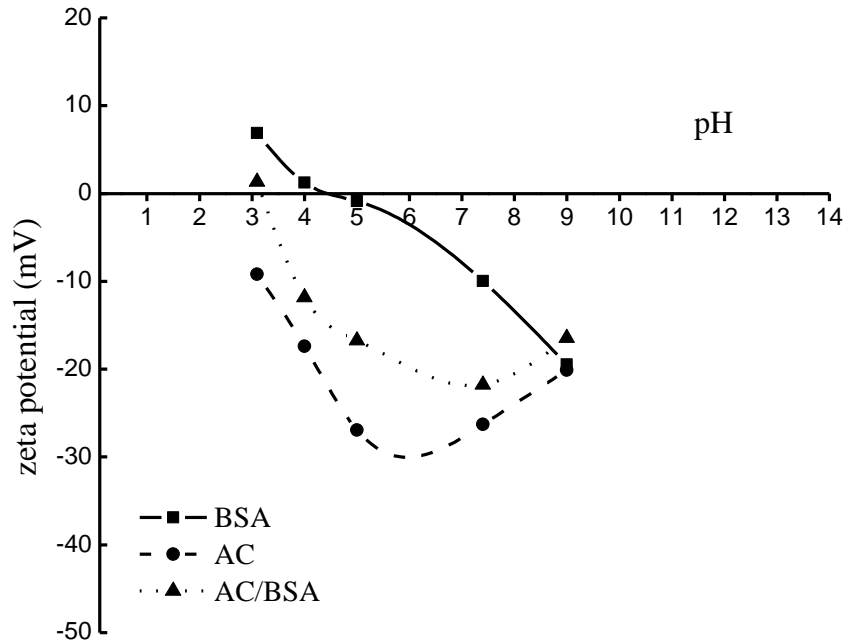


**Figure 7.** Zeta potential curve for AC/BSA adsorption.

**Adsorption equilibrium**

The BSA adsorption data are correlated with the isotherm models of Langmuir at Eq. (1) (34) and Freundlich at Eq. (2) (35),

$$\frac{1}{q_e} = \frac{1}{Q_0} + \frac{1}{Q_0 b} \frac{1}{C_e}$$ (Eq. 1)

$$q_e = K_f C_e^{1/n}$$ (Eq. 2)

where $C_e$ is the equilibrium concentration of BSA (mg/L), $Q_0$ the maximum adsorption capacity (mg/g), $b$ the Langmuir adsorption constant and $K_f$ and $1/n$ are Freundlich constants.

Experimental $q_e$ and $C_e$ values obtained for the adsorption of BSA on AC at various temperature and pH were compared with Langmuir and Freundlich models. Figures 8 and 9 show the linear graphs of Langmuir and Freundlich isotherm models given for pH 4 and 20 °C. In addition, the Langmuir and Freundlich model parameters obtained from the slope of the linear graphs for each pH and temperature, and the correlation coefficient squared ($R^2$) values indicating the compatibility of the models with the experimental data are given in Table 2. When Table 2 is examined, it is seen that experimental data at 20 °C for pH 5 and at 20 and 30 °C for pH 7.4 are not compatible with either the Langmuir or Freundlich models. The adsorption capacity calculated for the Langmuir model is $Q_0$, and it is observed

that the values increase at pH 5 and 7.4 as the temperature increases, and at pH 4, the $Q_0$ value is 160.3 mg/g at 20 °C; it decreases to 101.4 mg/g at 30 °C, and increases again to 159.0 mg/g at 40 °C. The maximum protein adsorption capacity was found to be almost the same at 20 and 40°C for pH 4. In a study conducted by Taskin *et al.* (36), the highest protein adsorption capacity for bovine serum albumin adsorption on modified activated carbon (2492 m$^2$/g) was found to be 136.77 mg/g. When the protein adsorption capacities were compared, it was found out that more BSA (160.3 mg/g) was adsorbed although the surface area of AC (1175 m$^2$/g) that we obtained was smaller than the surface area of the modified activated carbon.
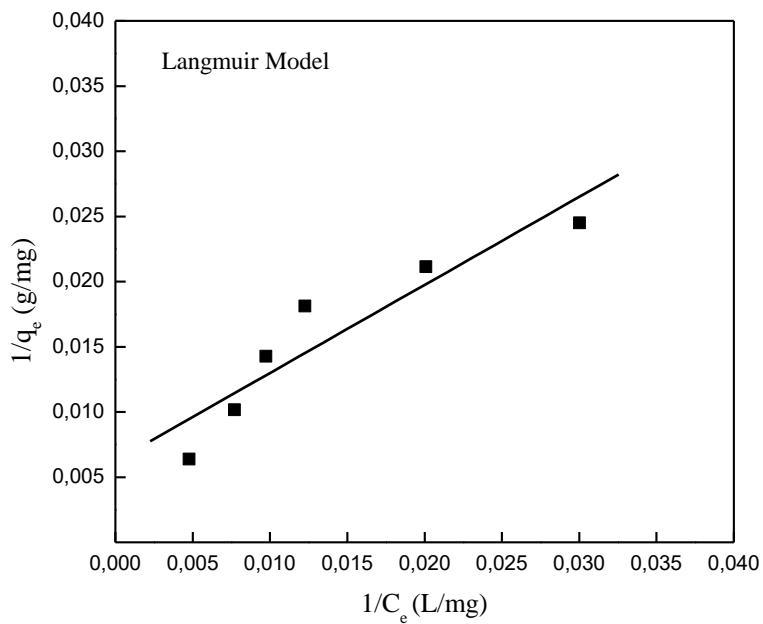


**Figure 8:** Langmuir Model curve obtained for AC/BSA adsorption at pH 4 and 20°C.
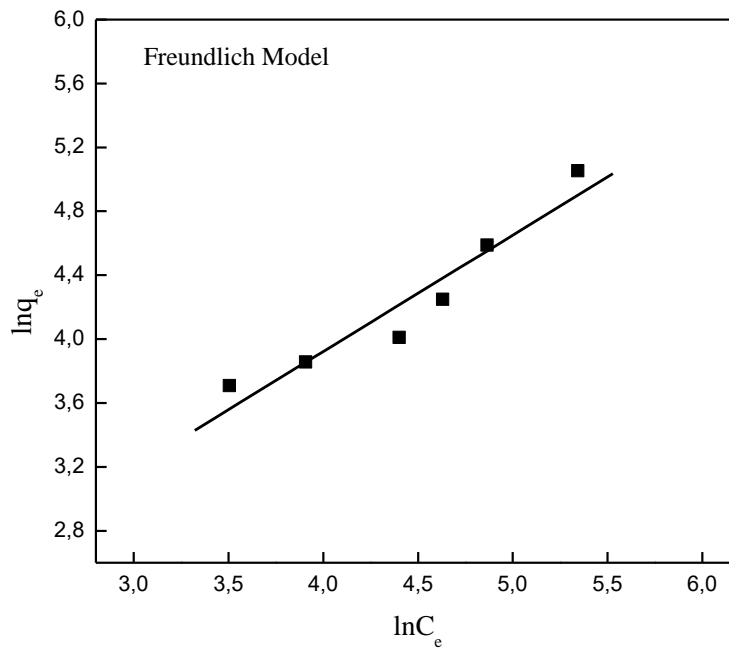
**Figure 9.** Freundlich model curve obtained for the AC/BSA adsorption at pH 4 and 20°C.

When the Freundlich model parameters are examined, it is seen that the $1/n$ values indicating the adsorption density are smaller than 1 in all pH environments. It is known that the closer the value of $1/n$ is to zero, the greater the density and heterogeneity of the adsorbed material on the adsorbent surface is (37). When the $R^2$ values in the models are close to unity, this is the indicative of the compatibility of that model with the experimental data. When the $R^2$ values of the Langmuir and Freundlich models in Table 2 are compared, it is seen that $R^2$ values are almost the same for both isotherm models.

**Table 2.** Langmuir and Freundlich model parameters calculated for AC/BSA adsorption system at different pHs and temperatures.

| pH | pH 4 | | | pH 5 | | | pH 7.4 | | |
|---|---|---|---|---|---|---|---|---|---|
| T (°C) | 20 | 30 | 40 | 20 | 30 | 40 | 20 | 30 | 40 |
| **Langmuir Model** | | | | | | | | | |
| $Q_0$ (mg/g) | 160.3 | 101.4 | 159.0 | - | 40.0 | 90.2 | - | - | 71.8 |
| b | 0.0092 | 0.00029 | 0.0053 | - | 0.005 | 0.010 | - | - | 0.003 |
| $R^2$ | 0.86 | 0.96 | 0.77 | - | 0.90 | 0.92 | - | - | 0.91 |
| **Freundlich Model** | | | | | | | | | |
| $K_f$ | 2.75 | 0.052 | 2.19 | - | 2.66 | 6.02 | - | - | 1.52 |
| 1/n | 0.728 | 0.877 | 0.692 | - | 0.386 | 0.431 | - | - | 0.548 |
| $R^2$ | 0.92 | 0.96 | 0.82 | - | 0.90 | 0.91 | - | - | 0.88 |

**Adsorption kinetics**

The kinetics of adsorption of BSA on activated carbon was studied on the basis of two simplified kinetic models, including pseudo-first-order and pseudo-second-order equations. The Lagergren pseudo-first-order kinetic model was represented as (38)

$$\log(q_e - q) = \log q_e - \frac{k_1}{2.303}t \qquad \text{(Eq. 3)}$$

and the pseudo-second-order equation was given by (39),

$$\frac{1}{(q_e - q)} = \frac{1}{q_e} + k_2 t \qquad \text{(Eq. 4)}$$

where $k_1$ (1/min) and $k_2$ (g/mg min) are the rate constants of the pseudo-first-order and second-order adsorption kinetics respectively. $q_e$ is the amount of protein adsorbed on the surface of the adsorbent at equilibrium (mg/g) and $q$ is the amount of protein adsorbed at any time (mg/g).

In order to analyze the adsorption mechanism of BSA on AC, the experimental rate data obtained by keeping the initial concentration of BSA and adsorbent amounts constant at different pH values and temperature were compared with the Lagergren's pseudo-first and pseudo-second order kinetic models. In order to obtain the first- and second-order rate constants of BSA adsorption on AC, changes in $\log(q_e\text{-}q)$ and $1/(q_e\text{-}q)$ values in time at 20, 30 and 40 °C at pH 4, 5 and 7.4 by keeping the absorbent amount constant are given in Figures 10 and 11 respectively. $k_1$, $k_2$, $q_e$ and $R^2$ values obtained by using the slope and the breakpoint of the straight lines in the graphs are given in Table 3. When the graphs and the chart obtained for AC were examined, $k_1$ values increased with increasing temperature at pH 4 and 5 but decreased with increasing temperature at pH 7.4. When $R^2$ values of the first- and second-order kinetic models were compared, $R^2$ values of the first order kinetic model were much closer to 1.0 than those of pseudo-first-order model at all temperatures and pHs. Therefore, BSA's adsorption rate on AC complies with the first-order kinetic model better. The rate of protein adsorption by the AC has been interpreted here in terms of the adherence of protein on the active sites of the adsorbent as well as its interparticle diffusion within the pores of the adsorbent (39, 40).
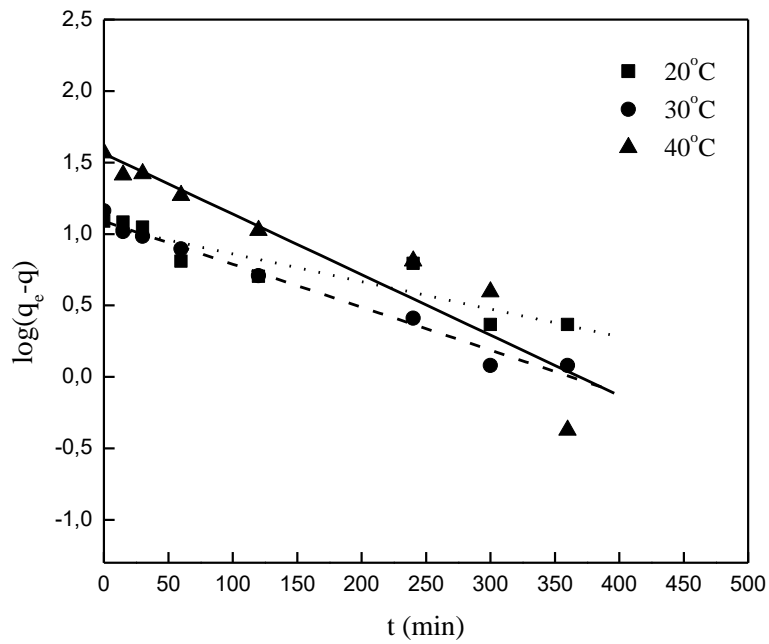
**Figure 10:** Pseudo-first-order kinetic curves for AC/BSA adsorption at pH 4.
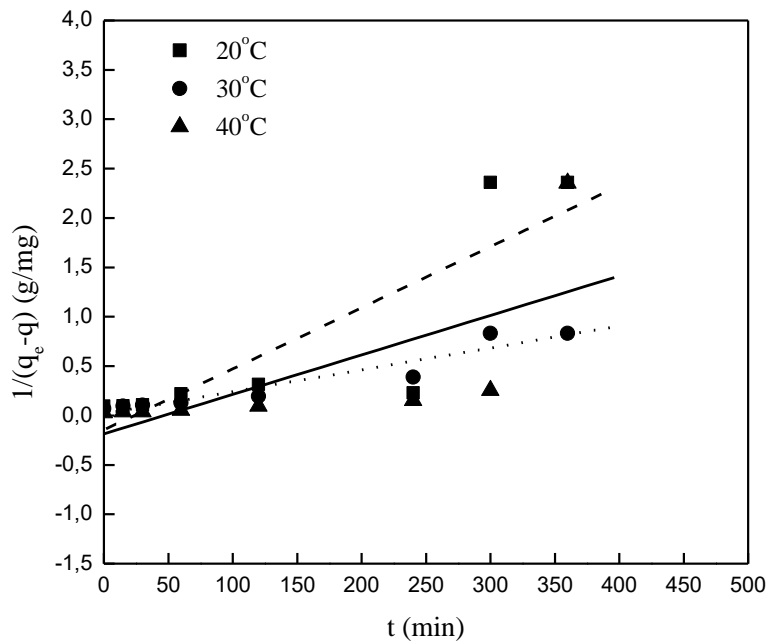


**Figure 11:** Pseudo-second-order kinetic curves for AC/BSA adsorption at pH 4.

**Table 3.** Pseoudo-first- and second-order kinetic parameters for AC/BSA adsorption system.

| pH | pH 4 | | | pH 5 | | | pH 7.4 | | |
|---|---|---|---|---|---|---|---|---|---|
| T (°C) | 20 | 30 | 40 | 20 | 30 | 40 | 20 | 30 | 40 |
| **Pseudo-first-order model parameters** | | | | | | | | | |
| $k_1$ (1/min) | 0.0044 | 0.0069 | 0.0097 | 0.0046 | 0.0064 | 0.0063 | 0.0071 | 0.0068 | 0.0055 |
| $R^2$ | 0.85 | 0.98 | 0.88 | 0.81 | 0.94 | 0.99 | 0.99 | 0.92 | 0.99 |
| **Pseudo-second-order model parameters** | | | | | | | | | |
| $k_2$ (g/mg min) | 0.0062 | 0.0022 | 0.0040 | 0.0017 | 0.0029 | 0.0005 | 0.0025 | 0.0026 | 0.0003 |
| $R^2$ | 0.73 | 0.91 | 0.49 | 0.72 | 0.89 | 0.96 | 0.91 | 0.77 | 0.89 |

**CONCLUSION**

AC was produced from the coal at 800 °C with single step $H_3PO_4/N_2+H_2O$ vapor activation. The surface properties and morphological characteristics of the AC produced were determined. Kinetic and electrostatic interactions and the adsorption of BSA on AC at different temperatures (20, 30 and 40 °C) and pH values (4, 5 and 7.4) were examined. According to the results obtained, the BSA adsorption capacity of AC decreased with increasing pH, but the adsorption increased with increasing temperature. However, it was also found that the BSA adsorption capacity at pH 4 decreased when the temperature increased from 20 to 30°C and had a similar adsorption capacity at 20 and 40 °C. The highest adsorption capacity was found to be 160.3 and 159 mg/g respectively at 20 and 40 °C at pH 4. Lagergren's first- and pseudo-second-order kinetic models were applied to BSA adsorption on AC at all pHs and temperatures. The results obtained show that the adsorption rate of BSA on AC complies with the first-order kinetic model in a better fashion. According to the results obtained, it can be also said that AC obtained from coal is cheaper and has potential to compete compared to other adsorbents in terms of eliminating the protein pollution.

**ACKNOWLEDGMENTS**

## REFERENCES

1. Lu JR, Zhao X, Yaseen M. Protein adsorption studied by neutron reflection. Current Opinion in Colloid & Interface Science. 2007;12(1):9-16.

2. Hinderliter A, Almeida PF, Creutz CE, Biltonen RL. Domain formation in a fluid mixed lipid bilayer modulated through binding of the C2 protein motif. Biochemistry. 2001;40(13):4181-91.

3. Rabe M, Verdes D, Seeger S. Understanding protein adsorption phenomena at solid surfaces. Advances in colloid and interface science. 2011;162(1):87-106.

4. Kalasin S, Santore MM. Non-specific adhesion on biomaterial surfaces driven by small amounts of protein adsorption. Colloids and Surfaces B: Biointerfaces. 2009;73(2):229-36.

5. Liu J, Lee ML. Permanent surface modification of polymeric capillary electrophoresis microchips for protein and peptide analysis. Electrophoresis. 2006;27(18):3533-46.

6. Roach P, Eglin D, Rohde K, Perry CC. Modern biomaterials: a review—bulk properties and implications of surface modifications. Journal of Materials Science: Materials in Medicine. 2007;18(7):1263-77.

7. Chen H, Yuan L, Song W, Wu Z, Li D. Biocompatible polymer materials: role of protein–surface interactions. Progress in Polymer Science. 2008;33(11):1059-87.

8. Cole MA, Voelcker NH, Thissen H, Griesser HJ. Stimuli-responsive interfaces and systems for the control of protein–surface and cell–surface interactions. Biomaterials. 2009;30(9):1827-50.

9. Huang N-P, Michel R, Voros J, Textor M, Hofer R, Rossi A, et al. Poly (L-lysine)-g-poly (ethylene glycol) layers on metal oxide surfaces: surface-analytical characterization and resistance to serum and fibrinogen adsorption. Langmuir. 2001;17(2):489-98.

10. Heuberger R, Sukhorukov G, Vörös J, Textor M, Möhwald H. Biofunctional polyelectrolyte multilayers and microcapsules: Control of non-specific and bio-specific protein adsorption. Advanced Functional Materials. 2005;15(3):357-66.

11. Zürcher S, Wäckerlin D, Bethuel Y, Malisova B, Textor M, Tosatti S, et al. Biomimetic surface modifications based on the cyanobacterial iron chelator anachelin. Journal of the American Chemical Society. 2006;128(4):1064-5.

12. Hlady V, Buijs J, Jennissen HP. [26] Methods for studying protein adsorption. Methods in enzymology. 1999;309:402-29.

13. Liou T-H. Development of mesoporous structure and high adsorption capacity of biomass-based activated carbon by phosphoric acid and zinc chloride activation. Chemical Engineering Journal. 2010;158(2):129-42.

14. Tsai W, Chang C, Wang S, Chang C, Chien S, Sun H. Preparation of activated carbons from corn cob catalyzed by potassium salts and subsequent gasification with $CO_2$. Bioresource Technology. 2001;78(2):203-8.

15. Hsu L-Y, Teng H. Influence of different chemical reagents on the preparation of activated carbons from bituminous coal. Fuel Processing Technology. 2000;64(1):155-66.

16. Lussier MG, Shull JC, Miller DJ. Activated carbon from cherry stones. Carbon. 1994;32(8):1493-8.

17. Hayashi J, Muroyama K, Gomes VG, Watkinson AP. Fractal dimensions of activated carbons prepared from lignin by chemical activation. Carbon. 2002;40(4):630-2.

18. Khalili NR, Campbell M, Sandi G, Golaś J. Production of micro-and mesoporous activated carbon from paper mill sludge: I. Effect of zinc chloride activation. Carbon. 2000;38(14):1905-15.

19. Kabe T, Ishihara A, Qian EW, Sutrisna IP, Kabe Y. Coal and coal-related compounds: structures, reactivity and catalytic reactions: Elsevier; 2004.

20. Teng H, Yeh T-S, Hsu L-Y. Preparation of activated carbon from bituminous coal with phosphoric acid activation. Carbon. 1998;36(9):1387-95.

21. Jagtoyen M, Thwaites M, Stencel J, McEnaney B, Derbyshire F. Adsorbent carbon synthesis from coals by phosphoric acid activation. Carbon. 1992;30(7):1089-96.

22. Kopac T, Toprak A. Preparation of activated carbons from Zonguldak region coals by physical and chemical activations for hydrogen sorption. International Journal of Hydrogen Energy. 2007;32(18):5005-14.

23. Lowry OH, Rosebrough NJ, Farr AL, Randall RJ. Protein measurement with the Folin phenol reagent. Journal of biological chemistry. 1951;193(1):265-75.

24. Gregg SJ, Sing KSW. Adsorption, surface area, and porosity: Academic Press; 1991.

25. Fu K, Yue Q, Gao B, Sun Y, Zhu L. Preparation, characterization and application of lignin-based activated carbon from black liquor lignin by steam activation. Chemical Engineering Journal. 2013;228:1074-82.

26. Lua AC, Yang T. Effect of activation temperature on the textural and chemical properties of potassium hydroxide activated carbon prepared from pistachio-nut shell. Journal of colloid and interface science. 2004;274(2):594-601.

27. Jung M-W, Ahn K-H, Lee Y, Kim K-P, Rhee J-S, Park JT, et al. Adsorption characteristics of phenol and chlorophenols on granular activated carbons (GAC). Microchemical Journal. 2001;70(2):123-31.

28. Ji Y, Li T, Zhu L, Wang X, Lin Q. Preparation of activated carbons by microwave heating KOH activation. Applied surface science. 2007;254(2):506-12.

29. Qu D. Studies of the activated carbons used in double-layer supercapacitors. Journal of Power Sources. 2002;109(2):403-11.

30. Vidal CV, Juan AO, Muñoz AI. Adsorption of bovine serum albumin on CoCrMo surface: effect of temperature and protein concentration. Colloids and Surfaces B: Biointerfaces. 2010;80(1):1-11.

31. Lu C, Chung Y-L, Chang K-F. Adsorption thermodynamic and kinetic studies of trihalomethanes on multiwalled carbon nanotubes. Journal of hazardous materials. 2006;138(2):304-10.

32. Lee W-K, Ko J-S, Kim H-M. Effect of electrostatic interaction on the adsorption of globular proteins on octacalcium phosphate crystal film. Journal of colloid and interface science. 2002;246(1):70-7.

33. Znidarsic WJ, Chen I-W, Shastri VP. ζ-potential characterization of collagen and bovine serum albumin modified silica nanoparticles: a comparative study. Journal of materials science. 2009;44(5):1374-80.

34. Langmuir I, The constitution and fundamental properties of solids and liquids: Part I. solids. Journal of the american chemical society. 1916;38: 2221-2295.

35. Freundlich H, Colloid and capillary chemistry. Methuen, London. 1926, pp 110-114.

36. Taşkın M, Özbek S, Demirhan E, Özbek B. BSA adsorption onto commercial activated carbon modified by microwave assisted chemical activation. 2016.

37. Uğurlu M. Adsorption of a textile dye onto activated sepiolite. Microporous and mesoporous Materials. 2009;119(1):276-83.

38. Largergren S. Zur theorie der sogenannten adsorption geloster stoffe. Kungliga Svenska Vetenskapsakademiens. Handlingar. 1898;24(4):1-39.

39. Ho Y-S, McKay G. Pseudo-second order model for sorption processes. Process biochemistry. 1999;34(5):451-65.

40. Orumwense F-F-O, Removal of lead from water by adsorption on a kaolinitic clay. J. Chem. Technol. Biotechnol. 1996;65:363.

# Adsorption of Metamizole Sodium by Activated Carbon in Simulated Gastric and Intestinal Fluids

**Elif ÇALIŞKAN SALİHİ[1]***

[1]Marmara University, Faculty of Pharmacy, Department of Basic Pharmaceutical Sciences, 34668, Haydarpasa, Istanbul, Turkey

**Abstract:** *In vitro* adsorption of metamizole sodium by activated carbon was studied at pH 1.2 and 7.5 in order to simulate gastric and intestinal fluids. In the first 5 minutes, more than eighty percent of the total adsorption occurred but the adsorption process achieved to the equilibrium in 1 hour. Time to reach equilibrium did not change with the changing pH, concentration of the adsorbate or the adsorbent amount. The equilibrium data followed the Langmuir model and therefore fitted to L-type in accordance with the Giles classification for adsorption isotherms. The maximum removal capacities of the activated carbon for metamizole sodium were calculated using Langmuir equation and found as 185.19 mg/g and 161.29 mg/g at pH 1.2 and 7.5, respectively.

**Keywords:** Adsorption, Metamizole sodium, Gastric fluid, Intestinal fluid, Dipyrone.

## INTRODUCTION

Metamizole sodium (MS), also known as dipyrone, is a pyrazolone derivative and represents analgesic and antipyretic activity. The molecular structure of MS is shown in Figure 1. It was withdrawn already in several countries due to its potentially fatal adverse effects. The most serious adverse effect of MS is agranulocytosis. Studies showed that MS overdose usually causes mild toxicity and occurs mainly at home by the oral route and in relation to a considerable number of suicide attempts. However, MS is still widely used as an over the counter preparation in adults and children in many countries (1). The use of MS during pregnancy and postpartum even exceeds the use of paracetamol in some of these countries. Studies report that metabolites of MS were found in the breast milk in concentrations similar to those in the maternal serum (2).
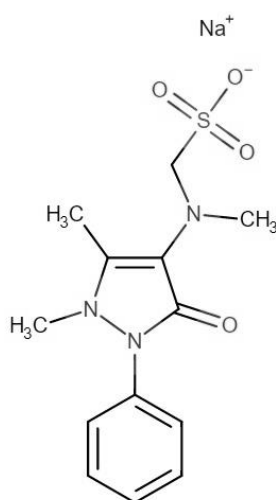


**Figure 1:** Chemical structure of MS (metamizole sodium).

Drug poisoning is a common and serious clinical problem. Because many drugs used do not have any specific antidote for the treatment of poisoning. If the specific antidote does not exist, gastrointestinal adsorbents are beneficial for the treatment of overdose or poisoning by preventing the further absorption of drug. Activated carbon is widely used as a gastrointestinal adsorbent and has been successfully applied in the cases of overdosing of many pharmaceuticals (3). Activated carbons are also commonly used in the industries relevant to water treatment, pharmaceutical and food as adsorbent materials due to their highly porous structure and large adsorption capacity. However, there are limited number of studies investigating the adsorption rate and capacity of activated carbon for a certain drug including the effect of pH on the adsorption (4-12). Nabais *et al.* have studied the adsorption of fluoxetine in activated carbons and activated carbon fibers at gastric and intestinal pH values and reported most of the materials tested have potential for treating potential fluoxetine intoxications (13).

In the literature, there was no study on the adsorption of MS on activated carbon or any other adsorbent. So, the objective of the current study was to explore the *in vitro* adsorption of metamizole sodium using commercial powder activated carbon in the simulated gastric and intestinal fluids. Adsorption studies were conducted at 37 °C (body temperature) using various contact times, adsorbent amounts and initial adsorbate concentrations. Data from the equilibrium studies were modeled by using Langmuir and Freundlich isotherm equations and adsorption capacities were calculated.

## MATERIALS AND METHODS

Powdered activated carbon (PAC) was obtained from Merck. Surface and textural characterization of PAC used have been described in detail elsewhere (4). Briefly, the surface area and $pH_{PZC}$ (PZC: point of zero charge) of PAC are 780 $m^2$/g and 9.5, respectively. MS was supplied by Sigma (≥98%).

The adsorption experiments were conducted in simulated gastric fluid (SGF) and simulated intestinal fluid (SIF). Stock solutions of MS were prepared in SGF (pH=1.2) which contains NaCl and concentrated HCl (pepsin omitted) and SIF (pH=7.5) which contains $NaH_2PO_4$ and NaOH (without pancreatin). All the solutions were prepared by using purified (MilliQ) water and used at once. 100 mL of MS solutions of a known concentration (10 to 100 mg/L) were shaken with PAC (25 to 250 mg) in glass containers at 37 °C for 1 hour using a thermostatic shaker with a water bath. Separation of the samples was done with microfilters (0.45 µm). Concentrations of MS in the samples were measured with a spectrophotometer (Shimadzu, UV-visible) at 225 nm. Concentrations of the samples were calculated using calibration curves prepared for MS. The same arrangement were used also for the kinetic experiments. Blank experiments (without adsorbent) were performed and all the experiments were repeated at least three times under identical conditions.

## RESULTS AND DISCUSSION

*In vitro* adsorption of MS was performed in both SGF and SIF. In order to find the time to reach equilibrium, adsorption experiments were carried out using various shaking times. In the first 5 minutes, more than eighty percent of the total adsorption occurred but the adsorption process achieved to the equilibrium in 1 hour (Figure 2). The time to reach equilibrium did not change with changing pH, adsorbate concentration and the amount of adsorbent. So the adsorption of MS was carried out using 1 hour as shaking time at body temperature, 37 °C. The amount of adsorption (q, mg/g) was calculated as given below:

$$q = \frac{(C_0 - C_t)V}{w}$$

(Eq. 1)

$C_0$ shows the initial concentration of MS (mg/L) and $C_t$ shows the concentration of MS (mg/L) at any time (t). V is the volume of MS solution used (L) and w is the mass of PAC (g).
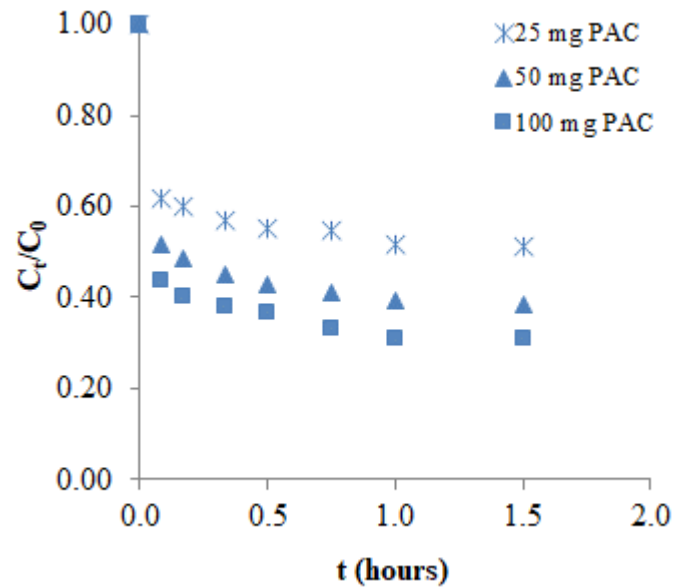


**Figure 2:** Effect of contact time on the adsorption of metamizole sodium (MS) on powder activated carbon (PAC).

Isotherm equations are used to model the interaction between the adsorbate and the adsorbent for the adsorption processes. Figure 3 and 4 are the Giles isotherms of MS on PAC at 37°C in SGF and SIF, respectively. The shapes of the isotherms in Figure 2 and 3 fit the L type in accordance with the Giles isotherm classification. L type means there is a high affinity between PAC and MS (14).
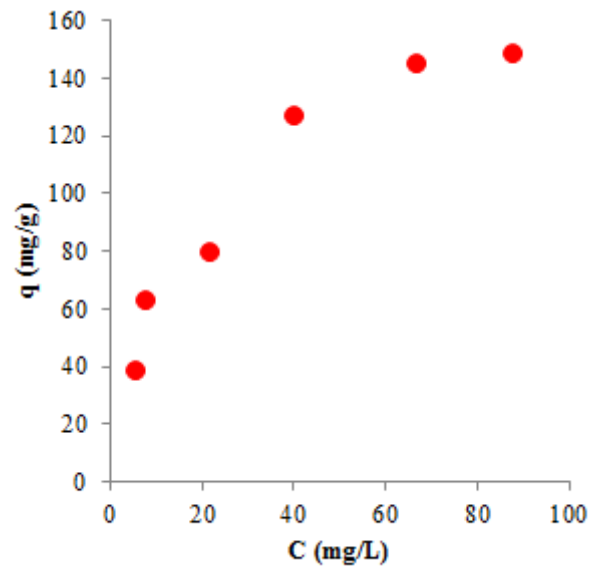
**Figure 3:** Giles isotherm for the adsorption of MS on PAC in SGF at 37°C.
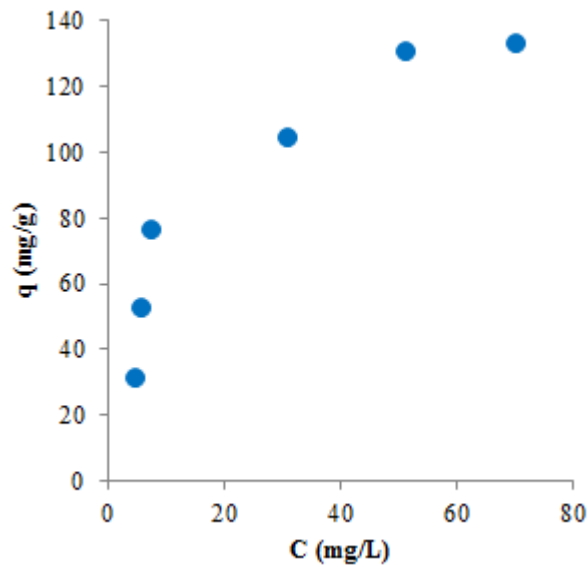


**Figure 4:** Giles isotherm for the adsorption of MS on PAC in SIF at 37°C.

Data obtained from equilibrium experiments were modeled by using the Langmuir (Figures 5a and 6a) and the Freundlich (Figure 5b and 6b) isotherm equations. Langmuir (15) and Freundlich (16) isotherm equations in their linear forms are respectively shown below.

$$\frac{C}{q} = \frac{1}{Qb} + \frac{C}{Q}$$

(Eq. 2)

$$\ln q = lnk + nlnC$$

(Eq. 3)

C shows the equilibrium concentration (mg/L); q shows the amount of adsorption at the equilibrium (mg/g); Q shows the maximum adsorption capacity (mg/g); b is the adsorption equilibrium constant (L/mg); k and n are Freundlich constants.

As seen in Table 1, the Langmuir model represents the adsorption of MS on PAC better than the Freundlich model. The Langmuir model indicates a localized adsorption with a monolayer coverage on the surface of the adsorbent where the adsorption heat is indepedent of the adsorbed amount of the material (17).



(a)                                                    (b)
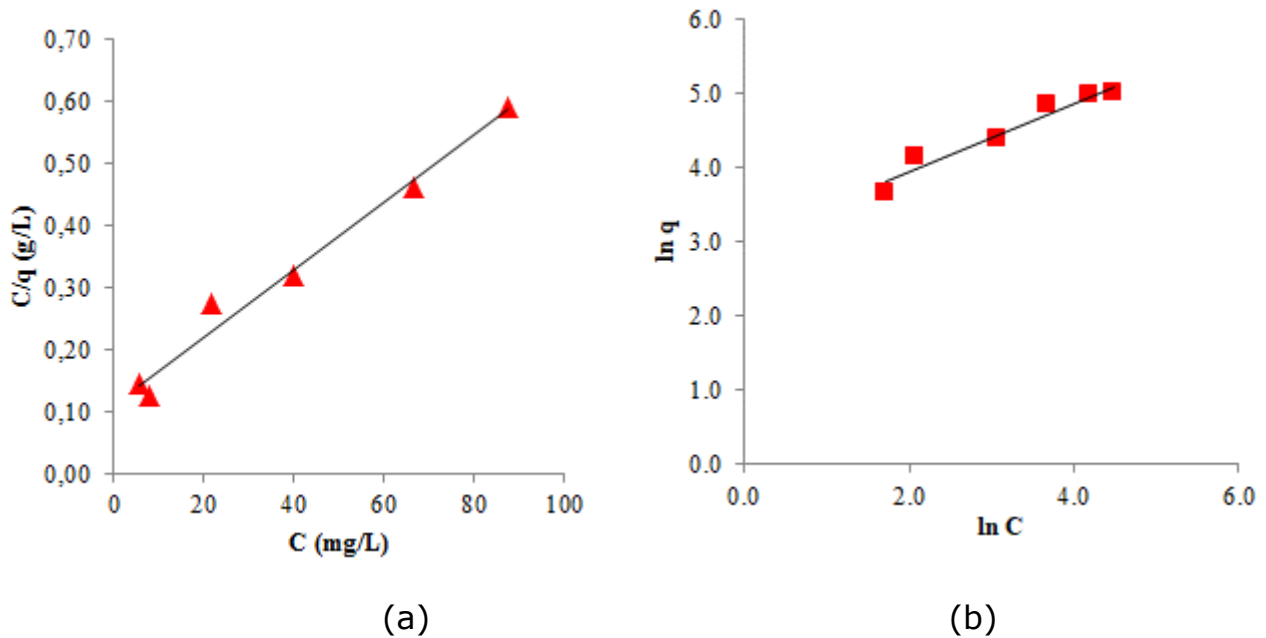
**Figure 5:** Langmuir and Freundlich isotherms for the adsorption of MS on PAC in SGF at 37 °C.



(a)                                                    (b)
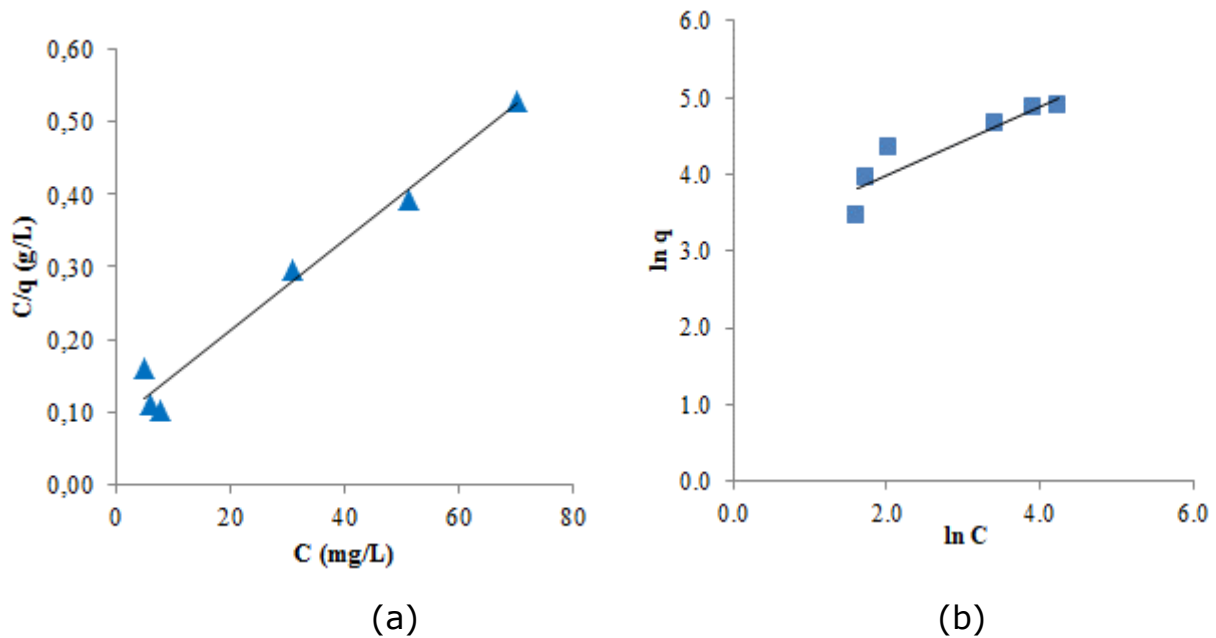
**Figure 6:** Langmuir and Freundlich isotherms for the adsorption of MS on PAC in SIF at 37°C.

**Table 1:** Isotherm parameters of the adsorption of MS PAC in SGF and SIF.

|  | Langmuir model | | | Freundlich model | | |
|---|---|---|---|---|---|---|
|  | Q (mg/g) | b(L/g) | $R^2$ | n | k | $R^2$ |
| SGF | 185.19 | 0.05 | 0.981 | 0.47 | 20.16 | 0.945 |
| SIF | 161.29 | 0.07 | 0.976 | 0.45 | 21.95 | 0.839 |

pKa (Ka: acidity constant) is an important parameter that controls the dissociation of adsorbate and effects the adsorption. This effect is closely related to the solution pH. MS (pKa = -1.2) exists its anionic form in the solution (18). Another parameter which importantly effects the adsorption is the surface charge of the adsorbent which is PAC in this study (4). PAC is an amphoteric material and has a point of zero charge (pH$_{PZC}$) of 9.5 which means that the charge of the surface is positive at the working pH values, 1.2 and 7.5. But the net positive charge on the surface at the pH 7.5 is lower than the one at the pH 1.2 which is more closer to the pH$_{PZC}$. The maximum adsorption capacity obtained at the pH 1.2 (in SGF) is higher than the one obtained at the pH 7.5 (in SIF). The adsorption capacity of PAC decreased with the increasing pH which shows the main role of electrostatic attraction on the adsorption of MS. The adsorption of MS occurs related to the electrostatic attraction forces between the anionic MS molecule and surface of PAC charged positively.

Dispersive (dispersion) and electrostatic interactions are the types of interactions which rule the adsorption of aromatic compounds on activated carbons. Dispersive interactions between the $\pi$-electrons of the aromatic rings of MS molecules and those of the graphene layers of PAC may be also contributive in this process (5, 19-23).
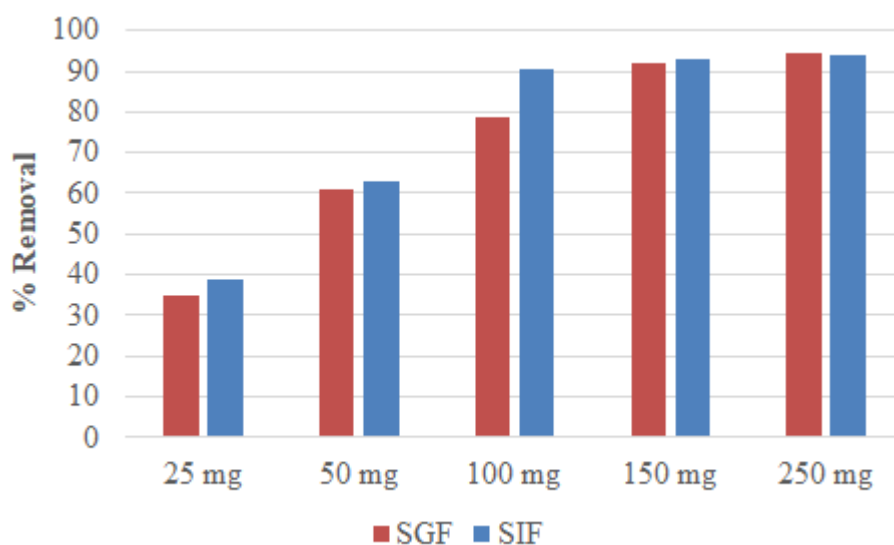


**Figure 7:** Comparison of % Removal of MS (metamizole sodium) for different amounts of PAC (powder activated carbon).

Figure 7 shows the effect of adsorbent amount on the removal of MS for various amounts of PAC. % Removal increases with an increase in the amount of PAC and stays almost constant at the adsorbent amounts higher than 100 mg. PAC used showed a high removal capacity for MS.

## CONCLUSIONS

Adsorption of MS (metamizole sodium) on PAC (powder activated carbon) was studied in simulated gastric and intestinal fluids at body temperature. The adsorption process achieved to the equilibrium in 1 hour, but more than eighty percent of the total adsorption occurred in the first 5 minutes. The maximum adsorption capacities of MS on PAC were calculated using the Langmuir isotherm model. The maximum adsorption capacity of MS in the simulated gastric fluid was found to be 185.19 mg/g which is higher than the one obtained in the simulated intestinal fluid found to be 161.29 mg/g. The adsorption capacity increased with decreasing pH. These results indicate the role of electrostatic attraction in this prosess. Electrostatic interactions played the main role for the adsorption of MS on PAC with a possible contribution of π-π dispersion interactions. Taking into account the equilibrium time and the adsorption capacities of the PAC, it can be concluded from the above that the adsorption of MS on PAC is a fast process with a high removal efficiency. Results of the present study is important for the treatment of overdose or poisoning by preventing the further absorption of drug.

## REFERENCES

1. Bentur Y, Cohen O. Dipyrone Overdose, Journal of Toxicology: Clinical Toxicology 2004; 42(3): 261-265.

2. Bar-Oz B, Bulkowstein M, Benyamini L, Greenberg R, Soriano I, Zimmerman D, Bortnik O, Berkovitch M. Use of antibiotic and analgesic drugs during lactation. Drug safety. 2003 Nov 1;26(13):925-35.

3. Otero M, Grande CA, Rodrigues AE. Adsorption of salicylic acid onto polymeric adsorbents and activated charcoal, Reactive & Functional Polymers 2004; 60: 203–213.

4. Çalışkan E, Göktürk S. Adsorption characteristics of sulfamethoxazole and metronidazole on activated carbon. Separation Science and Technology. 2010 Jan 29;45(2):244-55.

5. Çalışkan Salihi E, Aydın E. Adsorptive characteristics of isoniazid on powdered activated carbon: π−π Dispersion interactions at the solid–solution interface. Journal of Dispersion Science and Technology. 2017 Apr 3;38(4):457-462.

6. Cantürk Talman RY, Çalışkan Salihi E, Göktürk S, Baştuğ AS. Removal of ethacridine lactate from aqueous solutions onto bentonite and activated carbon. Fresenius Environmental Bulletin. 2015; 24(11), 3603-3608.

7. Kyzas GZ, Lazaridis NK, Deliyanni EA. Oxidation time effect of activated carbons for drug adsorption. Chemical engineering journal. 2013 Dec 31;234:491-9.

8. Kyzas GZ, Deliyanni EA. Modified activated carbons from potato peels as green environmental-friendly adsorbents for the treatment of pharmaceutical effluents. Chemical Engineering Research and Design. 2015 May 31;97:135-44.

9. Jain S, Vyas RK, Pandit P, Dalai AK. Adsorption of antiviral drug, acyclovir from aqueous solution on powdered activated charcoal: kinetics, equilibrium, and thermodynamic studies. Desalination and Water Treatment. 2014 Jul 29;52(25-27):4953-68.

10. Bajpai SK, Bhowmik M. Poly (acrylamide-co-itaconic acid) as a potential ion-exchange sorbent for effective removal of antibiotic drug-ciprofloxacin from aqueous solution. Journal of Macromolecular Science, Part A. 2010 Dec 29;48(2):108-18.

11. Guedidi H, Reinert L, Lévêque JM, Soneda Y, Bellakhal N, Duclaux L. The effects of the surface oxidation of activated carbon, the solution pH and the temperature on adsorption of ibuprofen. Carbon. 2013 Apr 30;54:432-43.

12. Baccar R, Sarrà M, Bouzid J, Feki M, Blánquez P. Removal of pharmaceutical compounds by activated carbon prepared from agricultural by-product. Chemical engineering journal. 2012 Nov 15;211:310-7.

13. Nabais JV, Mouquinho A, Galacho C, Carrott PJ, Carrott MR. In vitro adsorption study of fluoxetine in activated carbons and activated carbon fibres. Fuel Processing Technology. 2008; May 31;89(5):549-55.

14. Giles, CH, MacEwan, TH, Nakhwa, SN, Smith, DJ. Studies in adsorption. Part XI. A system of classification of solution adsorption isotherms, and its use in diagnosis of adsorption mechanisms and in measurement of specific surface areas of solids. Journal of the Chemical Society. 1960;   786: 3973-3993.

15. Langmuir I. The adsorption of gases on plane surfaces of glass, mica and platinum. Journal of the American Chemical society. 1918 Sep; 40(9): 1361-403.

16. Freundlich H. Über die adsorption in lösungen. Zeitschrift für physikalische Chemie. 1907 Oct 1;57(1):385-470.

17. Myers, D. (1999) Surfaces, Interfaces, and Colloids: Principles and Applications; New York: John Wiley & Sons, Inc.

18. Marra MC, Silva PL, Muñoz RA, Richter EM. Ultra-fast determination of scopolamine, orphenadrine, mepyramine, caffeine, dipyrone, and ascorbic acid by capillary electrophoresis with capacitively coupled contactless conductivity detection. Journal of the Brazilian Chemical Society. 2014 May;25(5):913-9.

19. Wu Y, Xi B, Hu G, Wang D, Li A, Zhang W, Lu L, Ding H. Adsorption of tetracycline and sulfonamide antibiotics on amorphous nano-carbon. Desalination and Water Treatment. 2016 Oct 7;57(47):22682-94.

20. Ji L, Chen W, Zheng S, Xu Z, Zhu D. Adsorption of sulfonamide antibiotics to multiwalled carbon nanotubes. Langmuir. 2009 Sep 3;25(19):11608-13.

21. Gao Y, Li Y, Zhang L, Huang H, Hu J, Shah SM, Su X. Adsorption and removal of tetracycline antibiotics from aqueous solution by graphene oxide. Journal of colloid and interface science. 2012 Feb 15;368(1):540-6.

22. Wibowo N, Setyadhi L, Wibowo D, Setiawan J, Ismadji S. Adsorption of benzene and toluene from aqueous solutions onto activated carbon and its acid and heat treated forms: influence of surface chemistry on adsorption. Journal of Hazardous Materials. 2007 Jul 19;146(1):237-42.

23. Rivera-Utrilla J, Sánchez-Polo M. The role of dispersive and electrostatic interactions in the aqueous phase adsorption of naphthalenesulphonic acids on ozone-treated activated carbons. Carbon. 2002 Dec 31;40(14):2685-91.

# THE LATEST ADVANCEMENTS IN THE ACYLATION REACTIONS VIA CROSS-DEHYDROGENATIVE COUPLING AND/OR METAL CATALYSTS

Soykan Agar[1*] iD, Omer T. Gunkara[2] iD

[1]Department of Chemistry, Faculty of Science and Arts, Istanbul Technical University, Maslak, Istanbul 34469, Turkey;
[2]Department of Chemistry, Faculty of Science and Arts, Yildiz Technical University, Davutpasa Campus, Istanbul, Turkey.

**Abstract:** There are quite many examples in the scientific literature regarding the acylation reactions, especially the metal-catalyzed acylation reactions, metal-free acylation reactions, metal-catalyzed acylation via cross-dehydrogenative coupling (CDC) reactions and metal-free acylation via cross-dehydrogenative coupling (CDC) reactions. In this review paper, the most important examples of these domains were brought together and their mechanisms were exhibited in a clear, chronological format. Following these, the best example study towards green chemistry with a metal-free and high-yielding route was mentioned and discussed to demonstrate what has achieved in this field regarding the new acylation reaction mechanisms using the advantages of cross-dehydrogenative coupling (CDC) reactions. The most prominent studies regarding these domains have been examined thoroughly and the latest progress in this field was explained in detail.

## INTRODUCTION

Without a doubt, synthetic chemists always aim developing novel chemical reaction pathways at all times while trying to improve the mildness of reaction conditions. Such a goal is necessary to maximize the energy and product efficiency, product selectivity, chemical pathway simplicity, and environmental health and safety. Depending on this, carbon−carbon bond formation is known to be the central part of many chemical syntheses, and discoveries where these types of carbon−carbon bond formation reactions have the potential to improve overall synthetic efficiency. The acylation of aromatic compounds possesses quite a significant shelf in the library of organic chemistry. The acyl variations of aromatic compounds are widely used in the fields of drug designs, pharmaceuticals and as the building blocks in the polymer chemistry (1-3).

In order to get some environmentally benign results in the field of organic synthesis, a brand new concept of cross-coupling reaction, cross-dehydrogenative coupling, was discovered. Under the conditions of oxidative medium, from the reaction of two C-H bonds, form directly varying C-C bonds. Such discoveries within this cross-dehydrogenative coupling field lead us to the direct and efficient formation of C-C bonds. Therefore, the main advantage of this issue when we lean onto the mechanistic details of CDC is that this area has the capability to become one of the most important foundations of green chemistry due to the possibility of the usage of mild medium conditions as well as serving as an auxiliary field for the technological application processes of aromatic organic syntheses; especially if there would be more studies concerning acylation reactions via metal free coupling reactions within mild conditions.

CDC reactions are mainly used to form bonds between $sp^3$-$sp^3$, $sp^3$-$sp^2$, $sp^3$-$sp$, $sp^2$-$sp^2$ (including Heck-type reaction), $sp^2$-$sp$ (Sonogashira type) and $sp$-$sp$ (Glaser reaction) carbon atoms and also $C(sp^3)$-N. Due to these plethora of varying bond formations that CDC reactions possess, the CDC definition consists of a group of reactions where the mechanism and reactivity varies and differs dramatically depending on the substrate. These above mentioned couplings can be roughly divided into four groups including CDC *via* Heck-type mechanism, direct arylation, CDC *via* ionic intermediates and CDC *via* radical intermediates (4).

The first group, CDC via Heck-type mechanism should be emphasized since it is a significant matter where this type mechanism (5) is a member of typical $sp^2$-$sp^2$ CDC reactions including alkene-alkene, arene-alkene and arene-benzoquinone coupling; and also an $sp^3$-$sp^2$ type; and a formal $sp^3$-$sp^2$ type concerning enolate-alkene, allyl-arene coupling. As it can be seen from the name of CDC via Heck-type mechanism, the mechanism is very similar to Heck Reaction itself. Even though the fact that the same reactivity may be achieved with transition metals such as Rh(II), Ru(III) and

Ir(I) complexes, Palladium (6) salts are generally chosen as the catalysts. The arene ring undergoes electrophilic palladation with an assistance of a ligand or achieved via a base mediated C-H insertion, along with a Pd(II) catalyst to generate arylpalladium intermediate. Subsequent carbopalladation of olefin forms the alkylpalladium complex that further proceeds through syn-β-H elimination to yield styrenyl product and Pd(0). The last step is the oxidation of Pd(0) to Pd(II) to complete the catalytic cycle. In an alternative proposed mechanism, the Pd(II) catalyst gets used to form coordination with the olefin which enhances its electrophilicity and tendency to undergo nucleophilic addition via the electron rich aromatic rings. Such catalytic systems in the CDC via Heck-type mechanism are not usually too complex as one might think of, since they require no or solely a simple ligand as the following examples; phosphines, N-protected amino acids or sulfoxides. Any organic or inorganic base can also be utilized on top of that. In the cases where the formation of more than one product is possible, the regio-selectivity is normally achieved by the introduction of a directing group onto the aromatic ring whereas the pyridyl-based groups are the most extensively used ones to direct transition-metal-catalyzed C−H activation reactions, both ortho- and meta- (7).

The second group of CDC reactions, the direct arylation, also known as 2-fold C-H activation, is used to form bonds between two arenes (8). The strategy of direct arylation is an alternative route to such very well-known and widely used methods as Suzuki, Stille, Negishi, Hiyama, Kumada cross-couplings which require independent synthesis and isolation of aryl halide or pseudohalide and arylmetal starting materials.

Unlike the first two mechanisms, the third group, CDC via ionic intermediates can be promoted by various transition metals involving Pd, Ru, Zr, Ni, Cu, Fe, Co and the list goes on and on whereas the last three are the most widely used ones. Although some exceptions are known, the ionic mechanism predominantly relies on the single electron transfer (SET) pathway (9). In its mechanism, C-C/N bond formation occurs between the electrophilic carbon species (carbocations) and carbon- or nitrogen-based nucleophiles such as amine, amide, carbanion, enamine, heteroaromatic structures.

The final group of CDC reactions, CDC via radical intermediates, is very similar to the one described above (the ionic one), except the fact that no ionic intermediates get formed. The newly generated carbon centered radical, directly reacts with another active specie such as a carbocation, carboanion, C-C multiple bond, forming further a second radical which later on gets oxidized either by an oxidant (10) or transition metal (11) yielding the desired product. The radical CDC is exclusively promoted by first row transition metal complexes in the periodic table such as Cu, Fe, Mn (in some cases vanadium oxo-species) via single electron transfer type of a pathway. Selective

C-H bond oxidation of a radical can be accomplished with phenols, electron-rich arenes, benzylic compounds and $C(sp^3)$-H bond α- to carbonyl or heteroatom (O or N) structures.

These all sub-categories of CDC reactions state one important message that CDC is a promising approach to minimize the byproduct formation and reduce the total number of steps of the organic syntheses (12-26). Acylation reactions are commonly used in these aforementioned mechanisms of CDC reactions, and since they take an important place along with the CDC reactions, in this review, the latest advancements of acylation reactions and their relationship with CDC reactions were examined and explained as expressed in the following studies.

**The Metal Catalyzed Acylation and Coupling Reactions**

Li and co-workers has quite an important paper published in 2010 regarding the study of copper catalyzed intramolecular C-H oxidation/acylation of formyl-*N*-arylformamides (27). In this study, indoline-2,3-dione was synthesized with the use of a copper catalysts by acylation. Indoline-2,3-diones were known to be the building blocks that are widely used. Until 2010, there were only two other synthetic routes for indoline-2,3-diones. However, with the addition of this new route, found by Li *et al.*, now it gained a third significant organic synthetic pathway (**Scheme 1**).
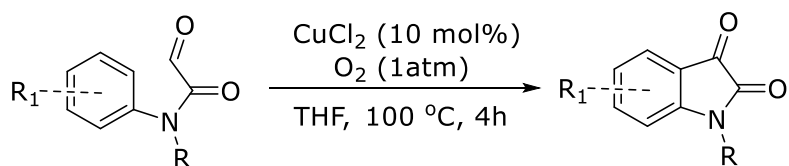


**Scheme 1:** The cyclization of phenylacetamide derivative with copper(II) chloride via Friedel Crafts acylation.

In the first step, Cu(I) gets oxidized to its second state. Then, Cu(II) forms a coordination complex with the aldehyde carbon and amide nitrogen and intermediate (I) gets synthesized. The $sp^2$ arene carbon couples to Cu(III) to yield intermediate (II), following the reductive elimination of intermediate (II) yielding the product and Cu(I) species. The control reaction was also studied in this paper in order to exhibit whether the mechanism is free radical or not. In the existence of radical terminating agents such as TEMPO and 1,1-diphenylethylene, the product was not affected since, the mechanism does not depend on any radical. Therefore, any possibility regarding that this is a free radical mechanism can be ruled out (**Scheme 2**).
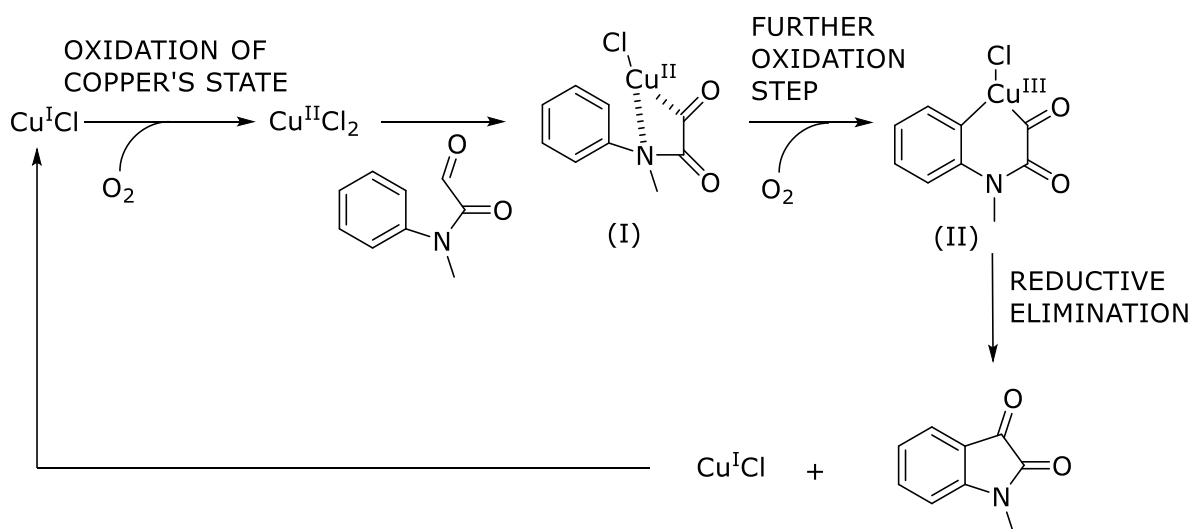
**Scheme 2:** The proposed mechanism of the cyclization of phenylacetamide derivative with copper(II) chloride via Friedel Crafts acylation.

In 2012, Zhu and co-workers published a study concerning Au(III)-catalyzed coupling reactions between alcohols and *N*-heterocycles via C−H bond activation. The scientific literature gained a new methodology regarding the acylation of *N*-heterocyclic compounds (28) (**Scheme 3**).
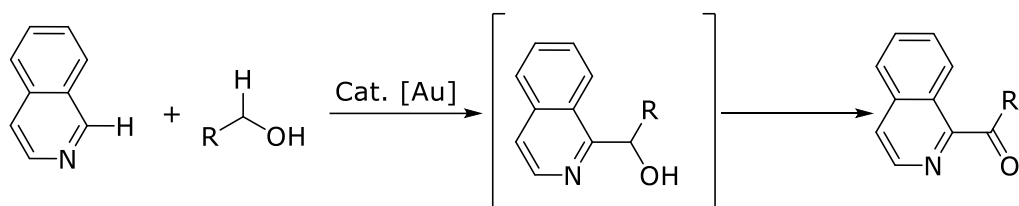


**Scheme 3:** Au-catalyzed dehydrogenative coupling between alcohols and isoquinoline.

In the first step, a *tert*-butoxide and hydroxyl radicals get formed under heat. With the hydrogen atom abstraction on the alpha position of ethanol, free radical intermediate (I) occurs. Then, this intermediate (I) reacts with the gold activated heterocyclic aromatic compound to yield intermediate (II). Intermediate (II) gets attacked by intermediate (I) to further yield intermediate (III) which is a metal complex of the heterocyclic aromatic compound. Following that, intermediate (III) gets rearomatized by the radical initiator *tert*-butoxide to yield the alcohol intermediate (IV). Then this alcohol intermediate (IV) is oxidized to the desired acylation product via Au/TBHP.

In the test reactions, it was observed that instead of the gold catalyst when some other metal catalysts were used, no product or some trace amounts of products were able to be obtained. This proves the necessity of the gold catalyst in the mechanism of this pathway (**Scheme 4**).
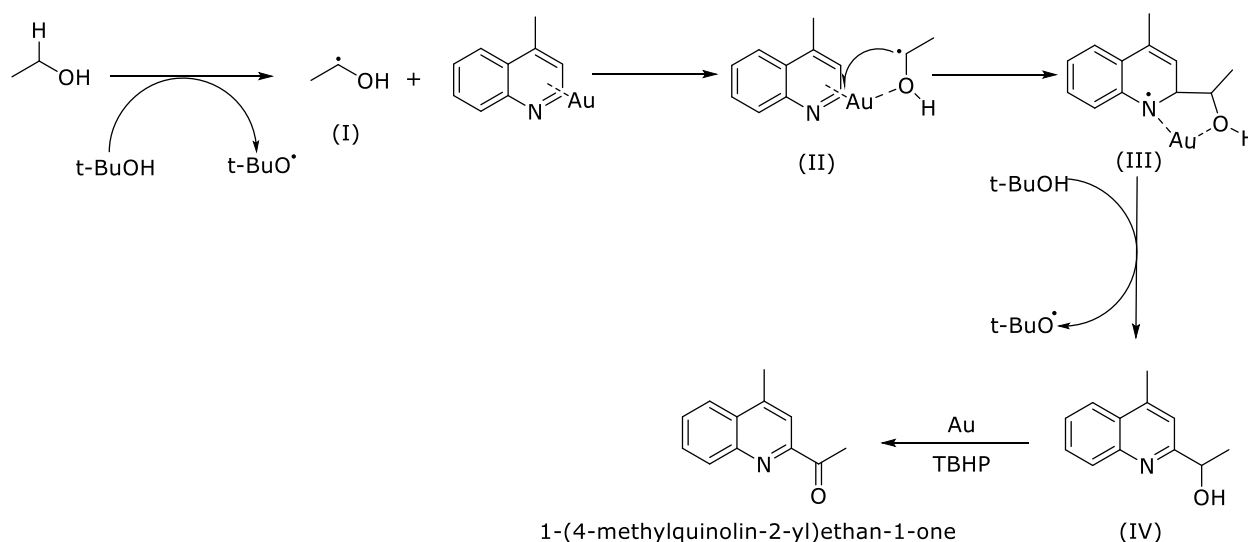
**Scheme 4:** The proposed mechanism of the Au-catalyzed dehydrogenative coupling reaction.

As it is well known, in the recent years, transition metal catalyzed decarboxylative cross coupling C-C bond formations have gained significant importance. Qi and co-workers in 2014, exhibited the silver-catalyzed decarboxylative acylation of arylglyoxylic acids (29). The result that they achieved in their study is quite an efficient pathway in the synthesis of non-symmetric diaryl ketones. In such a transformation reaction, alpha-oxocarboxylate was coupled with arylboronic acid via the corresponding silver(I) carbonate within the medium to give high yields and high functional group compatibility in aprotic polar solvents (**Scheme 5**).
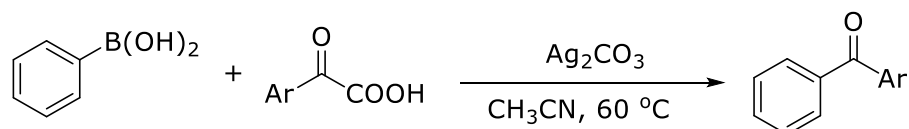


**Scheme 5:** Silver-catalyzed decarboxylative acylation of 2-*oxo*-2-phenylacetic acids with arylboronic acids.

The silver reacts with the arylglyoxylic acids derivative (2-*oxo*-2-phenylacetic acid) to give the corresponding silver salt. Then, decarboxylation occurs, acyl radical is generated *in situ*. Acyl radical attacks at the phenylboronic acid derivatives to obtain bis-aryl ketones (benzophenone derivatives) in good yields. After the product is obtained, the boronic acid radical [BH(OH)$_2$] reacts with silver radical and forms the boric acid and silver cation to complete/restart the cycle. When the radical trapping reagents, such as TEMPO got added into the reaction under the standard conditions independently, no desired product was detected, suggesting that a free radical course was involved in the reaction (**Scheme 6**).
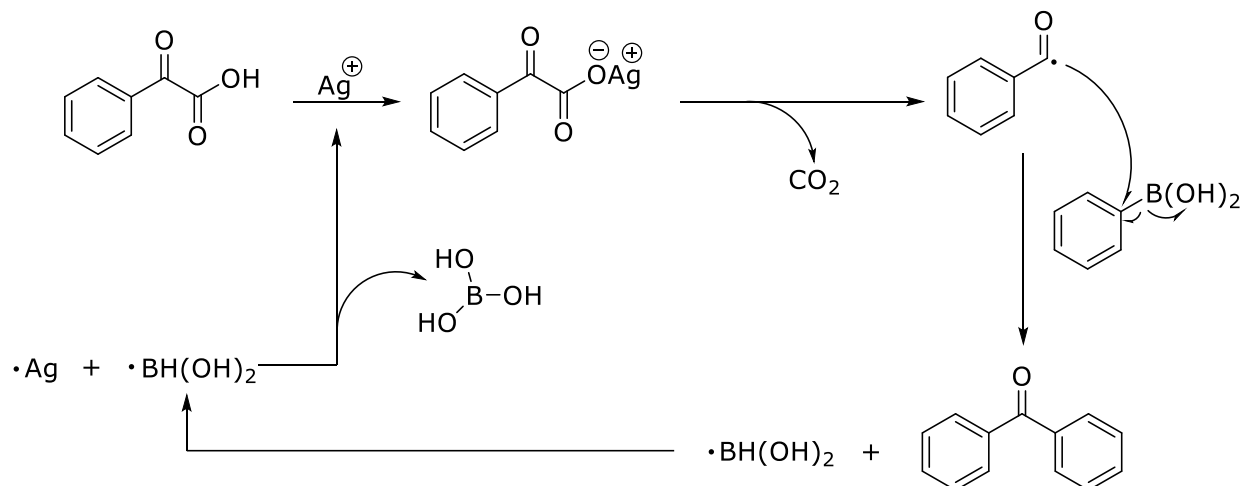
**Scheme 6:** The proposed mechanism of silver-catalyzed decarboxylative acylation of 2-*oxo*-2-phenylacetic acids with arylboronic acids.

The oxidation of alcohols into the aldehydes or ketones is one of the major and most significant reactions in terms of practical applications in the organic chemistry. In the same year, 2014, Nakazawa and co-workers, by using dehydrogenative reactions, synthesized the derivatives of 2-pyridylmethanol via iron complexes (30). Some series of acyl pyridine derivatives were successfully synthesized (**Scheme 7**).
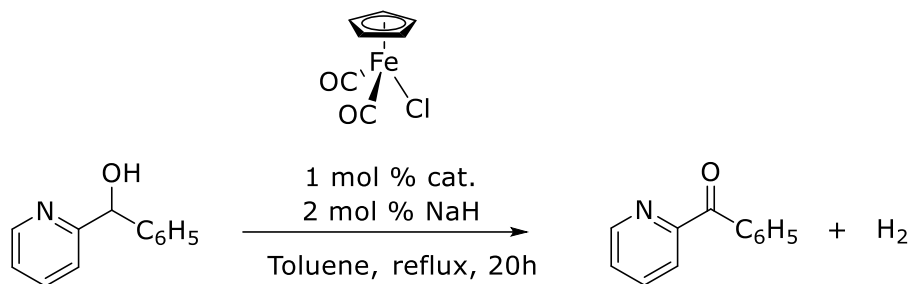


**Scheme 7:** The dehydrogenation of pyridin-2-ylmethanol via iron complex.

The alcohol reacts with the co-catalyst NaH to give the corresponding sodium alkoxide. Then this alkoxide reacts with iron complex to give the iron alkoxide complex. Following that, CO elimination occurs and the nitrogen atom in the attached pyridyl moiety displaces one of the CO ligands to give Intermediate (I). Dissociation of the intermediate (I) takes place, and the subsequent beta-hydride elimination produces the iron hydride complex (II) and the aldehyde product (2-pyridinecarboxyaldehyde). The nitrogen atom in the 2-pyridyl group within the first reactant is important for the iron catalyzed dehydrogenation since, 2-thiophenylmethanol (replacing nitrogen with sulfur) did not undergo dehydrogenation and 2-dimethylaminoethanol also did not undergo

dehydrogenation, indicating that the nitrogen atom in the aromatic ring (2-pyridyl) is important due to steric and/or electronic reasons. This vindicates the fact that nitrogen should be in the aromatic ring for this mechanism to work (**Scheme 8**).
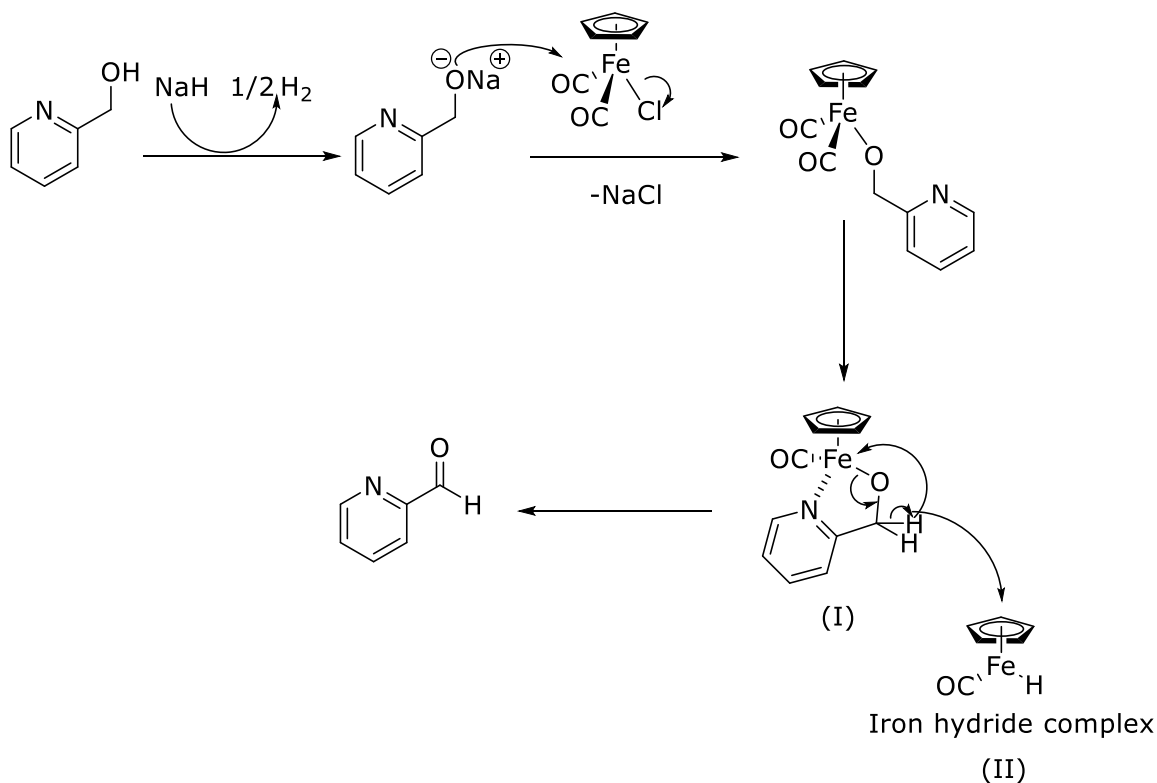


**Scheme 8:** The proposed mechanism of dehydrogenation of pyridin-2-ylmethanol via iron complex.

### The Metal-Free Acylation and Coupling Reactions

Gaunt and co-workers successfully synthesized bis-heteroaryl ketones beginning from heteroaryl aldehydes via N-heterocyclic carbene (NHC) catalyst in 2013 (31). Diaryl ketones can both be synthesized via Friedel Crafts reactions or the classical methodology of the addition of carbonyl compounds into the aryl-metal complexes. However, these mentioned synthetic pathways does not work with heteroaryl aldehydes since the organometallic reagents do not fit together with nucleophiles, and also Friedel-Crafts acylation requires π-electron-rich arenes to work better. That is the reason why the synthesis of bis-heteroaryl ketones via NHC catalyst beginning from heteroaryl aldehyde reactants is quite significant (**Scheme 9**).
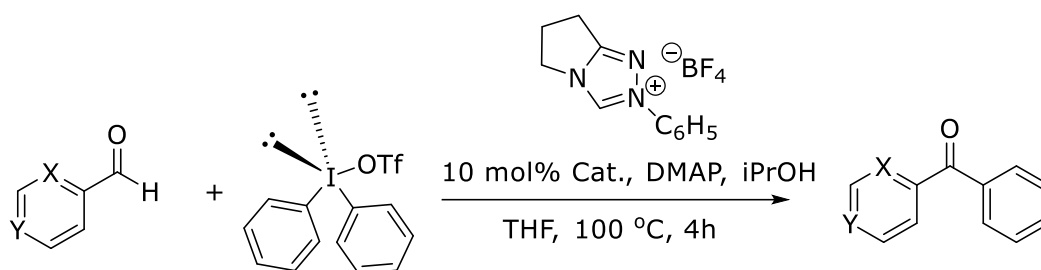
**Scheme 9:** The proposed mechanism of *N*-heterocyclic carbene-dependent bis-heteroaryl ketone formation via carbogenic nucleophilic transformation.

In this transformation, an NHC catalyst reacts with an aldehyde to form a transient carbogenic nucleophile, Breslow Intermediate (I) with a double bond. This Breslow intermediate's double bond is active to do a nucleophilic attack due to the reason that the nitrogen contributes to the ring aromaticity and the π electrons in the double bond easily attacks at the iodine. It should not be forgotten that triflate is a good leaving group. In the case of intermediate (II), the intermolecular rearrangement occurs and iodine leaves and following that in the case of intermediate (III), nitrogen draws electrons, "nitrogen-heterocyclic carbene" catalyst gets eliminated and the desired product bis-heteroaryl ketone is obtained. The catalytic cycle is now complete (**Scheme 10**).
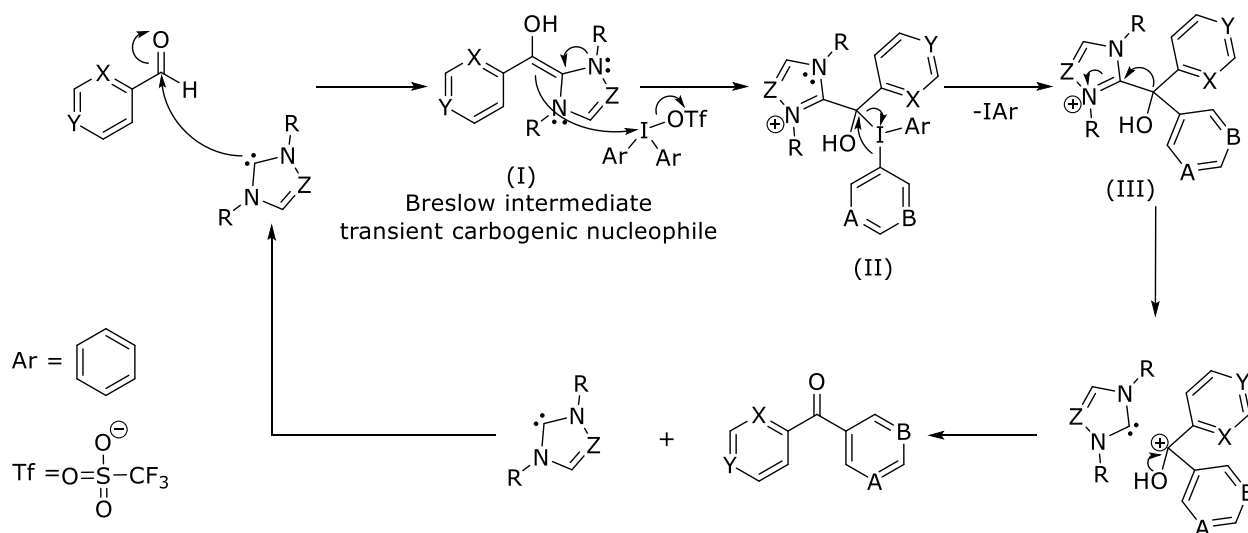


**Scheme 10:** The proposed mechanism of *N*-heterocyclic carbene dependent bis-heteroaryl ketone formation via carbogenic nucleophilic transformation.

**The Metal Catalyzed Acylation Reactions via Cross-Dehydrogenative Coupling**

With respect to a study of Zhaorigetu and co-workers in 2016 with the topic of "Replacing Pd(OAc)$_2$ with the supported palladium nanoparticles in ortho-directed CDC reactions of alkylbenzenes", the CDC reaction was achieved with the use of palladium nanoparticles instead of using palladium acetate. The "ortho-directing CDC reactions of alkylbenzenes" were possible to be achieved with the use of palladium nanoparticles since, the "supported palladium nanoparticle catalyzed ortho-directing C-C coupling reactions of 2-arylpyridines and aldehydes" were stated to be occurring without any repeatability problem. To express and prove how high efficiency and repeatability they possess, it can be said that "Pd/γ-Al$_2$O$_3$ catalyst with palladium nanoparticles with the mean diameter sizes of 3.21 nm" showed quite a high catalytic activity and even the best one, compared to the other series of supported palladium nanoparticles. On top of that, without losing any significant catalytic activity, Pd/γ-Al$_2$O$_3$ catalyst with palladium nanoparticles were able to be used five times.

To sum up the study, one can claim that the metallic state palladium is able to catalyze "ortho-directing CDC reaction of alkylbenzenes" including methyl, ethyl and propyl benzene variations for the synthesis of aromatic ketones and palladium states alter within the catalytic cycle. If someone decides to use high catalytic content in an organic reaction, it had been better to choose PdNP catalyst over Pd(OAc)$_2$ since the PdNP catalyst has some beneficial advantages such as higher catalytic activity, easy separation and recycling due to being a heterogeneous catalyst (**Scheme 11**) (32).
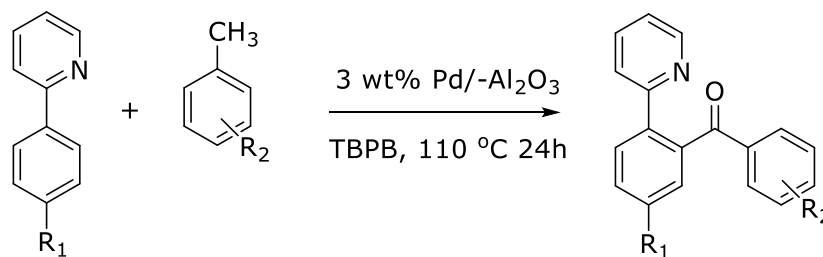


**Scheme 11:** The synthesis of aromatic ketones via C–H functionalization.

**The Metal-Free Acylation Reactions via Cross-Dehydrogenative Coupling**

Cross-dehydrogenative coupling (CDC) reactions have developed in time as some quite important tools for the synthesis of varying useful organic compounds due to their atom-economically shorter routes. In general, cross coupling reactions have been quite famous since the beginning of the 2000s depending on the fact that in the C-C bond constructions, they possess high regioselectivity and yields, and are especially quite efficient in the construction of varying complex architectures of the ubiquitous building blocks that can be mostly found in natural products. In order to improve new methodologies concerning much greener chemistry with high yields, C-H functionalization was

mostly emphasized nowadays and some quite progress has been observed in C-H bond activation in arenes. Within the last decade, these brand new discoveries have led to the achievement of C-H bond activation and C-C bond formation, solely emerging from two unfunctionalized structures possessing two different C-H bonds (33).

One of the main discoveries regarding this field has arrived in the year of 2015. Liu and co-workers published the oxidative dehydrogenative cross-coupling reaction of aldehydes along with the *N*-heterocyclic compounds (34). In their study, they successfully achieved the acylation of isoquinoline derivatives with varying aldehydes. As the oxidant, *tert*-butyl hydroperoxide (TBHP) and as the acid source trifluoroacetic acid (TFA) were used. TBHP/TFA was chosen due to the fact that in the oxidative cross-dehydrogenative coupling reactions of some varying *N*-heterocycles with diverse aldehydes (under metal free conditions), TBHP/TFA exhibited practical, scalable and highly efficient oxidation medium. These advantages results in the facile synthesis of broad range of structurally diverse C1-acyl substituted heterocycles since, the scope of these varying aldehyde components is broad and these aldehyde components, concerning both aromatic and aliphatic compounds, tolerate electronically varied substituents quite well (**Scheme 12**).
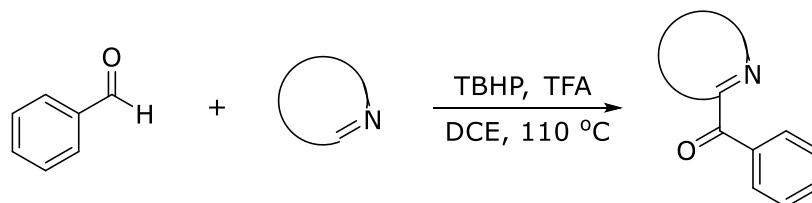


**Scheme 12:** TBHP/TFA mediated oxidative cross-dehydrogenative coupling of *N*-heterocycles with aldehydes.

Benzaldehyde is converted into its acyl radical in the presence of *tert*-butylhydroperoxide. "Nitrogen Heteroaryl" (quinoline derivatives) can be activated with TFA to facilitate the addition of intermediate (I) radical onto the "carbon-2 of protonated nitrogen heteroaryl" providing the radical cation intermediate (II). Then this radical cation reacts with the *tert*-butoxyl radical to yield the desired "acylated quinoline derivatives". When TEMPO is added, no product could be obtained stating that this pathway was in free radical nature (**Scheme 13**).
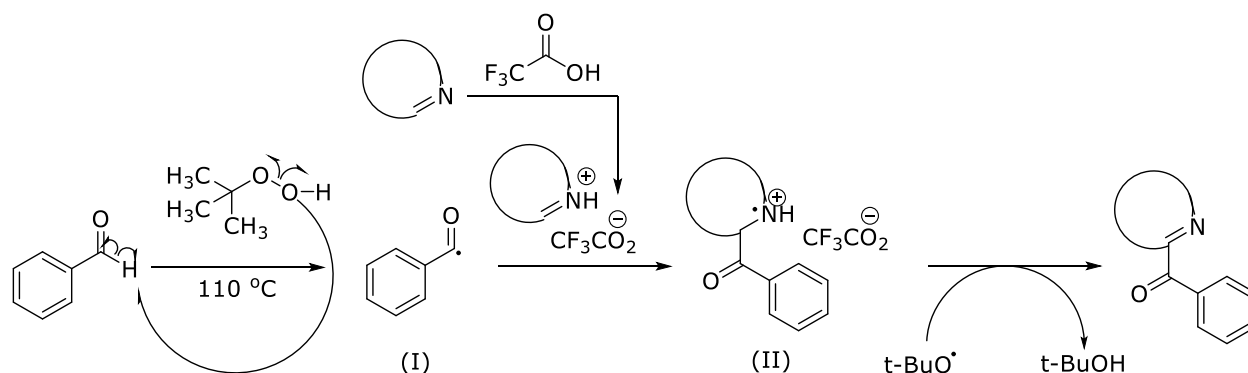
**Scheme 13:** The proposed mechanism of TBHP/TFA mediated oxidative cross-dehydrogenative coupling of *N*-heterocycles with aldehydes.

Most recently, the acylation of coumarins via CDC approach using aldehydes to serve as acylating agents was investigated in detail by Adib group (35), Qu (36) and Zhou (37). On top of these studies, Duan and co-workers illustrated the Ag-catalyzed diacylation of coumarins using oxocarboxylic acids as the acyl sources (38). In 2016, Adib and co-workers explained an efficient route for the intermolecular double $Csp^2$–H functionalization between aromatic aldehydes and 3-acetylcoumarins through $Csp^2$–$Csp^2$ bond formation leading to 4-aroylcoumarin derivatives (39) (**Scheme 14**).
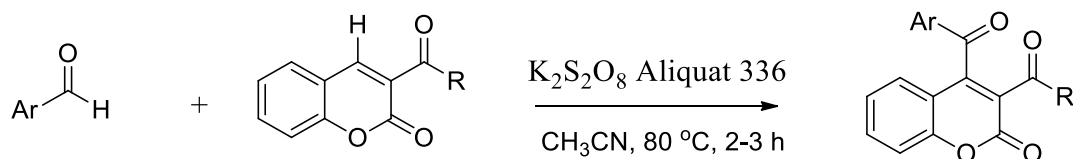


**Scheme 14:** The acylation of coumarins via CDC approach.

In order to vindicate the mechanism behind this theory, 4-methylbenzaldehyde and 3-acetylcoumarin were chosen as the model reaction substrates to optimize the CDC reaction conditions. In this optimization, the aim was to investigate the effect of several oxidants, solvents, additives, reaction temperature and time as well as various equivalents of oxidants and additives. Initially, this model reaction was tested in the presence of $K_2S_2O_8$ (1.0 equiv.) as the oxidant and Aliquat 336, tricaprylmethylammonium chloride, (40-42) (15 mol%) as the additive in acetonitrile at room temperature or 50°C for 2 h, but no product was formed. By rising the temperature to a higher degree like 80°C, 4-arylcoumarin was obtained with 65% yield. Subsequently, different quantities of $K_2S_2O_8$ and Aliquat 336 were utilized to improve the yield percentages. Increasing the amount of the additive Aliquat 336 to 30 mole percent led to the desired product 4-arylcoumarin to reach 78% yield. Ironically, increasing the amount of Aliquat 336 a bit more to 40 mole percent had no effect on the yield. Therefore, another parameter should be altered to see whether any further

effect on yield can occur or not. Thus, using 1.2 and 1.5 equiv. of $K_2S_2O_8$ along with 30 mole percent of Aliquat 336 resulted in the desired product 4-arylcoumarin to be obtained in 87% and 83% yields, respectively. Further rising the temperature to 100°C decreased the efficiency and yield percentage of the reaction. Some other additives such as NBS, $I_2$, KI and CuI were also screened in the study. However, they had no observable effect in this CDC reaction. Following these tests, the effects on efficiency of varying solvents were carried out with toluene, chlorobenzene, 1,4-dioxane, DCE, DMSO/$H_2O$ (1 : 1, v/v), DMSO and $H_2O$. However, carrying out the reaction in these solvents resulted in the 40–65% yields of 4-arylcoumarin and in DCE the product was not detected at all. Also, the reaction was performed in the solvent mixture of $CH_3CN/H_2O$ (1 : 1, v/v), and the yield was 82%. More testing was also done to indicate the fact that with the use of $(NH_4)_2S_2O_8$ and TBHP as the oxidants, the yield of 4-arylcoumarin decreased to 60% and 40%, respectively. Furthermore, oxidants such as $H_2O_2$ and DDQ were also inert in this CDC reaction. Without $K_2S_2O_8$ as the oxidant and Aliquat 336 as the additive, the completion of CDC reaction was not possible to proceed in $CH_3CN$ at 80°C after 2 h. So, the optimal conditions for the metal-free CDC acylation of cumarins were determined as the use of $K_2S_2O_8$ (1.2 equiv.), Aliquat 336 (30 mole percent), acetonitrile as the solvent, 80°C as the medium temperature and the duration is 2 hours. To understand and verify the mechanism of $K_2S_2O_8$/Aliquat 336 promoted acylation, the reaction between benzaldehyde and 3-acetylcoumarin was performed in the presence of a radical scavenger, 2,2,6,6-tetramethylpiperidin-1-yl-oxyl (TEMPO). 2,2,6,6-tetramethylpiperidino benzoate was obtained with 96% yield and the desired acylated product was not detected at all, proving that an acyl radical was involved in CDC catalytic cycle.

The whole mechanisms described earlier within the review for the use of acylation reactions of simple aromatic compounds and/or aromatic heterocyclic compounds tend to have low/moderate yields and only in some rare cases, have high yields and are quite far away from the green chemistry. However, if such an organic design would be made to make it greener in terms of no use of metal catalysts and if and only if there would a possibility to reach quite high yields without the cost of precision, then it would have become a more feasible, efficient and a compatible design and discovery within the boundaries of green chemistry. Therefore, if there would be such a study, researching a new organic pathway regarding the metal free CDC acylation of heterocyclic compounds such as pyridine derivatives, it would have been a huge contribution to the shelves of organic chemistry library. In that sense, a study with the name of ''Metal-free chemo- and regioselective acylation of pyridine derivatives with alcohols in water'' was published in 2017 (33). In that study, Kianmehr *et al*. described a new acylation methodology of pyridine derivatives without using metal catalysts. Beginning the synthesis from benzylic and aliphatic alcohols and using CDC reactions without metal catalysts in water medium, they were able to synthesize 2-acylpyridines for the first time with such a protocol and with such quite high yields as it is shown in (**Schemes 15-**

**19**). The reaction is compatible with accessible aliphatic alcohols and aromatic alcohols as the acylation sources and provides a new route to both alkanoyl- and aroylpyridines. In the general outline of the protocol shown in (**Scheme 15**), as a radical agent peroxydisulfate ($K_2S_2O_8$) was used. To prove the role of the peroxydisulfate as a radical agent in their mechanism, a control reaction was performed. When the reaction of pyridine was performed in the presence of 2,6-di-*tert*-butyl-4-methylphenol (BHT) as a radical-scavenger, no desired product was obtained.
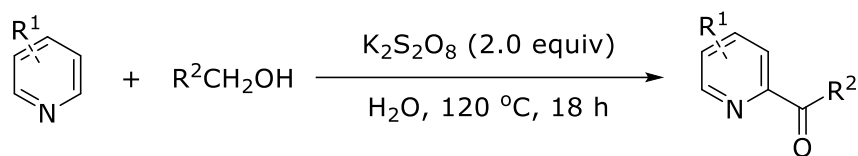


**Scheme 15:** The synthesis of 2-acylpyridine derivatives.
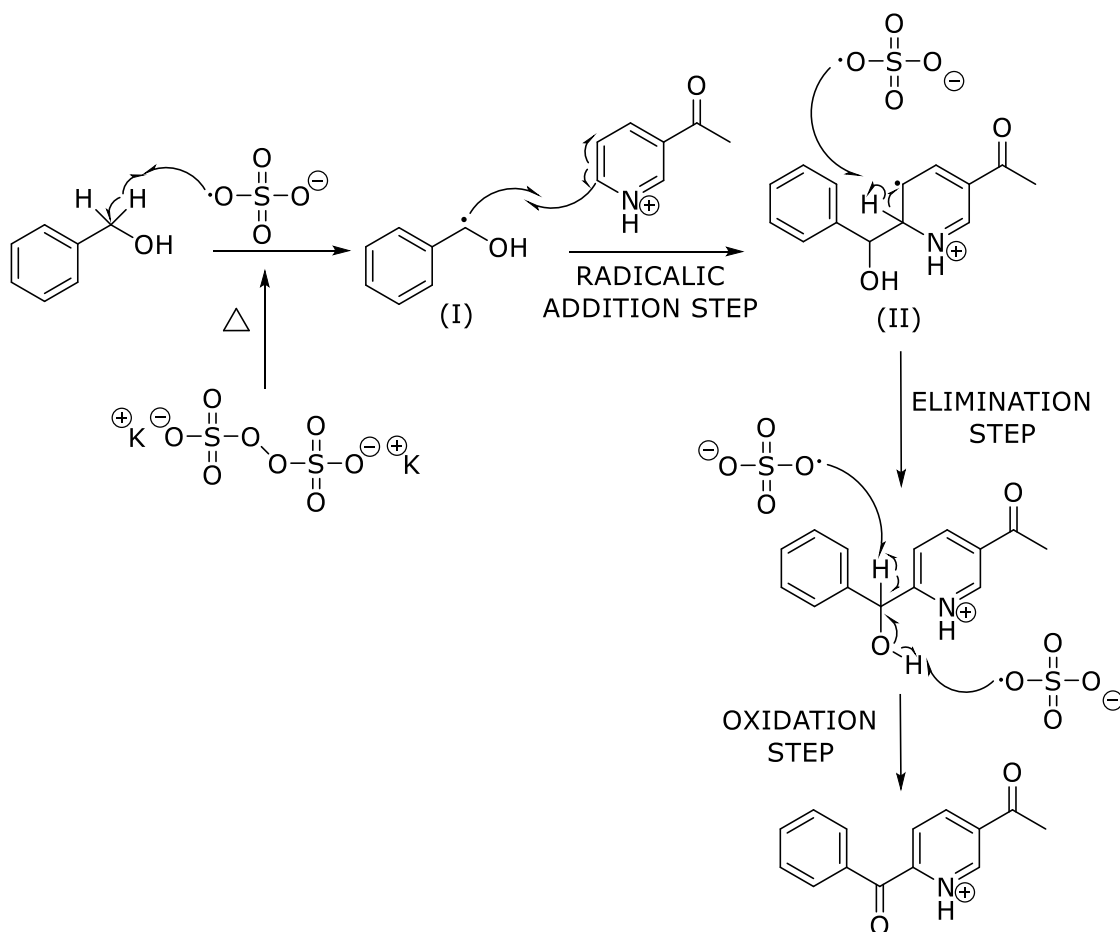


**Scheme 16:** The first proposed mechanism for the reaction.

In (**Scheme 16**), intermediate (I) is generated, *in situ*, through hydrogen atom abstraction from the benzyl alcohol in the presence of sulfate radical anion which is produced from peroxydisulfate ($K_2S_2O_8$). Radical addition of intermediate (I) to pyridine derivative occurs which gets protonated

under the reaction conditions, giving intermediate (II) which also leads to the formation of the product by elimination followed by oxidation (Medium: $H_2O$).

It should be further discussed that a second pathway (**Scheme 17**) is also possible for this acylation reaction using benzyl alcohols as the acylation sources. Benzyl alcohol is oxidized to benzaldehyde under the reaction conditions. Hydrogen atom abstraction from benzaldehyde in the presence of sulfate radical anion gives intermediate (III). The obtained free radical attacks the C-2 position of 3-acetylpyridine which is protonated under the reaction conditions, producing the corresponding free radical intermediate (IV). Finally, a hydrogen atom abstraction from the intermediate (IV) yields the desired product.
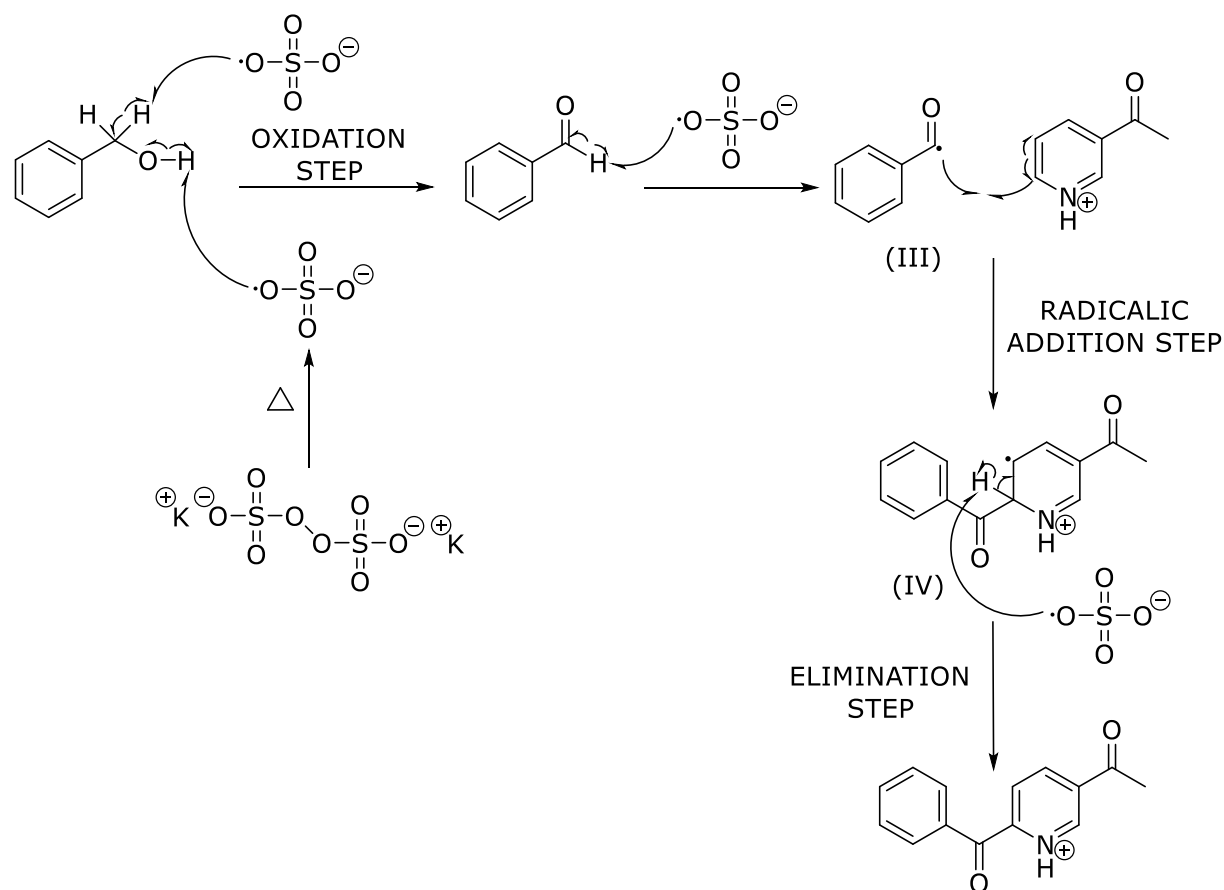


**Scheme 17:** The second proposed mechanism for the reaction.

This second pathway is confirmed by the observations with a test reaction concerning benzyl alcohol getting oxidized to benzaldehyde in the absence of pyridines under the reaction conditions and also with the fact that, the reaction proceeds successfully with benzaldehydes as the coupling partners instead of benzyl alcohols.

Why there are two proposed mechanisms in which neither of them can be ruled out, is a pretty good question that needs to be answered. If the 2nd pathway yields a product from benzaldehyde, then how can we make sure that the first pathway still works ?

Reaction 1
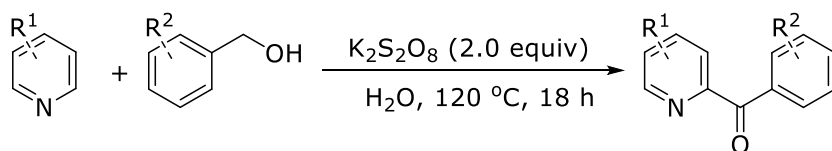


Reaction 2
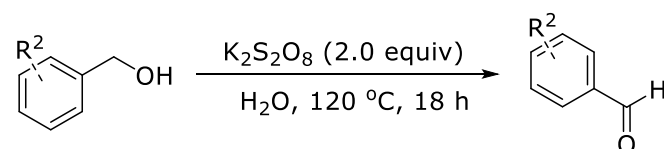


Reaction 3
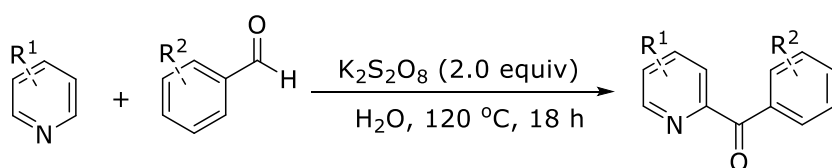


Reaction 4
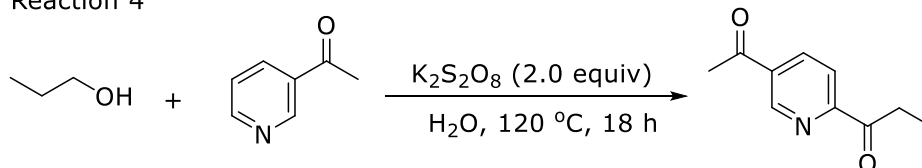


Reaction 5
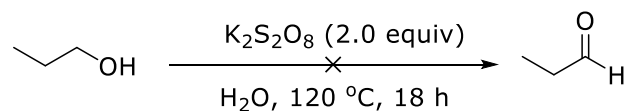


Reaction 6
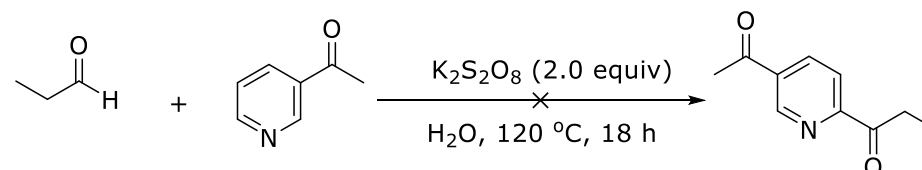


**Scheme 18:** The General Scheme of all test reactions.

Regarding this issue, (**Scheme 18**) will be helpful to comprehend the big picture behind it. In reaction 1, benzyl alcohol reacts with pyridine derivative yielding the final desired products, proving that the total reaction works. When it is taken a look at the reaction 2, the second proposed pathway is confirmed by the observation that was done where benzyl alcohol is oxidized to the corresponding aldehyde in the absence of pyridine (under the same reaction conditions). In the case of reaction 3, beginning the synthesis from the aldehyde immediately vindicates the second proposed pathway since it yields the final product. In reaction 4, when the aliphatic alcohol reacts with pyridine derivative, it yields the final product, showing that the total reaction works for aliphatics as well. In reaction 5, when it was again tried with the aliphatic alcohol but this time without pyridine, it was observed that the oxidation of ethanol and propanol to the corresponding aldehydes was not successful. This incident supports the first proposed mechanism. Therefore, any idea that may come into the mind to rule out the first mechanism cannot be possible after the incident of this test reaction. In the final reaction trial, the sixth one simply states that the total reaction failed to proceed when it was started from aliphatic aldehydes (ethanal and propanal) as the coupling partners where this again supports the first proposed mechanism.

The result that can be obtained from these test reactions is that the mechanisms concerning benzyl alcohol can both include the first and second proposed mechanisms. However, in the case of aliphatic alcohols, solely the first mechanism works. In the case of where benzyl alcohol is the reactant, benzylic radical due to its own aromaticity is more stable than the aliphatic alcohol in terms of getting attacked by a radical. Therefore, the second proposed mechanism's first oxidation step cannot occur when the aliphatic alcohol is the reactant.

All in all, Kianmehr *et al*. efficiently designed organic pathways which are practical methodologies for the chemoselective and regioselective synthesis of 2-acylpyridines, beginning from the pyridine and some varying aliphatic and benzylic alcohol reactants. Besides the good yields that can be seen in (**Scheme 19**), throughout the products of 6 to 9, the yields are moderately good when electron withdrawing groups such as cyanide, acetyl, ester are attached to the pyridine ring. Besides that, one of the main adventageous sides of this study is that it was performed within the water medium. Thus, this leads to the fact that it can be applied to decipher new materialistic discoveries especially in biotechnology and material science/engineering since the discovered routes to synthesize 2-acylpyridines are pretty straightforward, possess high yields, requires environmentally compatible and mild medium such as the use of water as a solvent and the benefit of not being forced to use any metal catalysts. Hence, if some new materials and compounds possessing good tolerance of various functional groups gets desired to be studied in the future, these kind of new acylation pathways just like the ones in this study, are always helpful for new technological advancements.

1 (87%)　　　　　2 (85%)　　　　　3 (83%)

4 (71%)　　　　　5 (85%)　　　　　6 (68%)

7 (82%)　　　　　8 (66%)　　　　　9 (89%)

10 (85%)　　　　　11 (86%)　　　　　12 (69%)
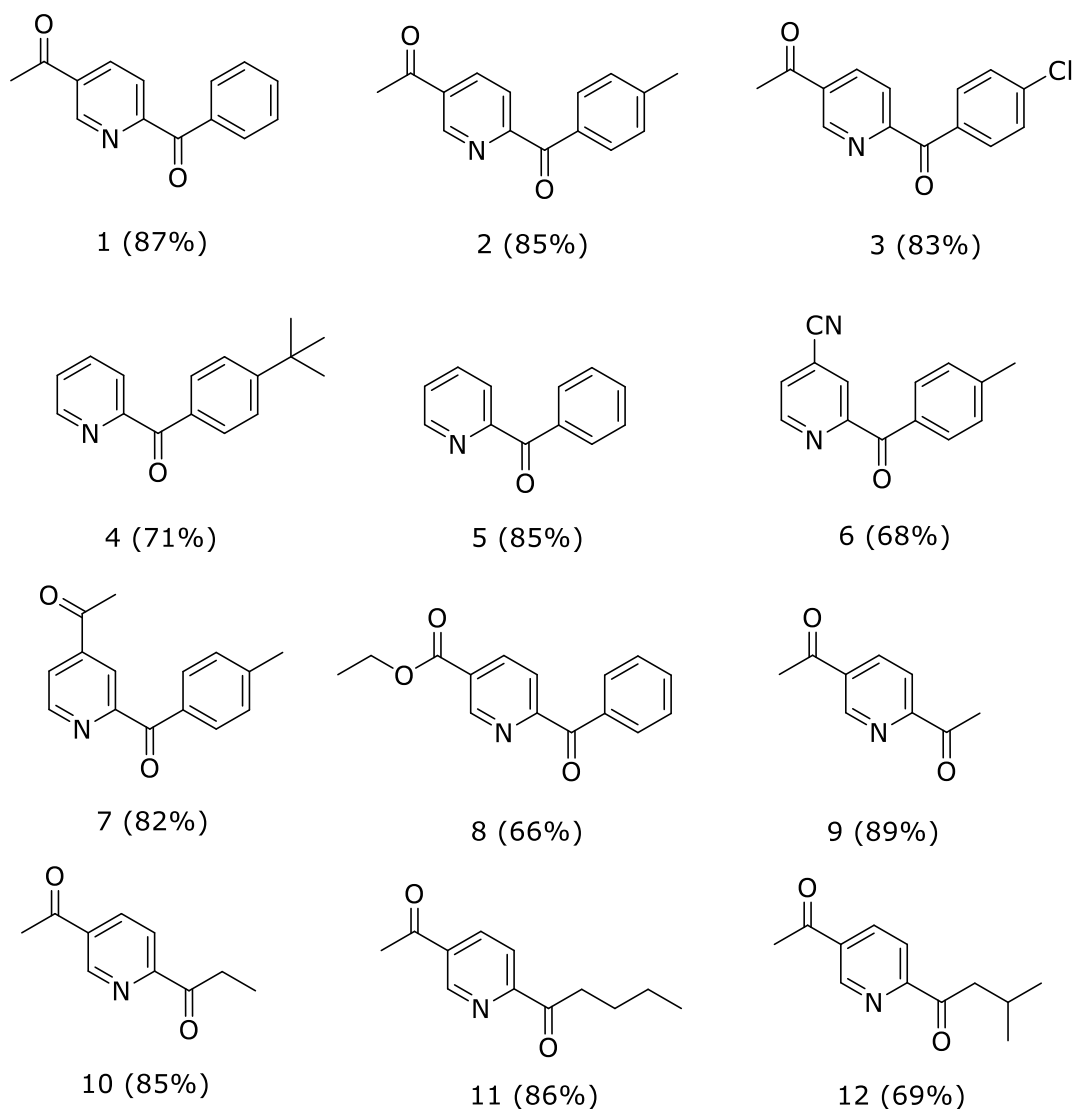
**Scheme 19:** Various products of 2-acylpyridines.

**CONCLUSION**

The acylation of aromatic compounds has quite a significant role both within the scientific advancement of organic chemistry itself and its technological applications in which serving as building blocks in the material science/engineering, drug designs, pharmaceuticals and polymer chemistry. Due to the importance of this field, different research institutes throughout the world try to decipher mechanisms concerning varying CDC reaction types for the use of acylation reaction in the organic chemistry. Thus, as it can be seen from what was mentioned earlier within the review paper, the corner stone mechanisms regarding the metal catalysts and/or metal-free CDC reactions for the use of acylation reactions in the aromatic compounds have been discussed comprehensively so far. Among the examined cross coupling reactions, Kianmehr *et al*.'s new protocol published in

2017, represents a more environmentally benign, practical, high yielding and cost effective methodology for the acylation of aromatic compounds.


## REFERENCES

1. Hashimoto I, Kawaji T, Badea FD, Sawada T, Mataka S, Tashiro M, et al. Regioselectivity of Friedel-Crafts acylation of aromatic compounds with several cyclic anhydrides. Res Chem Intermediat. 1996;22(9):855-69.

2. Freese U, Heinrich F, Roessner F. Acylation of aromatic compounds on H-Beta zeolites. Catal Today. 1999;49(1-3):237-44.

3. Ma ZH, Zhang XL, Wang H, Han ZG, Zheng XZ, Lin J. Syntheses, structures and catalytic activity for Friedel-Crafts reactions of substituted indenyl rhenium carbonyl complexes. J Coord Chem. 2017;70(4):709-21.

4. Yeung CS, Dong VM. Catalytic Dehydrogenative Cross-Coupling: Forming Carbon-Carbon Bonds by Oxidizing Two Carbon-Hydrogen Bonds. Chem Rev 2011;111(3):1215-1292.

5. Beccalli EM, Broggini G, Martinelli M. Sottocornola S, C-C, C-O, C-N bond formation on sp(2) carbon by Pd(II)-catalyzed reactions involving oxidant agents. Chem Rev 2007;107(11):5318-5365.

6. Huang H, Stewart T, Gutmann M, Ohhara T, Niimura N, Li YX, Wen JF, Bau R, Wong HNC. To Flip or Not To Flip? Assessing the Inversion Barrier of the Tetraphenylene Framework with Enantiopure 2,15-Dideuteriotetraphenylene and 2,7-Dimethyltetraphenylene. J Org Chem 2009;74(1):359-369.

7. Ling CMS, Keita T, Qinghao C, Natalya P, Eric S, Jin-Quan Y. Remote Meta-C−H Activation Using a Pyridine-Based Template: Achieving Site-Selectivity via the Recognition of Distance and Geometry. ACS Cent. Sci. 2015;1:394−399.

8. Lyons TW, Sanford MS. Palladium-Catalyzed Ligand-Directed C-H Functionalization Reactions. Chem Rev 2010;110(2):1147-1169.

9. Li ZP, Li CJ. Catalytic allylic alkylation via the cross-dehydrogenative-coupling reaction between allylic sp(3) C-H and methylenic sp(3) C-H bonds. J Am Chem Soc 2006;128(1):56-57.

10. Li XL, Hewgley JB, Mulrooney CA, Yang JM, Kozlowski MC. Enantioselective oxidative biaryl coupling reactions catalyzed by 1,5-diazadecalin metal complexes: Efficient formation of chiral functionalized BINOL derivatives. J Org Chem 2003;68(14):5500-5511.

11. Guo XW, Pan SG, Liu JH, Li ZP. One-Pot Synthesis of Symmetric and Unsymmetric 1,1-Bis-indolylmethanes via Tandem Iron-Catalyzed C-H Bond Oxidation and C-O Bond Cleavage. J Org Chem 2009;74(22):8848-8851.

12. Li CJ, Li Z. Green chemistry: The development of cross-dehydrogenative coupling (CDC) for chemical synthesis. Pure Appl. Chem. 2006;78:935–945.

13. Li Z, Bohle DS, Li CJ. Cu-catalyzed cross-dehydrogenative coupling: A versatile strategy for C–C bond formations via the oxidative activation of $sp^3$ C–H bonds. Proc. Natl. Acad. Sci. U. S. A. 2006;103:8928–8933.

14. Beccalli EM, Broggini G, Martinelli M, Sottocornola S. C−C, C−O, C−N Bond Formation on $sp^2$ Carbon by Pd(II)-Catalyzed Reactions Involving Oxidant Agents. Chem. Rev. 2007;107(11):5318–5365.

15. Li CJ. Cross-Dehydrogenative Coupling (CDC): Exploring C−C Bond Formations beyond Functional Group Transformations. Acc. Chem. Res. 2009;42(2):335–344.

16. Scheuermann CJ. Beyond Traditional Cross Couplings: The Scope of the Cross Dehydrogenative Coupling Reaction. Chem. Asian J. 2010;5:436–451.

17. Yoo, WJ, Li CJ. Cross-Dehydrogenative Coupling Reactions of sp3-Hybridized C–H Bonds. Top. Curr. Chem. 2010;292:281–302.

18. Yeung CS, Dong VM. Catalytic Dehydrogenative Cross-Coupling: Forming Carbon−Carbon Bonds by Oxidizing Two Carbon−Hydrogen Bonds. Chem. Rev. 2011;111(3):1215–1292.

19. Cho SH, Kim JY, Kwak J, Chang S. Recent advances in the transition metal-catalyzed twofold oxidative C–H bond activation strategy for C–C and C–N bond formation. Chem. Soc. Rev. 2011;40(10):5068–5083.

20. Sun CL, Li BJ, Shi ZJ. Direct C−H Transformation via Iron Catalysis. Chem. Rev. 2011;111(3):1293–1314.

21. Zhang C, Tang C, Jiao N. Recent advances in copper-catalyzed dehydrogenative functionalization via a single electron transfer (SET) process. Chem. Soc. Rev. 2012;41(9):3464–3484.

22. Song G, Wang F, Li X. C–C, C–O and C–N bond formation via rhodium(III)-catalyzed oxidative C–H activation. Chem. Soc. Rev. 2012;41:3651–3678.

23. Hirano K, Miura M. Copper-mediated oxidative direct C–C (hetero)aromatic cross-coupling. Chem. Commun. 2012;48:10704–10714.

24. Liu C, Liu D, Lei A. Recent Advances of Transition-Metal Catalyzed Radical Oxidative Cross-Couplings. Acc. Chem. Res. 2014;47(12):3459–3470.

25 Girard SA, Knauber T, Li CJ. The Cross-Dehydrogenative Coupling of $C_{sp3}$-H Bonds: A Versatile Strategy for C-C Bond Formations. Angew. Chem., Int. Ed. 2014;53:74–100.

26. Samanta R, Matcha K, Antonchick AP. Metal-Free Oxidative Carbon-Heteroatom Bond Formation Through C–H Bond Functionalization. Eur. J. Org. Chem. 2013;26:5769–5804.

27. Tang BX, Song RJ, Wu CY, Liu Y, Zhou MB, Wei WT, Deng G, Yin D, Li J. Copper-Catalyzed Intramolecular C H Oxidation/Acylation of Formyl-N-arylformamides Leading to Indoline-2,3-diones. J Am Chem Soc. 2010;132(26):8900-+.

28. Jiang HL, Xie J, Lin AJ, Cheng YX, Zhu CJ. The Au(III)-catalyzed coupling reactions between alcohols and N-heterocycles via C-H bond activation. Rsc Adv. 2012;2(28):10496-8.

29. Cheng K, Zhao BL, Qi CZ. Silver-catalyzed decarboxylative acylation of arylglyoxylic acids with arylboronic acids. Rsc Adv. 2014;4(89):48698-702.

30. Kamitani M, Ito M, Itazaki M, Nakazawa H. Effective dehydrogenation of 2-pyridylmethanol derivatives catalyzed by an iron complex. Chem Commun (Camb). 2014;50(59):7941-4.

31. Toh QY, McNally A, Vera S, Erdmann N, Gaunt MJ. Organocatalytic C-H bond arylation of aldehydes to bis-heteroaryl ketones. J Am Chem Soc. 2013;135(10):3772-5.

32. Bao YS, Zhang DL, Jia ML, Bao ZRGT. Replacing Pd(OAc)(2) with supported palladium nanoparticles in ortho-directed CDC reactions of alkylbenzenes. Green Chem. 2016;18(7):2072-7.

33. Kianmehr E, Pakbaznia A, Faghih N, Forournadi A. Metal-free chemo- and regioselective acylation of pyridine derivatives with alcohols in water. Tetrahedron. 2017;73(11):1407-12.

34. Chen J, Wan M, Hua J, Sun Y, Lv Z, Li W, et al. TBHP/TFA mediated oxidative cross-dehydrogenative coupling of N-heterocycles with aldehydes. Org Biomol Chem. 2015;13(47):11561-6.

35. Adib M, Rajai-Daryasarei S, Pashazadeh R, Tajik M, Mirzaei P. Regioselective transition metal-free acylation of coumarins via cross-dehydrogenative coupling reaction of coumarins and aldehydes. Tetrahedron Lett. 2016;57(33):3701-3705.

36. Yuan JW, Yin QY, Yang LR, Mai WP, Mao P, Xiao YM, Qu LB. Iron-catalyzed regioselective direct coupling of aromatic aldehydes with coumarins leading to 3-aroyl coumarins. RSC Adv. 2015;5: 88258-88265.

37. Zhao W, Xu L, Ding Y, Niu B, Xie P, Bian Z, Zhang D, Zhou A. Regioselective Coupling Reactions of Coumarins with Aldehydes or Di-tert-butyl Peroxide (DTBP) through a C(sp2)–H Functionalization Process. Eur. J. Org. Chem. 2016;2:325-330.

38. Wang H, Zhou SL, Guo LN, Duan XH. Diacylation of coumarins by silver-catalyzed decarboxylative cross-coupling. Tetrahedron. 2015;71(4):, 630-636.

39. Adib M, Pashazadeh R, Rajai-Daryasarei S, Kabirib R, Jahania M. Transition metal-free cross-dehydrogenative coupling acylation of coumarins by the $K_2S_2O_8$/ Aliquat 336 catalytic system: a versatile strategy towards 4-aroylcoumarin derivatives. RSC Adv. 2016;6: 110656-110660.

40. Starks CM. Phase-transfer catalysis. I. Heterogeneous reactions involving anion transfer by quaternary ammonium and phosphonium salts. J. Am. Chem. Soc. 1971;93(1):195-199.

41. Grudpan K, Taylor CG. Use of Aliquat-336 for the extraction of cadmium from aqueous solutions. Analyst, 1984;109:585-588.

42. Mikkola JP, Virtanen P, Sjoholm R. Aliquat 336®—a versatile and affordable cation source for an entirely new family of hydrophobic ionic liquids. Green Chem. 2006;8:250-255.

# Comparative Studies of Photophysicochemical Properties of Non-Peripherally Anisole/Thioanisole-Tetrasubstituted Gallium(III) Phthalocyanines Containing Oxygen/ Sulfur Bridge

**Armağan Günsel***

*Sakarya University, Department of Chemistry, TR54187 Serdivan, Sakarya, Turkey*

**Abstract:** In this work, we have presented the synthesis and characterization of gallium(III) phthalocyanines **(4-6)** which are non-peripherally tetra-substituted with anisole or thioanisole functional groups containing oxygen or sulfur bridge. Confirmation of the phthalocyanine structures performed with the cooperation of elemental analysis, FTIR, $^1$H-NMR, UV-Vis and MALDI-MS spectral data. Also, we have investigated and discussed the effects of non-peripherally tetra-substitution with different functional groups on the photochemical and photophysical properties (singlet oxygen quantum yield, photodegradation quantum yield, fluorescence quantum yield and fluorescent behavior). In every substituent, we obtained very similar singlet oxygen quantum yields as 0.64 for **(4)**, 0.56 for **(5)** and 0.65 for **(6)** suggesting their potential as photosensitizer in PDT treatment.

**Keywords:** Phthalocyanine, anisole, thioanisole, gallium, photochemistry.

## INTRODUCTION

Phthalocyanines (Pcs) are highly conjugated macrocycles which have the ability to form complexes with many different metals. Because of having their chemical, photophysical, and photochemical properties as well as their stability (1), Pcs have been used for development of photosensitizers in photodynamic therapy (2,3), dye-sensitized solar cells (4), organic semiconductors (5), electrochromic displays (6), non-linear optical materials (7), liquid crystals (8), chemical sensors (9), and electrochromic agents (10).

Because of their low solubility, unsubstituted phthalocyanines tend to be in the aggregated form in common organic solvents but they can become soluble in many solvents by attaching some functional groups such as methoxy or methylthio groups at peripheral or non-peripheral positions of Pcs. These kind of groups have extensively been used in both medical and industrial purposes like antiallergenic, antiartherogenic, antiinflammatory, antimicrobial, antioxidant, antithrombotic, cardioprotective, and vasodilatory effects. Non-peripheral substitution causes red-shift in the Q-band, suggesting optimal transparency into tissue in PDT(11–16).

The strong absorption of phthalocyanines in the region of 650-680 nm and high efficiency in producing reactive oxygen species (ROS), *e.g.* singlet oxygen ($^1O_2$), causing destruction of cancer cells, led to the development of photodynamic cancer therapy (PDT) over the last century. The variety of metal ion that is inserted to the inner core of phthalocyanines strongly influences the ROS production. Especially, phthalocyanines containing diamagnetic ions ($Zn^{2+}$, $In^{3+}$, $Ga^{3+}$*etc.*) exhibit sufficient photophysical and photochemical properties (triplet quantum yield, lifetime and singlet oxygen generation) because of high ROS yields for PDT(17,18).

In this paper, we have firstly presented the synthesis and characterization of anisole or thioanisole tetra-substituted gallium(III) phthalocyanines **(4-6)** containing oxygen or sulfur bridge at non-peripheral positions, which show good solubility in common organic solvents. Finally, the photochemical and photophysical properties (singlet oxygen quantum yield, photodegradation quantum yield, fluorescent quantum yields and fluorescent behavior) of the synthesized gallium(III) phthalocyanines **(4-6)** in DMSO were investigated to compare the effect of different substituent, which is very important for biological cell studies on PDT.

## EXPERIMENTAL

### Materials and Methods
3-(4-Methoxy-phenoxy)phthalonitrile **(1)**, 3-(4-(methylthio)phenoxy)phthalonitrile **(2)**, 3-(4-(methylthio)phenylthio)phthalonitrile **(3)** and 1(4), 8(11), 15(18), 22(25)-tetrakis (3-(4-(methylthio)phenylthio))phthalocyaninatogallium(III) chloride **(6)** were prepared according to

the procedures in literature (4,19,20). Some chemicals such as dimethyl sulfoxide (DMSO) and $GaCl_3$ were acquired from Merck and Alfa Aesar and used as received. UV-Vis spectra were acquired in a quartz cuvette on an Agilent Model 8453 diode array spectrophotometer. Perkin-Elmer Spectrum Two FT-IR spectrometer was used to acquire FT-IR spectra. All the products were purified by column chromatography on silica gel (Merck grade 60) from Aldrich. All reactions were achieved under a dry $N_2$ atmosphere. A Bruker 300 spectrometer was used to record ^{1}H NMR spectra. Mass spectra (MS) were analyzed by MALDI SYNAPT G2-Si Mass Spectrometer. Fluorescence spectra were measured using a Varian Eclipse spectrofluorometer using 1-cm path length cuvettes at room temperature. Photo-irradiations for singlet oxygen determination were measured using a General Electric quartz line lamp (300 W). A 600 nm glass cut off filter (Schott) and a water filter were used to filter off ultraviolet and infrared radiations, respectively. An interference filter (Intor, 700nm with a bandwidth of 40nm) was additionally placed in the light path before the sample. Light intensities were measured with a POWER MAX 5100 (Mol electron detector incorporated) power meter.

### Synthesis

*General procedure for the synthesis of gallium phthalocyanines (GaPcs): Reaction*: A mixture of **(1)** or **(2)** (0.100 g, ~0.39 mmol), $GaCl_3$ (0.018 g, 0.10 mmol) and a catalytic amount of DBU (1,8-diazabicyclo[5.4.0]undec-7-ene) in n-hexanol (2 $cm^3$) was refluxed at 160 °C in a sealed glass tube for 10 hours under $N_2$ atmosphere. After cooling to room temperature, the green crude product was cooled and precipitated by adding n-hexane and filtered. *Purification*: After being washed with methanol, it was purified by silica gel column chromatography ($CH_2Cl_2$/ethanol 50/2, v/v) and finally dried *in vacuo* at 100 °C. Solubility: Highly soluble in THF, $CH_2Cl_2$, DMSO, and DMF.

### 1(4), 8(11), 15(18), 22(25)-Tetrakis (3-(4-methoxy-phenoxy)phthalocyaninato gallium(III) chloride(4)

The product was soluble in $CHCl_3$, $CH_2Cl_2$, THF, DMF, and DMSO. Yield of **(4)**: 0.036 g (33%). Anal. calcd. For (%) $C_{60}H_{40}ClGaN_8O_8$ (1106.18 g/mol): C, 65.15; H, 3.64; N, 10.13; Found: C, 64.49; H, 3.80; N, 9.58. FT-IR ($u_{max}$/$cm^{-1}$): 3062 (Ar-H), 2948, 2914, 2855 (Aliph. C-H), 1722, 1625 (C=C), 1574, 1517, 1480, 1428, 1315, 1220, 1105, 892, 741. UV-Vis (DMSO): $\lambda_{max/nm}$ (log ε): 713 (4.65), 641 (3.98), 322 (4.45). ^{1}H-NMR (300 MHz, $CDCl_3$) δ ppm: 7.84-7.64 (m, 12H, Pc-H), 7.44-7.10 (m, 16H, Ar-H), 2.12 (s, 12H C$H_3$-OAr). MS (MALDI-TOF, 2,5-dihydroxybenzoic acid as matrix): m/z 1071.68 $[M-Cl+H]^+$.

### 1(4),8(11),15(18), 22(25)-Tetrakis (3-(4-(methylthio)phenoxy)phthalocyaninato gallium(III) chloride(5)

The product was soluble in $CHCl_3$, $CH_2Cl_2$, THF, DMF, and DMSO. Yield of **(5)**: 0.033 g (30%). Anal. calcd. For (%)$C_{60}H_{40}ClGaN_8O_4S_4$ (1170.45 g/mol): C, 61.57; H, 3.44; N, 9.57; Found: C,

60.55; H, 3.41; N, 9.71. FT-IR ($\upsilon_{max}/cm^{-1}$): 3049 (Ar-H), 2961, 2862 (Aliph. C-H), 1733, 1631 (C=C), 1560, 1521, 1447, 1431, 1314, 1221, 1105, 841, 702, 612. UV-Vis (DMSO): $\lambda_{max/nm}$ (log ε): 712 (4.65), 639 (3.96), 358 (4.15). $^1$H-NMR (300 MHz, CDCl$_3$) δ ppm: 7.79-7.55 (m, 12H, Pc-H), 7.38-7.14 (m, 16H, Ar-H), 2.20 (s, 12H C$H_3$-SAr). MS (MALDI-TOF, 2,5-dihydroxybenzoic acid as matrix): m/z 1135.88 [M-Cl+H]$^+$.

## Photophysical and Photochemical Studies

*Fluorescence quantum yields:* Fluorescence quantum yields ($\Phi_F$) were determined by the comparative method **(Eq. 1)(21)**,

$$\Phi_F = \Phi_{F(Std)} x \frac{F . A_{Std} . n^2}{F_{Std} . A . n_{Std}^2}$$

**(Eq. 1)**

where F and $F_{Std}$ are the areas under the fluorescentemission curves of the samples and the standard, respectively. A and $A_{Std}$ are the respective absorbances of the samples and standard (Unsubstituted ZnPc) at the excitation wavelengths, respectively. $n^2$and $n_{(Std)}^2$are the refractive indices of solvents used for the sample and standard, respectively. Unsubstituted ZnPc in DMSO ($\Phi_F$ = 0.20)(22) was used as the standard. Both the samples and standard were excited at the same wavelength. The absorbance of the solutions at the excitation wavelength ranged between 0.04 and 0.05.

*Singlet oxygen quantum yields:* Singlet oxygen quantum yield ($\Phi_\Delta$) determinations were carried out by using the experimental set-up described in the literature(23). Quantum yields of singlet oxygen photogeneration were determined in air (no oxygen bubbled) using the relative method with ZnPc as reference and DPBF (1,3-diphenylisobenzofuran) as the chemical quencher for singlet oxygen, using formula **(Eq. 2)**,

$$\Phi_\Delta = \Phi_\Delta^{Std} x \frac{R . I_{abs}^{Std}}{R^{Std} . I_{abs}}$$

**(Eq. 2)**

where $\Phi_\Delta^{Std}$is the singlet oxygen quantum yield for ZnPc standard ($\Phi_\Delta^{Std}$= 0.67 in DMSO(24)). R and $R_{Std}$ are the DPBF photobleaching rates in the presence of the respective samples and standard, respectively. $I_{abs}$ and $I_{abs}^{Std}$are the rates of light absorption by the samples and standard, respectively. To avoid chain reactions induced by DPBF in the presence of singlet oxygen (24,25), the concentration of quencher (DPBF) was lowered to ~3 x $10^{-5}$ mol dm$^{-3}$. Solutions of the sensitizer (containing DPBF) were prepared in the dark and irradiated in the Q band region using the set up described above. DPBF degradation was monitored at 417 nm. The light intensity of 7.05 x $10^{15}$ photons s$^{-1}$ cm$^{-2}$ was used for $\Phi_\Delta$ determinations.

*Photodegradation quantum yields:* Photodegradation quantum yield ($\Phi_d$) determinations were carried out using the experimental set-up described in literature (26). Photodegradation quantum yields were determined using formula **(Eq.3)**,

$$\Phi_d = \frac{(C_0 - C_t) \cdot V \cdot N_A}{I_{abs} \cdot S \cdot t}$$

**(Eq. 3)**

where "$C_0$" and "$C_t$" are the sample concentrations before and after irradiation respectively, "$V$" is the reaction volume, "$N_A$" is the Avogadro's constant, "$S$" is the irradiated cell area, "$t$" is the irradiation time, "$I_{abs}$" is the overlap integral of the radiation source light intensity and the absorption of the samples. A light intensity of $2.38 \times 10^{16}$ photons $s^{-1}$ $cm^{-2}$ was employed for $\Phi_d$ determinations.

## RESULTS AND DISCUSSION

### Synthesis and Spectroscopic Characterization
The characterization of all synthesized compounds was carried out with the aid of some spectroscopic methods such as FT-IR, $^1$H-NMR and UV-Vis spectroscopic methods, elemental analysis and mass spectra which gave very satisfactory results.

Non-peripherally tetrasubstituted phthalocyanines **(4)** and **(5)** were prepared by cyclotetramerization of 3-(4-methoxy-phenoxy)phthalonitrile **(1)** or 3-(4-(methylthio)phenoxy)phthalonitrile **(2)**. The preparation of phthalocyanines **(4)** and **(5)** from the aromatic dinitriles were carried out under the same reaction conditions by treatment of phthalonitriles **(1)** or **(2)** with GaCl$_3$ in dry n-hexanol and 1,8-diazabicyclo[5.4.0]undec-7-ene (DBU) at 160 °C, for 10 h **(Scheme 1)**.
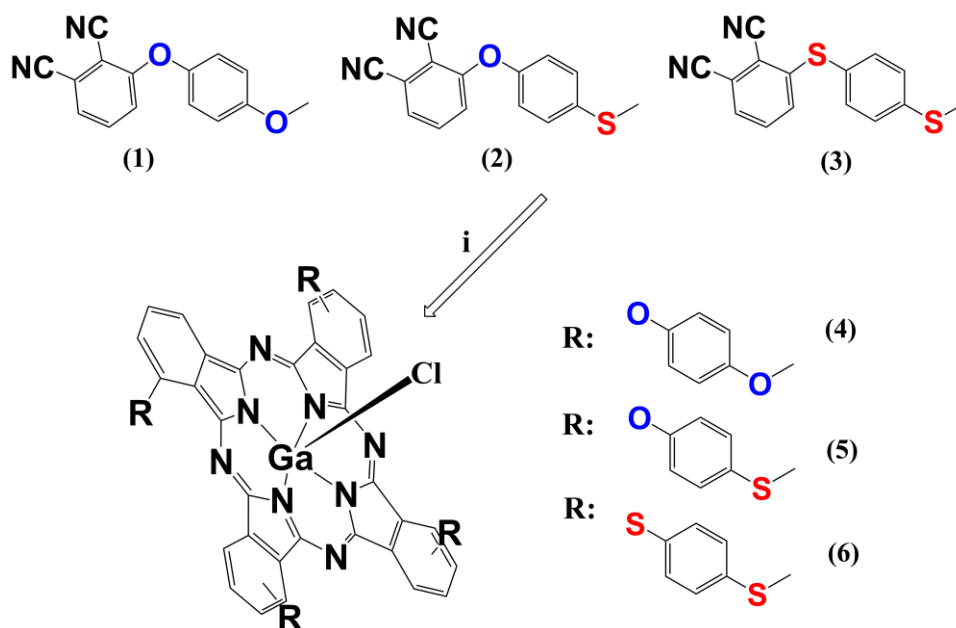
**Scheme 1.** General procedure for the synthesis of gallium phthalocyanines (GaPcs) **(4-6), i:** $GaCl_3$, 160 °C, for 10h, n-hexanol, and DBU.

The UV-Vis spectra of phthalocyanines **(4)** and **(5)** were recorded in DMSO. The UV-Vis spectra of phthalocyanines **(4)** and **(5)** were obtained as a single band of high intensity at 713 nm (Q) for **(4)**, 712 nm (Q) for **(5)**, respectively that are typical of phthalocyanine complexes. Phthalocyanines indicate characteristic B-band in addition to Q band absorption, in the UV region at 322 nm for **(4)** and 358 nm for **(5)** respectively.

In the FT-IR-spectra, after conversion into phthalocyanines **(4)** and **(5)**, the characteristic -C≡N peaks for **(1)** and **(2)** were not observed for **(4)** and **(5)** as expected and thus, proved the formation of these compounds **(4)** and **(5)** from the corresponding dinitriles **(1)** and **(2)**.

The synthesized phthalocyanine complexes **(4)** and **(5)** are very similar to each other and showed characteristic vibrations which belong to the ether groups at ~1220 $cm^{-1}$, the aromatic CH stretching at *ca.* 3049-3062 $cm^{-1}$ and the aliphatic CH stretching at *ca.* 2855-2961 $cm^{-1}$.

In $^1H$ NMR spectra of the phthalocyanines **(4)** and **(5)**, the obtained signals for the phthalocyanines **(4)** and **(5)** are quite broader compared to the signals of the starting compounds **(1)** and **(2)**. The protons were observed between 7.84-7.55 ppm on aromatic structure for Pc-ring, and between 7.44-7.10 ppm aromatic structure for functional groups. Additionally, the protons were observed at around 2.12 and 2.20 ppm respectively as singlet for the O-CH₃ and S-CH₃ groups.

In the MALDI-TOF mass spectra, the observation of the characteristic molecular ion peaks at m/z 1071.68 [M-Cl+H]$^+$ for **(4) (Figure 1.A)** and at m/z 1135.88 [M-Cl+H]$^+$ for **(5) (Figure 1.B)** confirmed the proposed structure.

Last, elemental analysis of both complexes gave satisfactory results corresponding to all synthesized compounds.
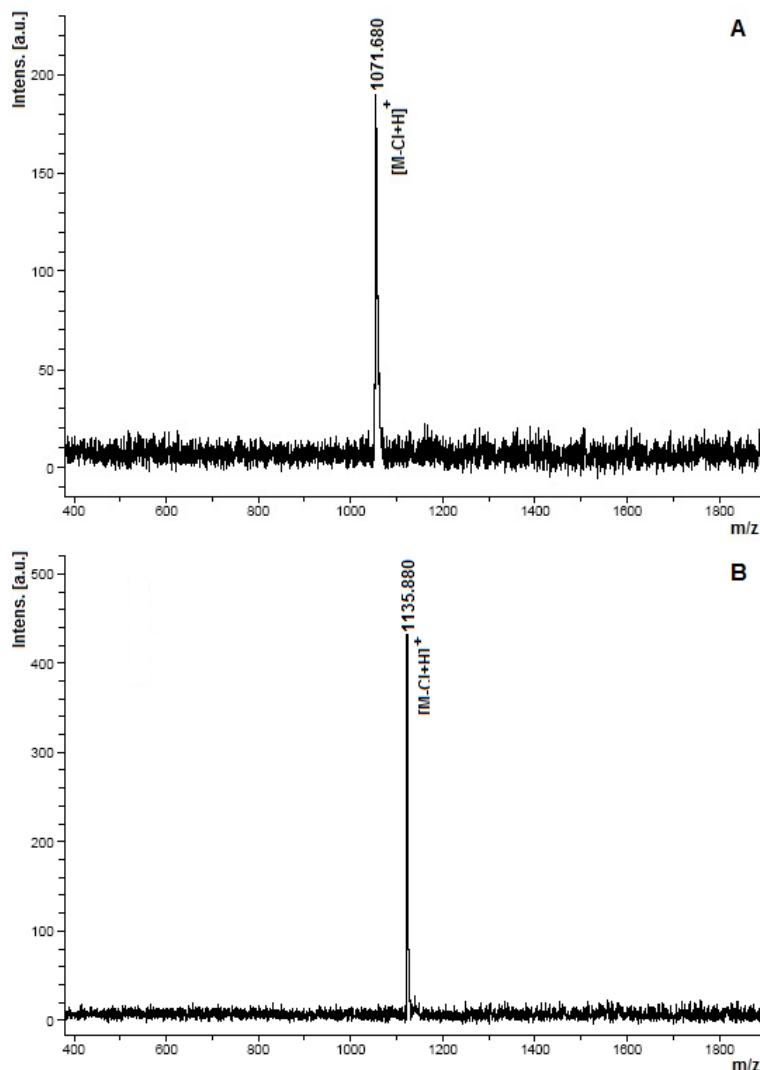


**Figure 1:** MALDI-TOF MS spectra of compound **(4, A)** and **(5, B)**.

**Aggregation studies**

An intense and sharp Q-band was observed in the absorption spectra of the phthalocyanines **(4-6)** in DMSO, exhibiting the evidence of the formation of non-aggregated forms. Dilution studies in DMSO were done to test the aggregation of the phthalocyanines **(4-6)(Figure 2.(A-C)** shows the spectra of the synthesized phthalocyanines **(4-6)** in DMSO at various concentrations). The increasing of the Pc concentration led to an increase in the intensity of absorption of the Q band. No new band formation was observed because of the aggregated forms(27,28). From these results, we can conclude that the phthalocyanines **(4-6)** did not aggregate in the solvent of

DMSO and the Lambert-Beer law was obeyed for the synthesized phthalocyanines at the concentration ranging from $3.59 \times 10^{-5}$ to $2.24 \times 10^{-6}$ M for **(4)**, $3.52 \times 10^{-5}$ to $2.20 \times 10^{-6}$ M for **(5)** and $3.65 \times 10^{-5}$ to $2.25 \times 10^{-6}$ M for **(6)** respectively.
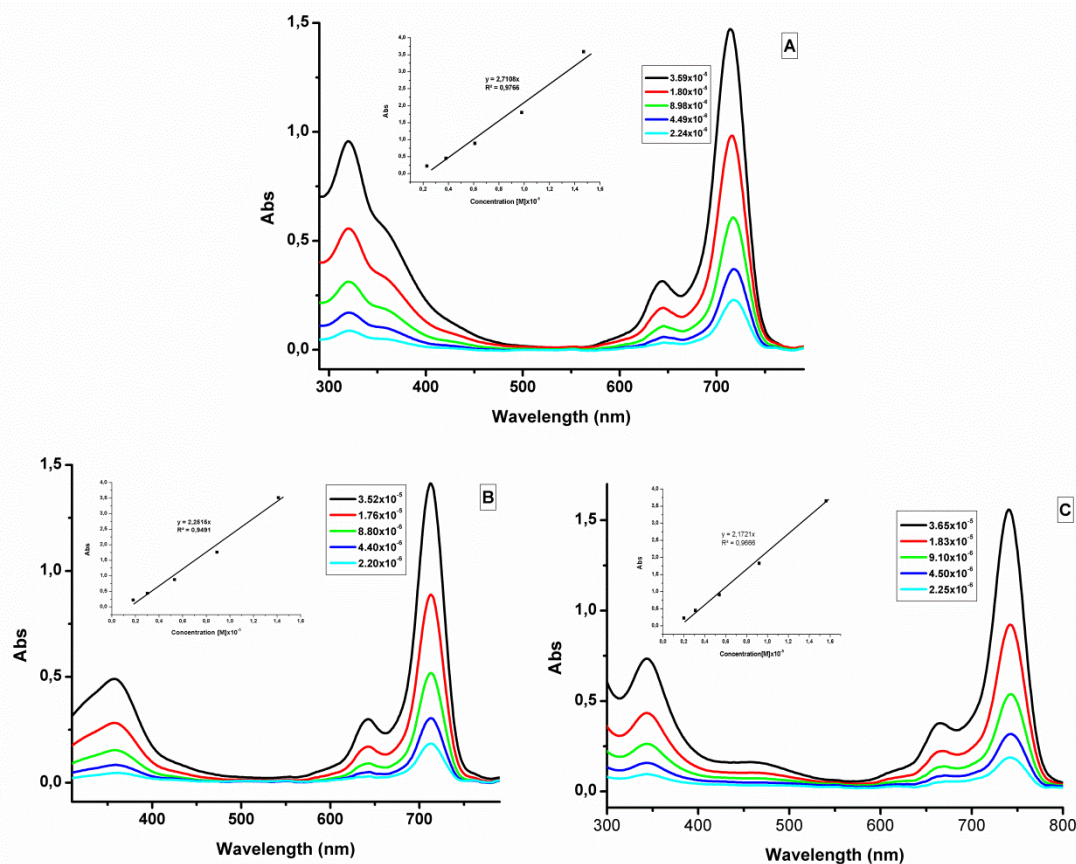


**Figure 2:** UV-Vis absorption spectra of the phthalocyanines **(4:A)**, **(5:B)** and **(6:C)** in DMSO at different concentrations.

**Photophysical and photochemical studies**

*Fluorescence quantum yields:* The measurement of fluorescent quantum yields was determined in DMSO. The comparison of spectra was also carried out under the same conditions **(**Figures 3 and 4**)**. While the complexes **(4)** and **(5)** have typical fluorescent behavior, the complex **(6)** shows that the fluorescence excitation spectrum is blue-shifted by about 10 nm relative to that of the absorption spectrum, suggesting a change in geometry upon excitation (20). The quantum yield results are; for **(4)** in DMSO 0.138, for **(5)** in DMSO 0.101 and for **(6)** in DMSO 0.050. The yields of the complexes **(4)** and **(5)** are almost similar but the complex **(6)** is lower fluorescent quantum yields than the complexes **(4)** and **(5).** These compounds have lower fluorescent quantum yields than standard GaPc ($\Phi_F$ = 0.30 in DMSO).
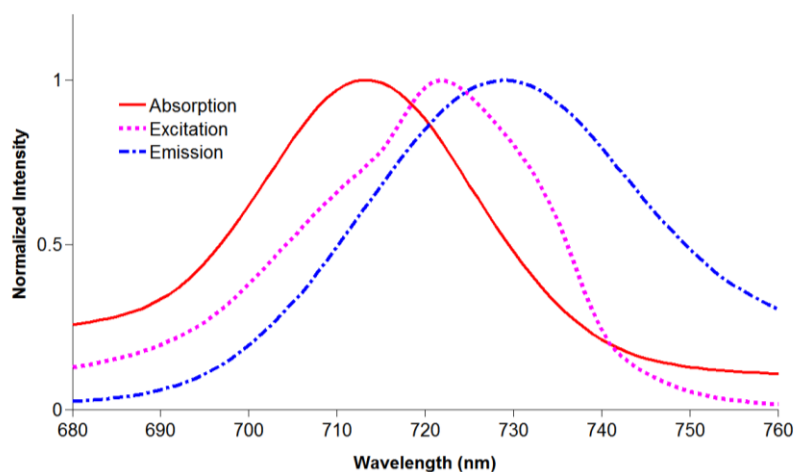
**Figure 3:** Absorption (713 nm), excitation (721 nm) and emission (729 nm) spectra of **(4)** in DMSO.
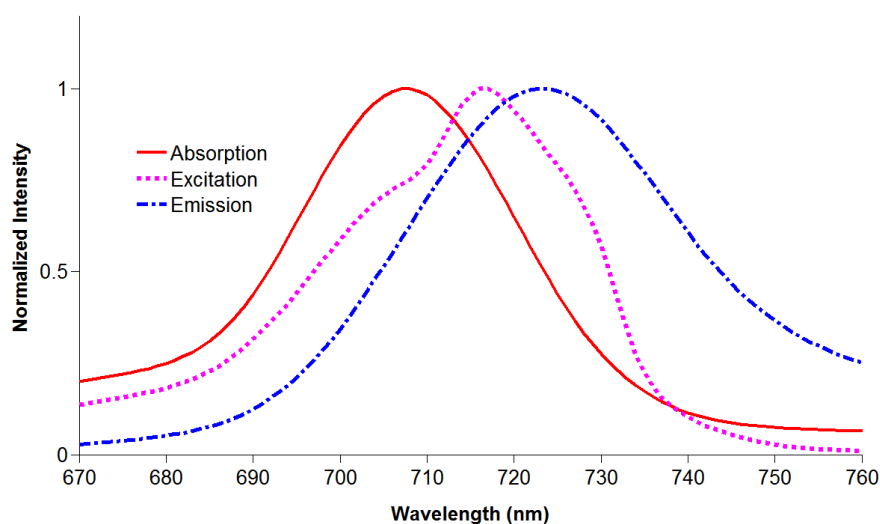


**Figure 4:** Absorption (708 nm), excitation (717 nm) and emission (723 nm) spectra of **(5)** in DMSO.

*Singlet oxygen quantum yields:* The singlet oxygen quantum yields in the presence of different substituents were determined in DMSO by following the chemical method based on the chemical quenching of DPBF (1,3-diphenylisobenzofuran) in order to investigate the effect of substituents (Figures 5,6, and 7). In every substituent, the complex showed similar quantum yields. As shown in Table 1, the highest quantum yield $\Phi_\Delta$ (0.65) is for complex (**6**), followed by complex (**4**) $\Phi_\Delta$ (0.64) and complex (**5**) $\Phi_\Delta$ (0.56). The yields of singlet oxygen for all synthesized complexes have very high values when compared to unsubstituted GaPc.
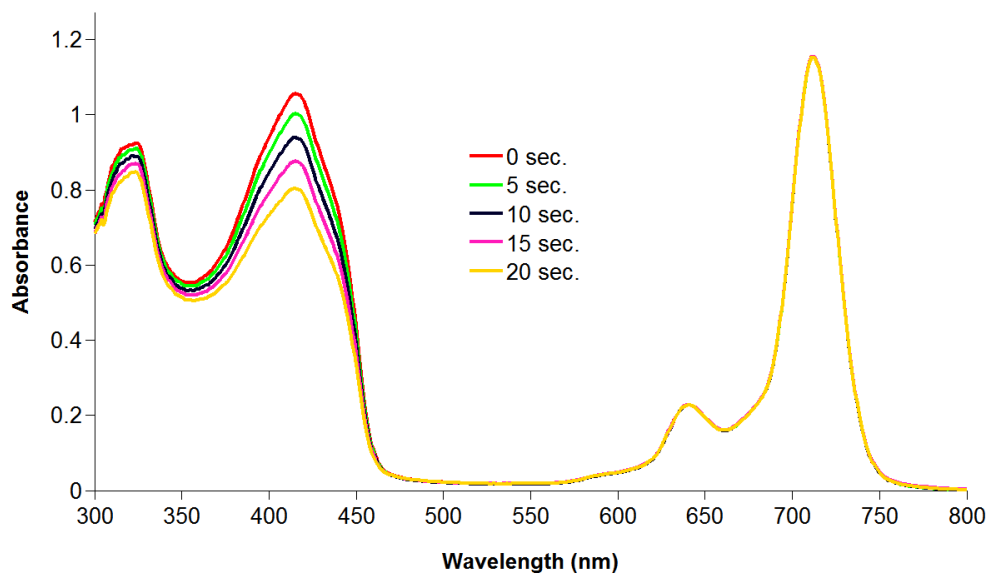
**Figure 5:** A typical spectrum for the determination of singlet oxygen quantum yield of **(4)** in DMSO.
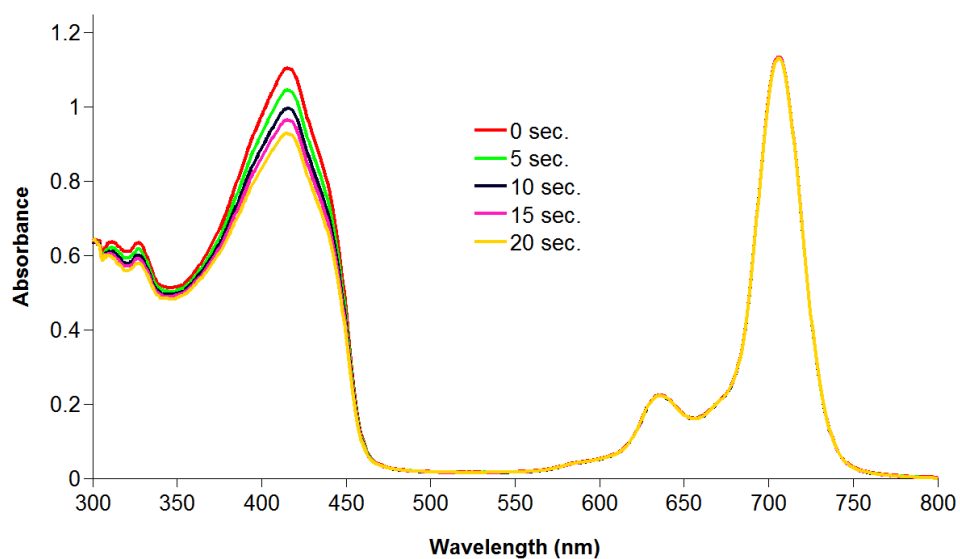


**Figure 6:** A typical spectrum for the determination of singlet oxygen quantum yield of **(5)** in DMSO.
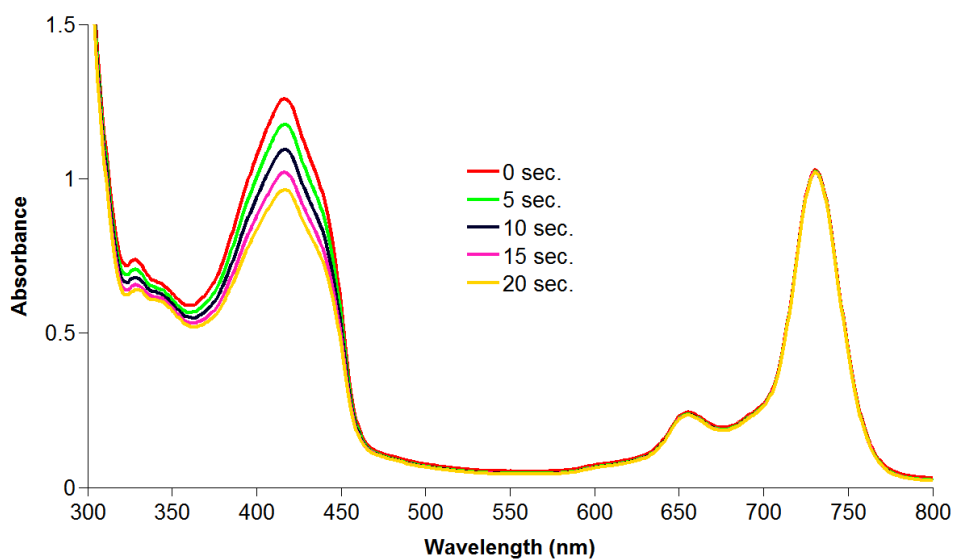
**Figure 7:** A typical spectrum for the determination of singlet oxygen quantum yield of **(6)** in DMSO.

*Photodegradation quantum yields:* The quantum yield values of the order $10^{-4}$ were given Table 1 and the spectral changes observed for the complexes are shown in (Figures 8,9, and 10). Unsubstituted GaPc complexes as a reference is less stable than these complexes. Photodegradation quantum yield ($\Phi_d$) value of complex **(5)** in DMSO ($\Phi_d$: 2,9 $\times 10^{-4}$) is less stable as compared to the other complexes. But in generally, it can be said that all the complexes are resistant to photochemical degradation.
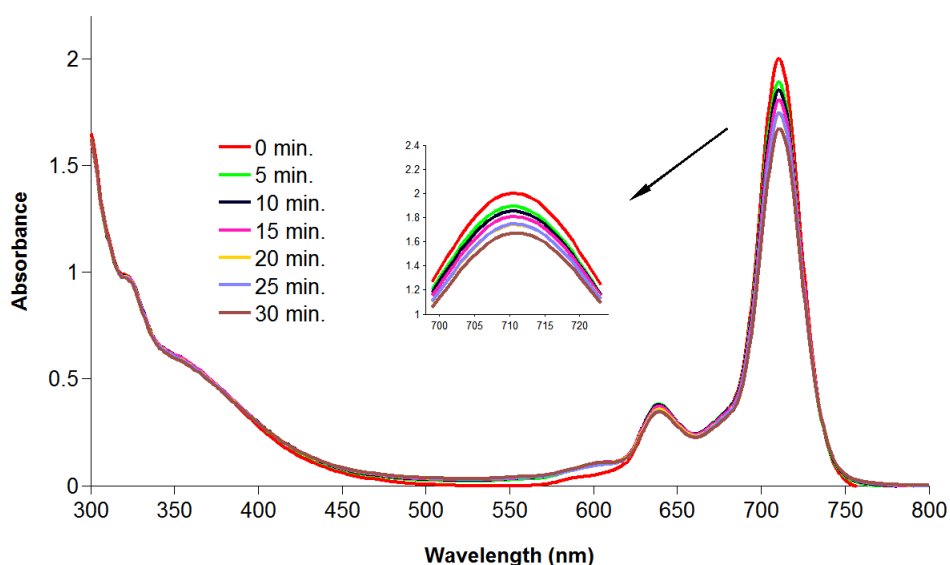


**Figure 8:** A typical spectrum for the determination of photodegradation of **(4)** in DMSO.
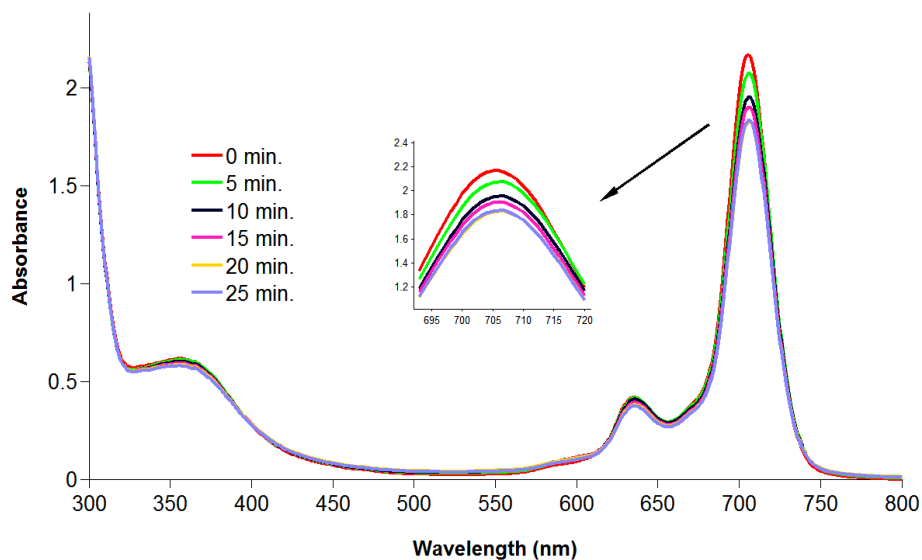
**Figure 9:** A typical spectrum for the determination of photodegradation of **(5)** in DMSO.
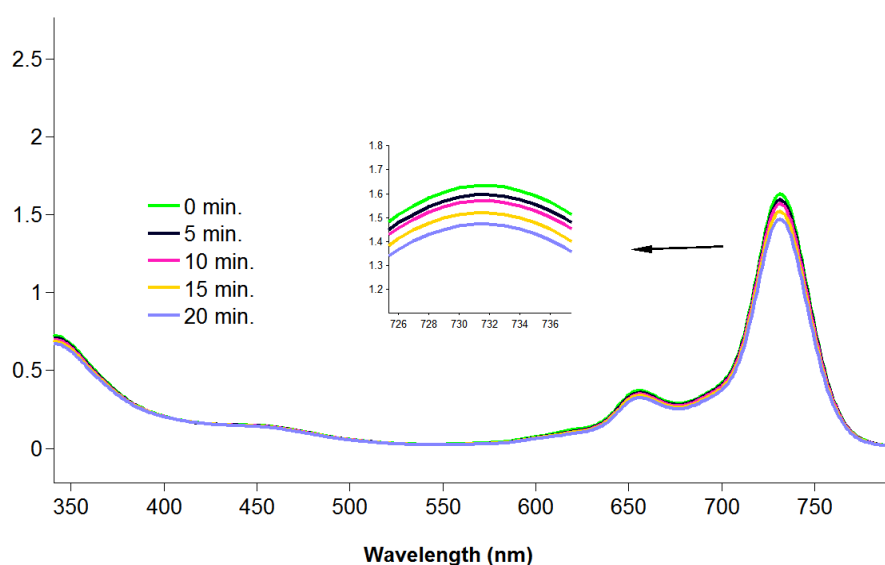


**Figure 10:** A typical spectrum for the determination of photodegradation of **(6)** in DMSO.

**Table 1:** Photophysical and photochemical properties of the complexes in DMSO.

| Complex | Q band, λmax, (nm) | Excitation, (nm) | Emission, (nm) | $\Phi_F$ | $\Phi_d$ $(10^{-4})$ | $\Phi_\Delta$ | Stokes shift, Δstokes, (nm) |
|---|---|---|---|---|---|---|---|
| **(4)** | 713 | 721 | 729 | 0.138 | 15 | 0.64 | 16 |
| **(5)** | 708 | 717 | 723 | 0.101 | 2.9 | 0.56 | 15 |
| **(6)** | 742 | 732 | 744 | 0.050 | 40 | 0.65 | 2 |
| GaPc[a] | - | - | - | 0.300 | 0.09 | 0.41 | - |

[a] Data from (29).

## CONCLUSION

In this paper, we have synthesized and characterized anisole or thioanisole tetra-substituted gallium(III) phthalocyanines **(4-6)** containing oxygen or sulfur bridge at the non-peripheral positions and then investigated and discussed the effects of different functional groups on the photochemical and photophysical properties. In every substituent, the complex exhibited similar quantum yield. The highest quantum yield $\Phi_\Delta$ (0.65) is for complex **(6)**, and then it is followed by complex **(4)** $\Phi_\Delta$ (0.64) and complex **(5)** $\Phi_\Delta$ (0.56).

**Conflict of interest:** The authors declare that they have no conflict of interest.

## REFERENCES

1.McKeown NB. Phthalocyanine materials : synthesis, structure, and function. Cambridge, U.K. ; New York : Cambridge University Press; 1998.

2.Güzel E, Günsel A, Bilgiçli AT, Atmaca GY, Erdogmus A, Yarasir MN. Synthesis and photophysicochemical properties of novel thiadiazole-substituted zinc (II), gallium (III) and silicon (IV) phthalocyanines for photodynamic therapy. Inorganica Chim Acta. 2017;467:169-76.

3.Günsel A, Güzel E, Bilgiçli AT, Atmaca GY, Erdogmus A, Yarasir MN. Synthesis and investigation of photophysicochemical properties of novel ketone-substituted gallium (III) and indium (III) phthalocyanines with high singlet oxygen yield for photodynamic therapy. J Luminescence. 2017;192:888-92.

4.Günsel A, Güzel E, Bilgiçli AT, Şişman İ, Yarasir MN. Synthesis of non-peripheral thioanisole-substituted phthalocyanines: Photophysical, electrochemical, photovoltaic, and sensing properties. J Photochem. Photobiol. A. 2017;348(Supplement C):57–67.

5.Günsel A, Kandaz M, Yakuphanoglu F, Farooq WA. Extraction of electronic parameters of organic diode fabricated with NIR absorbing functional manganase phthalocyanine organic semiconductor. Synth Met. 2011;161(15):1477–82.

6.Krasnov YS, Kolbasov GY, Tretyakova IN, Tomachynska LA, Chernii VY, Volkov SV. Dynamics of redox processes and electrochromism of films of zirconium (IV) phthalocyanines with out-of-plane β-dicarbonyl ligands. Solid State Ion. 2009;180(14):928–33.

7.de la Torre G, Vazquez P, Agullo-Lopez F, Torres T. Phthalocyanines and related compounds: organic targets for nonlinear optical applications. J Mater Chem. 1998;8(8):1671–83.

8.Basova TV, Hassan A, Durmus M, Gurek AG, Ahsen V. Orientation of the liquid crystalline nickel phthalocyanine films confined between electrodes. Synth Met. 2011;161(17–18):1996–2000.

9.Günsel A, Yaraşir MN, Kandaz M, Koca A. Synthesis, H- or J-type aggregations, electrochemistry and in situ spectroelectrochemistry of metal ion sensing lead(II) phthalocyanines. Polyhedron. 2010;29(18):3394–404.

10.Komatsu T, Ohta K, Fujimoto T, Yamamoto I. Chromic Materials .1. Liquid-Crystalline Behavior and Electrochromism in Bis(octakis-N-Alkylphthalocyaninato)lutetium(iii) Complexes. J Mater Chem. 1994;4(4):533–6.

11.Tillo A, Stolarska M, Kryjewski M, Popenda L, Sobotta L, Jurga S, vd. Phthalocyanines with bulky substituents at non-peripheral positions – Synthesis and physico-chemical properties. Dyes Pigments. 2016;127(Supplement C):110–5.

12.Sobotta L, Wierzchowski M, Mierzwicki M, Gdaniec Z, Mielcarek J, Persoons L, vd. Photochemical studies and nanomolar photodynamic activities of phthalocyanines functionalized with 1,4,7-trioxanonyl moieties at their non-peripheral positions. J Inorg Biochem. 2016;155:76–81.

13.Aydin M, Alici EH, Bilgicli AT, Yarasir MN, Arabaci G. Synthesis, characterization, aggregation, fluorescence and antioxidant properties of bearing (4-(methylthio)phenylthio) tetra substituted phthalocyanines. Inorganica Chim Acta. 2017;464:1–10.

14.Benavente-Garcia O, Castillo J, Marin FR, Ortuno A, Del Rio JA. Uses and properties of Citrus flavonoids. J Agric Food Chem. 1997;45(12):4505–15.

15.Middleton E, Kandaswami C, Theoharides TC. The effects of plant flavonoids on mammalian cells: Implications for inflammation, heart disease, and cancer. Pharmacol Rev. 2000;52(4):673–751.

16.Olivati CA, Riul JA, Balogh DT, Oliveira JO, Ferreira M. Detection of phenolic compounds using impedance spectroscopy measurements. Bioprocess Biosyst Eng. 2009;32(1):41–6.

17.Usuda J, Kato H, Okunaka T, Furukawa K, Tsutsui H, Yamada K, vd. Photodynamic therapy (PDT) for lung cancers. J Thorac Oncol. 2006;1(5):489–93.

18.Bacellar IOL, Tsubone TM, Pavani C, Baptista MS. Photodynamic Efficiency: From Molecular Photochemistry to Cell Death. Int J Mol Sci. 2015;16(9):20523–59.

19.Qinglong B, Chunhua Z, Chuanhui C, Wancheng L, Jin W, Guotong D, Synthesis, Photophysical Properties and Near Infrared Electroluminescence of 1(4),8(11),15(18),22(25)-Tetra-(methoxy-phenoxy)phthalocyanine. Chinese Journal of Chemistry. 2012;30:689-94.

20.Güzel E, Çetin Ş, Günsel A, Bilgiçli AT, Şişman İ, Yarasir MN. Comparative studies of photophysical and electrochemical properties of sulfur-containing substituted metal-free and metallophthalocyanines. Res Chem Intermed. :1–19.

21.Atmaca GY, Dizman C, Eren T, Erdogmus A. Novel axially carborane-cage substituted silicon phthalocyanine photosensitizer; synthesis, characterization and photophysicochemical properties. Spectrochim Acta Part -Mol Biomol Spectrosc. 2015;137:244–9.

22.Sen P, Atmaca GY, Erdogmus A, Dege N, Genc H, Atalay Y, vd. The Synthesis, Characterization, Crystal Structure and Photophysical Properties of a New Meso-BODIPY Substituted Phthalonitrile. J Fluoresc. 2015;25(5):1225–34.

23.Guzel E, Atmaca GY, Erdogmus A, Kocak MB. Novel sulfonated hydrophilic indium(III) and gallium(III) phthalocyanine photosensitizers: preparation and investigation of photophysicochemical properties. J Coord Chem. 2017;70(15):2659–70.

24.Yasa G, Erdogmus A, Ugur AL, Sener MK, Avciata U, Nyokong T. Photophysical and photochemical properties of novel phthalocyanines bearing non-peripherally substituted mercaptoquinoline moiety. J Porphyr Phthalocyanines. 2012;16(7–8):845–54.

25.Kirbac E, Atmaca GY, Erdogmus A. Novel highly soluble fluoro, chloro, bromo-phenoxy-phenoxy substituted zinc phthalocyanines; synthesis, characterization and photophysicochemical properties. J Organomet Chem. 2014;752:115–22.

26.Tayfuroglu O, Atmaca GY, Erdogmus A. Novel peripherally substituted zinc phthalocyanine: synthesis, characterization, investigation of photophysicochemical properties and theoretical study. J Coord Chem. 2017;70(18):3095–109.

27.Kobayashi N, Sasaki N, Higashi Y, Osa T. Regiospecific and Nonlinear Substituent Effects on the Electronic and Fluorescence-Spectra of Phthalocyanines. Inorg Chem. 1995;34(7):1636-.

28.Ozcesmeci I, Burat AK, Bayir ZA. Synthesis and photophysical properties of novel unsymmetrical metal-free and metallophthalocyanines. J Organomet Chem. 2014;750:125–31.

29. Durmus M, Ahsen V. Water-soluble cationic gallium(III) and indium(III) phthalocyanines for photodynamic therapy. J. Inorganic Biochem. 2010; 104: 297–309.

# Multi-Walled Carbon Nanotube Reinforced Polyimide Composites

**Burcu Oktay**✉ iD **, Sevil Türker**✉ iD **, Sevim Karataş**✉ iD **and Nilhan Kayaman-Apohan**✉ iD *

Marmara University, Department of Chemistry, 34722 Istanbul, Turkey

**Abstract :** Polyimides have a wide range of uses such as aeronautical applications of fuel cells, optics and electronic materials industry due to their outstanding thermal, mechanical and chemical properties. In this study, it was aimed to prepare composite polyimide films with amine-tethered multi-walled-carbon nanotubes (MWCNT). Firstly, to produce amine functional groups onto the surface of MWNCTs, MWCNTs were reacted with $H_2SO_4/HNO_3$, thionyl chloride and ethylenediamine. Then polyamic acid solution was prepared from 3',4,4'-benzophenone tetracarboxylic dianhydride (BTDA) and, 4'-oxydianiline (ODA). The functionalized carbon nanotube was added to the PAA solutions with certain amounts (1, 3, 4, 5 and 6 wt. % followed by stepwise thermal imidization. The thermal stability of the composite polyimide films were enhanced with addition of modified-carbon nanotube due to covalent interaction between polyimide based matrix and modified-carbon nanotube as a result of the imidization reaction. The addition of MWCNT increased the Tg of the BTDA-ODA-6% MWCNTs polyimide film from 275 to 304 °C with respect to the BTDA-ODA polyimide film. In addition, the mechanical properties of the films were improved. While the modulus of BTDA-ODA film was found as 743 MPa, with the introduction of MWCNT the modulus of BTDA-ODA-6% MWCNTs was increased up to 1119 MPa.

**Keywords:** Polyimide, carbon nanotube, nanocomposite.

**INTRODUCTION**

Multi-walled and single-walled carbon nanotubes (MWCNTs and SWCNTs) have superior chemical, electrical, and thermal performance (1). Despite their extraordinary properties, dispersion of carbon nanotubes into a polymer matrix is limited because of their hydrophobic character. To overcome this problem, the covalent and non-covalent chemical modifications of carbon nanotubes should be carried out (2).

Covalent chemical modification of CNTs allows a fine dispersion within a polymer matrix. Generally, the carboxylic acid or hydroxyl groups are created on the CNT surface by treatment with sulfuric and nitric acid. The functional groups make further reactions of carbon nanotubes possible (3,4).

Polyimides are a class of organic compounds that have received much attention owing to their excellent properties, such as superior thermal stability, mechanical properties and good chemical resistance (5). In addition, the composites can be used in advanced microelectronics and aerospace technologies due to their flexibility and radiation resistant properties (6). In recent years, a great amount of research has focused on the carbon nanotube/polyimide nanocomposites, to improve the properties of the polyimides. Incorporation of carbon nanotubes in polyimides has been shown to remarkably improve the mechanical and thermal properties of the resulting composites. Park et al. prepared carbon nanotube containing polyimide composites by in situ polymerization (7). Zhu *et al.* investigated the effect of carbon nanotubes on mechanical and electrical properties of the composites. The results showed that the composites containing carbon nanotubes had a higher tensile strength with good electrical properties (8). So *et al.* investigated the effect of carbon nanotubes on the morphological, mechanical, and electrical properties of MWNT-reinforced polyimides (9).

Non-covalent and covalent surface modifications have been used for functionalization of CNTs. Although, covalent surface modification can be better controlled to produce more stable nanomaterials (10). Commonly, the first step in this method is to incorporate carboxylic acid groups. In a second step, the carboxylic acid groups activated with thionyl chloride ($SOCl_2$) and then covalently attaching any molecule that contains a free-amine group such as ethylene diamine (11-14).

In this study, we focused on the modification of MWCNTs and the preparation of functionalized MWCNTs/polyimide composite films. Amine-tethered MWCNTs (MWCNTs-$NH_2$) were prepared by three step reactions. Firstly, MWCNTs were oxidized by a mixture

of $H_2SO_4$ and $HNO_3$, to produce surface carboxyl groups. Then, the COOH groups of MWCNTs were substituted with thionyl chloride and the resulting product was further reacted with ethylenediamine. Polyamic acid solutions were prepared by an *in situ* polymerization reaction from 3,3',4,4'-benzophenone tetracarboxylic dianhydride" (BTDA), 4,4'-oxydianiline (ODA) and various ratios of MWCNTs-$NH_2$ and followed by thermal imidization. The prepared composite films were characterized by scanning electron microscopy (SEM), Fourier transform-infrared spectroscopy (FT-IR), thermal gravimetric analysis (TGA), differential scanning calorimeter (DSC), and tensile and elongation tests.

## MATERIALS AND METHODS

### Reagents and Apparatus

Carbon nanotube (multi-walled, purity 95%, diameter: 10–15 nm, length: 0.1–10 μm, density: 1.7–2.1 $g/cm^3$) was purchased from Alfa Aesar. 4,4'-oxydianiline (ODA), thionyl chloride ($SOCl_2$) (≥99%), 3,3',4,4'-benzophenone tetracarboxylic dianhydride (BTDA), (3-aminopropyl)trimethoxysilane (97%), ethylenediamine and dimethylacetamide (DMAc) were purchased from Sigma Chem. Co. (St Louis, MO).

The structures of MWCNTs, in oxidized and amine-tethered forms, as well as polyamic acid and composite polyimides were investigated by Perkin Elmer ATR-FTIR spectrometer. The spectra were recorded in the frequency range of 4000-380 $cm^{-1}$. The morphology of the composite polyimide films were investigated by scanning electron microscopy (SEM) on Phillips XL 30 ESEM-FEG/EDAX. Thermogravimetric analysis (TGA) was carried out on Perkin–Elmer Thermogravimetric analyzer STA 6000 at heating rate of 10 °C/min from 30 to 750 °C in inert atmosphere. Differential scanning calorimeter studies were carried out on Pyris Diamond DSC (Perkin Elmer at a heating rate of 5 °C/min under $N_2$. Mechanical properties of the composite films were analyzed by standard tensile stress–strain tests using a Zwick Z010universal tensile tester (Istanbul, Turkey).

### Synthesis of amine-tethered MWCNTs (MWCNT-$NH_2$)

The modification of MWNCTs was carried out in three steps. At first, 1 g MWCNTs was refluxed in a mixture of sulfuric acid/nitric acid (3:1 v/v) at 120 °C for 4 h. The mixture was diluted with deionized water (2 L) and filtered. The oxidized product was dried at 50 °C. Then, the COOH groups of the oxidized MWCNTs were converted to acyl chloride (-COCl) groups with thionyl chloride at 70 °C for 24 h. The unreacted thionyl chloride was removed by heating at 80 °C. The product was dried in vacuum. Finally, 0.5 g of acyl

chloride functionalized MWCNTs was refluxed at 90 °C for 24 h with ethylene diamine to prepare amine-tethered MWCNTs (15). The reaction pathway is shown in Figure 1.
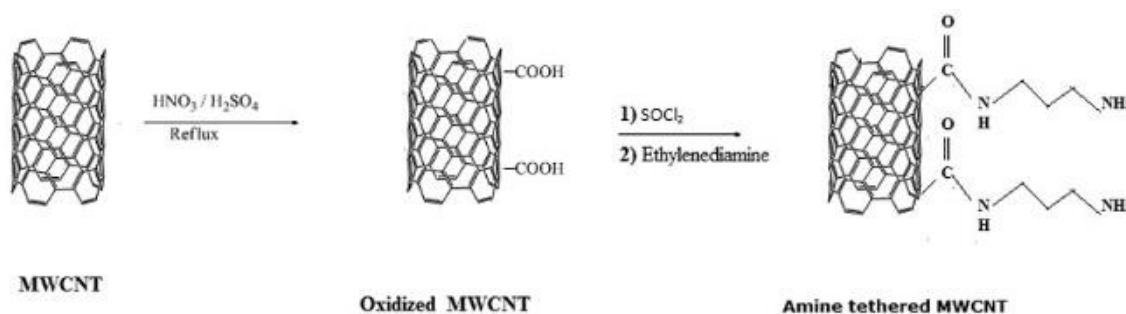


**Figure 1:** Modification of multi-walled carbon nanotube.

## Preparation of BTDA–ODA Polyamic acid Solution

The synthesis of the polyamic acid (PAA) precursor was followed according to literature (16). The solid concentration was afforded as a 20% (wt/v). Briefly, 9.011 g (0.045 mol) of ODA was dissolved in 80 mL DMAc until obtaining a clear solution. Then, 9.815 g (0.045 mol) of BTDA was partially added and the mixture was stirred for 24 h at room temperature. Table 1 summarizes the preparation method of PAA solutions.

**Table 1:** Composition of polyamic acid solutions.

| Codes | ODA (g) | BTDA (g) | Amine-tethered MWCNTs (%) |
|---|---|---|---|
| BTDA-ODA | 9.0108 | 9.8154 | - |
| BTDA-ODA-1%MWCNTs | 9.0108 | 9.8154 | 1 |
| BTDA-ODA-3% MWCNTs | 9.0108 | 9.8154 | 3 |
| BTDA-ODA-4% MWCNTs | 9.0108 | 9.8154 | 4 |
| BTDA-ODA-5% MWCNTs | 9.0108 | 9.8154 | 5 |
| BTDA-ODA-6% MWCNTs | 9.0108 | 9.8154 | 6 |

## Preparation of Amine-Tethered MWCNTs/Polyimide Films

One of the following (1, 3, 4, 5 or 6 wt%) amine-tethered MWCNTs were added to the PAA solution. The mixtures were sonicated for 10 min at room temperature and were cast on a glass substrate. Then, the glass substrate were dried stepwise at 80 °C, 100 °C, 150 °C, 200 °C and 300 °C for 1 h at each temperature. The schematic fabrication process of amine-tethered MWCNTs/polyimide films is shown in Figure 2. The polyimides were obtained in 89–95% yield. The strong chemical bond between amino groups of CNTs-ODA and PI matrix. During the polymerization and thermal imidization process, amine-tethered MWCNT tended to form strong chemical bond with BTDA-ODA polyimide (17). The prepared products were washed with ethanol and dried under vacuum.
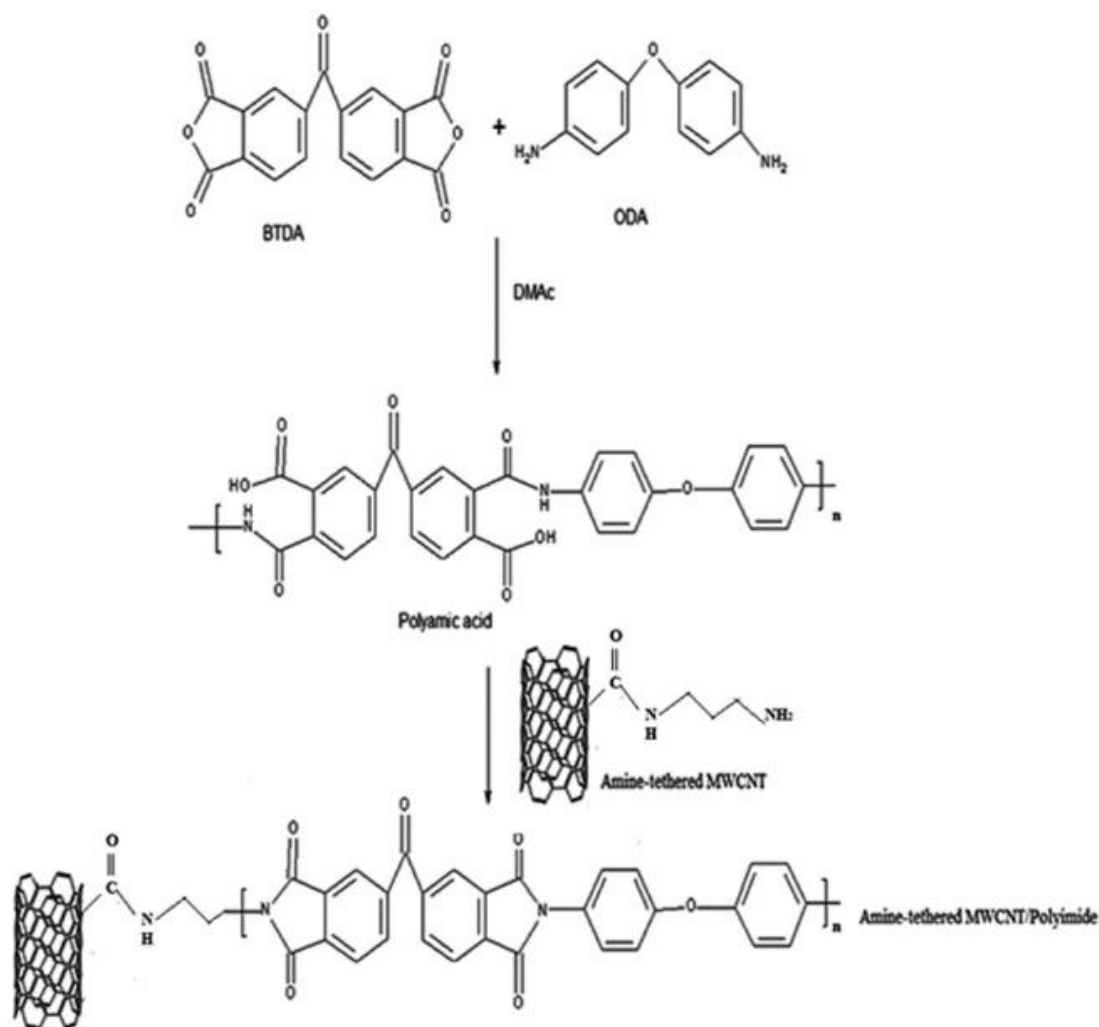
**Figure 2:** Preparation of amine-tethered MWCNTs/polyimide films.

## RESULTS

### Characterization of MWCNTs-NH$_2$

Figure 3 shows the FTIR spectra of MWCNT, MWCNTs-COOH and MWCNTs-NH$_2$. The band at 3700 cm$^{-1}$ corresponds to free hydroxyl groups. The broad band in the range of 3400-2800 cm$^{-1}$ is associated to the characteristic O-H stretching from carboxyl groups in the oxidized MWCNTs (O=C−OH and C−OH). The peak at 1560 cm$^{-1}$ is related to the carboxylate anion stretch mode (17). In the FTIR spectrum of the MWCNTs-NH$_2$, the peak at 3200 cm$^{-1}$ corresponds to the characteristic N-H stretching of the CONH group. The C-H stretching peaks at 2900 cm$^{-1}$ and 2845 cm$^{-1}$ indicate the covalent bonding of ethylene diamine on MWCNT. Evidently, as a result of the adsorption of CO on the MWCNT, broad bands in the C−O stretch region appeared. Two bands at a frequency higher than the gas-phase CO frequency are found: A band around 2330 cm$^{-1}$ and a band near 2108 cm$^{-1}$ (19,20).
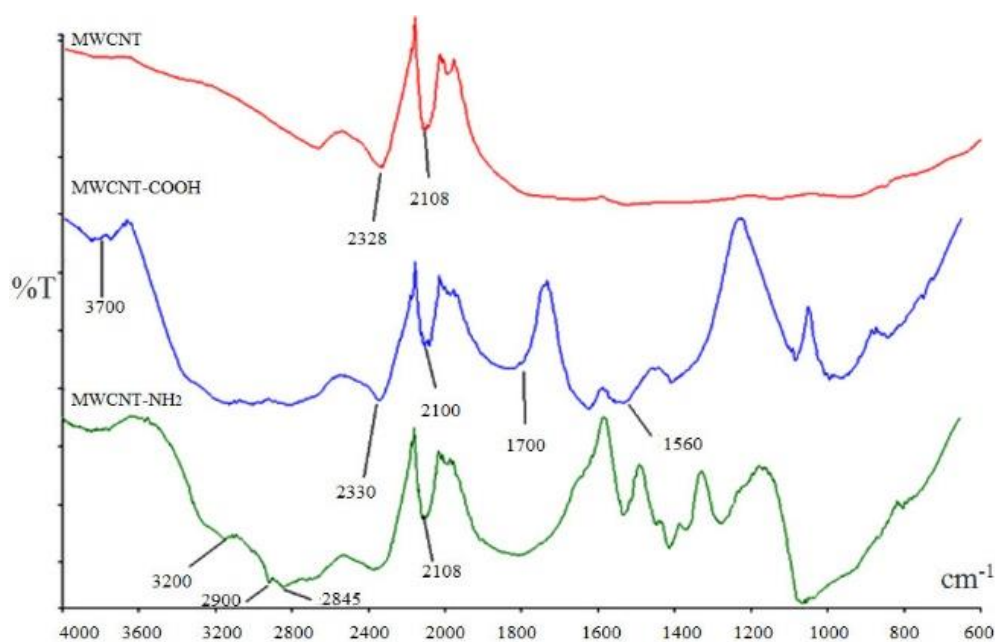
**Figure 3:** The FTIR spectra of MWCNT (in red), MWCNTs-COOH (in blue) and MWCNTs-NH$_2$ (in green).

**Structural Characterization of Polyimide Films**

Figure 4 shows the FTIR spectra of the polyamic acid and polyimide/MWCNTs films. In the spectrum of the polyamic acid (spectrum A), the characteristic amide band of polyamic acid is observed at 1617 cm$^{-1}$. As can be seen from spectrum B to F, the amide stretching peak disappeared after thermal imidization of polyamic acid solution. The absence of this peak indicates that imidization was successfully carried out. The new bands at 1777 and 1715 cm$^{-1}$ correspond to asymmetric and symmetric carbonyl stretching of the polyimides, respectively. The stretching absorptions of -C-N-C- were observed at 1370 cm$^{-1}$ and 1150 cm$^{-1}$ (21).
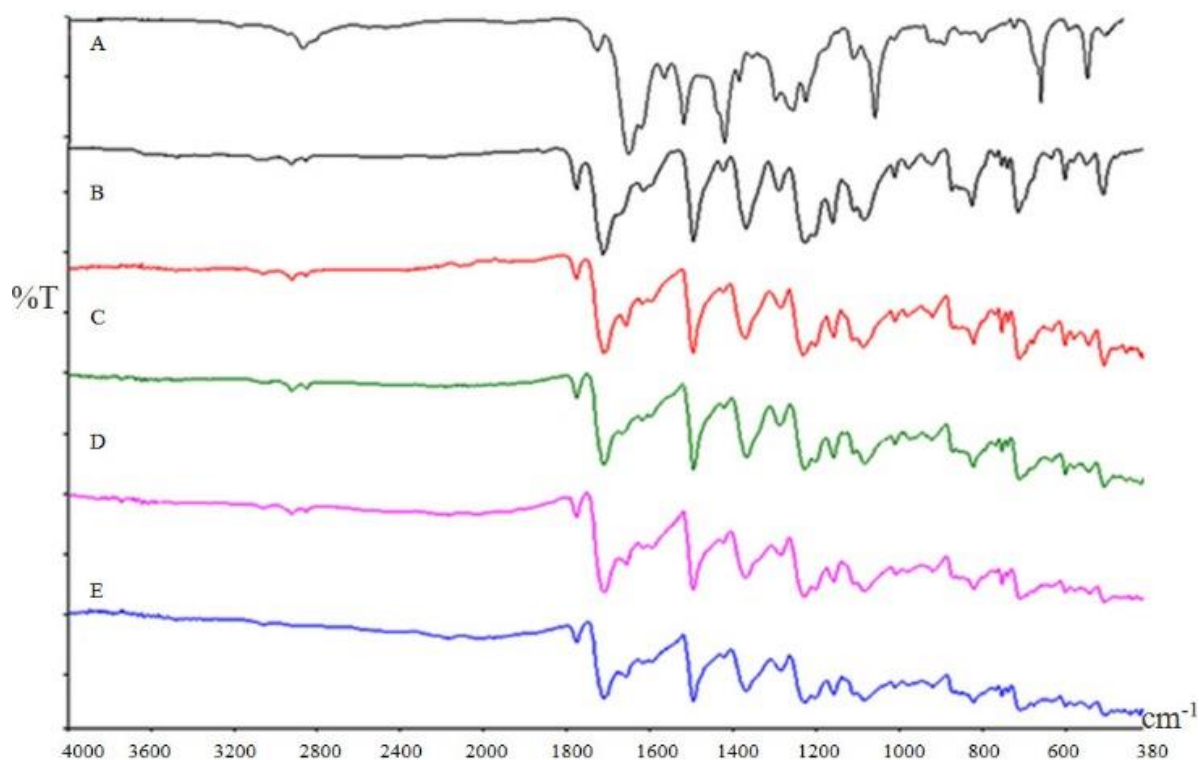
**Figure 4:** The FTIR spectra of the polyamic acid and polyimide/MWCNTs films. A)PAA, B) BTDA-ODA-%1 MWCNTs, C) BTDA-ODA-%3 MWCNTs, D) BTDA-ODA-%4 MWCNTs, E) BTDA-ODA-%5 MWCNTs and F) BTDA-ODA-%6 MWCNTs

## Morphology of Polyimide films

Morphology of the polyimide films were investigated by scanning electron microscopy (SEM). The SEM micrographs are shown in Figure 5a-d. Homogenous dispersion was obtained at a certain amount of MWCNTs as confirmed by SEM images. The amine-tethered MWCNTs were dispersed in the polyimide matrix in individual tubes. Carbon nanotubes tend to agglomerate due to strong interfacial forces such as van der Waals interactions and geometry (22). To overcome the agglomeration of MWCNTs by modification is a critical challenge. Kim *et al.* reported that the strong interfacial interactions between modified MWCNTs with polyimide matrix take place by covalent and hydrogen bonds. In addition, the modification of MWCNTs provides the chemical compatibility between the PI matrix and the modified CNTs (23). The addition of MWCNT changed the morphology of polyimide. It is said that the surface roughness of films increased.
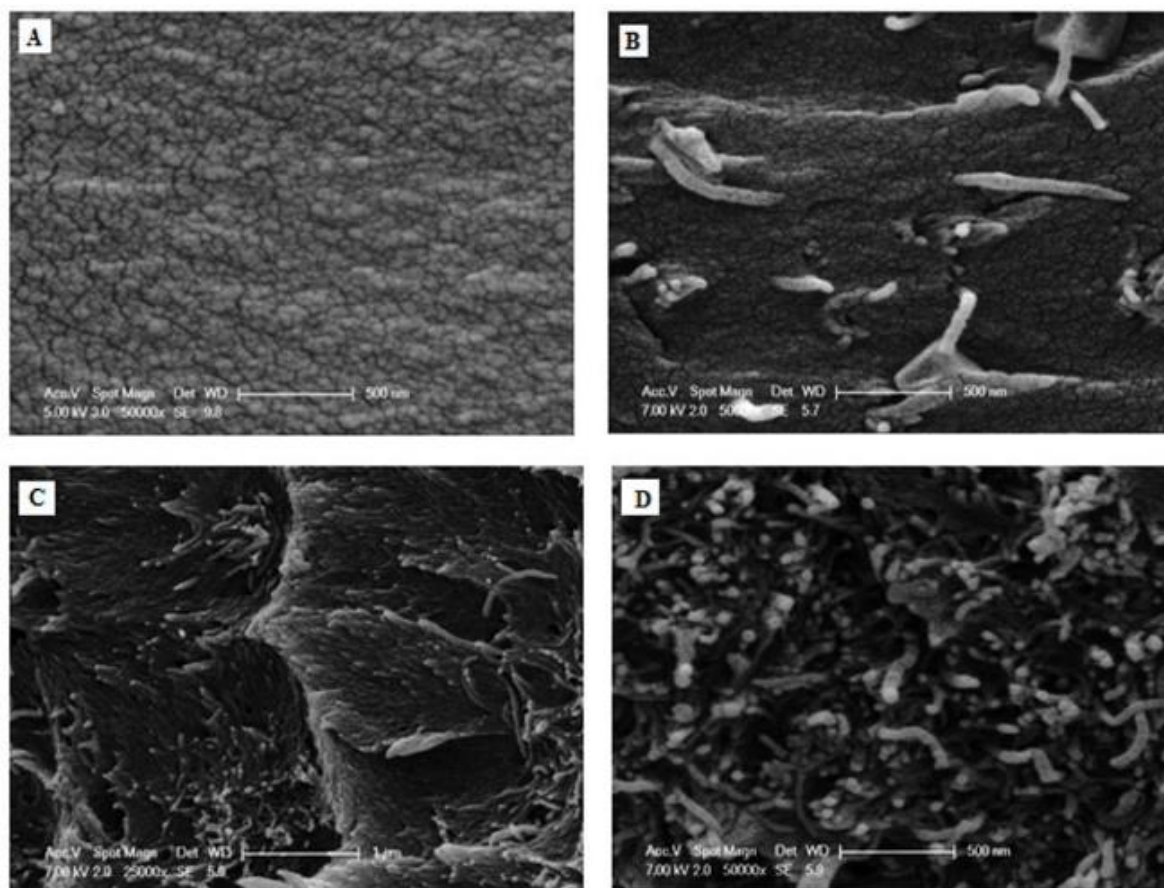
**Figure 5:** The SEM micrographs of (A) BTDA-ODA (50.000x), (B) BTDA-ODA-%1 MWCNTs (50.000x), (C) BTDA-ODA-%4 MWCNTs (25.000x) and (D) BTDA-ODA-%6 MWCNTs (50.000x).

**Thermal properties of MWCTs/polyimide composite films**

Figure 6 shows TGA curves of neat polyimide and MWCTs/polyimide composite films. 5 wt% weight loss temperatures (T%5), maximum weight loss temperatures ($T_{max}$%), and the residual char of the films are listed in Table 2. Aromatic polyimides exhibit high thermal stability because of their regular aromatic groups (24). The aromatic polyimides start to decompose after about 400 °C (25). As can be seen in Figure 6, TGA curves of the films exhibited one step degradation under nitrogen atmosphere. The maximum weight loss temperature ($T_{max}$) was found to slightly increase with increasing amount of modified-MWCNTs. It is known that MWCNTs make contribution to the thermal stability and decomposition rate (26). As expected, char yield of the polyimides gradually increased with addition of MWCNTs.
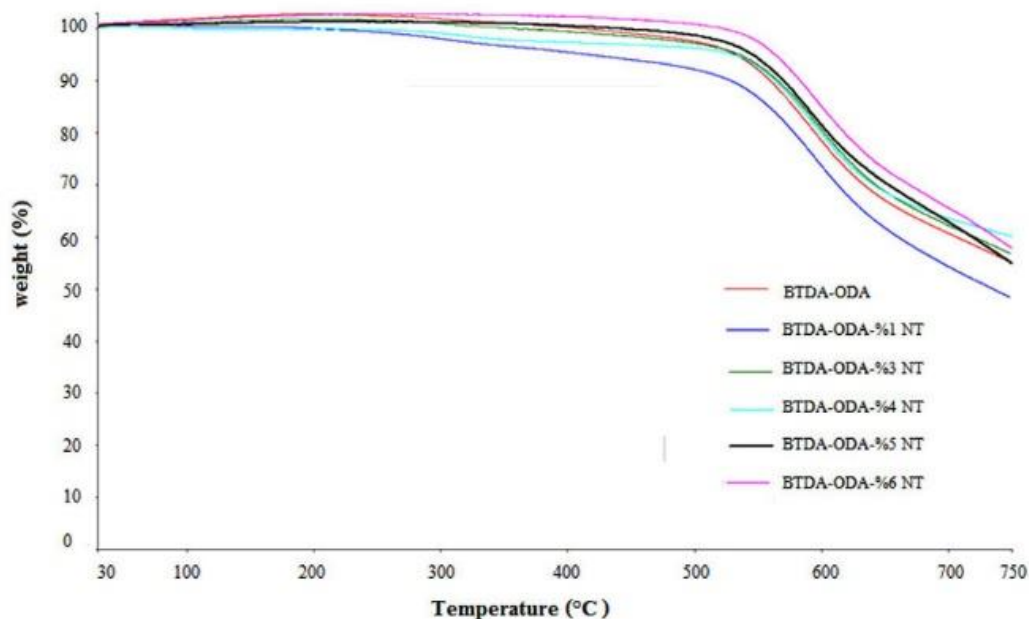
**Figure 6:** TGA thermograms of the BTDA-ODA polyimide and MWCNTs/Polyimide composite films in nitrogen atmosphere.

The glass transitions temperatures (Tg) of polyimide films were investigated by differential scanning calorimeter. The Tg for BTDA-ODA polyimide film was 275 °C. DSC curves show that the addition of MWCNTs causes Tg values of the MWCTs/polyimide composite films to increase. The results are listed in Table 2. The increasing Tg values demonstrated that amine modified MWCNTs were covalently bonded to the polyimide chains. The secondary network structure occurs by addition of MWCNTs to the BTDA-ODA crosslinked structure (27).

**Table 2:** Thermal and Mechanical properties of polyimide films.

| Codes | T%5 (T °C) | $T_{max}$ (T °C) | Char (%) | Tg (°C) | E-modulus (MPa) |
|---|---|---|---|---|---|
| BTDA-ODA | 415 | 553 | 48.45 | 275 | 743 |
| BTDA-ODA-1% MWCNTs | 535 | 603 | 55.33 | 277 | 1011 |
| BTDA-ODA-3% MWCNTs | 528 | 555 | 56.00 | 280 | 1036 |
| BTDA-ODA-4% MWCNTs | 531 | 565 | 60.10 | 287 | 1040 |
| BTDA-ODA-5% MWCNTs | 544 | 571 | 54.76 | 289 | 1091 |
| BTDA-ODA-6% MWCNTs | 563 | 590 | 57.56 | 304 | 1119 |

**Mechanical properties of MWCTs/polyimide composite films**

The Young's modulus of the composite polyimide films are given in Table 2. The presence of MWCNTs increased the modulus of composite films compared to BTDA-ODA neat film. The modulus of BTDA-ODA polyimide film was found as 743 MPa. However, the modulus of the composite polyimide films increased with addition of amine-tethered MWCNTs. The modulus of BTDA-ODA-1% MWCNT and BTDA-ODA-3% MWCNT composite polyimide films were found as 1011 and 1036 MPa, respectively. Moreover, %1, 2%, 3%, 4%, 5%

and 6% MWCNTs containing polyimide films showed higher modulus than BTD-ODA polyimide film.

**CONCLUSIONS**

BTDA-ODA polyimide and BTDA-ODA-MWCNTs composite polyimide films were successfully prepared via in situ polymerization process. MWCNTs were functionalized with amine groups, to bond with the polyimide matrix. The addition of amine functionalized MWCNTs into a BTDA-ODA polyimide led to obvious improvements in the thermal and mechanical properties. SEM investigations indicate that MWCNTs were homogeneously dispersed in the polyimide matrix. The successful modification and attachment of MWCNTs into the polymeric matrix will create various applications for nanocomposite area.

**REFERENCES**

1. Yang F, Li Y, Zhang S, Tao M, Zhao J, Hang C. Functionalization of multiwalled carbon nanotubes and related polyimide/carbon nanotubes composites. Synthetic Metals 2010; (160), 15–16,: 1805-1808.

2. Olalde B,  Aizpurua JM, García A, Bustero I, Obieta I, Jurado MJ. Single-Walled Carbon Nanotubes and Multiwalled Carbon Nanotubes Functionalized with Poly(l-lactic acid): a Comparative Study J. Phys. Chem. C. 2008; 112 (29): 10663–10667.

3. Meng L, Fu C , Lu Q. Advanced technology for functionalization of carbon nanotubes  Progress in Natural Science. 2009; (19), 7- 10: 801-810.4. J Nanomater, 83583 (2006), pp. 1-5.

4.Z.M. Dang, L. Wang, L.P. Zhang Surface functionalization of multiwalled carbon nanotube with trifluorophenyl. J Nanomater. 2006; (83583): 1-5.

5. Oktay B,  Toker RD, Kayaman-Apohan N. Superhydrophobic behavior of polyimide–siloxane mats produced by electrospinning. Polymer Bulletin. 2015: ( 72) , 11; 2831–2842.

6. Srivastava R, Banerjee S, Jehnichen D, Voit B, Böhme F. In Situ Preparation of Polyimide/Amino-Functionalized Carbon Nanotube Composites and Their B Properties. Macromol. Mater. Eng. 2009; (294): 96–102.

7. Park C, Ounaies Z, Watson KA, Crooks RE, Smith JE, Lowther SE. Dispersion of single wall carbon nanotubes by in situ polymerization under sonication. Chem. Phys. Lett. 2002;(364):303–8.

8. Zhu BK, Xie SH, Xu ZK, Xu YY. Preparation and properties of the polyimide/multi-walled carbon nanotubes (MWNTs). Compos Sci Technol 2006;(66):548–554.

9. So HH,  Cho Sahoo NG. Effect of carbon nanotubes on mechanical and electrical properties of polyimide/carbon nanotubes nanocomposites. Macromolecular Nanotechnology. European Polymer Journal. 2007; (43): 3750–3756.

10. Li R, Wang X, Ji Z, Sun B, Zhang H, Chang CH, et al. Surface Charge and Cellular Processing of Covalently Functionalized Multiwall Carbon Nanotubes Determine Pulmonary Toxicity. ACS Nano. 2013 Mar 26;7(3):2352–68.

11. Kim SW, Kim T, Kim YS, Choi HS, Lim HJ, Yang SJ, et al. Surface modifications for the effective dispersion of carbon nanotubes in solvents and polymers. Carbon. 2012 Jan;50(1):3–33.

12. Murugesan S, Myers K, Subramanian V (Ravi). Amino-functionalized and acid treated multi-walled carbon nanotubes as supports for electrochemical oxidation of formic acid. Applied Catalysis B: Environmental. 2011 Apr;103(3–4):266–74.

13. Xie H, Sheng C, Chen X, Wang X, Li Z, Zhou J. Multi-wall carbon nanotube gas sensors modified with amino-group to detect low concentration of formaldehyde. Sensors and Actuators B: Chemical. 2012 Jun;168:34–8.

14. Mugadza T, Nyokong T. Covalent linking of ethylene amine functionalized single-walled carbon nanotubes to cobalt (II) tetracarboxyl-phthalocyanines for use in electrocatalysis. Synthetic Metals. 2010 Oct;160(19–20):2089–98.

15. Vatanpour V, Safarpour M, Khataee A, Zarrabi H, Ehsan M, Kavian YM. A thin film nanocomposite reverse osmosis membrane containing amine-functionalized carbon nanotubes. Separation and Purification Technology. 2017: (184), 31; 135–143

16. Çakmakçı E, Güngör A. Preparation and characterization of flame retardant and proton conducting boron phosphate/polyimide composites. Polymer Degradation and Stability. 2013; (98), 5: 927-933.

17. Wang J, Jiao Q, Li H, Zhao Y, Guo B. In situ preparation of polyimide/amino-functionalized carbon nanotube composites and their properties. Polymer Composites. 2014 Oct;35(10):1952–9.

18. Atieh MA, Bakather OY, Al-Tawbini B,  Bukhari AA,  Abuilaiwi FA, Fettouhi MB. Effect of Carboxylic Functional Group Functionalized on Carbon Nanotubes Surface on the Removal of Lead from Water. Bioinorg Chem Appl. 2011:(2010); 2010: 603978.

19. Ţucureanu V, Matei A, Avram AM. FTIR Spectroscopy for Carbon Family Study. Critical Reviews in Analytical Chemistry. 2016 Nov;46(6):502–20.

20. V. Rakİc, V. Dondur, R. Hercıgonja. FTIR study of carbon monoxide adsorption on ion-exchanged X, Y and mordenite type zeolites. Journal of the Serbian Chemical Society. 2003: (4-5): 409-16.

21. So HH, Cho JW,  Sahoo NG. Effect of carbon nanotubes on mechanical and electrical properties of polyimide/carbon nanotubes nanocomposites. European Polymer Journal. 2007: (43), 9:750–3756.

22. Wang J, Pui DYH. Dispersion and Filtration of Carbon Nanotubes (CNTs) and Measurement of Nanoparticle Agglomerates in Diesel Exhaust. Chem Eng Sci. 2013: (85); 69–76.

23. Kim BS, Bae SH, Park YH, Kim JH. Preparation and Characterization of Polyimide/Carbon-Nanotube Composites. Macromolecular Research, 2007 (15),4: 357-362.

24. Ha CS., Mathews A.S. (2011) Polyimides and High Performance Organic Polymers. In: Advanced Functional Materials. Springer, Berlin, Heidelberg.

25. Ribeiro CR, Freeman BD,  Kalika DS, Kalakkunnath S. Pervaporative Separation of Aromatic/Aliphatic Mixtures with Poly(Siloxane-co-Imide) and Poly(Ether-co-Imide) Membranes. Ind Eng Chem Res  2013; (52): 8906−8916.

26. Mahajan A, Ákos AK, Zoltan K, Vilarinho PM. Studies on the thermal decomposition of multiwall carbon nanotubes under   different atmospheres. Materials Letters. 2013; (90),1:165-168.

27. Mo TC, Wang HW, Chen SY, Yeh YC. Synthesis and Characterization of Polyimide/ Multi-Walled Carbon Nanotube nanocomposites. Polymer Composites. 2008; (29), 4: 451-457.

**RESEARCH ARTICLE**

# Optical investigation of palladium(II) phthalocyanine including an aromatic group

## İbrahim Özçeşmeci [a*] and İdris Sorar [b*]

[a] Istanbul Technical University, Department of Chemistry, Maslak, TR-34469, Istanbul, Turkey
[b] Mustafa Kemal University, Department of Physics, Antakya, TR-31040, Hatay, Turkey

**Abstract:** Peripherally β-naphthoxy-substituted palladium(II) phthalocyanine was synthesized from corresponding phthalonitrile compounds. The palladium(II) phthalocyanine was characterized with ultraviolet–visible spectroscopy (UV-Vis), fourier transform-infrared spectroscopy (FT-IR), mass spectrometry, and elemental analysis techniques. Thin films of palladium(II) phthalocyanine were prepared using different organic solvents by spin coating technique. Transmittance and absorbance spectra of the thin films were studied in the wavelength range of 200–1000 nm. Optical band gaps of palladium(II) phthalocyanine thin films were also calculated.

**Keywords:** Phthalocyanine, β-naphthol, palladium, thin film, optical properties.

**Corresponding Author** Fax: +90 (212) 2856386; Tel.: +90 (212) 2857309
*e-mail* : ozcesmecii@itu.edu.tr

**Corresponding Author** Fax: +90 (326) 2455867; Tel.: +90 (326) 2455845
*e-mail* : sorar@mku.edu.tr

## INTRODUCTION

Phthalocyanines (Pcs) are macrocyclic compounds which are highly stable against elevated temperatures and light. The colors of Pcs range from dark blue to dark green. They attracted great interest due to their use as pigments. The electronic, optical, structural, and coordination properties of Pcs and their ability to be modified according to purpose have created quite different application areas for them than their classical uses. These applications include information technology, semiconductors, photodynamic agents, electrochromic devices, liquid crystalline materials, molecular materials and nonlinear optical materials, Langmuir-Blodgett films, and many catalytic processes (1, 2). Most of these applications are related to the planar π-configuration system of Pc as much as the structure of the central metal atom. The addition of substituents to the peripheral positions increases the distance between the Pc conjugated 18-π electron systems and facilitates their solubility. This allows the optical and optoelectronic properties of the molecule to be adjusted (3, 4).

There are many acquisition methods for thin films used in different technological fields. The coating techniques are divided into four basic methods in consideration of the physical condition of the coating material and the surface of the coating. These methods are coatings made from solid state, made from solution, made from liquid or semi-liquid state, and made from vapor phase (5). The spin coating method is one of the most commonly used processes for obtaining thin films of soluble Pc compounds containing substituent groups (6, 7). In this method, the final film thickness and other properties of thin film depend on the solution properties (concentration, drying speed, solid ratio, and surface tension) and processing conditions (rotation speed) (8, 9).

In this work, we have synthesized and characterized peripherally β-naphthoxy unit substituted palladium(II) phthalocyanine. We have also obtained thin films of palladium(II) phthalocyanine using different organic solvents [chloroform (CF), tetrahydrofuran (THF), dimethylformamide (DMF) and dimethyl sulfoxide (DMSO)] with spin coating technique and investigated their optical properties. Besides, optical band gaps of palladium(II) phthalocyanine thin films were also calculated.

## EXPERIMENTAL

### Equipments and Materials

FT-IR spectra were taken at Perkin Elmer Spectrum One FT-IR spectrometer. Mass spectra were recorded on Ultima Fourier Transform and Varian 711 mass spectrometers. Elemental analyses were recorded on the Instrumental Analysis Laboratory of the TUBITAK Marmara Research Centre. Electronic spectra were taken at Scinco SD 1000 single-beam ultraviolet-visible (UV-vis) spectrophotometer at room temperature. 4-nitrophthalonitrile was synthesized according to a

reported procedure (10). 4-(2-naphthoxy)phthalonitrile (1) was synthesized according to a procedure in the publications (11).

## Tetrakis(2-naphthoxy)phthalocyaninatopalladium(II) (2)

4-(2-naphthoxy) phthalonitrile (1) (0.270 g, 1 mmol) and $PdCl_2$ (0.044 g, 0.25 mmol) in 2.5 mL of N,N-(dimethylamino)ethanol (DMAE) were mixed in a glass tube. The mixture was stirred and heated at 145 °C for 24 h under $N_2$. The resulting blue mixture was cooled to room temperature and the crude product was precipitated by addition of water. It was filtered off and the precipitate was successively washed with water and cold acetone, cold ethanol, and lastly with n-hexane, and then dried *in vacuo*. Finally, pure palladium(II) phthalocyanine compounds were purified by chromatography on silica gel using dichloromethane/ethanol (25:1) mixture as eluent. The yield was 122 mg (41.21%). Melting point is over 200 °C. Anal. calc. for $C_{72}H_{40}N_8O_4Pd$: C, 72.82; H, 3.39; N, 9.44. Found: C, 72.86; H, 3.36; N, 9.42%; FT-IR, $(cm^{-1})$: 3055 (Ar -H), 1459, 1220, 1155, 964; UV-Vis $\lambda_{max}$ (nm) (log ε) in DMSO: 681 (4.81), 340 (4.71), 290 (4.97); MS: m/z 1187.012 $[M]^+$, 1205.977 $[M+H_2O]^+$

## Preparation of PdPc (2) thin films

Thin films were prepared in the following way: PdPc were dissolved in chloroform (CF), tetrahydrofuran (THF), dimethylformamide (DMF), and dimethyl sulfoxide (DMSO) by stirring with for 10 min. The resulting solutions were blue and homogeneous. The same amount of PdPc was used for each solvent and the concentration of all solutions was 10 mg/mL. Films were prepared on pre-cleaned microscope glass substrates by rotating them on a spin coater at a speed of 2000 rpm for 15 s. Finally, the films were dried at room temperature prior to optical measurement. Transmittance and absorbance spectra of the films were obtained by using a Thermo Scientific GENESYS 10S UV–vis spectrophotometer in the wavelength range of 200–1000 nm.

## RESULTS AND DISCUSSION

### Synthesis and characterization

The starting compound of 4-(2-naphthoxy) phthalonitrile (**1**) was a base-catalyzed aromatic nitro displacement of 4-nitrophthalonitrile with β-naphthol (11). Conversion of 4-(2-naphthoxy) phthalonitrile (**1**) into related palladium(II) phthalocyanine (**2**) was achieved in (N,N-(dimethylamino)ethanol) as a high boiling solvent in the presence of metal salt ($PdCl_2$) (Scheme 1) (12, 13). Tetrakis(2-naphthoxy)phthalocyaninatopalladium(II) (**2**) was characterized by FT-IR, mass, elemental analysis and UV–Vis spectroscopic techniques. The palladium(II) phthalocyanine product in this study is a mixture of positional isomers. It is because the phthalonitrile precursor has a single substituent. The positional isomers were hardly separated by chromatography (14).
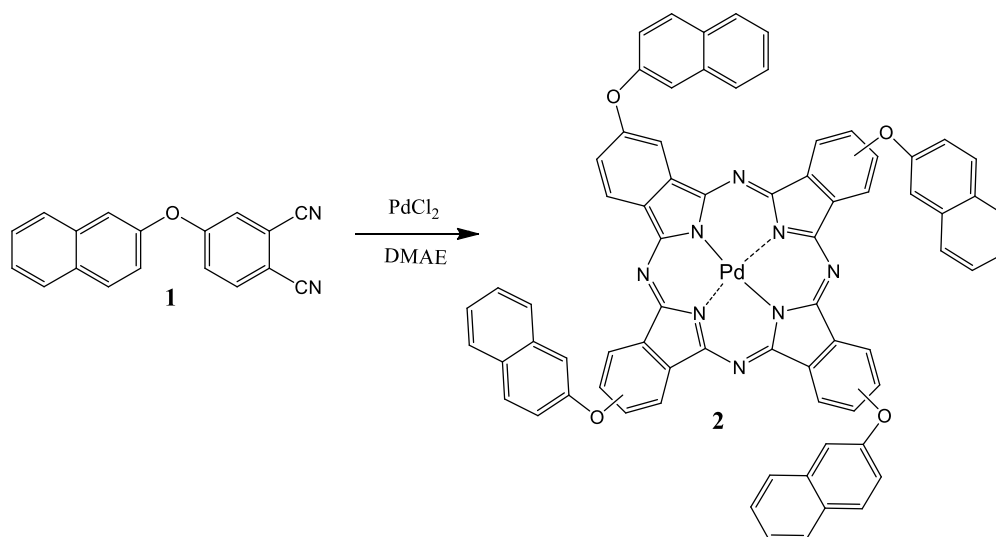
**Scheme 1.** Synthetic route of tetrakis(2-naphthoxy)phthalocyaninatopalladium(II) (2).

In the FT-IR spectrum of palladium(II) phthalocyanine (**2**), the typical C≡N stretch at ~ 2300 cm$^{-1}$ of 4-(2-naphthoxy) phthalonitrile (**1**) disappeared. Palladium(II) phthalocyanine (**2**) has expected IR vibration peaks due to aromatic CH stretching at 3050 cm$^{-1}$. The FT-IR spectrum for palladium(II) phthalocyanine (**2**), showed transmittance peaks around 1459, 1220, 1155 and 964 cm$^{-1}$ which may be assigned to phthalocyanine skeletal vibrations. The elemental analysis result of palladium(II) phthalocyanine (**2**) is consistent with the suggested structure. The mass spectrum of palladium(II) phthalocyanine (2) has the expected mass. The molecular ion peaks of **2** was observed at m/z= 1187.012 [M]$^+$ and 1205.977 [M+H$_2$O]$^+$ (Figure 1). The electronic absorption spectra of palladium(II) phthalocyanine (**2**), recorded in DMSO, show an intense Q bands at 681 nm (Figure 2). The B bands of **2** come out in the UV region around 340 nm. An intense broad electronic absorption band resulting from the п–п* transition of naphthalene groups emerge in the UV region at about 290 nm for **2** (15).
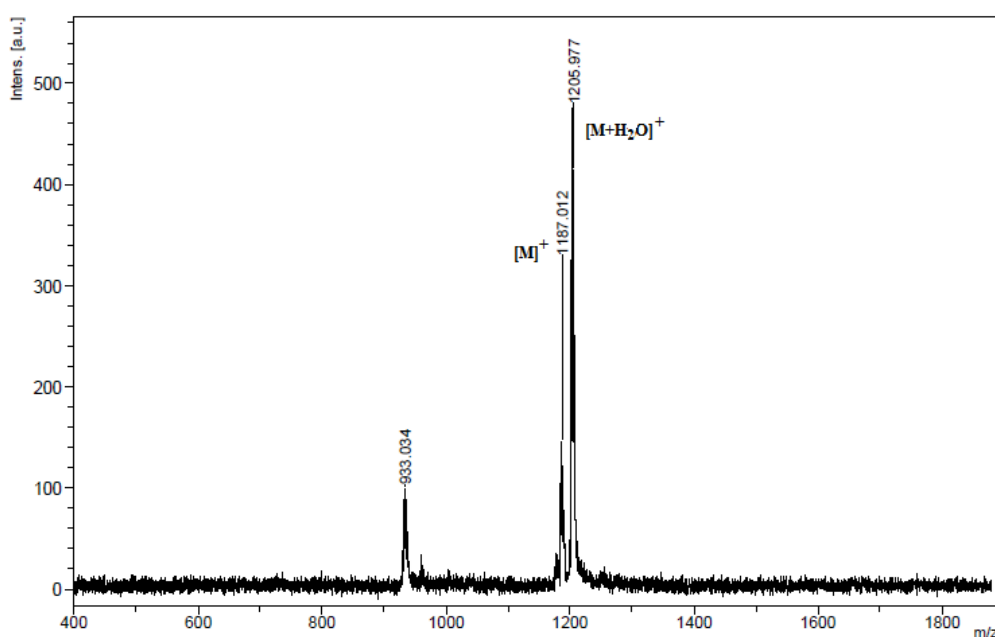


**Figure 1:** Mass spectrum of tetrakis(2-naphthoxy)phthalocyaninatopalladium(II) (**2**).
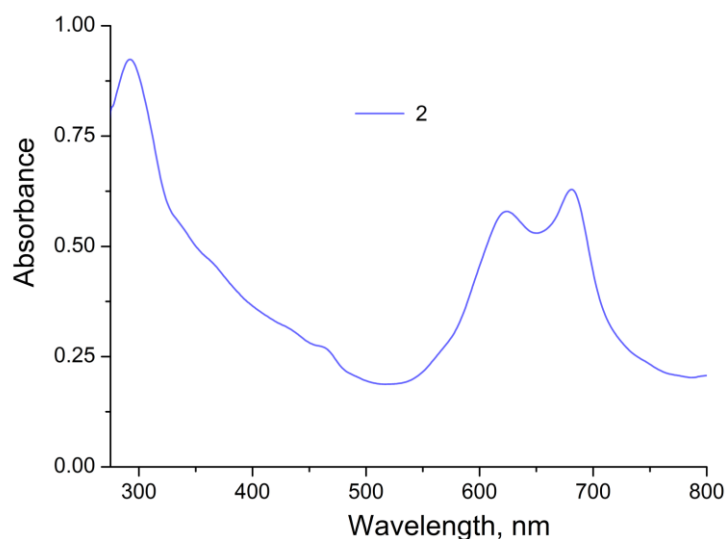
**Figure 2:** Absorption spectrum of (**2**) in DMSO (1.0 x10$^{-5}$ M).

### Optical results

The films prepared using DMF and DMSO solvents did not adhere completely to the surface but the film surfaces prepared using CF and THF solvents were found to be homogeneously coated. Transmittance spectra of the PdPc (**2**) films which were prepared by dissolving PdPc (**2**) in various solvents are shown in Figure 3. The peaks in the specific Q band region of PdPc (**2**) were best seen in films prepared using CF and THF solvents. Nevertheless, no picture was found in this region of the films prepared using DMF and DMSO solvents. This may be attributed to their low adhesion to the surface, or having less solubility of them compared to other two solvents and there may not be enough PdPc (**2**) on the surface of the films prepared with these solvents. The transmittance value of all films in the visible region and near infrared region is above 80%. It has been found that the solvents used to prepare PdPc (**2**) thin films have a significant effect on the transmittance and characteristic peaks in the Q band region of the spectrum. This is also clearly seen in Figure 4, in which the absorption spectrum is shown. There are studies showing that the amount of absorption in the Q band region can be adjusted by the concentration of the solvent and can be used for optical windowing purposes (9). In this study, it is seen that the use of different solvents is also effective in this region.
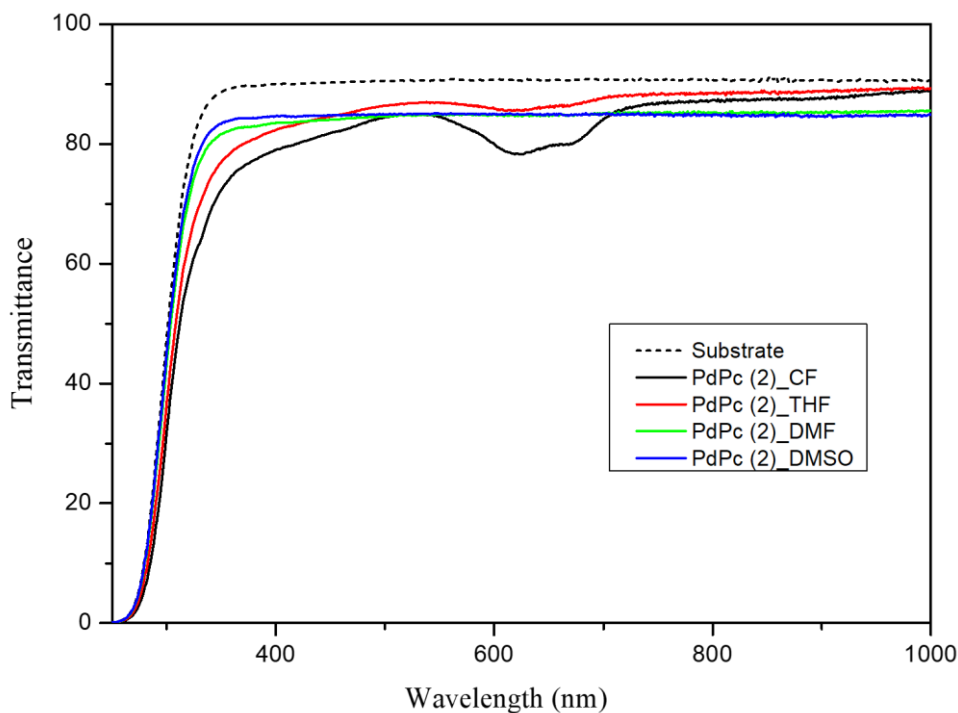
**Figure 3:** Transmittance spectra of PdPc (**2**) thin films as a function of solvents.
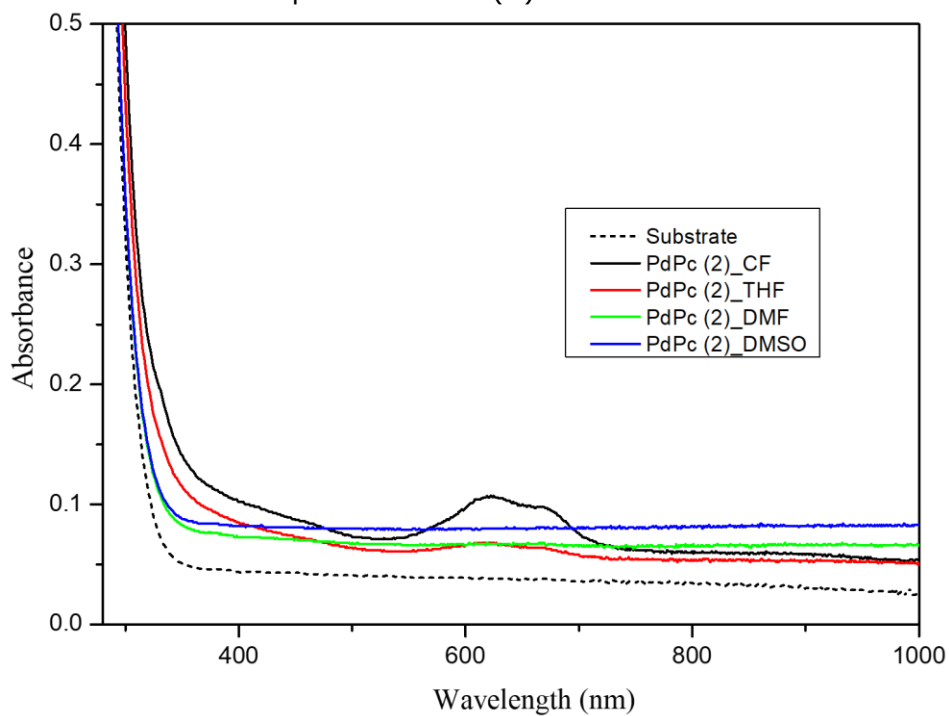


**Figure 4:** Absorption spectra of PdPc (**2**) thin films as a function of solvents.

Optical energy band gap of PdPc (**2**) films were calculated according to the following relation (16):

$$\alpha = A(h\nu - E_g)^m \qquad \text{(Eq. 1)}$$

where *A* is a constant, and m determines the type of the transition which is equal to 1/2 for direct allowed transitions. Extrapolation of the linear part to photon energy axis (Figure 5) gives

the energy band gaps of the films. They were found about 4.48, 4.51, 4.55 and 4.55 eV for PdPc (**2**) films as a function of solvents CF, THF, DMF and DMSO, respectively. It has been observed that films prepared using different solvents have changed the value of the energy band gaps.
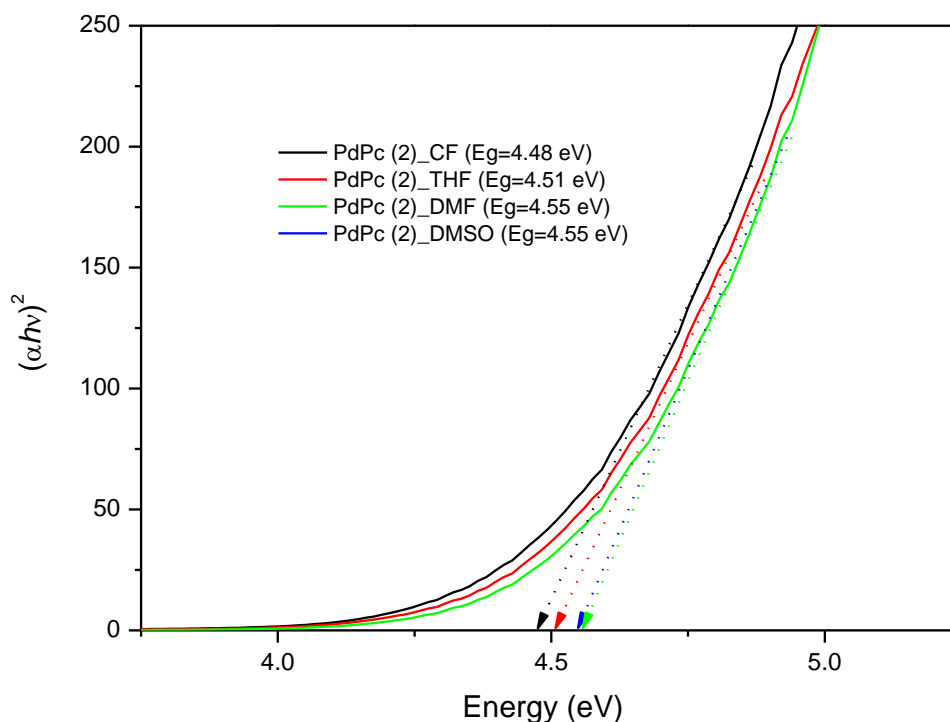


**Figure 5:** Relation between vs. photon energy for PdPc (2) thin films as a function of solvents.

**CONCLUSION**

In summary, we have synthesized and characterized peripherally β-naphthoxy substituted palladium(II) phthalocyanine (**2**). Thin films of palladium(II) phthalocyanine were prepared using different organic solvents by spin coating technique. The transmittance value of all films in the visible region and near infrared region is above 80%. The peaks in the specific Q region of PdPc (**2**) were best seen in films prepared using CF and THF solvents. It has been observed that energy band gaps of the films may be modulated by using different solvents. PdPc (**2**) thin films prepared by using different organic solvents especially CF exhibit a good absorption in the visible region of electromagnetic spectrum hence they could be good candidate for various device applications such as optical filters.

**ACKNOWLEDGEMENT**

## REFERENCES

1. McKeown NB. *Phthalocyanine Materials: synthesis, structure, and function*. Cambridge University Press: Cambridge, 1998.

2. Leznoff CC, Lever ABP. Phthalocyanines: properties and applications. Vols. 1–4. Eds. VCH Publishers: New York, USA, 1989.

3. Özçeşmeci İ, Güner S, Okur Aİ, Gül A. New phthalocyanines containing bulky electron rich substituents. J. Porphyrins Phthalocyanines. 2007; 11(07): 531–6.

4. Kurt Ö, Özçesmeci İ, Gül A, Koçak MB. Synthesis and photophysical properties of novel hexadeca-substituted phthalocyanines bearing three different groups. *J. Organomet. Chem.* 2014; 754: 8–15.

5. Seshan K. Handbook of Thin-Film Deposition Processes And Techniques, W. Andrew Publishing: Norwich, New York, U.S.A., 2002.

6. Özçesmeci İ, Sorar İ, Gül A. Optical studies on phthalocyanines substituted with phenylazonaphthoxy groups. Philos. Mag. 2016; 96(28): 2986–99.

7. Özçeşmeci M, Sorar İ, Hamuryudan E. Synthesis, optical and structural studies of tetrakis [4-(2', 3', 4', 5', 6'-pentafluorobenzyloxy) benzyloxy]-substituted metallo-phthalocyanines. Synth. Met. 2012; 162: 154–61.

8. Sorar İ, Şener MK, Tepehan F, Gül A. Structural and optical studies of tetra (tricarbethoxy)-substituted metallophthalocyanines. Thin Solid Films. 2008; 516: 2894–98.

9. Özçesmeci İ, Sorar İ, Gül A. Zinc (II) phthalocyanine as an optical window for visible region. Inorg. Chem. Commun. 2011; 14: 1254–57.

10. Young JG, Onyebuagu WJ. Synthesis and Characterization of Di-disubstituted Phthalocyanines, Org. Chem. 1990; 55: 2155–59.

11. Yenilmez HY, Özçeşmeci İ, Okur Aİ, Gül A. Synthesis and characterization of metal-free and metallophthalocyanines with four pendant naphthoxy-substituents. Polyhedron. 2004; 23: 787–91.

12. Özçeşmeci M. Synthesis, photophysical and photochemical properties of metal-free and zinc (II) phthalocyanines bearing α-naphtholbenzein units. J. Organomet. Chem. 2014; 767: 16–21.

13. Özçeşmeci İ, Yerli Y, Okur Aİ, Gül A. Synthesis and EPR studies of a near infrared absorbing tetrakis(2-naphthoxy)vanadyl-phthalocyanine. Inorg. Chem. Commun. 2009; 12: 625–27.

14. Hanack M, Schmid G, Sommeraner M, Chromatographic separation of the four possible structural isomers of a tetrasubstituted phthalocyanine: tetrakis(2-ethylhexyloxy)phthalocyaninatonickel(II). Angew. Chem. Int. Ed. Engl. 1993; 32 (10): 1422–24.

15. Özçesmeci İ, Koca A, Gül A. Synthesis and electrochemical and in situ spectroelectrochemical characterization of manganese, vanadyl, and cobalt phthalocyanines with 2-naphthoxy substituents. Electrochim. Acta. 2011; 56: 5102–14.

16. Tauc J, Grigorovici R, Vancu A, Optical properties and electronic structure of amorphous germanium. Phys. Status Solidi. 1966; 15: 627-37.

# An Effective Method to Synthesize 2,3-Dihydroquinazolin-4(1H)-One Using Phosphate Fertilizers (MAP, DAP and TSP) as Green Heterogeneous Catalysts

**Youssef MERROUN, Soukaina CHEHAB, Touriya GHAILANE, Said BOUKHRIS, Rachida GHAILANE, Nouzha HABBADI, Amina HASSIKOU, Brahim LAKHRISSI and Abdelaziz SOUIZI***

Laboratory of Organic, Organometallic and Theoretical Chemistry, University of IbnTofail, Faculty of Science, B.P. 133, 14000 Kenitra, Morocco

**Abstract:** In this work, an efficient, easy, and green process has been developed for the synthesis of 2,3-dihydroquinazolin-4(1H)-one from a condensation reaction of anthranylamide with various aromatic aldehyde using of phosphate fertilizers, mono-ammonium phosphate (MAP), di-ammonium phosphate (DAP) and triple super phosphate (TSP) as heterogeneous catalysts. The reaction conditions were optimized taking into account of some parameters which control the reaction, namely the nature and the volume of the solvent and the mass of catalyst. The results show that the catalysts used herein are very interesting because they present a good catalytic activity and they are reusable for at least five cycles without any degradation of their activity.

**INTRODUCTION**

Heterocyclic chemistry forms an important branch of organic chemistry because it comprises at least half of all organic chemistry research worldwide. In particular, heterocyclic structures form the basis of many pharmaceutical, agrochemical, and veterinary products. There are numerous biologically active molecules whose framework includes a six-member ring containing two nitrogen atoms fused to a phenyl ring. Most of these molecules are based on the skeleton the dihydroquinazolin-4(1H)–one.

The dihydroquinazolin-4(1H)–one derivatives are an interesting class that exhibits a wide range of pharmacological and biological activity such as antitumor (1), diuretic (2), anti-inflammatory (3), antianxietic (4), antifibrillatory (5), anti-hypertensive (6), vasodilating agent (7), analgesic (8), antihistaminic (9), anticancer (10), anticonvulsant (11), and antileishmanial (12). There are several methods in the literature for the synthesis of dihydroquinazolin-4(1H)–one, among which condensation of anthranylamide with aldehyde or ketones and three-component condensation isatoic anhydride, aldehyde and amine with an assortment of catalysts such as p-toluenesulfonic acid (p-TsOH) (13), acetic acid (14), silica-bonded S-sulfonic acid (15), $SnCl_2$ (16), Amberlyst-15 (17), aluminum tris (dihydrogen phosphate) ($Al(H_2PO_4)_3$) (18), $Al/Al_2O_3$ nanoparticles (19), $LaCl_3/nanoSiO_2$ (20), $Fe_3O_4$-SA-PPCA (21), β-cyclodextrin-$SO_3H$ (22), nanocrystalline sulfated zirconia (23), PEG-400 (24)  and ionic liquid-water (25). These methods have some disadvantages such as hard reaction conditions, low yields, and long reaction times, they also require tedious processing procedures, as well as the application of strongly acidic catalysts, non-recyclable, toxic and expensive. In addition, they use the toxic solvents. Therefore, these processes lead to a great loss of energy, as well as they are harmful to the environment.

As a continuation of our efforts to develop green synthetic methods, this work presents an easy, efficient, and ecological procedure for 2,3-dihydroquinazolin-4(1H)–one reaction using fertilizer phosphate catalysts, mono-ammonium phosphate (MAP), di-ammonium phosphate (DAP) and triple super phosphate (TSP) (26-28)which are solid catalysts, cheap, easy to reuse, and environmentally friendly. In this study, the recyclability, solvent effect, the influence of the catalyst amount and reaction time effect on the 2,3-dihydroquinazolin-4 (1H)–one synthesis were studied. The novelty of this method appears in the fact that the catalysts MAP, DAP, and TSP are available, cheap and natural, and their use in the organic synthesis contribute to economize the cost and the energy and thus to develop green chemistry.

## MATERIALS AND METHODS

All of the chemicals and reagents used in this work were purchased from Sigma Aldrich. For all reactions, the purity of the derivatives 2,3-dihydroquinazolin-4 (1H)–one was monitored by thin layer chromatography (TLC) using aluminum layers coated with F254 silica gel (Merck) plates using ethyl acetate and hexane as eluent. The melting points were recorded on a hot Kofler and show a good agreement with previous works.

### General procedure for the synthesis of 2,3-dihydroquinazolin-4(1H)–one

1 mmol of anthranylamide and 1 mmol of aromatic aldehyde were dissolved in 1 mL of EtOH in the presence of the catalyst MAP, DAP or TSP (Scheme 1). The reaction mixture was heated at reflux. The reaction is monitored by thin-layer chromatography (TLC) using (n-hexane/EtOAc, v/v). After the reaction completion, the product was purified by recrystallization from ethanol and the solid catalyst is readily removed by simple filtration. The catalyst may be reactivated later by washing with ethanol to remove the products that may be present on its surface and then dried before being reused. The products obtained were characterized on the basis of comparison of their melting points and their spectroscopic data with those of literature (29-31).

2-(4-Chlorophenyl)-2,3-dihydroquinazolin-4(1H)-one **3a**: $^1$H NMR(300 MHz, DMSO-d$_6$, delta, ppm): 8.35 (1H, s, NHCO), 7.63 (1H, s), 7.54-7.45 (4H, m), 7.26 (1H, t, Ar-H), 7.15 (1H, s, NH), 6.76 (1H, d, Ar-H), 6.69 (1H, t, Ar-H), 5.79 (1H, s, CH). $^{13}$C NMR (75 MHz, DMSO-$d_6$): δ 163.98, 148.13, 141.13, 133.87, 133.46, 129.23, 128.78, 127.85, 117.76, 115.42, 114.94, 66.25.

2-(4-Nitrophenyl)-2,3-dihydroquinazolin-4(1H)-one **3b**: $^1$H NMR ((300 MHz, DMSO-d$_6$, delta, ppm): 8.53 (1H, s, NHCO), 8.25 (2H, d), 7.75 (2H, d), 7.26 (1H, d), 7.34 (1H, s, NH), 7.27 (1H, t), 6.78 (1H, d), 6.69 (1H, t, Ar-H), 5.93 (1H, s, CH). $^{13}$C NMR (75 MHz, DMSO-$d_6$): δ 163.76, 149.78, 147.89, 147.71, 134.04, 129.28, 128.05, 127.88, 124.57, 124.05, 117.94, 115.37, 115.02, 65.77.

2-(4-Methyphenyl)-2,3-dihydroquinazolin-4(1H)-one **3c**: $^1$H NMR (300 MHz, DMSO-d$_6$, delta, ppm): 8.23 (1H, s, NHCO), 7.61 (1H, d, Ar-H), 7.37 (2H, b, Ar-H), 7.27-7.18 (3H, m), 7.05 (1H, s, NH), 6.74 (1H, d, Ar-H), 6.67 (1H, t, Ar-H), 5.71 (1H, s, CH), 2.30 (3H, s, CH$_3$). $^{13}$C NMR (75 MHz, DMSO-$d_6$): δ 164.10, 148.38, 139.13, 138.87, 133.18, 133.72, 129.27, 127.80, 127.26, 117.53, 115.47, 114.87.25, 66.84, 21.19.

2-Phenyl-2,3-dihydroquinazolin-4(1H)-one **3d**: ^{1}H NMR(300 MHz, DMSO-d$_6$, delta, ppm): 8.30 (1H, s, NHCO), 7.64 (1H, d, Ar-H), 7.51 (2H, d), 7.40 (3H, m), 7.25 (1H, t, Ar-H), 7.12 (1H, s, NH), 6.76 (1H, d, Ar-H), 6.69 (1H, t, Ar-H), 5.77 (1H, s, CH). ^{13}C NMR (75 MHz, DMSO-*d$_6$*): δ 164.08, 148.35, 142.10, 133.79, 128.93, 128.80, 127.83, 127.34, 117.59, 115.43, 114.88, 67.05.

2-(4-Methoxyphenyl)-2,3-dihydroquinazolin-4(1H)-one **3e**: ^{1}H NMR(300 MHz, DMSO-d$_6$, delta, ppm): 8.21 (1H, s, NHCO), 7.63 (1H, d, Ar-H), 7.43 (2H, d, Ar-H), 7.22 (1H, t, Ar-H), 7.03 (1H, s, NH), 6.94 (2H, d, Ar-H), 6.76 (1H, d, Ar-H), 6.67 (1H, t, Ar-H), 5.73 (1H, s, CH), 3.75 (3H, s, OCH$_3$). ^{13}C NMR (75 MHz, DMSO-d$_6$): δ 164.23, 159.92, 148.51, 133.91, 133.71, 128.71, 127.84, 117.58, 115.48, 114.90, 114.10, 66.84, 55.63.

2-(2,3-Dimethoxyphenyl)-2,3-dihydroquinazolin-4(1H)-one **3f**: ^{1}H NMR(300 MHz, DMSO-d$_6$, delta, ppm): 8.05 (1H, s, NHCO), 7.65 (1H, d, Ar-H), 7.27-7.22 (1H, t, Ar-H), 7.11-7.03 (3H, m), 6.81 (1H, s, NH),6.78-6.67 (2H, m), 6.06 (1H, s, CH), 3.83 (3H, s, OCH$_3$), 3.81 (3H, s, OCH$_3$). ^{13}C NMR (75 MHz, DMSO-*d$_6$*): δ 164.24, 152.72, 148.47, 146.60, 134.94, 133.72, 127.80, 124.37, 119.56, 117.54, 115.20, 114.91, 113.47, 61.69, 61.19, 56.28.

## RESULTS AND DISCUSSION

To start up, the 2,3-dihydroquinazolin-4(1H)–one synthesis reaction has been chosen (Scheme 1) as a model in order to study the catalytic activity of heterogeneous catalysts MAP, DAP and TSP. The results obtained are summarized in Table 1.
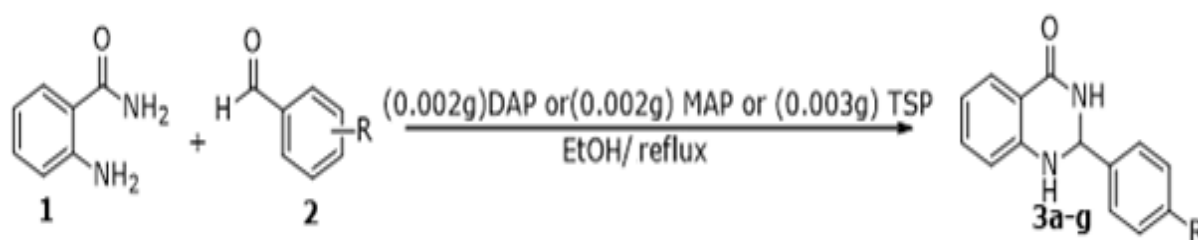


**Scheme 1.** Synthesis reaction of 2,3-dihydroquinazolin-4(1H)–one.

**Table 1.** Yields and reaction times obtained without catalyst and using MAP, DAP and TSP catalysts in case of the 2,3-dihydroquinazolin-4(1H)–ones synthesis [a].

| Entry | Catalyst | Time (min) | Yield (%) |
|-------|----------|------------|-----------|
| 1 | _ | 60 | trace |
| 2 | MAP | 30 | 83 |
| 3 | DAP | 40 | 80 |
| 4 | TSP | 40 | 86 |

[a] reaction conditions : anthranylamide (1 mmol), 4-chlorobenzaldehyde(1 mmol), EtOH(3 mL), 0.01 g of catalyst.

Table 1 shows that in absence of the catalysts, the product **3a** has been obtained as a trace within a reaction time of 60 min. When we added MAP, DAP and TSP as catalysts, the yields were 83, 80 and 86% respectively while the reaction times were shorter than the one obtained without a catalyst. Then, our work was concentrated on the improvement of the reaction yields by the determination the optimal conditions.

We consider at first the optimization of the reaction time of the synthesis of 2, 3-dihydroquinazolin-4(1H)–one, Figure 1 illustrated the reaction time concerning the conversion of 4-chlorobenzaldehyde to anthranylamide**.**
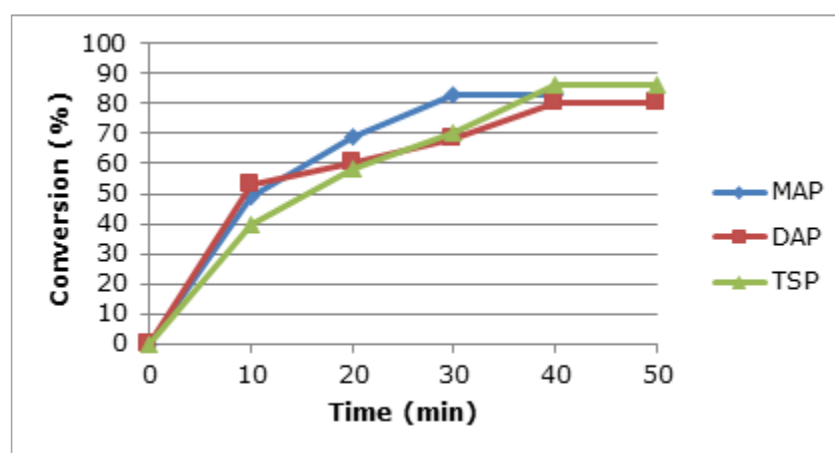


**Figure 1.** Reaction time optimization of 2,3-dihydroquinazolin-4(1H)–one synthesis.

From Figure 1, one can notice that the catalytic activity increases over time to reach a level representing the catalytic stability. The conversion rates obtained are respectively 83% for the catalyst MAP, 80% for the catalyst DAP and 86% for the TSP catalyst. Therefore, it can be concluded that the optimum reaction time is 30 min for the catalyst MAP and 40 min for catalysts DAP and TSP.

Then, the effect of certain porous polar solvents such as (EtOH, MeOH, BuOH), polar aprotic ($CH_3CN$, THF) and apolar aprotic (chloroform) was studied, the results are grouped in Table 2.

**Table 2.** Solvent effect on the synthesis of 2,3-dihydroquinazolin-4(1H)−one [a].

| Entry | Solvent | Time (min) | | | Yield (%)[b] | |
|:---:|:---:|:---:|:---:|:---:|:---:|:---:|
| | | MAP | DAP | TSP | MAP | DAP |
| 1 | EtOH | 30 | 40 | 40 | 83 | 80 |
| 2 | MeOH | 30 | 40 | 40 | 81 | 80 |
| 3 | n-Butanol | 30 | 40 | 40 | 78 | 76 |
| 4 | Acetonitrile | 30 | 40 | 40 | 70 | 74 |
| 5 | Chloroform | 30 | 40 | 40 | 67 | 70 |
| 6 | THF | 30 | 40 | 40 | 62 | 64 |

[a] Reaction conditions: anthranylamide (1 mmol), 4-chlorobenzaldehyde (1 mmol), solvent (3 mL), 0.01 g of catalyst.

[b]Isolated yields.

According to the obtained results, the reaction is carried out more easily in ethanol, due to its high dipole moment and high dielectric constant which allows the separation of the charges, thus facilitating the product **3a** formation with yields by 83, 80 and 86% for the three catalysts MAP, DAP, and TSP respectively.

The use of another solvent such as $CH_3CN$, chloroform, and THF gives the final product **3a** with lower yields than those obtained in ethanol, this can be probably explained by their dipole moment and constant dielectric which are lower than those of ethanol, it can be deduced, that the ethanol has been chosen as the solvent for the reaction of 2, 3-dihydroquinazolin-4(1H)−one.

Among the main parameters that control the cost of the reaction is the solvent volume used. For this reason, we envisage studying the influence of volume of the solvent on the reaction yield, this is carried out by varying the volume of the ethanol from 3 to 1 mL in case of the model reaction. The results are summarized in Table 3.

**Table 3.** Solvent volume effect on the 2,3-dihydroquinazolin-4(1H)-one synthesis [a].

| Entry | Volume | Time (min) | | | Yield (%)[b] | |
|:---:|:---:|:---:|:---:|:---:|:---:|:---:|
| | | MAP | DAP | TSP | MAP | DAP |
| 1 | 1 mL | 30 | 40 | 40 | 85 | 83 |
| 2 | 2 mL | 30 | 40 | 40 | 84 | 81 |
| 3 | 3 mL | 30 | 40 | 40 | 83 | 80 |

[a] Reaction conditions : anthranylamide (1 mmol), 4-chlorobenzaldehyde (1 mmol), EtOH (x mL), 0.01 g of catalyst.

[b]Isolated yields.

Table 3 shows that the best yield corresponds to 1 mL of ethanol, but when one increases the volume until 3 mL we observe a reduction of the yield of the reaction, this may be due to the deactivation of the interaction between the reactants and the catalyst by the formation of a layer on the surface of the catalyst. Thus, it can be concluded that the optimum volume for carrying out this reaction is 1 mL.

In the next step, it is fundamental to determine the optimum catalyst mass, thus we studied the influence of the amounts of catalysts MAP, DAP, and TSP on the yield on the reaction, the mass of catalyst has been varied from 0.001 to 0.01 g, the results are collected in Table 4.

**Table 4.** Catalyst amount optimization for the synthesis of 2,3-dihydroquinazolin-4(1H)-one synthesis[a].

| Entry | Amount of catalyst (g/mol %) | | | Time (min) | | | Yield %[b] | |
|:---:|:---:|:---:|:---:|:---:|:---:|:---:|:---:|:---:|
| | MAP | DAP | TSP | MAP | DAP | TSP | MAP | DAP |
| 1 | 0.001/0.8 | 0.001/0.7 | 0.001/0.4 | 30 | 40 | 40 | 92 | 89 |
| 2 | 0.002/1.7 | 0.002/1.5 | 0.002/0.8 | 30 | 40 | 40 | 96 | 94 |
| 3 | 0.003/2.6 | 0.003/2.3 | 0.003/1.2 | 30 | 40 | 40 | 96 | 93 |
| 4 | 0.004/3.3 | 0.004/3.1 | 0.004/1.7 | 30 | 40 | 40 | 95 | 90 |
| 5 | 0.005/3.5 | 0.005/3.8 | 0.005/2.2 | 30 | 40 | 40 | 92 | 89 |
| 6 | 0.006/5.2 | 0.006/4.6 | 0.006/2.6 | 30 | 40 | 40 | 91 | 87 |
| 7 | 0.007/6.1 | 0.007/5.3 | 0.007/2.9 | 30 | 40 | 40 | 88 | 85 |
| 8 | 0.008/6.9 | 0.008/6.1 | 0.008/3.4 | 30 | 40 | 40 | 87 | 84 |
| 9 | 0.009/7.8 | 0.009/6.8 | 0.009/3.9 | 30 | 40 | 40 | 86 | 82 |
| 10 | 0.01/8.5 | 0.01/7.6 | 0.01/4.3 | 30 | 40 | 40 | 85 | 83 |

[a]Reaction conditions: Anthranylamide(1 mmol), 4-chlorobenzaldehyde(1 mmol), EtOH(1 mL), x g of catalyst. [b]Isolated yields.

The results presented in Table 4 show that the optimum masses of MAP, DAP and TSP catalysts were respectively 0.002 g (1.7 mol %), 0.002 g (1.5 mol %) and 0.003 g (1.2 mol %). Beyond these masses, the yields of the reaction decrease, this is explained by the dispersion of the reagents on the surface of the catalysts.

After having optimized reaction conditions, namely the reaction time, the solvent nature as well as its volume and the mass of the catalyst. It is fundamental to examine the evolution turnover number (TON) and turnover frequency (TOF) in function of the catalysts mass used, for the pilot reaction. Table 5 present the calculated values.

**Table 5.** TON and TOF values for MAP, DAP and TSP catalysts used in the synthesis of 2,3-Dihydroquinazolin-4(1H)-One.

| Amount of catalyst (g ) | Time (h) | | | TON | | | TOF(h$^{-1}$) | |
|---|---|---|---|---|---|---|---|---|
| | MAP | DAP | TSP | MAP | DAP | TSP | MAP | DAP |
| 0.001 | 1/2 | 2/3 | 2/3 | 116.27 | 131.57 | 232.55 | 232.54 | 199.34 |
| 0.002 | 1/2 | 2/3 | 2/3 | **58.82** | **66.66** | 117.64 | **117.64** | **101.00** |
| 0.003 | 1/2 | 2/3 | 2/3 | 38.46 | 43.47 | **83.33** | 77.28 | 65.86 |
| 0.004 | 1/2 | 2/3 | 2/3 | 29.41 | 32.25 | 58 .82 | 58 .82 | 48.86 |
| 0.005 | 1/2 | 2/3 | 2/3 | 28.57 | 26.31 | 45.45 | 57.14 | 39.86 |
| 0.006 | 1/2 | 2/3 | 2/3 | 19.23 | 21.73 | 38.46 | 38.46 | 32.92 |
| 0.007 | 1/2 | 2/3 | 2/3 | 16.39 | 18.86 | 34.48 | 32.78 | 28.57 |
| 0.008 | 1/2 | 2/3 | 2/3 | 14.49 | 16.39 | 29.41 | 28.98 | 24.83 |
| 0.009 | 1/2 | 2/3 | 2/3 | 12.82 | 14.70 | 25.64 | 25.64 | 22.27 |
| 0.01 | 1/2 | 2/3 | 2/3 | 11.62 | 13.15 | 23.25 | 23.24 | 19.92 |

TON and TOF values in bold correspond to the amounts, 0.002 g for MAP and DAP and 0.003 g for TSP, that were used in this study.

The high values of TON and TOF were found for 0.001 g for the three catalysts. From the table above, it is clear that The TON and TOF increase when the mass of catalyst decrease. Their values are higher between 0.001 and 0.003 g of each catalyst. Such as it showed before and by considering the optimum reaction time, the best yields were obtained using 0.002 g for MAP and DAP and 0.003 g for TSP this led to the yield about 95% for the pilot reaction.

One of the most important characteristics of a catalyst is its activity which is linked to the evaluation of its stability and its capacity to be reused for several times without any loss of efficiency. The reusability of  MAP, DAP, and TSP catalysts has been studied under the optimum reaction conditions determined above, after completion of the reaction, the

catalyst was filtered and washed several times with ethanol and then dried, the results are presented in Figure 2.
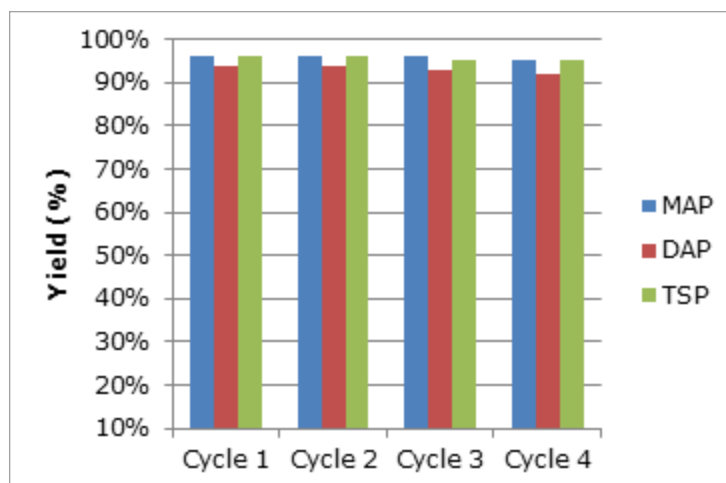


**Figure 2.** Recyclability of catalyst MAP, DAP and TSP.

According to Figure 2, it is observed that the yields remain unchanged as a function of the number of regeneration cycles; this suggests that there is no loss of catalytic activity, even after four times of reusability of the catalysts. Thus, one can deduce that the long term durability of these catalysts is excellent.

After optimizing the reaction conditions of 2, 3-dihydroquinazolin-4(1H)-one synthesis, this process was generalized for the derivatives of 2, 3-dihydroquinazolin-4(1H)-one synthesis, using various aromatic aldehydes substituted with anthranylamide (Scheme 1). The melting points were determined and showed a good agreement compared to those given in the literature, the results are presented in Table 6.

**Table 6.** Generalization to the synthesis of 2,3-dihydroquinazolin-4(1H)-one derivatives.

| Compound no | R | Yield (%) / Time (min) | | | Melting point (°C) |
|:---:|:---:|:---:|:---:|:---:|:---:|
| | | MAP | DAP | TSP | Found |
| **3a** | 4-Cl | 96/30 | 94/40 | 96/40 | 204-205 |
| **3b** | 4-NO$_2$ | 89/30 | 91/35 | 92/35 | 199-200 |
| **3c** | 4-CH$_3$ | 92/27 | 93/30 | 95/32 | 232–233 |
| **3d** | H | 93/20 | 90/28 | 94/25 | 219-220 |
| **3e** | 4-OCH$_3$ | 95/30 | 96/40 | 93/40 | 192−193 |
| **3f** | 2,3-OCH$_3$ | 85/35 | 81/40 | 79/40 | 220-221 |
| **3g** | 4-N(CH$_3$)$_2$ | 90/30 | 89/40 | 90/40 | 227-228 |

The results show that whatever the grouping of the aldehyde electron donor (Cl, OH, OCH$_3$, CH$_3$) or electron attractors (NO$_2$), the products are obtained with excellent yields in very short reaction times.

The proposed the catalytic mechanism for the condensation of an aromatic aldehyde and anthranylamide, using MAP catalyst, for the synthesis of 2,3-dihydroquinazolin-4 (1H)-one (Scheme 2).
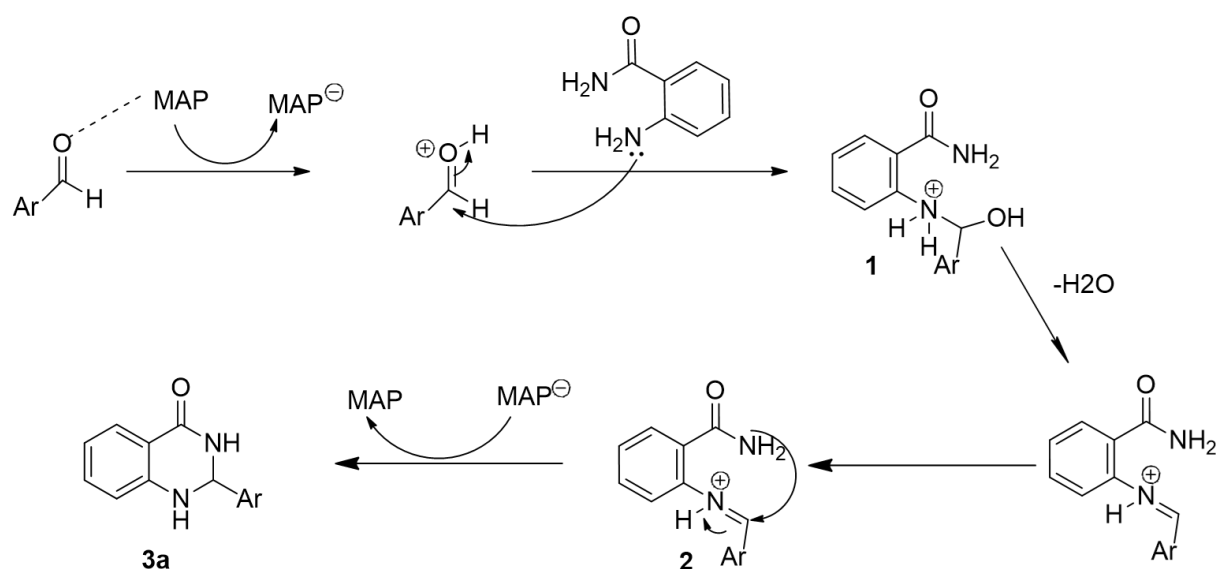
**Scheme 2.** A plausible mechanism for the formation of 2,3-dihydroquinazolin-4(1H)-one.

From this scheme, the probable mechanism for the synthesis of 2,3-dihydroquinazolin-4 (1H)-one, first the protonation of the carbonyl group with MAP take place, subsequently the amino group of anthranylamide makes a nucleophilic attack on the activated carbonyl group, since the amino is more reactive than the amide, which allows the formation of an imine intermediate 1, which then leads to the elimination of a molecule of water, followed by an intramolecular nucleophilic attack of the amide group on the imine carbon 2, finally deprotonation occurs for the formation of the desired product 3a, as shown in the Scheme 2.

For the DAP and TSP, the catalytic mechanisms must be similar to the one given in Scheme 2 since the three catalysts act with the reagent by a proton exchange as they are potential donors of the proton.

After determining the best-operating conditions for the synthesis of 2, 3-dihydroquinazolin-4(1H)–one, it would be interesting to compare the catalyst activities of MAP, DAP, and TSP used herein with those given in the literature. The results are summarized in Table 7.

**Table 7.** Efficiency comparison of various catalysts used in the condensation of anthranylamides and benzaldehyde condensation in various reaction conditions.

| Entry | Catalyst | Reaction conditions | Time | Yield (%) |
|-------|----------|---------------------|------|-----------|
| 1 | MAP | EtOH/reflux | 20 min | 93 |
| 2 | DAP | EtOH/reflux | 28 min | 90 |
| 3 | TSP | EtOH/reflux | 25 min | 94 |
| 4 | $Al^{3+}$-ExIC | EtOH/reflux | 6h | 95(34) |
| 5 | $Sc(OTf)_3$ | $CH_2Cl_2$/RT | 4 h | 94(35) |
| 6 | $ZnCl_2$ | EtOH/80°C | 3 h | 59 (36) |
| 7 | $LaCl_3$ | EtOH /80°C | 1,5 h | 79 (36) |
| 8 | PEG-400 | 100-110°C | 10 h | 85(24) |
| 9 | $[MIMC_4SO_3H][HSO_4]$ | 110°C | 1,5 | 69 (37) |
| 10 | CAN | $H_2O$/60°C | 2h | 92(38) |
| 11 | Trifluoroethanol | Reflux | 1,5h | 90(39) |
| 12 | Oxalic Acid | EtOH :$H_2O$ /80°C | 45min | 88(40) |

**For 11 and 12 entries, homogenous catalysts were used.**

From Table 7, one can deduce that the catalysts MAP, DAP and TSP possess an interesting catalytic activity and provide short times and excellent yields of the 2, 3-dihydroquinazolin-4(1H)–one synthesis compared to catalysts $Al^{3+}$-ExIC, $Sc(OTf)_3$, $ZnCl_2$, $LaCl_3$, PEG-400, $[MIMC_4SO_3H][HSO_4]$, trifluoroethanol and oxalic acid that give low yields and along reaction times.

**CONCLUSION**

To sum up, an environmentally friendly method, for the synthesis of derivatives 2,3-dihydroquinazolin-4(1H)–one by condensation of anthranylamide with aromatic aldehyde using phosphate fertilizers (MAP, DAP, and TSP) as heterogeneous catalysts, was developed. The operational conditions were optimized namely the nature and volume of solvent as well as the amount of catalyst. The products were obtained with excellent yields in short reaction times and the catalysts can be used for at least four times without any loss in its catalytic activity. These results are better than the ones given in previous works. Moreover, the catalysts are natural and cheap and their use is harmful to the environment.

Therefore, this method can be used for the synthesis of a wide series of heterocyclic compounds in the way to protect the environment against chemical pollution.

## REFERENCES

1. Birch HL, Buckley GM, Davies N, Dyke HJ, Frost EJ, Gilbert PJ, et al. Novel 7-methoxy-6-oxazol-5-yl-2,3-dihydro-1H-quinazolin-4-ones as IMPDH inhibitors. Bioorg Med Chem Lett. 2005;15(23):5335-9.

2. Cohen E, Klarberg B, Vaughan JR. QUINAZOLINONE SULFONAMIDES AS DIURETIC AGENTS. J Am Chem Soc. 1959;81(20):5508-9.

3. Yadav MR, Shirude ST, Parmar A, Balaraman R, Giridhar R. Synthesis and anti-inflammatory activity of 2,3-diaryl-4(3H)-quinazolinones. ChemHeterocyl Compd. 2006; 42(8):1038-1045.

4. Carlo M, Anna B, Isabella S, Maria S, Andrea R, Rosella F, et al. Synthesis and evaluation as NOP ligands of some spiro[piperidine-4,2'(1'H)-quinazolin]-4'(3'H)-ones 3 and spiro[piperidine-4,5'(6'H)-[1,2,4]triazolo[1,5-c]quinazolines]. Chem Pharm Bull (Tokyo). 2006;54(5):611-622.

5. Bonola G, Da Re P, Magistretti MJ, Massarani E, Setnikar I. 1-Aminoacyl-2,3-dihydro-4(1H)-quinazolinone derivatives with choleretic and antifibrillatory activity. J Med Chem.1968;11(6):1136-9.

6. Hess HJ, Cronin TH, Scriabine A. Antihypertensive 2-amino-4(3H)-quinazolinones. J Med Chem. 1968;11(1):130-6.

7. Levin JI, Chan PS, Bailey T, Katocs AS, Venkatesan AM. The synthesis of 2,3-dihydro-4(1H)-quinazolinone angiotensin II receptor antagonists. Bioorg Med Chem Lett. 1994;4(9):1141-6.

8. Okumura K, Oine T, Yamada Y, Hayashi G, Nakama M. 4-Oxo-1,2,3,4-tetrahydroquinazolines. I. Syntheses and pharmacological properties of 2-methyl-3-aryl-4-oxo-1,2,3,4-tetrahydroquinazolines and their 1-acyl derivatives. J Med Chem. 1968;11(2):348-52.

9. Alagarsamy V, Solomon VR, Murugan M. Synthesis and pharmacological investigation of novel 4-benzyl-1-substituted-4H-[1,2,4]triazolo[4,3-a]quinazolin-5-ones as new class of H1-antihistaminic agents. Bioorg Med Chem. 2007;15(12):4009-15.

10. Chinigo GM, Paige M, Grindrod S, Hamel E, Dakshanamurthy S, Chruszcz M, Minor W, Brown M. Asymmetric Synthesis of 2,3-Dihydro-2-arylquinazolin-4-ones: Methodology and Application to a Potent Fluorescent Tubulin Inhibitor with Anticancer Activity. J Med Chem. 2008;51(15):4620-31.

11. White DC, Greenwood TD, Downey AL, Bloomquist JR, Wolfe JF. Synthesis and anticonvulsant evaluation of some new 2-substituted-3-arylpyrido[2,3-d]pyrimidinones. Bioorg Med Chem. 2004;12(21):5711-7.

12. Sharma M, Chauhan K, Shivahare R, Vishwakarma P, Suthar MK, Sharma A, et al. Discovery of a New Class of Natural Product-Inspired Quinazolinone Hybrid as Potent Antileishmanial agents. J Med Chem. 2013;56(11):4374-92.

13. Baghbanzadeh M, Salehi P, Dabiri M, Kozehgary G. Water-Accelerated Synthesis of Novel Bis-2,3-dihydroquinazolin-4(1 H )-one Derivatives. Synthesis. 2006;(2):344-8.

14. Karimi-Jaberi Z, Arjmandi R. Acetic acid-promoted, efficient, one-pot synthesis of 2,3-dihydroquinazolin-4(1H)-ones. MonatshefteFürChem - Chem Mon. 2011;142(6):631-5.

15. Niknam K, Mohammadizadeh MR, Mirzaee S. Silica-bonded S-sulfonic Acid as a Recyclable Catalyst for Synthesis of 2,3-Dihydroquinazolin-4(1H)-ones. Chin J Chem. 2011;29(7):1417-22.

16. Yoo CL, Fettinger JC, Kurth MJ. Stannous Chloride in Alcohol: A One-Pot Conversion of 2-Nitro-N -arylbenzamides to 2,3-Dihydro-1 H -quinazoline-4-ones. J Org Chem. 2005;70(17):6941-3.

17. Surpur MP, Singh PR, Patil SB, Samant SD. Expeditious One-Pot and Solvent-Free Synthesis of Dihydroquinazolin-4(1H)-ones in the Presence of Microwaves. Synth Commun. 2007;37(12):1965-70.

18. Shaterian HR, Oveisi AR, Honarmand M. Synthesis of 2,3-Dihydroquinazoline-4(1 H )-ones. Synth Commun. 2010;40(8):1231-42.

19. Kassaee MZ, Rostamizadeh S, Shadjou N, Motamedi E, Esmaeelzadeh M. An efficient one-pot solvent-free synthesis of 2,3-dihydroquinazoline-4(1H)-ones via Al/Al2O3 nanoparticles. J Heterocycl Chem. 2010;47(6):1421-4.

20. Tarannum S, Ahmed N, Siddiqui ZN. LaCl3/nano-SiO2: A novel nanocatalyst for efficient synthesis of functionalized 2,3-dihydroquinazolinones. CatalCommun. 2015;66:60-6.

21. Ghorbani-Choghamarani A, Azadi G. Synthesis, characterization, and application of Fe 3 O 4 -SA-PPCA as a novel nanomagnetic reusable catalyst for the efficient synthesis of 2,3-dihydroquinazolin-4(1H)-ones and polyhydroquinolines. RSC Adv. 2015;5(13):9752-8.

22. Wu J, Du X, Ma J, Zhang Y, Shi Q, Luo L, Song B, Yang S, Hu D. Preparation of 2,3-dihydroquinazolin-4(1H)-one derivatives in aqueous media with β-cyclodextrin-SO3H as a recyclable catalyst. Green Chem. 2014;16(6):3210-3217.

23. Abdollahi-Alibeik M, Shabani E. Nanocrystalline sulfated zirconia as an efficient solid acid catalyst for the synthesis of 2,3-dihydroquinazolin-4(1H)-ones. J Iran Chem Soc. 2014;11(2):351-9.

24. Yerram P, Chowrasia R, Seeka S, Tangenda SJ. Polyethylene glycol (PEG-400) as a medium for novel and efficient synthesis of 2-phenyl-2,3-dihydroquinazolin-4(1H)-one derivatives. Eur J Chem. 2013;4(4):462-6.

25. Chen J, Su W, Wu H, Liu M, Jin C. Eco-friendly synthesis of 2,3-dihydroquinazolin-4(1H)-ones in ionic liquids or ionic liquid–water without additional catalyst. Green Chem. 2007;9(9):972.

26. Bahammou I, Esaady A, Boukhris S, Ghailane R, Habbadi N, Hassikou A, et al. Direct use of mineral fertilizers MAP, DAP, and TSP as heterogeneous catalysts in organic reactions. Mediterr J Chem. 2016;5(6):615.

27. Sibous S, Boukhris S, Ghailane R, Habbadi N, Hassikou A, Souizi A. easy synthesis of 3,4-dihydropyrimidin -2-(1h)-ones using phosphate fertilizers MAP, DAP and TSP as efficient catalysts. J Turk Chem. Soc Sect A Chem. 2017;4(2):477-488.

28. Sibous S, Ghailane T, Houda S, Ghailane R, Boukhris S, Souizi A. Green and efficient method for the synthesis of 1,5-benzodiazipines using phosphate fertilizers as catalysts under free solvent. Mediterr J Chem. 2017;6(3):53.

29. Wang M, Zhang TT, Song ZG. Eco-friendly synthesis of 2-substituted-2,3-dihydro-4(1H)-quinazolinones in water. Chin Chem Lett. 2011;22(4):427-30.

30. Shaterian HR, Oveisi AR. PPA-SiO 2 as a Heterogeneous Catalyst for Efficient Synthesis of 2-Substituted-1,2,3,4-tetrahydro-4-quinazolinones under Solvent-free Conditions. Chin J Chem. 2009;27(12):2418-22.

31. Benzekri Z, Serrar H, Boukhris S, Souizi A. FeCl3/Egg shell: An Effective Catalytic System for the Synthesis of 2,3-Dihydroquinazolin-4(1H)-ones at Room Temperature. J Turk Chem. Soc. Sect A Chem. 2017;4(3):775-786.

32. Chen J, Wu D, He F, Liu M, Wu H, Ding J, et al. Gallium(III) triflate-catalyzed one-pot selective synthesis of 2,3-dihydroquinazolin-4(1H)-ones and quinazolin-4(3H)-ones. Tetrahedron Lett. 2008;49(23):3814-8.

33. Rostami A, Tavakoli A. Sulfamic acid as a reusable and green catalyst for efficient and simple synthesis of 2-substituted-2,3-dihydroquinazolin-4(1H)-ones in water or methanol. Chin Chem Lett. 2011;22(11):1317-20.

34. Kancherla M, Badathala V. Aluminium exchanged Indian clay as an efficient reusable green catalyst for synthesis of 2, 3-dihydroquinazolin-4(1H)-one derivatives. J Porous Mater. 2017;24(5):1187-96.

35. Vasudhevan S, Joel Karunakaran R. Synthesis, Characterisation of 2,3-Dihydroquinazolinone Derivatives and their Antimicrobial Studies. Int J ChemTech Res. 2013;5(6):2844-53.

36. Shang Y-H, Fan L-Y, Li X-X, Liu M-X. Y(OTf)3-catalyzed heterocyclic formation via aerobic oxygenation: An approach to dihydroquinazolinones and quinazolinones. Chin Chem Lett. 2015;26(11):1355-8.

37. Yassaghi G, Davoodnia A, Allameh S, Zare-Bidaki A, Tavakoli-Hoseini N. Preparation, Characterization and First Application of Aerosil Silica Supported Acidic Ionic Liquid as a Reusable Heterogeneous Catalyst for the Synthesis of 2,3-Dihydroquinazolin-4(1H)-ones. Bull Korean Chem Soc. 2012;33(8):2724-30.

38. M W, J. J G, Z. G S, L W. Cerium(IV) ammonium nitrate catalyzed green synthesis of 2-substituted 2,3-dihydro- quinazolin-4(1H)-ones using a grinding technique. ChemHeterocycl Compd. 2011;47(7):851–855.

39. Qiao RZ, Xu BL, Wang YH. A facile synthesis of 2-substituted-2,3-dihydro-4(1H)-quinazolinones in 2,2,2-trifluoroethanol. Chin Chem Lett. 2007;18(6):656-8.

40. Karhale S, Survase D, Bhat R, Ubale P, Helavi V. A practical and green protocol for the synthesis of 2,3-dihydroquinazolin-4(1H)-ones using oxalic acid as organocatalyst. Res ChemIntermed. 2017;43(7):3915-24.

# Electrochemical xanthine biosensor based on zinc oxide nanoparticles–multiwalled carbon nanotubes–1,4-benzoquinone composite

## Berna Dalkıran[1], Ceren Kaçar[1], Pınar Esra Erden[1,2], Esma Kılıç[1]

[1]Ankara University, Faculty of Science, Department of Chemistry, Ankara, TURKEY
[2]Gazi University, Polatlı Faculty of Science and Arts, Department of Chemistry, Ankara, TURKEY

**Abstract:** Zinc oxide nanoparticles (ZnONPs), multiwalled carbon nanotubes (MWCNTs) and 1,4-benzoquinone (BQ) dispersed in chitosan (CS) matrix were used to construct a xanthine biosensor. Xanthine oxidase (XOx) was immobilized onto BQ-MWCNTs-ZnO–CS composite modified glassy carbon electrode (GCE) using glutaraldehyde as the crosslinking agent. The parameters of the construction process and the experimental variables for the biosensor were optimized. The xanthine biosensor showed optimum response within 10 s, and the sensitivity was 39.4 µA/mMcm$^2$ at +0.25 V (vs. Ag/AgCl). The linear working range of the biosensor was found to be $9.0\times10^{-7}$–$1.1\times10^{-4}$ M with a detection limit of $2.1\times10^{-7}$ M. The biosensor exhibited good long-term stability and reproducibility. The presented biosensor was also used for monitoring the freshnesses of chicken and beef flesh.

**Keywords:** Xanthine, biosensor, zinc oxide nanoparticles, carbon nanotubes, mediator.

**INTRODUCTION**

Xanthine concentration in biological fluids is used as an index for the diagnosis of various disorders such as xanthinuria, renal failure and gout. Moreover, xanthine attracted much attention as a marker for estimating the meat freshness in food industry (1). Therefore, direct, rapid, accurate and low cost measurement of xanthine in samples is of great interest in clinical analysis and food industry. Electrochemical enzyme electrodes that combine the sensitivity of electroanalytical methods with the bioselectivity of the enzyme are promising alternatives for sensitive, specific and rapid determination of xanthine (2).

Carbon nanotubes (CNTs) have been widely used in biosensor applications due to their unique properties such as high electrocatalytic effect, large surface area, mechanical strength, chemical stability, strong adsorption ability and biocompatibility (3, 4). Nowadays, the modification of CNTs with other nanomaterials such as metal or metal oxide nanoparticles (MONPs) is of great importance since the composite materials possess characteristics of the individual constituents and have favorable synergistic effects (5, 6).  It is well known that ZnO is a semiconductor with band gap of 3.37 eV and has some beneficial electronic and optical properties. ZnO nanoparticles also have potential in biosensing applications because of their unusual features including rapid electron transfer ability, chemical stability, biocompatibility, large surface area, high catalytic efficiency, non-toxicity, and strong adsorption ability (7, 8). ZnONPs and MWCNTs composite has already used in fabricating biosensors. Wang *et al*., reported the development of a lactate biosensor based on the synergistic action of MWCNTs and ZnONPs (9). Palanisamy *et al*., immobilized hemoglobin at MWCNTs/ZnO composite modified GCE to develop an amperometric biosensor for $H_2O_2$ determination (7). Haghighi and Bozorgzadeh decorated ZnONPs on MWCNTs to construct an electrochemiluminescence lactate biosensor (10). Ma and Tian fabricated a hemoglobin biosensor based on ZnO coated MWCNTs and nafion composite and studied the direct electron transfer and electrocatalysis of hemoglobin (11). Zhang *et al*., reported a ZnO/MWCNTs/CS nanocomposite based electrochemical DNA biosensor (12). Hu *et al*., constructed a glucose biosensor based on ZnO nanoparticle and MWCNTs modified GCE and investigated the direct electron transfer of glucose oxidase enzyme (13).

The catalytic oxidation of xanthine in the presence of XOx enzyme takes place according to the following equation:

$$Xanthine + O_2 \xrightarrow{\text{XOx}} Uric\ acid + H_2O_2$$

Electrooxidation of $H_2O_2$ generated by the enzymatic reaction is widely used for the amperometric determination of xanthine (14). High potentials used for the electrooxidation of $H_2O_2$ make the electrode sensitive to common interferences. The use of artificial electron transfer mediators including Prussian blue, colloidal gold, ferrocene and its derivatives, cobalt phthalocyanine and ferricyanide to

eliminate the influence of interferences is a common approach in xanthine enzyme electrodes (15, 16, 17, 18).

Herein, we report a novel biosensor based on MWCNTs, ZnONPs and BQ composite. Such composite is expected to give enhanced response characteristics towards xanthine due to the synergic action of its components. Moreover, the use of BQ is expected to provide an interference free biosensor by lowering the operating potential. To the best of our knowledge, no study has yet been published based on the MWCNTs, ZnONPs and BQ composite for the amperometric detection of xanthine.

## MATERIALS AND METHODS

### Reagents

XOx from Microbial source, ZnONPs (<100 nm particle size (TEM)), $K_3Fe(CN)_6$, $K_4Fe(CN)_6.3H_2O$, uric acid, sodium dihydrogen phosphate dihydrate, glutaraldehyde, disodium hydrogen phosphate dihydrate, Nafion, sodium benzoate, creatine, caffeine, theophylline and ascorbic acid were obtained from Sigma (St. Louis, MO, USA). Xanthine, BQ and glucose were purchased from Fluka (Buchs, Switzerland). MWCNTs (O.D. <8 nm; I.D. 2–5 nm; length 10–30 μm) were bought from Cheaptubes Inc. (Brattleboro, USA). CS (medium molecular weight) was obtained from Aldrich. Standard xanthine solution was prepared by dissolving xanthine in 0.10 M NaOH. All aqueous solutions were prepared using deionized water.

### Apparatus

Electrochemical studies were carried out in a three-electrode cell. Ag/AgCl electrode, platinum wire and GCE were employed as reference, counter and working electrodes, respectively. The electrochemical setup also involved a computerized IviumStat.h electrochemical analyzer (Ivium Technologies, Netherlands). Scanning electron microscopy (SEM) images were taken from Carl Zeiss AG, EVO® 50 Series. 0.1 M KCl aqueous solution containing 5.0 mM $K_3[(Fe(CN)_6]$, 5.0 mM $K_4[(Fe(CN)_6]$ (redox probe) was used for the cyclic voltammetry (CV) and electrochemical impedance spectroscopy (EIS) experiments. Cyclic voltammograms (CVs) were recorded between (−1.0)–(+1.0)V at a scan rate of 50 mV s$^{-1}$. EIS experiments were conducted with a frequency range of $10^6$–0.5 Hz under open circuit potential ($E_{OCP}$) conditions (0.2 V). Phosphate buffer solution (PBS; 0.05 M pH 7.5) was the supporting electrolyte for the amperometric measurements.

### Enzyme Electrode Preparation

In this study, modified and unmodified GCEs were used as working electrodes. GCE was polished according to the procedure reported elsewhere (19). 0.50 g CS was dissolved in 50.0 mL acetate buffer solution (pH 5.0) under magnetic stirring. 10 mg MWCNTs and 10 mg ZnONPs were ultrasonicated in 10.0 mL CS solution to achieve a final concentration of 1 mg mL$^{-1}$ MWCNTs and 1 mg mL$^{-1}$ ZnONPs. 10 mg BQ was added to MWCNTs-ZnO-CS mixture and ultrasonicated. 10 μL of the

BQ-MWCNTs-ZnO-CS mixture was cast onto the GCE surface and allowed to dry for 2 h at room temperature. 10 µL XOx solution (0.025 Units µL$^{-1}$) was drop-cast on BQ-MWCNTs-ZnO-CS/GCE surface and allowed to dry. XOx/BQ-MWCNTs-ZnO-CS/GCE was treated with glutaraldehyde vapor for 10 min to achieve the crosslinking of the enzymes. 7.5 µL Nafion solution (0.25%) was cast on the resulting electrode and dried. The fabrication procedure of the xanthine biosensor is shown in Scheme 1.
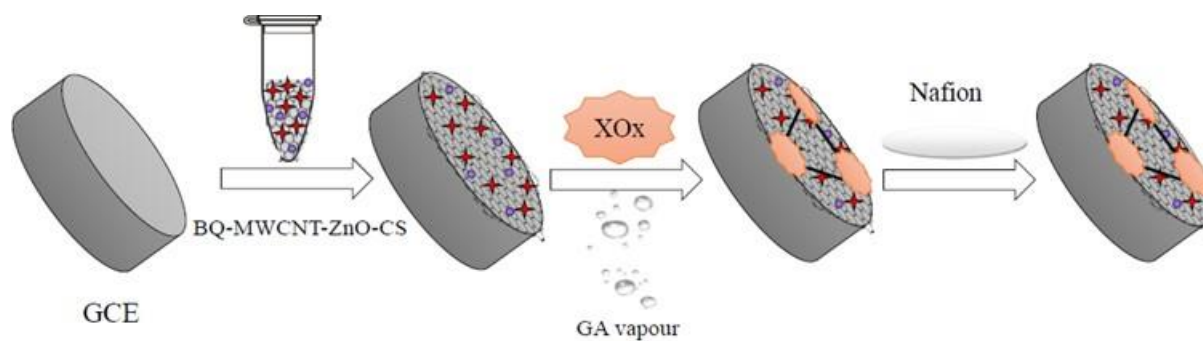


**Scheme 1.** The fabrication procedure for the XOx/BQ-MWCNTs-ZnO-CS/GCE.

MWCNTs ● ZnO ✦ BQ 🔶 XOx ⬭ CS — GA ⬭ Nafion

## RESULTS AND DISCUSSION

### Morphological studies

SEM images of (a) ZnO-CS/GCE, (b) BQ-CS/GCE, (c) MWCNTs-ZnO-CS/GCE, (d) BQ-MWCNTs-ZnO-CS/GCE and (e) XOx/BQ-MWCNTs-ZnO-CS/GCE are depicted in Figure 1. Images a and b show that ZnONPs or BQ are well dispersed in CS matrix. In image c structures corresponding to MWCNTs and ZnONPs can be seen. The porous structure of the resulting BQ-MWCNTs-ZnO composite (image d) is very suitable for enzyme immobilization. After XOx immobilization the porous structure of the BQ-MWCNTs-ZnO-CS composite changed to a more regular form (image e).
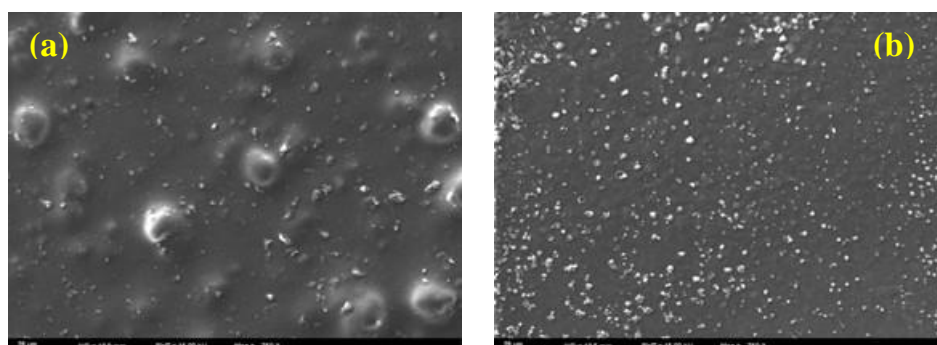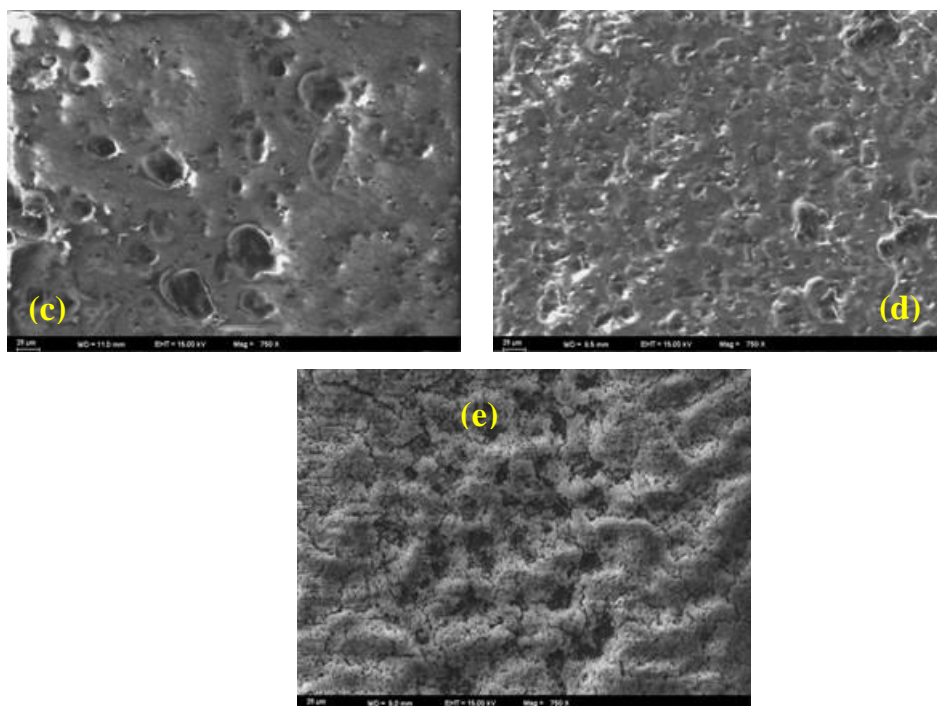
**Figure 1.** SEM images of (a) ZnO-CS/GCE, (b) BQ-CS/GCE, (c) ZnO-MWCNTs-CS/GCE, (d) BQ-MWCNTs-ZnO-CS/GCE, (e) XOx/BQ-MWCNTs-ZnO-CS/GCE (20 μm; EHT = 15.00 kV; Mag = 750×)

## Electrochemical studies

Electrochemical characteristics of the modified and unmodified electrodes were investigated by CV and EIS studies. Figure 2A shows the CVs recorded for BQ-MWCNTs-ZnO-CS/GCE (curve a) and XOx/BQ-MWCNTs-ZnO-CS/GCE (curve b) in $[Fe(CN)_6]^{3-/4-}$ redox probe. Oxidation and reduction peaks corresponding to the redox probe were obtained at BQ-MWCNTs-ZnO-CS composite modified GCE (curve a). After the XOx enzyme was introduced into the composite peak currents decreased dramatically indicating that the immobilized enzyme layer hindered the electron transfer (curve b) (20).
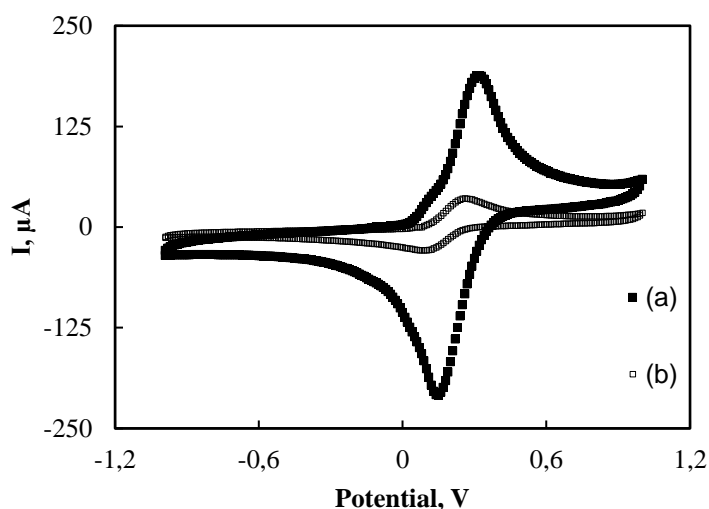


**Figure 2A.** CVs of (a) BQ-MWCNTs-ZnO-CS/GCE and (b) XOx/BQ-MWCNTs-ZnO-CS/GCE in 0.10 M KCl solution containing 5.0 mM $Fe(CN)_6^{3-/4-}$ at 50 mVs$^{-1}$.
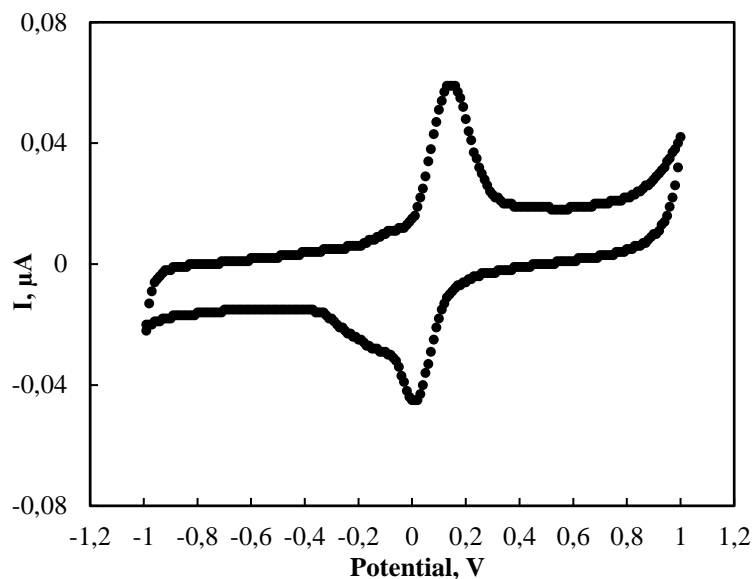
**Figure 2B.** CV of BQ-MWCNTs-ZnO-CS/GCE in 0.05 M PBS containing 0.1 M KCl at 50 mVs$^{-1}$.

The CV of BQ-MWCNTs-ZnO-CS/GCE recorded in 0.05 M PBS containing 0.1 M KCl (Figure 2B) exhibited one anodic peak ($Epa$= +0.18 V) at forward scan of the potential and one cathodic peak ($Epc$=+0.02 V) at backward scan of the potential. These peaks correspond to the oxidation and reduction peaks of BQ (21).

The Nyquist plot (Figure 3) shows EIS studies of unmodified GCE (curve a), BQ-MWCNTs-ZnO-CS/GCE (curve b) and XOx/BQ-MWCNTs-ZnO-CS/GCE (curve c). In Nyquist plot the diameter of the semicircle portion at higher frequencies corresponds to the charge transfer resistance ($R_{ct}$), which controls the electron transfer kinetics of the redox probe at the electrode interface (22). In our study the $R_{ct}$ of BQ-MWCNTs-ZnO-CS/GCE (55 Ω) was found to be lower than the $R_{ct}$ of the bare GCE (1250 Ω). This indicates a decreased resistance and improved electron transfer efficiency for the BQ-MWCNTs-ZnO-CS/GCE. After immobilization of XOx onto BQ-MWCNTs-ZnO-CS composite, the value of $R_{ct}$, increased to 480 Ω revealing that the immobilization of XOx cause hindrance to electron transfer due to the insulating property of the enzyme. The increase in $R_{ct}$ further confirms the successful immobilization of the enzymes onto the BQ-MWCNTs-ZnO-CS composite.
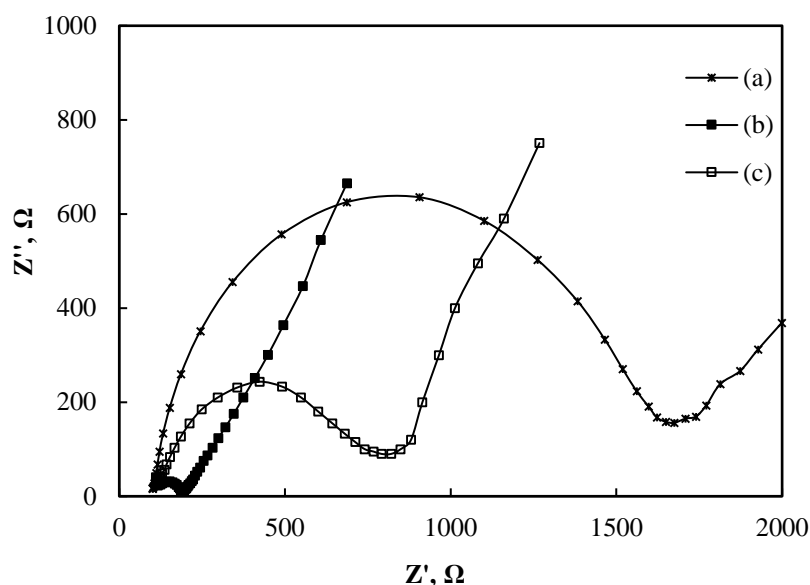
**Figure 3.** The Nyquist curves of in (a) unmodified GCE, (b) BQ-MWCNTs-ZnO-CS/GCE and (c) XOx/BQ-MWCNTs-ZnO-CS/GCE in 0.10 M KCl solution containing 5.0 mM $Fe(CN)_6^{3-/4-}$.

**Optimization studies**

Effects of MWCNTs, ZnONPs, BQ and enzyme amount were studied in order to optimize the composition of the biosensor. All optimization studies were conducted in 0.05 M PBS (pH 7.5) containing 0.05 mM xanthine and response currents of the biosensor were recorded. Effect of MWCNTs amount on biosensor response was investigated using different MWCNTs amounts as 0.5 mg $mL^{-1}$; 1.0 mg $mL^{-1}$; 1.5 mg $mL^{-1}$; 2.0 mg $mL^{-1}$ and 2.5 mg $mL^{-1}$. 10 µL of these solutions were used for electrode construction and the amperometric response of the electrodes were recorded. The highest current response was observed with the electrode prepared with 1.0 mg $mL^{-1}$ MWCNTs and this value was selected as the optimum MWCNTs amount. MWCNTs amounts higher than 1.0 mg $mL^{-1}$ did not increase the biosensor response.

Different ZnONPs amounts from 0.5 mg $mL^{-1}$ to 4.0 mg $mL^{-1}$ were used for biosensor construction to study the the effect of ZnONPs amount on biosensor response. The highest biosensor response was obtained with 1.0 mg $mL^{-1}$ ZnONPs and this value was used for all further experiments. BQ amount was varied between 0.5 mg $mL^{-1}$ and 3 mg $mL^{-1}$ to optimize the mediator amount. The response current of the biosensor increased with the mediator amount up to 1 mg $mL^{-1}$ and then decreased with increasing BQ amount. Therefore, 1.0 mg $mL^{-1}$ BQ was used for biosensor construction. The decrease in the response current of the biosensor at high MWCNTs, ZnONPs or BQ concentrations could be due to an increase in the diffusion barrier for the electroactive species toward electrode surface (6-19).

Various XOx amounts (0.06; 0.12; 0.25 and 0.50 U) were immobilized onto the BQ-MWCNTs-ZnO-CS/GCE to optimize the enzyme amount (Figure 4). It is clear from the figure that the response current increased from 0.06 to 0.25 U and then decreased. The highest response current was recorded with

0.25 U XOx and this value was selected as the optimum enzyme loading. The current decrease at higher enzyme loading (>0.25 U) may be attributed to the blocking of the electrode surface by the large amount of immobilized protein (23, 24).
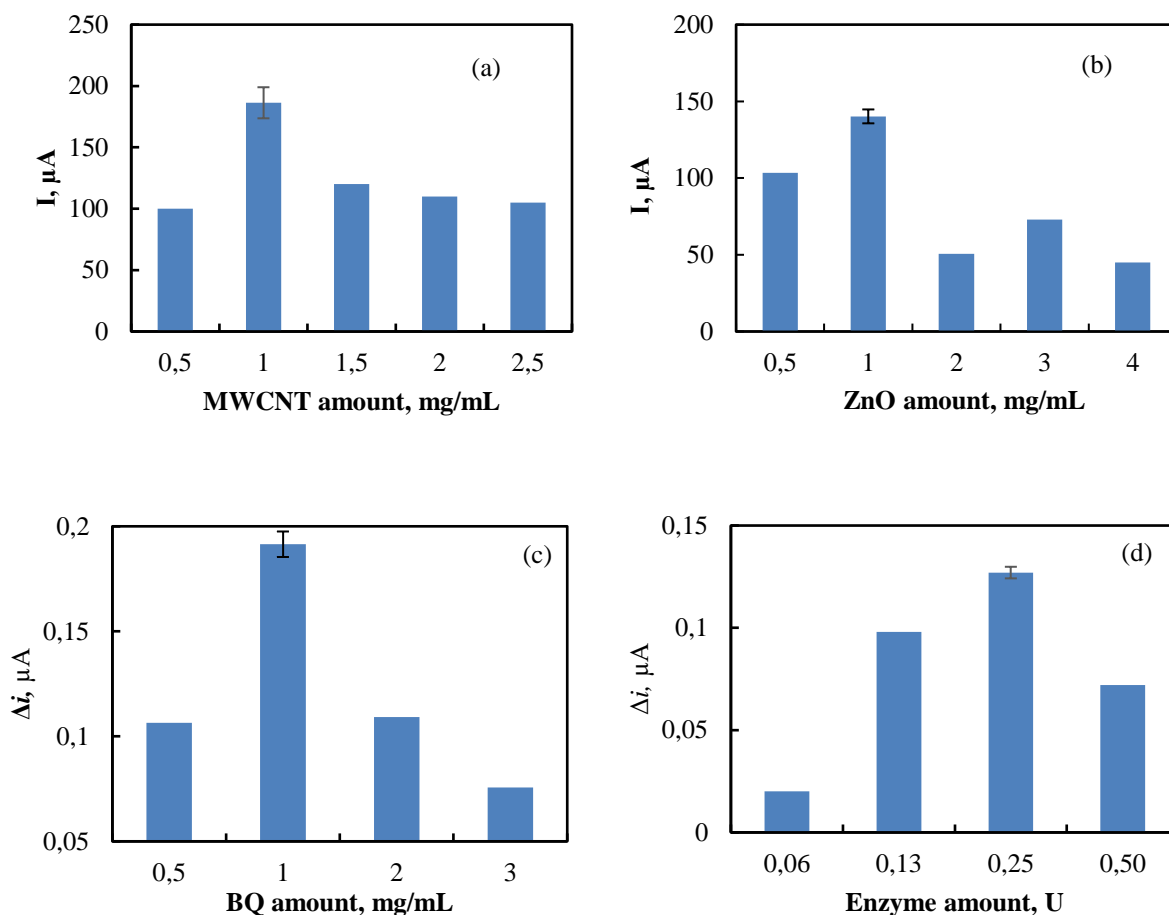


**Figure 4.** Effects of (a) MWCNTs, (b) ZnONPs, (c) BQ and (d) XOx amount on the response of the XOx/BQ-MWCNTs-ZnO-CS/GCE (in 0.05 M PBS at +0.25 V, error bars indicate the standard deviation of three measurements).

Operating potential is another critical parameter for biosensor response and selectivity. The amperometric response of the xanthine biosensor to 0.05 mM xanthine was measured at different operating potentials between (+0.10)–(+0.30) V. This potential range was selected due to the oxidation and reduction peaks of BQ (Figure 2B). The highest biosensor response was recorded at +0.25 V (data not shown). Therefore, all further measurements were performed at +0.25 V.

In this study, we have used BQ as the artificial electron transfer mediator in order to minimize the effects of common interfering substances normally present in real samples. The purposed response mechanism for the XOx/BQ-MWCNTs-ZnO-CS/GCE can be illustrated as follows:

$$\text{Xanthine} + \text{H}_2\text{O} \xrightarrow{\text{XOx}} \text{Uric acid}$$

$$XO_{x_{red}} + BQ \rightarrow XO_{x_{Ox}} + H_2BQ$$

$$H_2BQ \xrightarrow{\text{Electrode}(+0.25V)} BQ$$
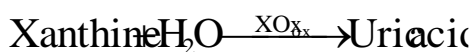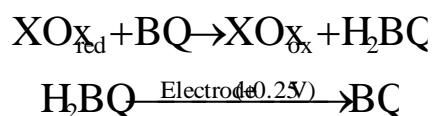
In the response mechanism of the presented biosensor BQ accepts electrons from the reduced XOx and H2BQ is produced. At an operating potential of +0.25 V H2BQ is reoxidized to form BQ on the surface of the electrode. The current is directly proportional to xanthine concentration.

The effect of pH on biosensor response was studied in the pH range of 6.0-8.5 in the presence of 0.05 mM xanthine. Figure 5 shows that the optimum response current was obtained at pH 7.5, and this pH was selected as the optimum pH. This value is compatible with the pH values reported for the previous xanthine biosensors (25-27).
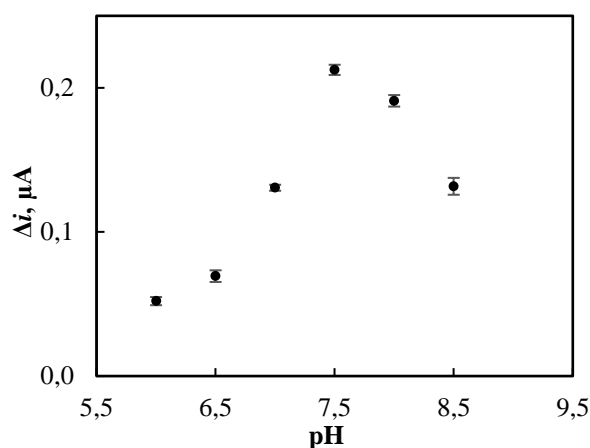


**Figure 5.** Effect of pH on the response of the XOx/BQ-MWCNTs-ZnO-CS/GCE (in 0.05 M PBS at +0.25 V, error bars indicate the standard deviation of three measurements)

**Analytical characteristics**

The amperometric response of the biosensor to successive injection of xanthine was studied. The biosensor showed a fast response to xanthine and achieved 95% of steady current within 10 s. The relationship between response current (µA) and xanthine concentration was linear from $9.0 \times 10^{-7}$ to $1.1 \times 10^{-4}$ M with the linear equation being $\Delta i = 2.80\ c + 0.02$ ($R^2 = 0.992$) (Figure 6). Detection limit of the xanthine biosensor was calculated according to the $3S_b/m$ criterion where $m$ is the slope of the calibration curve and $S_b$ was estimated as the standard deviation of 10 different amperometric signals recorded for the lowest xanthine concentration (0.9 µM) in the linear range and found as $2.1 \times 10^{-7}$ M (28). The sensitivity of the biosensor was found to be 39.4 µA/mMcm$^2$. This detection limit is much lower than the detection limits obtained in previously reported xanthine biosensors (17, 29, 30). Similar detection limits for xanthine biosensors were also reported in the literature (1, 31, 32).

$\Delta i = 2.80\, c + 0.02$
$R^2 = 0.9919$
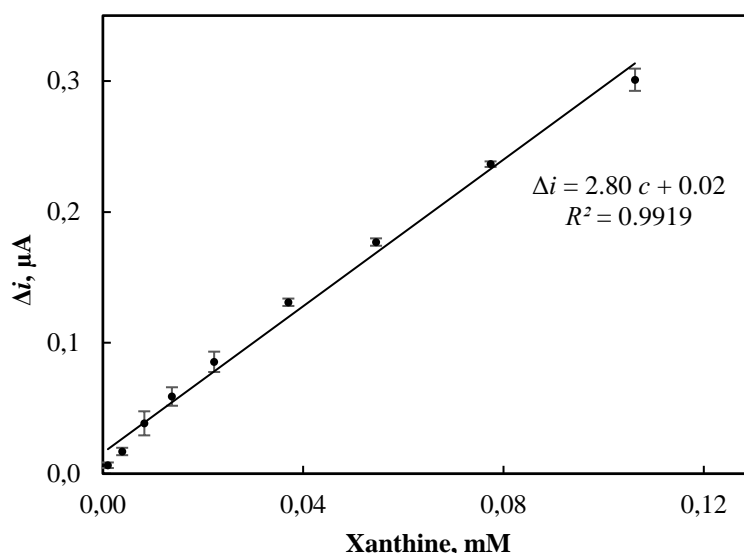
**Figure 6.** Calibration graph of XOx/BQ-MWCNTs-ZnO-CS/GCE after successive xanthine injections into a stirred solution of PBS (0.05 M; pH 7.5) at an operating potential of +0.25 V.

Successive calibration curves (n=5) were obtained by the use of the same electrode to determine the repeatability of the xanthine biosensor. The relative standard deviation (RSD) of the sensitivity values was 4.0% revealing the good repeatability of the XOx/BQ-MWCNTs-ZnO-CS/GCE. The long-term stability of the XOx/BQ-MWCNTs-ZnO-CS/GCE was studied by recording the current response at a xanthine concentration of 0.5 mM over a period of 25 days. The biosensor was stored at 4 °C between the measurements under a dry atmosphere. The XOx/BQ-MWCNTs-ZnO-CS/GCE maintained 95% of the initial current response even after about 25 days. This suggests that use of BQ-MWCNTs-ZnO-CS composite ensures good stability of the biosensor.

The selectivity study of the XOx/BQ-MWCNTs-ZnO-CS/GCE was performed by comparing the amperometric response before and after the injection of various interferents such as glucose, ascorbic acid, sodium benzoate, uric acid, and creatine along with xanthine in 0.05 M PBS. Amperometric responses were obtained by injection of 0.03 mM xanthine and 0.01 mM interfering species. The interference was determined as the percentage of the current signal obtained for detecting 0.03 mM xanthine, which was contributed by the addition of a particular interfering substance. The results showed that, sodium benzoate, glucose, creatine, caffeine, and theophylline practically have no interference in the analysis of xanthine. The interference caused by ascorbic acid and uric acid to 0.03 mM xanthine was about 2% and 10% respectively. The good selectivity of the presented biosensor towards xanthine detection may be attributed to the low operating potential of +0.25 V and presence of Nafion layer that can minimize the interference effect.

To evaluate the performance of the presented xanthine biosensor, a comparison of different parameters obtained by various biosensors for xanthine detection are given in Table 1. The results

presented in this table show that the different characteristics of the proposed biosensor are better in some cases or comparable with the other xanthine biosensors reported so far.

**Analysis of meat samples**

To evaluate the possible analytical application of the xanthine biosensor, the variation of xanthine content in meat samples with storage time was investigated.

For this purpose, chicken meat was chopped and homogenized. This homogenate was then portioned into five equal parts. One of these parts was then mechanically stirred for 45 min in 20 mL of deionized water for xanthine extration and then centrifuged at 4000 rpm for 10 min. This homogenate was filtered through a Whatman filter membrane. The filtrate was diluted to 25.0 mL with deionized water. The same sample preparation route was applied to the other meat sample (beef). To study the effect of storage time on freshness of meat, the other parts were stored at +4°C up to 9 days and the samples were analyzed for xanthine concentration every 2 days. The xanthine concentration in chicken and beef meat were measured by the purposed biosensor at different storage times ranging from 1 to 9 days using the standard addition method. Aliquots of standard xanthine solution was added to several portions of the chicken and beef meat extracts, to obtain a multiple addition calibration curve. Xanthine concentration in chicken and beef meat extracts calculated from the calibration curves were $0.36\pm0.01$ and $0.47\pm0.01$ mg L$^{-1}$ ($n=3$) on the first day, respectively. Figure 7 shows the results of the real sample analysis. It is clear from the figure that xanthine content increased with the storage time of meat samples. It was 5.4 times higher for the chicken sample and 1.6 times higher for the beef sample at day 9 than those at day 1. The increase in xanthine accumulation with storage time is an expected result (32). The experimental results indicated that the presented XOx/BQ-MWCNTs-ZnO-CS/GCE can be used for the monitoring of xanthine accumulation with storage time in meat samples.
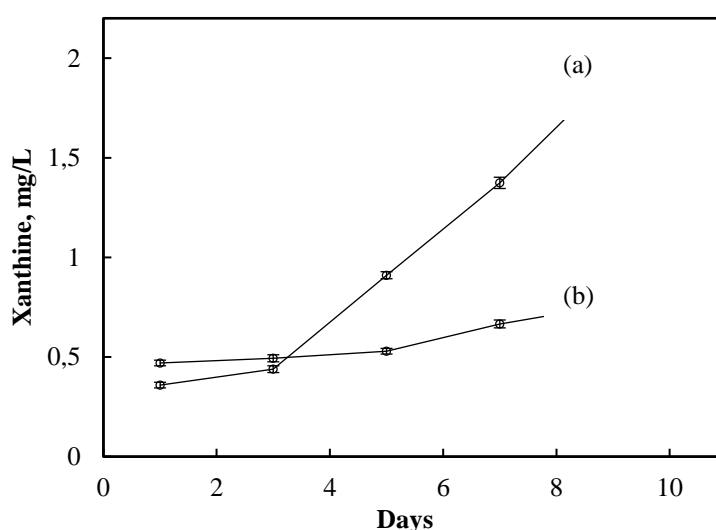


**Figure 7.** Variation of xanthine level in chicken (a) and beef (b) during storage at +4°C.

**Table 1.** Comparison of various amperometric xanthine biosensors reported in the last decade.

| Enzyme /Working potential | Electrode composition/Immobilization technique | Linearity/Detection limit | Resp. time | Interf. | Storage stability | Ref. |
|---|---|---|---|---|---|---|
| XOx/−0.4V vs. SCE | Silica sol-gel film/XOx/CNT/GCE | 0.2–10 µM/0.1 µM | 6 s | − | 5% loss after 90 days | [33] |
| XOx/0.05 V vs. Ag/AgCl | PB/SPTE/Cross-linking | $1\times10^{-7}-4.98\times10^{-6}$ M /0.10 µM | − | − | − | [18] |
| XOx/−0.05 V vs. Ag/AgCl | Graphite electrode modified with platinum and and palladium | 1.5–70 µM/$1.5\times10^{-6}$ M | 60 s | AA, UA (nr) | − | [27] |
| XOx/+0.4 V vs. Ag/AgCl | Au-NPs/PVF/Pt | $2.5\times10^{-6}-5.6\ 10^{-4}$ M/0.75 µM | − | AA (17.2%) | 18 days (40% loss) | [26] |
|  | Pt-NPs/PVF/Pt/Electro deposition | $2.0\times10^{-6}-6.6\ 10^{-4}$ M /0.60 µM |  | AA (20.5%) | 23 days (40% loss) |  |
| XOx/+0.5 V vs. Ag/AgCl | PVF-perchlorate matrix/Pt electrode/Electro deposition | $4.3\times10^{-7}-2.84\times10^{-3}$ M/0.13 µM | 15 s | AA, UA (nr) | 25 days (42% loss) | [34] |
| XOx/+0.05 V vs. Ag/AgCl | Phenazine methosulfate as mediator/ Edge-plane pyrolytic graphite/ Adsorpsion | $1.0\times10^{-5}-1.8\times10^{-3}$ M/0.25 nM | − | AA, UA (nr) | 4 weeks (22% loss) | [35] |
| XOx/+0.25 V vs. Ag/AgCl | 1,4-benzoquinone/CPE | $1.9\times10^{-7}-5.5\times10^{-6}$ M and $5.2\times10^{-5}-8.2\times10^{-4}$ M/0.1 µM $1.9\times10^{-7}-2.1\times10^{-6}$ M; | 100 s | AA (18.2%), UA (3.6%) | 14 days | [25] |
| XOx/+0.30 V vs. Ag/AgCl | PVF/CPE/Cross-linking | $1.9\times10^{-6}-1.0\times10^{-5}$ M and $5.2\times10^{-5}-8.2\times10^{-4}$ M/0.1 µM | 50 s | AA(18.4%), UA (2.5%) | 7 days |  |
| XOx/+0.50 V vs. Ag/AgCl | CS/Fe-NPs@Au/PGE/Electro deposition | $1\times10^{-7}-3\times10^{-4}$ M/0.1 µM | 3s | AA (10%), UA (nr) | 100 days (25% loss) | [1] |
| XOx/+0.50V vs. Ag/AgCl | Gold coated Fe-NPs/CS/Covalent immobilization | 1–300 µM/0.1 µM | 3s | AA (nr) | 25% loss after 100 days | [36] |
| XOx/+0.35 V vs. Ag/AgCl | Poly(glycidyl methacrylate-co-vinylferrocene)/MWCNT/PGE/Covalent immobilization | $2\times10^{-6}-2.8\times10^{-5}$ M; $2.8\times10^{-5}-4.6\times10^{-5}$; $4.6\times10^{-5}-8.6\times10^{-5}$/0.12 µM | 4 s | AA, UA (nr) | 25 days (30% loss) | [28] |
| XOx/+0.25 V vs. Ag/AgCl | XOx/BQ-MWCNTs-ZnO-CS/GCE/Cross-linking | $9.0\times10^{-7}-1.1\times10^{-4}$ M/$2.1\times10^{-7}$ M | 10 s | AA (2%), UA (10%) | 25 days (5% loss) | This work |

*SPTE : screen-printed three-electrode; PVF : polyvinylidene fluoride; CPE: carbon paste electrode; PGE : pencil graphite electrode; nr:no response

**CONCLUSION**

A new biosensor for xanthine analysis was developed based on the BQ-MWCNTs-ZnO-CS composite modified GCE. The purposed biosensor exhibited a low response time (10 s), satisfactory repeatability (4.0%), good sensitivity (39.4 µA/mMcm$^2$), wide linear range ($9.0 \times 10^{-7} - 1.1 \times 10^{-4}$ M), and low detection limit ($2.1 \times 10^{-7}$ M). Moreover, the biosensor showed good selectivity due to the low operating potential. In conclusion, the presented biosensor can be utilized to detect the xanthine content in chicken and beef samples for the evaluation of meat freshness.

**ACKNOWLEDGMENTS**

**REFERENCES**

1. Devi R, Batra B, Lata S, Yadav S, Pundir, CS. A method for determinationof xanthine in meat by amperometric biosensor based on silver nanoparticles/cysteine modified Au electrode. Process Biochem. 2013; 48(2): 242–9.

2. Ronkainen NJ, Halsall HB, Heineman WR. Electrochemical biosensors. Chem. Soc. Rev. 2010; 39(5): 1747-63.

3. Anik Ü, Çubukçu M. Examination of the electroanalytic performance of carbon nanotube (CNT) modified carbon paste electrodes as xanthine biosensor transducers. Turk. J. Chem. 2008; 32: 711-9.

4. Jacobs CB, Peairs MJ, Venton, BJ. Review: Carbon nanotube based electrochemical sensors for biomolecules. Anal. Chim. Acta 2010; 662(2): 105-27.

5. Lin J, He C, Zhang L, Zhang S. Sensitive amperometric immunosensor for a-fetoprotein based on carbon nanotube/gold nanoparticle doped chitosan film. Anal. Biochem. 2009; 384: 130–5.

6. Kaçar C, Dalkiran B, Erden PE, Kiliç E. An amperometric hydrogen peroxide biosensor based on Co3O4 nanoparticles and multiwalled carbon nanotube modified glassy carbon electrode. Appl. Surf. Sci. 2014; 311: 139-46.

7. Palanisamy S, Cheemalapati S, Chen SM. Highly sensitive and selective hydrogen peroxide biosensor based on hemoglobin immobilized at multiwalled carbon nanotubes–zinc oxide composite electrode. Anal. Biochem. 2012; 429(2): 108-15.

8. Kavitha T, Gopalan AI, Lee KP, Park SY. Glucose sensing, photocatalytic and antibacterial properties of graphene–ZnO nanoparticle hybrids. Carbon 2012; 50(8): 2994-3000.

9. Wang YT, Yu L, Wang J, Lou L, Du WJ, Zhu ZQ, Peng H, Zhu JZ.  A novel L-lactate sensor based on enzyme electrode modified with ZnO nanoparticles and multiwall carbon nanotubes. J. Electroanal. Chem. 2011; 661: 8-12.

10. Haghighi B, Bozorgzadeh S. Fabrication of a highly sensitive electrochemiluminescence lactate biosensor using ZnO nanoparticles decorated multiwalled carbon nanotubes. Talanta 2011; 85(4): 2189-93.

11. Ma W, Tian D. Direct electron transfer and electrocatalysis of hemoglobin in ZnO coated multiwalled carbon nanotubes and Nafion composite matrix. Bioelectrochem. 2010; 78(2): 106-12.

12. Zhang W, Yang T, Huang D, Jiao K, Li G. Synergistic effects of nano-ZnO/multi-walled carbon nanotubes/chitosan nanocomposite membrane for the sensitive detection of sequence-specific of PAT gene and PCR amplification of NOS gene. J.  Membr. Sci. 2008; 325(1): 245-51.

13. Hu F, Chen S, Wang C, Yuan R, Chai Y, Xiang Y, Wang C. ZnO nanoparticle and multiwalled carbon nanotubes for glucose oxidase direct electron transfer and electrocatalytic activity investigation. J. Mol. Catal. B: Enzym. 2011; 72(3): 298-304.

14. Liu Y, Nie L, Tao W, Yao S. Full Paper Amperometric study of au-colloid function on xanthine biosensor based on xanthine oxidase immobilized in polypyrrole layer. Electroanal. 2004; 16: 1271–8.

15. Zhao J, O'daly JP, Henkens RW, Stonehuerner J, Crumbliss AL. A xanthine oxidase/colloidal gold enzyme electrode for amperometric biosensor applications. Biosens. Bioelectron. 1996; 11(5): 493-502.

16. Kilinc E, Erdem A, Gokgunnec L, Dalbasti T, Karaoglan M, Ozsoz M. Buttermilk based cobalt phthalocyanine dispersed ferricyanide mediated amperometric biosensor for the determination of xanthine. Electroanal. 1998; 10(4): 273-5.

17. Arslan F, Yaşar A, Kılıç E. An amperometric biosensor for xanthine determination prepared from xanthine oxidase immobilized in polypyrrole film. Artif. cells blood substit. biotechnol. 2006; 34(1): 113-28.

18. Teng Y, Chen C, Zhou C, Zhao H, Lan M. Disposable amperometric biosensors based on xanthine oxidase immobilized in the Prussian blue modified screen-printed three-electrode system. Sci. China Chem. 2010; 53(12): 2581-6.

19. Dalkiran B, Kacar C, Erden PE, Kilic E. Amperometric xanthine biosensors based on chitosan-Co 3 O 4-multiwall carbon nanotube modified glassy carbon electrode. Sens. Actuators B Chem. 2014; 200: 83-91.

20. Zhang S, Wang N, Niu Y, Sun C. Immobilization of glucose oxidase on gold nanoparticles modified Au electrode for the construction of biosensor. Sens. Actuators B Chem. 2005; 109: 367–74

21. Jakobs RCM, Janssen LJJ, Barendrecht E. Hydroquinone oxidation and p-benzoquinone reduction at polypyrrole and poly-N-methylpyrrole electrodes. Electrochim. Acta, 1985; 30(10): 1313-21.

22. Pajkossy T, Jurczakowski R. Electrochemical impedance spectroscopy in interfacial studies. Curr. Opin. in Electrochem. 2010; 1: 53-8.

23. Mulchandani, A., Pan, A.S. and Wilfred, C. 1999. Fiber–Optic Enzyme Biosensor for Direct Determination of Organophosphate Nerve Agents. Biotechnol. Prog., 15, 130–4.

24. Kanyong, P., Pemberton, R.M., Jackson, S.K. and Hart, J.P. 2013. Development of an amperometric screen–printed galactose biosensor for serum analysis. Analytical Biochemistry 435, 114–9.

25. Shan D, Wang Y, Xue H. Cosnier S. Sensitive and selective xanthine amperometric sensors based on calcium carbonate nanoparticles. Sens. Actuators B Chem. 2009; 136: 510–5.

26. Jain U, Narang J, Rani K, Chauhan N. Synthesis of cadmium oxide and carbon nanotube based nanocomposites and their use as a sensing interface for xanthine detection. RSC Adv.2015; 5: 29675-83.

27. Erden P, Pekyardımcı Ş, Kılıç E. Amperometric enzyme electrodes for xanthine determination with different mediators. Acta Chim. Slov., 2012; 59(4): 824-32.

28. Borisova B, Ramos, J, Díez, P, Sánchez, A, Parrado, C, Araque, E, Villalonga, R, Pingarrón, J.M. A Layer-by-Layer Biosensing Architecture Based on Polyamidoamine Dendrimer and Carboxymethylcellulose-Modified Graphene Oxide. Electroanalysis 2015; 27: 2131–8.

29. Baş SZ, Gulce H, Yıldız S, Gulce A. Amperometric biosensors based on deposition of gold and platinum nanoparticles on polyvinylferrocene modified electrode for xanthine detection. Talanta 2011; 87: 189–96.

30. Dodevska T, Horozova E, Dimcheva N. Design of an amperometric xanthine biosensor based on a graphite transducer patterned with noble metal microparticles. Cent. Euro. J. Chem. 2010; 8: 19–27.

31. Dervisevic M, Custiuc E, Çeviki E, Şenel M. Construction of novel xanthine biosensor by using polymeric mediator/MWCNT nanocomposite layer for fish freshness detection. Food Chem. 2015; 181: 277-83.

32. Devi R, Yadav S, Pundir CS. Au-colloids–polypyrrole nanocomposite film based xanthine biosensor. Colloids Surf. A Physicochem. Eng. Asp. 2012; 394: 38-45.

33. Gao Y, Shen C, Di J, Tu Y. Fabrication of amperometric xanthine biosensors based on direct chemistry of xanthine oxidase, Mater. Sci. Eng. C 2009; 29: 2213–6.

34. Bas S.Z, Gulce H, Yıldız S. Amperometric xanthine biosensors based on electrodeposition of platinum on polyvinylferrocenium coated Pt electrode, J. Mol. Catal. B: Enzym 2011; 72: 282–8.

35. Kalimuthu P, Leimkuhler S, Bernhardt P.V. Low-potential amperometric enzyme biosensor for xanthine and hypoxanthine, Anal. Chem. 2012; 84: 10359–65.

36. Devi R, Yadav S, Nehra R, Yadav S, Pundir C.S. Electrochemical biosensor based on gold coated iron nanoparticles/chitosan composite bound xanthine oxidase for detection of xanthine in fish meat, J. Food Eng. 2013; 115: 207–14.